Engineering Structures 358 (2026) 122448



Contents lists available at ScienceDirect

Engineering Structures

journal homepage: www.elsevier.com/locate/engstruct

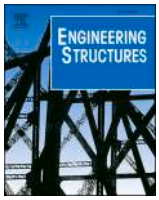



Full-scale shake table tests on hybrid CFS–EPS lightweight structures: Experimental program and global seismic response

George Taranu [1]

"Gheorghe Asachi" Technical University of Iasi, Faculty of Civil Engineering and Building Services, Department of Structural Mechanics, no. 1, D. Mangeron street, Iasi 700050, Romania

ARTICLE INFO

Keywords:
Hybrid CFS–EPS panels
ThermaSteel system
Full-scale shake-table tests
Lightweight modular structures

ABSTRACT

This paper investigates the seismic performance of single-storey hybrid cold-formed steel–expanded polystyrene (CFS–EPS) ThermaSteel modules through full-scale shake-table testing. Two rectangular units, THS 24–388 and THS 24–389, were assembled from prefabricated CFS–EPS panels with different steel sheet thicknesses, EPS densities, and wall layouts. The specimens were tested on the ANCO R250–3123 shake table using recorded motions (1977 Vrancea, 2023 Türkiye) and spectrum-compatible artificial accelerograms scaled to the Romanian seismic code P100–1/2013 elastic spectrum (ag = 0.40 g; corner periods representative of stiff and soft soil). THS 24–388 was subjected mainly to shorter-duration inputs, whereas THS 24–389 was tested with longer-duration and higher-intensity motions to increase cumulative demand. Impulse-based identification consistently revealed two dominant low-order in-plane components, with periods in the ranges 0.12–0.14 s and 0.20–0.22 s, and equivalent viscous damping ratios of about 2–3% of critical, with modest stiffness degradation over the campaigns. Peak interstorey drifts remained below P100–1/2013 serviceability limits for THS 24–388 and below ultimate drift limits for THS 24–389, including runs at or slightly above the design-level table acceleration. No significant damage was observed in THS 24–388, while THS 24–389 developed localized base-track distortion and fastener bearing at panel joints without global instability or fastener pull-out. The results show that properly detailed hybrid CFS–EPS modules can satisfy drift and stability objectives under design-level and selected above-design-level shaking, and they highlight the role of wall layout, seismic panel placement, and anchorage detailing in moderate-to-high seismic regions.

1. Introduction

Lightweight prefabricated structures have become a key direction in modern construction because of their reduced mass, rapid assembly, and improved energy efficiency. Among these systems, cold-formed steel (CFS) structures provide a robust and modular framework for low- and mid-rise buildings, combining low self-weight with favourable strength-to-stiffness ratios and ease of industrialized production [1,2]. When properly detailed according to contemporary design standards, thin-walled CFS members can offer reliable global stability and ductile behavior under horizontal actions.

Expanded polystyrene (EPS) is another material widely adopted in building envelopes due to its excellent thermal insulation, low density, and ease of shaping into modular panels [3]. Numerous hybrid configurations have been investigated, including EPS–concrete sandwich panels [4], EPS combined with cementitious or mineral-matrix layers, and EPS–OSB or EPS–steel sheet panels used mainly as enclosure and insulation systems [5,6]. In most of these systems, the EPS core acts primarily as insulating or filling material, while concrete, mortar or sheathing skins provide the structural resistance and control stiffness and ductility under seismic loading. Classical structural insulated panels (SIP) with OSB or steel sheathing also belong to this category, where the load path is governed by the stiff skins and the foam core is essentially non-structural.

Within this broader context, CFS systems have evolved into a mature structural solution for low-rise residential and modular buildings. Their advantages—reduced self-weight, prefabrication potential and favourable strength-to-stiffness ratios—are well documented in design standards and research studies [2,7,8]. A large body of work has shown that the global seismic behaviour of CFS walls and buildings is typically connection-dominated, and that stiffness degradation, pinching, and hysteretic dissipation depend on the detailing of sheathing, fasteners,

E-mail address: george.taranu@academic.tuiasi.ro.
[1] orcid id: 0000–0002-5662–8484

https://doi.org/10.1016/j.engstruct.2026.122448
Received 23 November 2025; Received in revised form 7 February 2026; Accepted 24 February 2026
Available online 23 March 2026
0141-0296/© 2026 The Author(s). Published by Elsevier Ltd. This is an open access article under the CC BY license (http://creativecommons.org/licenses/by/4.0/).

tracks, and anchorage. Italian research teams led by Landolfo and Fiorino developed extensive experimental programmes that were important for the seismic calibration of CFS systems: the seminal work in [9] defined ductility and stiffness degradation of typical screw connections under cyclic loading, while [10] proposed one of the earliest performance-based procedures for the seismic design of light-steel walls. Subsequent developments in [11,12] supported the forthcoming second-generation Eurocodes for lightweight steel shear walls. Full-scale dynamic campaigns further validated these approaches, including stable hysteretic response and overstrength with ductile detailing and system-level performance under quasi-static and dynamic loading [13–18]. These studies provide a reference background for interpreting system-level indicators such as period shift, drift demand, acceleration amplification, and hysteresis in lightweight steel structures. The contribution of diagonal bracing to lateral stiffness was quantified in [19]. More recent investigations extended the focus toward hybrid and modular configurations: [20,21] confirmed the reliability of thin-walled shear walls under multiaxial seismic actions, [22] demonstrated the feasibility of prefabricated hybrid frame–wall modules, and [5,26] highlighted the potential of thin-walled systems for energy-efficient building envelopes.

EPS-based hybrid panel systems form another important family of lightweight solutions. EPS–concrete sandwich panels, in which the foam core acts as insulation between reinforced-concrete layers, have shown moderate stiffness retention and satisfactory energy dissipation under seismic loading [4]. Cementitious EPS boards evaluated in [23] demonstrated that, when EPS is confined within a mineral matrix, the hybrid system can sustain shake-table excitations without significant degradation. Hybrid panels combining EPS with glass-fibre-reinforced mineral matrices, investigated in [24] and dynamically tested in [25] exhibited stable hysteretic response and limited cracking under cyclic actions. Despite these promising results, EPS has been used almost exclusively as a non-structural or insulating component. To the best of the author's knowledge, no published full-scale shake-table programme has examined EPS–CFS wall modules where the panelized system acts as the primary lateral-load-resisting system and where system-level response metrics (drift, period/stiffness evolution, acceleration amplification, hysteresis, and damage progression) are reported for seismic excitation.

Hybridization strategies that combine cold-formed and hot-rolled steel members have shown potential for improving lateral resistance and energy dissipation. Experimental investigations reported in [26] demonstrated that mixed systems can enhance stiffness and damping compared with conventional solutions. In parallel, the critical review in [27] emphasizes that lightweight modular construction—particularly based on panelized steel systems—has become an important option for rapid post-disaster reconstruction, thanks to its fast assembly and predictable seismic performance. However, no previous study has assessed a hybrid EPS–CFS wall system behaving as a fully structural element under earthquake excitation. Such a configuration would merge the stiffness and ductility of galvanized thin-walled steel members with the insulation and damping characteristics of EPS, providing an integrated solution for seismic and energy-efficient buildings.

Romania lies within the Vrancea intermediate-depth seismic zone, one of the most active in Europe. The national seismic design code P100–1/2013 [28] prescribes high design ground accelerations and significant spectral amplification at intermediate and long periods. European practice follows EN 1998–1 (Eurocode 8) [29] in conjunction with EN 1993–1-3 [7] for cold-formed steel members. This regulatory context imposes stringent requirements on drift control and deformation capacity, which are particularly demanding for lightweight systems where stiffness degradation may become critical.

The literature survey leads to three main observations: (1) CFS systems exhibit well-documented seismic performance and are supported by mature international codes [2,7,12]; (2) EPS-based hybrid system provide clear thermal and weight advantages but only limited structural resistance [4,23]; and (3) full-scale shake-table evidence for EPS–CFS hybrid wall modules acting as primary structural seismic elements remains limited in the open literature. Given Romania's high seismicity and the increasing interest in energy-efficient modular buildings, full-scale dynamic verification of such hybrid panels becomes both scientifically necessary and practically relevant. The present shake-table campaign addresses this gap by quantifying system-level stiffness degradation, hysteretic energy dissipation, and observed failure mechanisms of full-scale hybrid EPS–CFS modules. The results complement earlier studies on thin-walled cold-formed steel frames and mineral-matrix composite systems [24,25,30] and provide global-response targets for future numerical modelling. In this paper, steel–EPS interaction is discussed only at system level (contact-mediated coupling and geometric confinement), while interface/material characterization and any verification of shear transfer or strain compatibility are intentionally deferred to a companion study.

2. Research objectives and scope

2.1. Background and motivation

The ThermaSteel construction system, shown in Fig. 1, was developed and patented in the United States in the late 1980s as a lightweight prefabricated wall and floor panel combining galvanized cold-formed steel framing with an expanded polystyrene (EPS) core. The panels, manufactured by ThermaSteel Inc. in Radford, Virginia, have been used extensively in residential and modular construction throughout North America. The design philosophy integrates thin-gauge galvanized steel profiles bonded to a rigid EPS core, producing a hybrid element that simultaneously provides structural framing, thermal insulation, sheathing, and vapor barrier functions [31].

Fig. 1 illustrates the main panel typologies (X, I, B, C, H, S, F, R), the manufacturing workflow, and examples of completed buildings. In conventional use, these panels are employed mainly as enclosure and load-sharing elements. In contrast to sandwich EPS–concrete walls and SIP systems with OSB or steel sheathing, the present configuration relies on a steel framework embedded in and continuously bonded to the EPS core, with no stiff concrete or thick sheathing skins. The EPS core may contribute to contact-mediated coupling and confinement effects at the panel level and helps reduce thermal bridges along the thin-walled steel members, leading to a distinct class of lightweight hybrid walls compared to previously studied EPS–concrete or SIP solutions.

Despite their practical diffusion, ThermaSteel systems have not been verified experimentally under strong-motion conditions representative of high-seismicity regions such as the Vrancea zone. The in-plane seismic response, stiffness and damping evolution, and damage mechanisms of full-scale hybrid CFS–EPS modules remain undocumented. In addition, there is limited quantitative evidence on how such systems perform relative to drift limit states in modern codes and how they might be integrated into performance-based seismic design frameworks. These gaps motivate the full-scale shake-table campaign reported in this paper.

2.2. Experimental objectives

The overarching objective of this study is to evaluate, through full-scale shake-table tests, the seismic performance of single-storey hybrid CFS–EPS modules constructed from ThermaSteel panels. The work is designed to extend existing knowledge on lightweight structural panels by:

- quantifying the global dynamic properties (fundamental periods and mode shapes) of two full-scale modules with different steel sheet thicknesses and EPS densities;
- assessing stiffness degradation and equivalent viscous damping under increasing seismic demand, including the influence of strong-motion duration;



Fig. 1. Thermasteel hybrid CFS–EPS panel system. (a) Main panel typologies: exterior (X), interior (I), below-grade (B), ceiling (C), hurricane-resistant (H), shear wall (S), concrete floor (F), and roof (R) panels; (b) manufacturing and assembly stages of multi-storey buildings; (c) completed residential structures built in the United States [31].

- relating measured interstorey drifts to serviceability and ultimate limit states from P100–1/2013 and EN 1998–1, in order to frame the response in a performance-based design perspective;
- documenting local and global damage mechanisms and their correlation with wall layout, connection detailing, and input motion characteristics.

Each specimen was instrumented with triaxial accelerometers and laser displacement transducers to record bidirectional accelerations and inter-storey drifts. The excitation protocol included:

- recorded ground motions (most notably the 1977 Vrancea earthquake scaled to 0.4 g);
- modified and artificial accelerograms generated for spectral compatibility with P100–1/2013 and EN 1998–1;
- impulse tests for modal identification.

The two specimens, THS 24–388 and THS 24–389, are nominally similar in geometry but differ in panel configuration and material properties, providing a controlled basis for comparison. The test programme combines recorded and spectrum-compatible artificial ground motions scaled up to and slightly beyond the code-based design level, so that both serviceability and near-damage states can be observed. The resulting dataset is intended to support subsequent numerical modelling and future derivation of design parameters such as behaviour factors and drift limits for hybrid CFS–EPS wall systems.

2.3. Scope and limitations

The study focuses on the in-plane seismic response of two single-storey ThermaSteel modules assembled with standard manufacturer detailing and representative of compact residential units. Within this scope, the work reports (i) impulse-based identification of dominant dynamic properties, (ii) peak drift demand, (iii) absolute and relative acceleration response (including amplification), (iv) stiffness/period evolution through the test stages, and (v) observed damage mechanisms and their localization.

Several limitations apply. Only two full-scale specimens were tested, so statistical generalization is not possible. Excitation was applied primarily along one horizontal direction; parasitic components were monitored but did not govern the response. Non-structural finishes, interior partitions, and variable gravity loads were not included. Out-of-plane wall behaviour, long-term degradation, thermal/fire performance, and multi-storey configurations are outside the scope of this paper. By providing the first full-scale seismic assessment of ThermaSteel hybrid panels, this research closes a significant knowledge gap and complements earlier studies on thin-walled cold-formed steel frames and mineral-matrix composite systems [25,30]. The results show how a prefabricated technology can be evaluated and adapted for the demands of European seismic design regions, opening the way toward broader implementation of hybrid EPS–CFS systems in earthquake-resistant construction.

This paper reports full-scale shake-table testing, instrumentation, data processing, and system-level response metrics. It does not include independent material- or interface-level characterization of EPS, steel–EPS interaction, fasteners, or concrete, and it does not attempt to infer constitutive or contact parameters from the global response. Accordingly, interpretations of the EPS role are restricted to system-level observations. Dedicated material/interface testing and FE model calibration/validation will be presented in a companion study, using the present results as global-response targets; EPS shear properties (e.g., shear modulus and rate effects) are not measured herein and are not inferred from the system-level response.

The modules were assembled following standard manufacturer detailing and were not intended as code-qualified dissipative CFS shear-wall designs with a prescribed capacity-designed fuse mechanism. Therefore, the expected strength of a designated ductile fuse and an overstrength hierarchy are not defined. Energy dissipation is interpreted at system level from the measured hysteretic response and observed damage, with plausible mechanisms including localized slip/friction

and bearing/yielding around fasteners and thin-gauge tracks at panel joints and anchorage regions, while brittle modes such as screw pull-out/fracture and global stud buckling were not observed within the tested demand range. Consequently, the discussion is framed in terms of global response metrics (period shift, drift demand, acceleration amplification, and hysteretic energy), rather than a code-calibrated behaviour factor.

3. Materials and methodology

3.1. Materials

The experimental specimens were constructed from prefabricated ThermaSteel hybrid panels manufactured at ThermaSteel Inc., Radford, Virginia (USA), and subsequently shipped to the Technical University of Iași (TUIASI) for full-scale assembly and testing. Each panel consists of thin-walled galvanized cold-formed steel (CFS) framing embedded in and bonded to an expanded polystyrene (EPS) core, forming a light-weight hybrid element that provides both load-bearing and thermal

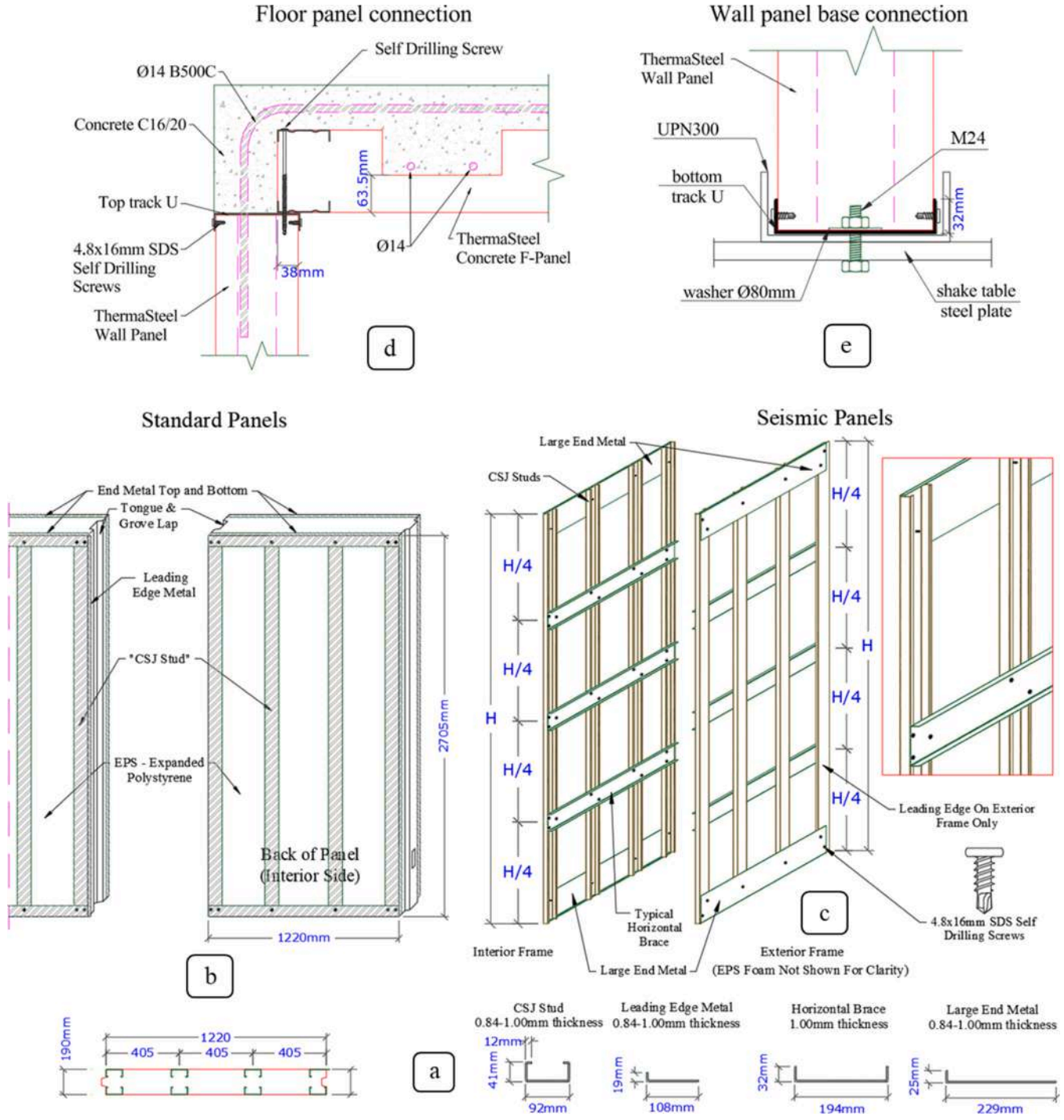

Fig. 2. Standard and seismic Thermasteel hybrid panels. (a) typical C-shaped studs, leading edge members, and horizontal braces; (b) Standard wall panel configuration (model X); (c) Seismic panel configuration (model S); (d) Floor panel connection; (e) Wall panel base connection.

functions. The EPS is moulded directly around the steel framing, which limits local separation under cyclic loading and promotes continuous contact between the two materials at the panel level; however, the degree of interface shear transfer is not directly quantified in this experimental campaign.

The framing (Fig. 2) is made of cold-formed C-shaped profiles fabricated from galvanized low-carbon steel conforming to ASTM A653, structural grade SS37. The nominal yield strength and elastic modulus of the steel are given in Table 1. Sheet thickness is 0.84 mm for specimen THS 24–388 and 1.00 mm for specimen THS 24–389, reflecting the two configurations used in practice. Vertical studs are spaced at regular intervals and connected to U-shaped tracks at the top and bottom by 4.8 × 16 mm self-drilling Grabber screws made of AISI 1018 steel. Details of the floor-to-wall and base connections are shown in Fig. 2(d) and (e), respectively.

The EPS core is produced according to ASTM C578 [35] as a closed-cell expanded polystyrene with nominal densities of 16.9 kg/m^3 for THS 24–389 and 24 kg/m^3 for THS 24–388. The corresponding elastic moduli and compressive strengths are summarized in Table 1. The foam is moulded around the steel frame under controlled conditions in the factory. Reducing the likelihood of voids at the steel–EPS interface improves the continuity of contact between the materials. In this paper, the EPS role is discussed only at system level; no independent EPS shear tests, steel–EPS interface tests, or strain-compatibility measurements were performed. Material/interface characterization and FE calibration are deferred to a companion study.

Reinforced concrete elements (foundation beams and floor slab) are made of C16/20 concrete with BST 500 C reinforcing bars, while the mechanical properties of the steel, EPS, screws, rebars, and concrete are all summarized in Table 1.

3.2. Description of the structural models

Two full-scale single-storey ThermaSteel modules, denoted THS 24–388 and THS 24–389, were designed and constructed for the shake-table tests. Both specimens have a rectangular footprint of approximately 3.6 m × 2.8 m and a storey height of about 2.7 m, representative of a small residential unit. The modules comprise four exterior walls, labelled A–B and 1–2, with door and window openings arranged to match typical architectural layouts. Plan and elevation views are shown in Fig. 3. The effective mass $m = 4415$ kg corresponds to the tested module as assembled (RC slab and supporting RC elements plus the steel/EPS superstructure), and is the value used consistently for base shear and damping-related computations. The footprint (3632 mm × 2794 mm) was selected to comply with the shake-table facility constraints (platform clear dimensions, payload and stroke limits) while enabling a full-scale (1:1) ThermaSteel module with standard door/window openings and manufacturer detailing. It represents the smallest practical unit that still develops three-dimensional box behaviour with realistic panel joints and anchorage.

The two specimens share the same overall geometry and boundary conditions but differ in panel configuration and material properties. THS 24–388 uses standard wall panels with thinner steel sheets and higher EPS density (24.0 kg/m^3). THS 24–389 employs panels with thicker steel and a lower EPS density (16.9 kg/m^3), and dedicated seismic panels placed along selected wall lines (Wall A and Wall 2). These panels include additional CFS members and edge stiffeners around openings, as well as specific detailing at panel joints, providing higher in-plane stiffness and improved energy dissipation capacity. In both modules, wall panels are joined along their vertical edges using tongue-and-groove laps and rows of self-drilling screws, which provide structural continuity and ensure airtightness of the enclosure. Horizontal braces and edge channels complete the framing, creating a continuous load path around the perimeter. The resulting configurations are intended to represent realistic single-storey residential units assembled according to standard ThermaSteel practice.

The compact footprint should not be interpreted as intrinsically ‘beneficial’ for strength or ductility; it mainly affects the global mass and wall distribution within a single module. The response is therefore reported using normalized, transferable metrics (e.g., drift ratio, period shift and acceleration amplification), rather than absolute displacements. In a companion study, a finite-element model calibrated against the present full-scale tests will be used to extend the assessment to larger modules and multi-module configurations under comparable intensity measures.

3.3. Anchorage system and assembly procedure

The specimens were anchored to the ANCO R250–3123 shake table using a rigid steel adapter frame fabricated from UPE 300 channels and bolted to the table platform (Fig. 4(a)). The ThermaSteel base U-tracks were aligned with the adapter frame and clamped using M24 bolts with 80 mm flat washers (Fig. 4(a)), providing distributed bearing and limiting local indentation at the steel–EPS contact, as the EPS core bears against the base track. The vertical wall panels were then seated in the base U-tracks and fixed to the track flanges by lateral self-drilling screws in accordance with the manufacturer’s detailing (Fig. 4(b)). No vertical threaded rods were used at the base connection.

After wall installation, prefabricated roof panels were placed on top of the walls and fastened to the upper U-profiles using self-drilling screws, forming a closed box configuration (Fig. 4(c)). A timber formwork was erected around the perimeter, and a reinforced concrete slab (C16/20) was cast directly on top of the ThermaSteel roof/floor panels (Fig. 4(d)). The rib reinforcement and top mesh were detailed to provide in-plane diaphragm action and distribute lateral loads among the walls. The concrete was cured for ten days before formwork removal; the measured compressive strength at this age was consistent with the nominal value in Table 1. The completed assemblies are shown in Fig. 5 for THS 24–388 and THS 24–389.

3.4. Instrumentation and data acquisition

The dynamic response of the structures was measured using a combination of wireless accelerometers and non-contact laser displacement

Table 1
Materials properties.

Element	Type	Elastic modulus (E)	Compressive strength (f_c)	Tensile yield strength (f_y)	Tensile ultimate strength (f_u)
Steel sheet C profiles [32]	ASTM A653 SS Grade 37	200 GPa		255 MPa	310 MPa
Expanded Polystyrene ASTM C578 [32]	16.9 kg/m^3 – THS 24-389	3 MPa	60 kPa		
	24 kg/m^3 – THS 24-388	8 MPa	120 kPa		
Self-Drilling Screws for profile connections [33]	Grabber 4.8 × 16 mm AISI 1018	210 GPa		310 MPa	448 MPa
Rebars	B500C	200 GPa		500 MPa	550 MPa
Concrete	C16/20	24 GPa	20 MPa		

Note: Material values are from standards/manufacturer data; material/interface tests for FE calibration are outside the scope and will be reported separately.

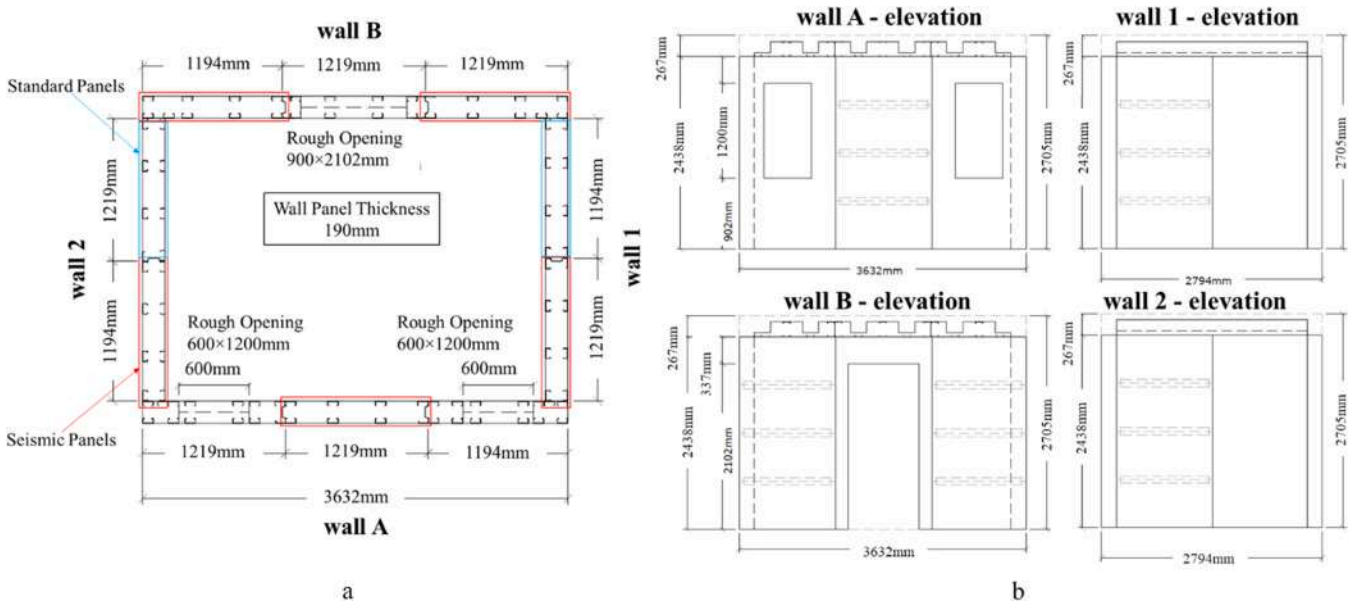

Fig. 3. Configuration of the ThermaSteel test structure. (a) Plan view; (b) Elevations of the tested structure.



Fig. 4. Assembly sequence of the full-scale ThermaSteel hybrid structure. (a) Shake-table platform prepared with the steel foundation frame; (b) assembly of ThermaSteel wall panels; (c) top view during installation of roof panels; (d) placement of reinforcing steel for the concrete floor slab.

sensors. The sensor locations on the walls and along the base are shown in the instrumentation layouts in Fig. 6 and Fig. 7.

Absolute accelerations were recorded with G-LINK-200–8G wireless accelerometers, each with a measurement range of ±8 g and a sensitivity of 0.1 m/s^2. One accelerometer (A_0) was mounted on the shake-table platform to capture the input motion, while three accelerometers (A_1–A_3) were installed at the roof level to record the bidirectional response of the modules. The internal timing module of the system ensured synchronized data acquisition across all accelerometer channels, with a sampling frequency adequate for the frequency range of interest (up to several tens of hertz).

Relative displacements were monitored with optoNCDT ILR 2250 laser displacement sensors mounted at the lower corners of the structures (Fig. 7). Four sensors, Dx_1–Dx_4, measured displacements along the X direction, and four sensors, Dy_1–Dy_4, measured displacements along the Y direction. The devices provide a resolution of 5 μm and an operating range of ±100 mm, which was sufficient to capture both service-level drifts and the largest excursions attained during the most severe tests.

Data acquisition and control were implemented using SensorConnect [38] for the accelerometers and sensortool [39] for the laser sensors, enabling synchronized real-time recording of all channels. The raw



Fig. 5. Full-scale ThermaSteel hybrid structures tested on the ANCO R250–3123 shake table. (a) Specimen THS 24–388, wall B view; (b) Specimen THS 24–389, wall A view; (c) Specimen THS 24–389, wall 2 view.

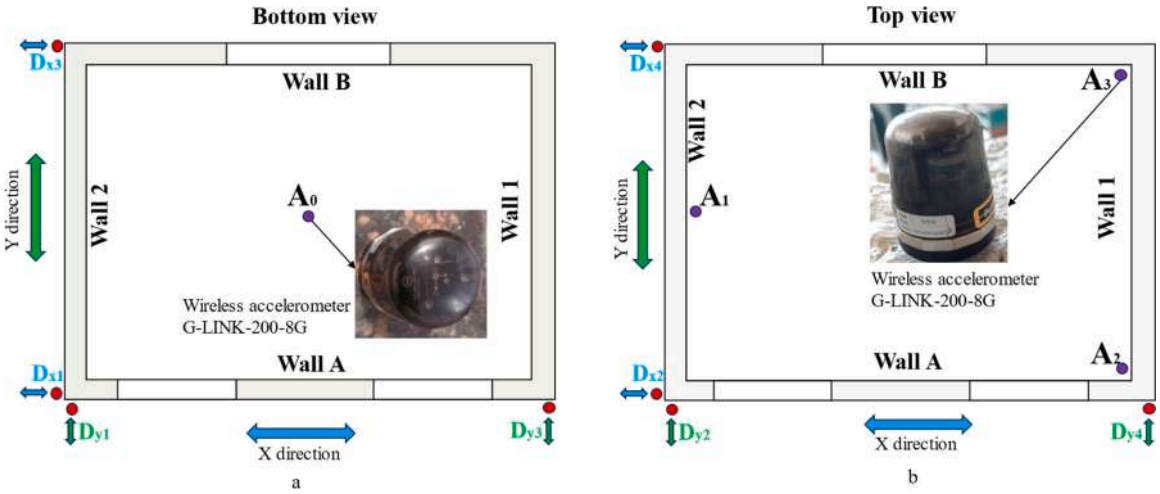

Fig. 6. Instrumentation layout for the ThermaSteel hybrid structures. (a) Plan view of base accelerometer (A_0); (b) Plan view of roof accelerometers (A_1–A_3) using G-LINK-200–8G wireless sensors.

acceleration records were processed using a second-order Butterworth band-pass filter in the 0.3–30 Hz range and then double integrated to obtain displacements. Filter cut-off frequencies were chosen to remove low-frequency drift and high-frequency noise while preserving the frequency content relevant for the global response of the structures. Strain gauges were not used in this campaign; therefore, the present dataset does not include component-level strain histories for studs, tracks, or fastener regions.

3.5. *Seismic testing platform and excitation protocol*

The system of the shake table consists of three hydraulic actuators arranged at 120° around the table and anchored to a massive reinforced concrete reaction block. In its standard configuration, the table can reproduce three translational degrees of freedom. For the present campaign, the control strategy enforced motion primarily along the longitudinal X direction of the modules, corresponding to their most flexible in-plane axis, while reference signals in the transverse Y direction and vertical Z direction were set to zero. Measured parasitic motions in Y and Z remained small, typically below 10–15% of the peak X acceleration. Their response spectra in the period range relevant to the dominant low-order response components identified for the specimens (approximately $T \approx 0.12$–0.22 s) were significantly lower than those in the X direction, confirming that parasitic motions did not govern the global response.

The excitation protocol combined recorded and artificial ground motions representative of the Romanian seismic context. Recorded accelerograms from the 1977 Vrancea earthquake and the 2023 Türkiye earthquake were baseline-corrected, filtered, and scaled by constant intensity factors so that their elastic response spectra matched, in an average sense, the target P100–1/2013 design spectrum in the period range surrounding the fundamental period of the structures. Artificial accelerograms were generated to be compatible with the P100–1/2013 Type 1 spectrum for $a_g = 0.40$ g and corner periods $T_c = 0.7$ s and $T_c = 1.6$ s, corresponding to stiff and soft soil conditions. Standard spectral-matching procedures were used to obtain records whose 5%-damped

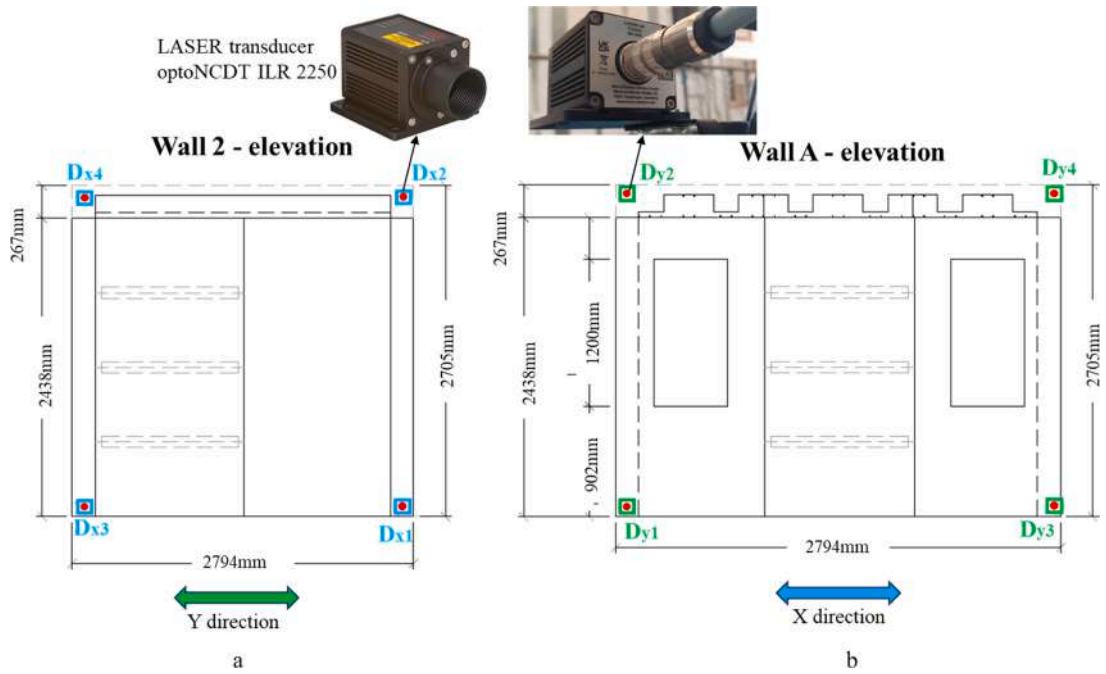

Fig. 7. Arrangement of LASER displacement sensors. (a) Dx_1–Dx_4 - X direction; (b) Dy_1–Dy_4) – Y direction.

response spectra remained within a narrow tolerance band (of the same order as in P100–1/2013) around the target in a broad period range relevant for low-rise buildings.

For specimen THS 24–388, the programme employed mainly short-duration records (less than about 30 s), including scaled versions of the recorded motions and an artificial accelerogram compatible with Tc = 0.7 s. For THS 24–389, the test sequence combined similar recorded motions with longer-duration artificial accelerograms (40–50 s) compatible with Tc = 1.6 s, thus imposing higher cumulative damage demands while keeping peak spectral ordinates close to the design level. The input motions were applied in intensity steps, from low amplitudes for modal identification to table peak accelerations at and slightly above the design level, so that both serviceability and near-damage states could be reached and documented.

4. Experimental program

The two full-scale hybrid ThermaSteel structures were subjected to

Table 2
Experimental test for model THS 24-388.

Test no.	Tag	Duration [s]	Action type/ Description	Frequency [Hz]	PGA X aprox. [g]	PGA Y aprox. [g]	Max. shake table absolute displacement in X direction [mm]	Max. shake table absolute displacement in Y direction [mm]
8-I1	388-F0	5	impulse	5.04				
8-S1	VN77_0-50	8	Vrancea 1977 modified – 50%		0.11	0.025	2	0.5
8-S2	VN77_0-65	8	Vrancea 1977 modified – 65%		0.14	0.027	3	1
8-S3	VN77_0-90	8	Vrancea 1977 modified – 90%		0.188	0.035	4	1
8-S4	VN77_0-125	8	Vrancea 1977 modified – 125%		0.25	0.037	10	2
8-I2	388-F1	5	impulse	4.65				
8-S5	TKM_0-25	15	Türkiye 2023 modified – 25%		0.16	0.09	4	1
8-S6	TKM_0-35	15	Türkiye 2023 modified – 35%		0.23	0.10	10	2
8-S7	TKM_0-55	15	Türkiye 2023 modified – 55%		0.35	0.12	8	2
8-S8	TKM_0-75	15	Türkiye 2023 modified – 75%		0.50	0.155	17	3
8-I3	388-F2		impulse	4.63				
8-S9	AR_0-25	15	artificial earthquake 0 – 25%		0.14	0.042	3	0.5
8-S10	AR_0-35	15	artificial earthquake 0 – 35%		0.205	0.047	5	1
8-S11	AR_0-45	15	artificial earthquake 0 – 45%		0.27	0.07	7	2
8-S12	AR_0-70	15	artificial earthquake 0 – 70%		0.41	0.08	9	3
8-I4	388-F3	5	impulse	4.63				

an extensive shake-table campaign comprising more than 40 seismic excitations with progressively increasing intensity. The full campaign included additional runs (not tabulated here); Tables 2–3 report the representative subset discussed in the paper. The program was designed to reproduce, in a controlled manner, a wide range of seismic demand levels, from serviceability up to near-collapse conditions, while monitoring the evolution of dynamic properties, damage patterns and stiffness degradation.

For the purposes of this paper, only the most representative excitations from the full campaign are discussed in detail. The selected actions are summarized in Table 2 for specimen THS 24–388 and in Table 3 for specimen THS 24–389, where peak ground accelerations, maximum table displacements and key characteristics of each input motion are reported. Details on the generation and spectral matching of the recorded and artificial accelerograms are given in Section 4.5.

4.1. Test sequence for specimen THS 24-388

The first structure, THS 24–388, was subjected to a sequence of earthquake simulations based on:

- modified versions of the 1977 Vrancea record and the 2023 Türkiye record, scaled to several intensity levels, and
- an artificial accelerogram generated to match the P100–1/2013 design spectrum for ag = 0.40 g and corner period Tc = 0.7 s, representative of stiff soil conditions.

The sequence started with low-amplitude motions, intended to characterize the quasi-elastic response and to provide baseline data for the initial dynamic properties. Subsequently, the same records were applied at increasing scale factors, so that their 5%-damped response spectra approached and slightly exceeded the P100–1/2013 target spectrum in the period range around the fundamental period of the structure.

As shown in Table 2, the peak ground accelerations imposed in the longitudinal X direction reached values up to about 0.50 g. The effective durations of the records used for THS 24–388 were typically shorter than 30 s, which results in relatively limited cumulative damage demand. No global instability or loss of load-bearing capacity was observed at the end of the program, although noticeable stiffness reduction and damage accumulation were recorded and are discussed in 6.

4.2. Test sequence for specimen THS 24-389

The second structure, THS 24–389, was tested after the completion of the THS 24–388 campaign. The test matrix was constructed so as to enable a meaningful comparison between the two specimens and, at the same time, to expose the second structure to a more demanding seismic environment.

Several ground motions applied to THS 24–388, including the modified Vrancea 1977 and Türkiye 2023 records and the first artificial accelerogram, were repeated on THS 24–389, in many cases at higher intensity levels. In addition, five further artificial accelerograms were introduced. These new records were generated to be compatible with a different target spectrum, still defined by ag = 0.40 g but with a longer corner period Tc = 1.6 s, representative of more unfavourable long-period conditions relevant for the Vrancea intermediate-depth source.

Tables 2–3 show that the two campaigns were not strictly ‘same-

Table 3
Experimental test for model THS 24-389.

Test no.	Tag	Duration [s]	Action type/ Description	Frequency [Hz]	PGA X aprox. [g]	PGA Y aprox. [g]	Max. shake table absolute displacement in X direction [mm]	Max. shake table absolute displacement in Y direction [mm]
9-I1	389-F0	5	impulse	5.70				
9-S1	TKS_1-25	20	Türkiye 2023 scaled −25%		0.26	0.098	10	2
9-S2	TKM_0-25	20	Türkiye 2023 modified – 25%		0.18	0.092	7	1
9-S3	VN77_1-50	20	Vrancea 1977 scaled – 100%		0.20	0.07	8	2
9-S4	AR_0-35	15	artificial earthquake 0 – 35%		0.19	0.06	7	1
9-S5	AR_5-20	50	artificial earthquake 5 – 20%		0.22	0.076	8	1
9-I2	389-F1	5	impulse	5.30				
9-S6	TKS_1-35	20	Türkiye 2023 scaled −35%		0.23	0.046	8	2
9-S7	TKM_0-35	20	Türkiye 2023 modified – 35%		0.18	0.098	7	1
9-S8	VN77_1-125	20	Vrancea 1977 scaled – 125%		0.26	0.05	9	2
9-S9	AR_0-50	15	artificial earthquake 0 – 50%		0.22	0.076	10	2
9-S10	AR_5-50	50	artificial earthquake 5 – 50%		0.25	0.088	11	2
9-I3	389-F2	5	impulse	4.60				
9-S11	TKS_1-80	20	Türkiye 2023 scaled −80%		0.48	0.12	32	5
9-S12	TKM_0-80	20	Türkiye 2023 modified – 80%		0.43	0.11	30	4
9-S13	VN77_1-200	20	Vrancea 1977 scaled – 200%		0.39	0.06	18	3
9-S14	AR_0-80	15	artificial earthquake 0 – 80%		0.42	0.11	25	3
9-S15	AR_5-80	50	artificial earthquake 5 – 80%		0.44	0.11	31	5
9-S16	AR_5-100	50	artificial earthquake 5 – 100%		0.61	0.14	65	10
9-I4	389-F3	5	impulse	4.50				

record' repetitions. A limited set of input motions was repeated at both specimens (TKM_0–25, TKM_0–35 and AR_0–35), while the remaining sequence for THS 24–389 was intentionally intensified (higher PGA levels, longer durations and additional spectrum-compatible artificial motions) based on the response observed in THS 24–388. Therefore, the comparison is carried out using (i) the repeated motions where available and (ii) intensity-banded comparisons within the same motion families (TKM_0 and AR_0), complemented by normalized response metrics (drift demand, acceleration amplification, and stiffness/frequency shift).

As a result, THS 24–389 was subjected both to higher peak spectral ordinates and to longer strong-motion durations than THS 24–388. The artificial accelerograms used for the second specimen typically had effective durations between 40 and 50 s, almost double those employed in the first campaign, leading to higher cumulative damage demands for similar peak acceleration levels. The peak table accelerations in the X direction reached values up to approximately 0.61 g (Table 3), significantly above the code-based design level.

The acceleration time histories of the main input motions in the longitudinal direction are plotted in Fig. 9 for THS 24–388 and in Fig. 10 for THS 24–389, providing a direct visual comparison of the different records, intensity levels and durations. Response spectra of the three main input motions used for each specimen are reported in Fig. 14.

4.3. Impulse tests and dynamic identification

In addition to the earthquake simulations, impulse tests were conducted at several stages of the experimental program for both specimens in order to identify their dominant dynamic properties and to track stiffness and damping evolution. The identified periods/frequencies and equivalent damping ratios are reported as system-level metrics and are not used to back-calculate EPS material parameters.

Each impulse test consisted of applying a short-duration impact with a rubber hammer in the longitudinal and transverse directions while the shake table was kept at rest. The resulting free-vibration response was recorded by the accelerometers installed at the roof and foundation levels. The acceleration time histories were processed using Fast Fourier Transform (FFT) analysis to obtain amplitude spectra, from which the dominant peaks associated with the fundamental and higher modes were identified.

The decay of the displacement or velocity envelopes was used to estimate equivalent viscous damping ratios by means of the logarithmic decrement method. Impulse tests were repeated at the initial, intermediate and final stages of the seismic programs listed in Tables 2 and 3, allowing the variation of the fundamental period and damping ratio with increasing damage to be quantified. The corresponding trends for both specimens are presented and discussed in 6. Fig. 10 shows a representative free-vibration acceleration record at the roof of model THS 24–389, illustrating the lightly damped single-degree-of-freedom-type response dominated by the first in-plane lateral mode.

5. Experimental results

5.1. Dynamic identification

Impulse tests performed at the beginning and at selected stages of the campaigns allowed identification of the dominant system-level dynamic properties. The Fourier amplitude spectra of the free-vibration responses (Fig. 11) reveal two stable low-order peaks in the in-plane measurements, with frequencies typically around 4.6–5.0 Hz ($T \approx 0.20$–0.22 s) and 7.2–8.5 Hz ($T \approx 0.12$–0.14 s), depending on specimen and test stage (Tags F0–F3 in Tables 2–3). The ≈ 7.2–8.5 Hz peak corresponds to the short-period component that is most evident in the transverse in-plane response, whereas the ≈ 4.6–5.0 Hz peak represents the lowest-frequency global component observed in the X-direction records. Higher-frequency contributions are comparatively small in the measured signals.

The comparison between phases F0 and F3 shows modest reductions of the dominant frequency for both specimens, with larger changes for THS 24–389, which was subjected to higher intensities and longer-duration motions. Quantitatively, the dominant frequency decreased from 5.04 Hz (F0) to 4.63 Hz (F3) for THS 24–388 (≈8% drop), and from 5.70 Hz (F0) to 4.50 Hz (F3) for THS 24–389 (≈21% drop), as reported in Tables 2–3. Assuming approximately constant participating mass during each campaign, these shifts correspond to effective in-plane stiffness reductions of about 16% and 38%, respectively ($k \propto f^2$). A noticeable drop occurs between the initial identification stage (F0) and the first post-excitation stage (F1), whereas later stages (F2–F3) remain closer. This trend is interpreted as an initial seating/adjustment effect of a lightweight panelized system (closure of tolerances, fastener/track seating, initiation of micro-slip and local bearing at joints/anchorage). This initial reduction is not attributed to macroscopic base slippage; the base interface was ensured by the rigid UPE 300 adapter frame and dense M24 bolting/clamping (Fig. 4(a)), and no visible base shift was observed during testing.

5.2. Acceleration response

Figs. 12 and 13 show representative X-direction absolute acceleration time histories measured at the shake table (A0) and at the roof level (A1) for both specimens (sensor locations in Fig. 6). For THS 24–388 (VN77_0–125, TKM_0–75 and AR_0–75), the imposed base peak accelerations span approximately 0.25–0.50 g, while the roof response remains bounded and dominated by low-order in-plane components consistent with the impulse-test identification (5.1; Tables 2–3). For THS 24–389 (VN77_1–200, TKS_1–80 and AR_5–100), the base peaks reach about 0.61 g; despite higher intensity and longer duration, the roof response remains stable, without indications of dynamic instability. The corresponding 5%-damped acceleration response spectra of the selected input motions, computed for the commanded table acceleration in X at the applied scaling levels, are reported in Fig. 14. Fig. 12–14 therefore describe the same set of actions: time histories (Figs. 12–13) and their

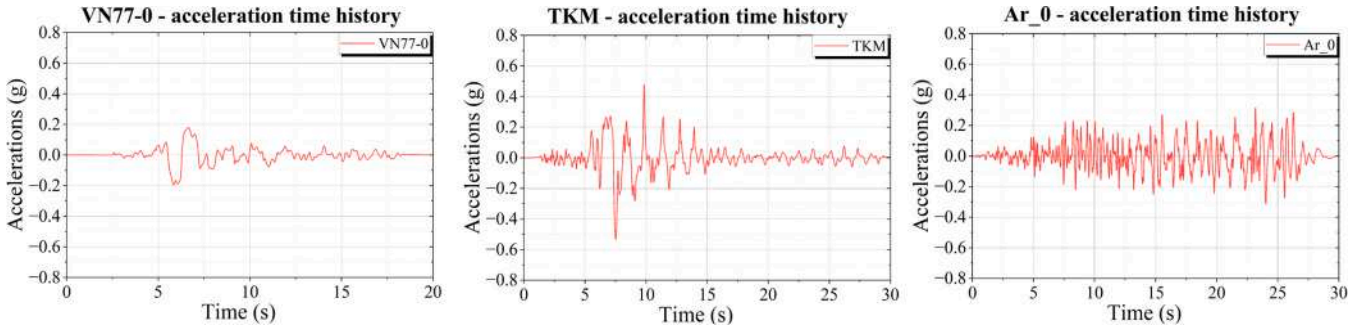

Fig. 8. Acceleration time histories used for model THS-24–388.

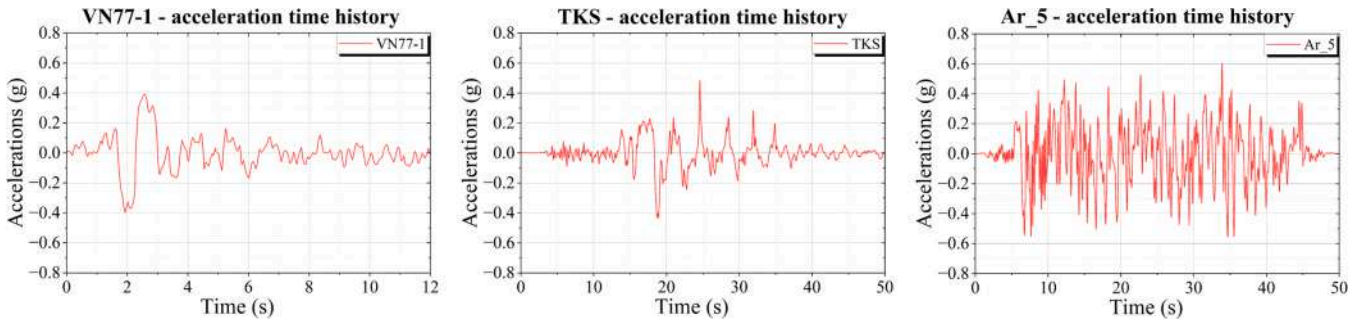

Fig. 9. Acceleration time histories used for model THS-24–389.

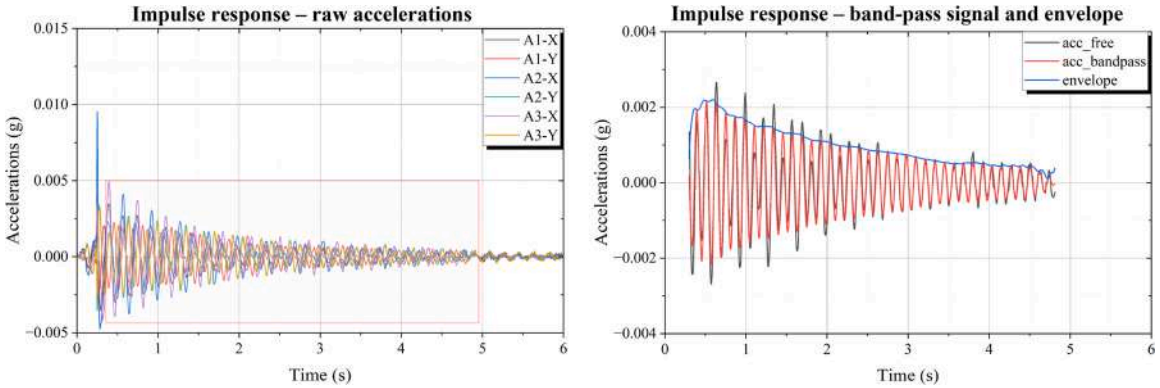

Fig. 10. Impulse free-vibration acceleration time histories for FFT analysis model THS-24–389.

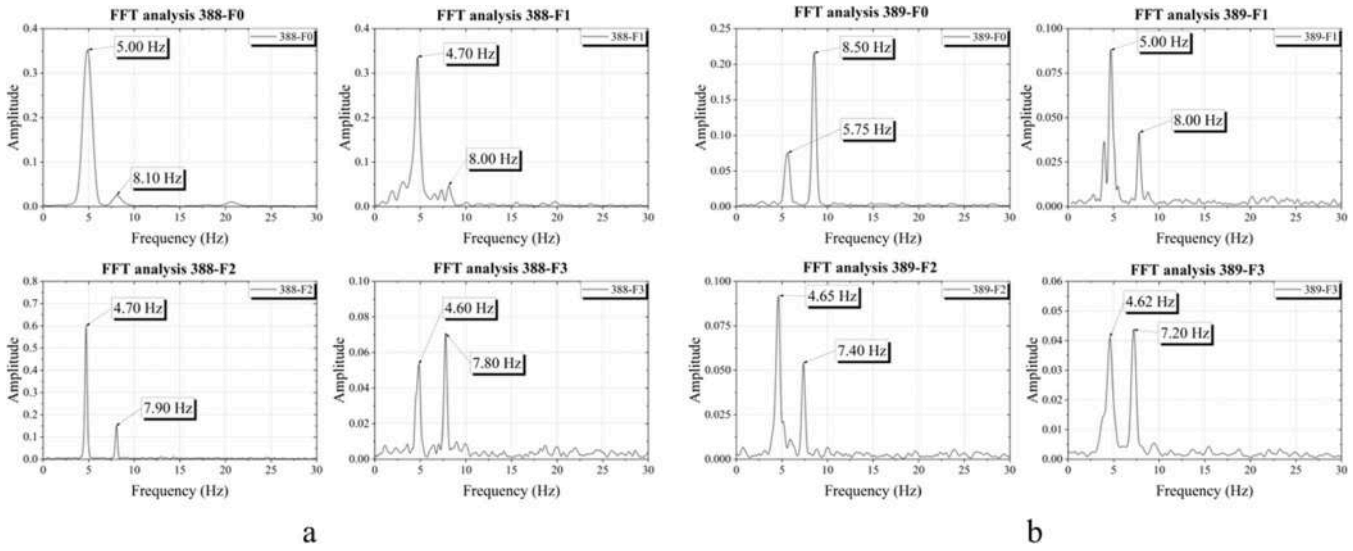

Fig. 11. FFT analysis of free-vibration tests for phases F0–F3 of models: (a) THS 24–388; (b) THS 24–389.

spectra (Fig. 14), presented separately for the two campaigns.

Acceleration amplification is quantified by the peak-based amplification factor $A_f = a_{A1,\text{peak}}/a_{A0,\text{peak}}$, where $a_{A0,peak}$ *and* $a_{A1,peak}$are the peak absolute accelerations of the base and roof channels over the same record. The representative records confirm amplification from base to roof (A_f > 1) for both specimens. For THS 24–389, roof peaks reach about 1.5 g in the long-duration artificial motion AR_5–100 (Table 3). Across the representative records, the peak-based amplification is typically of the order of 2–4, with larger instantaneous ratios possible for long-duration motions where the largest roof peaks occur intermittently.

These trends are consistent with predominantly low-order response, where amplification depends on the overlap between input spectral ordinates and the dominant period range identified from impulse tests (≈0.12–0.22 s). Long-duration motions can increase scatter through modest period elongation and progressive activation of mild nonlinearities at joints and anchorage regions.

Fig. 14 illustrates spectrum compatibility with respect to the P100–1/2013 elastic spectrum used for scaling. At the applied scaling levels, the selected inputs approach or locally exceed the reference spectrum over the dominant short-period interval relevant to the tested modules, supporting interpretation of the results in a code-consistent acceleration- and drift-based performance framework for the design-

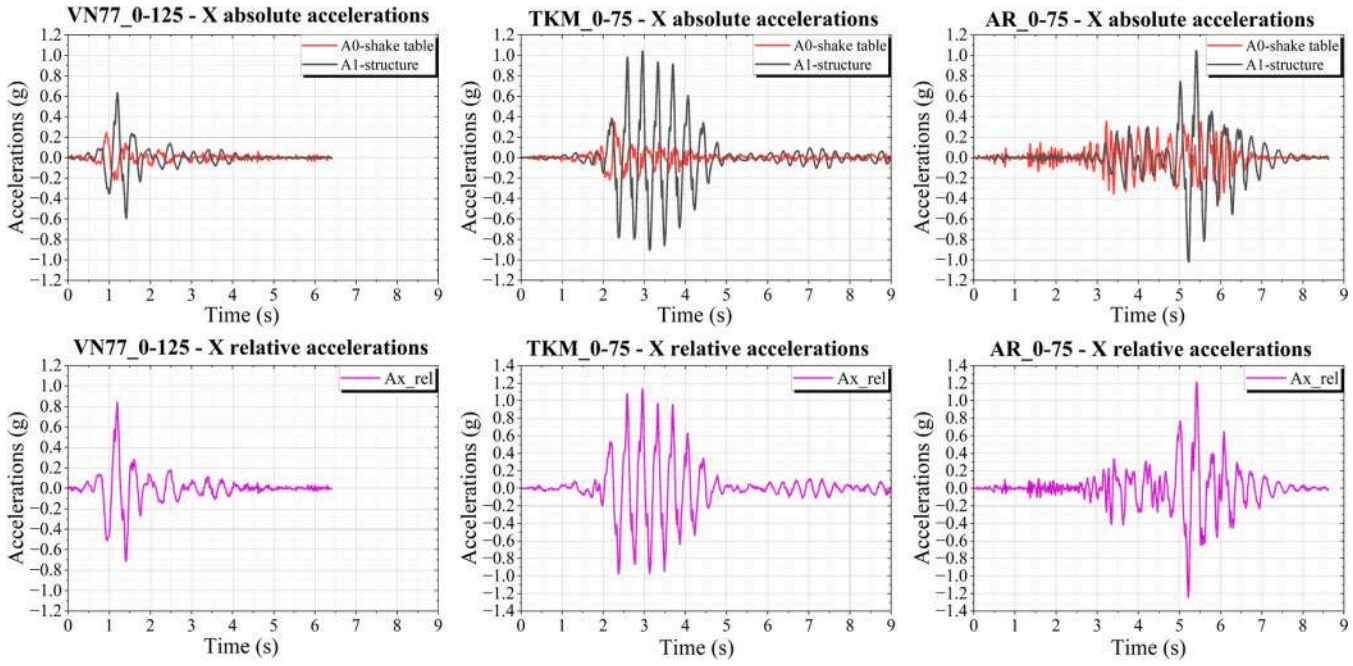

Fig. 12. Absolute and relative X-direction accelerations for THS 24–388 model.

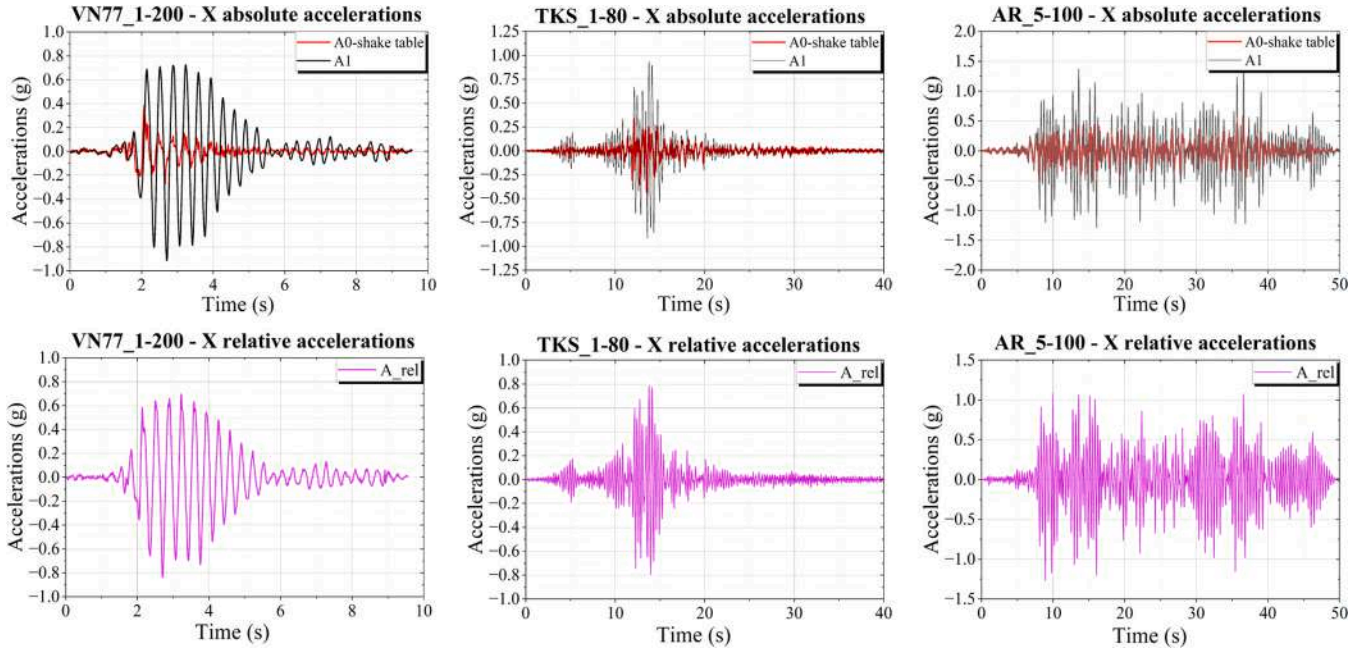

Fig. 13. Absolute and relative X-direction accelerations for the THS 24–389 model.

level and selected above-design-level shaking considered.

5.3. Displacement-based performance and verification of interstory drift

The displacement-based performance of the two structures was evaluated in terms of absolute and relative roof displacements along the X direction. Figs. 15 and 16 show the time histories of absolute and relative displacements for THS 24–388 under VN77_0–100, TKM_0–75 and AR_0–75, and for THS 24–389 under VN77_1–200, TKS_1–80 and AR_5–100. The relative displacement was computed as the difference between the average readings of the displacement transducers Dx2 and Dx1, mounted at the roof and at the base, respectively.

According to the Romanian seismic design code P100–1/2013 (Annex E), admissible interstorey drift limits are defined at the serviceability limit state (SLS) as 0.005 h for brittle non-structural elements and 0.008 h for non-brittle components, and at the ultimate limit state (ULS) as 0.025 h, where h is the storey height. For the tested modules, $h = 2705$mm, resulting in SLS limits of 13.5 mm (brittle) and 21.6 mm (non-brittle), and a ULS limit of 67.6 mm.

The evolution of displacement demand with increasing intensity was assessed by relating the applied scaling levels to the maximum drift ratio, computed as $\mathrm{IDR}_{\max} = \max|\Delta u(t)|/H$, where $\Delta u(t)$is the roof-to-base relative displacement in the X direction and $H = 2705$mm. Representative traces show that drift generally increases with seismic

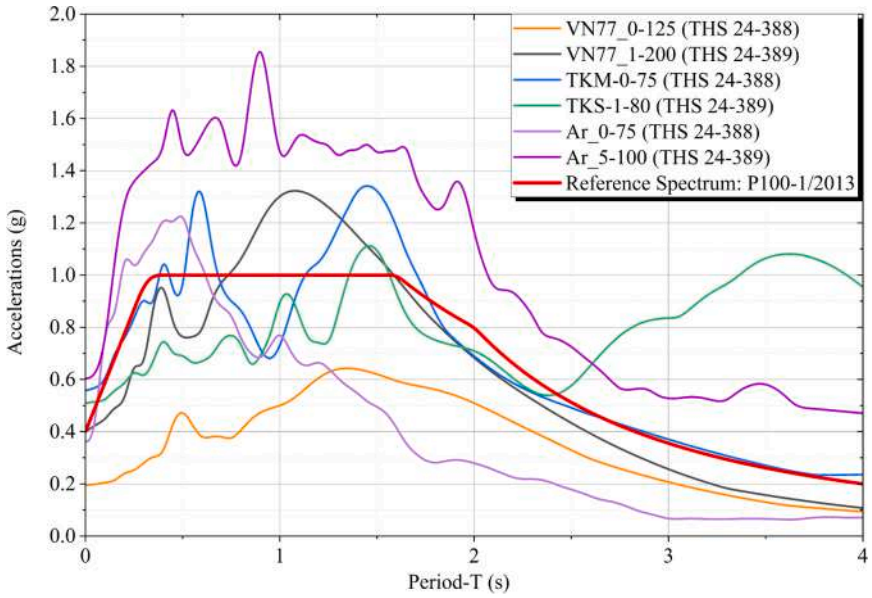

Fig. 14. 5%-damped acceleration response spectra of the three main input motions shown in Fig. 12 (THS 24–388) and Fig. 13 (THS 24–389), computed for the commanded X-direction table acceleration at the applied scaling levels; the P100–1/2013 elastic spectrum is shown for reference.

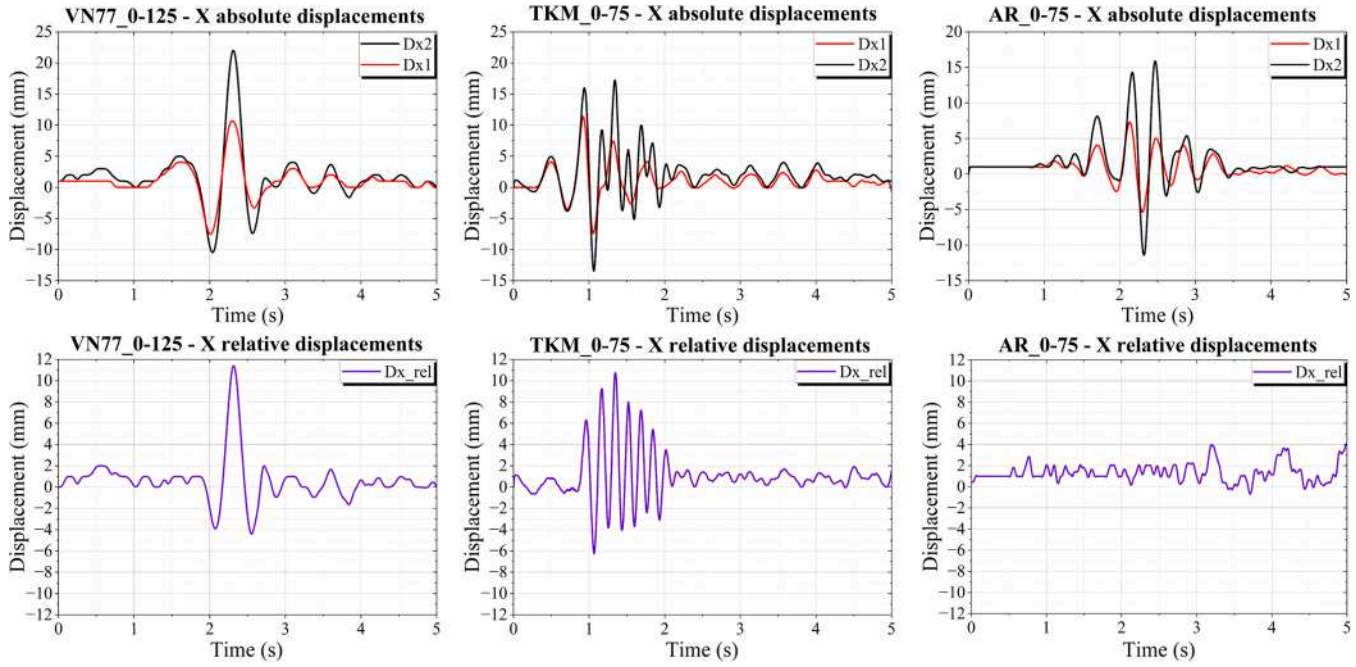

Fig. 15. Absolute and relative X-direction displacements for the THS 24–388 model.

demand, but it is also sensitive to record duration and spectral shape. For THS 24–388, peak relative displacements are about 11 mm (VN77_0–125), 10 mm (TKM_0–75) and 4 mm (AR_0–75), corresponding to $IDR_{max} \approx 0.41\%$, 0.37% and 0.15%, respectively. For THS 24–389, the corresponding peaks are about 22 mm (VN77_1–200), 22 mm (TKS_1–80) and 53 mm (AR_5–100), giving $IDR_{max} \approx 0.81\%$, 0.81% and 1.96%. The higher drift demand under the long-duration artificial motion is consistent with cumulative response effects and the modest period elongation identified from the impulse tests (Tables 2–3).

For THS 24–388, the maximum relative roof displacement in the most demanding runs remains around 10–11 mm, with displacement histories that are nearly symmetric about zero and with negligible residual offsets, indicating an essentially elastic response. As summarized in Table 4, drift remains below the SLS non-brittle limit of 0.008 h (21.6 mm).

For THS 24–389, longer-duration and higher-intensity motions produce larger drifts. The most severe test AR_5–100 (base peak acceleration about 0.61 g) yields a maximum relative displacement of 53 mm, i.e., $IDR_{max} \approx 2.0\%$. This exceeds the SLS limits for non-structural components but remains below the ULS limit of 0.025 h (67.6 mm). Overall, the results indicate compliance with serviceability requirements at lower-to-moderate intensities and preservation of life-safety performance even for selected above-design-level and long-duration excitations.

Although THS 24–389 uses thicker steel framing, it was subjected to intentionally more demanding inputs (higher cumulative demand and

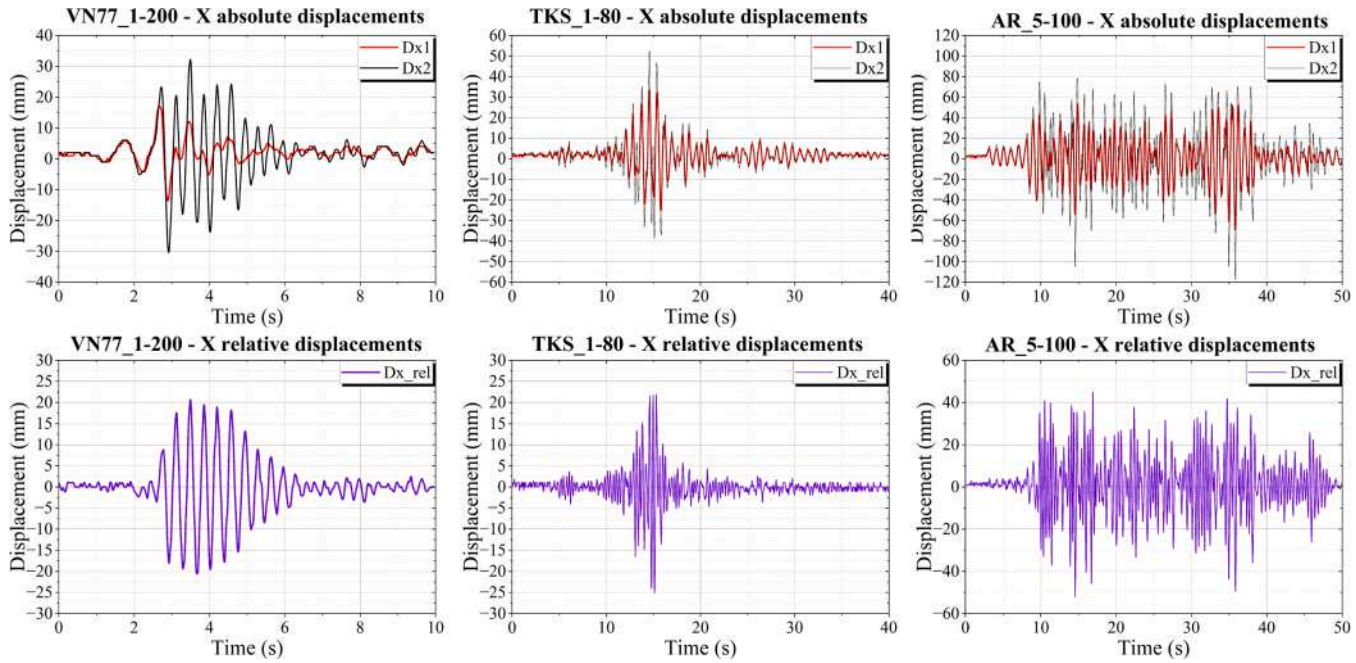

Fig. 16. Absolute and relative X-direction displacements for the THS 24–389 model.

Table 4
Summary of interstory drifts compared to admissible values.

Tested structure	Test name	Shake table maximum absolute acceleration (g)	Experimental test maximum interstory drift (mm)	SLS – admissible maximum drift *0.008h=21.6* (mm)	ULS – admissible maximum drift *0.025h=67.5* (mm)
THS 24-388	VN77_0-100	0.25	10.6	<	<
	TKM_0-75	0.50	10.7	<	<
	AR_0-75	0.41	10.5	<	<
THS 24-389	VN77_1-200	0.39	22	<	<
	TKS-1-80	0.48	25	>	<
	AR_5-100	0.61	53	>	<

long-duration artificial motions), which resulted in larger drift ratios than THS 24–388; therefore, comparisons should be interpreted at comparable intensity bands and repeated motions. Nevertheless, the overall deformation demand remains within the range typically associated with damage-control or life-safety performance levels for low-rise light construction.

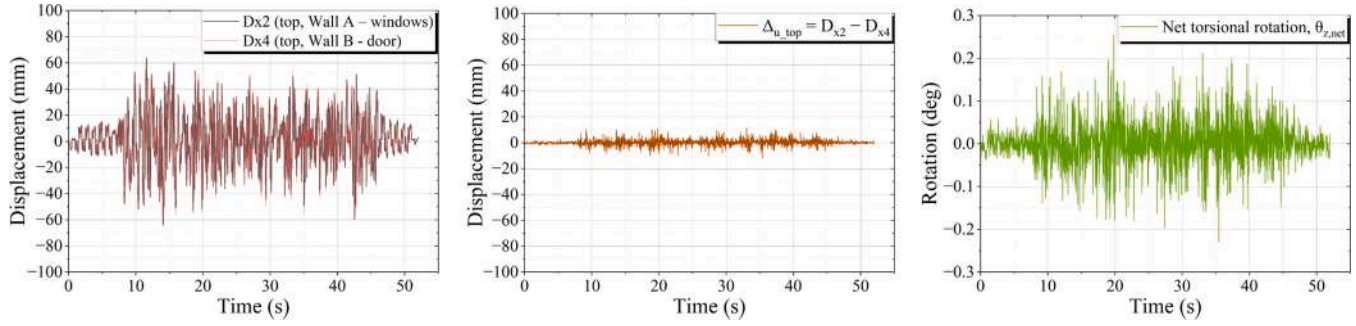

Fig. 17. Torsional response indicators for the maximum-intensity artificial ground motion for the THS 24–389 model: roof-level displacements in X at the two opposite sensor lines (Dx2 on Wall A and Dx4 on Wall B).

5.4. Torsional response indicators from corner/roof displacement measurements

Because specimen THS 24–389 has an asymmetric wall layout, torsional effects were quantified from the roof-level displacement measurements, as shown in Fig. 17.

Fig. 17 quantifies the coupled translational–torsional response of the asymmetric configuration (THS 24–389) using the roof displacement measurements. The peak differential roof displacement was $\max|\Delta u_{\text{top}}| \approx 13.0\text{mm}$, which corresponds to a peak net torsional rotation of $\max|\theta_{z,\text{net}}| \approx 0.29^{\circ}$ for $B = 2794\text{mm}$. These results indicate a measurable but moderate torsional component, which increases local corner demand relative to the average roof translation.

The identified ζ values are system-level equivalent viscous damping ratios derived from the decay of the global free-vibration response. They therefore capture the combined effect of all dissipation sources in the assembled module (connection slip/bearing, frictional micro-slip at interfaces, local yielding of thin-gauge tracks, and material damping), and should not be interpreted as a direct measure of the intrinsic, material-level viscoelastic damping of EPS. A change in EPS density may influence stiffness and local deformation distribution, yet it may produce only a marginal change in the global ζ if the dominant dissipation is governed by joints and frictional mechanisms typical of CFS/LSF systems.

Because ζ is identified from low-amplitude impulse/free-vibration decay at selected stages, it reflects an approximately linearized system response and is less sensitive to amplitude-dependent hysteretic mechanisms that develop under the strongest shaking.

5.5. Determination of the fraction of critical damping

The damping ratio was evaluated from the impulse-response tests by analysing the free-vibration signal recorded on channel A2 at the upper level, which provided the best signal-to-noise ratio. Peaks of the same sign were extracted from the decaying part of the response, starting immediately after the maximum amplitude of the impulse. For two successive peaks x_i and $x_{i+1}$of the same sign, the logarithmic decrement is defined as

$$\delta_i = \ln(x_i/x_{i+1}). \tag{1}$$

The average logarithmic decrement δ was obtained by averaging δ_i over the first 10–12 successive peak pairs. The fraction of critical damping ξ was estimated using the classical relationship for lightly damped systems,

$$\xi \approx \frac{\delta}{2\pi}, \tag{2}$$

The vibration period $T$was determined from the time interval between successive peaks, and the corresponding natural circular frequency was computed as $\omega_n = 2\pi/T$. Assuming an equivalent SDOF representation with total mass $m = 4415kg$ and identified ω_n, the critical viscous damping coefficient was computed as $c_{cr} = 2m\omega_n$. The equivalent viscous damping coefficient was then obtained as $c_{eq} = \xi\, c_{cr}$.

For THS 24–389, the identified damping ratio increased from about 2.0% to about 2.4% between phases F0 and F3, remaining within a narrow range throughout the test sequence. For THS 24–388, the identified damping ratios ranged from about 2.9% in the initial configuration (based on the long-duration F0 record) to about 3.3% at the end of the campaign. In both cases, the identified ξ values are consistent with published system-level damping for cold-formed steel and light steel framing systems under dynamic identification and shake-table related contexts, which is typically in the low single-digit range and may increase with cumulative demand depending on mode, amplitude, and damage state (Table 5). The modest increase of $\xi$with increasing demand suggests a progressive activation of benign dissipation mechanisms, such as friction and local connection slip, rather than unstable damage patterns. In the absence of interface-level measurements, the observed differences are discussed as system-level effects of steel–EPS interaction (contact coupling and confinement), rather than as demonstrated composite action.

Table 5
Literature benchmark of equivalent viscous damping ratios for cold-formed steel (CFS) / light steel framing (LSF) systems under dynamic testing.

Ref.	Structural system / specimen	Test type and identification	Reported damping ratio ζ (%)	Notes (context for comparison)
This study (THS 24-388)	Full-scale single-storey hybrid CFS–EPS module	Impulse/free-vibration decay (logarithmic decrement)	2.9 → 3.3	Narrow range over the campaign (system-level damping).
This study (THS 24-389)	Full-scale single-storey hybrid CFS–EPS module	Impulse/free-vibration decay (logarithmic decrement)	2.0 → 2.4	Slight increase with test phase (system-level damping).
Macillo et al., 2017 [34]	Shaking-table tests on a CFS building sheathed with gypsum panels (multi-storey mock-up)	Dynamic identification from random/vibration tests; reported in Table 4	Typically, ~1–3 before EQ; up to ~2–5 after stronger shaking	Paper explicitly reports damping ranges for "bare" vs "complete construction" and post-earthquake increases.
Wang et al., 2018 [35]	Full-scale CFS building (system identification campaign; multiple modes)	White-noise based modal ID across damage states	Fundamental mode often > 5 during serviceability states; higher modes ~3	Damping increases with damage and excitation amplitude; first longitudinal mode reported > 5% at serviceability sequence.
Taranu et al., 2023 [30]	Scaled-down CFS structural skeleton (no claddings) on shake table	Experimental modal properties + numerical THA;	~1–2 (reported as 0.01–0.02)	This is a bare CFS skeleton; damping is not intended to represent finished wall systems. The paper reports experimental damping values and (separately) damping values adopted in modelling.

5.6. Seismic performance evaluation

Additional insight into the deformation behaviour is provided by the force–displacement hysteresis loops plotted in Fig. 18 for THS 24–388 and in Fig. 19 for THS 24–389. For the first model, the loops corresponding to VN77_0–75, TKM_0–75 and AR_0–75 remain narrow and almost linear, with only slight widening at the largest excursions. This is consistent with the small drift demands reported in Table 4 and with the limited reduction of the fundamental frequency, and confirms that the structure responded predominantly in the elastic range with minor energy dissipation and negligible damage.

The base shear was estimated from inertia forces using the measured accelerations in the controlled X direction. The absolute acceleration at the roof slab $A_1(t)$ was converted into a relative acceleration with respect to the table motion $A_0(t)$, i.e., $a_{\text{rel}}(t) = A_1(t) - A_0(t)$. The

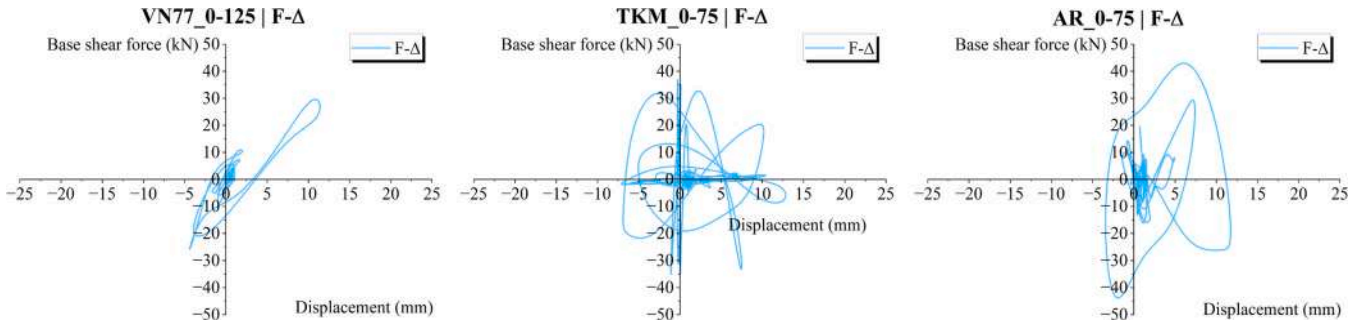

Fig. 18. Force–displacement hysteresis loops for the THS 24–388 model.

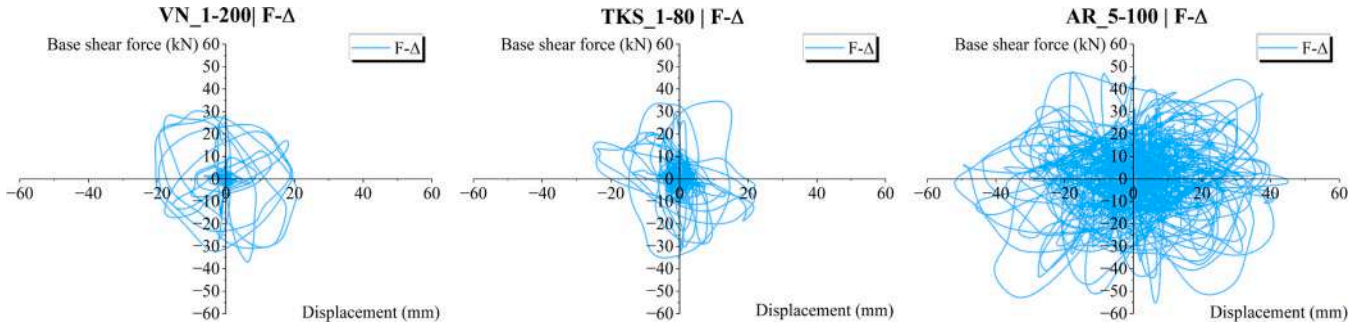

Fig. 19. Force–displacement hysteresis loops for the THS 24–389 model.

inertia-based base shear was then computed as $V_b(t) = m \bullet a_{\text{rel}}(t)$, with $m = 4415$ kg (effective mass of the as-tested assembly) and $a_{\text{rel}}(t)$ expressed in m/s^2(signals recorded in *g*were converted using $1g = 9.81$ m/s^2). The reported force–displacement loops therefore represent system-level inertia-based base shear versus relative displacement.

For THS 24–389, the loops associated with VN77_1–200 and TKS_1–80 display a more pronounced but still stable hysteretic behaviour, while the AR_5–100 test produces the widest cycles. The latter reflects increased energy dissipation and moderate stiffness degradation at higher drift levels, in line with the larger interstorey drifts and the slightly higher damping ratios identified for this specimen. The displacement coordinate in the hysteresis plots is the measured relative displacement in X, $\Delta(t) = u_{\text{top}}(t) - u_{\text{base}}(t)$, computed from the corresponding top and base LVDT channels (same line of action), and processed with a 12 Hz Butterworth low-pass filter to reduce high-frequency noise.

In comparative terms, THS 24–388 exhibits a nearly elastic stiffness with limited loop area, characteristic of a system operating well within the serviceability range, whereas THS 24–389 shows broader, yet stable, cycles that are typical of controlled inelastic response at damage-control or life-safety performance levels. The absence of pinching and the lack of strength deterioration in the loops of THS 24–389 indicate that the dominant inelastic mechanisms are localized and do not compromise the global lateral load-carrying capacity of the modules.

5.7. Failure mechanisms

5.7.1. Specimen THS 24-388

The overall behaviour of specimen THS 24–388 remained essentially elastic throughout the entire test sequence, including the highest-intensity input AR_0–75. Video snapshots of Wall B during peak displacements (Fig. 20 (a–b)) show a reversible sway motion of the module with no visible cracking or local damage. A slight tendency of uplift of the concrete slab from the wall anchorage can be observed at the



Fig. 20. Video frame detail of wall B, model THS 24–388, Video snapshots of specimen THS 24–388 during during peak sway of the TKM_0–75 action: (a) displacement to the left; (b) displacement to the right.

opposite edge in both directions of motion, but the connection remains intact and no separation develops along the perimeter.

A detailed visual inspection at the end of the campaign confirmed the absence of structural damage in the primary components. No plastic deformation of the cold-formed steel members was identified, no debonding between the EPS core and the steel profiles was observed, and no screw connections were found to be rotated, displaced or partially pulled out. Minor defects were limited to superficial coating irregularities and small marks in the EPS, with no consequence for the load-bearing behaviour.

Figs. 21 and 22 illustrate typical views of the base region, the concrete diaphragm and the interior corners, all of which remained undamaged, with only limited rocking and gap opening at the steel foundation frame.

5.7.2. Specimen THS 24-389

In contrast, specimen THS 24–389, which was subjected to higher and spectrally more demanding motions (including AR_5–100), exhibited localized but clearly identifiable damage at the base and at several screw connections. After the AR_5 excitation, the lower steel profiles at the corners of the module showed local out-of-plane distortions, especially at the intersections of Walls 1 with A and B and Walls 2 with A and B. As documented in Fig. 23(a–b), the lateral parts of the U-tracks became locally wavy, indicating plastic deformation of the thin flanges. In the same regions, some anchorage screws appeared partially unscrewed, although no complete pull-out or fracture was observed. The EPS core was locally compressed and slightly extruded at the interface, but the global anchorage between the walls and the steel foundation frame remained effective.

Additional damage concentrated at panel-to-panel joints on both the interior and exterior faces (Figs. 24 and 25). Several screws along vertical joints and at diaphragm–wall connections were found to be partially unscrewed, and the surrounding holes in the thin-gauge sheets exhibited plastic deformation and enlargement. Close-up views show tilted screw heads and elongated holes, indicating local bearing and partial pull-through deformation in the sheet steel, accompanied by slight crushing of the EPS backing.

Despite these local mechanisms, the damage pattern remained non-brittle and distributed: no screw was completely pulled out, no connector fractured, and no buckling of the main studs was detected. The hybrid system dissipated energy mainly through local yielding in the sheet around the fasteners and through limited deformation of the base tracks, while the global stability and load-carrying capacity of the module were preserved.

6. Conclusions

This paper reports full-scale shake-table testing, instrumentation, data processing, and system-level response metrics for two single-storey hybrid CFS–EPS modules built with ThermaSteel panels (THS 24–388 and THS 24–389). The input set combined recorded motions and spectrum-compatible artificial accelerograms scaled to the Romanian code P100–1/2013 elastic spectrum for ag = 0.40 g, covering both stiff- and soft-soil corner periods (Tc = 0.7 s and Tc = 1.6 s). Selected runs reached or slightly exceeded the design-level intensity at the table.

Impulse tests and FFT analyses identified two stable low-order components in the in-plane response, with dominant peaks around 4.6–5.0 Hz ($T \approx 0.20$–0.22 s) and 7.2–8.5 Hz ($T \approx 0.12$–0.14 s), depending on specimen and test phase. Over the campaigns, period elongation remained modest for THS 24–388 and larger for THS 24–389, consistent with the higher intensities and longer-duration motions applied. The associated frequency shifts indicate limited-to-moderate system-level stiffness reduction, with no evidence of global lateral instability.

Equivalent viscous damping ratios identified from impulse/free-vibration decay remained within a narrow range of about 2–3% of critical for both modules. These values represent global, assembly-level damping dominated by connection-related and frictional mechanisms typical of lightweight steel systems. They should not be interpreted as intrinsic viscoelastic damping of EPS, and the modest sensitivity to EPS density is consistent with a joint-dominated dissipation mechanism under the applied identification procedure.

In displacement-based terms, THS 24–388 exhibited a predominantly elastic response. Peak drift ratios did not exceed about 0.4% of storey height, hysteresis loops remained narrow and near-linear, and residual deformations were negligible. THS 24–389 developed larger deformation demands under the intensified and longer-duration sequence, reaching peak drift ratios on the order of 2% in the most severe run. The hysteretic response remained stable, with no pinching or strength deterioration, indicating controlled inelasticity concentrated in connections rather than loss of global capacity.

Observed damage mechanisms were localized and non-brittle. THS 24–388 exhibited no structural damage. THS 24–389 developed localized distress at base tracks and panel joints (track distortion and fastener bearing/pull-through), accompanied by slight local EPS crushing, while avoiding brittle modes such as screw pull-out/fracture and global stud buckling. The global load path remained intact throughout the campaign.

Because the two test programmes were not strictly identical, quantitative comparison relied on repeated motions where available and on intensity-banded comparisons within the same motion families, supported by normalized metrics (drift ratio, period shift, acceleration amplification, and hysteresis shape). Within repeated motions and comparable intensity bands, the configuration with thicker steel framing exhibited a more favourable system-level response, despite the higher cumulative demand applied to THS 24–389.

A limitation of the present dataset is the absence of local strain measurements and independent material/interface tests. Therefore, interpretations are kept at system level. Component-level demand quantification and EPS/interface characterization will be addressed in a



Fig. 21. Absence of the local damage in specimen THS 24–388: (a) base region showing limited rocking and gap opening at the steel foundation frame; (b) undamaged concrete diaphragm and door header at the end of testing.



Fig. 22. Interior views of specimen THS 24–388: (a) corner at roof level with undamaged ring beam and studs; (b) base connection on the steel foundation frame, showing no visible yielding or tearing of the steel components.



Fig. 23. Damage at base joints in specimen THS 24–389: (a) EPS crushing and relative slip at the wall corner; (b) gap opening and local compression of the EPS at the longitudinal wall–foundation interface.



Fig. 24. Fastener deformation in specimen THS 24–389: (a) tilting and bearing deformation of screws at interior plates; (b) partial pull-through of screw heads at an exterior panel joint with local crushing of the EPS backing.

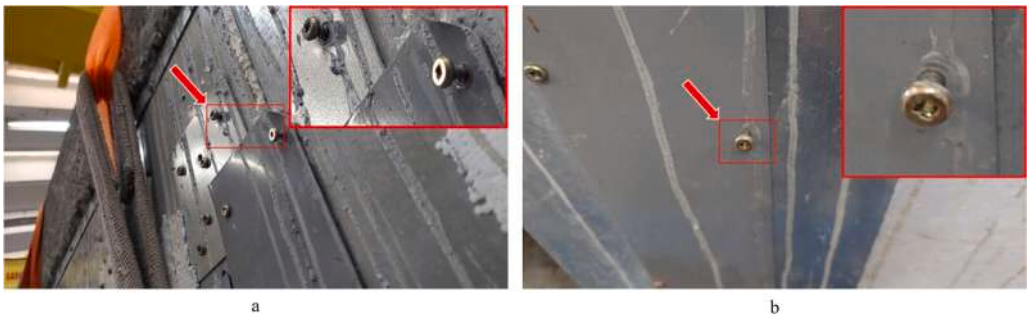

Fig. 25. Local plastic deformation of screws in specimen THS 24–389 at diaphragm–wall and exterior joints.

companion study.

Design implications

The results indicate that the global seismic response of ThermaSteel-type hybrid CFS–EPS modules is governed primarily by wall layout, connection detailing, and the characteristics of the input motion, especially spectral overlap with the short-period range and motion duration. Although peak table acceleration is an important intensity measure, the maximum drift demand was also influenced by duration and by how the

response spectrum covers the dominant period range of the modules. This supports using a drift-based verification framework consistent with code practice, while explicitly considering spectrum shape and duration effects when selecting records for assessment of lightweight, short-period systems.

Wall layout should be treated as a primary design variable. Concentrating openings and seismic panels on selected wall lines may increase torsional sensitivity and corner demands. Even when torsional rotation remains moderate, differential corner response can increase local demand at joints and anchorage. Layout checks should therefore include a torsional-sensitivity verification based on stiffness distribution and on corner-response indicators.

At higher demand, the controlling inelastic mechanisms were connection- and track-driven, concentrated at base tracks and panel joints. Track distortion and fastener bearing/pull-through governed stiffness degradation and energy dissipation, while global stud buckling and brittle connector failures were not observed. This implies that seismic reliability depends strongly on anchorage robustness and joint detailing. Distributed base clamping, adequate track thickness, detailing that limits local bearing and pull-through, and avoidance of stress concentrations at corners and wall ends are critical to maintain stable hysteresis and preserve the global load path.

Roof-level accelerations showed consistent amplification relative to the table, as expected for first-mode-dominated lightweight systems. This has direct implications for acceleration-sensitive non-structural components and contents. Design checks should not rely solely on base/PGA scaling. They should account for expected floor amplification, using either code-consistent floor-response procedures or experimentally supported amplification factors for comparable systems and period ranges.

Finally, the reported response metrics are intentionally normalized and transferable. Drift ratios, period shift, acceleration amplification, and hysteresis shape provide direct calibration targets for subsequent numerical modelling and for extrapolation to larger modules or multi-module configurations, under comparable intensity measures. Any claims of verified composite shear transfer or strain compatibility between CFS and EPS should be avoided without dedicated interface testing, and modelling assumptions in this respect should be stated explicitly as assumptions until validated.

CRediT authorship contribution statement

George Taranu: Writing – review & editing, Writing – original draft, Resources, Project administration, Methodology, Investigation, Funding acquisition, Data curation, Conceptualization.

Funding

This research was supported by the research contract no. 31160 / 04.09.2024, entitled “Research and experimental testing for structural elements and systems with Thermasteel panels”, funded through the Technical University “Gheorghe Asachi” of Iași. The financial support provided under this contract covered the design, preparation and execution of the full-scale shake-table tests.

Additional information

Video shaking table experiment:

- Model THS 24–388 https://youtu.be/gNKNPZ7_pco
- Model THS 24–389 https://youtu.be/XDudUWT1-5g

Declaration of Competing Interest

The author declares that there are no known competing financial interests or personal relationships that could have appeared to influence the work reported in this paper

Acknowledgements

The author acknowledges the contribution of SC ABC Constructii Civile și Industriale SRL, Romania and ThermaSteel Inc., USA, for supplying the materials, joints and accessories needed for conducting the laboratory investigations.

Data availability

Data will be made available on request.

References

[1] Dubina D, Ungureanu V, Landolfo R. Design of Cold-Formed Steel Structures. ECCS Eur Conv Constr Steel 2012.
[2] American Iron and Steel Institute. AISI S100-24: North American Specification for the Design of Cold-Formed Steel Structural Members. Washington: AISI; 2024.
[3] Ramli Sulong NH, Mustapa SAS, Abdul Rashid MK. Application of expanded polystyrene (EPS) in buildings and constructions: A review. J Appl Polym Sci 2019; 136:47529. https://doi.org/10.1002/APP.47529;SUBPAGE:STRING:FULL.
[4] Huang Y, Yang C, Ji X, Lu D, Song Q. Seismic response of expanded polystyrene (EPS) sandwiched concrete panels system in buildings: Damage distribution and correlation analysis of parameters. J Build Eng 2024;91:109608. https://doi.org/10.1016/J.JOBE.2024.109608.
[5] Liang H, Roy K, Fang Z, Lim JBP. A Critical Review on Optimization of Cold-Formed Steel Members for Better Structural and Thermal Performances. 2022;12: 34 Buildings 2022;12:34. https://doi.org/10.3390/BUILDINGS12010034.
[6] Liu C, Mao X, He L, Chen X, Yang Y, Yuan J. A new demountable light-gauge steel framed wall: Flexural behavior, thermal performance and life cycle assessment. J Build Eng 2022;47:103856. https://doi.org/10.1016/J.JOBE.2021.103856.
[7] European Comitte for Standardization. EN 1993-1-3. Eurocode 3: Design of Steel Structures, Part 1.3: General Rules, Supplementary Rules for Cold-formed Thin Gauge Members and Sheeting, 2024. Brussels, Belgium: CEN; 2024.
[8] European Comitte for Standardization. EN 1993-1-5: 2006/A1:2017 - Eurocode 3 - Design of steel structures - Part 1-5: Plated structural elements 2017.
[9] Fiorino L, Della Corte G, Landolfo R. Experimental tests on typical screw connections for cold-formed steel housing. Eng Struct 2007;29:1761–73. https://doi.org/10.1016/J.ENGSTRUCT.2006.09.006.
[10] Landolfo Raffaele, Fiorino Luigi, Iuorio Omella. A Specific Procedure for Seismic Design of Cold-Formed Steel Housing 2010. ⟨https://www.researchgate.net/publication/258930474_A_Specific_Procedure_for_Seismic_Design_of_Cold-Formed_Steel_Housing⟩ (accessed November 3, 2025).
[11] Fiorino L, Shakeel S, Macillo V, Landolfo R. Seismic response of CFS shear walls sheathed with nailed gypsum panels: Numerical modelling. ThinWalled Struct 2018;122:359–70. https://doi.org/10.1016/J.TWS.2017.10.028.
[12] Fiorino L, Campiche A, Shakeel S, Landolfo R. Seismic design rules for lightweight steel shear walls with steel sheet sheathing in the 2nd-generation Eurocodes. J Constr Steel Res 2021;187. https://doi.org/10.1016/j.jcsr.2021.106951.
[13] Dao TN, van de Lindt JW. Seismic Performance of an Innovative Light-Frame Cold-Formed Steel Frame for Midrise Construction. J Struct Eng 2013;139:837–48. https://doi.org/10.1061/(ASCE)ST.1943-541X.0000683.
[14] Nakata N., Schafer B.W., Madsen R.L. Seismic design of multi-story cold-formed steel buildings: The CFS-NEES archetype building. Structures Congress 2012 - Proceedings of the 2012 Structures Congress, 2012. https://doi.org/10.1061/9780784412367.134.
[15] Speicher M.S., Olivares I., Schafer B.W. Seismic Evaluation of a 2-Story Cold-Formed Steel Framed Building using ASCE 41-17 n.d. https://doi.org/10.6028/NIST.TN.2116.
[16] Peterman KD, Madsen RL, Schafer BW. Experimental seismic behavior of the CFS-NEES building: System- level performance of a full-scale two-story light steel framed building. 22nd Int Spec Conf Recent Res Dev ColdForm Steel Des Constr 2014.
[17] Fiorino L, Bucciero B, Landolfo R. Shake table tests of three storey cold-formed steel structures with strap-braced walls. Bull Earthq Eng 2019;17:4217–45. https://doi.org/10.1007/S10518-019-00642-Z.
[18] Fiorino L, Macillo V, Landolfo R. Shake table tests of a full-scale two-story sheathing-braced cold-formed steel building. Eng Struct 2017;151:633–47. https://doi.org/10.1016/j.engstruct.2017.08.056.
[19] Shi Y, Ran X, Xiao W, Ke K, Xiang Y, Deng R. Experimental and numerical study of the seismic behavior of cold-formed steel walls with diagonal braces. ThinWalled Struct 2021;159. https://doi.org/10.1016/j.tws.2020.107318.
[20] Xiang Y, Zhou X, Shi Y, Zhou J, Ke K, Deng F. Study on the seismic performance of cold-formed thin-walled steel frame with K-shaped braced shear panel. ThinWalled Struct 2023;184. https://doi.org/10.1016/j.tws.2022.110449.
[21] Xing Y, Wang W, Zhao O. Experimental, numerical and analytical studies on full-scale cold-formed steel center-sheathed shear walls subjected to combined loading. Eng Struct 2024;307. https://doi.org/10.1016/j.engstruct.2024.117910.
[22] Wu H, Tu T, Sui L, Yan F, Zhou T. A novel modular CFS composite frame-wall structure: Experimental investigation and numerical analysis. J Constr Steel Res 2024;218. https://doi.org/10.1016/j.jcsr.2024.108702.

[23] Lee AJ, Kelly H, Jagoda R, Rosenfeld A, Stubee E, Colaco J, et al. Affordable, safe housing based on expanded polystyrene (EPS) foam and a cementitious coating. 2006;41 J Mater Sci 2006;41(21):6908–16. https://doi.org/10.1007/S10853-006-0223-4.
[24] Taranu G., Lungu I., Taranu N., Budescu M. Load Carrying Elements and Structural Modular Systems Made of Synthetic Fibres Reinforced Mineral Matrix Composite 2013. https://doi.org/10.4028/www.scientific.net/AEF.8-9.327.
[25] Taranu G, Taranu N, Toma IO. Shake table test of a structural model made of glass fiber reinforced mineral matrix composite. 1st Croat Conf Earthq EngCroCEE 2021. https://doi.org/10.5592/CO/1CroCEE.2021.183.
[26] Liu S, Feng R. Seismic performance of a hybrid system combining hot-rolled steel frame with steel-sheathed cold-formed steel shear wall. Eng Struct 2025;344:121363. https://doi.org/10.1016/J.ENGSTRUCT.2025.121363.
[27] Deng EF, Zong L, Ding Y, Zhang Z, Zhang JF, Shi FW, et al. Seismic performance of mid-to-high rise modular steel construction - A critical review. ThinWalled Struct 2020;155. https://doi.org/10.1016/j.tws.2020.106924.
[28] M.D.R.A.P. P100-1/2013: Cod de proiectare seismic-partea I-Prevederi de proiectare pentru cladiri/ Seismic design code-part I-Design provisions for buildings 2013.
[29] European Comittee for Standardization. EN 1998-1: Eurocode 8: Design of structures for earthquake resistance – Part 1: General rules, seismic actions and rules for buildings. 2004.
[30] Taranu G, Ungureanu V, Nagy Z, Alexa-Stratulat MS, Toma IO, Luca SG. Shake table test and numerical analyses of a thin-walled Cold-Formed Steel structure: Part 1 — Investigation of the structural skeleton without claddings. ThinWalled Struct 2023;182:110258. https://doi.org/10.1016/J.TWS.2022.110258.
[31] Structural Insulated Panel Manufacturer | ThermaSteel Inc n.d. ⟨https://thermasteelinc.com/⟩ (accessed November 4, 2025).
[32] ThermaSteel Resources | Technical Data, Product Info & Installation Guides n.d. ⟨https://thermasteelinc.com/resources/⟩ (accessed November 6, 2025).
[33] Product Specification Manual 2020 “The Professional’s Choice” TM n.d.
[34] Macillo V, Bucciero B, Terracciano MT, Pali T, Fiorino L, Landolfo R. Shaking table tests on cold-formed steel building sheathed with gypsum panels. Ce/Pap 2017;1:2847–56. https://doi.org/10.1002/CEPA.336.
[35] Wang X., Hutchinson T.C. System identification of a mid-rise cold-formed steel framed building under earthquake and post-earthquake fire tests. Eleventh U.S. National Conference on Earthquake Engineering, Los Angeles: 2018.

buildings

MDPI

Article

Nonlinear Seismic Reassessment of an Existing Reinforced Concrete Frame Building: Influence of Masonry Infills Under Intermediate-Depth and Shallow Crustal Earthquake Records

George Taranu

Department of Structural Mechanics, Faculty of Civil Engineering and Building Services, "Gheorghe Asachi" Technical University of Iasi, 700050 Iasi, Romania; george.taranu@academic.tuiasi.ro

Abstract

This paper presents a nonlinear time-history reassessment of an existing reinforced concrete frame building originally designed in 2007 according to the Romanian seismic code P100-1/2006 and re-evaluated under current seismic demand. Two three-dimensional solid finite-element models were developed in ANSYS Workbench 2025 R2: a bare reinforced concrete frame and an infilled frame with masonry panels. A distinctive feature of the modelling strategy is the explicit representation of longitudinal and transverse reinforcement embedded in the concrete solids, which allows direct tracking of steel stress demand and post-cracking load transfer. The models were subjected to bidirectional ground motions from the Vrancea 1977 and 1990 earthquakes and the Türkiye 2023 earthquake, scaled to the P100-1/2013 target spectrum for the investigated site. The results show that masonry infills markedly increase global stiffness and reduce displacement-related demand, with substantially lower roof displacements and interstorey drift measures in the infilled configuration. The bidirectional response remains predominantly translational, while the local stress and inelasticity fields indicate qualitative concentration zones in the frame, masonry panels, and staircase region. Overall, the study shows that masonry infills can strongly modify the actual seismic response of existing reinforced concrete frame buildings and should be considered explicitly in performance assessment.

Keywords: nonlinear time-history; reinforced concrete frames; masonry infills; 3D solid FEM; explicit reinforcement modelling; Vrancea and Türkiye earthquakes

Check for updates

Academic Editors: María Victoria Requena García de la Cruz and Madalena Ponte

Received: 21 February 2026
Revised: 28 March 2026
Accepted: 30 March 2026
Published: 1 April 2026

Copyright: © 2026 by the author. Licensee MDPI, Basel, Switzerland. This article is an open access article distributed under the terms and conditions of the Creative Commons Attribution (CC BY) license.

1. Introduction

The seismic performance of reinforced concrete (RC) frame buildings with masonry infill walls remains a critical issue in regions exposed to strong ground motions, including Romania and Türkiye. The 4 March 1977 Vrancea earthquake caused widespread damage and collapse of RC buildings in Romania, highlighting the vulnerability of mid-rise frame structures with infill walls and limited ductile detailing [1,2]. More recently, the 6 February 2023 Kahramanmaraş earthquake sequence in Türkiye produced severe damage and collapse in many RC frame buildings with masonry infills (Figure 1), showing that this structural typology continues to dominate seismic risk in the current building stock [3–5]. Post-earthquake reconnaissance in Türkiye has repeatedly pointed to brittle infill failure, soft-story mechanisms, and inadequate confinement and detailing in RC members as frequent contributors to damage and collapse [3–5]. These observed damage mechanisms provide important background for the present study, although the current numerical model

is focused primarily on global response and does not explicitly simulate brittle out-of-plane infill collapse mechanisms.



Figure 1. Partially collapsed reinforced concrete apartment buildings with masonry infill walls, Gaziantep, Türkiye, February 2023.

RC frames with masonry infills exhibit complex in-plane and out-of-plane seismic behaviour. Their response depends on infill strength and stiffness, opening layout, RC detailing quality, and the frame–infill interaction. In many design-oriented studies, infills were ignored in structural modelling and treated as non-structural components, although they can significantly modify global dynamic response and damage distribution [6–9]. Research indicates that infills can increase lateral stiffness and strength and reduce global drifts. At the same time, they may induce short-column effects, torsional irregularities, and abrupt stiffness degradation after cracking and crushing [7–10]. Reviews and experimental–numerical studies therefore stress the need for reliable modelling strategies to capture these competing effects in performance-based assessment [6–9].

Over the last two decades, modelling approaches for masonry-infilled RC frames have ranged from equivalent diagonal strut models to detailed finite-element formulations [7,8,10,11]. Simplified macro-models support efficient nonlinear static or dynamic analyses in practice. More refined approaches aim to reproduce cracking, interface sliding, and possible out-of-plane failure modes [7,8,10,11]. Nonlinear static procedures and nonlinear time-history analyses have been used to study ductility capacity, strength degradation, and collapse mechanisms in prototype and existing infilled frames [10–14]. These studies show that including infills can lead to markedly different estimates of seismic demand than bare-frame models, especially for interstorey drifts and the development of plastic mechanisms [10–14].

The influence of infill distribution and mechanical properties on global performance has also been widely investigated. Parametric and case-study analyses indicate that vertical or plan irregularities in infill layout can trigger soft-story or torsional mechanisms. Different masonry types and opening ratios can also modify capacity curves and fragility functions [15–19]. Large-scale experimental campaigns provide key evidence for calibration and validation, and they highlight the coupling between in-plane and out-of-plane actions and the tendency for damage concentration in specific stories [18,20]. These findings are particularly relevant for existing buildings not detailed according to modern capacity-design and confinement rules.

Despite the extensive literature, gaps remain for the seismic reassessment of existing RC frame buildings in Eastern Europe. Many studies address generic prototypes, low-rise buildings, or structures designed either without seismic provisions or according to international standards such as Eurocode 8 [21]. Fewer works focus on buildings designed according to older Romanian provisions such as P100-1/2006 [22], which still represent a substantial share of the current building stock [15,23–25]. Moreover, only a limited

number of studies combine three-dimensional nonlinear time-history analysis of an actual multi-story building with explicit modelling of masonry infills, using recorded motions from both the 1977 Vrancea event and the 2023 Türkiye earthquakes for direct comparison [3,4,20,26]. The influence of infills on drift profiles and on the distribution of local demands in RC members under these two distinct seismotectonic scenarios is therefore not yet well quantified.

The present study addresses these issues through a nonlinear reassessment of an existing multi-story RC frame building designed in 2007 according to P100-1/2006 and located in a high-seismicity region of Romania. The building is analysed using detailed three-dimensional nonlinear finite-element models with and without masonry infills, subjected to recorded ground motions from the 1977 Vrancea earthquake and the 2023 Türkiye earthquake sequence. The time-history inputs are scaled to the current Romanian seismic hazard level (a_g = 0.40 g, P100-1/2013 [27]), whereas the original 2007 design used a_g = 0.32 g with a reduced design spectrum using a behaviour factor q = 4.5. By comparing two structural configurations—bare and infilled RC frames—under three recorded earthquakes (Vrancea 1977, Vrancea 1990, and Türkiye 2023), the study evaluates six nonlinear response-history cases and examines how masonry infills modify the global and local response, including fundamental periods, base shear demand, interstorey drifts, and the development of plastic mechanisms. The results are discussed in relation to observed damage in Romania and Türkiye and to recent research on infilled RC frames [3–6,10–21,26], with the aim of supporting seismic re-evaluation and retrofit decisions for buildings designed to earlier code generations.

The general historical discussion and fatality statistics are not repeated here, since the manuscript focuses on a mechanics-based comparison between code-era design assumptions and present-day nonlinear reassessment under updated hazard levels.

In Romania, seismic activity is largely controlled by the Vrancea intermediate-depth source. During the last century, several large Vrancea earthquakes with moment magnitude above 7 have affected the country. The 1940 event (Mw 7.6, focal depth about 150 km) caused 593 deaths, while the 1977 Vrancea earthquake (Mw 7.5) resulted in 1578 fatalities [28–30]. Figure 2 illustrates representative examples of severe structural damage and partial collapse in Bucharest during the 1977 event [31,32]. The observed differences in casualties between earthquakes and across regions reflect a combination of factors, including magnitude and source characteristics, site effects, urban density, and the prevailing structural typology. Low-rise, horizontally spread building stocks generally imply lower occupant concentration per unit footprint than mid-rise apartment blocks. They can also lead to different damage patterns, because the dominant periods and failure mechanisms differ from those of multi-story RC frames with infills.



Figure 2. Partial collapse of reinforced concrete buildings in Bucharest during the 1977 Vrancea earthquake (**a**)—general view of failure of Wilson apartment building, (**b**)—general view of the collapse of the multi-story Continental building before removal of the wreckage [1].

2. Case-Study Building and Original Seismic Design

The case-study structure is a social housing block with one basement, ground floor, two typical stories and a habitable attic (D + P + 2E + M), located in Panciu (Vrancea County), in one of the highest seismic hazard zones of Romania. In the original design, the site parameters were taken as $a_g = 0.32$ g and $T_c = 1.0$ s according to P100-1/2006. The building belongs to importance class C and importance–exposure class III (γI = 1.0) and was designed as a cast-in-place reinforced concrete (RC) frame system with medium ductility and behaviour factor q = 4.5 [22].

The load-bearing system consists of lamellar RC frames in both principal directions. Beams have a 25 × 60 cm cross-section, while columns include L-, T- and rectangular shapes, typically 25 cm in the minor dimension and 60–100 cm in the major one. Floors are solid RC slabs 20 cm thick, cast monolithically with the beams. The basement slab at −2.65 m is 10 cm thick, while stair flights are 13 cm thick and landings 15 cm thick. The roof is a timber pitched structure supported by RC ring beams at attic level. Foundations are continuous strip footings with RC pedestals at about −3.15 m. Footing widths are 1.60 m (reinforced concrete) and 2.20 m (plain concrete blocks), designed for a conventional bearing pressure of 150 kPa, with subgrade modulus $k_s \approx 20{,}000$ kN/m^3.

The architectural layout is typical for Romanian social housing. The basement contains storage rooms, technical spaces, and circulation areas. The ground floor, upper stories, and attic contain apartments. In plan, the building comprises two 5.10 m bays and seven 3.30 m bays in the longitudinal direction, with a constant storey height of 2.85 m above the basement. The exterior enclosure walls are made of hollow ceramic masonry blocks with 5 cm external thermal insulation. The original calculation notes indicate a masonry thickness of 25 cm for the exterior walls. Interior partitions consist of 25 cm thick masonry walls (the same hollow ceramic block type as the exterior enclosure) and plasterboard walls (1 cm gypsum board on each side of cold-formed steel studs with mineral wool infill). The roof is a pitched timber structure composed of rafters, purlins, posts, and wall plates supported by RC ring beams at attic level. In the original 2007 structural design model developed in Robot Structural Analysis Professional 2006 according to P100-1/2006, the exterior masonry walls were considered only through their gravity load contribution acting on the slabs and were not included as structural members in the seismic analysis. Accordingly, the original seismic model was a bare-frame idealisation and no frame–infill interaction was considered.

Concrete class C16/20 (Bc20) and reinforcing steel grades PC52 and OB37 were specified in the original design documentation. The documented reinforcement diameters include Ø22 and Ø16 bars for PC52 and Ø8 and Ø10 bars for OB37. In general, the larger-diameter PC52 bars were used for the main longitudinal reinforcement of RC members, while the smaller-diameter OB37 bars were used exclusively for transverse reinforcement (stirrups and ties in beams and columns) and were not employed as main longitudinal reinforcement in any structural member. The design followed NP 007-97 [33] for RC frames, STAS 10107/0-90 [34] for concrete members, CR0 and CR1-1-3 for actions, and the seismic code P100-1/2006. In this original modelling approach, the masonry enclosure and partition walls were treated as non-structural components and were not assigned any in-plane lateral stiffness contribution. Modal response spectrum analysis was conducted using the P100-1/2006 design spectrum for the Vrancea region ($a_g = 0.32$ g, $T_c = 1.0$ s). In this original design context, the seismic demand was reduced through the behaviour factor q = 4.5, in line with code-based force design. For this value, the plateau spectral acceleration is of the order of $S_d(T) \approx 0.18$ g in the period range relevant to the fundamental mode, leading to a design base shear of the order of 0.18 times the seismic weight in each principal direction.

These values are reported to document the original force-based design assumptions and should not be interpreted as direct predictors of nonlinear time-history demand.

Figure 3 documents key construction stages and provides visual confirmation of the executed configuration and materials. The images show the slab and beam reinforcement prior to concreting, the erection of RC frames, and the progressive construction of hollow clay masonry infill walls between columns and beams. The final images illustrate completed infills with openings, balcony and stair-core detailing, and the installation of the timber roof structure. These photographs are used primarily as qualitative evidence of the presence, extent, and construction sequence of the infills, which later motivates their explicit inclusion in the nonlinear finite-element models.



Figure 3. Construction stages of the RC frame building (**a**)—slab and beam reinforcement; (**b**,**c**)—erection of RC frames and masonry infills; (**d**)—installation of the timber roof structure.

The foundations consist of continuous strip footings and pedestals under the main columns, as detailed in the foundation plan in Figure 4. Footing widths range between 1.60 m and 2.20 m, depending on column loads and soil bearing capacity. The typical floor formwork plan in Figure 5 shows the arrangement of beams and solid slabs, including stair-core and balcony openings, and was used to verify consistency between architectural and structural layouts and to define tributary areas for gravity loads.

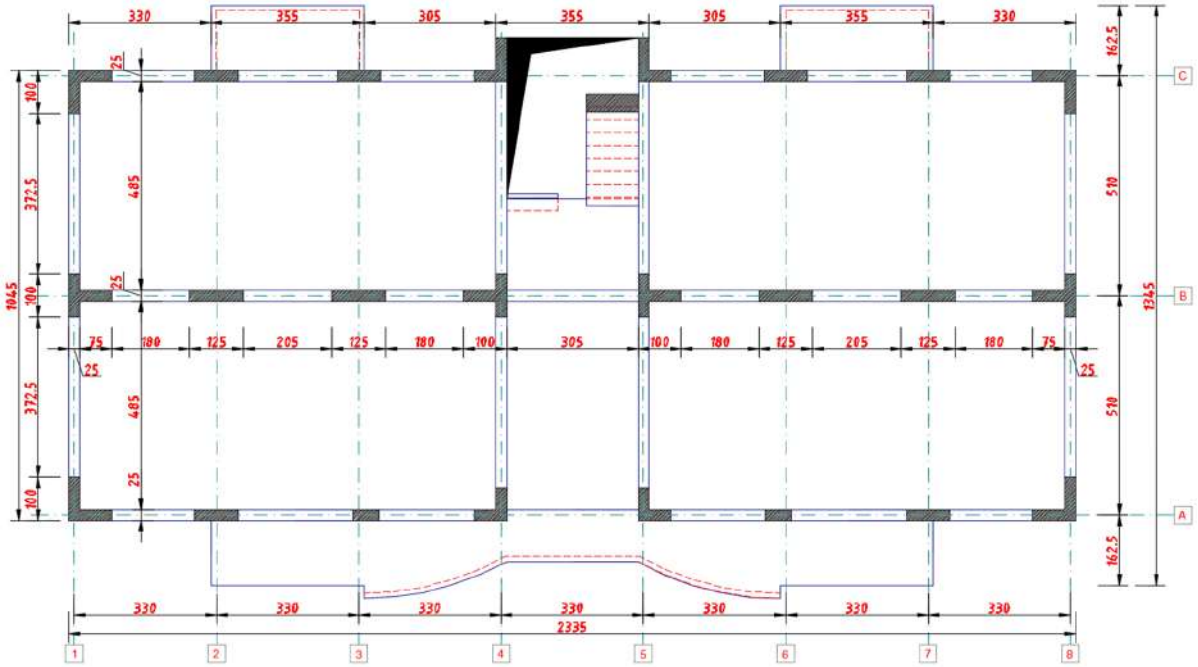

Figure 4. Typical floor formwork plan with beam and slab layout.

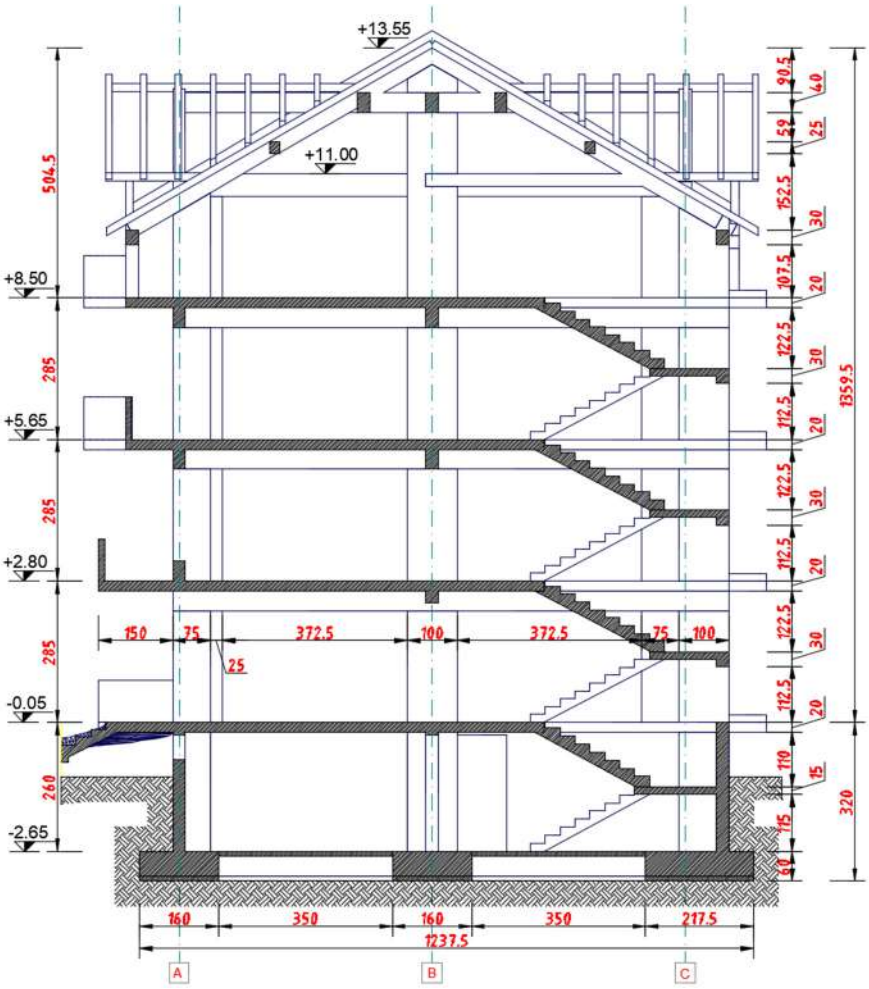

Figure 5. Transversal section.

Table 1 summarises the main subsystems and materials as specified in the original design and clarifies their role in the original analytical model. For the later nonlinear

reassessment, the same material classes are retained as a starting point, while nonlinear constitutive laws are introduced for concrete and explicit reinforcement representations are adopted, consistent with the objectives of time-history simulation.

Table 1. Materials and components in the original building (as designed).

Subsystem/Component	Material (As Specified)	Structural Role in Original Design Model
Beams, columns, slabs, stairs	Reinforced concrete, class C16/20	Primary lateral and gravity system
Reinforcement	Steel types PC52-Ø22, Ø16 and OB37–Ø8, Ø10	Reinforcement of RC members
Foundations	Reinforced concrete	Gravity and seismic load transfer to soil
Exterior infill/envelope walls	25 cm thick hollow ceramic masonry blocks + 5 cm external thermal insulation	Non-structural in original seismic model (gravity load only)
Interior partitions	Masonry partitions and gypsum-board walls (1 cm) on cold-formed steel studs with mineral wool infill	Non-structural in original seismic model (gravity load only)
Roof	Timber pitched roof (rafters, purlins, boarding) supported by RC ring beams	Gravity system; limited in-plane diaphragm action

3. Seismic Actions and Ground Motion Selection

The case-study building is located in the Vrancea seismic region, which controls the hazard for most of Romania. Intermediate-depth events, with focal depths typically between 70 and 150 km, generate long-period motions that can strongly affect mid-rise reinforced concrete frame buildings over large areas, including Bucharest and eastern Romania. The current Romanian seismic code P100-1/2013 specifies the design ground acceleration and elastic response spectrum for this source. For the investigated site, the code parameters are $a_g = 0.40$ g and corner period $T_c = 1.0$ s. These parameters define the target elastic spectrum used to scale the selected ground-motion records for the nonlinear time-history analyses.

3.1. Overview of the Selected Earthquakes

Three recorded earthquakes were selected to represent two distinct seismotectonic scenarios relevant to the present study: intermediate-depth Vrancea motions, which govern seismic hazard in Romania, and a shallow-crustal Turkish motion used as a contrasting scenario. The set includes the 4 March 1977 Vrancea earthquake, the 1990 Vrancea earthquake sequence, and the 6 February 2023 Kahramanmaraş, Türkiye, earthquake sequence. Their main characteristics and the rationale for their inclusion are summarised in Table 2.

Table 2. Summary of the earthquake scenarios considered in the study.

Earthquake Scenario	Date	Magnitude	Seismotectonic Type	Selected Role in the Analysis	Main Relevance to the Study
Vrancea 1977 [35]	4 March 1977	Mw 7.4	Intermediate-depth Vrancea source	Romanian reference motion	Benchmark event for the governing seismic source of the case-study building
Vrancea 1990 [35]	30 May 1990	Mw 6.9	Intermediate-depth Vrancea source	Additional Vrancea motion	Source-consistent comparison within the same Romanian hazard environment
Türkiye 2023 [35,36]	6 February 2023	Mw 7.8	Shallow-crustal strike-slip source	Contrasting comparative motion	Examination of response sensitivity to a different tectonic setting and waveform character

The final compatibility of the selected records with the Romanian seismic demand was imposed subsequently through scaling to the P100-1/2013 target spectrum, as described in Section 3.3.

3.2. Strong-Motion Records

For each earthquake, one accelerogram was selected from the Engineering Strong-Motion (ESM) database, which provides uniformly processed waveforms and metadata for the Euro-Mediterranean region. The selected records were chosen to limit variability due to local site effects and to ensure seismotectonic relevance for the comparative study [35].

- Vrancea 1977: station A39 (Romania), event RO-1977-0001, two horizontal components (HN-N and HN-E).
- Vrancea 1990: station A1856 (Romania), event RO-1990-0003, two horizontal components (HN2 and HN3).
- Türkiye 2023: station 3138 (network TK), event INT-20230206_0000008, two horizontal components (HNN and HNE).

The raw peak ground accelerations at the recording sites are approximately 0.17–0.20 g for Vrancea 1977, 0.011–0.019 g for Vrancea 1990, and 0.75–0.90 g for the 2023 Türkiye record in the horizontal directions (values from the processed ESM records used in this study). Only the two horizontal components were considered in the structural analyses, in agreement with common code practice for ordinary buildings, where the vertical component is typically assessed separately. In the nonlinear analyses, the two horizontal components were applied simultaneously along the global X and Y axes of the numerical model; no SRSS combination was used for the input motion.

Each pair of horizontal components was scaled using a single factor so that the resulting response spectrum matches the P100-1/2013 target elastic spectrum defined by $a_g = 0.40\,\mathrm{g}$ and $T_c = 1.0\,\mathrm{s}$ over the selected period range. This scaling ensures a consistent intensity level for comparing the response under different records and structural configurations. Figure 6 shows the scaled acceleration time histories of the selected records, for both horizontal components (N–S and E–W). The plots highlight the different duration and pulse content of the Vrancea and Türkiye motions, while maintaining a consistent intensity level after scaling.

3.3. Record Processing and Spectral Scaling

All accelerograms were downloaded in processed form from ESM database and then re-processed using the online ITACA (ITalian ACcelerometric Archive v4.0)/ESM (the Engineering Strong-Motion Database) tools to ensure a uniform treatment of all records. A causal band-pass filter with cut-off frequencies 0.2–25 Hz was adopted for all components, following common practice for building-scale analyses in the Euro-Mediterranean region. The raw ESM records had an initial sampling interval of 0.005 s. For the nonlinear time-history analyses, the records were trimmed to the time windows of interest and resampled to a constant time step of $\Delta_t = 0.05$ s in order to reduce computational effort while preserving the response quantities relevant to the investigated structure. The main details of the raw ESM records and of the final scaled inputs used in the numerical model are summarised in Table 3.

Table 3 reports the individual scale factors applied to each record pair and documents the final scaled inputs used in the nonlinear analyses. The adopted three-record suite should not be interpreted as a statistically representative record ensemble, but as a limited comparative set defined to explore the sensitivity of the structural response to different input characteristics under a common reference intensity level.

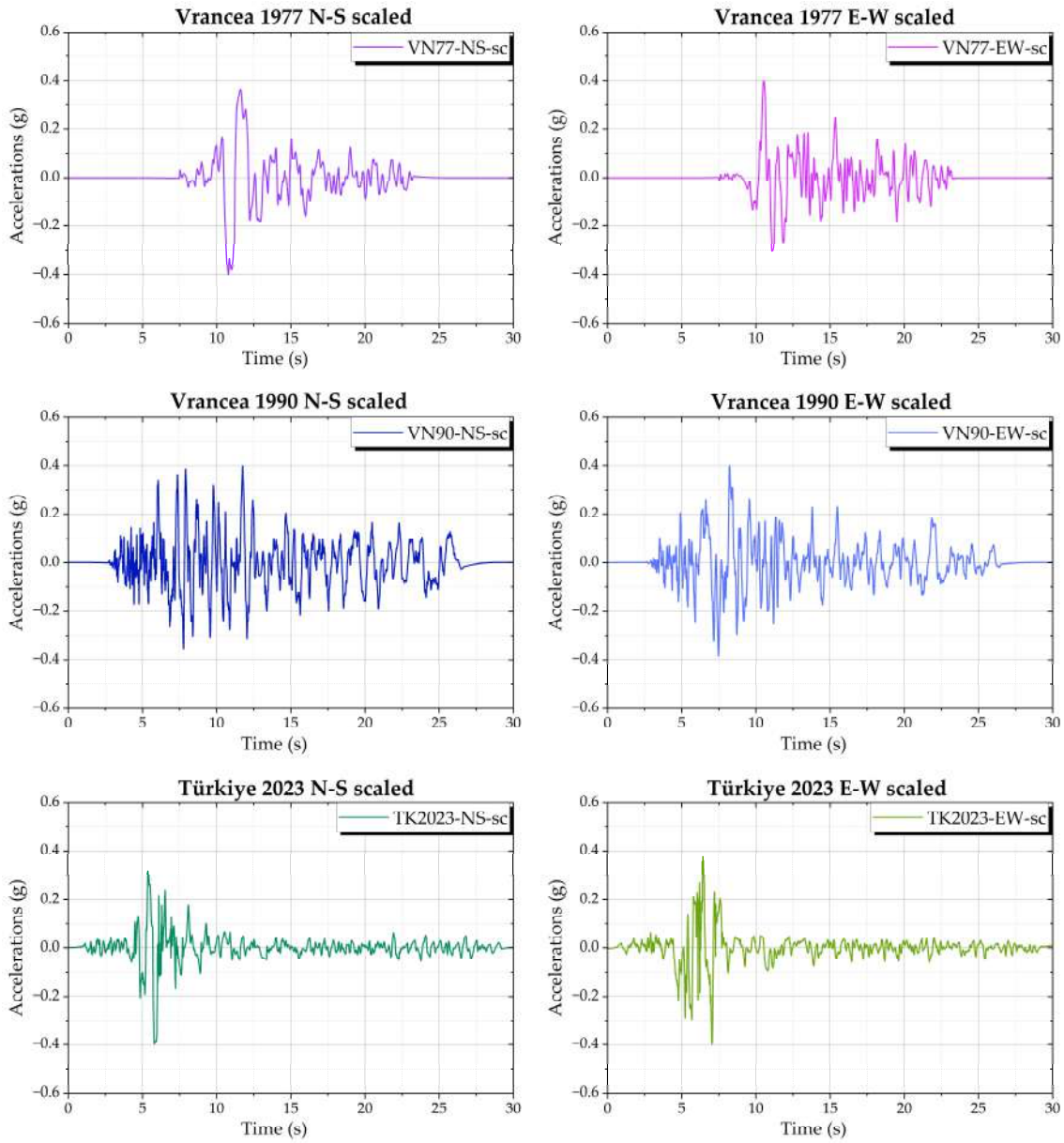

Figure 6. Scaled horizontal acceleration time histories of the selected records: Vrancea 1977 (**top**), Vrancea 1990 (**middle**), and 2023 Türkiye (**bottom**). For each event, the N–S component is shown on the left and the E–W component on the right, after scaling to the P100-1/2013 target elastic spectrum (a_g = 0.40 g, T_c = 1.0 s).

Each pair of horizontal components was scaled by a single factor so that the geometric-mean, 5%-damped elastic response spectrum matches, in an average least-squares sense, the P100-1/2013 elastic target spectrum for the considered site over the period range 0.1–2.0 s. This fixed period band was adopted directly, rather than a relative interval of the form 0.2 T1–1.5 T1, in order to cover the full response range relevant to the investigated structure. The target spectrum corresponds to the local site conditions and the building importance category, with a_g = 0.40 g and T_c = 1.0 s, while the remaining spectral parameters follow the code definitions. Figure 7 compares the resulting record spectra with the P100-1/2013 elastic target and, for reference, with the P100-1/2006 design and elastic spectra.

Table 3. Details of the raw ESM records and the final scaled inputs used in nonlinear time-history analysis.

Record	ESM Event ID/ Station	Components Used in Model	EC8 Site Class	Epicentral Distance (km)	Raw Δ_t (s)	Final Δ_t in Analysis (s)	Final Input Duration (s)	Raw PGA X (g)	Raw PGA Y (g)	Final Scaled PGA X (g)	Final Scaled PGA Y (g)	Scale Factor	Average Misfit of Pair [%]	Maximum Misfit of Pair [%]
Vrancea, Romania 1977	RO-1977-0001/A39–Bucharest-Building Research Institute	HNE → X, HNN → Y	C	164.4	0.005	0.05	18.0	0.1697	0.1979	0.3532	0.3858	1.99	5.2	24.4
Vrancea, Romania 1990	RO-1990-0003 A1856–Istrita	HN2 → X, HN3 → Y	A	78.8	0.005	0.05	15.0	0.0110	0.0192	0.3191	0.4003	20.65	6.3	26.9
Türkiye 2023	INT-20230206_0000008/3138–Hassa Hatay	HNE → X, HNN → Y	B	65.0	0.005	0.05	18.0	0.7595	0.9067	0.2582	0.4006	0.442	3.3	21.0

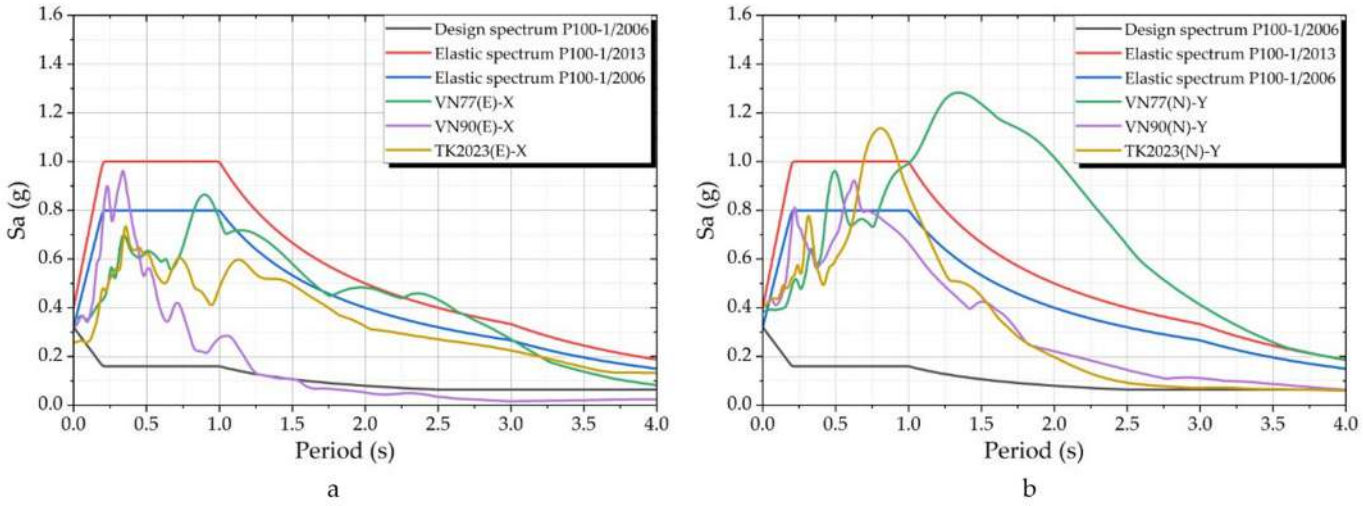

Figure 7. 5%-damped elastic response spectra of the selected and scaled records compared with Romanian code spectra: (**a**) E–W component applied along the global X axis (longitudinal direction of the model); (**b**) N–S component applied along the global Y axis (transversal direction of the model).

Table 3 reports the applied scale factors, component mapping, EC8 site class, raw and scaled PGA values, retained record durations, and the average and maximum spectral misfit values obtained after matching over 0.1–2.0 s. After scaling, the spectral ordinates of the selected records over the period range of interest become comparable and consistent with the reference design level adopted in this study. The selected suite remains limited and does not support broad statistical inference. However, within this three-record comparative set, the main directional trend is stable: the infilled configuration consistently shows lower displacement-related demand than the bare-frame configuration. At the same time, the magnitude of the response reduction and the local inelastic indicators remain record-dependent. The final retained input durations were 18 s for the Vrancea 1977 record, 15 s for the Vrancea 1990 record, and 18 s for the Türkiye 2023 record.

3.4. Justification of the Selected Suite

The selected suite of three records was defined primarily for comparative, scenario-based assessment, on the basis of source type and structural relevance rather than spectral-shape similarity alone. Two records (Vrancea 1977 and Vrancea 1990) represent the intermediate-depth Vrancea source, which governs the seismic hazard for the Romanian case-study site, while the 2023 Türkiye record was included as a contrasting shallow-crustal strike-slip motion in order to examine the effect of a different waveform character on the same RC frame building. To limit variability associated with local site effects, records with documented relatively firm site conditions were preferred. The final spectral compatibility with the Romanian code demand was then imposed through scaling to the P100-1/2013 target spectrum. Accordingly, the adopted suite should be interpreted as a limited comparative set, not as a statistically representative hazard-consistent record ensemble.

The Vrancea 1977 record represents the reference major event that strongly influenced the evolution of Romanian seismic regulations and produced severe damage in building typologies comparable to the case-study structure. The Vrancea 1990 record corresponds to the strongest Vrancea event after 1977 and provides an additional sample from the same source, representative of a lower-magnitude but more frequent scenario that can still generate significant shaking in Bucharest and other urban areas. The VN90 record required the largest scale factor because its recorded intensity was much lower than the adopted reference level. This should not be interpreted directly as the poorest spectral-shape compatibility, which was evaluated separately through the post-scaling misfit indicators

reported in Table 3. Within the present limited comparative suite, VN90 produced the most demanding response in several global measures after scaling. This governing character should therefore be understood in the context of the adopted common target intensity and the scaled waveform characteristics, rather than as a direct intrinsic ranking of the original unscaled source record.

The 2023 Türkiye record introduces a different tectonic context, with shallow strike-slip faulting and waveform features often associated with near-fault effects, including pronounced velocity pulses and relatively shorter effective durations. This event is considered because it caused extensive collapse of reinforced concrete frame buildings with unreinforced masonry infills, which share key vulnerability drivers with many residential buildings in Romania. By scaling all records to the same P100-1/2013 elastic target spectrum, the influence of record-to-record differences in frequency content, duration, and cumulative hysteretic demand on the nonlinear seismic response of the building can be assessed in a consistent framework.

4. Numerical Modelling and Analysis Procedure

The seismic response of the case-study building was analysed in ANSYS Workbench 2025 R2 using detailed three-dimensional finite-element models. The model was developed to capture stiffness degradation, force redistribution, and reinforcement activation after concrete cracking. The load-bearing RC members (beams, columns, slabs, and stair flights) were modelled with 3D solid elements. Two structural configurations were investigated: a bare RC frame and an infilled RC frame, in which masonry panels were introduced in the corresponding bays.

Two analysis levels were used. The first level was intended as a verification step for global dynamic characteristics. The second level provided the final nonlinear time-history response.

- Approach 1 (verification). A modal-based transient workflow was used to check fundamental periods, mode shapes, and global mass participation. This step served as a consistency check of the 3D FE idealisation and as a benchmark against the linear-elastic reference model. Because the response is obtained through modal superposition, the dynamic response remains essentially linear, even if nonlinear constitutive laws are assigned at material level.
- Approach 2 (final). Nonlinear transient time-history analyses were performed by direct time integration. In this approach, nonlinear constitutive laws were activated and reinforcement was introduced explicitly using ANSYS reinforcement capabilities, so that the post-cracking load transfer to steel is represented in a physically consistent manner.

4.1. Linear-Elastic Reference Model in Robot

The original design model prepared in 2007 was developed in Robot Structural Analysis Profesional 2006. Beams and columns were represented by frame elements, while floor slabs were assumed to act as rigid diaphragms. The model was used for code-based checks according to P100-1/2006.

In the present study, the same geometry of the Robot model was recomputed using the elastic response spectrum of P100-1/2013 while keeping the original member cross-sections. The resulting fundamental periods and principal mode shapes served as reference values for the ANSYS models. Linear response-spectrum indicators, such as base-shear and interstorey drift demand, are used later only as a baseline for interpreting the nonlinear time-history results. To document the consistency of the 3D ANSYS idealisation at the linear-elastic level, Table 4 compares the main modal characteristics of the bare-frame model

obtained in Robot and in ANSYS. The comparison is limited to global dynamic properties, since nonlinear time-history analyses were not performed in Robot and the objective of the present study was not an inter-software comparison of nonlinear seismic response.

Table 4. Comparison of the main linear-elastic modal characteristics of the bare RC frame in Robot and ANSYS.

Quantity	Robot	ANSYS, 200 × 200 mm Mesh	Difference vs. Robot	ANSYS, 100 × 100 mm Mesh	Difference vs. Robot
f1 [Hz]	4.1700	4.4669	+7.1%	4.4089	+5.7%
T1 [s]	0.240	0.224	−6.6%	0.227	−5.4%
f2 [Hz]	4.9700	5.5851	+12.4%	5.4851	+10.4%
T2 [s]	0.201	0.179	−11.0%	0.182	−9.4%
f3 [Hz]	5.7000	6.7955	+19.2%	6.6406	+16.5%
T3 [s]	0.175	0.147	−16.1%	0.151	−14.2%
Dominant Y modal mass contribution [%]	75.61	78.42	+3.7%	77.79	+2.9%
Dominant X modal mass contribution [%]	72.72	76.38	+5.0%	73.15	+0.6%

The Robot model was used only as the original linear-elastic design/reference model of the bare RC frame. No nonlinear time-history analyses were carried out in Robot. Therefore, the comparison is limited to the main global modal characteristics of the bare structural system. The dominant Y translational mode corresponds to Mode 1, while the dominant X translational mode corresponds to Mode 3 in the compared models.

4.2. Nonlinear 3D Model in ANSYS

The three-dimensional ANSYS model reproduces the geometry of the building above the basement slab. Only the superstructure was modelled. The real building includes a basement level with reinforced concrete perimeter walls, which was not represented explicitly. Instead, the slab above the basement was adopted as the support plane. All nodes at this level were fully restrained, corresponding to a fixed-base condition provided by a stiff basement box. This idealisation neglects soil–structure interaction and potential basement wall flexibility.

Figure 8 illustrates the numerical geometry used in the analyses. Figure 8a shows the discrete reinforcement layout for the RC members, represented through embedded bar reinforcement. Figure 8b shows the concrete solids for beams, columns, slabs, and stairs in the bare-frame configuration. Figure 8c presents the complete infilled-frame model, where masonry panels are included in the corresponding bays. In the final nonlinear analyses, the RC members were represented with explicit embedded reinforcement, including both longitudinal and transverse bars, as illustrated in Figure 8a. The reinforcement steels PC52 and OB37 were modelled with multilinear isotropic hardening laws, and their main material properties are reported in Table 5.

Concrete beams, columns, slabs, and stair flights were discretised (Figure 9) with three-dimensional solid finite elements (ANSYS SOLID186). A mesh-sensitivity check was carried out for the bare RC frame model in order to verify the adequacy of the adopted discretisation for the main global response quantities. The reference mesh used in the nonlinear analyses employed a nominal global element size of 200 × 200 mm, with local refinement to 100 × 100 mm in selected regions with smaller structural dimensions or higher expected stress gradients. Additional trial analyses with finer elements below

100 × 100 mm led to a major increase in computational effort, with about 300% more elements and nodes, nearly twelve times longer runtimes, and up to about three times larger disc-space demand, even for the bare-frame model. In contrast, the differences in the main global response indicators remained small, of the order of about 2%. Therefore, the adopted mesh was considered a reasonable compromise for full-building nonlinear time-history analyses.

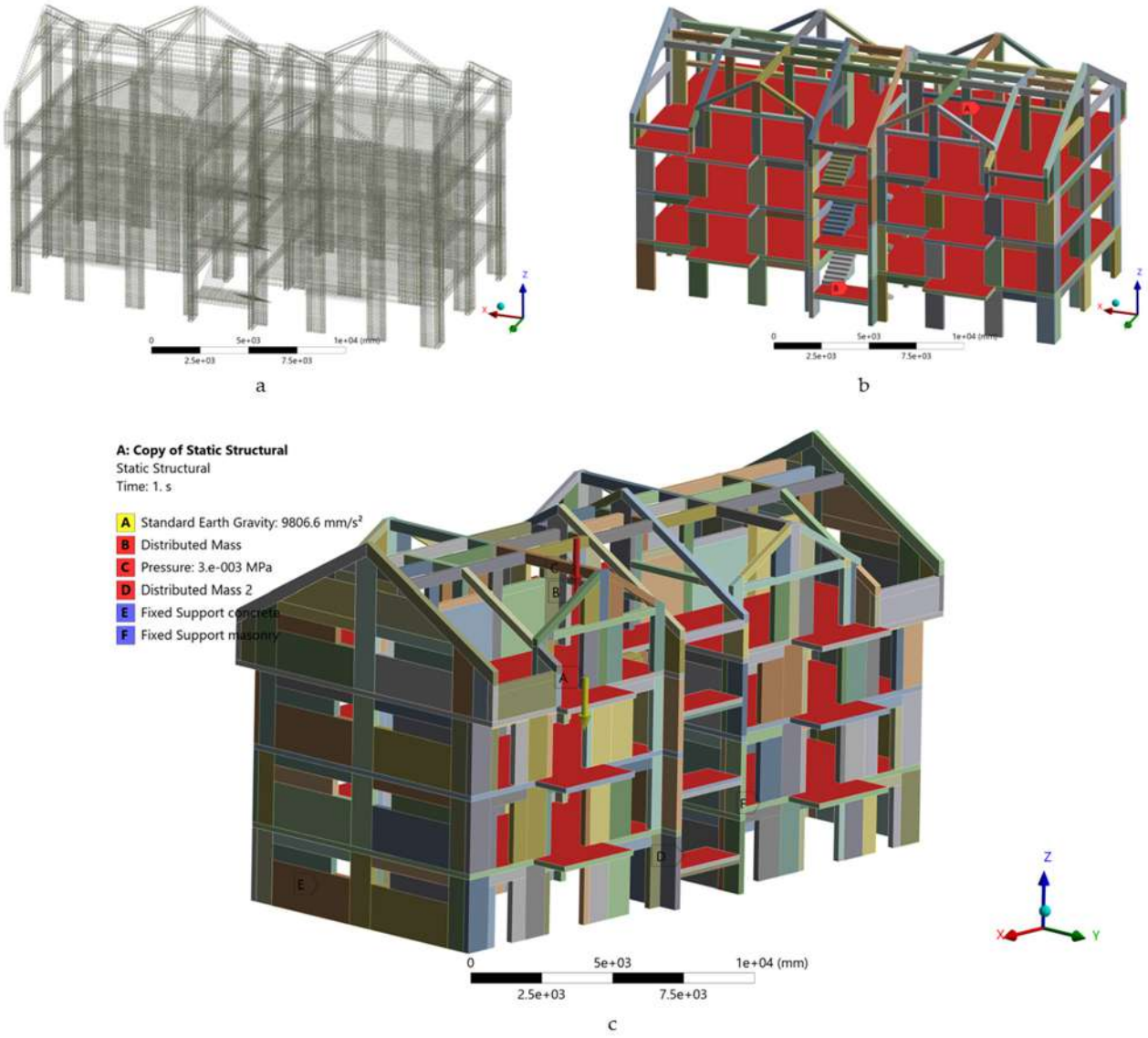

Figure 8. Geometry of the three-dimensional FE models used in ANSYS: (**a**) discrete reinforcement layout for RC members, modelled as embedded bar reinforcement; (**b**) concrete solids for beams, columns, slabs, and stairs (bare-frame configuration); (**c**) complete infilled-frame model, including the RC frame and masonry infill panels.

Local mesh refinement was introduced only in selected beams, columns, and masonry wall regions whose characteristic dimensions were smaller than 200 mm, in order to improve the representation of local stress gradients while keeping the full-building nonlinear response-history analyses computationally tractable. In addition, the refined 100 × 100 mm mesh yielded first-mode frequencies of 4.4089, 5.4851, and 6.6406 Hz, compared with 4.4669, 5.5851, and 6.7955 Hz for the adopted mesh, corresponding to differences of only about 1.3–2.3%. This confirms that the main global dynamic characteristics are only weakly affected by further mesh refinement. For the bare RC frame model, the global mesh was gener-

ated with a nominal element size of 200 mm, resulting in 581,913 nodes and 261,341 solid elements. For the infilled configuration (RC + M), the discretisation was extended to the masonry panels; the executed model contains 295,765 solid elements and 1,017,386 nodes, reflecting the increased computational demand associated with the frame–infill interfaces. A coarser discretisation was retained in regions with smoother stress fields to maintain feasible runtimes for nonlinear time-history analyses. Self-weight was included through material density. Additional permanent loads from finishes and partitions were applied as surface loads on slab elements.

Table 5. Materials properties used in ANSYS.

Property	Concrete (Drucker–Prager)	Masonry Infill (Drucker–Prager)	Reinforcement PC52 (MISO)	Reinforcement OB37 (MISO)
Density ρ [kg/m^3]	2500	1600	7850	7850
Young's modulus E [GPa]	28	2	200	200
Poisson's ratio ν [–]	0.20	0.15	0.30	0.30
Bulk modulus K [GPa]	15.556	0.95238	166.67	166.67
Shear modulus G [GPa]	11.667	0.86957	76.923	76.923
Uniaxial compressive strength f_{cu} [MPa]	16	3	–	–
Uniaxial tensile strength f_{tu} [MPa]	1.8	0.3	–	–
Biaxial compressive strength f_{bc} [MPa]	20	5	–	–
Tensile yield strength $f_{y,t}$ [MPa]	–	–	355	255
Tensile ultimate strength $f_{u,t}$ [MPa]	–	–	510	320
Plasticity model	Drucker–Prager	Drucker–Prager	Multilinear isotropic hardening	Multilinear isotropic hardening

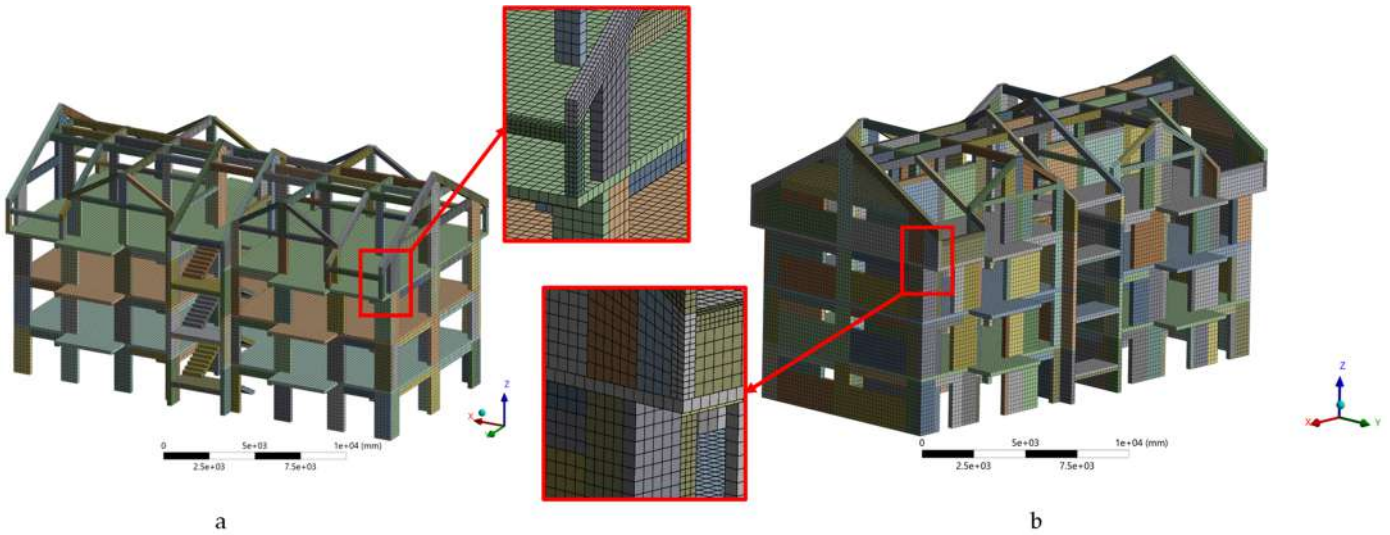

Figure 9. Three-dimensional FE models used in ANSYS and corresponding mesh discretization: (**a**) bare RC frame; (**b**) RC frame with masonry infill panels.

In the nonlinear ANSYS model, the masonry infills were represented as homogenised continuum solids with equivalent properties representative of hollow ceramic masonry (ρ = 1600 kg/m^3, E = 2 GPa, ν = 0.15, f_{cu} = 3 MPa, f_{tu} = 0.3 MPa, f_{bc} = 5 MPa). Mortar joints were not modelled as a separate material phase; their influence was included implicitly within the equivalent masonry properties. Both exterior enclosure walls and interior masonry partition walls (all 25 cm thick hollow ceramic blocks) were discretised as three-dimensional solid finite elements in the RC + M model and therefore contributed their own stiffness, mass, and inertial effects directly. In the bare RC model, these walls were not represented geometrically; instead, their gravity contribution was included through the equivalent slab-level permanent action of 500 kg/m^2. The plasterboard partition walls and the timber roof structure were not discretised explicitly in either model. Their contribution was accounted for through the permanent-load definition, with the plasterboard-related load included in the adopted slab-level permanent action (300 kg/m^2 for RC + M, 500 kg/m^2 for RC).

Material models and key parameters adopted in ANSYS for concrete, masonry infills, and reinforcement are summarised in Table 5. Concrete nonlinear behaviour was represented using a Drucker–Prager plasticity model with a tension cut-off based on the uniaxial tensile strength. Thus, the adopted concrete formulation was not a Concrete Damage Plasticity, smeared-cracking, or Willam–Warnke model. The concrete parameters were assigned from the specified material class of the existing building, namely C16/20 (Bc20), using engineering values suitable for full-building nonlinear solid modelling. No dedicated inverse calibration against material-level cyclic tests was performed for the concrete constitutive law. This modelling choice was adopted to obtain stable nonlinear response under cyclic loading with a limited parameter set, consistent with the scale and objective of the present building-level analyses.

Two reinforcement representations were used, in line with the two analysis levels. In the verification step, reinforcement was not introduced explicitly and the model was used primarily to check global dynamic characteristics. In the final nonlinear analyses, longitudinal and transverse reinforcement was introduced explicitly using the embedded reinforcement capability in ANSYS. In this formulation, the reinforcement bars are embedded within the host concrete solid elements through a kinematic constraint, so that their deformation follows the displacement field of the surrounding concrete. This corresponds to an idealised perfect-bond assumption between steel and concrete. Therefore, no explicit bond–slip interface law was introduced, and local slip transfer was not modelled separately. Reinforcing steels (PC52 and OB37) were modelled using a multilinear isotropic hardening law, and steel demand was assessed through the von Mises equivalent stress. This explicit reinforcement representation was adopted to capture the contribution of steel after concrete cracking and crushing initiate, to track reinforcement stress demand directly, and to avoid an excessively brittle numerical response at the structural level.

4.3. Nonlinear Infilled-Frame Model

The infill-to-frame interaction was modelled using bonded surface-to-surface contact. This assumption was adopted to reflect the execution sequence of the case-study building, in which the masonry panels were erected first and the reinforced-concrete columns and beams were subsequently cast in the dedicated gaps defined by the masonry layout. Compared with conventional infill walls constructed after completion of the RC frame, this sequence is expected to produce a stronger interface engagement and more efficient force transfer between frame and masonry. In the numerical model, this behaviour was idealised as fully bonded contact, with no separation or sliding allowed at the interface and with both compression and shear transferred across the contact surfaces. This choice should

therefore be interpreted as a strongly engaged infill scenario for the analysed building, not as a general interface model for all RC frame–masonry systems. Accordingly, the RC + M results represent an upper-bound estimate of infill stiffness to the global response and a lower-bound estimate of drift demand under the adopted interface idealisation. Masonry infill panels were modelled as continuum solids governed by the same Drucker–Prager framework, using reduced stiffness and strength parameters representative of hollow ceramic masonry. The uniaxial compressive strength, tensile strength, and biaxial compressive strength were taken as $f_c = 3\,\text{MPa}$, $f_t = 0.3\,\text{MPa}$, and $f_{bc} = 5\,\text{MPa}$, respectively, with linear-elastic properties $E = 2\,\text{GPa}$ and $\nu = 0.15$. The nonlinear direct-integration analyses performed for the bare-frame model were then repeated for the infilled configuration under the same set of scaled ground motions, in order to isolate the influence of the masonry panels on both global response and local demand in RC members and reinforcement.

4.4. Damping, Numerical Integration and Loading Protocol

Rayleigh damping was adopted for all transient analyses. The Rayleigh coefficients were calibrated from the eigenvalue analyses of each structural configuration, because the modal properties differ between the bare RC frame and the infilled frame. For the infilled model, the first six eigenfrequencies range from 5.868 to 16.169 Hz, while for the bare RC-frame model (with discrete reinforcement) they range from 4.467 to 14.25 Hz. In both cases, the low-order modes capture a substantial fraction of the effective translational mass (cumulative fractions ≈0.81–0.84 in X and Y).

Rayleigh damping was adopted using mass and stiffness-proportional terms. The modal damping ratio is given by

$$\zeta(\omega) = \frac{\alpha}{2\omega} + \frac{\beta\omega}{2} \tag{1}$$

where α is the mass-proportional coefficient $\left[\text{s}^{-1}\right]$, β is the stiffness-proportional coefficient $[\text{s}]$, and $\omega = 2\pi f$ is the circular frequency. In the executed ANSYS model, the coefficients were introduced as $\alpha = 2.705$ and $\beta = 7.22 \times 10^{-4}$ for the RC + M model and $\alpha = 1.595$ and $\beta = 1.504 \times 10^{-3}$ for the RC model, calibrated to provide approximately 5% damping in the low-mode range governing the global response. The coefficients α and β were obtained by imposing $\zeta(\omega_1) = \zeta(\omega_2) = 0.05$ for two selected modal frequencies.

Nonlinear time-history analyses were performed using implicit direct time integration. For the bare RC frame model, a constant time step $\Delta t = 0.05\,\text{s}$ was adopted over an analysis step end time of 15/18/20 s. For the infilled configuration (RC + M), automatic time stepping was enabled, with an initial time step $\Delta t_0 = 0.005\,\text{s}$, a minimum time step of 0.001 s, and a maximum time step of 0.05 s, to improve robustness when stiffness changes occur due to the frame–infill interaction. A direct solver was used. Geometric nonlinearity was activated in the nonlinear transient analyses (large deflection: On). Nonlinear equilibrium iterations were performed using a Full Newton–Raphson scheme with line search enabled, while stabilisation was kept off. Force convergence was activated with a tolerance of 5% and a minimum reference force of 1 N, whereas the remaining convergence checks (moment, displacement, rotation, and energy) were left program-controlled.

Permanent actions were applied prior to the seismic excitation. Self-weight was introduced through standard earth gravity $\left(g = 9806.6\,\text{mm/s}^2\right)$ using the material densities defined for concrete, reinforcement, and masonry. Non-structural permanent actions (finishes and partitions) were introduced at slab level in two consistent forms: as additional distributed mass and as uniformly distributed permanent pressure loads. Table 6 presents the permanent-action budget adopted for the two structural configurations and the corresponding modelling strategy. In both models, the self-weight of concrete and

reinforcement was introduced explicitly through density and gravity. In the bare RC model, the equivalent slab-level permanent action of 500 kg/m^2 includes floor finishes, screed, plaster, and the contribution of masonry walls not represented explicitly. In the RC + M model, the slab-level value of 300 kg/m^2 includes only floor finishes, screed, and plaster, because the masonry panels were modelled explicitly as solid elements and therefore contributed their own weight and inertial mass directly. Accordingly, the different slab-level values reflect two different representations of masonry mass, not a major difference in total structural weight.

Table 6. Mass budget and modelling representation of permanent actions in the two numerical models.

Load Component	Bare RC Model	Bare RC Model	RC + M Model	RC + M Model	How It Was Defined in the Model
	kg/m^2	kN/m^2	kg/m^2	kN/m^2	
Floor finishes	60	0.60	60	0.60	Added at slab level as equivalent distributed mass and as uniform permanent pressure
Screed and levelling layers	180	1.80	180	1.80	Added at slab level as equivalent distributed mass and as uniform permanent pressure
Plaster/ceiling finishing	60	0.60	60	0.60	Added at slab level as equivalent distributed mass and as uniform permanent pressure
Exterior and interior masonry walls not modelled explicitly	200	2.00	0	0	Included only in the bare RC model as equivalent slab-level mass and pressure, because walls were not represented explicitly
Masonry infill walls modelled explicitly as solids	0	0	explicit	explicit	In the RC + M model, wall self-weight and inertial mass were introduced directly through masonry solid elements, density ρ = 1600 kg/m^3
Total slab-level equivalent permanent action	500	5.00	300	3.00	Same values applied both as distributed mass and as uniform permanent pressure in the gravity pre-step

Note: For the RC + M model, the masonry walls were not added again as slab-level equivalent mass, because they were represented explicitly by solid elements. For a 25 cm-thick masonry wall with density 1600 kg/m^3 and storey height 2.85 m, the corresponding self-weight is approximately 1140 kg/m, i.e., 11.18 kN/m.

The seismic input was imposed as base acceleration at the restrained support plane (the slab above the basement), with the two horizontal components applied simultaneously along the global X and Y axes. Thus, the final analyses were performed as bidirectional nonlinear time-history analyses, rather than by SRSS combination of separate unidirectional responses. For each structural configuration (bare and infilled), three ground-motion cases were analysed (Vrancea 1977, Vrancea 1990, and Türkiye 2023), and each record was scaled to the target intensity level $a_g = 0.40$ g as described in Section 3.

4.5. Response Quantities and Post-Processing

The response assessment was performed consistently for both structural configurations (bare RC frame and RC frame with masonry infill) and for all three input motions (Vrancea 1977, Vrancea 1990, and Türkiye 2023), scaled to $a_g = 0.40$ g. The global coordinate system follows the numerical model convention. The X axis is the longitudinal building direction and the Y axis is the transversal direction. The two horizontal acceleration components were applied simultaneously along X and Y.

The primary kinematic outputs were storey displacements and interstorey drifts along the transversal direction, because the lateral response discussed in this section refers to Y. Absolute nodal displacements $u_i(t)$ were extracted at representative points for the basement and each storey. The reporting levels are denoted as B, $S1$, $S2$, $S3$, and roof R (level 4). Interstorey drift histories were computed from displacement differences between consecutive levels as follows:

$$\Delta_{\mathrm{i}}(t) = u_i(t) - u_{i-1}(t) \tag{2}$$

The corresponding drift ratios were obtained as follows:

$$\theta_i(t) = \frac{\Delta_i(t)}{H_i} \tag{3}$$

where $H_i = 2.85$ m for all storeys except the top level. For the fourth level, the storey height was 4.00 m.

Global force–deformation behaviour was quantified through base shear–roof displacement hysteresis loops. The base shear in the transversal direction, $V_b(t)$, was taken from the reaction force at the fixed support plane, consistent with the global axes shown in the model. The roof displacement $u_R(t)$ was the total displacement at level 4 along Y. The hysteresis curves V_b—u_R were plotted for each analysis case to compare stiffness, strength, and energy dissipation between the bare and infilled frames.

Peak demand measures were reported using absolute maxima over the full record. For each response history $x(t)$, the peak was defined as $\max \mid x(t) \mid$. The reported peaks were

$$u_{\max} = \max \mid u(t) \mid, \Delta_{\max} = \max \mid \Delta(t) \mid, V_{b,\max} = \max \mid V_b(t) \mid, M_{b,\max} = \max \mid M_b(t) \mid$$

where $M_b(t)$ is the base moment component taken from the support reactions, in the global system, in agreement with the transversal action effects. Alongside these peak values, the raw time histories were retained for traceability and for identifying the time instants associated with peak responses.

To characterise the nonlinear response mechanisms, field outputs were extracted at the time instants associated with critical peaks and were reported as contour plots. The adopted fields included maximum and minimum principal stresses in the continuum materials, equivalent plastic strain as an indicator of inelastic demand, and reinforcement stress measures for the steel bars. Reinforcement demand was reported through peak stresses in the steel domains, to highlight the most stressed zones under each ground motion and to enable direct comparisons between the bare and infilled configurations. These plots were complemented by the displacement fields along X and Y to confirm the deformation patterns and the directional consistency of the response.

All outputs were extracted in a consistent manner across cases, using the same level definitions, sign conventions, and peak metrics. This ensured that differences between RC and RC + M models reflect physical effects of stiffness, mass, and interaction mechanisms, rather than changes in post-processing rules.

As illustrated in Figure 10, response quantities were extracted at predefined points along the building height in the global coordinate system (X longitudinal, Y transversal). The results reported in Section 5 refer to the transversal response (Y) at these locations.

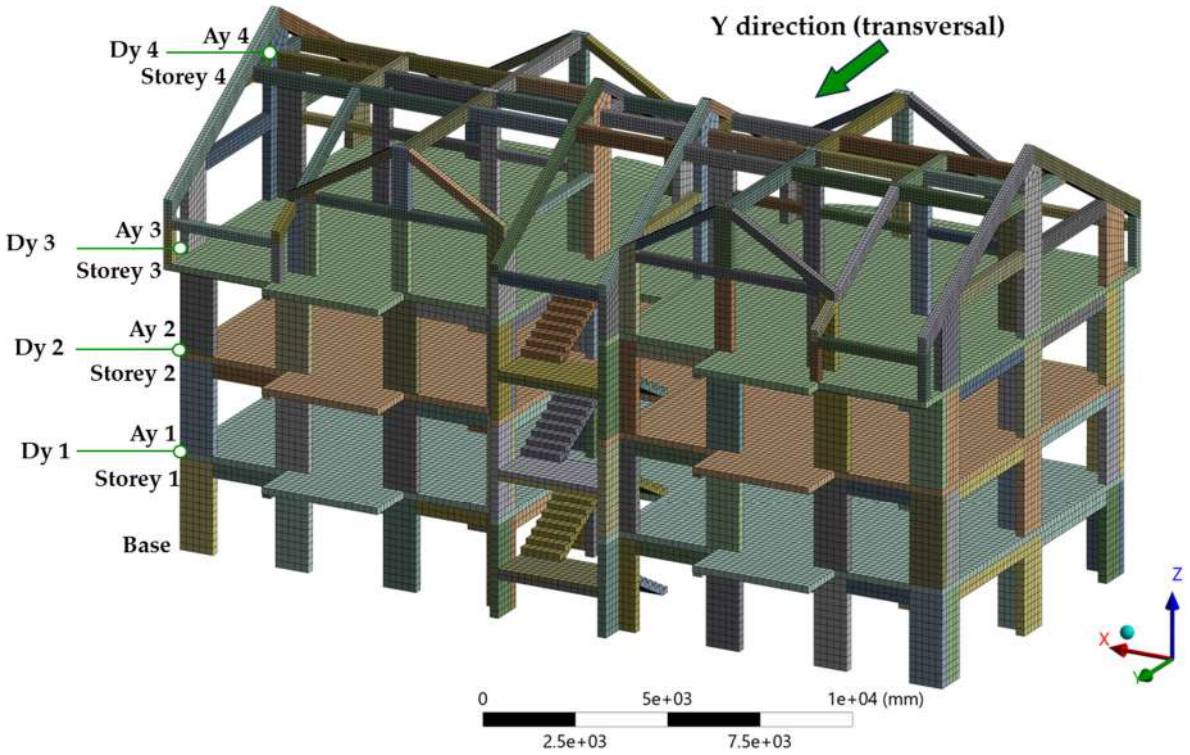

Figure 10. FE model showing the global coordinate system and the marked points used to extract transversal (Y) displacements and accelerations.

5. Results and Discussion

All response quantities were extracted consistently with the global axes used in the FE model, with X = longitudinal and Y = transversal. The two horizontal components were applied simultaneously. The results below focus on the transversal (Y) response because it governs the reported base shear–roof displacement hysteresis and the interstorey drift checks.

5.1. Modal Analysis Results

A linear eigenvalue (modal) analysis was first performed for both structural configurations to characterise the dynamic properties that govern the subsequent nonlinear time-history response. The same global coordinate system was used as in the transient analyses, with X taken as the longitudinal direction and Y as the transversal direction. Modal properties are reported in terms of natural frequency, period, and translational mass participation in X and Y.

Table 7 summarises the first three modes for the bare RC frame and the infilled configuration (RC + M). The periods were computed as $T = 1/f$. For the bare RC frame, the first three natural frequencies were 4.4669 Hz, 5.5851 Hz, and 6.7955 Hz, corresponding to periods of 0.2239 s, 0.1790 s, and 0.1472 s. For RC + M, the corresponding frequencies increased to 5.8680 Hz, 6.9433 Hz, and 7.5634 Hz, with periods of 0.1704 s, 0.1440 s, and 0.1322 s. This systematic increase indicates a higher global stiffness when masonry infill panels are included, as expected from the added in-plane stiffness and the interaction between infills and the RC frame.

The effective modal mass confirms that the response is dominated by global translations in the low modes. Mode 1 is primarily a transversal (Y) translation for both models, with effective mass of about 939.35 t (RC) and 945.16 t (RC + M), and corresponding Y mass ratios of 0.784 and 0.776. Mode 3 is primarily a longitudinal (X) translation, with effective mass of about 914.91 t (RC) and 918.73 t (RC + M), and X mass ratios of 0.764 and 0.754.

Mode 2 is torsional, which is reflected by its comparatively small translational mass ratios in both directions. Therefore, the dominant lateral translational behaviour is captured by modes 1 and 3, while mode 2 mainly describes twisting of the structural system.

Table 7. Modal properties and translational mass participation (X and Y) for the bare RC frame and the RC frame with masonry infills (RC + M).

Model	Mode	Frequency, f (Hz)	Period, T (s)	Effective Mass X (t)	Ratio X	Effective Mass Y (t)	Ratio Y
RC	1	4.4669	0.2239	0.02	1.607×10^{-5}	939.35	0.784
RC	2	5.5851	0.1790	29.06	0.024	3.9574×10^{-3}	3.3016×10^{-6}
RC	3	6.7955	0.1472	914.91	0.764	0.03	2.2394×10^{-5}
RC + M	1	5.8680	0.1704	0.02	1.9853×10^{-5}	945.16	0.776
RC + M	2	6.9433	0.1440	63.41	0.052	0.15	1.2567×10^{-4}
RC + M	3	7.5634	0.1322	918.73	0.754	2.9724×10^{-3}	2.4390×10^{-6}

Figure 11 shows the first three mode shapes (total deformation) for both models. The deformed shapes are in line with the mass-participation results, with a predominantly translational fundamental mode, a torsional second mode, and a higher translational mode in the orthogonal direction. These modal characteristics provide the baseline for interpreting the differences observed later in roof displacement, interstorey drift, and base reaction demands under the bidirectional seismic input.

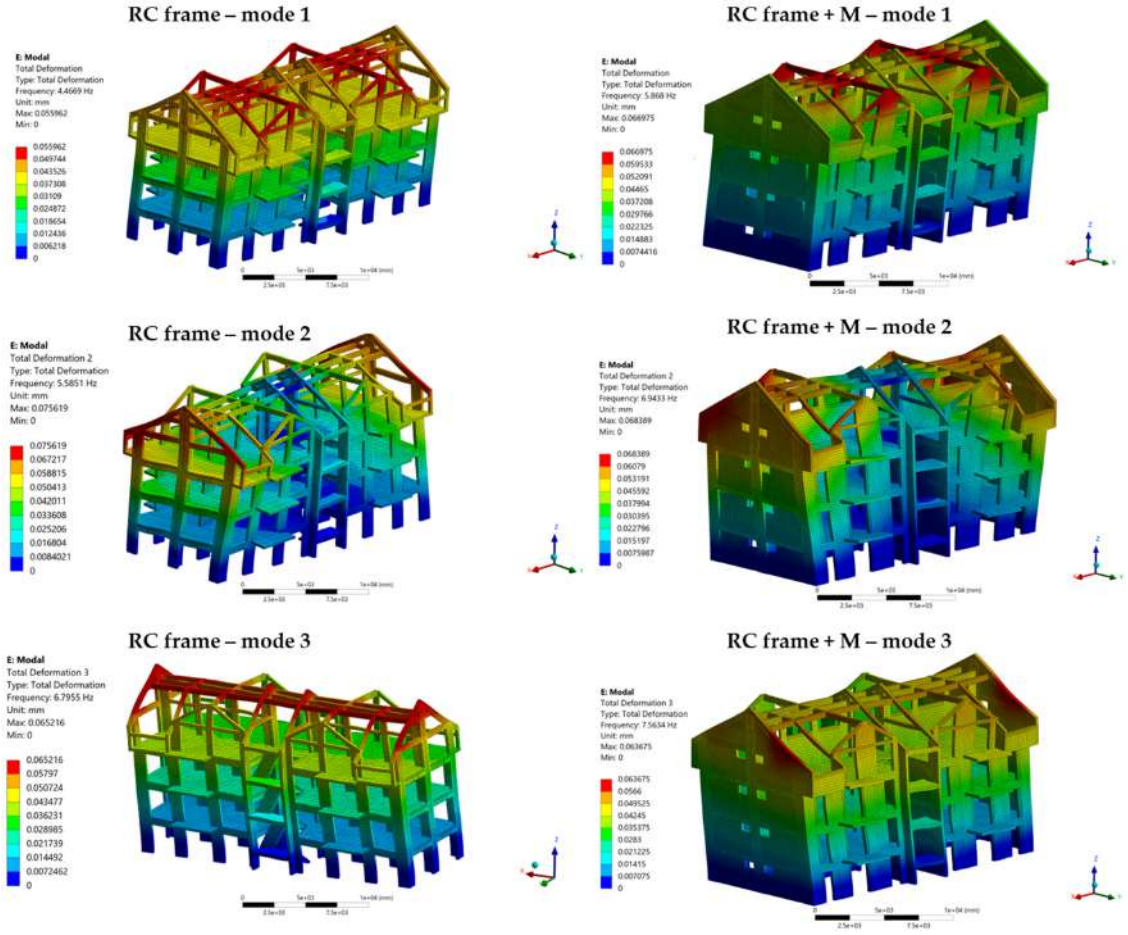

Figure 11. First three vibration mode shapes (total deformation) from the modal analysis: bare RC frame and RC frame with masonry infills, RC + M.

5.2. Peak Roof Displacements and Relative Interstorey Displacements

The peak lateral response was evaluated along the transversal direction (Y) using floor displacements relative to the base, $u_i(t)$, extracted at the reporting levels *B*, *S*1, *S*2, *S*3, and roof *R*. Interstorey drift increments $\Delta_i(t)$ and drift ratios $\theta_i(t)$ were computed as defined in Section 4.5. The discussion below focuses on the governing storeys *B*–*S*1 and *S*1–*S*2, for which the storey height is $H = 2.85\,\text{m} = 2850\,\text{mm}$.

Table 8 summarises the peak roof displacement u_r, the maximum drift increment $\Delta_{\max}$, the governing storey where $\Delta_{\max}$ occurs, and the resulting peak drift ratio $\theta_{\max}$. The infilled configuration (RC + M) exhibits a marked reduction in both u_r and $\Delta_{\max}$ for all three input motions. The largest demand occurs for VN90, where the bare RC frame reaches $u_r = 14.26\,\text{mm}$ and $\theta_{\max} = 0.1733\%$, while RC + M remains limited to $u_r = 3.38\,\text{mm}$ and $\theta_{\max} = 0.0407\%$. Using the admissible drift limits typically adopted from P100-1/2013 (SLS $\theta_{\text{adm}} = 0.5\%$ and ULS $\theta_{\text{adm}} = 2.5\%$, reported here as conservative reference values), all computed drifts remain well below both thresholds.

Table 8. Peak displacements and interstorey drift increments along Y.

Model	Record	u_r (mm)	$\Delta_{\max}$ (mm)	Governing Storey (For $\Delta_{\max}$)	$\theta_{max}=\frac{\Delta_{max}}{2850}$	θ_{max} (%)	θ_{adm} SLS (%)	θ_{adm} ULS (%)
RC + M	VN77	2.74	0.92	B–S1 or S1–S2	0.000323	0.0323	0.5	2.5
RC + M	VN90	3.38	1.16	S1–S2	0.000407	0.0407		
RC + M	TK2023	3.03	1.02	S1–S2	0.000358	0.0358		
RC	VN77	9.87	3.35	S1–S2	0.001175	0.1175		
RC	VN90	14.26	4.94	S1–S2	0.001733	0.1733		
RC	TK2023	9.93	3.35	S1–S2	0.001175	0.1175		

Note: θ_{adm} depends on the type of non-structural components; the conservative value $\theta_{\text{adm}} = 0.5\%$ is reported here.

Deformation patterns at peak roof response confirm global sway in the Y direction. For the bare RC frame, the displacement contours show a more flexible response with larger storey translations and a clearer drift concentration in the lower storeys, reflecting the governing S1–S2 drift increments reported in Table 8 (Figure 12). In contrast, the RC + M configuration develops a stiffer global response, with reduced displacement amplitudes and a more restrained deformation field due to the in-plane contribution of the masonry infills (Figure 13).

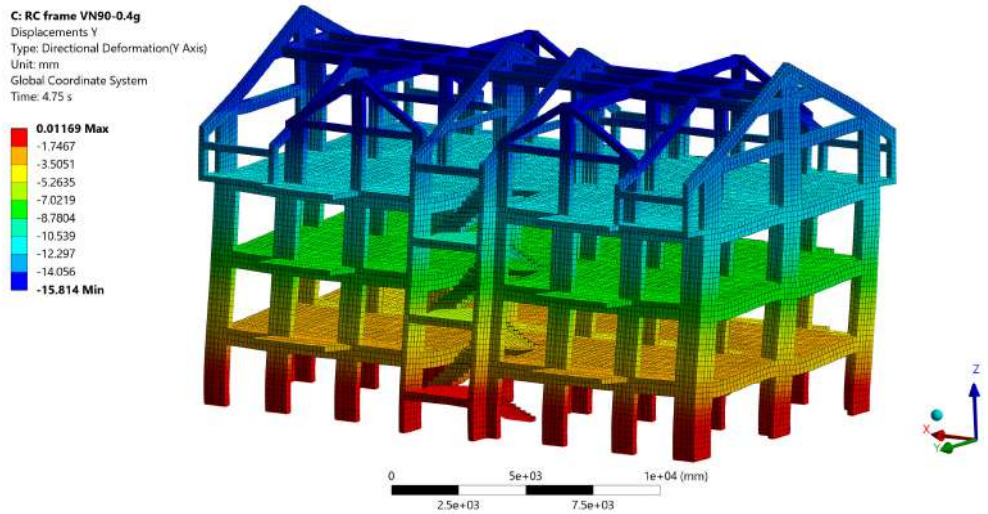

Figure 12. Transversal (Y) displacement contours (Directional Deformation, u_Y) at the time of peak roof response for the bare RC frame–VN90 scenario.

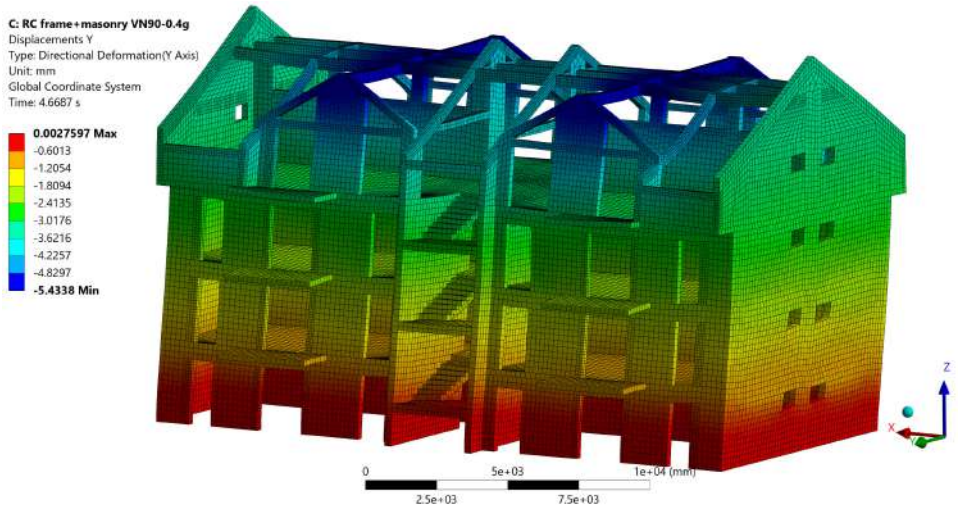

Figure 13. Transversal (Y) displacement contours (Directional Deformation, u_Y) at the time of peak roof response for the RC frame with masonry infills, RC + M–VN90 scenario.

The peak displacement profiles along height provide a compact comparison across all records (Figure 14). For each motion, the peak transversal displacement increases monotonically from *B* to *R*, which indicates sway-dominated response. The RC + M curves remain clustered in a narrow band, with roof peaks limited to about 2.7–3.4 mm, while the bare RC frame reaches about 9.9–14.3 mm. The separation between the RC and RC + M profiles at every level quantifies the stiffness increase introduced by the infills and explains the reduction in drift demand reported in Table 8.

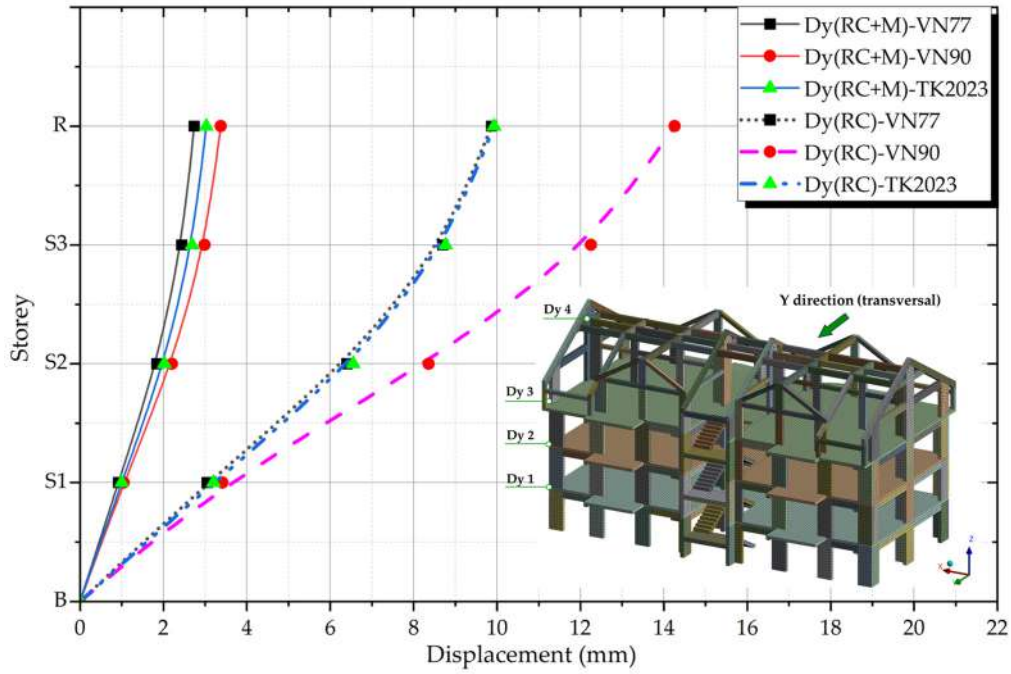

Figure 14. Peak floor displacements along the transversal direction (Y) for RC and RC + M under VN77, VN90, and TK2023, reported at levels B, S1, S2, S3, and roof R; inset shows the monitoring points and the global coordinate system.

To complement the detailed discussion of the transversal response, Table 9 summarises the peak bidirectional displacement response under simultaneous X–Y excitation. The results show that the peak roof displacement is larger in the Y direction for all analysed cases (Figure 15), both for the bare RC frame and for the RC + M model, confirming that

the transversal direction governs the global translational roof response. In contrast, the maximum relative interstorey displacement is more direction-dependent: for the bare RC frame, the largest values remain associated with the Y direction, whereas in the RC + M configuration the maximum relative displacement becomes slightly larger in the X direction. The torsional-response indicator is evaluated as

$$\phi_{z,max} = \frac{|Y_2 - Y_1|}{L_X} \quad (4)$$

and the relative torsional indicator was defined as

$$\eta_t = \frac{|Y_2 - Y_1|}{u_{Y,\,max}} \times 100 \quad (5)$$

where Y_1 and Y_2 are the transversal displacements of the two opposite roof-edge points, POI 1 and POI 2, L_X = 23.35 m is their plan distance, and $u_{Y,\max}$ is the peak global roof displacement in the transversal direction. Thus, $\phi_{z,\max}$ estimates the roof rotation about the vertical axis, while η_t expresses the torsional component relative to the dominant translational roof response. Both indicators remain small in all six cases, indicating a predominantly translational roof response. However, the bare RC model consistently develops larger torsional response than the RC + M configuration, which suggests that the masonry infills not only reduce the global displacement demand but also limit the torsional component of the roof motion.

Table 9. Compact summary of the peak bidirectional displacement response under simultaneous X–Y excitation, including maximum roof displacements, maximum relative interstorey displacements, edge-point transversal displacements at roof level (Y_1 and Y_2), and roof torsional-response indicators.

Record	Model	$u_{X,max}$ [mm]	$u_{Y,max}$ [mm]	$\Delta_{X,max}$ [mm]	$\Delta_{Y,max}$ [mm]	Y_1 [mm]	Y_2 [mm]	$\phi_{Z,\max}$ [mrad]	η_t [%]
VN77	RC + M	1.97	2.74	1.49	0.92	2.43	2.35	0.003	2.92
VN77	RC	4.17	9.87	0.57	3.35	8.67	8.14	0.023	5.37
VN90	RC + M	1.70	3.38	2.09	1.16	2.98	2.9	0.003	2.37
VN90	RC	5.36	14.26	0.44	4.94	12.22	11.77	0.019	3.16
TK2023	RC + M	1.63	3.03	1.62	1.02	2.68	2.84	0.007	5.28
TK2023	RC	4.54	9.93	0.49	3.35	8.75	9.48	0.031	7.35

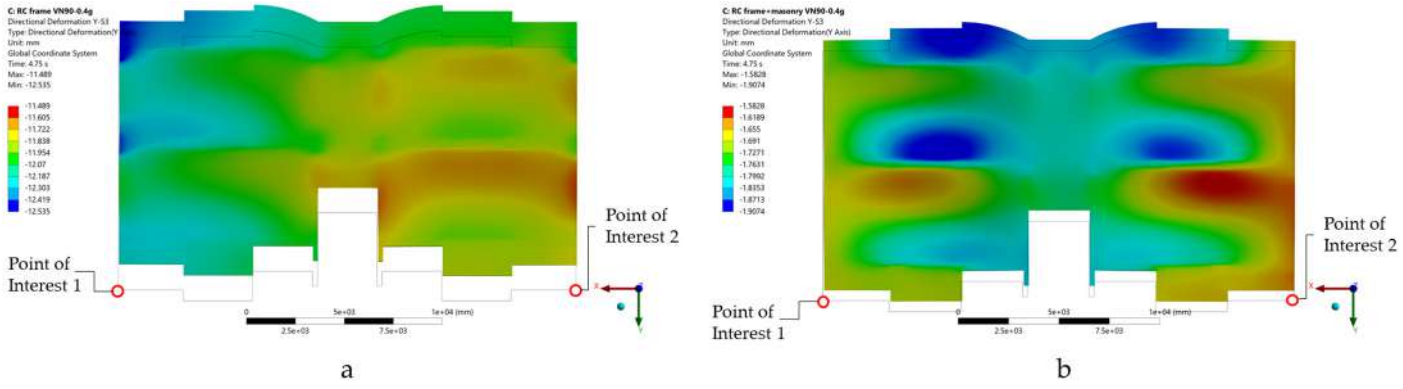

Figure 15. Directional displacement in Y direction: (**a**) RC frame VN90; (**b**) RC frame + masonry (VN90).

For completeness, Figure 16 compares the roof displacement time histories $u_R(t)$ (Dy4, Y) for both configurations and all three records, illustrating the consistent amplitude reduction produced by the infills, most pronounced for VN90.

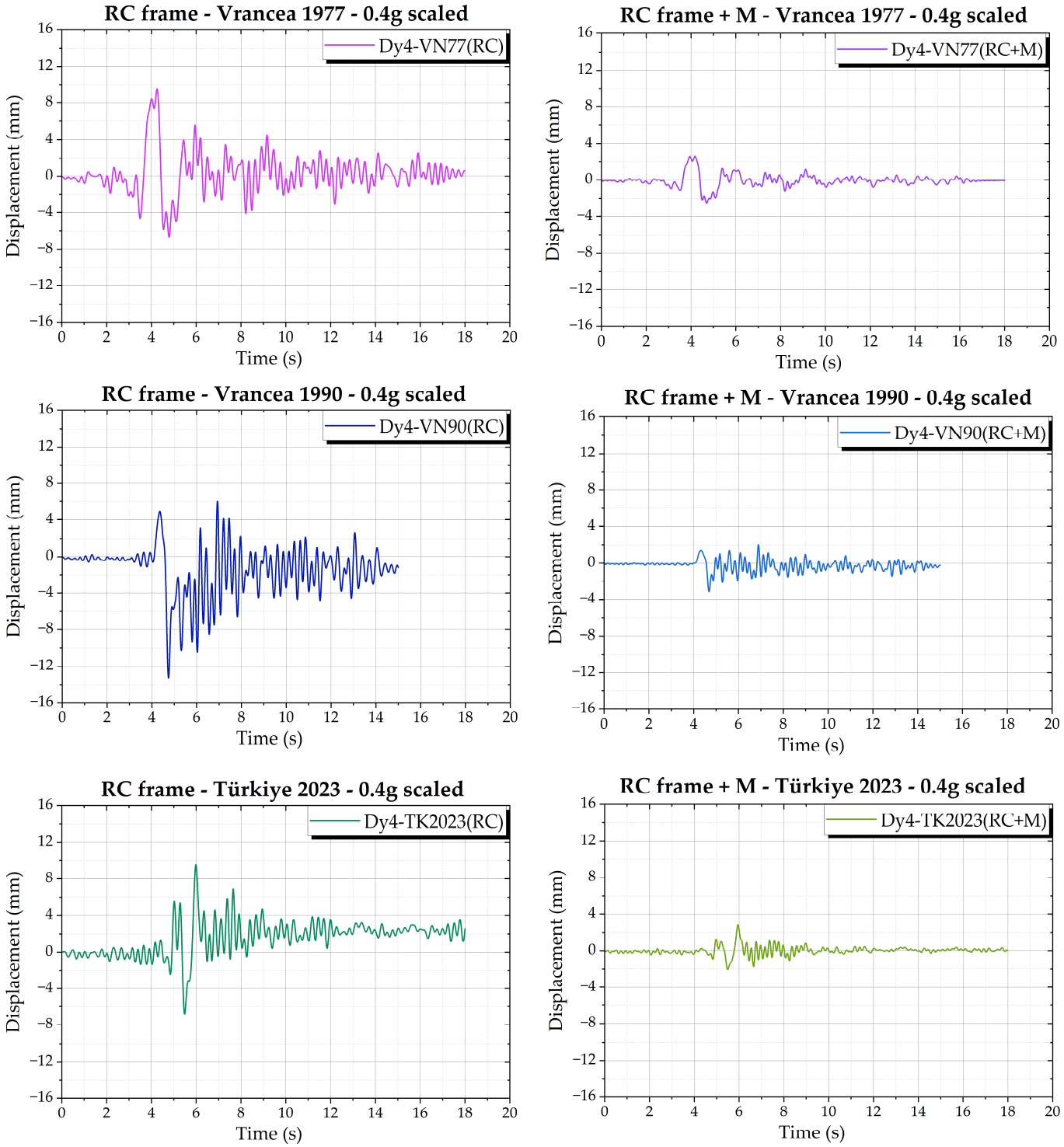

Figure 16. Roof displacement time histories along Y (Dy4) for the bare RC frame (**left** column) and RC + M (**right** column) under VN77, VN90, and TK2023 (0.4 g scaled).

5.3. Peak Floor Accelerations

Peak absolute accelerations in the transversal direction were extracted at the same reporting levels used for displacements, namely Base (B), S1, S2, S3, and roof R. For each record and level, the reported value is the absolute maximum of the acceleration time history, $A_{Y,\max} = \max_t \mid a_y(t) \mid$, evaluated over the full record duration.

Table 10 summarises the results in both mm/s^2 and g. A consistent height amplification is observed for both structural configurations, with the roof governing the peak accelerations in all cases. For the infilled configuration (RC + M), the roof peaks range from 710 to 2068 mm/s^2 (0.072–0.211 g), depending on the input record. For the bare frame (RC), the roof demand is substantially higher, reaching 4801 mm/s^2 (0.490 g) under VN90. This trend supports the displacement results, where the bare frame shows a more flexible global response and therefore develops larger vibration amplitudes under the same bidirectional excitation, while the masonry infills increase lateral stiffness and reduce global sway and associated acceleration amplification.

Table 10. Peak floor accelerations along Y, $A_{Y,\max}$.

Level	RC + M–VN77		RC + M–VN90		RC + M–TK2023		RC–VN77		RC–VN90		RC–TK2023	
	(mm/s^2)	(g)	(mm/s^2)	(g)	(mm/s^2)	(g)	(mm/s^2)	(g)	(mm/s^2)	(g)	(mm/s^2)	(g)
Base	0	0	0	0	0	0	0	0	0	0	0	0
S1	225	0.023	600	0.061	411	0.042	465	0.047	1458	0.149	633	0.065
S2	445	0.045	1300	0.133	878	0.090	1154	0.118	2884	0.294	1616	0.165
S3	620	0.063	1803	0.184	1206	0.123	1705	0.174	4072	0.415	2450	0.250
R	710	0.072	2068	0.211	1379	0.141	2012	0.205	4801	0.490	2907	0.296

The bidirectional roof acceleration response also confirms that the seismic demand is not governed exclusively by the transversal direction. The peak roof acceleration along X reaches 0.072 g, 0.211 g, and 0.141 g for the RC + M model under VN77, VN90, and TK2023, respectively, and 0.205 g, 0.490 g, and 0.296 g for the bare RC model. For comparison, the corresponding peak values along Y are 0.071 g, 0.233 g, and 0.116 g for RC + M, and 0.200 g, 0.425 g, and 0.202 g for RC. These results show that, unlike the peak roof displacements, the acceleration response remains more balanced between the two horizontal directions.

Figure 17 compares the roof acceleration histories (Ay 4) for RC and RC + M under VN77, VN90, and TK2023 (0.4 g scaled). The VN90 input produces the largest roof accelerations, and the reduction provided by infills is visible as a clear drop in peak amplitudes and a narrower response envelope for RC + M across all three records.

5.4. Base Reactions and Global Force–Deformation Response

The global lateral behaviour was further assessed using (i) the support reactions at the fixed base and (ii) base shear–roof displacement hysteresis loops in the transversal direction. The base shear, F_Y, was taken from the reaction resultants at the constrained support component, consistent with the global axes. The roof displacement was taken as the Y - direction displacement at level R (Dy4). The F_Y—Dy4 loops (Figure 18) provide a compact measure of global stiffness, strength demand, and energy dissipation under the bidirectional input.

Figure 18 shows that the bare RC frame develops substantially larger lateral excursions, with wider loops and a lower initial slope, indicating a more flexible global response. The infilled configuration (RC + M) exhibits a much steeper response with markedly reduced displacement demand, and the loops remain narrow, in agreement with the increased in-plane stiffness contribution of the masonry infills. However, this beneficial effect does

not apply uniformly to all response measures. As shown in Table 11, the peak absolute transversal base shear F_Y is slightly higher in the RC + M model than in the bare RC model for all three records. This indicates that the infills reduce global translations and drift demand but may also attract comparable or somewhat larger base shear because of the increased lateral stiffness of the system.

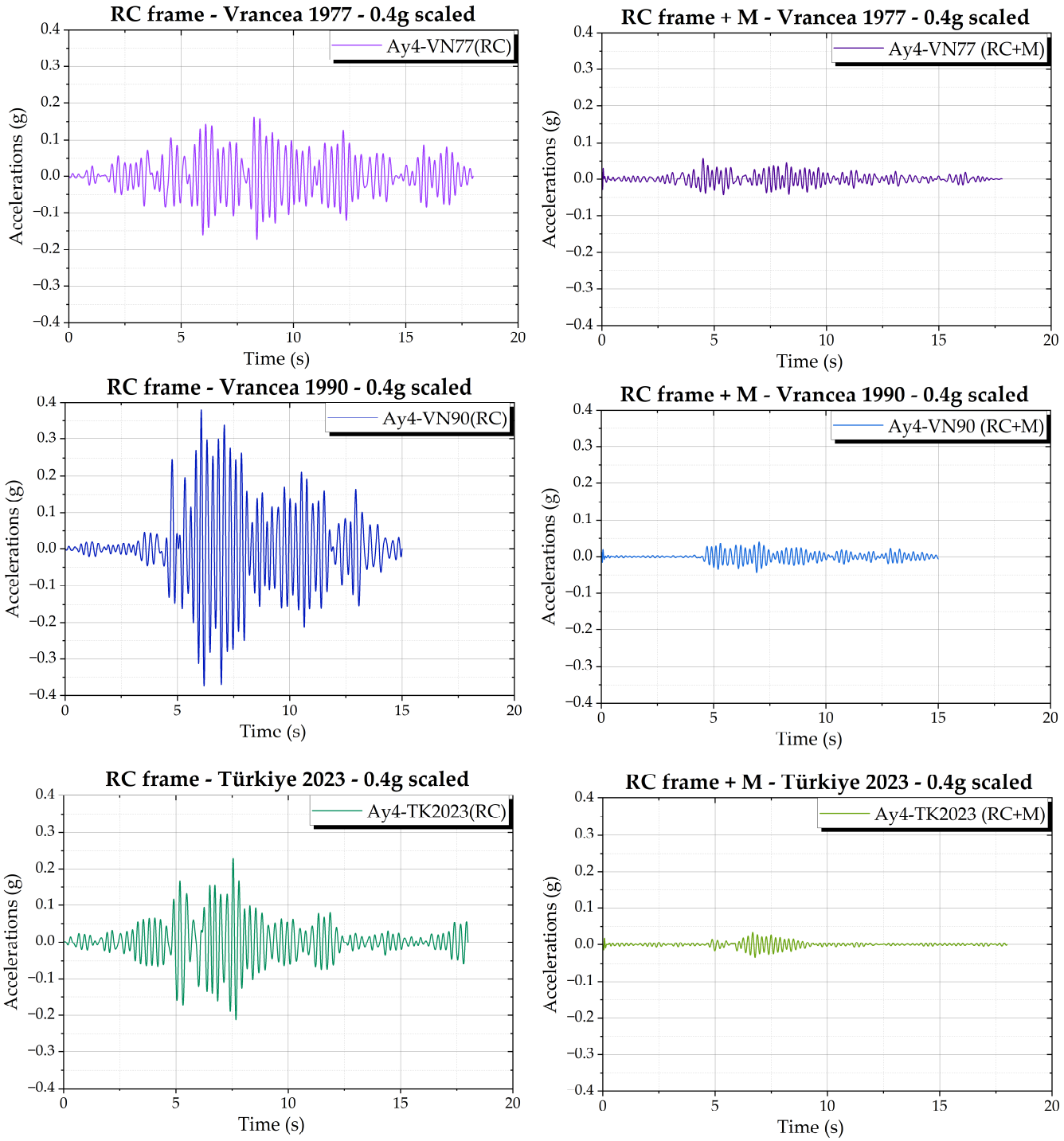

Figure 17. Roof acceleration time histories along the transversal direction (Ay4, Y) for the bare RC frame and the RC frame with masonry infills (RC + M) under VN77, VN90, and TK2023 (0.4 g scaled).

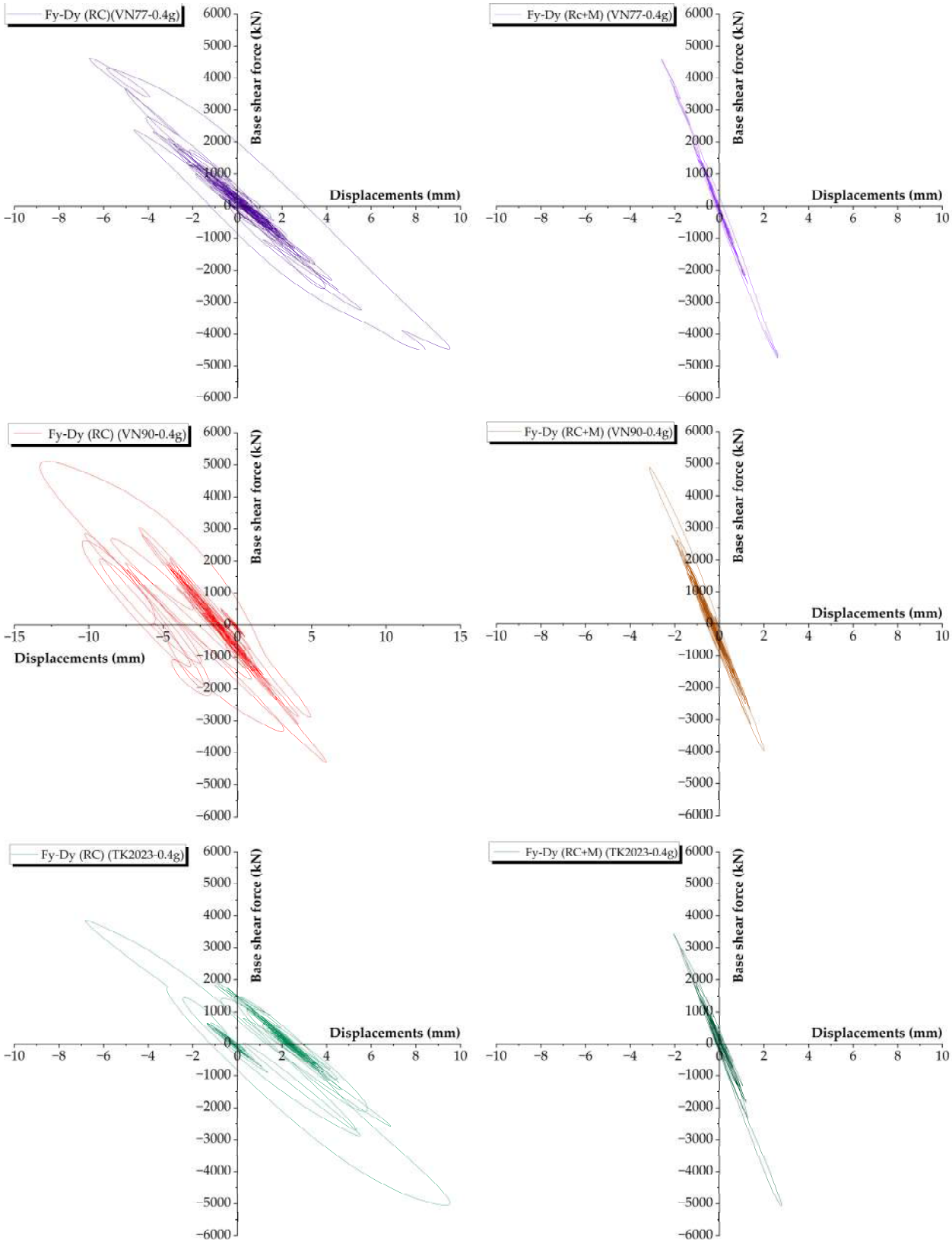

Figure 18. Base shear–roof displacement hysteresis loops in the transversal direction: F_y (base reaction) versus Dy4 (roof displacement along Y).

Table 11 reports the extreme (signed) reaction components extracted from the transient analyses. The vertical reaction F_Z remains practically constant across records for each model, reflecting the dominant gravity contribution and the constraint conditions at the

base. The transversal base shear component F_Y reaches the largest absolute values among the horizontal reactions and is compatible with the relative severity of the records observed in the displacement and acceleration results. The bending moments M_X and M_Y also increase in magnitude for the cases that generate higher lateral demand, providing an additional indicator of global overturning effects at the base.

Table 11. Extreme base reaction resultants (support reactions) for each record (global system).

Component	Units	RC + M–VN77	RC + M–VN90	RC + M–TK2023	RC–VN77	RC–VN90	RC–TK2023
M_X	kNm	−34,143	−39,318	−30,861	−36,287	−42,265	−32,540
M_Y	kNm	23,054	−21,085	−19,462	26,493	36,990	27,643
M_Z	kNm	1205.3	1281.2	1425.6	−3755.4	7643	2899.4
F_X	kN	3725.7	−3091.7	−2942.2	4423.5	5393.4	4315.6
F_Y	kN	−4825.9	5311.9	−5397.7	4700.9	5197.6	−5129.7
F_Z	kN	18,130	18,130	18,130	18,155	18,155	18,155

5.5. Stress Demand and Inelastic Indicators

Local response was assessed using stress and strain-type field outputs extracted from the 3D solid FE models. For concrete and masonry, the principal-stress fields were used to separate tension- and compression-dominated regions. Here, the maximum principal stress σ_1 is used as a practical indicator for regions where tensile cracking may develop when $\sigma_1 > 0$, while the minimum principal stress σ_3 is used as an indicator for compression-dominated regions when $\sigma_3 < 0$. Note that σ_1 is the largest principal value and may remain negative in fully compressive stress states; therefore, tensile regions are identified only where σ_1 becomes positive.

For reinforced concrete members, inelastic demand was tracked using the 'Equivalent Plastic Strain' field in the concrete solids. For reinforcement, steel demand was evaluated using the 'Equivalent (von Mises) Stress' in the rebar domains, in line with J2 plasticity, and directly comparable to the steel yield strength f_y. Accordingly, the contour plots are used here to identify qualitative demand patterns and relative concentration zones, rather than to infer validated crack paths or discrete local failure mechanisms.

For clarity, the contour plots are shown for the VN90 case, which produced the largest global response measures within the analysed scaled suite at $a_g = 0.40$ g. The figures should therefore be interpreted as illustrative worst-case results for the adopted comparative framework, while the other records remain represented through the peak summaries reported in Table 9. In this way, VN90 is used to illustrate spatial patterns, while VN77 and TK2023 remain covered through global extremes.

For each field quantity, the contour snapshot was taken at the time instant when that specific quantity reaches its peak. Therefore, the 'Maximum Principal Stress' contour is extracted at the time when the maximum tensile principal stress peaks, while the 'Minimum Principal Stress' contour is extracted at the time when the most negative compressive principal stress occurs. The same approach is used for equivalent plastic strain and for rebar von Mises stress. This avoids mixing non-synchronous maxima and keeps each map physically consistent.

Figures 19–22 show that positive σ_1 values (tension) are limited and localised, with peak values (up to about 3 MPa), whereas σ_3 reaches markedly higher magnitudes in compression (up to about 25 MPa in the bare RC frame). In many zones, σ_1 remains negative, indicating a fully compressive stress state.

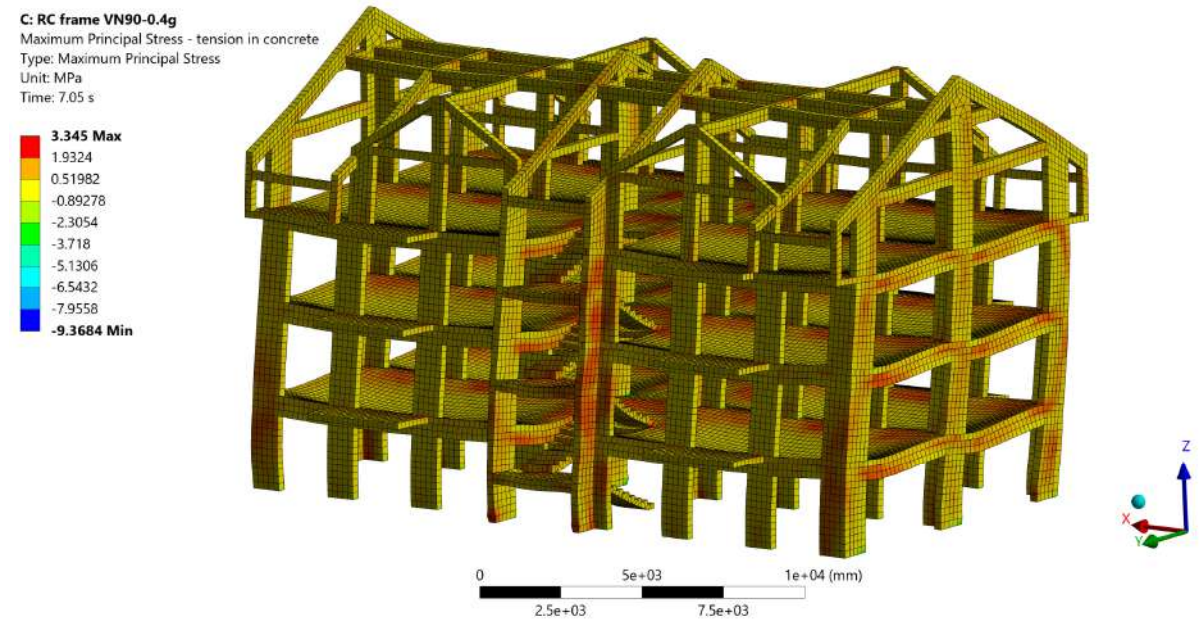

Figure 19. Maximum principal stress in concrete elements RC frame model, VN90-0.4 g scenario.

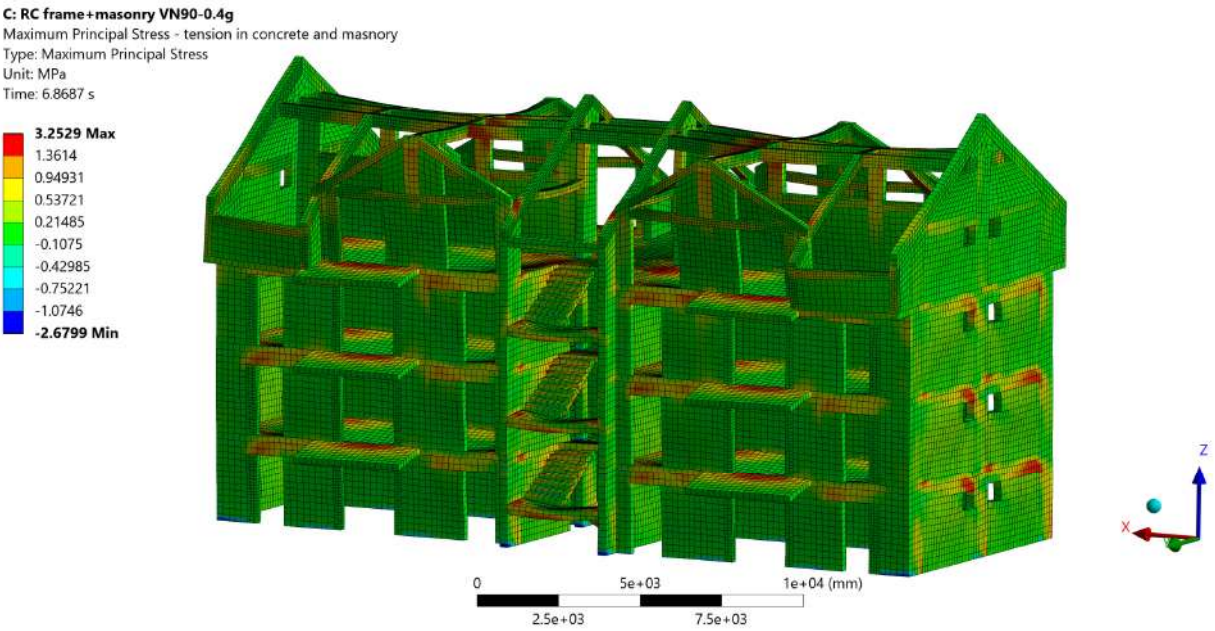

Figure 20. Maximum principal stress in concrete and masonry elements RC frame + masonry model, VN90-0.4 g scenario.

In the RC + M configuration, the compressive principal stress field suggests engagement of the masonry panels in the transversal direction, with compression trajectories qualitatively consistent with a strut-like in-plane response. Tensile stress indicators in masonry are concentrated mainly around openings and near panel corners, where the stress field changes more abruptly (Figures 19–22).

Figures 23 and 24 show that equivalent plastic strain concentrations are more pronounced in the bare RC frame than in the infilled model, which suggests the larger drift demand of the bare RC configuration. In the RC frame, equivalent plastic-strain indicators are concentrated mainly at the base of columns, especially for perimeter columns, and near beam ends adjacent to beam–column joints. Localised concentrations also appear in

the staircase zone, at the connections between landings and adjacent RC members, where stiffness discontinuities and force transfer details amplify local demand (Figures 23 and 24).

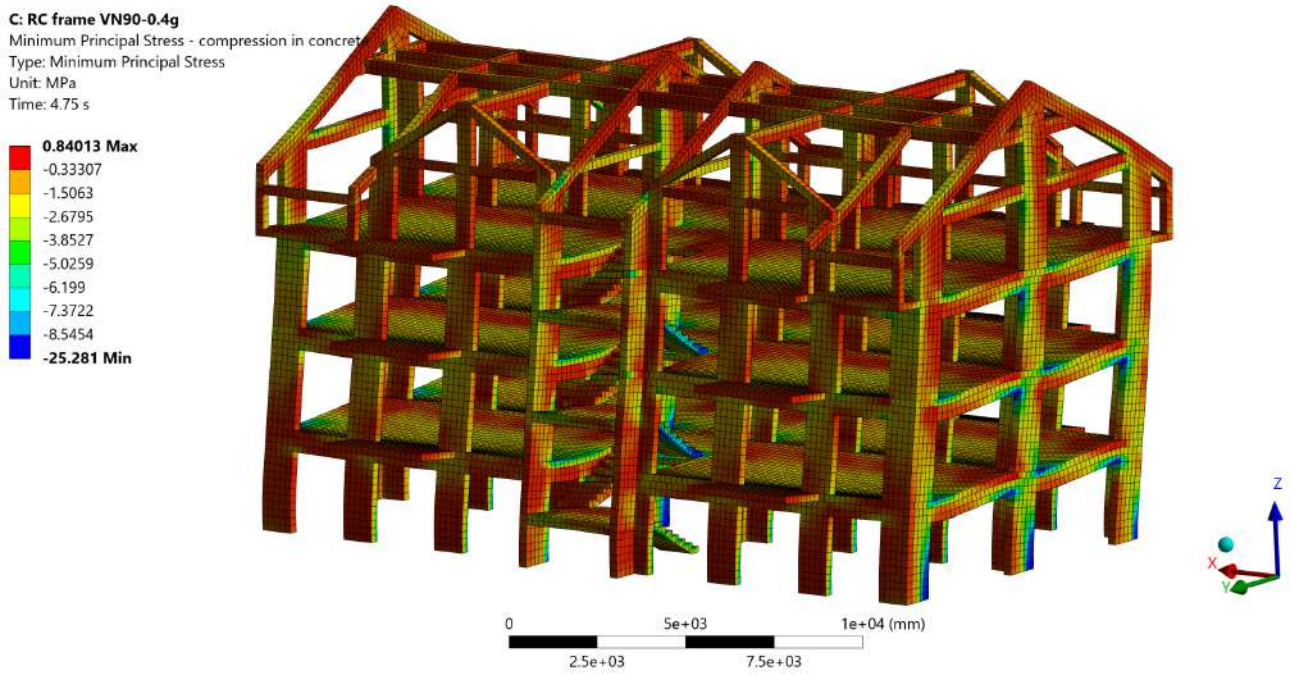

Figure 21. Minimum principal stress in concrete elements RC frame model, VN90-0.4 g scenario.

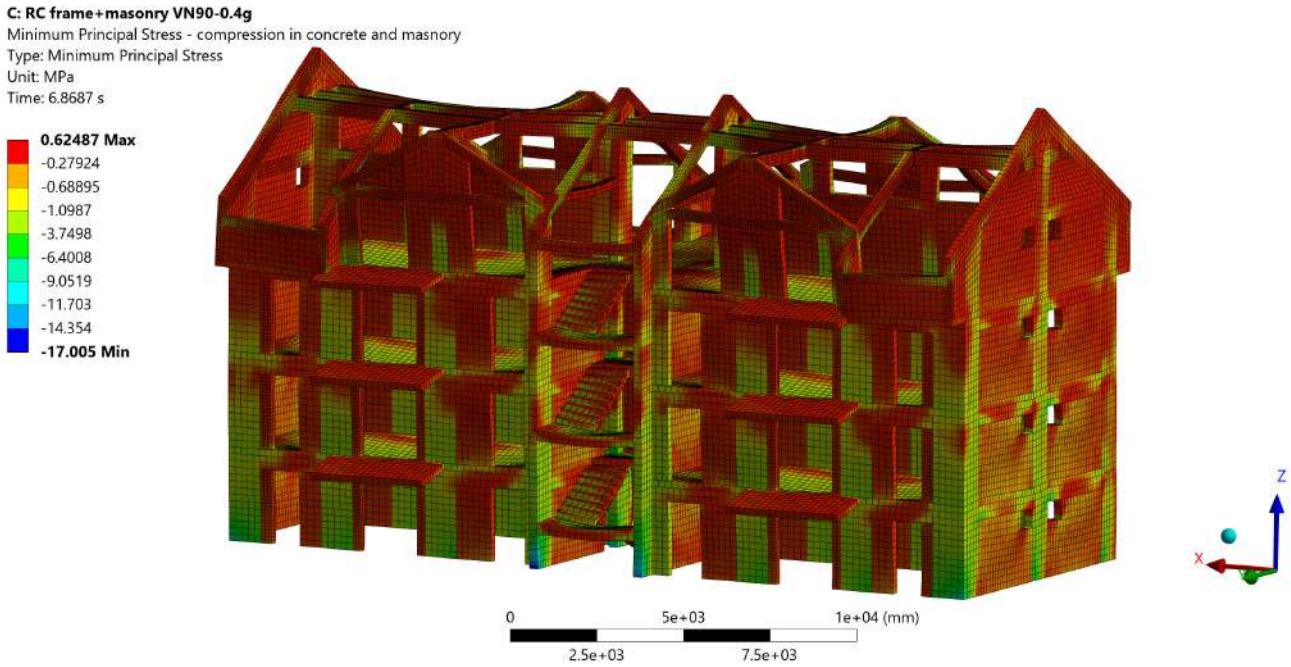

Figure 22. Minimum principal stress in concrete and masonry elements RC frame + masonry model, VN90-0.4 g scenario.

In the RC + M model, plastic strain in concrete is generally reduced, while inelastic indicators in masonry concentrate around openings and their corners, along infill-to-frame boundary regions in the transversal direction, and near the base storey. These zones are qualitatively compatible with increased local demand near geometric discontinuities and interface transfer regions. (Figures 23 and 24).

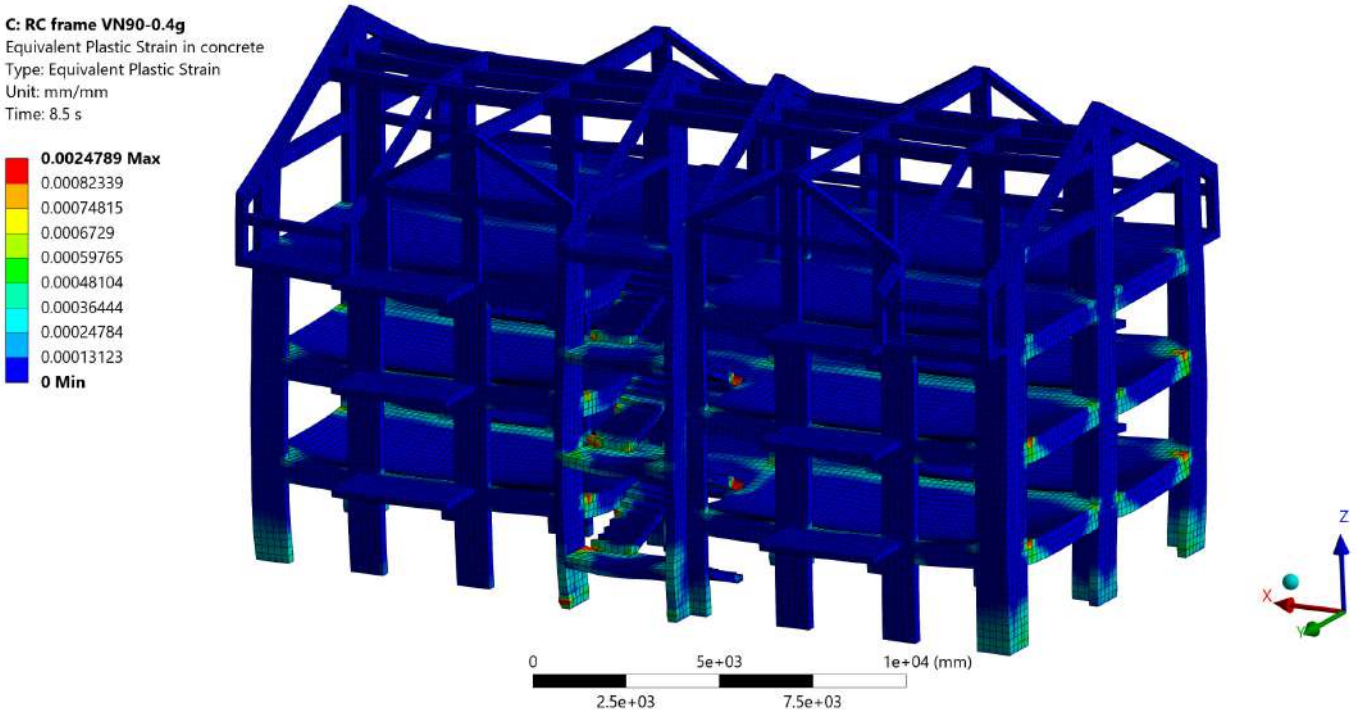

Figure 23. Equivalent plastic strain in concrete elements RC frame model, VN90-0.4 g scenario.

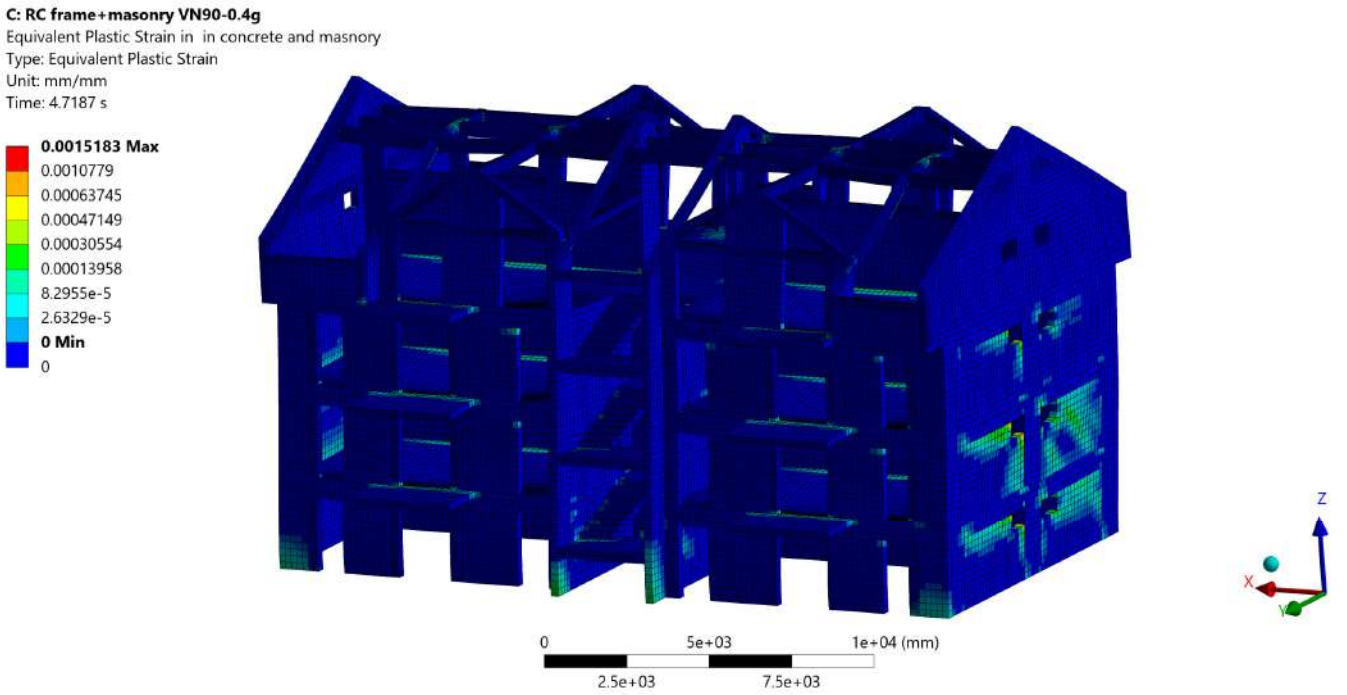

Figure 24. Equivalent plastic strain in concrete and masonry elements RC frame + masonry model, VN90-0.4 g scenario.

Figures 25 and 26 show that the reinforcement von Mises stress in the bare RC frame reaches about 360 MPa, close to the yielding range of the PC52 steel.

The highest steel-stress indicators are observed in (i) the longitudinal reinforcement at beam ends adjacent to columns, (ii) the extreme bars at the base of columns, and (iii) the staircase region, where landings connect into the surrounding frame and local force transfer is intensified (Figures 25 and 26). This spatial pattern may be influenced by the torsional contribution identified in Mode 2, although the present model does not

support a fully validated local damage interpretation. For the RC + M model, peak rebar stresses remain much lower (about 121 MPa), which is consistent with the reduced drift and reduced curvature demand in beams and columns under the same scaled intensity (Figures 25 and 26).

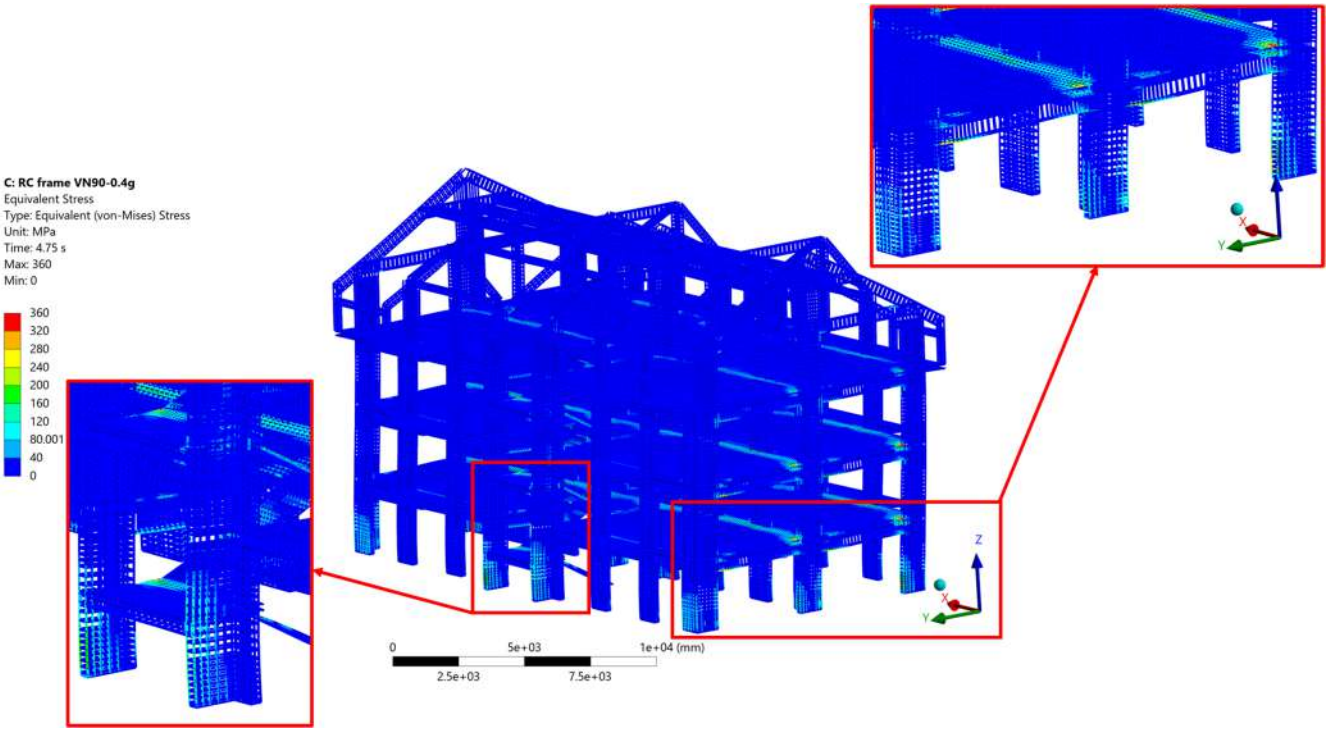

Figure 25. Equivalent von Mises stress in reinforcement (steel rebars) RC frame model, VN90-0.4 g scenario.

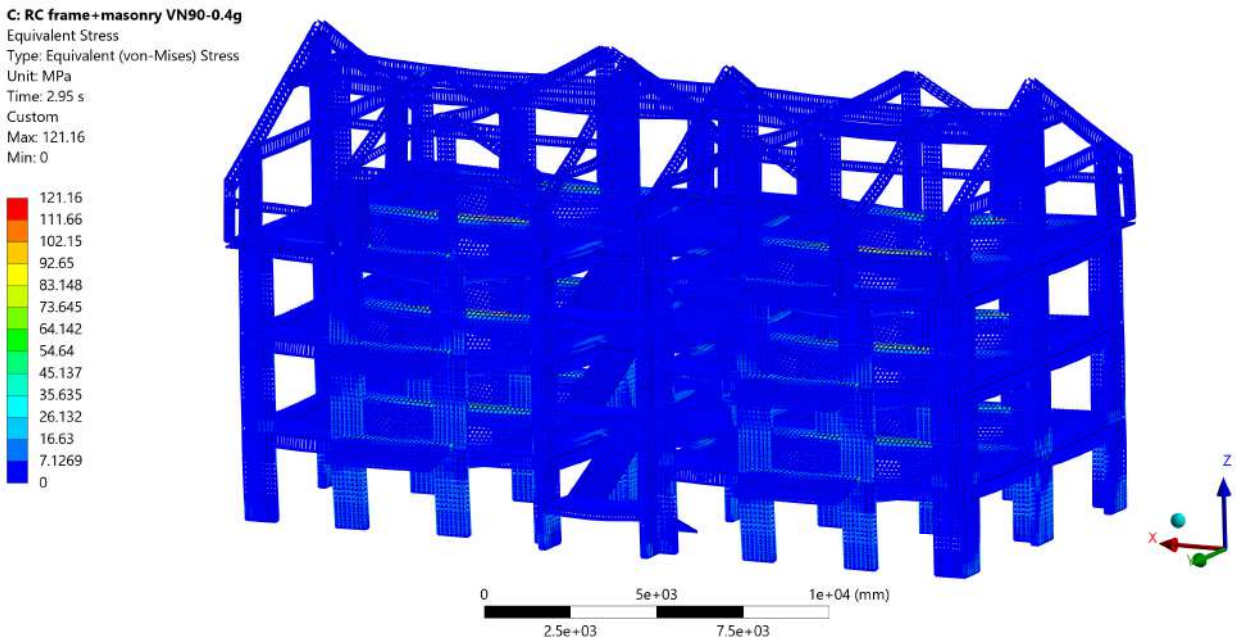

Figure 26. Equivalent von Mises stress in reinforcement (steel rebars) RC frame + masonry model, VN90-0.4 g scenario.

Table 12 consolidates the extreme values across all three records. For the bare RC frame, peak tensile principal stress is about 2.8–3.345 MPa, peak compressive principal stress mag-

nitude is about 20.55–25.28 MPa, peak equivalent plastic strain is about 0.0021–0.0025, and peak rebar von Mises stress is about 338–360 MPa. For RC + M, peak tensile principal stress is about 3.25–3.32 MPa, peak compressive principal stress magnitude is about 13.46–17.01 MPa, peak equivalent plastic strain is about 0.0011–0.0015, and peak rebar von Mises stress is about 121–127 MPa. These results are compatible with the global response metrics. Masonry infills reduce lateral deformation demand and, consequently, limit both concrete inelastic demand and reinforcement stress demand at the considered design-level intensity.

Table 12. Extreme values of maximum and minimum principal stress in concrete elements, equivalent von Mises stress in steel rebar reinforcements and equivalent plastic strain.

Model	Scenario	Maximum Principal Stress (Tension in Concrete) (MPa)	Minimum Principal Stress (Compression in Concrete) (MPa)	Equivalent Plastic Deformation (mm/mm)	Equivalent von Mises Stress (Steel Rebar Reinforcement) (MPa)
RC frame	VN77	2.8	24.14	0.0025 − c	357.88
	VN90	3.345	25.28	0.0025 − c	360
	TK2023	2.81	20.55	0.0021 − c	338
RC frame + masonry	VN77	3.32	13.46	0.0011 − m	123.03
	VN90	3.25	17.005	0.0015 − m	121.16
	TK2023	3.3	16.07	0.0014 − m	127.25

6. Discussion and Implications

The adopted intensity level $a_g = 0.40$ g corresponds to the current design level for the investigated site to P100-1/2013. At this level, the analysed building satisfies the drift-based checks used in this study, with peak drift ratios remaining below the reference serviceability threshold $\theta_{adm} = 0.5\%$. Under the present modelling assumptions, the results therefore indicate an acceptable global response of the analysed structure at the investigated intensity level. However, this should not be interpreted as a general statement that the building possesses a performance margin above the minimum requirements of the original code, because the present reassessment is based on a single intensity level, a limited comparative record set, fixed-base conditions, a bonded frame–infill interface, simplified constitutive laws, and no explicit treatment of soil–structure interaction or interface uncertainty. The results also indicate that the infills strongly influence stiffness and deformation demand at $a_g = 0.40$ g. With infills included (RC + M), global drifts and reinforcement stresses remain comparatively low, whereas the bare-frame configuration (RC) becomes more clearly drift-governed, with localised inelastic demand at column bases and beam ends and higher steel stress demand in critical regions. Extrapolation to substantially higher intensity levels (e.g., 0.6 g and above) should be treated as qualitative in the present work, since such analyses were not performed. Even so, the observed demand concentration trends indicate likely zones of increased response at higher intensities, especially around openings, panel corners, RC end regions, and the staircase vicinity.

In the present study, the most restrictive requirement remains the global stiffness (drift) condition, which is also the response measure most sensitive to the presence of infills. At the same time, this beneficial contribution should be interpreted with appropriate caution in engineering practice, because the properties, continuity, and degradation mechanisms of masonry infills may vary substantially from one building to another. Therefore, for code-type verification of new RC frames, it remains prudent not to rely on infills as guaranteed

primary lateral-resisting components. For the assessment of existing buildings, however, the present results show that infills can strongly modify the actual structural response and should be represented explicitly whenever their contribution is expected to be significant.

7. Limitations

The reported results should be interpreted within the adopted modelling assumptions. The base was idealised as fully fixed at the slab above the basement; soil–structure interaction and potential basement flexibility were not modelled. The frame–infill interface was idealised as bonded contact, reflecting the observed construction sequence of the case-study building. Even so, this assumption may overestimate the initial stiffness and modify local damage localization when compared with more compliant frictional, separating, or bond-degrading interfaces. Therefore, the RC + M results should be interpreted as a strongly engaged infill scenario, not as a general prediction for all masonry-infilled RC frames.

Concrete and masonry were represented using Drucker–Prager-type constitutive laws, while reinforcement was modelled with a multilinear isotropic hardening law. The concrete and masonry parameters were assigned from specified material classes and engineering assumptions suitable for building-scale nonlinear modelling; dedicated calibration from material or interface tests was not performed. In addition, the concrete–reinforcement interaction was idealised through embedded reinforcement with perfect bond, and no explicit bond–slip law was introduced. Accordingly, local bar slip, anchorage deterioration, and interface degradation effects were not represented explicitly. For these reasons, the reported local stress and plastic-strain fields should be interpreted as qualitative demand patterns rather than as validated predictions of explicit crack paths or discrete local failure modes. Rayleigh damping was kept constant during each nonlinear analysis, with one value assigned to the bare RC model and a different value assigned to the RC + M model. Although this distinction reflects the different global dynamic characteristics of the two configurations, the adopted damping formulation remains simplified and may not fully represent amplitude-dependent energy dissipation at larger damage levels. In addition, local stress and plastic-strain maps remain mesh-dependent to some extent; a more refined discretisation would be more appropriate for dedicated local sub-models, but this was outside the scope of the present full-building analysis.

The selected seismic input suite remains limited to three bidirectional record pairs, and one motion required a relatively large amplification factor to reach the adopted reference intensity. Therefore, the record-specific nonlinear results should be interpreted comparatively and scenario-wise, rather than as statistically robust estimates of structural demand. Within this limited suite, the main comparative trend remains stable, namely the systematic reduction in displacement-related demand in the infilled configuration, whereas the absolute response amplitudes and local inelasticity indicators remain record-dependent. No dedicated time-step sensitivity study or convergence-sensitivity study for local stress/plastic-strain peaks was carried out in the present revision, because such checks would require rerunning the full 3D nonlinear time-history analyses and were beyond the computational scope of this study. Finally, although the present 3D solid modelling framework can represent global three-dimensional response and qualitative stress redistribution within the masonry panels under bidirectional excitation, it was not calibrated or configured to predict brittle out-of-plane infill failure mechanisms explicitly, such as separation from the RC frame, local loss of support, rocking instability, or panel expulsion.

8. Conclusions

This study re-assessed an existing RC frame building designed according to P100-1/2006 by means of nonlinear three-dimensional solid finite-element models with explicit

reinforcement. Two structural configurations were analysed: a bare frame (RC) and an infilled frame (RC + M), subjected to bidirectional time-history input from the Vrancea 1977, Vrancea 1990, and Türkiye 2023 earthquakes, scaled to the P100-1/2013 target spectrum for the investigated site.

The results show that masonry infills markedly increase the global stiffness of the building. The fundamental frequency increases from 4.4669 Hz for the bare frame to 5.8680 Hz for the infilled configuration, while the fundamental period decreases from 0.2239 s to 0.1704 s. For both models, the first mode is dominated by translation in the Y direction, the second mode is torsional, and the third mode is dominated by translation in the X direction. In the analysed case study, the presence of infills therefore has a major influence on the global dynamic properties of the structure.

Under the adopted bonded frame–infill interface idealisation, the infilled configuration shows substantially lower displacement-related demand than the bare-frame configuration. Peak roof displacements in the transversal direction decrease from 9.87 to 14.26 mm to 2.74–3.38 mm, while peak relative interstorey displacements decrease from 3.35 to 4.94 mm to 0.92–1.16 mm. The governing storey is typically located between S1 and S2, and the maximum drift ratio remains low, reaching about 0.173% in the most demanding bare-frame case. These results indicate that, for the analysed building, masonry infills can strongly improve stiffness and drift-sensitive global response.

The beneficial influence of infills is not uniform for all demand measures. Although the infilled model shows lower displacement demand and lower roof acceleration in the governing VN90 case, the peak base shear F_y is slightly higher in the RC + M model for all three analysed records. This indicates that the increased stiffness provided by the infills reduces deformations but may also attract comparable or somewhat larger force demand. The bidirectional response remains predominantly translational, while the torsional component stays secondary and is consistently smaller in the infilled configuration.

The local response fields indicate different concentration patterns in the two models. In the bare frame, plastic-strain indicators are concentrated mainly at perimeter column bases and beam ends. In the infilled model, the highest local demand shifts towards masonry discontinuities around openings and panel corners, as well as towards the base storey and staircase region. These local fields should be interpreted as qualitative response indicators rather than as validated predictions of explicit crack paths or discrete local failure modes.

These conclusions apply in the current analysis framework, including fixed-base conditions, bonded frame–infill interface, Drucker–Prager-type constitutive laws for concrete and masonry, multilinear isotropic hardening for reinforcement, and constant Rayleigh damping with different values assigned to the RC and RC + M models. Accordingly, the RC + M results should be interpreted as a strongly engaged infill scenario for the investigated case study, not as a general prediction for all reinforced concrete frame buildings with masonry infills. For the assessment of existing buildings, however, the results show that masonry infills can significantly modify the actual seismic response and should therefore be considered explicitly whenever their contribution is expected to be relevant.

Supplementary Materials: The following supporting information can be downloaded at https://www.mdpi.com/article/10.3390/buildings16071392/s1, TK2023.xlsx—Time History acceleration Turkey 2023; VN1990.xlsx—Time History acceleration; VN1977.xlsx—Time History acceleration; Spectre.xlsx—Comparative Spectrum; TH-displacements.xlsx—Time History displacements response; TH-acceleration.xlsx—Time History acceleration response; Reaction.xlsx—Base reaction; Acceleration peak.xlsx—Peak Accelerations; stresses.xlsx—Maximum Principal Stresses; Displacements peak.xlsx—Maximum displacements.

Funding: This research received no external funding.

Data Availability Statement: Data is contained within the article or Supplementary Material.

Conflicts of Interest: The author declares no conflicts of interest.

References

1. Fattal, G.; Simiu, E.; Culver, C. *Observations on the Behavior of Buildings in the Romania Earthquake of March 4, 1977*; National Bureau of Standards: Washington, DC, USA, 1977. [CrossRef]
2. Mihail Ifrim Earthquake of March 4, 1977 in Romania-Damage and Strengthening of Structures. In *Proceedings of the 3rd Canadian Conference on Earthquake Engineering, Montréal, QC, Canada, 4–6 June 1979*; Canadian National Committee for Earthquake Engineering: Vancouver, BC, Canada, 1979; pp. 825–836.
3. Sonmez, E.; Eryilmaz Yildirim, M.; Aydin, M.F.; Koroglu, F.B. Seismic Performance Assessment of Structural Systems in the Aftermath of the 2023 Kahramanmaraş Earthquakes: Observations and Fragility Analyses. *Earthq. Spectra* **2025**, *41*, 198–218. [CrossRef]
4. Cilsalar, H.; Anil, O. Investigation of Seismic Collapse Performance of RC Frames with Strengthened Masonry Infill Walls under February 6, 2023 Earthquakes in Türkiye. *Bull. Earthq. Eng.* **2025**, *23*, 4499–4524. [CrossRef]
5. Marinković, M.; Butenweg, C. Behaviour and Damage of Masonry Infill Walls during the Earthquake Sequence in Turkey 2023: What Can Be Done to Prevent Extensive Damage of Infilled RC Structures? In *Proceedings of the 16th International Scientific Conference "Planning, Design, Construction and Building Renewal", Novi Sad, Serbia, 16–17 November 2023*; Departman za građevinarstvo i geodeziju, Fakulteta tehničkih nauka, Univerziteta u Novom Sadu: Novi Sad, Serbia, 2023.
6. Kaushik, H.B.; Rai, D.C.; Jain, S.K. Code Approaches to Seismic Design of Masonry-Infilled Reinforced Concrete Frames: A State-of-the-Art Review. *Earthq. Spectra* **2006**, *22*, 961–983. [CrossRef]
7. Dias-Oliveira, J.; Rodrigues, H.; Asteris, P.G.; Varum, H. On the Seismic Behavior of Masonry Infilled Frame Structures. *Buildings* **2022**, *12*, 1146. [CrossRef]
8. Asteris, P.G.; Cotsovos, D.M.; Chrysostomou, C.Z.; Mohebkhah, A.; Al-Chaar, G.K. Mathematical Micromodeling of Infilled Frames: State of the Art. *Eng. Struct.* **2013**, *56*, 1905–1921. [CrossRef]
9. Wang, B.; Guo, X.; Xuan, Y.; Fan, X.-Q.; Chen, B. The Effects of Infilled Walls on Seismic Performance of RC Frame Structures with Eccentrically Placed Open Corridor. *Sustainability* **2022**, *14*, 5299. [CrossRef]
10. Pohoryles, D.A.; Bournas, D.A. A Unified Macro-Modelling Approach for Masonry-Infilled RC Frames Strengthened with Composite Materials. *Eng. Struct.* **2020**, *223*, 111161. [CrossRef]
11. Angelucci, G.; De Luca, F.; De Risi, R.; Mollaioli, F.; Spacone, E. Simplified Model for the Seismic Performance of Masonry Infilled RC Buildings. *Eng. Struct.* **2025**, *342*, 120903. [CrossRef]
12. Martinelli, E.; Lima, C.; De Stefano, G. A Simplified Procedure for Nonlinear Static Analysis of Masonry Infilled RC Frames. *Eng. Struct.* **2015**, *101*, 591–608. [CrossRef]
13. Gentile, R.; Pampanin, S.; Raffaele, D.; Uva, G. Non-Linear Analysis of RC Masonry-Infilled Frames Using the SLaMA Method: Part 1—Mechanical Interpretation of the Infill/Frame Interaction and Formulation of the Procedure. *Bull. Earthq. Eng.* **2019**, *17*, 3283–3304. [CrossRef]
14. Vahed, M.; Habibi, A. Seismic Evaluation of Set-Back RC Frames with and without Masonry Infill Walls. *Earthq. Struct.* **2025**, *28*, 173. [CrossRef]
15. Falcão Moreira, R.; Varum, H.; Castro, J.M. Influence of Masonry Infill Walls on the Seismic Assessment of Non-Seismically Designed RC Framed Structures. *Buildings* **2023**, *13*, 1148. [CrossRef]
16. Kong, J.; Su, Y.; Zheng, Z.; Wang, X.; Zhang, Y. The Influence of Vertical Arrangement and Masonry Material of Infill Walls on the Seismic Performance of RC Frames. *Buildings* **2022**, *12*, 825. [CrossRef]
17. Messaoudi, A.; Chebili, R.; Mohamed, H.; Rodrigues, H. Influence of Masonry Infill Wall Position and Openings in the Seismic Response of Reinforced Concrete Frames. *Appl. Sci.* **2022**, *12*, 9477. [CrossRef]
18. Lubrano Lobianco, A.; Del Zoppo, M.; Rainieri, C.; Fabbrocino, G.; Di Ludovico, M. Damage Estimation of Full-Scale Infilled RC Frames under Pseudo-Dynamic Excitation by Means of Output-Only Modal Identification. *Buildings* **2023**, *13*, 948. [CrossRef]
19. Venghiac, V.-M.; Neagu, C.-P.; Taranu, G.; Rotaru, A. Time History Analyses of a Masonry Structure for a Sustainable Technical Assessment According to Romanian Design Codes. *Sustainability* **2023**, *15*, 2932. [CrossRef]
20. Kallioras, S.; Pohoryles, D.A.; Bournas, D.; Molina, F.J.; Pegon, P. Seismic Performance of a Full-Scale Five-Story Masonry-Infilled RC Building Subjected to Substructured Pseudodynamic Tests. *Earthq. Eng. Struct. Dyn.* **2023**, *52*, 3649–3678. [CrossRef]
21. *EN 1998-1*; Eurocode 8; Design of Structures for Earthquake Resistance—Part 1: General Rules, Seismic Actions and Rules for Buildings. European Committee for Standardization: Brussels, Belgium, 2004.
22. *P100-1/2006*; Seismic Design Code—Part I: Design Provisions for Buildings. Ministry of Public Works and Territory Planning: Bucharest, Romania, 2006.

23. Pavel, F. An Updated Perspective of the Impact of the 1940 Vrancea Earthquake on Design and Construction Practices in Romania. *Buildings* **2024**, *14*, 1152. [CrossRef]
24. Sococol, I.; Mihai, P.; Toma, I.-O.; Olteanu-Donţov, I.; Venghiac, V.-M. Stress-Strain Relation Laws for Concrete and Steel Reinforcement Used in Non-Linear Static Analytical Studies of the Moment Resisting Reinforced Concrete (RC) Frame Models. *Bull. Polytech. Inst. Iaşi Constr. Archit. Sect.* **2021**, *67*, 17–29. [CrossRef]
25. Olteanu, I.; Canarache, R.M.; Budescu, M. Case Study on Vulnerability Increase for a Reinforced Concrete Frame Structure. *Math. Model. Civ. Eng.* **2015**, *11*, 38–45. [CrossRef]
26. Ibrahim, A.R.; Makhloof, D.A.; Ren, X. Seismic Performance and Collapse Analysis of RC Framed-Wall Structure Excited with Turkey/Syria Destructive Earthquake. *Structures* **2024**, *59*, 105774. [CrossRef]
27. *P100-1/2013*; Seismic Design Code-Part I-Design Provisions for Buildings. Ministry of Public Works and Territory Planning: Bucharest, Romania, 2013.
28. Georgescu, E.-S.; Pomonis, A. Building Damage vs. Territorial Casualty Patterns during the Vrancea (Romania) Earthquakes of 1940 and 1977. In Proceedings of the 15th World Conference on Earthquake Engineering, Sociedade Portuguesa de Engenharia Sismica (SPES), Lisbon, Portugal, 24–28 September 2012.
29. Bala, A.; Toma-Danila, D. The Strong Romanian Earthquakes of 10.11.1940 and 4.03.1977. Lessons Learned and Forgotten? In *Proceedings of the Symposium Commemorating 75 Years from November 10, 1940 Vrancea Earthquake. The 1940 Vrancea Earthquake. Issues, Insights and Lessons Learnt*; Radu, V., Constantin, I., Eds.; Springer: Cham, Switzerland; Bucharest, Romania, 2016; pp. 19–35. Available online: https://link.springer.com/book/10.1007/978-3-319-29844-3 (accessed on 26 December 2025).
30. INFP. Bridging the Gap Between Seismology and Earthquake Engineering: From the Seismicity of Romania Towards a Refined Implementation of Seismic Action EN 1998-1 (2004) in Earthquake Resistant Design of Buildings (BIGSEES Project). Available online: http://bigsees.infp.ro/ (accessed on 26 December 2025).
31. Bunea, G.; Atanasiu, G.M. Structural response analysis for RC frame structures under seismic action. *Bull. Polytech. Inst. Jassy Constr. Archit. Sect.* **2023**, *68*. [CrossRef]
32. Georgescu, E.-S.; Steinbrueck, K. New Archival Evidence on the 1977 Vrancea, Romania Earthquake and Its Impact on Disaster Management and Seismic Risk. In *Seismic Hazard and Risk Assessment*; Springer: Cham, Switzerland, 2018.
33. *NP 007-97*; Design Code for Reinforced Concrete Frame Structures. Ministry of Public Works and Territory Planning: Bucharest, Romania, 1997.
34. *STAS 10107/0-90*; Civil and Industrial Buildings—Design and Detailing of Concrete, Reinforced Concrete and Prestressed Concrete Structural Elements. Ministry of Public Works and Territory Planning: Bucharest, Romania, 1990.
35. Engineering Strong Motion Database ESM. Available online: https://esm-db.eu/processing/select (accessed on 11 March 2026).
36. Hussaini, S.S.; Karimzadeh, S.; Rezaeian, S.; Lourenço, P.B. Broadband Stochastic Simulation of Earthquake Ground Motions with Multiple Strong Phases with an Application to the 2023 Kahramanmaraş, Turkey (Türkiye), Earthquake. *Earthq. Spectra* **2025**, *41*, 2399–2435. [CrossRef]

Disclaimer/Publisher's Note: The statements, opinions and data contained in all publications are solely those of the individual author(s) and contributor(s) and not of MDPI and/or the editor(s). MDPI and/or the editor(s) disclaim responsibility for any injury to people or property resulting from any ideas, methods, instructions or products referred to in the content.

buildings

MDPI

Article

Buckling Behavior of Perforated Cold-Formed Steel Uprights: Experimental Evaluation and Comparative Assessment Using FEM, EWM, and DSM

George Taranu [1,*], Serban Iacob [2] and Nicolae Taranu [2]

[1] Department of Structural Mechanics, Faculty of Civil Engineering and Building Services, The "Gheorghe Asachi" Technical University of Iasi, 700050 Iasi, Romania
[2] Department of Civil Engineering, Faculty of Civil Engineering and Building Services, The "Gheorghe Asachi" Technical University of Iasi, 700050 Iasi, Romania; serban.iacob@student.tuiasi.ro (S.I.); nicolae.taranu@academic.tuiasi.ro (N.T.)
* Correspondence: george.taranu@academic.tuiasi.ro

Abstract: This paper presents an experimental and numerical investigation of the axial compression behavior of perforated cold-formed steel upright profiles commonly used in pallet racking systems. The primary objective is to examine how slenderness influences the failure modes and load-bearing capacity of these structural elements. Three column lengths, representative of typical vertical spacing in industrial rack systems, were tested under pin-ended boundary conditions. All specimens were fabricated from 2 mm thick S355 steel sheets, incorporating web perforations and a central longitudinal stiffener. Experimental results highlighted three distinct failure mechanisms dependent on slenderness: local buckling for short columns (SS-340), combined distortional–flexural buckling for medium-length columns (MS-990), and global flexural buckling for slender columns (TS-1990). Finite Element Method (FEM) models developed using ANSYS Workbench 2021 R1 software accurately replicated the observed deformation patterns, stress concentrations, and load–displacement curves, with numerical results differing by less than 5% from experimental peak loads. Analytical evaluations performed using the Effective Width Method (EWM) and Direct Strength Method (DSM), following EN 1993-1-3 and AISI S100 specifications, indicated that EWM tends to underestimate the ultimate strength by up to 15%, whereas DSM provided results within 2–7% of experimental values, especially when the entire net cross-sectional area was considered fully effective. The originality of the study is the comprehensive evaluation of full-scale, perforated, stiffened cold-formed steel uprights, supported by robust experimental validation and detailed comparative analyses between FEM, EWM, and DSM methodologies. Findings demonstrate that DSM can be reliably applied to perforated sections with moderate slenderness and adequate web stiffening, without requiring further local reduction in the net cross-sectional area.

Keywords: cold-formed steel; axial compression; finite element analysis (FEA); steel storage racks

check for updates

Academic Editor: You-Fu Yang

Received: 9 April 2025
Revised: 24 April 2025
Accepted: 1 May 2025
Published: 6 May 2025

Citation: Taranu, G.; Iacob, S.; Taranu, N. Buckling Behavior of Perforated Cold-Formed Steel Uprights: Experimental Evaluation and Comparative Assessment Using FEM, EWM, and DSM. *Buildings* **2025**, *15*, 1561. https://doi.org/10.3390/buildings15091561

Copyright: © 2025 by the authors. Licensee MDPI, Basel, Switzerland. This article is an open access article distributed under the terms and conditions of the Creative Commons Attribution (CC BY) license (https://creativecommons.org/licenses/by/4.0/).

1. Introduction

In recent decades, rapid industrialization and economic expansion have led to an increasing demand for efficient and robust steel pallet rack systems. These structures are typically constructed from cold-formed steel, which provides an optimal balance between lightweight design and high strength [1–4].

However, the presence of perforations significantly affects the stability and load-bearing capacity of uprights, necessitating a detailed analysis of axial compression behavior [5,6]. Several experimental and numerical studies have examined perforated uprights, investigating buckling resistance and failure mechanisms. Neiva et al. found that the Direct Strength Method (DSM) tends to overestimate load-carrying capacity, leading to modifications in the distortional buckling curve [7,8]. Similarly, Ren et al. explored the interaction between distortional and global buckling, concluding that perforations adversely impact structural performance [9].

Further research by Shaker et al. confirmed that DSM, in its current form, fails to accurately predict failure modes in cold-formed steel sections without modifications. To improve structural performance, Taheri et al. proposed reinforcement techniques using spacers and bolts, demonstrating enhanced load-bearing capacity and reduced distortional buckling risks [10]. Meanwhile, Bernuzzi et al. emphasized the importance of evaluating stiffness in beam-to-column joints and base connections, as these factors heavily influence overall structural stability [11].

Pham et al. (2023) extended the applicability of the Direct Strength Method (DSM) to cold-formed steel channels featuring web perforations subjected to shear forces. The study proposed improved design procedures, emphasizing accurate predictions of shear capacity affected by web openings [12]. This reference supports discussions about limitations and enhancements of DSM for perforated sections, providing context on why further investigation into alternative or complementary analytical approaches is necessary.

Martins et al. (2021) conducted extensive numerical and experimental analyses on the interaction between distortional and global buckling modes in cold-formed steel columns. Their research provided valuable insights into the strength reduction resulting from these complex interactions, emphasizing the need for advanced analytical and numerical modeling [13].

Ye et al. (2022) performed numerical studies on perforated cold-formed steel columns under axial compression, evaluating the influence of various perforation patterns on the structural stability and buckling resistance. They proposed guidelines for efficient design practices based on Finite Element Method (FEM) simulations [14].

Xiang et al. (2021) developed simplified design methods specifically for cold-formed steel columns with built-up box sections, addressing buckling behavior and strength prediction. Their findings demonstrated simplified analytical methods that align closely with FEM and experimental results [15].

Shaker et al. (2022) conducted experimental investigations on stiffened, perforated cold-formed steel sections subjected to axial compression, emphasizing the impact of triangular and circular perforations. Their study highlighted limitations of the Direct Strength Method (DSM) in accurately predicting buckling and failure modes for these profiles. They demonstrated that conventional DSM requires modification—such as those proposed by Zhao et al.—to reliably estimate the ultimate capacity of stiffened perforated uprights. This study further underscores the necessity of refined analytical methods and careful numerical modeling for perforated cold-formed steel sections [16].

Although DSM offers a simplified and efficient approach, it presents certain limitations—particularly in the case of members with perforations, where mode interaction (e.g., local–distortional) and assumptions about net section effectiveness may affect its accuracy. These aspects are further investigated in this study.

The steel uprights are designed using perforated cold-formed profiles, allowing adjustable shelf configurations [17]. The image in Figure 1 illustrates the real-life loading and bracing conditions, including high and low bay arrangements, which are critical for evaluating the axial and lateral performance of the structural members. Figure 2 represents

the manufacturing and application process of perforated cold-formed steel upright profiles used in industrial pallet racks.



Figure 1. Typical industrial pallet rack system used in retail or warehouse environments.

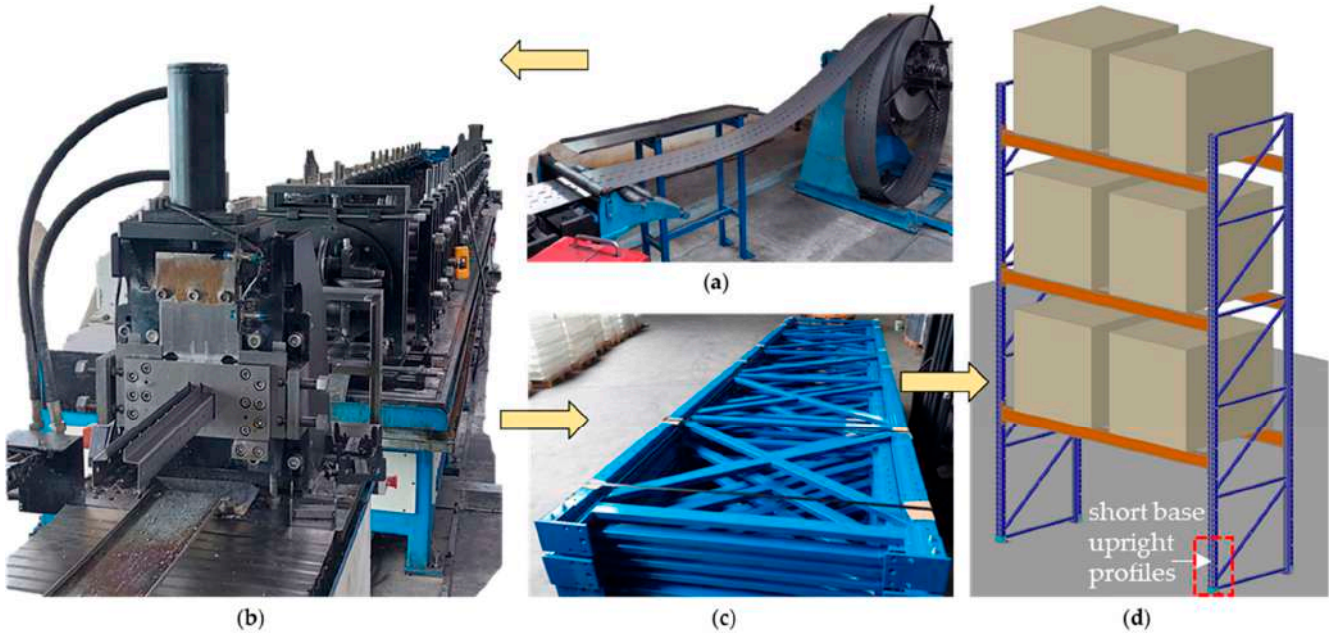

Figure 2. Cold-forming process of steel rack components: (**a**) perforated steel strip; (**b**) cold roll forming machine; (**c**) vertical frame storage ready for transportation; (**d**) assembled interior rack.

Cold-formed steel profiles are commonly manufactured from low-carbon steel sheets, with thicknesses ranging from 0.8 mm to 4.0 mm. The most frequently used steel grades in Europe include S355MC, S420MC, S460MC, S500MC, S550MC, S600MC, S650MC, S700MC, and S900MC, with selection based on application-specific requirements [18]. Understanding

material behavior and stress–strain characteristics is essential for improving finite element model (FEM) calibration and predicting failure modes in rack structures [19–23].

Although these contributions have improved the understanding of buckling phenomena, certain research gaps persist. Specifically, there remains limited investigation regarding the coupled buckling behavior of cold-formed perforated uprights at intermediate slenderness levels. Furthermore, detailed characterizations of realistic geometric imperfections, important for accurate finite element modeling, are rarely reported explicitly.

This paper addresses these specific gaps by presenting a comprehensive experimental, numerical, and analytical investigation into the axial compression behavior of cold-formed perforated steel upright profiles. Particular emphasis is placed on accurately capturing global–local–distortional mode interactions, especially for profiles of intermediate slenderness. Three realistic column lengths—340 mm, 990 mm, and 1990 mm—corresponding to typical bracing node spacings in pallet rack configurations are systematically studied. The chosen section dimensions (85 × 52 mm, 2 mm thick, steel grade S355) are representative of commonly utilized commercial profiles, allowing direct application of the results in practical design contexts.

A novel contribution of this research is the careful calibration of FEM, including measured geometric imperfections and realistic boundary conditions, significantly enhancing model fidelity compared to prior studies. Additionally, this study critically evaluates the applicability and limitations of simplified analytical methods, such as the Effective Width Method (EWM), particularly highlighting scenarios where DSM or enhanced analytical models may offer superior predictive capabilities.

The results presented herein provide valuable benchmark data and validated numerical models, supporting future research aimed at optimizing upright cross-sections, improving structural reliability, and assessing full-scale seismic performance of pallet rack systems.

2. Experimental Program

2.1. Materials

Materials used for storage rack systems must comply with the Romanian seismic design guide GP 128-2014 [24] specifically developed for commercial storage racks subjected to seismic actions. The materials used for storage rack systems must be suitable for cold forming, welding, and galvanizing. Their mechanical properties must comply with the requirements specified in EN 1993-1-1, EN 1993-1-3, [25,26], EN 1090-1+A1, and EN 1090-2+A1 [27,28], which regulate the execution of metal structures.

The mechanical properties considered for steel include the following:

- Yield strength: f_y.
- Ultimate tensile strength: f_u.
- Longitudinal modulus of elasticity: $E = 210,000$ Mpa.
- Shear modulus: $G \approx 81,000$ Mpa.
- Poisson's ratio: $\mu = 0.3$. Thermal expansion coefficient: $\alpha_t = 12 \times 10^{-6} \left(\frac{1}{^{\circ}\mathrm{C}}\right)$.
- Density: $\rho = 7850\ \mathrm{kg/m^3}$.

Additionally, other steel types suitable for cold forming may be used, provided they meet the specific bending and mechanical property requirements outlined in EN 15512 [29] a standard dedicated explicitly to the design of adjustable pallet racking systems. These steels must exhibit an ultimate-to-yield strength ratio f_u/f_y of at least 1.05.

Steels whose mechanical properties have been validated through standardized testing methods, such as those specified by EN ISO 6892-1 [30], may also be employed if they satisfy minimum performance criteria prescribed by structural design standards. In this

study, mechanical properties were verified experimentally by tensile testing a sample of five specimens, ensuring the steel age did not exceed 12 months at the sampling moment, in accordance with EN 15512.

For accurate finite element model calibration, tensile tests were conducted according to EN ISO 6892-1, on steel specimens identical to those used in vertical elements of the studied metal storage racks. The tensile specimens were machined in accordance with EN ISO 6892-1, using a flat dog-bone geometry with the following dimensions: 174.1 mm total length, 50 mm gauge length, 10 mm reduced section width, and 2.0 mm thickness, identical to the wall thickness of the upright profiles. The fillet radius was 30 mm, as illustrated in Figure 3a. Figure 3b presents representative stress–strain curves from these tests, and Table 1 summarizes specimen geometry alongside mechanical properties, including yield strength, ultimate tensile strength, and modulus of elasticity, obtained from experimental results.

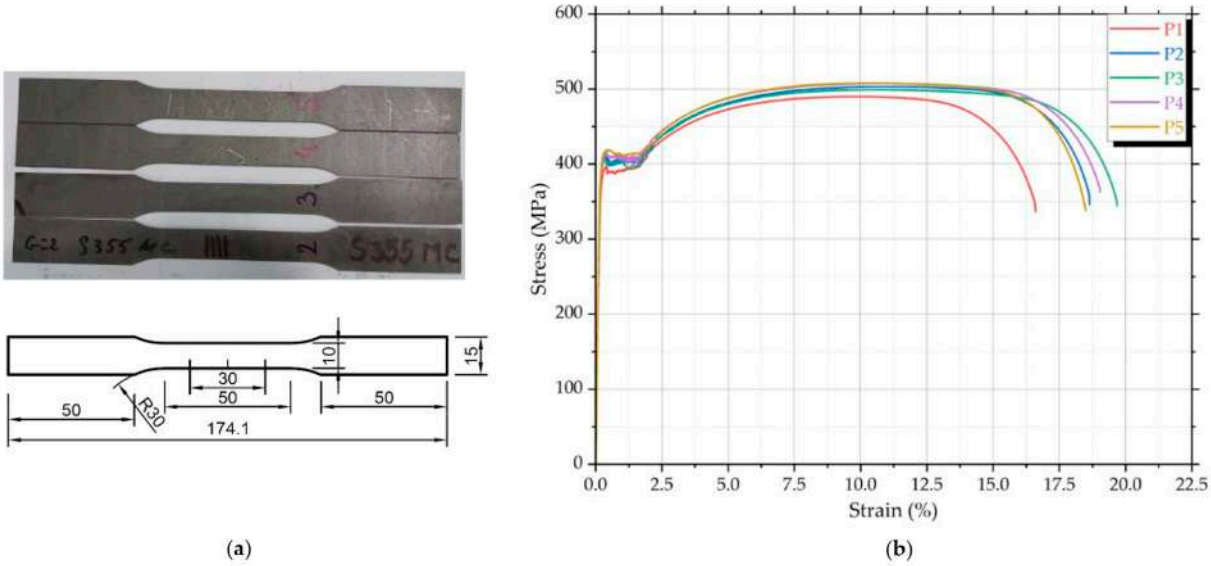

Figure 3. Tensile specimens and stress–strain curves for S355MC steel: (**a**) tested samples and specimen geometry in milimeters and (**b**) engineering stress–strain curves from five tests (P1–P5).

Table 1. Specimen and material properties used for axial compression testing.

Specimen	Length (mm)	Cross-Section Area A (mm^2)	Moment of Inertia I_y, I_z (mm^4)	Material	Yield Strength f_{yb} (MPa)	Ultimate Strength f_u (MPa)	Modulus of Elasticity E (MPa)
SS-340	340	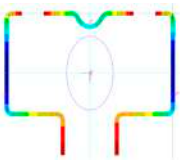	$I_y = 491,749$ $I_z = 270,184$	S355MC	355	430	210,000
MS-990	990						
TS-1990	1990	$A_g = 555$ $A_{eff} = 511$					

Figure 3b shows the stress–strain curves from tensile tests on five steel specimens (P1–P5) used in the upright elements of the storage racks. All curves show consistent elastic behavior with a modulus of elasticity around 210 GPa, confirming material uniformity. The yield strength ranges from 420 to 440 MPa, and the ultimate tensile strength reaches 490–515 MPa, giving a strength ratio $f_u/f_y > 1.1$, in line with EN 15512 requirements. Most specimens show good ductility with total elongation between 15% and 20%. Specimen P1

fractured earlier, possibly due to a local imperfection. The post-yield behavior indicates stable strain hardening, suitable for structural applications and accurate FEM calibration. Table 1 summarizes specimen geometry and mechanical properties (yield strength, ultimate tensile strength, and modulus of elasticity) obtained.

2.2. Methodology

2.2.1. Test Specimens and Geometry

Figure 4 presents the detailed technical drawings of the tested specimens, including cross-sections, elevation views, and the 3D configuration. The specimens include end plates used for load application during axial compression tests. All specimens share the same cross-sectional profile of 85 mm × 52 mm, with a nominal wall thickness of 2 mm. The total lengths investigated were 340 mm, 990 mm, and 1990 mm, corresponding to realistic upright segment lengths between bracing nodes in commercial pallet racks.

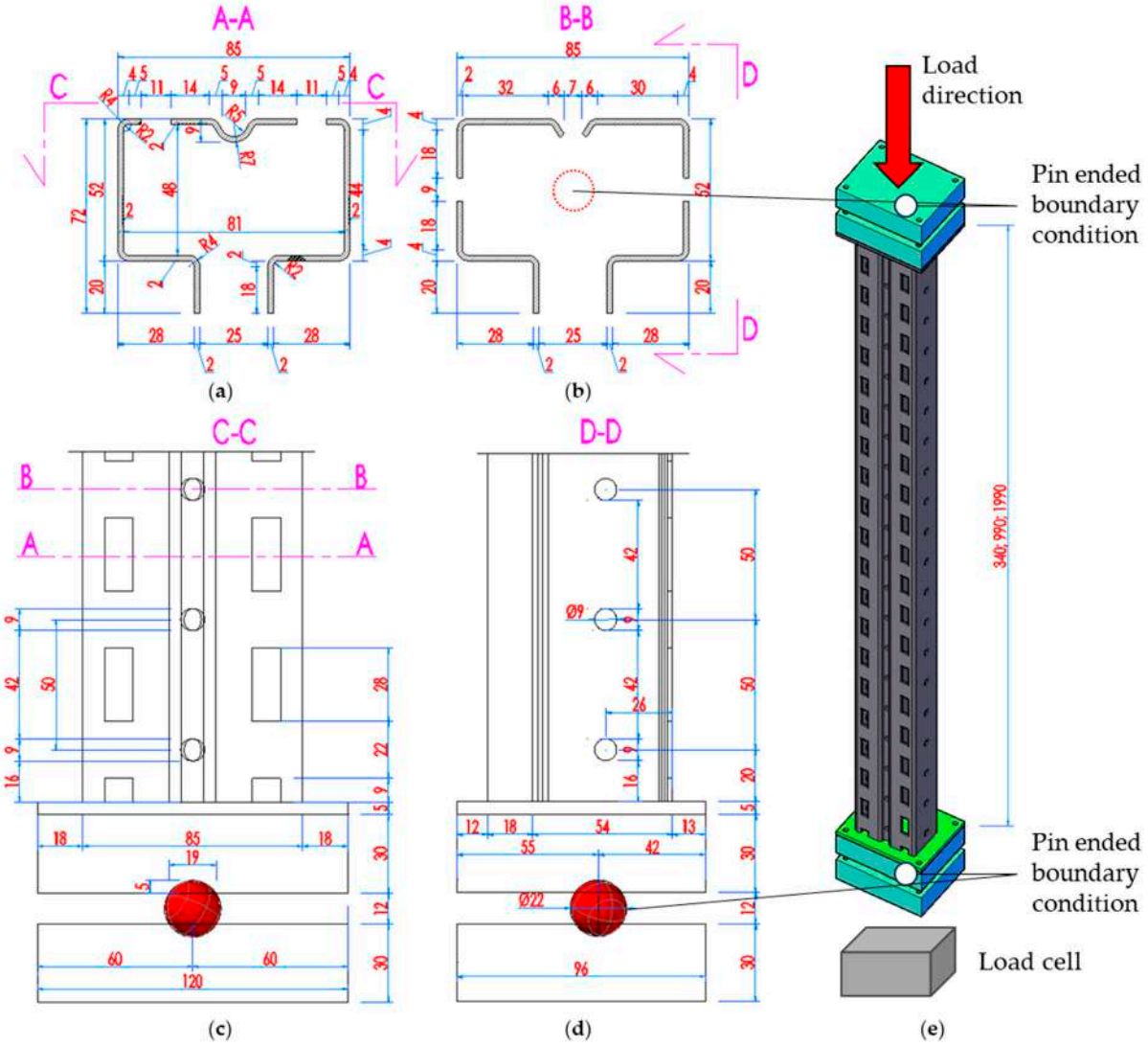

Figure 4. Technical drawings and dimensions in millimeters of the specimens. (**a**) Cross-section A-A; (**b**) cross-section B-B; (**c**) front elevation segment with the end plates; (**d**) lateral elevation segment with the end plates; (**e**) 3D view of the specimen.

The three specimen lengths—340 mm (SS-340), 990 mm (MS-990), and 1990 mm (TS-1990)—were selected to represent realistic vertical spacing between bracing nodes in industrial pallet rack systems. These values also span a representative range of

non-dimensional slenderness ($\overline{\lambda}$), from stocky columns susceptible to local buckling to intermediate-length members exhibiting coupled distortional–global interaction, and slender profiles governed by global flexural buckling. The chosen lengths reflect standard commercial configurations and are consistent with typical dimensions found in European racking design practice. This selection enabled a systematic investigation of the influence of slenderness on buckling behavior and compressive resistance.

In all tests, spherical hinges were used at both ends of the specimens, positioned at the centroid of the cross-section, in accordance with the recommendations provided in Annex A.2 of the Romanian seismic design guideline GP 128-2014. This configuration ensures concentric axial loading and minimizes the influence of end restraints or unintentional moments. The offset distances of 55 mm (top) and 42 mm (bottom) account for the physical dimensions of the hinge assembly and end plates, ensuring that the applied force passes directly through the section's centroidal axis. This setup simulates ideal pin-ended boundary conditions, enabling meaningful comparisons with analytical models and FEM simulations.

2.2.2. Test Setup and Procedure

Axial compression tests were performed on three groups of cold-formed perforated steel uprights with different lengths, representing typical vertical segments between bracing nodes in industrial pallet rack systems. All specimens were fabricated from S355 steel and had a uniform cross-section of 85 × 52 mm with a wall thickness of 2 mm. Their geometric characteristics, including cross-sectional views and end plate configuration, are detailed in Figure 4, while the visual appearance of the specimens prior to testing is presented in Figure 5.

- Short specimens (SS-340, length 340 mm): Five specimens were tested using a Zwick/Roell 1000SP universal testing machine with a capacity of 1000 kN. Axial force and displacement were recorded directly via the machine's integrated sensors. The test configuration for these specimens is shown in Figure 6a,b.
- Medium specimens (MS-990, length 990 mm): Another set of five specimens was tested in a 3000 kN hydraulic testing machine. An external load cell and a linear displacement transducer were employed to improve measurement precision. Data were recorded and processed using an external digital acquisition system. The test setup for MS-990 specimens is depicted in Figure 6c.
- Tall specimens (TS-1990, length 1990 mm): The tallest columns illustrated in Figure 6d, were tested in a custom experimental rig using a hydraulic jack with a 300 kN capacity. An external 100 kN load cell was used for accurate force monitoring.

Although three different testing rigs were employed—each selected to match the specific load capacity and geometric constraints of the specimen series—all machines were equipped with calibrated load cells and displacement transducers, and the same loading rate and boundary conditions were applied. This ensured consistency across tests. The load–displacement responses showed no systematic deviation attributable to the testing equipment, confirming that the use of multiple rigs did not influence the results. This approach was necessary due to significant differences in specimen size and expected behavior.



Figure 5. Appearance of the specimens prepared for testing (units milimiters): (**a**) SS-340; (**b**) MS-990; (**c**) TS-1990.

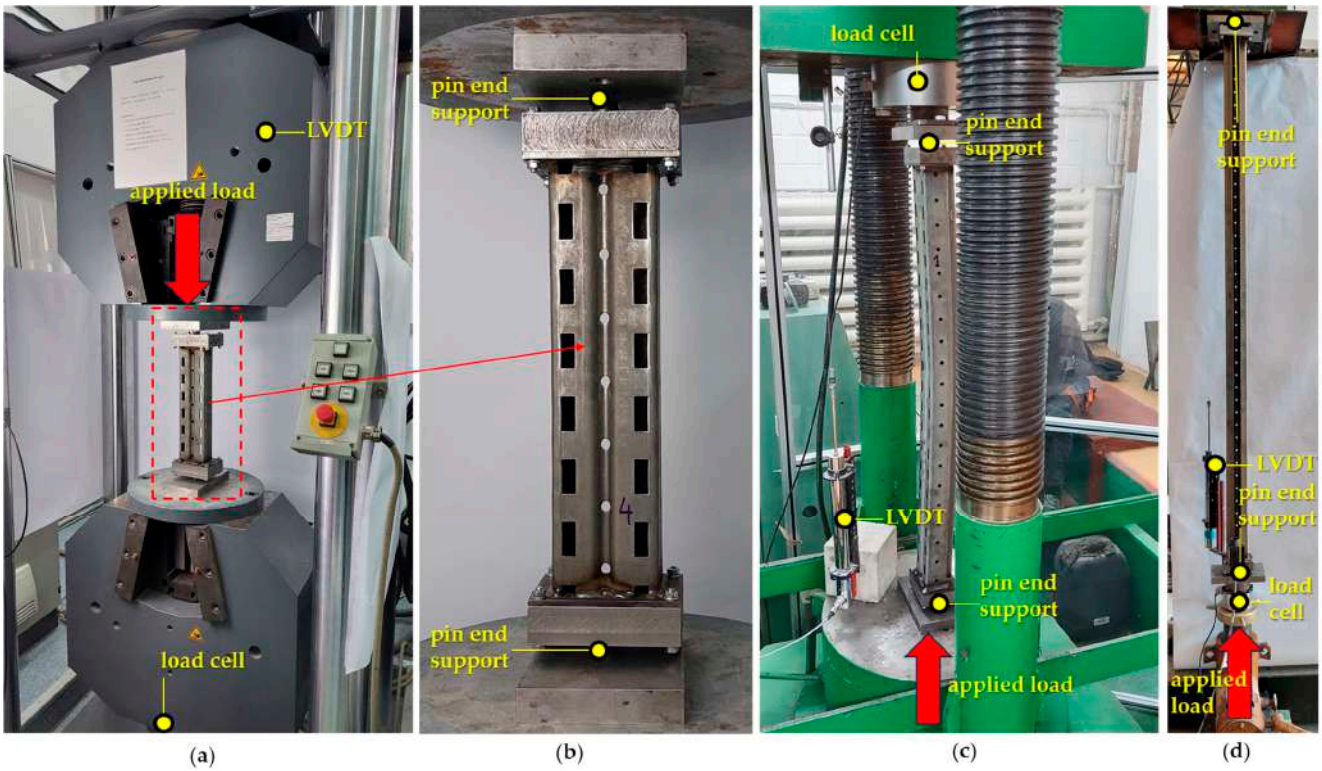

Figure 6. Experimental setup for axial compression testing of: (**a**) Zwick/Roell 1000SP universal testing machine for SS-340; (**b**) close-up view of the specimen SS-340; (**c**) MS-990 specimen tested in a 3000 kN universal testing machine; (**d**) TS-1990 specimens tested with a 300 kN hydraulic jack.

For the SS-340 and MS-990 series, five identical specimens were tested to ensure statistical reliability, capture potential variability due to manufacturing imperfections, and construct average load–displacement curves with confidence. In the case of the TS-1990 specimens, three tests were performed due to practical constraints related to the size of the test rig and availability of material. Nevertheless, the results showed consistent global buckling behavior and closely matched numerical predictions, which supports the validity of the conclusions drawn for slender members. This testing strategy enabled a robust comparison across all three slenderness categories while maintaining experimental feasibility.

All tests were conducted with articulated boundary conditions at the base, as prescribed by Annex A.2 of GP 128-2014, which reflects the typical behavior of uprights in pallet racking systems. The top end of each specimen was left free to displace laterally, simulating the unbraced length between two real-world bracing nodes. Axial loads were applied concentrically through welded steel end plates to ensure uniform stress distribution and minimal eccentricity. A constant loading rate of approximately 1 kN/s was maintained throughout the tests to avoid dynamic effects and ensure repeatability. The test was terminated when a clear local or global failure was observed, or when the applied load dropped below 80% of the peak value. This criterion ensures the capture of post-peak behavior while avoiding unnecessary loading beyond structural relevance. A similar approach, based on a predefined strength loss threshold, is also reported in recent experimental studies on cold-formed steel members [31].

Displacement evolution and failure modes were visually monitored and documented throughout testing. The experimental protocol was designed to meet current industry standards for cold-formed steel members, ensuring both reproducibility and data quality. The results obtained were used to calibrate the finite element models, enabling accurate comparisons between numerical simulations and experimental outcomes.

3. Experimental Test Results

3.1. SS-340 Specimens

The axial compression tests conducted on the short specimens (SS-340) revealed consistent mechanical behavior across all five samples. The load–displacement curves, shown in Figure 7a, indicate an initial linear response followed by a gradual nonlinear hardening, reaching peak loads between 195 and 203 kN. After reaching maximum capacity, all specimens exhibited a softening response, with displacement at failure ranging from 1.9 mm to 2.2 mm.

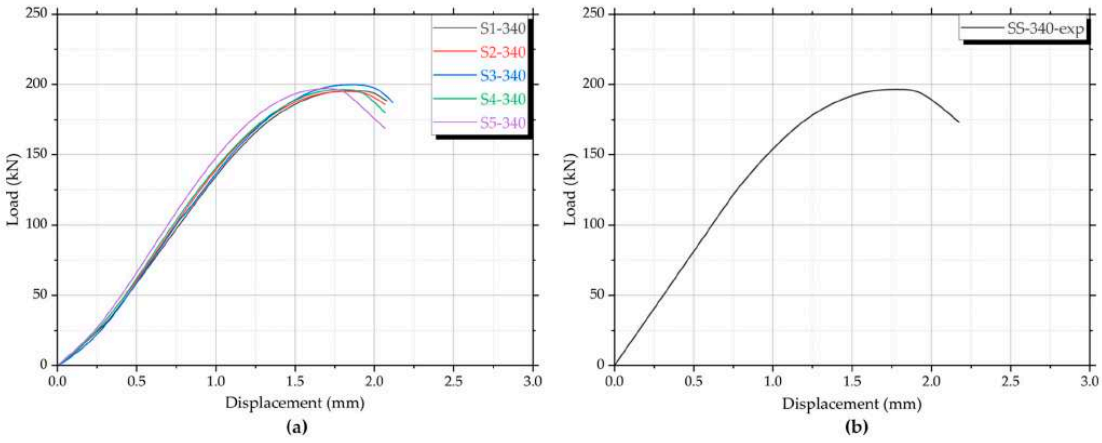

Figure 7. Experimental load–displacement curves for the short specimens SS-340 under axial compression: (**a**) individual results; (**b**) average results.

The average load–displacement curve shown in Figure 7b reaches a peak load of 196 kN at a displacement of 1.75 mm. After the peak, the curve exhibits a moderately descending trend, which reflects the progressive development of local buckling in the web region near the perforations.

After testing, the specimens exhibited various degrees of deformation. Failure patterns are presented in Figure 8. The images show that failure was initiated by local buckling in the web zone, particularly near perforations and dimples, which act as stress concentrators. Although some global deformation was visible, the short length and high stiffness of the SS-340 specimens prevented full-column buckling. The observed failure was thus dominated by local instability phenomena, initiated around geometric discontinuities. All specimens exhibited local buckling initiated in the web zone near perforations. The deformations involved both inward flange distortion and out-of-plane bending of the web. In some cases, buckling occurred at multiple perforations simultaneously, producing compound deformation shapes.

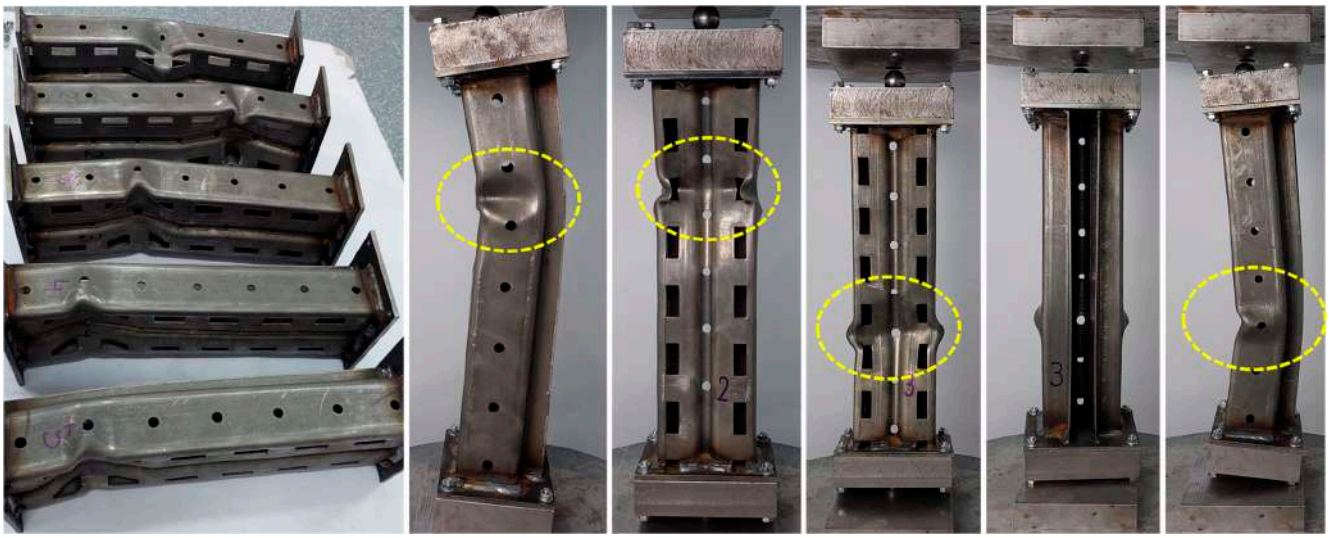

Figure 8. Detailed views of failure patterns for SS-340 specimens following axial compression.

Plastic deformations remained confined to local zones. No material tearing or rupture was observed. The failure mode was governed by geometric instability—such as local buckling and flange distortion—rather than by ultimate material failure (e.g., tearing or rupture). Plastic yielding occurred locally, but the specimens retained integrity throughout the test.

3.2. MS-990 Specimens

The experimental load–displacement curves for the MS-990 specimens are shown in Figure 9. The individual curves in Figure 9a indicate consistent structural behavior across the five tests. All specimens follow a similar path: an initial linear elastic region, followed by a nonlinear hardening phase, reaching peak load, and ending with a post-peak softening.

The maximum load values range from approximately 128 kN to 143 kN, with most specimens reaching peak strength between 1.7 mm and 2.1 mm of axial displacement. This small variation suggests a moderate sensitivity to initial geometric imperfections or local instability effects caused by the perforations.

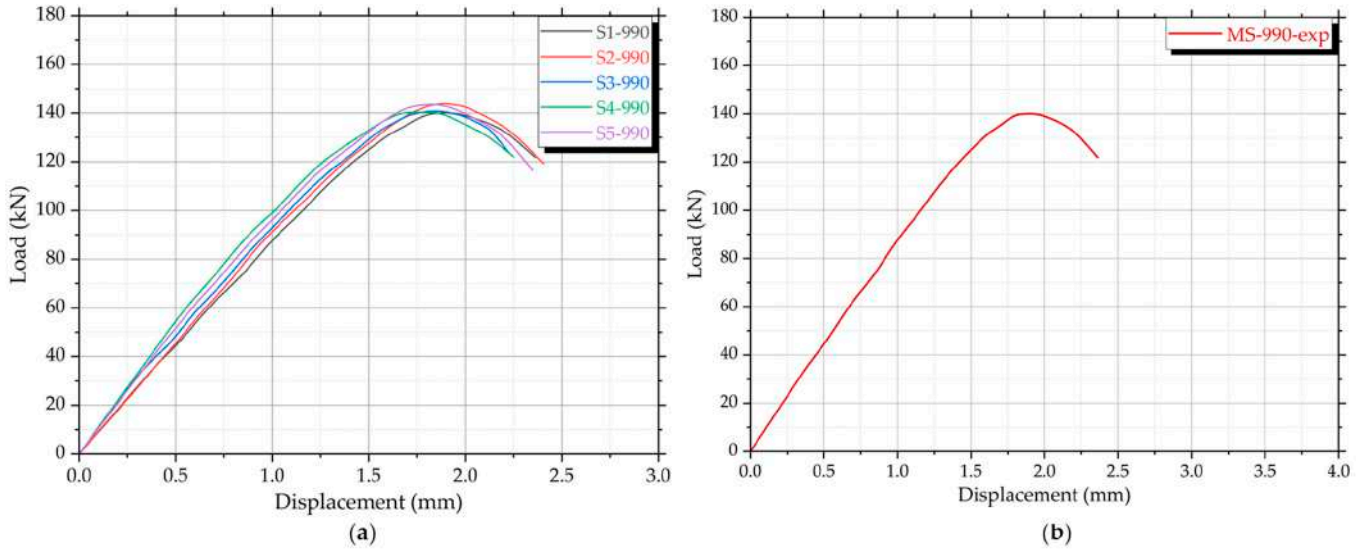

Figure 9. Experimental load–displacement curves for the medium specimens MS-990 under axial compression: (**a**) individual results; (**b**) average results.

The average response, shown in Figure 9b, confirms this trend. The maximum load reaches 140 kN, followed by a softening branch that extends until a displacement of about 2.4 mm.

The general shape of the curves reflects a deformation mechanism initiated by distortional buckling, observed as local flange and web distortions near mid-height, which then triggered a gradual global lateral deflection. This interaction reduced axial stiffness and governed the post-peak response. The deformation pattern was stable, with no abrupt load drops or material failure, and was similar for all tested specimens.

The post-test deformation patterns of MS-990 specimens are shown in Figure 10. All five columns exhibited smooth global flexural buckling, with lateral deflection occurring in a single direction and maximum curvature concentrated near the mid-span. The dashed yellow lines highlight the lateral displacement path observed during and after loading.

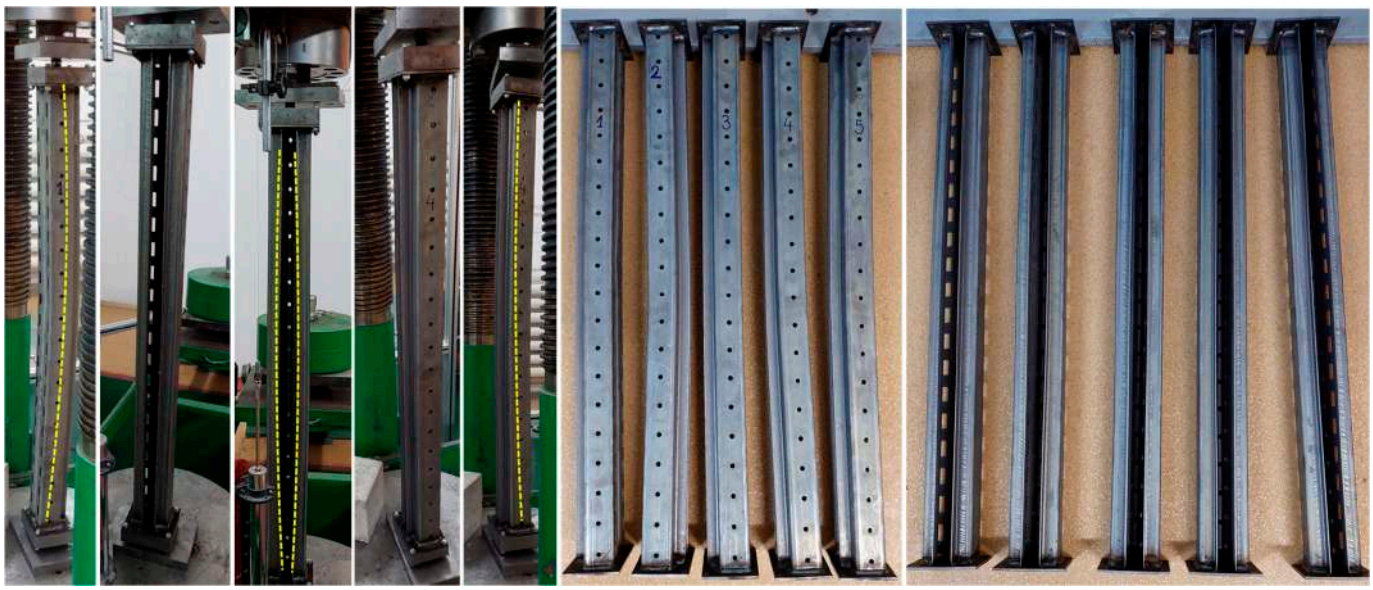

Figure 10. Experimental results for MS-990 specimens after axial compression tests.

Some specimens present slight asymmetry in the deflected shape, suggesting the influence of geometric imperfections or eccentricities during load application. Despite the global nature of the failure, localized distortion of the cross-section can also be observed in the web regions, particularly near perforations, where the local stiffness is reduced.

In the unloaded state, viewed from both the front and rear faces, the residual deformation confirms the presence of elastic–plastic global buckling. No visible tearing or crushing was observed, indicating that material failure did not occur. Instead, the deformation was governed by geometric instability, with residual bowing retained after unloading.

This behavior aligns with the experimental curves shown earlier, where the softening branch reflects the gradual loss of axial capacity due to second-order effects from large displacements.

3.3. TS-1990 Specimens

The experimental results for the tall specimens (TS-1990) are shown in Figure 11. The individual load–displacement curves in Figure 11a indicate consistent behavior across the three tested columns. All specimens follow a similar path with an initial linear elastic region, followed by a smooth transition into a nonlinear range. The load reaches a maximum between 85 kN and 91 kN, occurring at axial displacements ranging from 3.6 mm to 4.1 mm. The average curve in Figure 11b confirms this trend, with a peak load of 89 kN reached at a displacement of 3.9 mm.

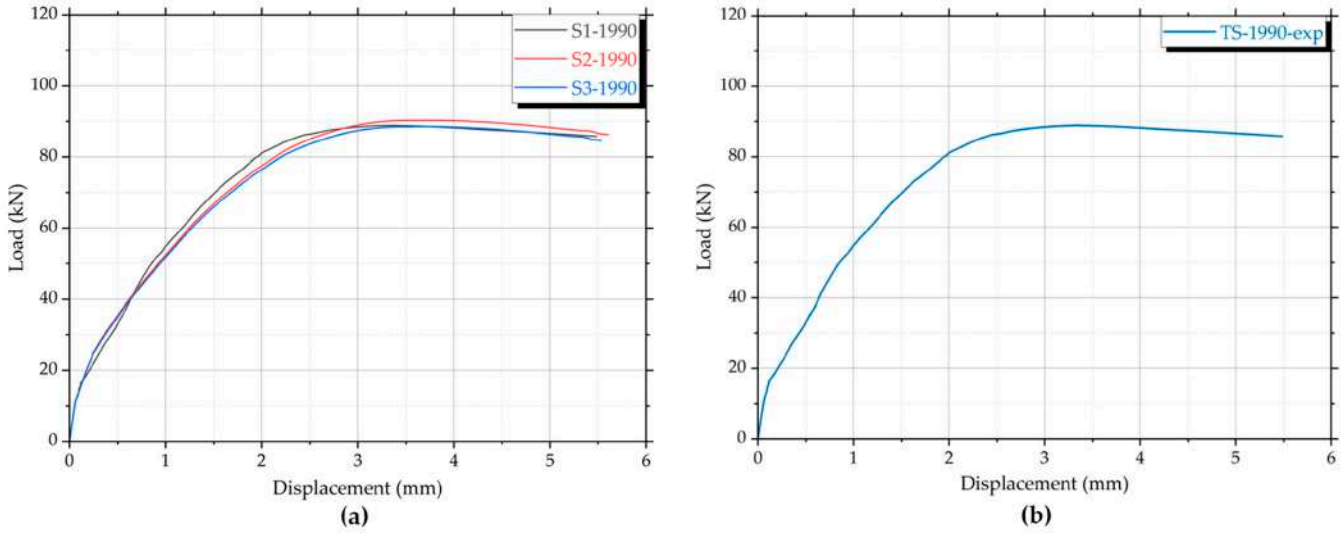

Figure 11. Experimental load–displacement curves for the tall specimens TS-1990 under axial compression: (**a**) individual results; (**b**) average results.

Post-peak behavior shows a gradual decline in axial load, indicating a softening response associated with large lateral deflections. No sudden drop or brittle failure was observed.

The average load–displacement curve shown in Figure 11b presents three distinct linear segments, each corresponding to a different phase in the structural response of the TS-1990 specimens. The initial linear portion represents the elastic axial compression phase, characterized by uniform shortening and negligible lateral deformation. The second segment, with a noticeably reduced slope, reflects the onset of global flexural buckling, during which the columns develop increasing lateral deflection while continuing to carry axial load. The final segment, with a descending trend, corresponds to the post-peak softening phase, governed by large deflections, redistribution of stresses, and progressive loss of axial stiffness. No material rupture occurred, but the strength degradation is attributed to geometric nonlinearity and second-order effects typical of slender column behavior.

Photographic documentation of the deformed specimens is provided in Figure 12. All three specimens exhibit global flexural buckling, with pronounced lateral deflection centered at mid-height. The deformation path is smooth and continuous, with no evidence of local buckling near the perforations. The dashed yellow lines indicate the curvature profiles developed during testing.



Figure 12. Experimental results for TS-1990 specimens after axial compression tests.

Residual deformation observed after unloading confirms that the instability occurred in the plastic range. The high slenderness of the TS-1990 columns resulted in a flexural response dominated by global mode behavior, with minimal influence from local or distortional effects.

Unlike the shorter specimens, which displayed web and flange distortions around perforations, the TS-1990 profiles remained stable in the cross-sectional plane. The absence of localized deformation modes is consistent with the slenderness effect and longer effective buckling length of these specimens.

4. Numerical Analysis

4.1. Calibration of the Finite Element Model Based on Tensile Test

To accurately define the mechanical behavior of the S355MC steel used for cold-formed profiles, a finite element simulation of the uniaxial tensile test [32] was conducted using ANSYS [33]. The aim was to calibrate the material model by comparing the simulated stress–strain response with experimental results obtained from the tensile tests described in Section 2.1.

In order to address the research gaps identified in the Introduction, the numerical modeling strategy was specifically designed to capture the coupled buckling behavior observed in members with intermediate slenderness, as well as to account for realistic geometric imperfections. To this end, an eigenvalue buckling analysis was first performed to identify the critical mode shapes, and the first buckling mode was then scaled and introduced as an initial imperfection in the nonlinear analysis. This approach enables the simulation to reproduce complex instability phenomena, such as local–distortional and distortional–global mode interactions, which were especially relevant for the MS-990 specimens. The modeling assumptions and boundary conditions were chosen to mirror the test conditions as closely as possible.

The geometry of the standard tensile coupon was created in AutoCAD 2013 and imported into ANSYS as a 3D solid SAT file. The mesh consisted of SOLID186 elements, which are 20-node high-order hexahedral elements suitable for nonlinear analyses. A maximum element size of 2 mm was used, resulting in 5594 nodes and 728 solid elements, as shown in Figure 13a.

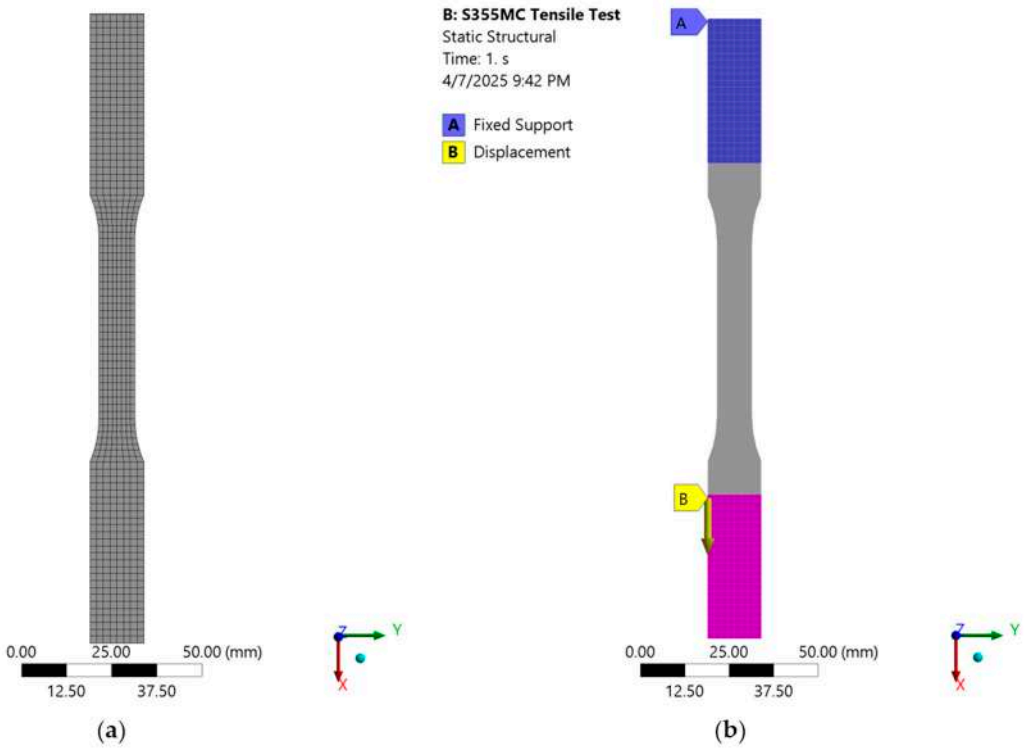

Figure 13. Numerical setup for the tensile test simulation of S355MC steel using ANSYS: (**a**) finite element mesh using SOLID186; (**b**) boundary conditions showing fixed support at the top and imposed displacement at the bottom.

The boundary conditions included a fixed support applied to one end of the specimen, restraining all degrees of freedom. At the opposite end, a prescribed displacement of 15 mm was imposed in the axial (Y) direction to simulate the loading as Figure 13b shows. The

analysis was performed under static structural conditions with large deformation enabled and automatic time stepping activated.

The material was defined as a multilinear isotropic hardening plastic model using true stress–strain data obtained from experimental conversion. The conversion from engineering to true values followed the standard relations shown below:

$$\sigma_{\text{true}} = \sigma_{\text{eng}} \cdot (1 + \varepsilon_{\text{eng}}) \tag{1}$$

$$\varepsilon_{\text{true}} = \ln(1 + \varepsilon_{\text{eng}}) \tag{2}$$

$$\varepsilon_{\text{elastic}} = \frac{\sigma_{true}}{E} \tag{3}$$

$$\varepsilon_{\text{plastic}} = \varepsilon_{total} - \varepsilon_{elastic} \tag{4}$$

where

- σ_{eng}, ε_{eng}: engineering stress and strain;
- σ_{true}, ε_{true}: true stress and strain, used for defining the material in the numerical model;
- $\varepsilon_{\text{elastic}}$: elastic component of the total strain;
- $\varepsilon_{\text{plastic}}$: plastic strain used to define the hardening curve;
- $E = 210,000$ MPa: Young's modulus of elasticity.

The comparison between the experimental, true, and FEM-generated stress–strain curves is shown in Figure 14. The FEM curve was obtained by applying the true stress–strain values in ANSYS and running a tensile simulation of a calibrated test specimen. The very good agreement observed confirms that the material model reproduces the mechanical behavior of the tested steel with sufficient accuracy, and it can be reliably used in the numerical modeling of the full compression tests.

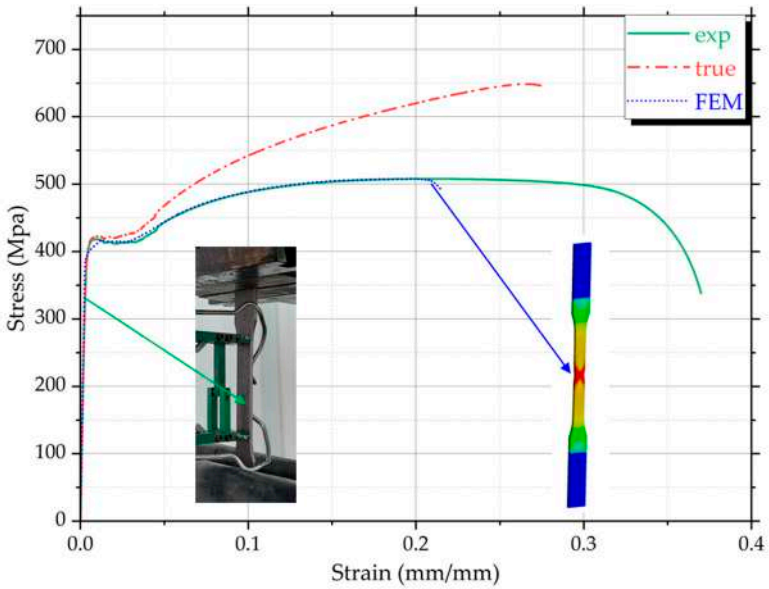

Figure 14. Comparative stress–strain curves for the S355MC steel used in numerical analyses.

Figure 15 shows the main results from the finite element simulation of the tensile test on the S355MC steel specimen. In Figure 15a, total deformation reaches the imposed 15 mm, with uniform elongation along the gauge length, indicating correct boundary conditions and mesh quality. Figure 15b presents the equivalent plastic strain, with a maximum of 0.3838 mm/mm near the center of the reduced section, matching the expected necking zone. Figure 15c shows the von Mises stress distribution, with a peak of 677.47 MPa

in the same area, confirming the model captures post-yield behavior using the applied hardening law.

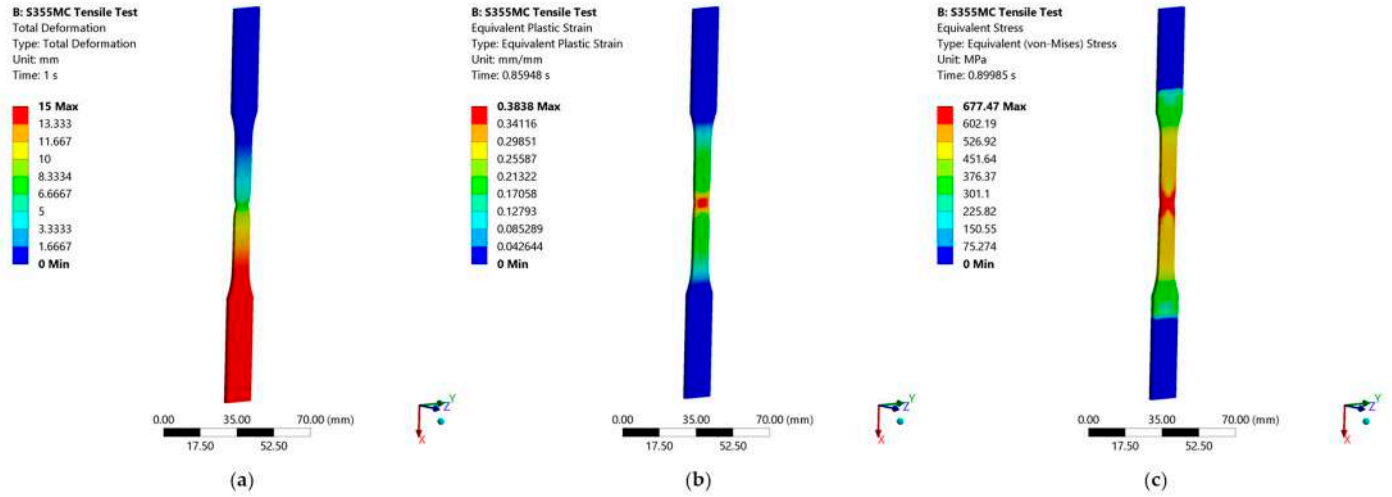

Figure 15. Simulation results for the tensile test of the S355MC steel specimen: (**a**) total deformation; (**b**) equivalent plastic strain; (**c**) equivalent von Mises stress distribution.

The material model implemented in the finite element simulations used the true stress–strain curve, derived from the experimentally obtained engineering data. While the engineering yield strength was approximately 430–440 MPa, the true stress corresponding to the maximum plastic strain reached values up to 650 MPa. This value was used as the upper limit of the multilinear plasticity model to correctly capture the strain hardening behavior of the S355MC steel in the FEM analyses. This approach ensures a more realistic simulation of post-yield deformation and energy dissipation.

4.2. Numerical Modeling and Analysis of the SS-340 Specimen Under Axial Compression

The SS-340 specimen was simulated using a multi-step finite element analysis in ANSYS. The 3D solid model was created in AutoCAD and imported in (.sat) format. The finite element mesh (Figure 16) used SOLID186 elements, with 257,816 nodes and 73,656 elements, providing sufficient resolution to capture both local and global instabilities. A mesh convergence study was performed to ensure reliable prediction of local buckling behavior. The selected mesh, based on SOLID186 elements, was validated by comparing results across multiple mesh densities, with variations in peak load below 2%. Additionally, local mesh refinement was applied around perforations and web zones to accurately capture stress concentrations and deformation localization.

The full test setup, including end plates and spherical supports, was replicated (Figure 17). Contact behavior was defined as frictional, with a coefficient of 0.1, to simulate the pin-ended boundary conditions. The base was fixed, while a remote vertical displacement was applied at the top, allowing axial movement without lateral restraint.

An initial eigenvalue buckling analysis identified the critical buckling shape, which was then introduced as a geometric imperfection in a subsequent nonlinear static analysis. The large deflection option was enabled to account for geometric nonlinearity.

The first buckling mode obtained from the linear eigenvalue analysis was used to introduce initial geometric imperfections in the nonlinear simulations. A scaling factor equal to 1/1000 of the column length was applied to the eigenmode shape, consistent with standard practice for cold-formed steel members and recommendations from EN 1993-1-5 [34] and related studies. This amplitude ensures the triggering of instability while maintaining physical realism.

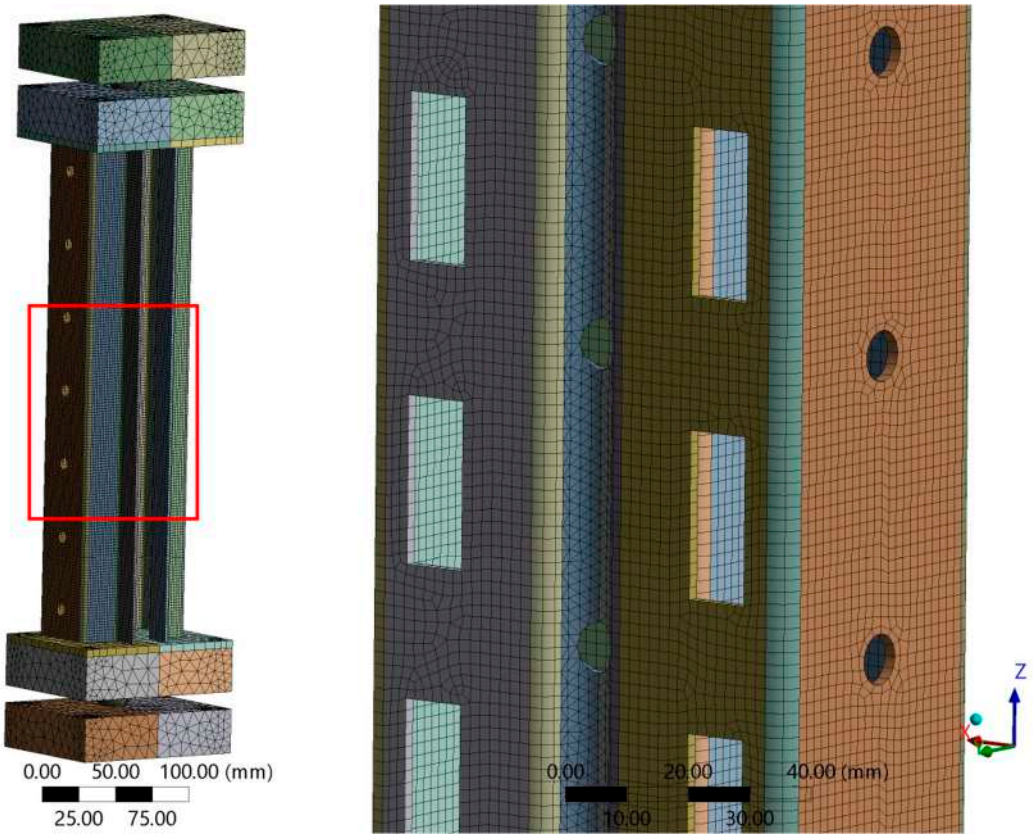

Figure 16. Finite element mesh of the SS-340 model.

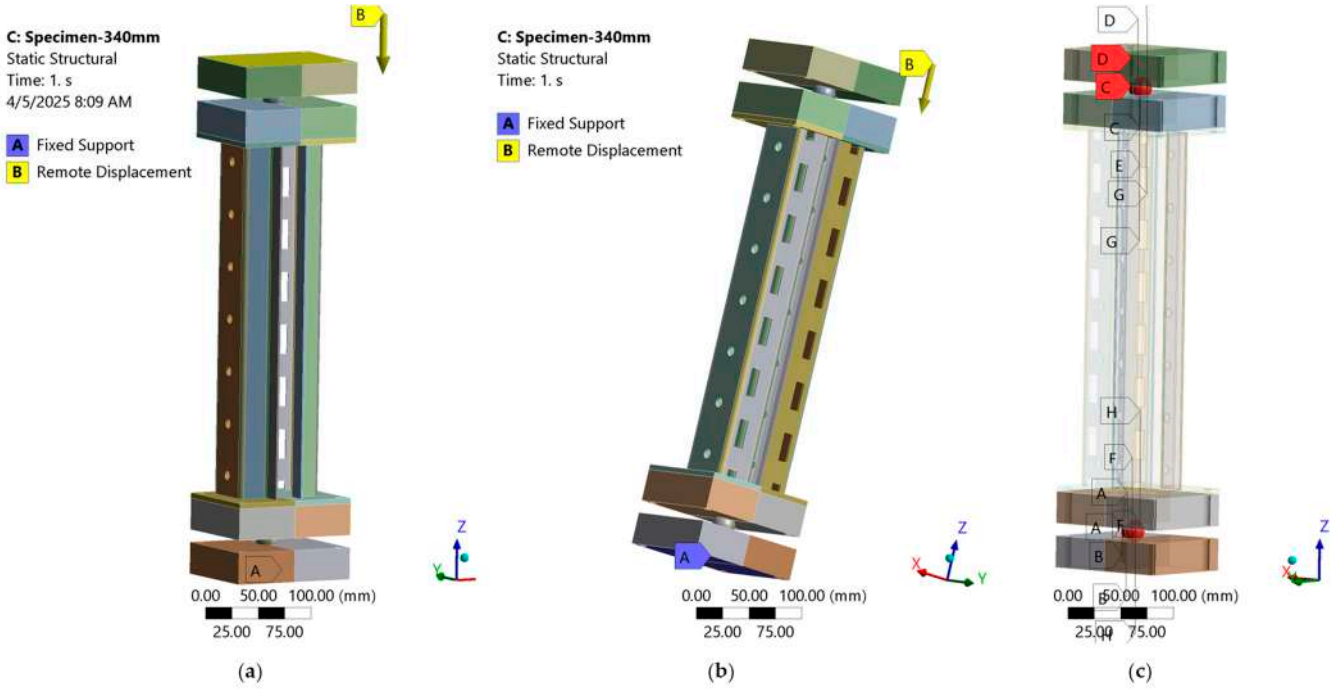

Figure 17. Numerical modeling setup for the SS-340 specimen: (**a**,**b**) the boundary conditions; (**c**) the frictional contact modeling details at the pin-ended supports.

Results from the nonlinear simulation (Figure 18a) show significant out-of-plane deflection near mid-height, consistent with flexural buckling. The corresponding eigenmode shown in Figure 18b confirms the location and shape of the instability. Total deformation

reached 13 mm Figure 19a, with minor vertical shortening observed along the *Z*-axis, as shown in Figure 19b.

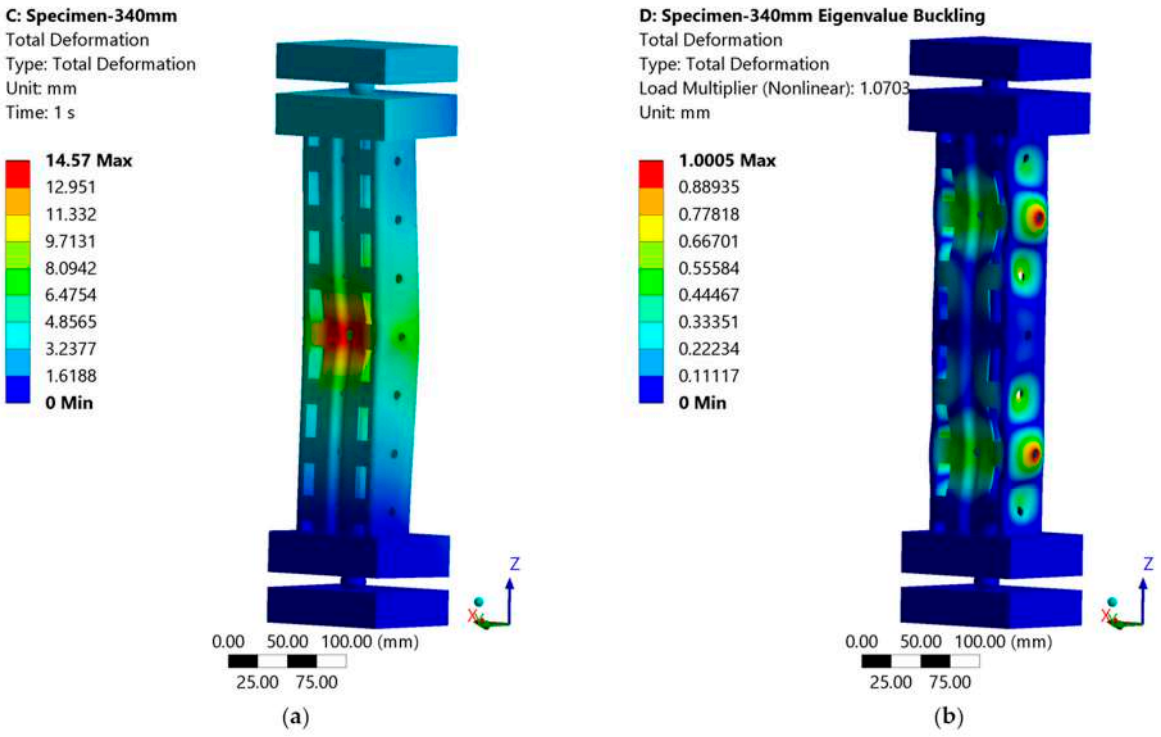

Figure 18. Deformed shape of the SS-340 specimen: (**a**) nonlinear structural static analysis; (**b**) first buckling mode from eigenvalue analysis.

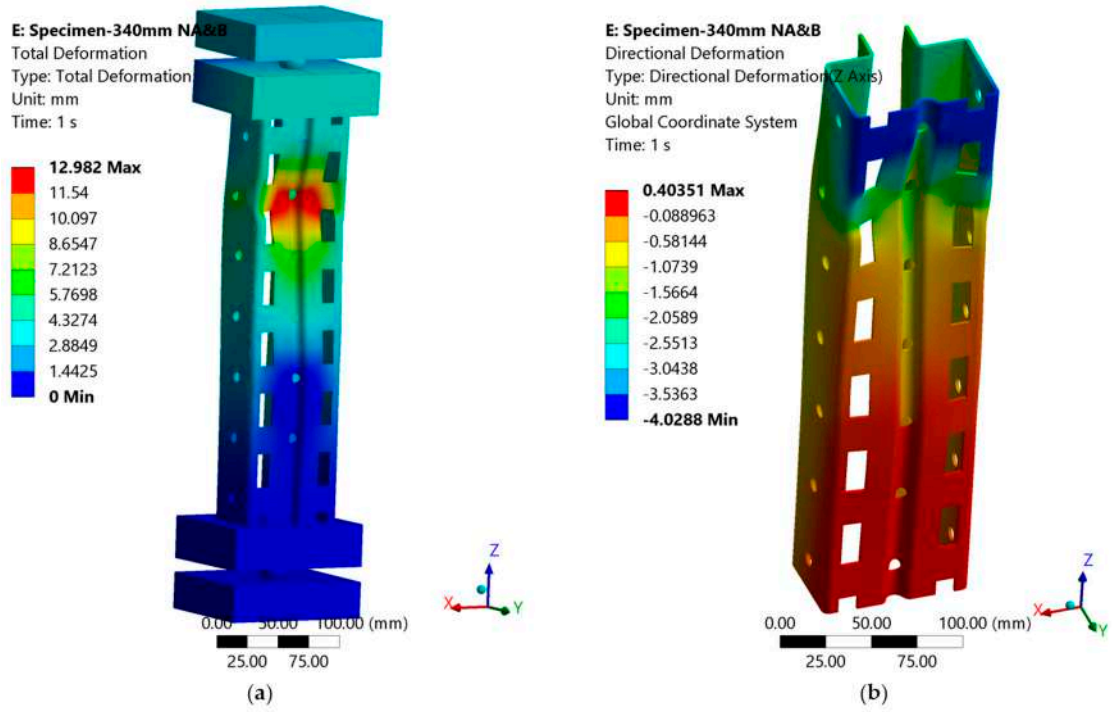

Figure 19. Nonlinear analysis following eigenvalue analysis of the SS340 specimen: (**a**) total deformation; (**b**) directional deformation along the Z axis.

Von Mises stress results presented in Figure 20 show stress concentrations above 650 MPa near perforations at mid-height, matching the zones of observed plastic deforma-

tion in the physical tests. These stresses correspond to the experimentally observed failure features Figure 20c.

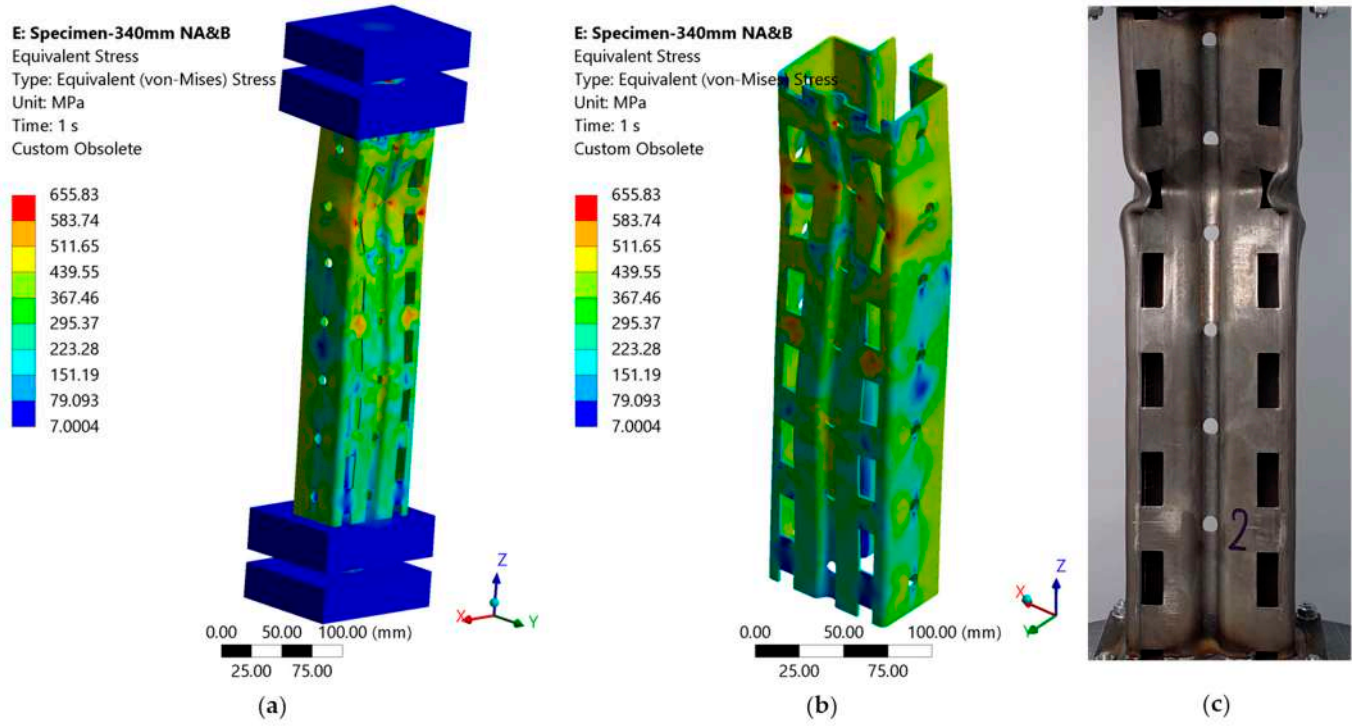

Figure 20. Equivalent von Misses Stress distribution: (**a**) the complete model; (**b**) upright profile with hidden end plates; (**c**) experimentally tested specimen for visual comparison of the failure mode.

The load–displacement curve comparison in Figure 21 indicates that the simulation accurately follows the experimental trend, with a minor overestimation of initial stiffness.

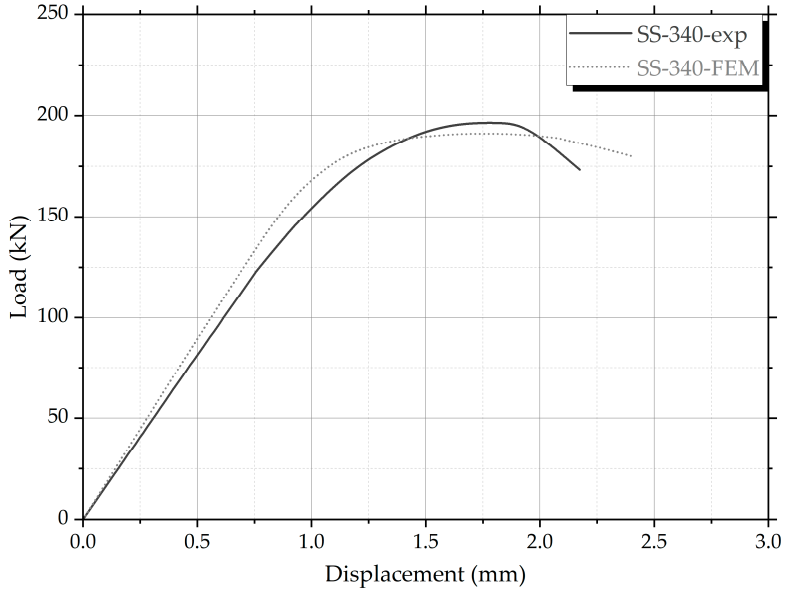

Figure 21. Load–displacement response comparison between experimental and numerical results for the SS-340 specimen.

4.3. Numerical Modeling and Analysis of the MS-990 Specimen Under Axial Compression

The MS-990 simulation followed the same modeling strategy. The geometry was exported from AutoCAD to ANSYS, and a 3D model was meshed using 98,260 SOLID186

elements and 575,874 nodes (Figure 22). Contact between the spherical ends and plates was modeled using TARGE170 and CONTA174 elements, with a friction coefficient of 0.1.

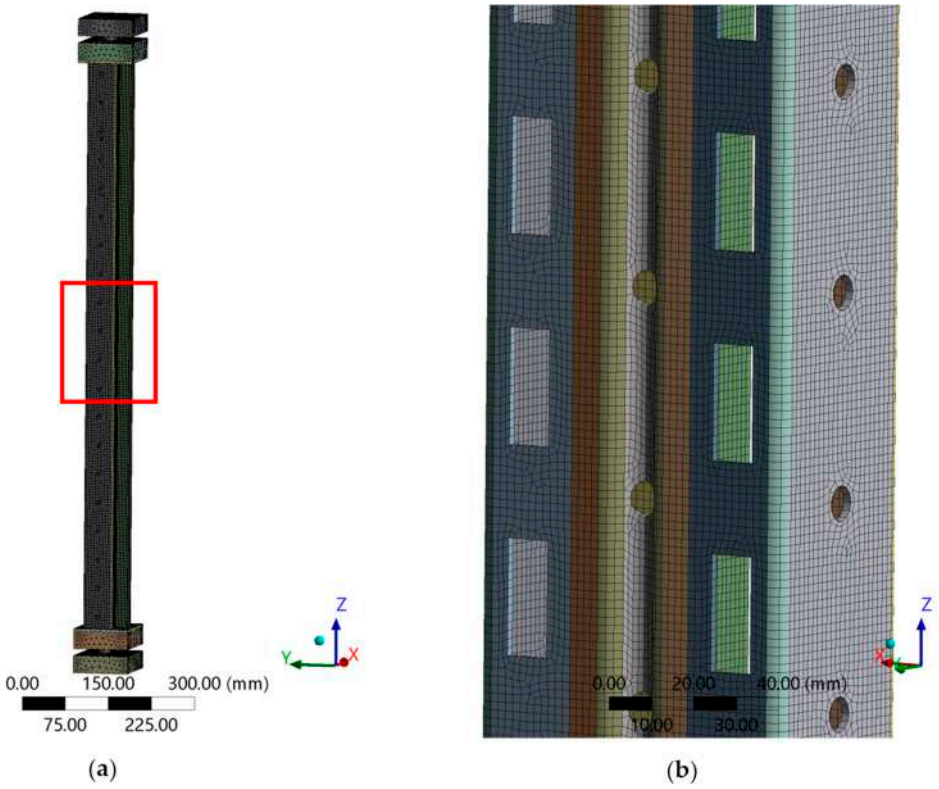

Figure 22. Finite element mesh of the MS-990 model. (**a**) finite element mesh; (**b**) mesh detail around perforations.

The boundary conditions replicated the test setup: a fixed base and remote displacement at the top (Figure 23). A nonlinear static analysis was followed by eigenvalue buckling and then a nonlinear post-buckling analysis.

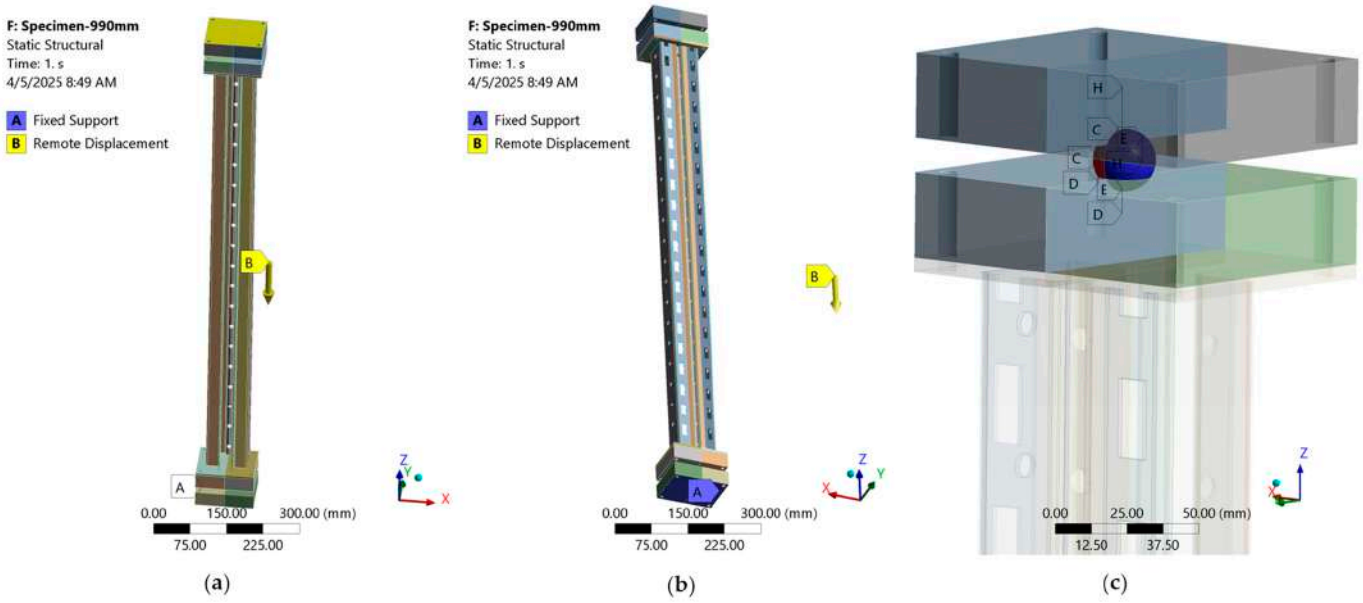

Figure 23. Boundary conditions for the MS-990 specimen: (**a**) remote displacement top view, (**b**) fixed support bottom view and (**c**) pin-ended contact detail.

Figure 24 shows the deformation shape from the static and eigenvalue analyses. The final deformed shape from the post-buckling analysis (Figure 25) highlights lateral deformation at mid-height. Equivalent stress contours (Figure 26) show stress localization around perforations, similar to the failure observed experimentally (Figure 27).

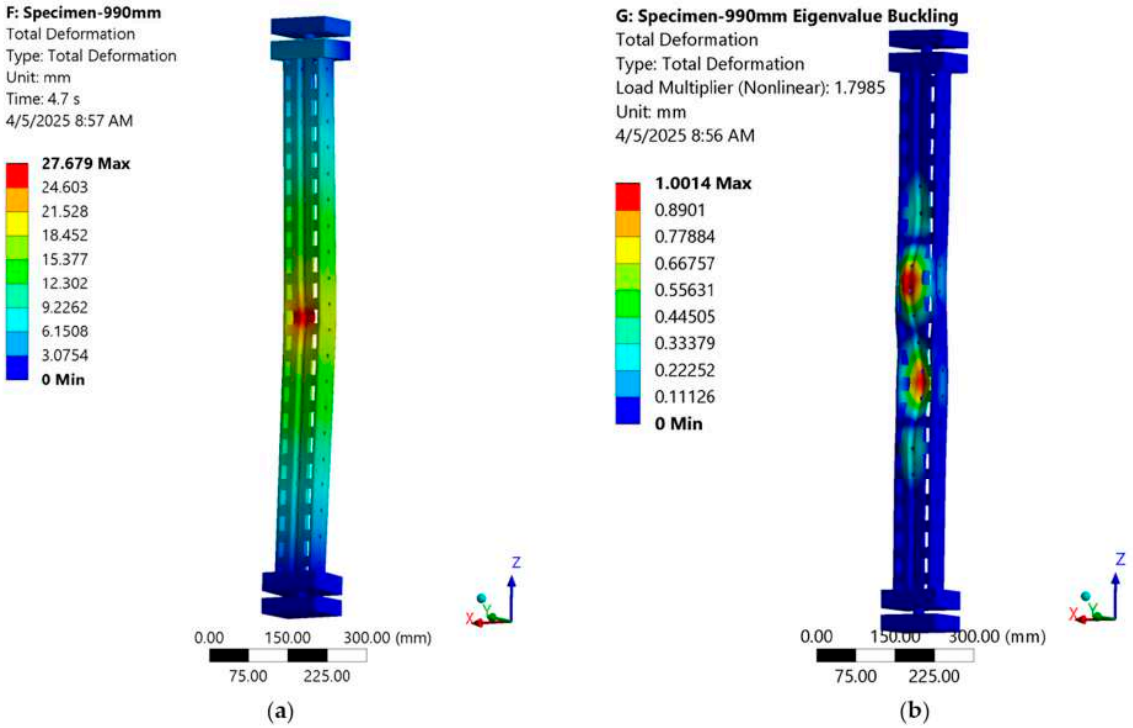

Figure 24. MS-990 specimen deformation: (**a**) nonlinear static analysis; (**b**) first buckling mode from eigenvalue analysis.

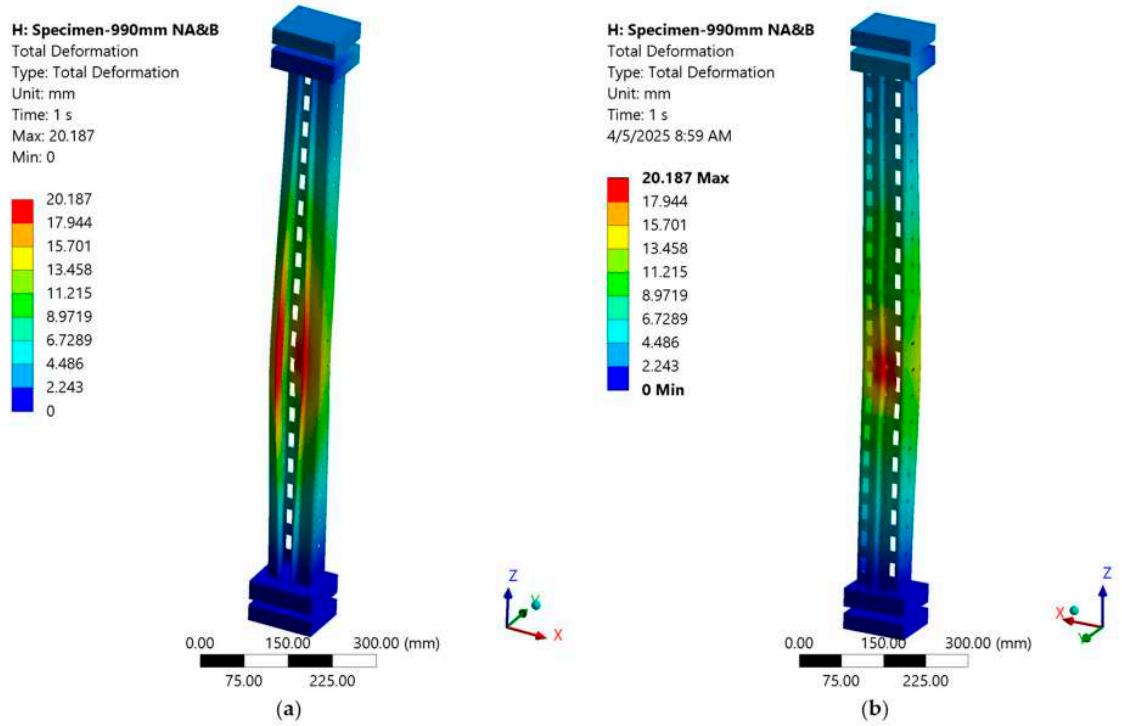

Figure 25. Total deformation of the MS-990 specimen from nonlinear post-buckling analysis: (**a**) front view; (**b**) back view.

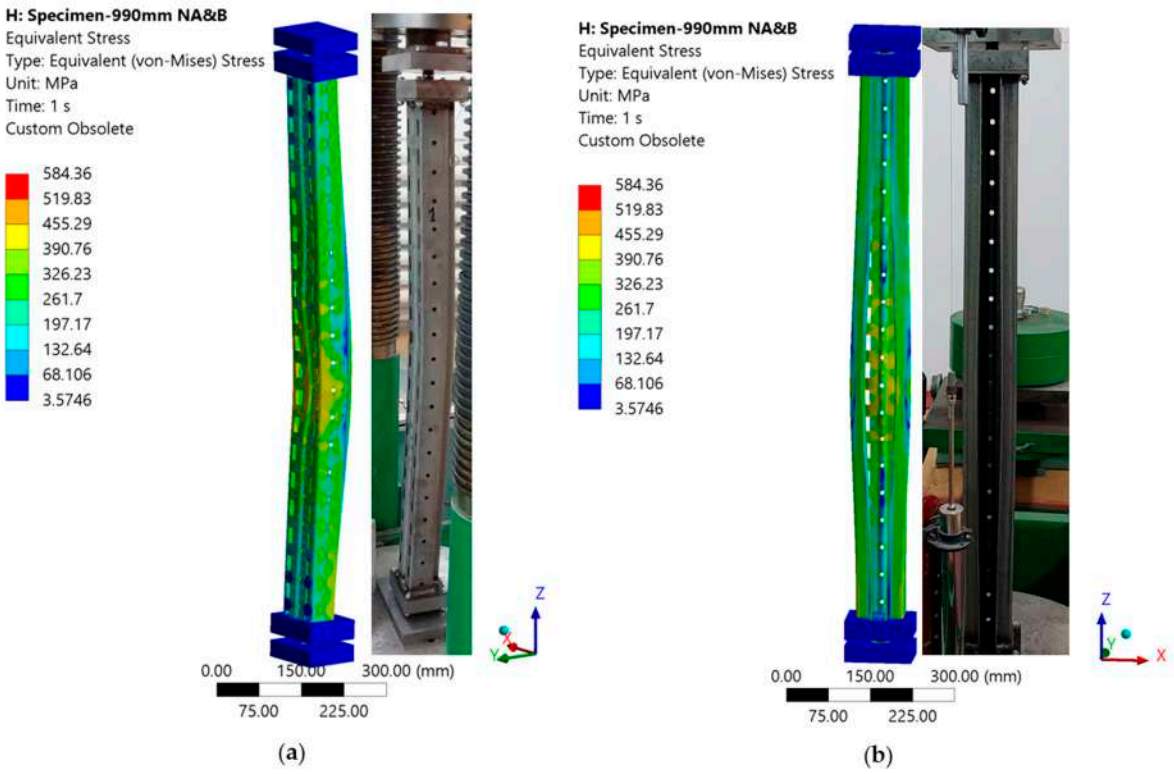

Figure 26. Equivalent von Mises stress distribution for the MS-990 specimen and comparison with experimental failure: (**a**) front view; (**b**) back view.

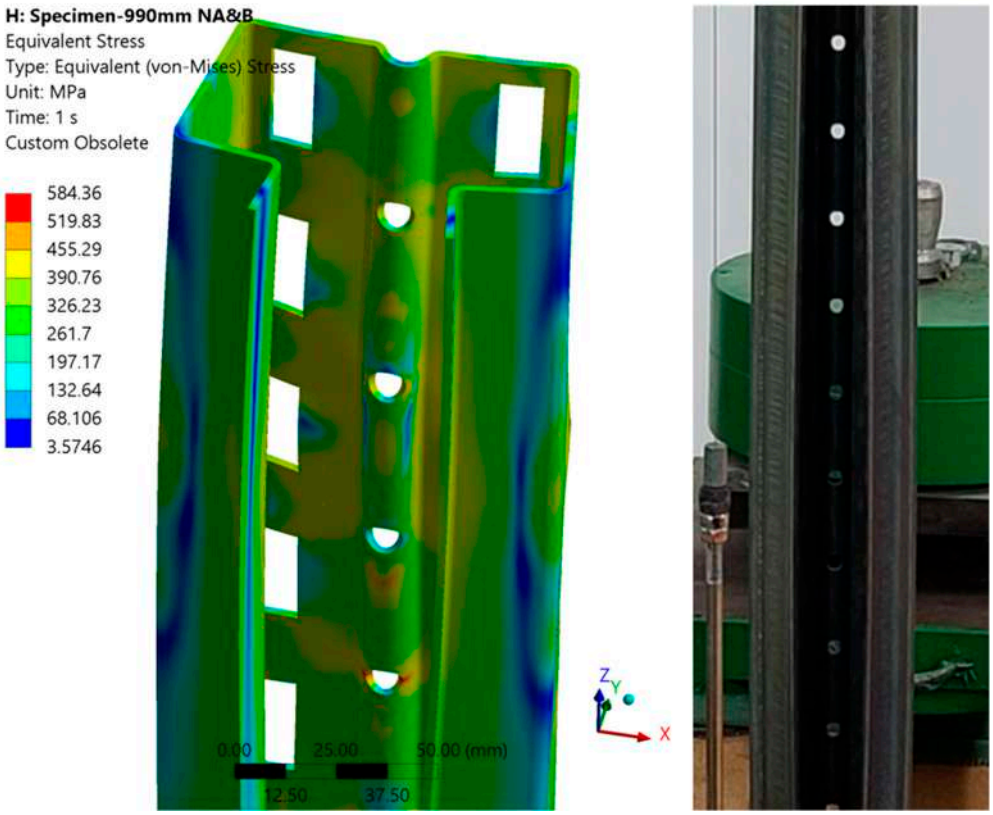

Figure 27. Stress concentration and failure localization in the middle part of the MS-990 specimennumerical von Mises stress mapand experimental observation.

The load–displacement response in Figure 28 shows good agreement between simulation and tests, both in terms of stiffness and maximum load.

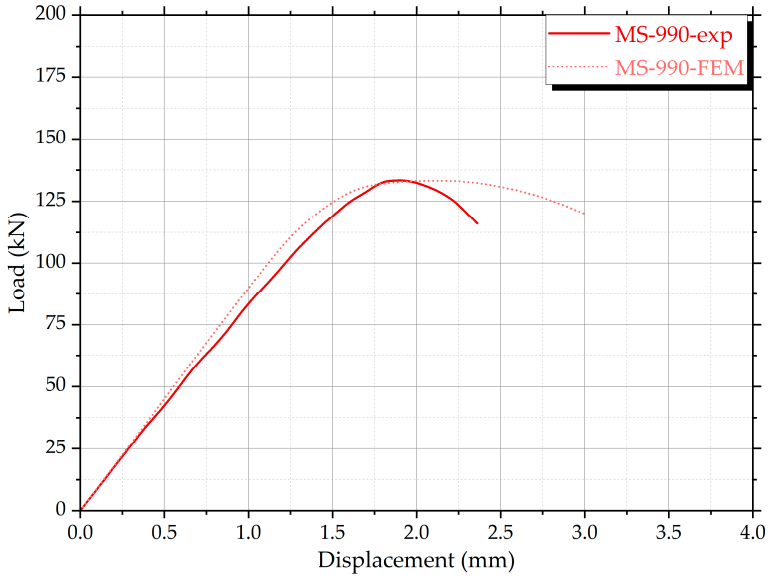

Figure 28. Load–displacement response comparison between experimental and numerical results for the MS-990 specimen.

4.4. Numerical Modeling and Analysis of the TS-1990 Specimen Under Axial Compression

The TS-1990 model included all geometric features and test conditions, with mesh refinement near perforations (Figure 29). The mesh included 166,433 elements and 1,109,982 nodes. Boundary conditions are shown in Figure 29a, with a fixed base and imposed vertical displacement at the top.

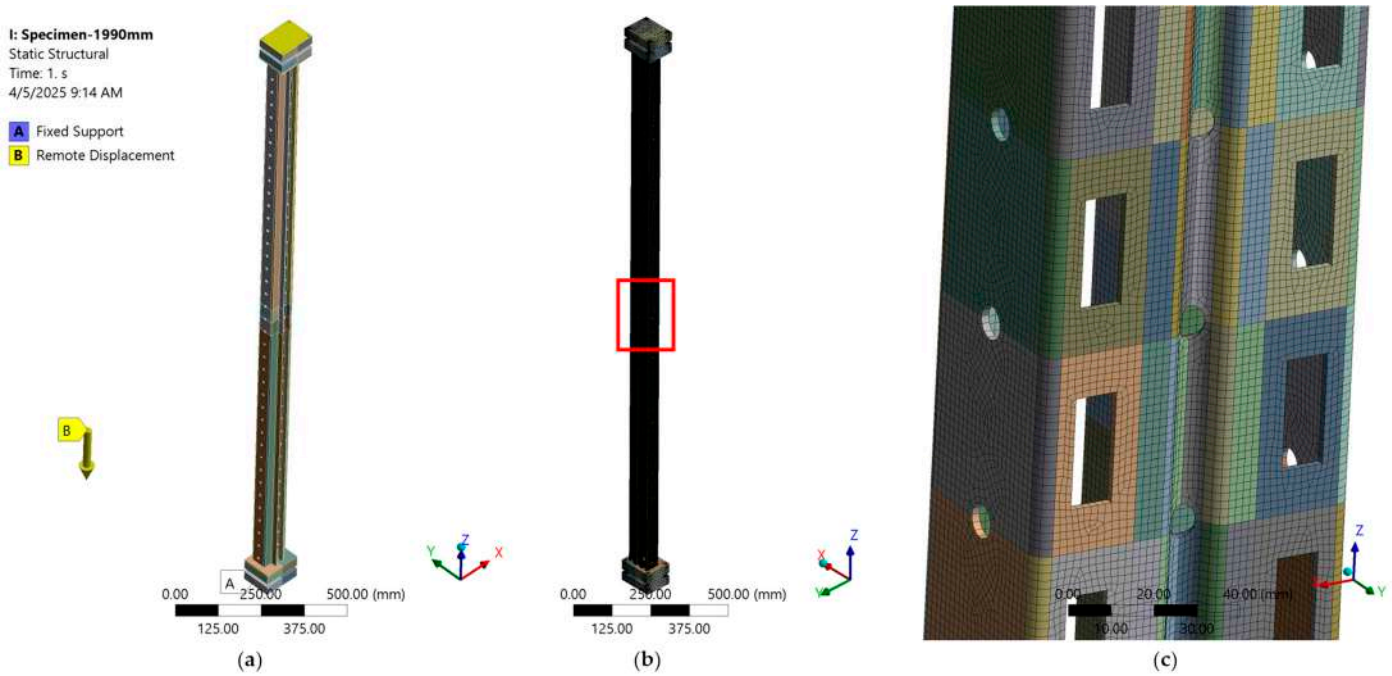

Figure 29. Numerical model of the TS-1990 specimen: (**a**) boundary conditions; (**b**) finite element mesh; (**c**) mesh detail around perforations.

A nonlinear static analysis was performed first, as shown in Figure 30a, followed by eigenvalue buckling, as shown in Figure 30b, which identified a higher-order mode with local distortional features. A final nonlinear analysis incorporating imperfections, as shown in Figure 30c, produced a realistic deflection profile. Von Mises stress results (Figure 31) show peak stresses near perforations, aligning with failure zones in tested specimens.

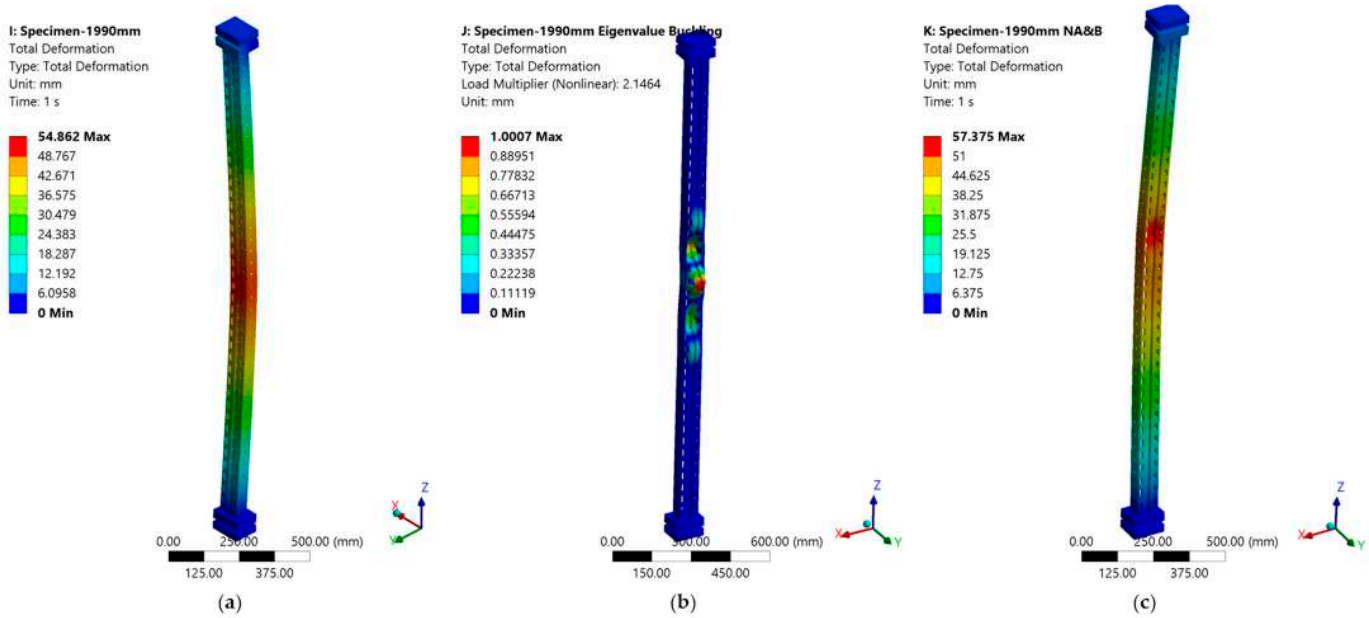

Figure 30. TS-1990 specimen results: (**a**) nonlinear static analysis; (**b**) first buckling mode from eigenvalue analysis; (**c**) nonlinear analysis after eigenvalue analysis.

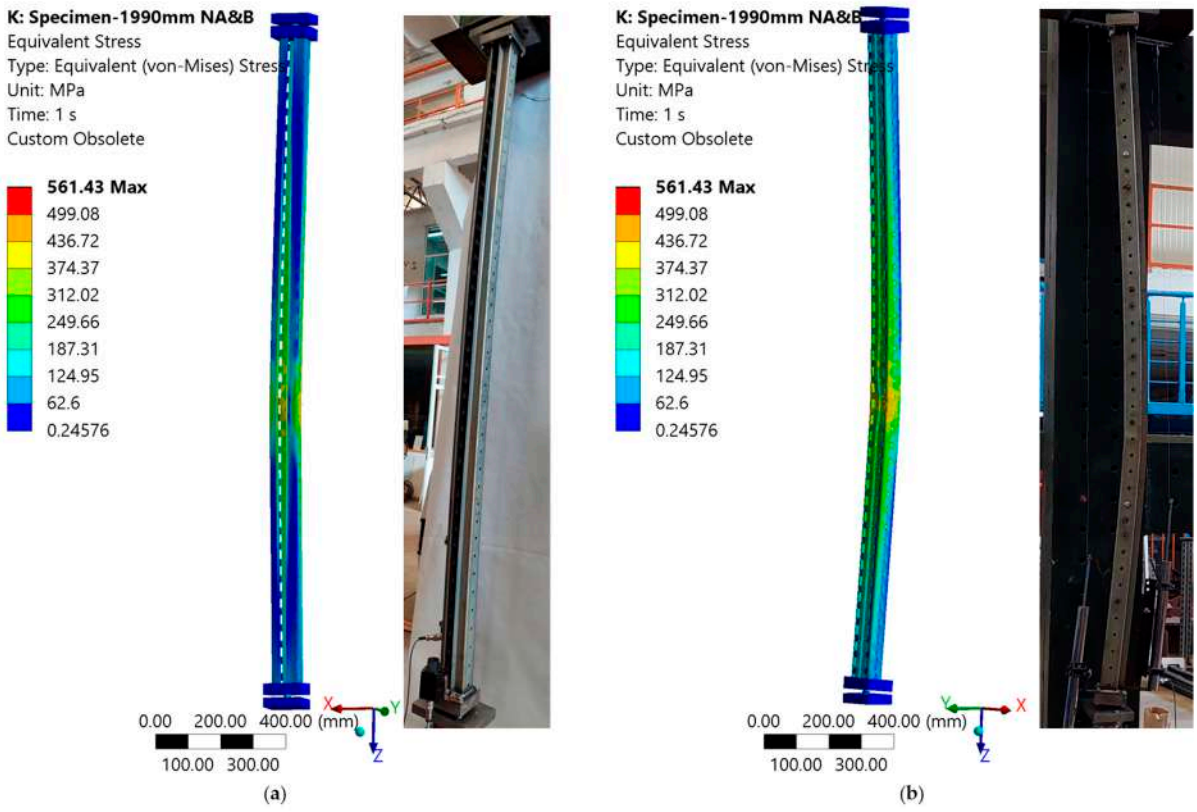

Figure 31. Von Mises stress distribution for the TS-1990 specimen and comparison with experimental failure mechanism: (**a**) back view; (**b**) front view.

Load–displacement curves (Figure 32) show close agreement between numerical and experimental results, with minor differences in post-peak displacement. This multistep modeling approach proved effective in capturing the instability and failure behavior of cold-formed perforated profiles under axial compression.

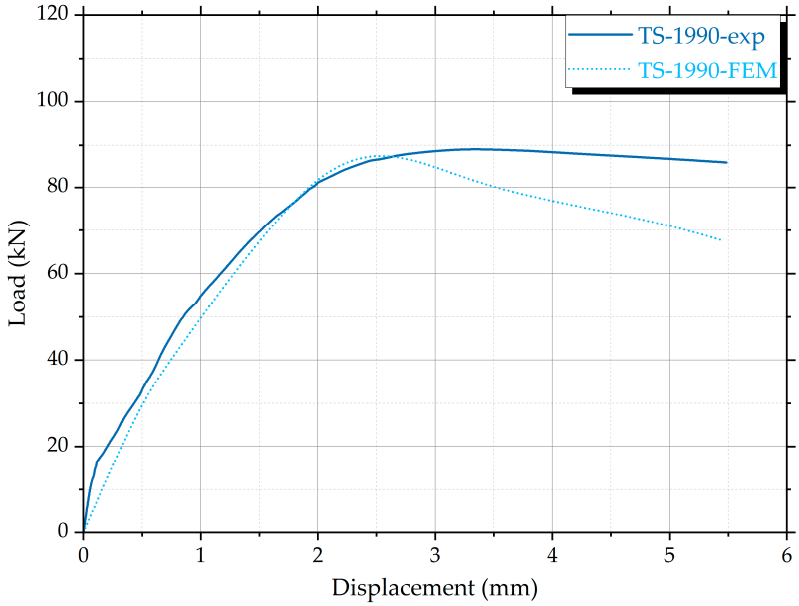

Figure 32. Load–displacement response comparison between experimental and numerical results for the TS-1990 specimen.

5. Design of Cold-Formed Thin-Walled Columns Under Axial Compression

This chapter presents the analytical design approach for cold-formed steel columns subjected to axial compression, based on the provisions of EN 1993-1-3 and EN 1993-1-1. The studied members are open-section perforated uprights commonly used in pallet rack systems. Their structural response is governed by the interaction of local, distortional, and global buckling modes, intensified by web perforations and thin-walled geometry.

5.1. Effective Width Method

Given this complex behavior, the Effective Width Method (EWM) is adopted as the recommended design procedure in Eurocode for cold-formed sections. This method accounts for the influence of local instabilities by reducing the effective area of individual plate elements in compression, leading to a reduced axial resistance.

Although EWM has limitations in predicting distortional or interactive buckling for perforated profiles, it remains the most widely used codified method due to its standardized framework and compatibility with current European design norms. Its stepwise application allows a conservative estimate of the column capacity, particularly when used alongside calibrated numerical and experimental validation.

For the studied upright profiles, the gross cross-sectional area is 555 mm^2, while the net area, obtained by subtracting the perforated regions, is 511 mm^2. In accordance with EN 1993-1-3, no further reduction to this net area was applied when calculating the effective cross-sectional area. This is justified by the fact that all plate elements (web, flanges, lips) have width-to-thickness ratios (b/t) lower than 30, which is below the limit slenderness for local buckling as defined in the Eurocode. Furthermore, the presence of a longitudinal stiffener in the web improves the local stability of the section. Therefore, the entire net area was considered fully effective in both EWM and DSM calculations.

The calculation steps followed for the current study are summarized in Tables 2 and 3, based on EN 1993-1-3 Annex A, adapted for sections with openings.

Table 2. Design of cold-formed thin-walled columns under axial compression using Effective Width Method (EWM).

Step	Design of Cold-Formed Thin-Walled Columns Under Axial Compression Using Effective Width Method (EWM)		Specimen		
			SS-340	**MS-990**	**TS-1990**
1	Gross section yield load Gross cross-sectional properties are first calculated based on the nominal geometry of the profile, neglecting any local imperfections. These include area A, centroidal distances, moments of inertia, and section moduli.				
2	Material properties are established from tensile tests, specifically the yield strength $f_y = 355$ MPa and modulus of elasticity $E = 210,000$ MPa. For cold-formed profiles, the design strength is taken as f_y/γ_{M1} where $\gamma_{M1} = 1.1$ is the partial safety factor.				
3	Local buckling effects are considered by computing effective widths for flat elements (web and flanges) using Section 5.2 of EN 1993-1-3. The slenderness of each plate is evaluated, and reduction factors are applied to determine the effective cross-sectional area $A_{eff} = 511$ mm^2				
4	Axial resistance N_{Rd}				
	$N_{Rd} = A_{eff} \cdot \frac{f_y}{\gamma_{M1}}$	(5)	165 kN	165 kN	165 kN
5	Elastic critical buckling load N_{cr} The elastic critical buckling load for a pin-ended column is given by:				
	$N_{cr} = \frac{\pi^2 \cdot E \cdot I_z}{(k \cdot L)^2}$	(6)	4844 kN	571 kN	141 kN
6	Non-dimensional slenderness $\overline{\lambda}$				
	$\overline{\lambda} = \sqrt{\frac{A_{eff} \cdot f_y}{N_{cr}}}$	(7)	0.194	0.563	1.133
7	Reduction factor for global buckling (χ) The buckling reduction factor is determined from:				
	$\phi = 0.5 \cdot \left[1 + \alpha\left(\overline{\lambda} - 0.2\right) + \overline{\lambda^2}\right]$	(8)	0.502	0.718	1.30
	$\chi = \frac{1}{\phi + \sqrt{\phi^2 - \overline{\lambda^2}}}$	(9)	1.0	0.82	0.516
8	Design compressive resistance $N_{b,Rd}$				
	$N_{b,Rd} = \chi \cdot A_{eff} \cdot \frac{f_y}{\gamma_{M1}}$	(10)	165 kN	141 kN	85 kN

In the above table, A_{eff} is the effective cross-sectional area accounting for local buckling 511 mm^2; f_y is the yield strength of steel 355 MPa; N_{cr} is the elastic critical buckling load [kN]; E is the modulus of elasticity of steel 210,000 MPa; I_z is the moment of inertia about the weak axis 270,184 mm^4; L is the buckling length of the member 340/990/1990 [mm]; k is the effective length factor (typically 1.0 for pinned supports); α is the imperfection factor, which depends on the buckling curve, i.e., for cold-formed members, buckling curve b is commonly used: α = 0.34; $N_{b,Rd}$ is the design axial compressive resistance [N]; γ_{M1} is the partial safety factor for member resistance (commonly 1.1).

Table 3. Design of cold-formed thin-walled columns under axial compression using Direct Strength Method (DSM).

Step	Design of Cold-Formed Thin-Walled Columns Under Axial Compression Using Direct Strength Method (DSM)	Specimen		
		SS-340	**MS-990**	**TS-1990**
1	Gross section properties A		511 mm^2	
2	Material properties f_y		355 MPa	
	Moment of inertia I		270,184 mm^4	
	Modulus of elasticity E		210,000 MPa	

Table 3. *Cont.*

Step	Design of Cold-Formed Thin-Walled Columns Under Axial Compression Using Direct Strength Method (DSM)		Specimen		
			SS-340	**MS-990**	**TS-1990**
3	Elastic critical buckling loads				
	$P_{crG} = \frac{\pi^2 \cdot E \cdot I}{(k \cdot L)^2}$	(11)	4844 kN	571 kN	141 kN
4	Nominal yield load				
	$P_y = A \cdot f_y$	(12)	181 kN	181 kN	181 kN
5	Non-dimensional slenderness				
	$\lambda = \sqrt{\frac{P_y}{P_{cr}}}$	(13)	0.194	0.563	1.133
6	Buckling reduction factor (global mode)				
	$\phi = 0.5 \cdot \left[1 + \alpha \cdot (\lambda - 0.2) + \lambda^2\right]$	(14)	0.518	0.721	1.3
	$\chi = \frac{1}{\phi + \sqrt{(\phi^2 - \lambda^2)}}$	(15)	1	0.855	0.516
7	Nominal compressive strength				
	$P_n = P_y \cdot \chi$	(16)	181 kN	155 kN	93 kN
8	Design compressive resistance				
	$N_{b,\,Rd} = \frac{P_n}{\gamma_{M1}}$	(17)	165 kN	141 kN	85 kN

Note: This study was conducted between 2022 and 2023, when the applicable versions of the design standards were EN 1993-1-3:2006 [26] and AISI S100-16 [35]. Updated versions have been published since then, but were not available at the time of the analysis. The authors acknowledge these developments and will consider them in future work.

5.2. Direct Strength Method DSM

The Direct Strength Method (DSM) [34] provides a simplified yet robust approach for determining the axial compressive resistance of cold-formed steel members, especially those with complex cross-sectional geometries and perforations. Unlike the traditional Effective Width Method (EWM), which requires iterative reduction in individual flat elements based on local buckling, DSM allows the use of the entire gross or net cross-sectional area, while capturing instability effects through the calculation of non-dimensional slenderness and buckling mode-specific reduction factors.

In this study, DSM was applied in accordance with the design philosophy introduced in AISI S100 and conceptually aligned with EN 1993-1-3 provisions. The method uses elastic critical buckling loads (local, distortional, and global) to define the slenderness parameters that govern the reduction in axial capacity. These values can be obtained from analytical formulations or numerical tools such as CUFSM (Constrained and Unconstrained Finite Strip Method). Once the critical loads are known, the DSM enables a direct estimation of the nominal and design strengths without requiring an effective section reconstruction.

The applicability of DSM is particularly advantageous for perforated profiles, where the presence of holes complicates the use of EWM due to irregular plate boundaries and stress concentrations. In the tested uprights, DSM results showed very good agreement with experimental data, confirming that the interaction between buckling modes is properly captured and that the net section assumption is sufficiently conservative and realistic.

6. Results and Discussion

The comparative analysis between the experimental, numerical (FEM), and analytical (EWM; DSM) results is presented in Figure 33 and Table 4. The load–displacement curves

illustrate the overall response of the three specimen groups under axial compression. Experimental results are plotted against the numerical predictions obtained through nonlinear finite element analysis.

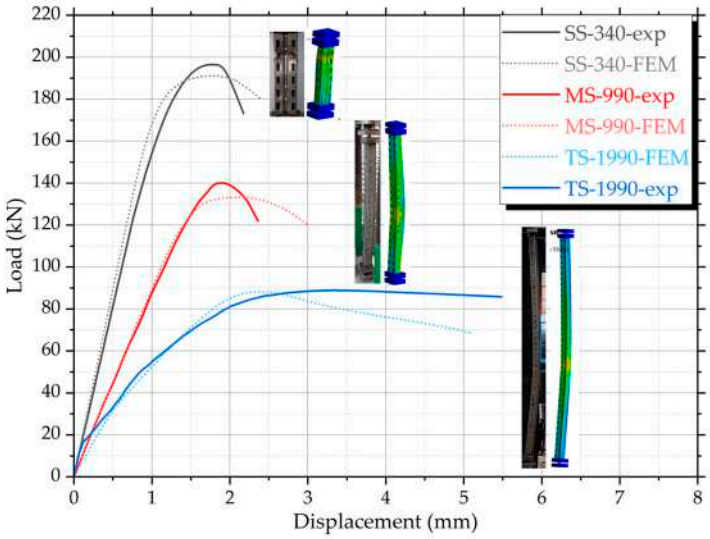

Figure 33. Load–displacement curves for the three tested specimens (SS-340, MS-990, TS-1990): comparison between experimental results and finite element simulations (FEM).

Table 4. Comparison between experimental, numerical (FEM), and analytical (EWM), (DSM) axial compressive resistance values for the tested specimens.

Specimen	Experimental	FEM	EWM	DSM
SS-340	196	185	165	165
MS-990	136	134	141	141
TS-1990	89	86	85	85

The behavior of the MS-990 series, both experimentally and numerically, confirmed the occurrence of distortional–global buckling interaction, particularly around mid-height, where localized deformation in the flanges and web transitioned into global lateral displacement. This confirms that members with intermediate slenderness are prone to coupled buckling phenomena, and justifies their inclusion as a distinct case in the study. The close agreement between test results and FEM simulations indicates that the adopted imperfection modeling strategy, based on eigenmodes, is suitable for capturing the nuanced instability mechanisms in perforated cold-formed sections.

Table 4 presents a comparative evaluation of axial compressive resistance values obtained through experimental testing, finite element modeling (FEM), and analytical methods based on the Effective Width Method (EWM) and the Direct Strength Method (DSM).

In all analyses, the net cross-sectional area was considered fully effective, without applying additional local reduction factors. This assumption is supported by several arguments. Firstly, all plate elements exhibit moderate slenderness, with width-to-thickness ratios below the critical limits established by EN 1993-1-3 for cold-formed unstiffened elements. Secondly, the presence of a longitudinal stiffener in the web significantly improves local stability, reducing the likelihood of premature buckling around perforations. Thirdly, the experimental results confirmed that no local tearing or early failure occurred in the web or flange zones near openings. All observed failures developed through geometric instability rather than material failure. These findings validate the decision to apply the full net area in both the DSM-based design calculations and the finite element modeling, and they align with the excellent agreement between test results and numerical predictions.

For the SS-340 specimen, the experimental value (196 kN) slightly exceeds the numerical (185 kN) and analytical results (165 kN), as expected for a stocky, short member. This small variation can be attributed to conservative simplifications in both analytical and numerical models that slightly underestimate peak behavior.

In the case of MS-990, the experimental result (136 kN) is marginally higher than the FEM (134 kN) and analytical estimations (141 kN). This deviation can be explained by the post-processing of the test data, where the original load–displacement curves were smoothed to remove local noise, which may have artificially elevated the recorded peak load. Nonetheless, the agreement remains within acceptable bounds, and the results confirm the mixed buckling behavior—initiated by local or distortional effects and followed by global flexure.

For the TS-1990 specimen, all values cluster between 85 and 89 kN, indicating a dominant global buckling mode with minimal influence from local or distortional instability. The consistency across all methods supports the assumption of linear behavior and confirms that the tested geometry behaves as a slender member under axial compression.

An important justification in both FEM and DSM analyses is the use of the net cross-sectional area without applying local reduction factors. Although the profiles include perforations, the web and flange panels exhibit width-to-thickness ratios not exceeding 25, which is well below the critical slenderness limit ($b/t \approx 30$) specified in EN 1993-1-3 for unstiffened elements. Furthermore, the presence of a longitudinal stiffener in the web enhances the stability of the critical panels, while the perforated zones behave as short cantilever segments without influencing the global stability.

Thus, it is technically justified to consider the entire net area as fully effective, both in numerical modeling and analytical estimation. The excellent agreement with experimental results supports this assumption and confirms that no significant local buckling compromised the resistance capacity.

7. Conclusions

This study investigated the axial compression behavior of cold-formed steel upright profiles with perforated webs and longitudinal stiffeners, commonly used in industrial pallet racking systems. Based on a combined experimental, numerical, and analytical approach, the following technical conclusions can be drawn:

1. Buckling modes are strongly dependent on member slenderness:
    - Short specimens (SS-340) primarily exhibited local buckling near perforations.
    - Medium-length specimens (MS-990) displayed distortional–global mode interaction.
    - Tall specimens (TS-1990) were governed by global flexural buckling, with no significant local deformation.
2. The finite element models developed in ANSYS accurately reproduced the following:
    - Load–displacement behavior.
    - Deformation patterns.
    - Stress concentration zones near perforations, confirming the validity of the material calibration and boundary condition modeling.
3. The Direct Strength Method (DSM) provided the closest agreement with experimental results, especially for the MS-990 and TS-1990 specimens. Specifically, DSM predictions for MS-990 differed by +3.7%, and for TS-1990 by –4.5%, relative to experimental peak loads. These values were identical to those obtained using EWM in this case, but this should be interpreted with caution due to the idealized assumptions used. DSM's ability to incorporate elastic critical loads and full net section properties makes it generally more reliable than EWM in predicting buckling strength for perforated members.

4. The Effective Width Method (EWM), while conservative, remains suitable for design purposes but may significantly underestimate capacity in members where distortional buckling and global modes dominate.
    - Despite the presence of perforations, the net cross-sectional area could be considered fully effective in both FEM and DSM analyses for the specific profiles tested, due to the following factors:
    - Moderate width-to-thickness ratios ($b/t < 30$).
    - The stabilizing effect of the longitudinal web stiffener.
    - The absence of premature local failures the experimental and numerical results.

    However, this conclusion applies only to the tested cross-sections and slenderness levels. Caution is advised when extending this assumption to more slender profiles or different perforation configurations, as local effects may become more significant.
5. The combination of full-scale testing and calibrated FEM analysis offers a robust design benchmark for future parametric studies and code development related to cold-formed perforated sections.

8. Future Research

The present investigation lays the groundwork for further studies focused on optimizing the structural performance of perforated upright members in industrial pallet racks. The validated finite element model, supported by experimental results and analytical assessments, can be confidently used in a series of parametric studies aimed at enhancing the cross-sectional geometry of cold-formed steel uprights. By systematically varying geometric parameters (e.g., flange width, lip length, perforation layout), future work will identify improved design configurations that maximize axial capacity while ensuring manufacturability and cost-efficiency.

Another important direction involves the development of retrofitting techniques to strengthen existing racking systems installed over three decades ago. Many of these legacy structures were designed according to outdated standards and may not meet current performance or safety requirements under seismic or accidental loading. The failure modes observed in this study—especially distortional–global interaction—highlight potential vulnerabilities in such systems. Future work will investigate the use of stiffeners, bracing elements, or local reinforcements to increase buckling resistance and delay instability. The FEM model calibrated in this study will support quantitative evaluation of these strengthening techniques.

Research will also be extended to include additional structural components such as beam-to-upright connections and lateral bracing systems, as well as the global seismic behavior of full pallet rack assemblies. Through dynamic simulations and testing on subassemblies, performance-based design recommendations will be developed to improve the resilience and ductility of storage racks under seismic or accidental loads.

In this context, the validated FEM framework may be adapted to simulate dynamic and seismic loading, incorporating time-dependent effects, strain-rate sensitivity, and cyclic degradation. These developments represent a logical extension of the current static analysis toward more comprehensive performance evaluation under extreme loading conditions.

Author Contributions: Conceptualization, G.T. and N.T.; methodology, S.I.; software, G.T.; validation, N.T.; formal analysis, G.T.; investigation, S.I.; resources, G.T.; data curation, S.I.; writing—original draft preparation, G.T.; writing—review and editing, N.T.; visualization, S.I.; supervision, G.T.; project administration, G.T.; funding acquisition, G.T. All authors have read and agreed to the published version of the manuscript.

Funding: The experimental work was financially supported under contract TUIASI 27233/15.09.2021. The APC was funded by TUIASI.

Institutional Review Board Statement: Not applicable.

Informed Consent Statement: Not applicable.

Data Availability Statement: The data that support the findings of this study are available from the corresponding author upon request.

Acknowledgments: The author gratefully acknowledges the support and collaboration of SKAT KART SRL, Romania, for providing the materials necessary for this research.

Conflicts of Interest: The authors declare no conflicts of interest. The funders had no role in the design of the study; in the collection, analyses, or interpretation of data; in the writing of the manuscript; or in the decision to publish the results.

References

1. Hancock, G.J. Cold-Formed Steel Structures. *J. Constr. Steel Res.* **2003**, *59*, 473–487. [CrossRef]
2. Schafer, B.W. Cold-Formed Steel Structures around the World. *Steel Constr.* **2011**, *4*, 141–149. [CrossRef]
3. Tunca, O.; Erdal, F.; Sağsöz, A.E.; Çarbaş, S. Structural Features of Cold-Formed Steel Profiles. *Chall. J. Struct. Mech.* **2018**, *4*, 77. [CrossRef]
4. Hancock, G.J. Cold-Formed Steel Structures: Research Review 2013–2014. *Adv. Struct. Eng.* **2016**, *19*, 393–408. [CrossRef]
5. Crisan, A.; Ungureanu, V.; Dubina, D. Behaviour of Cold-Formed Steel Perforated Sections in Compression. Part 1—Experimental Investigations. *Thin-Walled Struct.* **2012**, *61*, 86–96. [CrossRef]
6. Baldassino, N.; Bernuzzi, C.; di Gioia, A.; Simoncelli, M. An Experimental Investigation on Solid and Perforated Steel Storage Racks Uprights. *J. Constr. Steel Res.* **2019**, *155*, 409–425. [CrossRef]
7. Neiva, L.H.d.A.; Sarmanho, A.M.C.; Faria, V.O.; de Souza, F.T.; Starlino, J.A.B. Numerical and Experimental Analysis of Perforated Rack Members under Compression. *Thin-Walled Struct.* **2018**, *130*, 176–193. [CrossRef]
8. Miyazaki, J.P.d.L.; de Carvalho, A.S.; Martins, C.H.; Rossi, A. Evaluation of the Interaction between Distortional–Global Buckling in Perforated Cold-Formed Steel Rack Sections. *Structures* **2023**, *54*, 808–824. [CrossRef]
9. Ren, C.; He, Y.; Wu, Z.; He, W.; Dai, L. Experiments and Numerical Predictions of Cold-Formed Steel Members with Web Perforations under Combined Compression and Minor Axis Bending. *Eng. Struct.* **2022**, *256*, 114022. [CrossRef]
10. Taheri, E.; Firouzianhaji, A.; Usefi, N.; Mehrabi, P.; Ronagh, H.; Samali, B. Investigation of a Method for Strengthening Perforated Cold-Formed Steel Profiles under Compression Loads. *Appl. Sci.* **2019**, *9*, 5085. [CrossRef]
11. Bernuzzi, C.; Pellegrino, C.; Simoncelli, M. Characterization of Existing Steel Racks via Dynamic Identification. *Buildings* **2021**, *11*, 603. [CrossRef]
12. Pham, D.K.; Pham, S.H.; Pham, V.B.; Pham, C.H.; Hancock, G.J. Direct Strength Design of Cold-Formed Channels with Web Openings in Shear. *J. Struct. Eng.* **2023**, *149*, 04023022. [CrossRef]
13. Martins, A.D.; Camotim, D.; Dinis, P.B. On the Distortional-Global Interaction in Cold-Formed Steel Columns: Relevance, Post-Buckling Behaviour, Strength and DSM Design. *J. Constr. Steel Res.* **2018**, *145*, 449–470. [CrossRef]
14. Ye, J.; Quan, G.; Yun, X.; Guo, X.; Chen, J. An Improved and Robust Finite Element Model for Simulation of Thin-Walled Steel Bolted Connections. *Eng. Struct.* **2022**, *250*, 113368. [CrossRef]
15. Zhou, X.; Xiang, Y.; Shi, Y.; Xu, L.; Zou, Y. Simplified Design Method of Cold-Formed Steel Columns with Built-up Box Sections. *Eng. Struct.* **2021**, *228*, 111532. [CrossRef]
16. Shaker, F.M.F.; Mamdooh, Z.; Deifalla, A.; Yehia, M.M. Experimental Investigations of the Behavior of Stiffened Perforated Cold-Formed Steel Sections Subjected to Axial Compression. *Buildings* **2022**, *12*, 812. [CrossRef]
17. Dai, L.; Chen, Y.; Cheng, L.; Ren, C. Buckling Behavior and Design of Cold-Formed Thin-Walled Steel Storage Rack Upright Frames. *Structures* **2025**, *75*, 108685. [CrossRef]
18. *EN 10149-2:2013*; Hot Rolled Flat Products Made of High Yield Strength Steels for Cold Forming Part 2: Technical Delivery Conditions for Thermomechanically Rolled Steels. BSI Standards Publication: London, UK, 2013.
19. Vujanac, R.; Miloradović, N.; Vulović, S.; Pavlović, A. A Comprehensive Study into the Boltless Connections of Racking Systems. *Metals* **2020**, *10*, 276. [CrossRef]
20. Andrade, T.L.; Júnior, P.A.A.M.; de Paula, W.A. Tensile Test: Comparison Experimental, Analytical and Numerical Methods. *Int. J. Adv. Eng. Res. Sci.* **2017**, *4*, 87–90. [CrossRef]
21. Ungureanu, V.; Luka·evi ć, I.; Both, I.; Dubina, D. Numerical Investigations on Built-up Cold-formed Steel Beams for Long Spans. *Ce/Pap.* **2021**, *4*, 2277–2284. [CrossRef]

22. Cabezas, E.E.; Celentano, D.J. Experimental and Numerical Analysis of the Tensile Test Uing Sheet Specimens. In Proceedings of the First South-American Congress on Computational Mechanics—MECOM, Santa Fe, Argentina, 28–31 October 2002.
23. Mahmood, A.; Al-Samarai, R.A.; Fadhil, N.A. Comparative Study on Mechanical Properties of Steel by Numerical Analysis and Experimental Tests. *REVISTA AUS* **2019**, *26*, 333–340. [CrossRef]
24. *GP 128-2014*; Guide for the Calculation and Design of Steel Rack Structures for Display and Storage in Commercial Spaces Subject to Seismic Action; More Doctors for Rural Australia Program (MDRAP). Oxford University Press: Oxford, UK, 2014. (In Romanian)
25. *EN 1993-1-1*; Eurocode 3: Design of Steel Structures—Part. 1-1: General. Rules and Rules for Buildings. European Comittee for Standardization: Brussels, Belgium, 2005.
26. *EN 1993-1-3:2006*; Eurocode 3: Design of Steel Structures, Part. 1.3: General. Rules, Supplementary Rules for Cold-Formed Thin Gauge Members and Sheeting. European Comittee for Standardization: Brussels, Belgium, 2006.
27. *EN 1090-1:2009+A1:2011*; Execution of Steel Structures and Aluminium Structures—Part 1: Requirements for Conformity Assessment of Structural Components. European Standardisation Organisations: Brussels, Belgium, 2011.
28. *EN 1090-2:2018+A1:2024*; Execution of Steel Structures and Aluminium Structures—Part 2: Technical Requirements for Steel Structures. European Standardisation Organisations: Brussels, Belgium, 2024.
29. *EN 15512:2020+A1:2022*; Steel Static Storage Systems—Adjustable Pallet Racking Systems—Principles for Structural Design. European Standardisation Organisations: Brussels, Belgium, 2022.
30. *ISO 6892-1:2019*; Metallic Materials—Tensile Testing—Part 1: Method of Test at Room Temperature. International Organization for Standardization. International Organization for Standardization: Geneva, Switzerland, 2019.
31. Li, Z.J.; Gong, J.; Shao, Y.B.; Huang, W.F.; Zhang, X. Axial Compressive Behaviors of Multi-Cavity Concrete-Filled Double-Skin Tubular Stub Columns. *J. Constr. Steel Res.* **2024**, *216*, 108619. [CrossRef]
32. Petrík, A.; Ároch, R. Usage of True Stress-Strain Curve for FE Simulation and the Influencing Parameters. *IOP Conf. Ser. Mater. Sci. Eng.* **2019**, *566*, 012025. [CrossRef]
33. Ansys | Engineering Simulation Software. Available online: https://www.ansys.com/ (accessed on 19 October 2021).
34. *EN 1993-1-5:2006/A1:2017*; Eurocode 3: Design of Steel Structures—Part. 1-5: Part 1-5: Plated structural elements. European Comittee for Standardization: Brussels, Belgium, 2017.
35. *AISI S100-16*; North American Specification for the Design of Cold-Formed Steel Structural Members. American Iron an Steel Institute AISI: Washington, DC, USA, 2016.

Disclaimer/Publisher's Note: The statements, opinions and data contained in all publications are solely those of the individual author(s) and contributor(s) and not of MDPI and/or the editor(s). MDPI and/or the editor(s) disclaim responsibility for any injury to people or property resulting from any ideas, methods, instructions or products referred to in the content.

Thin-Walled Structures 182 (2023) 110258

Contents lists available at ScienceDirect

Thin-Walled Structures

journal homepage: www.elsevier.com/locate/tws

Full length article

Shake table test and numerical analyses of a thin-walled Cold-Formed Steel structure: Part 1 — Investigation of the structural skeleton without claddings

George Taranu [a,*], Viorel Ungureanu [b], Zsolt Nagy [c], Mihai-Sergiu Alexa-Stratulat [a], Ionut-Ovidiu Toma [a], Septimiu-George Luca [a]

[a] The "Gheorghe Asachi" Technical University of Iasi, Faculty of Civil Engineering and Building Services, Department of Structural Mechanics, 700050, D. Mangeron no. 1, Iasi, Romania

[b] Politehnica University of Timisoara, Department of Steel Structures and Structural Mechanics, 300224, Ioan Curea no. 1, Timisoara, Romania

[c] Technical University of Cluj-Napoca, Faculty of Civil Engineering, No. 28, Memorandumului Street, Cluj-Napoca, 400114, Romania

ARTICLE INFO

Keywords:
Thin-walled cold-formed steel profiles
Seismic action
Shake table experimental testing
Nonlinear analysis

ABSTRACT

CFS structures are classified as structures with low ductility. Due to this, they are not recommended for medium to high seismic areas. The paper presents the results of a complex experimental program coupled with numerical investigations on the behavior of Cold Formed Steel (CFS) structures under seismic actions. The scaled-down model skeleton was made of DX51D+Z C-shaped 89 × 41 × 12 × 1 mm steel elements connected by 4.8 × 16 mm self-tapping screws (STS) and 5.5 × 25 mm self-drilling screws (SDS). This structure represents a replica of constructive solutions for single-story or one or two-storey structures that are frequently met in South-Eastern Europe, including highly active seismic areas.

The main purpose of the research program is to gather both quantitative and, more importantly, accurate information regarding structural response to dynamic actions characterized by input accelerations equal in amplitude to the maximum values specified in seismic design codes, up to PGA = 0.40 g. The damage of the joints and the reduction in the structural stiffness due to cyclic loads, such as the ones produced by earthquakes, change the structure's eigen period and significantly influence the structure's response to seismic actions. Larger gravitational loads lead to more extensive damage of the joints. The developed numerical model based on the experimentally determined connection axial rigidity can offer accurate results in terms of the fundamental frequency of vibration, relative accelerations and displacements. However, for a more accurate capturing of the local damages and onset of failure mechanisms, more complex numerical models are needed, which take into account non-linear material behavior.

The results presented in this paper help to design these structures as only the skeleton and serve as a starting point for future research work aimed to assess the influence of the sheathing on the global response of CFS structures to seismic actions. Additionally, research in the direction of improved joints with better energy dissipation properties is also pursued by the authors.

1. Introduction

The behavior of civil engineering structures to seismic motions is a continuous matter of investigation for researchers around the world. Besides ensuring the safety of the inhabitants and mitigating the damages to the structures and the stored goods in the framework of performance-based design, buildings also need to become economic and sustainable in the sense that their maximum performance should be obtained with the least material consumption. Currently available seismic design codes, such as EN 1998-1 [1] or the Romanian code [2] include a lot of information and details on the seismic design of steel structures. Based on their specifications, Thin-Walled Cold-Formed Steel Structures (TWCFSS) are classified as having low dissipative capabilities and the verification of structural elements included in Class 4 is made in accordance with EN 1993-1-3 [3], and EN 1993-1-5 [4], respectively. The seismic design codes limit the behavior factor q to 1.5 in [1] and to 1 in [2] because such structural systems without cladding materials have low energy dissipation capabilities. The values of the behavior factor q and the associated ductility classification which are given in the design codes, characterize the balance between resistance and energy-dissipation capacity. "For the design of structures classified as

* Corresponding author.
E-mail addresses: george.taranu@academic.tuiasi.ro (G. Taranu), viorel.ungureanu@upt.ro (V. Ungureanu), zsolt.nagy@dst.utclus.ro (Z. Nagy), mihai-sergiu.alexa-stratulat@staff.tuiasi.ro (M.-S. Alexa-Stratulat), ionut-ovidiu.toma@academic.tuiasi.ro (I.-O. Toma), septimiu-george.luca@academic.tuiasi.ro (S.-G. Luca).

https://doi.org/10.1016/j.tws.2022.110258
Received 24 May 2022; Received in revised form 11 August 2022; Accepted 10 October 2022
Available online 1 November 2022
0263-8231/© 2022 The Author(s). Published by Elsevier Ltd. This is an open access article under the CC BY license (http://creativecommons.org/licenses/by/4.0/).

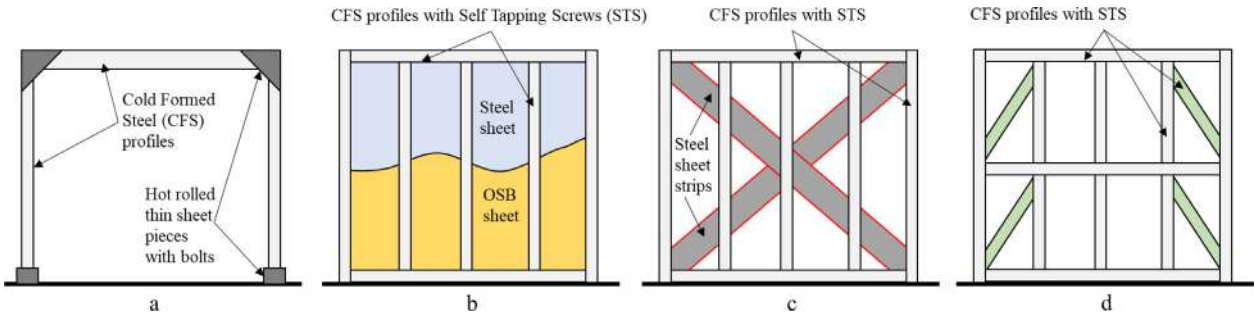

Fig. 1. Structural type systems: (a) frame system; (b) panel; (c) panel with strips diagonal; (d) panel with diagonals system.



Fig. 2. Real House structural systems — personal archive: (a) Romania, 2018, (b) Germany, 2018.

low-dissipative, no account is taken of any hysteretic energy dissipation and the behavior factor may not be taken, in general, as being greater than the value of 1.5 considered to account for overstrengths". "The behavior factor q is an approximation of the ratio of the seismic forces that the structure would experience if its response was completely elastic with 5% viscous damping, to the seismic forces that may be used in the design, with a conventional elastic analysis model, still ensuring a satisfactory response of the structure" [1]. In this study, the behavior factor was not used. Based on the presented results future numerical analyses will be developed in order to determine the appropriate value of the behavior factor for such types of structures.

The seismic behavior of hot-rolled steel structures was the main subject of research until 1990. Several approaches were considered from scaled-down models to structural sub-systems, to individual structural elements. A very powerful equipment used in such experimental investigations, both for hot-rolled and cold-formed steel structures, is the shake table. It is the only equipment that can simulate real seismic motions of either past earthquakes or artificially generated ones. However, due to its high initial and maintenance costs, most experimental works included pseudo-dynamic tests on structural elements or parts of structures that can lead to obtaining similar results. Another alternative would be the use of numerical simulations where various parameters could be changed and many different scenarios could be considered. However, these numerical models should be validated by laboratory tests in order to ensure the accuracy of the obtained results [5,6].

Thin-walled cold-formed steel structures elements started to attract more and more attention from 1990 because of their gradual implementation in civil engineering structures. Their use has seen a continuous grow and a significant number of studies were published in USA [7–13], Italy [14–22], Romania [23–28], Turkey [29], UK [30,31] or Asia [32–43]. Each study considered different CFS profiles, structural system of connectors for joining the elements. The most used structural typologies consisted in 3D frames with built-up cross-sections for the elements or framing elements to form rigid systems for structural applications. Fig. 1 presents 4 of the main CFS structural systems that are currently in use. The solution presented in Fig. 1a is that of a portal frame using built-up cross-sections for the elements. The elements are connected at the nodes by means of hot-rolled steel plates and bolts. These are the so-called moment-resisting frames where the seismic force is dissipated due to the moment–rotation capacity of the joint. On the other hand, in case of framing systems made of shear wall panels, Fig. 1b, sheathing with either Oriented Strand Boards — OSB panels or corrugated steel sheets, the seismic force is dissipated by the panels/sheets and the connectors used to fix the panels onto the steel framing.

In the case of framing systems with vertical studs and diagonal steel strips, as shown in Fig. 1c, the seismic force is resisted by the framing and the diagonal elements. On the other hand, the truss-like framing system with rigid diagonal elements, Fig. 1d, is able to dissipate the seismic energy mainly through the diagonal elements. In either of the presented structural systems, the presence of OSB, corrugated steel sheet or any other sheathing panels greatly contribute to the dissipation mechanism of the seismic force. The efficiency of a scaled down two storey model, using the same structural approach presented in Fig. 1c, to seismic motion was demonstrated in a series of shake table tests conducted in 2009 at the "Gheorghe Asachi" Technical University of Iasi [44]. Additional experimental investigations on different structural typologies were conducted from 2016 to the present day [7,8,20,37,45]. Such research works contribute to the general knowledge on the seismic behavior of steel structural systems and can be used to calibrate numerical models in order to conduct complex parametric investigations.

The structural model used in the present research is based on a framing concept with truss-like diagonal elements located in the marginal panels, as shown in Fig. 1d. Such system is frequently met in practice all over Europe, including in highly seismic active areas. Fig. 2 presents two examples of such structures built in Romania (see Fig. 2a), and Germany (see Fig. 2b), in 2018.

Fig. 3 presents an overview of a ground-floor building made from a combination of thin-walled cold-formed steel lipped channel profiles having the dimensions 89 × 41×12 × 1 mm and plain channel profiles with dimensions of 358 × 78×4 mm.

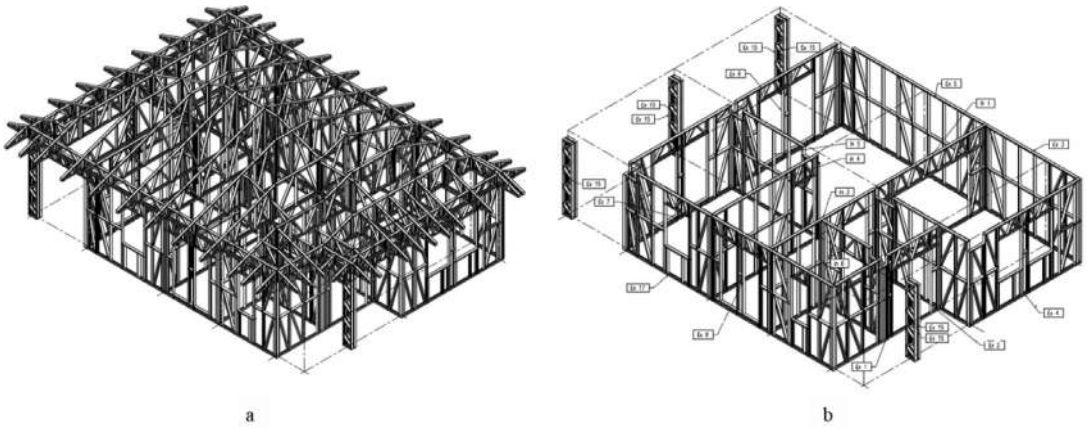

Fig. 3. Axonometry of typical one storey structural systems made of TWS profiles C89x41x12x1: (a) general assembly; (b) wall panel system.

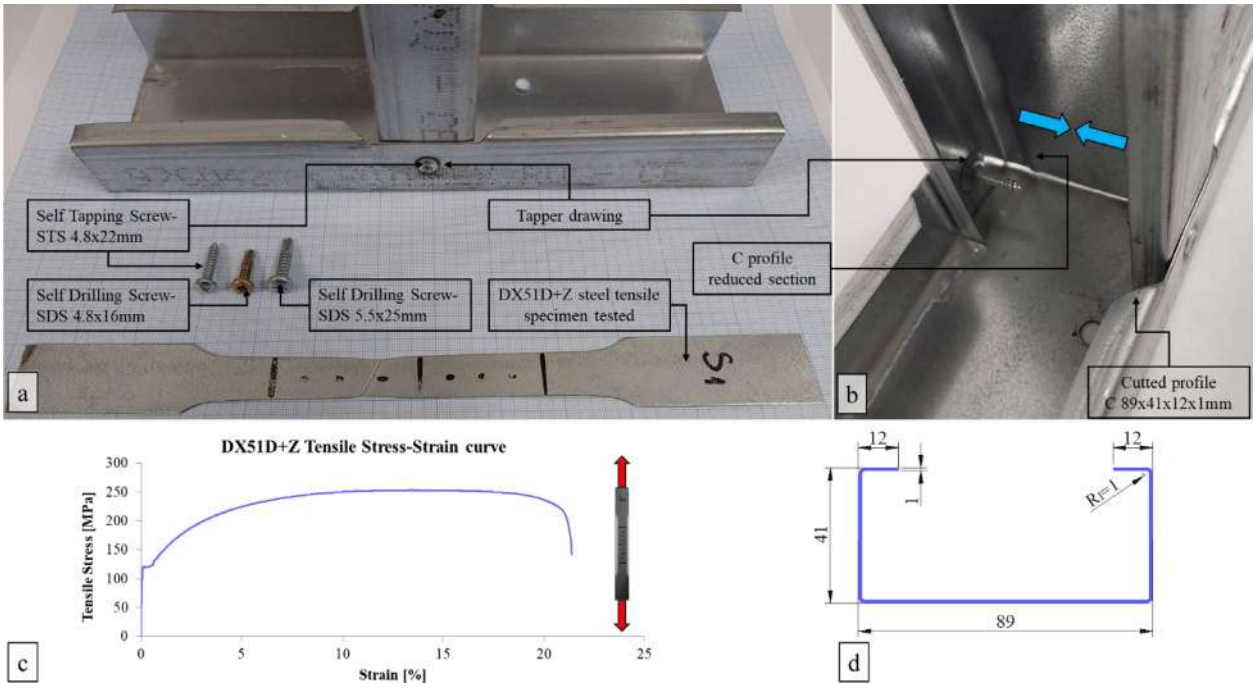

Fig. 4. (a) Materials and typical *T* joint connection; (b) perspective view of the connection with the interior; (c) average experimental tensile stress–strain curve of DX51D+Z steel sheet; (d) C profile section dimensions.

The lipped channels of 89 × 40×12 × 1 mm represents a relatively advantageous solution both for the end-user (beneficiary) and building-contractor due to its small overall dimensions. However, their use in structural elements to resist seismic loads should be considered only after significant experimental work in the laboratory. Such work could offer insightful information that can be used in the design practice. The obtained results are important data to calibrate numerical models based on FEM.

The present paper presents the results obtained from laboratory investigation on the material properties, behavior of T-joints to static and cycling loading scenarios and shake table tests to assess the behavior of the structural system made of CFS frames with truss-like diagonal elements in the central panels. The experimental program is accompanied by numerical simulations in order to create a computer model that is able to simulate, as accurately as possible, the real behavior of the scaled-down model to seismic actions. Both linear and non-linear analyses were conducted to render evident the differences between the two approaches.

2. Materials and methodology

2.1. Structural materials and connectors

The material properties of the steel sheet and connectors are presented in Table 1. The steel sheet used to obtain the steel profiles by cold-forming was DX51D+Z. Self-Tapping Screws (STS) with dimensions of 4.8 × 22 mm were used to connect the elements of the framing whereas Self Drilling Screws (SDS) with dimensions of 5.5 × 25 mm were used to connect the shear walls to each other. Additionally, the diagonal elements were connected by means of 4.8 × 16 mm SDS. The material properties of the steel sheet were experimentally determined by means of direct tensile tests on specimens cut from the profile web [46]. The material properties of the STS and SDS were the ones given by the manufacturer. The average stress–strain curve for the DX51D+Z steel is presented in Fig. 4a and the dimensions of the C-shaped profile are shown in Fig. 4b.

Table 1
Materials properties.

Element	Type	Elastic modulus (GPa)	Tensile yield strength (MPa)	Tensile ultimate strength (MPa)
Steel sheet C profiles — Fig. 4(a)	DX51D+Z	210	120 (exp)	250 (exp)
SDS — Fig. 4 (a) for profile connections ISO 15481 class (5.6) [47]	4.8 × 16 mm	210	300 [48]	500 [48]
SDS — Fig. 4 (a) for panel connections ISO 15481 class (5.6) [47]	5.5 × 25 mm	210	300 [48]	500 [48]
STS — Fig. 4 (a) for profile connections ISO 7049 class (5.6) [49]	4.8 × 22 mm	210	300 [48]	500 [48]

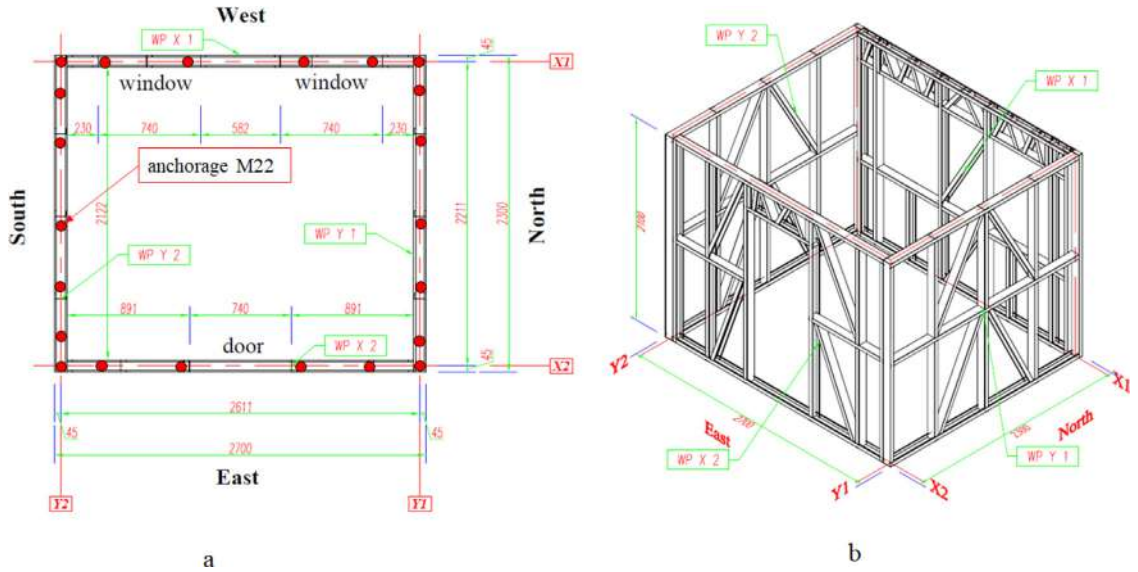

Fig. 5. (a) Plan view of the structural model; (b) Axonometry of the wall panels.

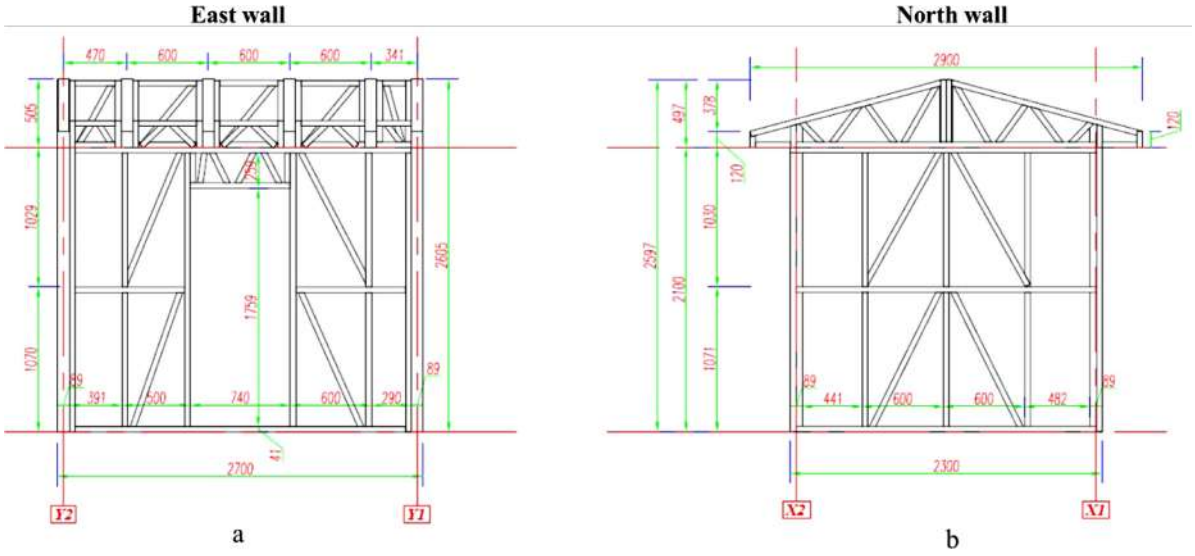

Fig. 6. Front views of the walls: (a) East wall, X1 direction; (b) North wall, Y1 direction.

2.2. Structural model assembly

The scaled-down model, presented in Fig. 5, had the in-plane dimensions of 2700 × 2300 mm, wall height of 2100 mm and the total height (at the ridge) of 2597 mm. The model was made of four panels. The roof was made of trusses with inclined upper chords, as shown in Fig. 6, transversally positioned (Y direction in Fig. 5). The stiffness of the roof was ensured by using truss panels located on top of the longitudinal wall panels (X direction in Fig. 5) and at the middle of transversal wall panels. The longitudinal wall panels had openings for windows and doors.

Fig. 5a presents the in-plane view of the model whereas Fig. 5b presents the axonometric view of the wall panels. The North–South direction of the model coincides with the X axis of the shake table along which the shaking motions will be induced. The East wall has a door opening with the dimensions of 740 × 1759 mm and the opposite, West,

Table 2
Similarity relationship and Cauchy similitude scaling factors.

Parameter	Symbol	Prototype	Model	Scale factor (prototype/ model)	Scale factor value
Length	L	3240 (mm)	2700 (mm)		
Width	w	2760 (mm)	2300 (mm)	$L_p/L_m = \lambda$	1.2
Height	h	3126 (mm)	2605 (mm)		
Steel profile section	sps	C 89 × 40 × 12 × 1 (mm)	C 89 × 40x12 × 1 (mm)	$L_p/L_m = \lambda$	1
Elasticity modulus	E	210000 (N/mm^2)	210000 (N/mm^2)	$e = E_p/E_m$	1
Specific mass	ρ	7850 (kg/m^3)	7850 (kg/m^3)	$\rho = \rho_p/\rho_m$	1
Mass	m	506 (kg)	293 (kg)	$m = m_p/m_m = \lambda^3$	1.728
Displacement	d			$d = d_p/d_m = \lambda$	1.2
Velocity	v			$v = v_p/v_m$	1
Acceleration	a			$a_p/a_m = 1/\lambda$	0.833
Time	t			$t_p/t_m = \lambda$	1.2
Frequency	f			$f_p/f_m = \frac{1}{\lambda}$	0.833

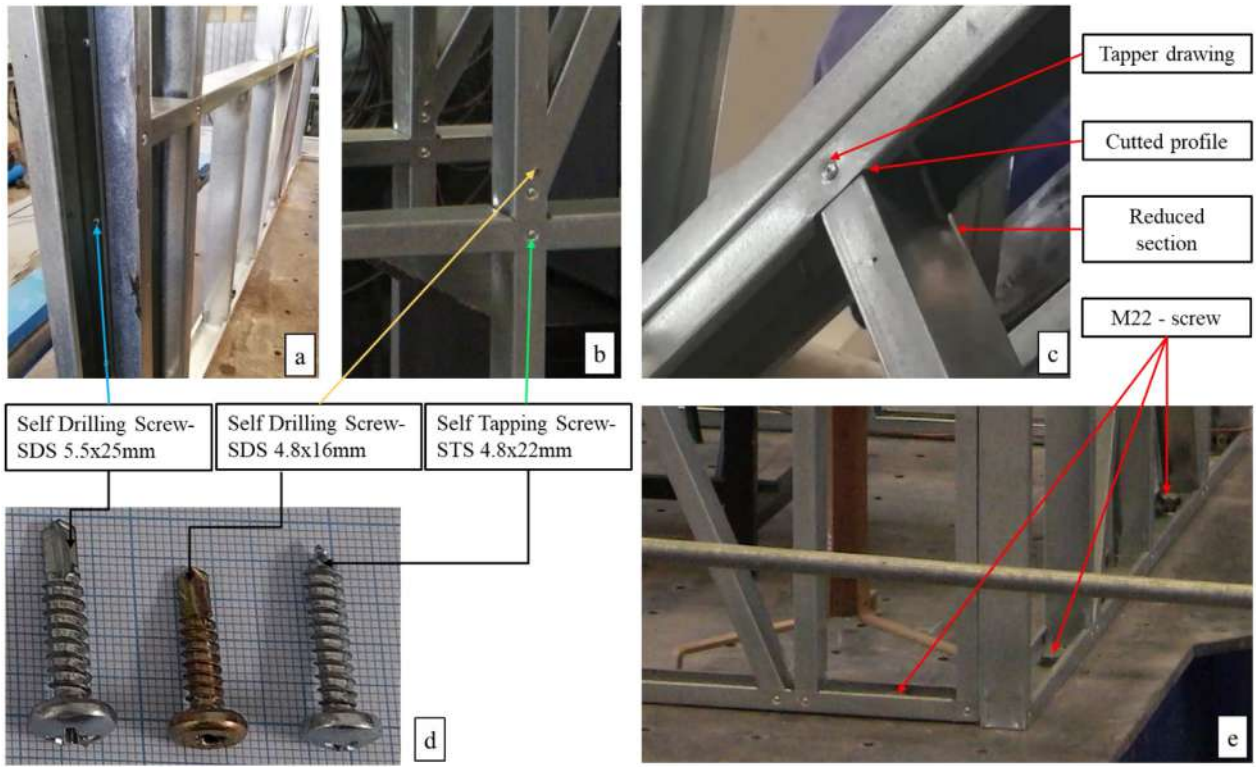

Fig. 7. Connection details: (a) panel intersection connection; (b) current joint of diagonals; (c) upper part T joint connection; (d) screws details; (e) base fixing detail.

wall had two window openings with dimensions of 740 × 1000 mm. The X1 and X2 represent the axes of the longitudinal walls and Y1 and Y2 represent the axes of the transversal walls.

The geometrical dimensions of the East wall and North wall are presented in Fig. 6. North and South wall panels are identical to one another whereas East and West wall panels have different configuration to accommodate the door and window openings. The wall framing panels were obtained by connecting the CFS elements by means of 4.8 × 16 mm STS that fit in the drawings located at the theoretical longitudinal axes of the steel profiles. The model was fixed on the shake table by 14 M22 bolts (4 bolts in both X1 and X2 directions and 3 bolts on both Y1 and Y2 directions).

The scaling down of the model was bound by the dimensions of the ANCO R250 shake table. Table 2 summarizes the values of the scaling factor based on the Cauchy law of similarity [50,51].

The joining of the steel profiles presented drawings, the diagonal members and the struts had reduced cross-sectional height and the clipping of the C-profile flanges was performed for the contour elements. Details of the joint layouts are presented in Fig. 7.

2.3. Test set-up and data acquisition

The experimental program took place at the Department of Structural Mechanics from the "Gheorghe Asachi" Technical University of Iasi. The 3-DOFs ANCO R-250 shake table has the in-plane dimensions of 3000 × 3000 mm. The 600 kN electro-hydraulic actuators are located at 120 degrees, as shown in Fig. 8. The frequency range is between 0–30 Hz whereas the maximum acceleration can reach 3 g. The fixing on the models on the shake table can be done using M22 bolts in a grid having the 200 step-size in both in-plane directions.

The scaled-down model was fitted with 4 PT5 A displacement transducers denoted as D_{x1} … D_{x4} in Fig. 8. The shaking motion was applied in the X direction, as shown in Fig. 8. The response of the model, in terms of accelerations, was recorded by means of four DYTRAN 3202 A accelerometers (A_{x1}, A_{x2}, A_{y1} and A_{y2}) located at the eaves, as shown in Fig. 9. The sampling frequency of the ESAM traveler data acquisition system was set at 50 recordings/ second/ channel.

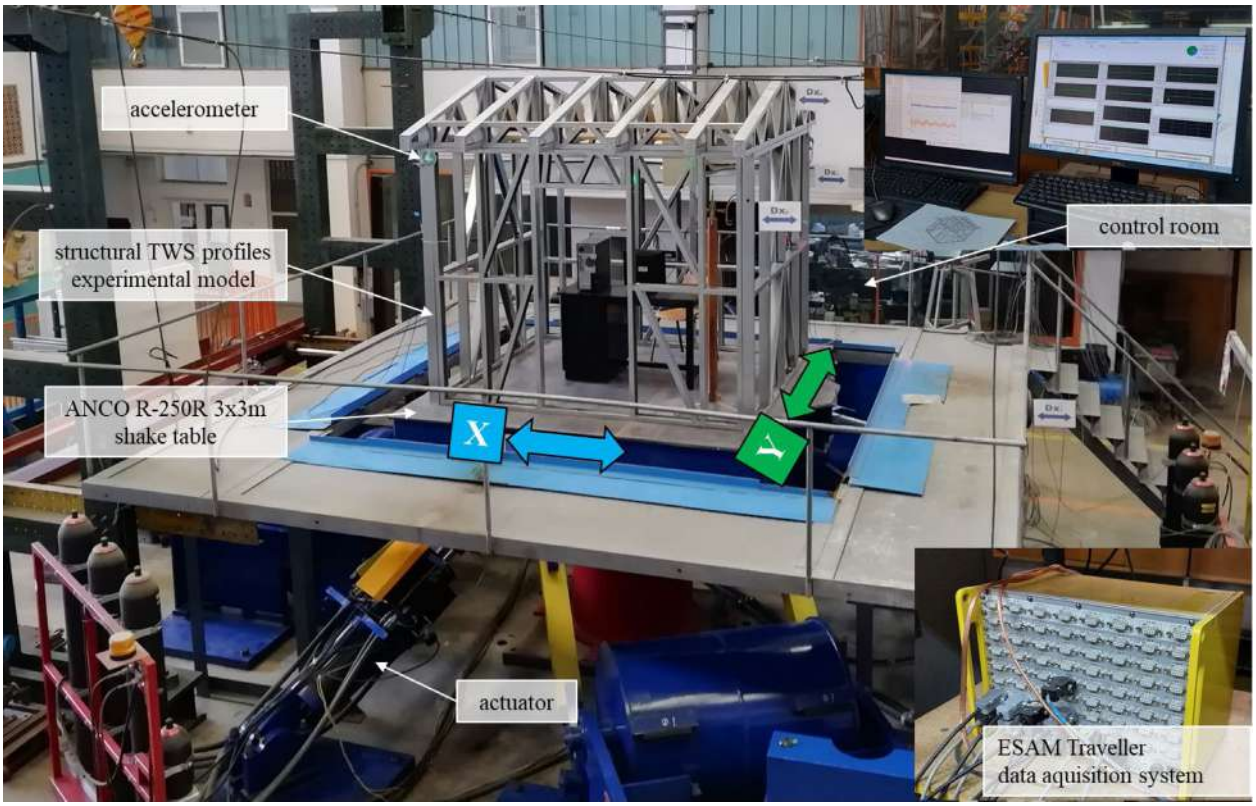

Fig. 8. View of the model on the shake table and instrumentation position.

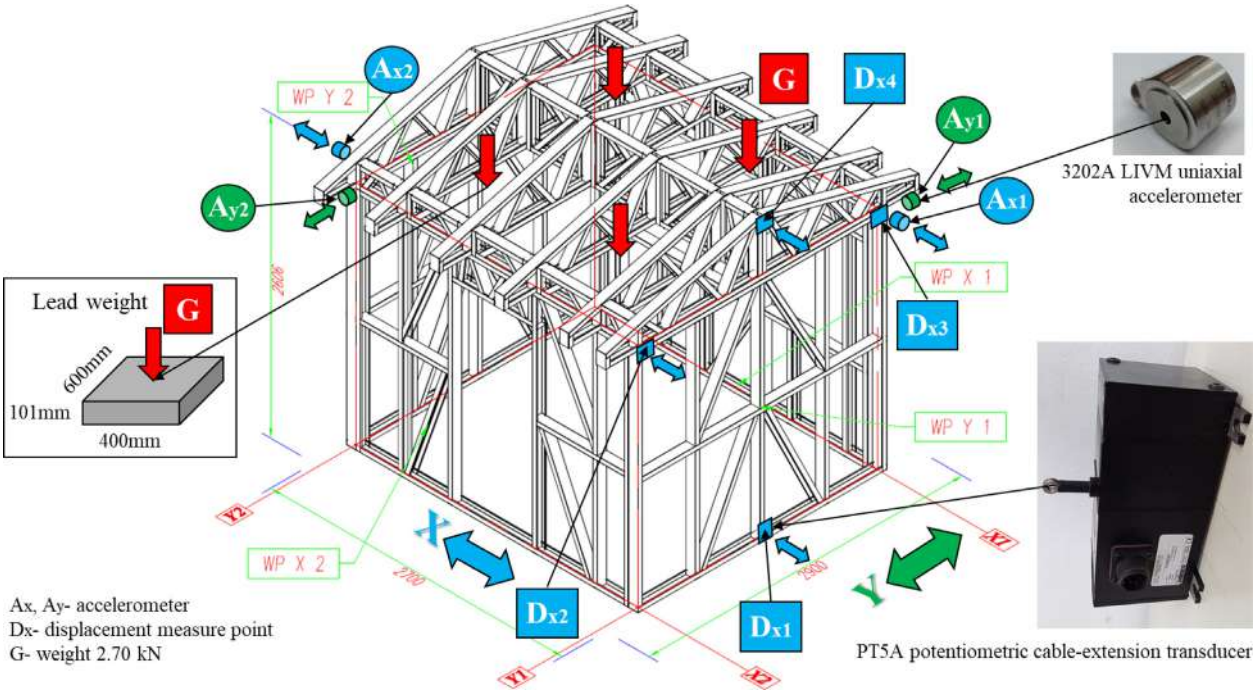

Fig. 9. Axonometry of the structural model with displacement LVDT positions.

3. Experimental program

3.1. Dynamic motions

According to the seismic design codes [1,2] and taking into account the seismic zoning of Romania, shown in Fig. 10, there are three distinct values for the corner/control period T_C: 0.7 s, 1.0 s and 1.5 s. The peak ground acceleration (PGA) in the Vrancea area, epicentral zone, is 0.4 g for a return period of 225 years and a 20% probability of being exceeded in 50 years. Sine beat loading function was chosen with 1 Hz, 1.5 Hz and 6 Hz frequencies and acceleration amplitudes between 0.14 g and 0.71 g.

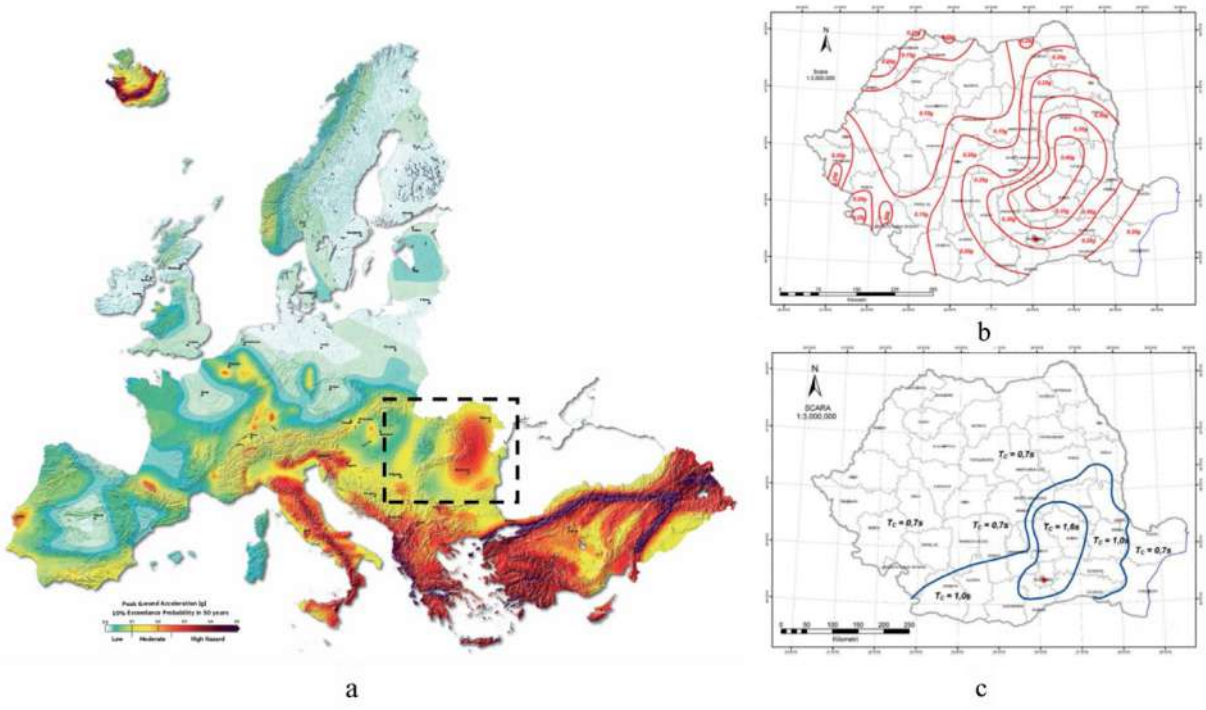

Fig. 10. (a) Europe seismic map [52]; (b) Romania — PGA for a RMI of 225 years and 20% probability of exceedance in 50 years; (c) Zonation of Romania based on the control/corner period T_C, of the response spectrum [2].

3.2. Loading scenarios

The experimental program considered two distinct cases in terms of live loads: bare frame without any additional gravitational loads (Unloaded-UL) and additional masses located at the top part of the walls. The additional masses, shown in Fig. 9, consisted of lead weights, each weighing 275 kg. They were symmetrically located at the ceiling level representing an equivalent load of 1.80 kN/m^2. The dynamic characteristics of the model were firstly determined after which shaking motions were induced following a sine-beat function with different frequencies and different amplitudes of accelerations.

The total load $q = q_1 + q_2 + q_3 + q_4 = 1.80$ kN/m^2 represented the contribution of permanent and partial snow loads considered with their most unfavorable intensities:

- Tile roof $q_1 = 0.75$ kN/m^2;
- Additional steel profiles for cladding: $q_2 = 0.12$ kN/m^2;
- Covering elements: $q_3 = 0.3$ kN/m^2;
- 40% of the snow load with $s = 2.5$ kN/m^2: $q_4 = 0.63$ kN/m^2;

Table 3 summarizes the loading protocol. The different frequencies of the sine-beat function as well as levels of accelerations would offer sufficient data to better understand the behavior of the CFS model to seismic actions.

There are two categories of tests presented in Table 3. The tests denoted with F are those for which the fundamental frequency of vibration was measured in the initial, undamaged state, and after each series of dynamic tests. The tests denoted with T are the test involving the dynamic sine-beat motions. The number in the test designation means the frequency of the shaking motion. Hence, F0-UL-1 Hz represents the test conducted to determine the fundamental frequency of vibration in the initial, unloaded (UL) state. Consequently, T10-L-1 represents test number 10, conducted on the loaded model (L) and the shaking motion had a frequency of 1 Hz.

3.3. Cyclic loading tests on T-joints

The shake table tests were preceded by cyclic loading tests on the T-joints with different configurations in terms of used connectors: type A with 4.8 × 16 mm SDS, type B with 4.8 × 22 mm STS and Tapper drawing and type C using a combination of types A and B. A detailed presentation of the research work can be found in [46]. For the purpose of this study, only type B joints were considered.

In case of structures subjected to seismic motions, the behavior of joints to cycling loads is very important because it can give information related to the possible deformations and decrease of rigidity. The cyclic tests were conducted in accordance with the methodology outlined in [53,54]. Five T-joint specimens were considered. They were first subjected to 20, displacement controlled, cyclic tests with a maximum amplitude of +/−1 mm and a loading rate of 0.083 mm/s. After the 20 cycles, the amplitude was increased to +/−2 mm and the loading rate to 0.167 mm/s and an additional 20 cycling tests were performed. An electro-hydraulic Zwick/Roell 1000SP universal testing machine was used to run this part of the experimental program (see Fig. 11).

4. Experimental results

4.1. Results of cyclic tests on the T-joint

Fig. 12 presents the average load–displacement curves obtained during the cyclic tests. It can be observed that for a maximum displacement of +/−1 mm, Fig. 12a, the stiffness on the tensile part of the test is almost constant with a value of 2300 N/mm and did not decrease significantly after 20 loading cycles. The peak load corresponding to the maximum displacement of 1 mm was 2300 N la 1 mm. On the compression part of the curve however, two different behaviors could be observed: from 0 to −0.5 mm the average value of the stiffness was 2200 N/mm. From −0.5 mm to −1.0 mm the stiffness increased to 8896 N/mm. A more evident decrease in the value of the stiffness can be observed after 20 loading cycles, especially for displacements between −0.5 mm to −1.0 mm. The variation in the applied force amplitude with the number of loading cycles, both in the tensile and compression ranges of the load–displacement curve is presented in Fig. 12c. It can be observed that the intensity of the applied load in the tensile range is almost constant whereas a significant decrease could be seen in the compression range. The value of the secant stiffness,

Table 3
Experimental test.

Current no.	Test label	Description	Dead load (kN/m^2)	Action type	Action frequency (Hz)	Action period (s)	Action max. abs. acceleration (g)	Percent of max. PGA seismic design code (0.4g)	Max. shake table abs. displacement in X direction (mm)
1	F0-UL-1Hz	Unloaded model (UL) tests	0	Sine beat	1	1	-	-	-
2	T1-UL-1						0.21	52.5%	52.44
3	T2-UL-1						0.31	77.5%	73.34
4	T3-UL-1						0.43	107.5%	102.4
5	F1-UL-1Hz				1.5	0.667	-	-	-
6	T4-UL-1.5						0.36	90%	39.88
7	T5-UL-1.5						0.51	127.5%	55.62
8	T6-UL-1.5						0.71	177.5%	76.85
9	F2-UL-1.5Hz				6	0.167	-	-	-
10	T7-UL-6						0.14	35%	1.26
11	T8-UL-6						0.23	57.5%	2.56
12	T9-UL-6						0.33	82.5%	3.87
13	F3-UL-6Hz						-	-	-
14	F4-L-1Hz	Loaded model (L) tests	1.80	Sine beat	1	1	-	-	-
15	T10-L-1						0.22	55%	52.92
16	F5-L-1Hz						-	-	-
17	T11-L-1 (FEM correlation)						0.31	77.5%	72.89
18	F6-L-1Hz						-	-	-
19	T12-L-1 (collapse)						0.46	115%	100.49

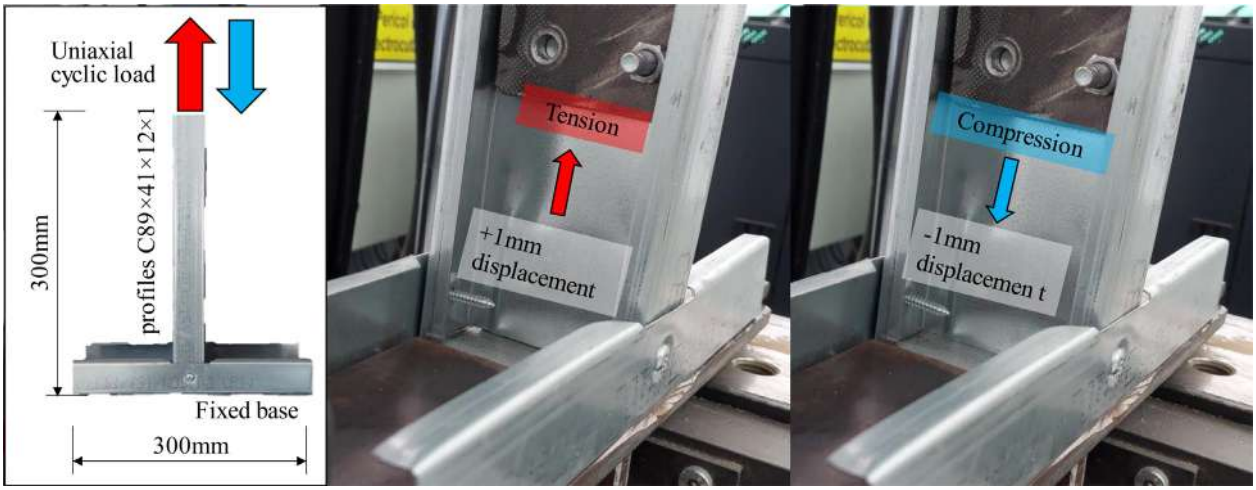

Fig. 11. Tension–Compression cyclic loading experimental test +/−1 mm @0.083 mm/s.

after 20 loading cycles, stabilized around de 2300 N/mm. After the initial test, a second round of cyclic tests were conducted on the same samples of T-joints with double the amplitude of the displacement: +/−2 mm. This resulted in a decrease in the values of the secant stiffness by approximately 30%, Fig. 12b, and almost constant intensity of the applied load both in tension and a smaller decrease of the load in compression, Fig. 12d.

4.2. Dynamic properties of the scaled down-model

The fundamental frequency of vibration for the unloaded, undamaged model was determined using the free-vibration decay method. The scaled-down model was then subjected to a first set of seismic motions at a motion frequency of 1 Hz (tests T1–T3 from Table 3). The fundamental frequency of vibration was then measured again at the end of the first series of tests. The experimental program continued with a second series of seismic motions with a motion frequency of 1.5 Hz. After a third determination of the fundamental frequency, the bare frame model was subjected to a third series of shake table test with a frequency of 6 Hz (tests T7–T9, Table 3). The change in the fundamental frequency of vibration from one series of tests to another, for the bare frame, is presented in Fig. 13a. The model was then loaded, as described in Section 3.2. The addition of masses changed the fundamental frequency from 8.09 Hz to 2.98 Hz, a 278% decrease. For the loaded model only one test was conducted for the motion frequency of 1 Hz but with different amplitudes (tests T10–T12, Table 3). The change in the fundamental frequency for the loaded model is presented in Fig. 13b

Based on the obtained data it can be concluded that the model exhibited some slight damages which is reflected in a decrease of the fundamental frequency from 8.28 Hz to 8.09 Hz for the unloaded scenario, a 2.41% decrease compared to the initial stage. A more significant decrease in the value of the fundamental frequency could be observed when the model was loaded with additional masses, the change being 31.21%.

4.3. Response of the model in accelerations

Fig. 14 presents the input versus recorded accelerations at the level of the shake table and at the top part of the walls for the model as an average value of the records given by accelerometers A_{x1} and A_{x2} (see Fig. 9). It can be observed that for the first series of tests (input frequency 1 Hz and different values for the acceleration amplitudes) the model behaves rigidly, with very small values of the relative accelerations computed as the difference between the absolute accelerations at the top of the walls and the absolute accelerations recorded at the

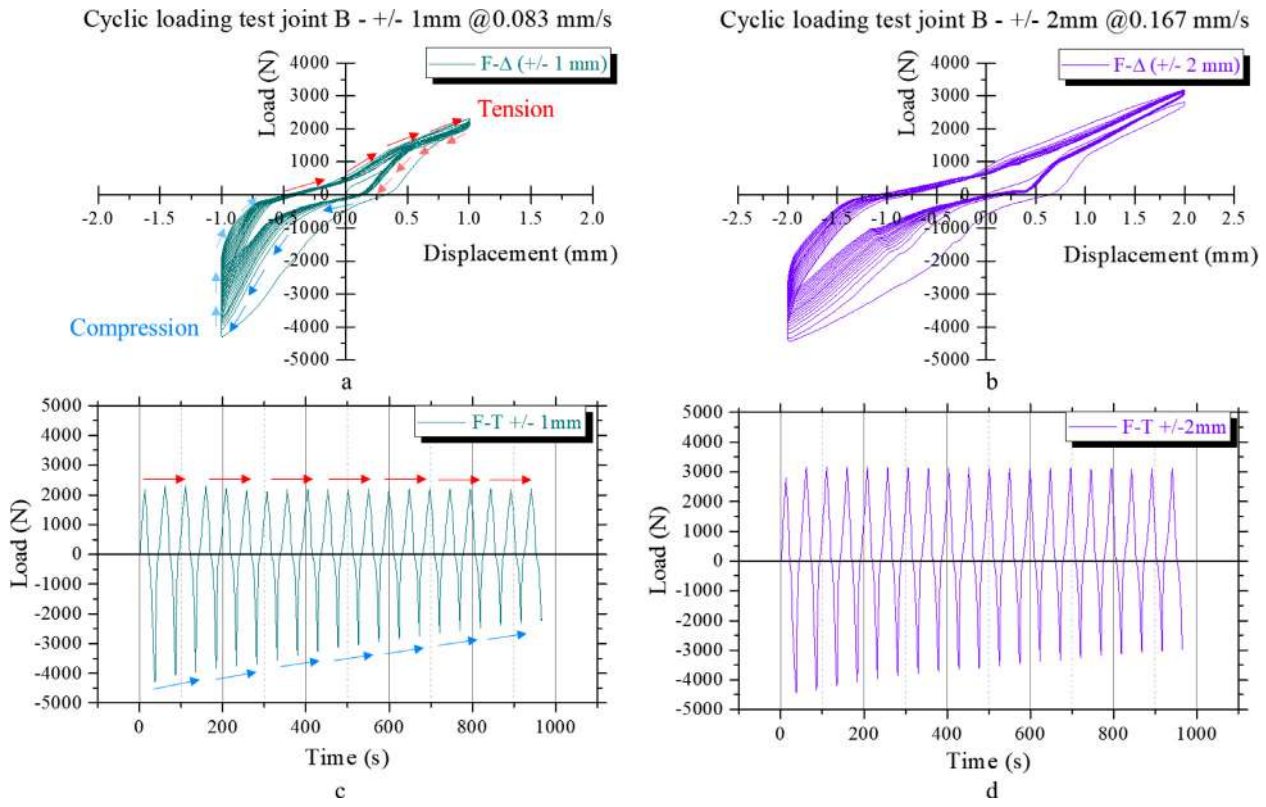

Fig. 12. Tension–Compression cyclic test results: (a) joint B +/−1 mm @0.083 mm/s; (b) joint B +/−2 mm @0.167 mm/s; (c) Load vs. time evolution of cyclic test with +/−1 mm; Load vs. time evolution of cyclic test with +/−2 mm.

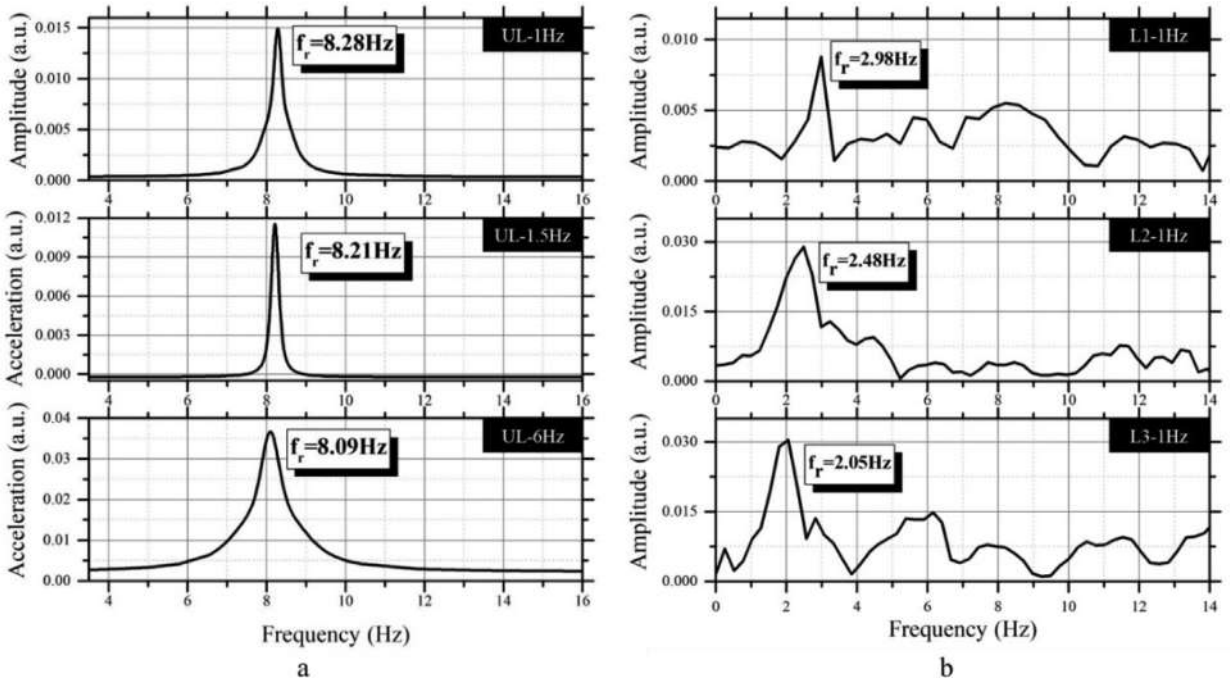

Fig. 13. Results of dynamic identification in terms of natural frequency (a) -Unloaded Model — UL; (b) Loaded Model — L..

level of the shake table. There is, however, an instance during test T3 when the maximum amplitude of the relative acceleration was 0.48 g.

Increasing the frequency of the input motion to 1.5 Hz did not result in significant change in the behavior of the model. It can be seen that the model and the shake table are in phase with one-another. The amplitude of the relative acceleration was reached a maximum of 0.34 g during test T5. From the data of the two series of tests it can be concluded that no significant amplifications were observed.

Increasing the frequency of the input motion to 6 Hz resulted in significant amplifications of the response. In test T9, even though the amplitude of the input motion was 0.33 g, the maximum relative acceleration was 1.76 g. This could be explained by the fact that the

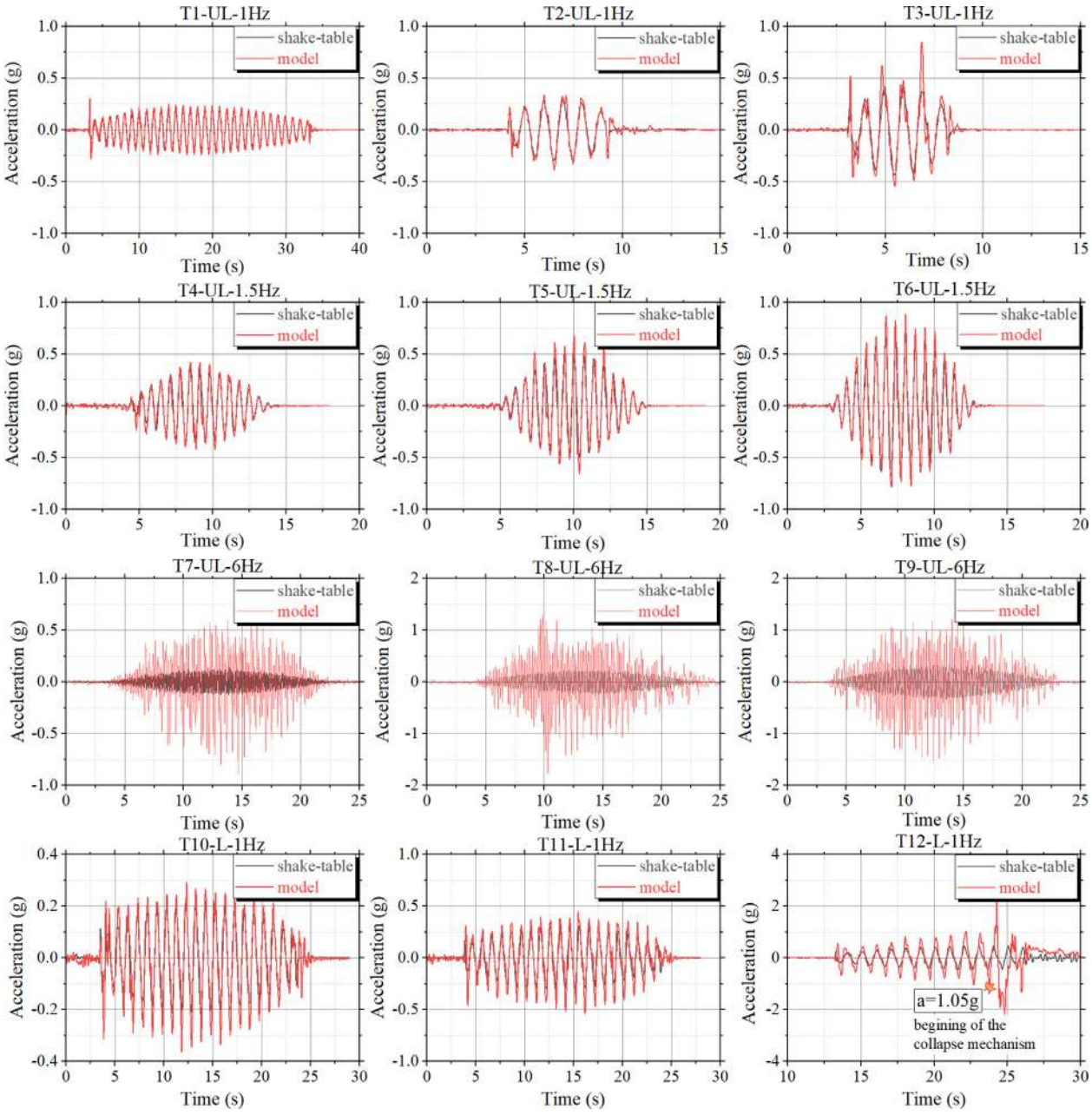

Fig. 14. Absolute acceleration vs. time of the experimental tests.

frequency of the input motion is closer to the fundamental frequency of vibration of the model and therefore significant amplifications of the response were observed.

When the model was loaded by additional masses, the amplitude of relative accelerations increased from 0.4 g in case of test T11 to 0.92 g in case of test T12 before the failure mechanisms started to develop. When the amplitude of the absolute acceleration of the model exceeded 1.05 g, the model failed, and the test was stopped. This can be seen from the last graph in Fig. 14 when the input and response motions are clearly out of phase and significant amplifications of the input amplitude were observed.

4.4. Relative lateral displacements

Fig. 15 presents the time histories of the relative lateral displacements computed as the difference between the average values measured by the displacement transducers D_{x2} and D_{x3} and the displacements recorded by D_{x1} (see Fig. 9).

The recorded data is consistent to what was presented in Fig. 14. Lower values of the relative lateral displacements were observed for the first two series of test with input frequencies of 1 Hz and 1.5 Hz, irrespective of the acceleration amplitudes. The maximum relative lateral displacement for the first series of tests was obtained for test T3, 2.99 mm, whereas for the second series the maximum relative displacement was 3.07 mm.

When the frequency of the input motion increased to 6 Hz, significant amplification of the response was observed during tests T8 and T9 for which the relative lateral displacements were 12.8 mm and 13.44 mm, respectively.

The loaded model exhibited significantly larger relative displacements from 22.75 mm for test T10 to 55.03 mm for test T12 before the failure mechanisms started to develop. A relative displacement of 283.14 mm was recorded when the collapse of the model occurred.

Table 4 summarizes the results in terms of fundamental frequencies of vibration as well as maximum amplitudes of relative accelerations and displacements.

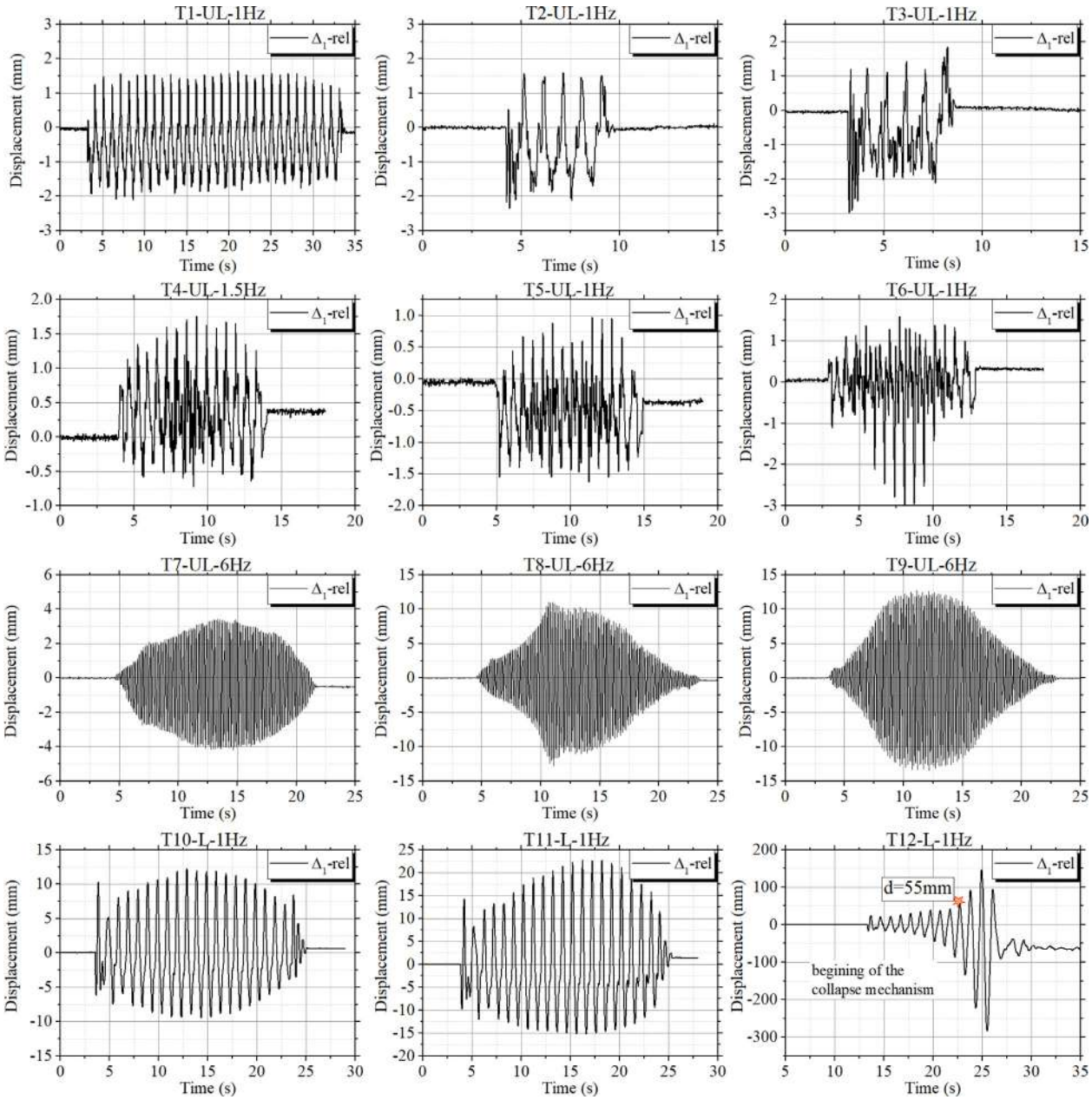

Fig. 15. Relative displacement vs. time: (a) Unloaded tests T3, T6, T9; (b) Loaded model tests T10, T11, T12.

4.5. Base shear–relative displacement curves

Fig. 16 presents the base shear–relative displacements curves for the tests of highest amplitude of the input motion in case of the bare frame model (T3, T6 and T9) as well as all three tests conducted on the loaded frame (tests T10–12).

According to the Romanian seismic design code, the maximum relative displacement in case of serviceability limit state (SLS) should be less than $0.005H$ where H is the height of the structure. For the model presented in this research work the maximum allowable displacement in case of SLS would be 10.5 mm.

$$d_r^{SLS} = 0.005H = 0.005 \cdot 2100 = 10.5 \text{ mm} \quad (1)$$

In case of ultimate limit state (ULS), the relative displacement should not exceed $d_r^{ULS} = 0.025H$, where H is the height of the structure. For the model presented in this research work the maximum allowable displacement in case of ULS is 52.5 mm.

$$d_r^{ULS} = 0.025H = 0.025 \cdot 2100 = 52.5 \text{ mm} \quad (2)$$

Analyzing the data presented in Fig. 16 it can be concluded that the scaled down model behaves linearly for the most part of the tests although in case of test T9 larger values were obtained for the relative lateral displacement which could mean that some of the joints exhibited larger deformations. For the loaded model, the relative displacement exceeds 20 mm in case of test T11 and a decrease in the overall stiffness can be observed. The values of the relative displacement become more significant during test T12, reaching 55.03 mm which represent the onset of the failure mechanisms.

4.6. Failure mechanisms

4.6.1. T-joints subjected to cyclic loading

The following failure mechanisms could be observed during the cyclic tests performed on the T-joints with 4.8 × 22 mm STS. Their order of development is presented in Fig. 17. Due to the cyclic loading the screw, which can be assumed as a small cantilever, tilts downwards due to the tensile force being applied, mechanism (a), almost at the

Table 4
Experimental test results.

Test no.	Test label	Natural frequency *(Hz)*	A_{TX} PGA abs shake table *(g)*	A_x abs. max structure (g)	A_x rel. max (g)	$\Delta_{1max} = D_{x3} - D_{x1}$ *(mm)*	$\Delta_{2max} = D_{x4} - D_{x1}$ *(mm)*
1	F0-UL-1Hz – F.D.T*	8.285	-	-		-	-
2	T1-UL-1Hz	-	0.21	0.30	0.25	2.11	2.47
3	T2-UL-1Hz	-	0.31	0.38	0.21	2.35	3.05
4	T3-UL-1Hz	-	0.43	0.84	0.48	2.99	5.06
5	F1-UL-1Hz – F.D.T	8.28	-	-		-	-
6	T4-UL-1.5Hz	-	0.36	0.42	0.27	1.76	1.39
7	T5-UL-1.5Hz	-	0.51	0.68	0.34	1.63	2.15
8	T6-UL-1.5Hz	-	0.71	0.88	0.25	3.07	3.40
9	F2-UL-1.5Hz – F.D:T	8.21	-	-		-	-
10	T7-UL-6Hz	-	0.14	0.89	0.77	4.18	5.01
11	T8-UL-6Hz	-	0.23	1.77	1.72	12.80	17.05
12	T9-UL-6Hz	-	0.33	1.52	1.76	13.44	18.48
13	F3-UL-6Hz – F.D.T	8.09	-	-		-	-
14	F4-L-1Hz – F.D.T	2.98	-	-		-	-
15	T10-L-1Hz	-	0.22	0.36	0.23	12.33	14.87
16	F5-L-1Hz – F.D:T	2.48	-				
17	T11-L-1Hz FEM correlation	-	0.31	0.53	0.40	22.75	27.78
18	F6-L-1Hz – F.D.T	2.05	-				
19	T12-L-1Hz collapsed	-	0.46	1.05 3.54**	0.92 2.17**	55.03 283.14**	86.04 294.82**

*F.D.T – frequency determination test
** near collapse

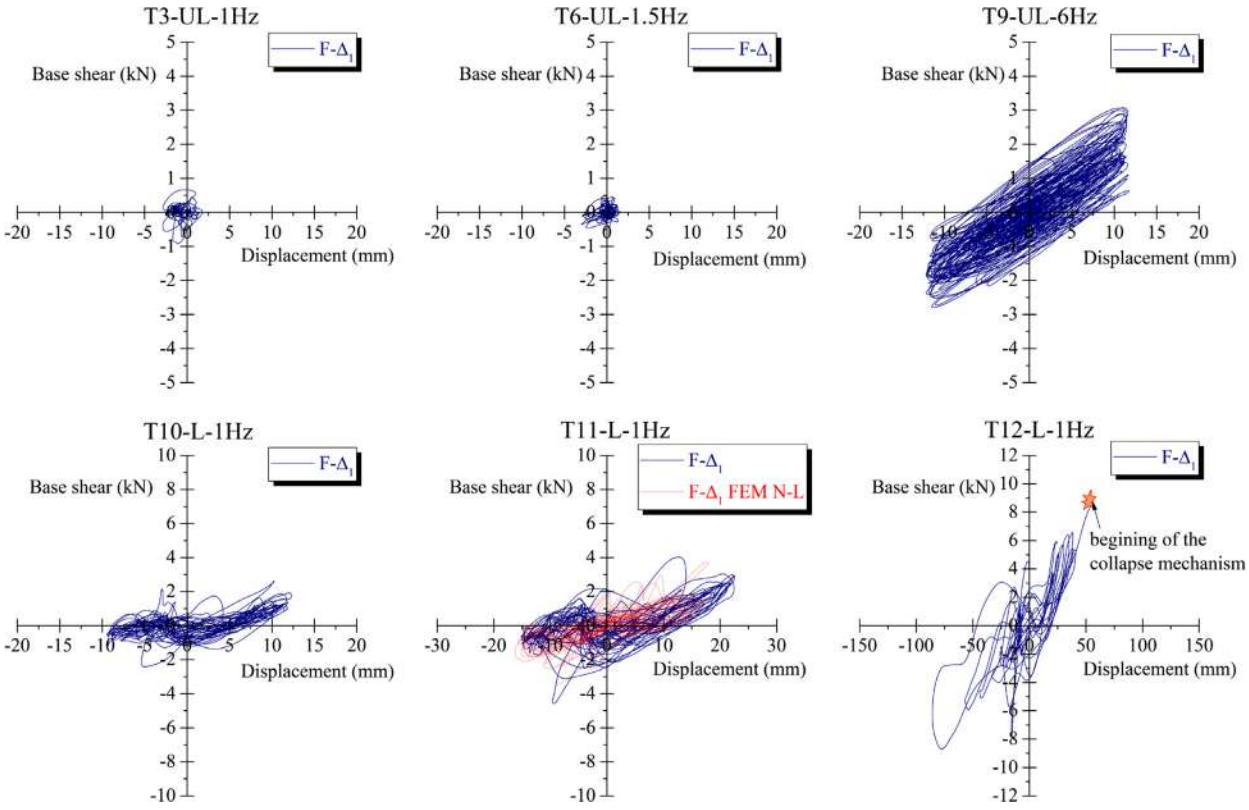

Fig. 16. Base shear vs. displacement graphs.

same time with the onset of plastic deformations of the edges of the pre-drilled holes, mechanism (b). The wall of the clipped steel profile (the chord) is subjected to bending and rotates outwards creating a gap between the chords and the strut during the application of the tensile load, mechanism (d). The excessive rotation is restrained due to the contacts between the chord and the strut. At the same time, the gap the occurs between the steel profiles lowers the friction force and leads to the unscrewing of the STS, mechanism (c).

4.6.2. Bare steel frame model subjected to seismic actions

After the first two series of tests were conducted at frequencies of 1 Hz and 1.5 Hz, no visible deformations could be observed at the joints between the CFS profiles, especially at the ends of the diagonal elements (the most loaded ones). When the frequency of the shaking motion increased to 6 Hz, significant amplifications of the response were recorded in terms of accelerations and relative displacements. The model was inspected once again and no visible damages could be detected for the elements and the joints of the framing in X direction.

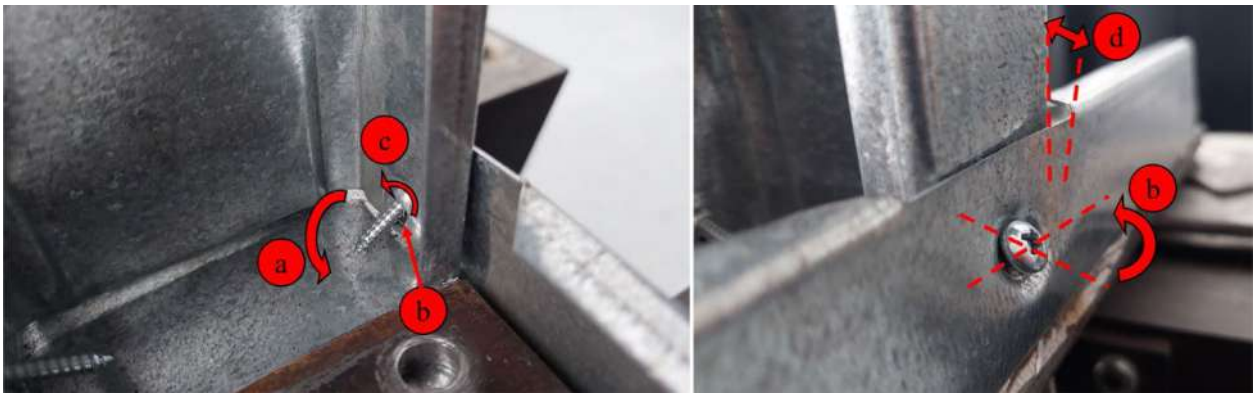

Fig. 17. Failure mechanism in joints during cyclic tests.

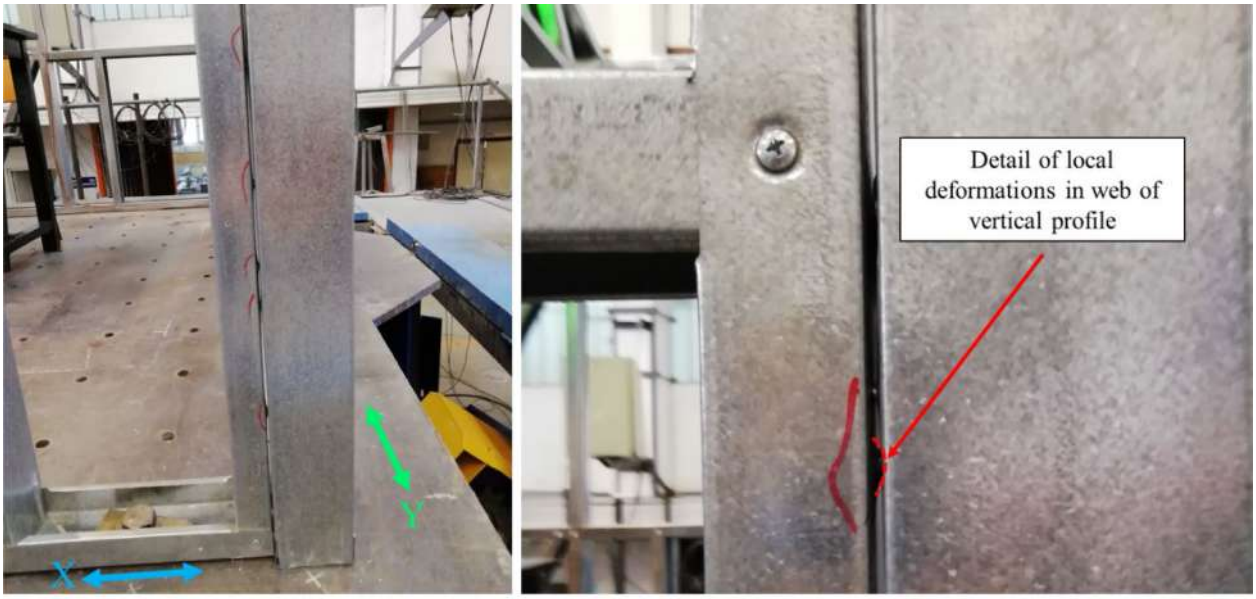

Fig. 18. Deformations of the joints between panels: (a) panel intersection; (b) detail of the deformation.

However, local deformation could be observed at the joints between the framing panels in X and Y directions, as shown in Fig. 18.

During test T11, after the model was loaded with additional masses, the maximum recorded relative displacements was 22 mm. There were still no other visible damages than the ones already identified during the previous tests. During test T12 the model exhibited a relative displacement of 55.03 mm which represented the onset of the failure mechanism, almost at the same time for all 6 locations presented in Fig. 19.

The exact order of the failure mechanisms occurrence in Fig. 19 could not clearly be established because of the extremely short time interval between their occurrences. In case of mechanism **1**, local buckling of the lower chord of the wall framing was observed on both East and West walls (see Fig. 5) which could be caused due to the fixing of the model onto the shake table coupled with the eccentricities between the centerline of the struct and the diagonal element. The axial force it the joint between the diagonal element and the lower chord produced normal stresses that exceeded the yield strength of the material leading to excessive plastic deformations and pulling out of the screw.

Mechanism **2** occurred at the upper end of the diagonal element adjacent to the door gap in the East wall along axis X2 (see Fig. 9). The failures occurred due to the local buckling of the horizontal element connecting the diagonal element and the vertical one forming the door gap. A similar failure mechanism was identified on the opposite side of the door gap. The 3rd failure mechanisms occurred at the joint between the vertical element and the lower end of the upper diagonal in the East wall. Both the vertical and horizontal elements failed due to local buckling because the joint between the diagonal element and the vertical one was stronger than the other joints due to the presence of an additional screw.

Mechanism **4** occurred in the upper part of the door gap, in the vertical element due to torsional buckling. The presence of the truss system to stiffen the upper part of the door gap led to significant differences in lateral stiffness which may have triggered the failure mechanism 4.

Mechanism **5** occurred due to local buckling of the horizontal element at the top of the door gap in Eastern wall coupled with pulling out of the screw. Mechanism **5** may have influenced the occurrence of mechanism **4** due to the fact that the upper left panel of the door gap lost its in-plane stability.

Mechanism **6** occurred in the Western, at the top end of the lower diagonal element from the panel located between the two windows opening. The failure occurred due to the tearing of the material in the diagonal element.

There were also other local damages identified throughout the model in the form of local crushing of the steel sheet at the edges of



Fig. 19. Failure details mechanisms captured from video recording of the experiment.

the holes of local deformation at the joints between the walls (corners of the model) but without pulling out of the screws.

5. Numerical modeling

5.1. General considerations

The numerical modeling of CFS structures can be accomplished by means of two frequently used approaches aimed at accurately simulating the real behavior of the structure. One of the frequently met approaches in the scientific literature [55–60] consists in using 2D or even 3D elements. Coupled with a non-linear material behavior, this approach leads to very accurate results, but it requires expensive hardware and a lot of time to run the simulations especially in case of complex structures.

On the other hand, the approach presented in the design codes [3, 61,62] suggests that the joints are the most vulnerable components of the CFS structures. The numerical investigations conducted in case of such an approach should take into account the second order effect and the real stiffness of the joints. The latter can be obtained from experimental testing. The numerical models presented in this paper consist in linear and non-linear models with infinitely (1) rigid joints and (2) semi-rigid joints. The rigidity of the latter was considered as constant or having a parabolic variation.

Starting from previously published results [46] and considering the results obtained through cyclic tests on T-joints, the finite element structural model based on 1D-beam pin-connected elements was used to simulate the behavior of the experimental model subjected to a similar loading scenario as in test T11.

5.2. The numerical model

Robot Structural Analysis Professional was used to generate the numerical model [63]. Depending on the type of analysis, linear or non-linear, the joints may be defined by means of their axial stiffness k_x depending on the considered scenario:

1. For the bare frame model:
    a. Linear with joints defined with elastic option k_x = 5650 N/mm and simple supports;
    b. Linear with rigid joints defined by $k_x = \infty$ and simple supports;
    c. Nonlinear with k_x = 5650 N/mm — parabolic and uplift supports.
2. For the loaded model (additional masses considered):
    a. Linear with joints defined with elastic option k_x = 5650 N/mm and simple supports;
    b. Linear with rigid joints defined by $k_x = \infty$ and simple supports;
    c. Nonlinear with k_x = 2300 N/mm — parabolic and uplift supports.

Fig. 20a presents the conceptual design/definition of the joint in the local coordinate system of each bar element. Based on the experimentally obtained data from direct tensile tests, Fig. 20b, and cyclic tests, Fig. 20c, the values of the joint stiffness both in tension and compression were assessed as a mean value of 2300 N/mm. The program allows the user to choose from several options on how to define the end releases for each degree of freedom as: fixed (fully restrained, infinite rigidity), fixed values of rigidity or by means of a parabolic variation [63]. Fig. 21 presents the numerical model highlighting the bar ends at the joints.

The geometry of the numerical model was generated based on the exact dimensions of the experimental model, including the eccentricities of the elements at the joints. Rigid joints were considered between the walls. The support conditions were chosen as pin supports at the location of the bolts fixing the model on the shake table. In the case of the non-linear numerical model, FEM N-L, additional uplift support conditions were generated on the surface of the lower chord of the wall framing. Such support conditions have a restrained displacement in the negative direction of the global Z axis (downwards) but the upward displacement was allowed. A graphical representation of the location of supports is presented in Fig. 22. Table 5 summarizes the characteristics of each numerical model considered in the paper.

Newmark method was used for the Time History Analysis (THA) for which the Rayleigh Damping coefficients were computed based on ω_1 = 14.72, ξ_1 = 0.02 and ω_2 = 25.54, ξ_2 = 0.02. The resulting values were $\alpha = 0,3735$ and $\beta = 0,00099$. A 0.02 s time step size was considered which was similar to the time interval for data acquisition during the

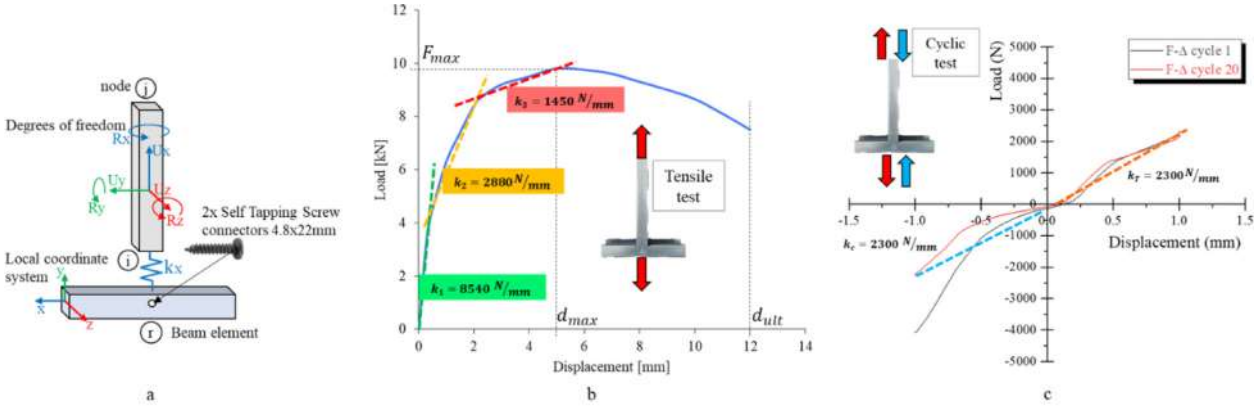

Fig. 20. Definition of beam element end-releases in Robot Structural Analysis (a) joint of beam FEM schematic concept; (b) load–displacement experimental monotonic data test; (c) load–displacement cyclic data test.

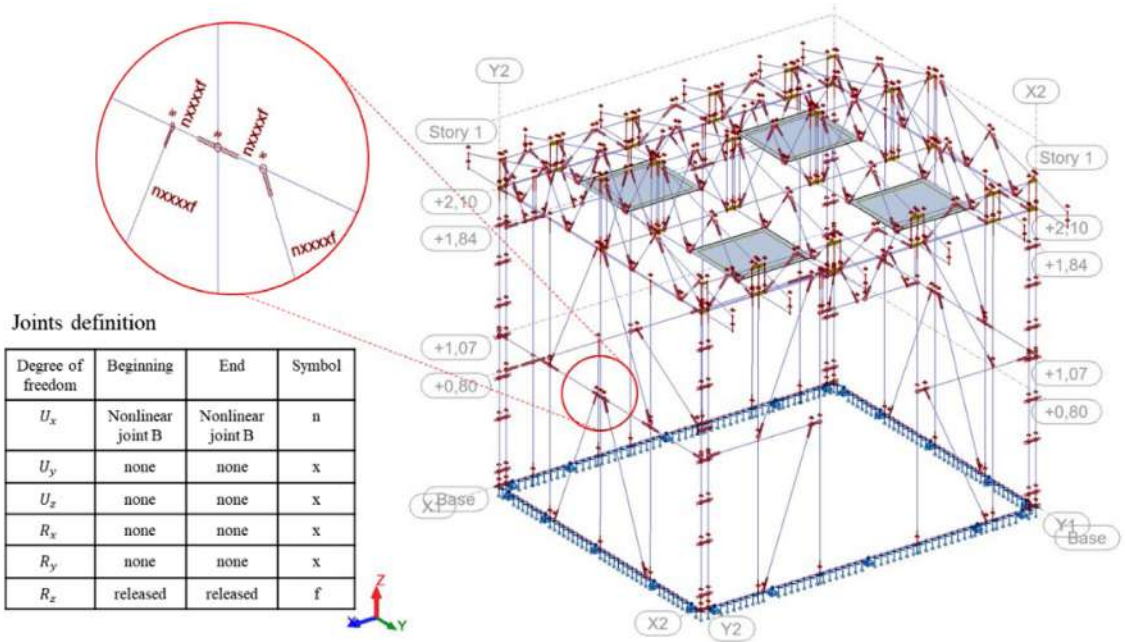

Fig. 21. Numerical model FEM N-L with beam elements and joints definition.

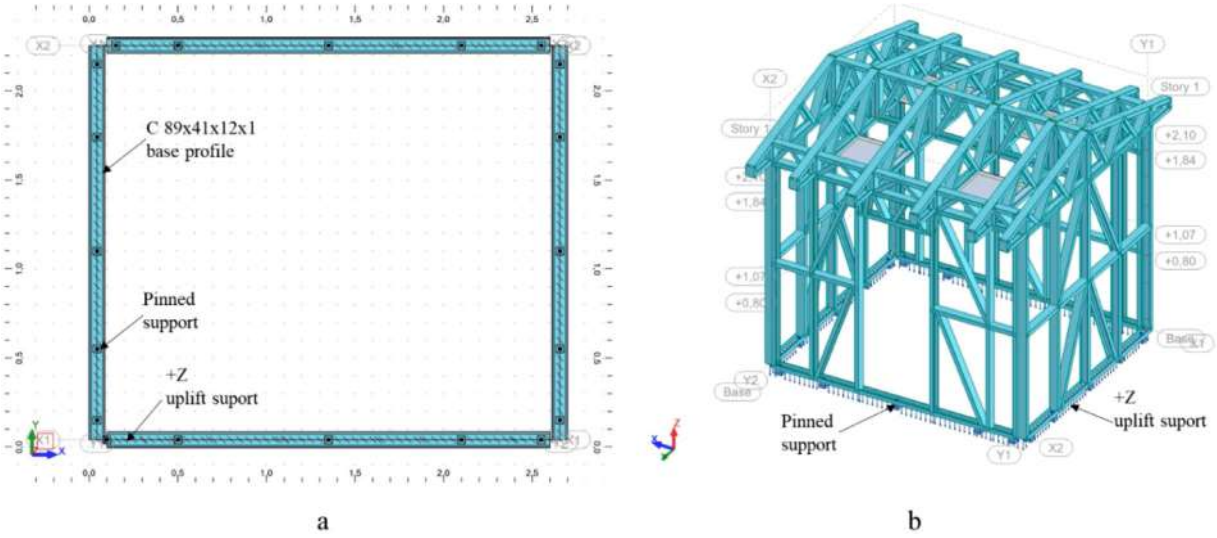

Fig. 22. Numerical model FEM N-L geometry (a) base plan view with supports; (b) 3D spatial model.

Table 5
Numerical models characteristics.

Model analysis type	Number of nodes	Number of bars	Bar finite elements	Rigid links	Releases	Non-linear releases	Supports	Unidirectional supports (uplift +Z)	Static degree of freedom	Time-History analysis method
Linear $k_x = 2300$ N/m	1193	312	897	105	256	–	200		6920	Modal decomposition
Linear $k_x = \infty$	1193	312	897	105	256	–	200		6920	Modal decomposition
Nonlinear $k_x = 2300$ N/mm	1193	312	897	105	–	256	200	181	7101	Newmark method

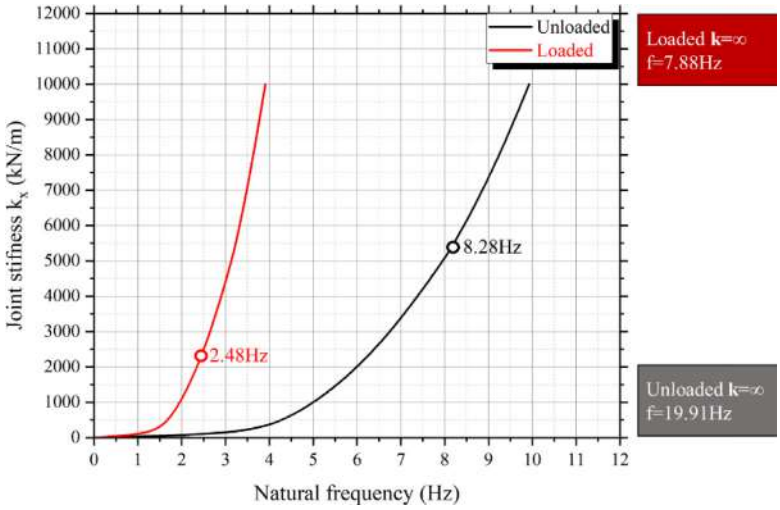

Fig. 23. Joint stiffness vs. natural frequency of the FEM Nonlinear model.

experimental program. The accelerograms used in the numerical model were the ones recorded at the level of the shake table, in both X and Y directions, during test T11-L-1 Hz.

5.3. Dynamic properties of the model

In order to calibrate the model from the point of view of the fundamental frequency of vibration, a set of modal analyses were conducted for which the main parameter was the axial stiffness at the joints. The considered range was between 100 N/mm up to 10000 N/mm. Fig. 23 presents the variation of the fundamental frequency with the change of the axial stiffness at the joints (end of bars). It can be observed that the values of the axial stiffness for which the fundamental frequency of the numerical model matched the experimental data, in both bare/unloaded and loaded frame configurations, were 5650 N/mm and 2300 N/mm, respectively. The axial rigidities exhibited lower values compared to the ones obtained by means of direct tensile tests but similar to the ones obtained during the cyclic tests. For the case of bare/unloaded structure, the considered value of the stiffness should be the one corresponding to the linear elastic range. In case of the loaded structure, already subjected to a three series of seismic motions, the axial rigidity at the joints should be reduced because of the innate displacements that may occur in the joint areas The results obtained from the numerical investigations suggested that the axial rigidity at the joints should be equal to the average value of the secant stiffness obtained from the cyclic tests and presented in Fig. 20c.

Fig. 24 presents the first two mode shapes of the bare/unloaded structural model. It can be observed that both mode shapes are translational ones in X and Y directions, respectively. Fig. 25 presents the first two mode shapes for the loaded structure.

Table 6 summarizes the results obtained from the modal analyses for all considered scenarios. From the presented data it can be observed that for the numerical model for which the joints were considered to have infinite axial rigidity, the obtained dynamic characteristics of the model differ significantly from the experimental results. It can, therefore, be concluded that this approach would lead to erroneous results.

5.4. Time history analyses

A similar accelerogram to the one corresponding to experimental test T11-L-1 Hz was considered in the numerical model. Both linear and non-linear analyses were run.

Fig. 26 present the response of the model in terms of accelerations and displacements. For comparative purposes, the experimentally obtained results and the numerical ones for different types of THA analyses were plot on the same graph. The output for the numerical model was considered to be at node 65 which corresponds to A_{x1} and D_{x3} on the real model (see Fig. 9).

It can be observed that there are significant differences between the results obtained from each of the two numerical models for which linear analysis was considered. The difference between the two models consisted in the way the axial rigidity was considered at the joints: infinite axial rigidity and finite axial rigidity with a value of 2300 N/mm. At the same time, the numerical model for which a non-linear analysis was considered, lead to similar results as the linear analysis case but with axial rigidity at the nodes defined based on the experimental data. For both graphs presented in Fig. 26, the numerical results are very close to the experimental data during the first 10 s on the THA. After that, the experimental model started to exhibit local damages which could not be captured in the numerical model. For this to happen, nonlinear material behavior should also be considered in the numerical simulations which would lead to a more demanding calculation effort.

Fig. 27 presents the deformed shape of the structure in each of the considered scenarios for the THA: (a) nonlinear with $k_x = 2300$ N/mm

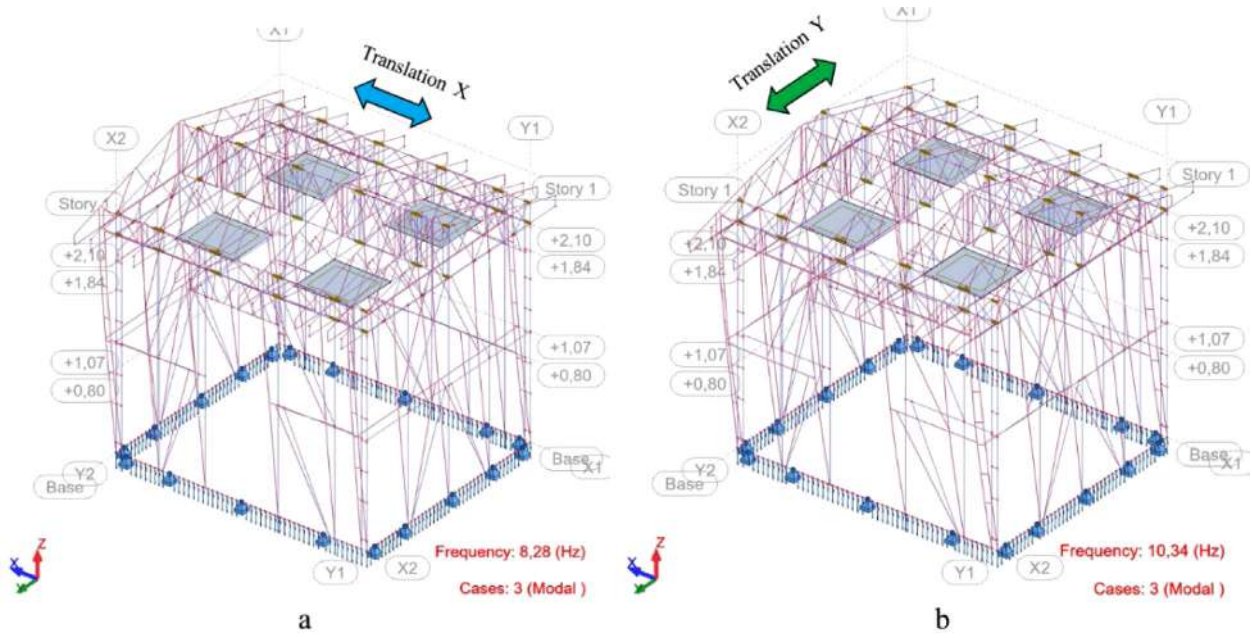

Fig. 24. Vibration modes of nonlinear unloaded-UL model: (a) 1st mode — translation in X direction; (b) 2nd mode — translation in Y direction.

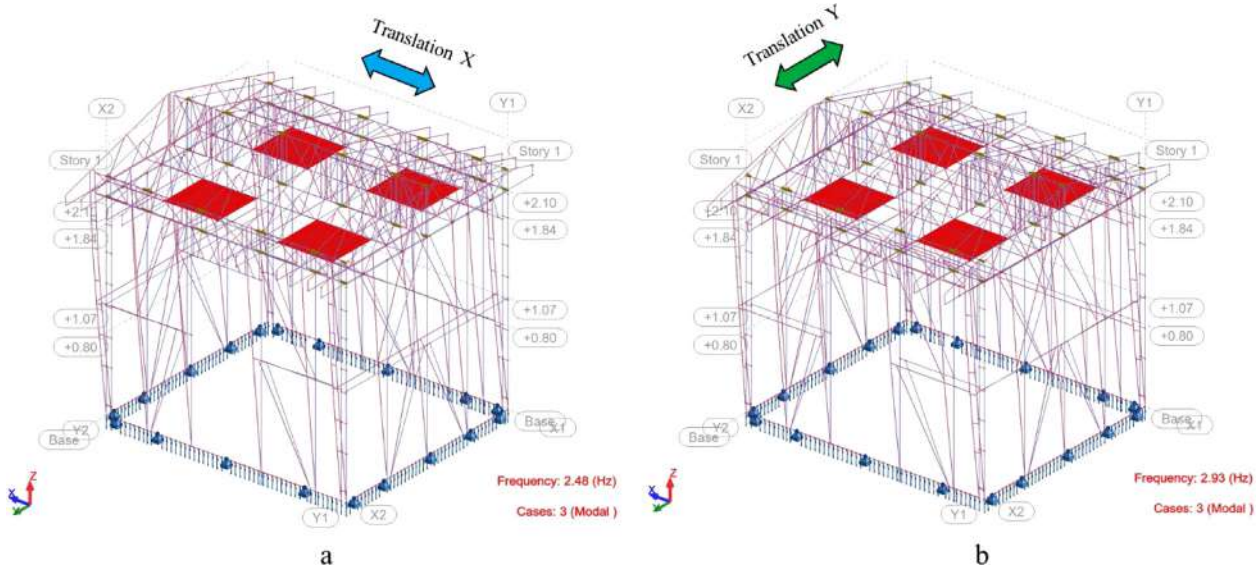

Fig. 25. Vibration modes of nonlinear loaded-L model: (a) 1st mode — translation in X direction; (b) 2nd mode — translation in Y direction.

Table 6
Dynamic analysis results.

Model	Mode	Frequency (Hz)	Period (sec)	Current mass Ux (%)	Current mass Uy (%)	Total mass (kg)	Pulsation	Damping
Unloaded	1	8.28	0.12	83.78	0.01	293	52.05	0.01
FEM k_x = 5650 N/mm	2	10.34	0.10	0.02	84.40	293	64.97	0.01
Unloaded	1	19.93	0.06	85.10	0.01	293	112.04	0.04
FEM k_x=inf	2	26.14	0.05	0.01	84.48	293	125.09	0.04
Unloaded Experimental	1	8.28	0.12	–	–	293	52.05	0.01
Loaded	1	2.48	0.40	96.44	0.05	1496	16.21	0.01
FEM k_x = 2300 N/mm	2	2.73	0.37	0.07	96.66	1496	18.34	0.01
Loaded	1	7.88	0.13	96.89	0	1496	49.54	0.04
FEM k_x = inf	2	10.45	0.10	0	96.78	1496	65.67	0.04
Loaded Experimental	1	2.48	0.40	–	–	1496	15.58	0.02

(b) linear with k_x = 2300 N/mm and (c) linear with k_x = ∞. The maximum intensity of the axial force obtained during the THA for the three considered scenarios is shown in Fig. 28.

It can be observed that the lateral displacements of the linear and nonlinear models with k_x = 2300 N/mm are much larger than in the case of infinite rigidity at the nodes. At the same time, the obtained

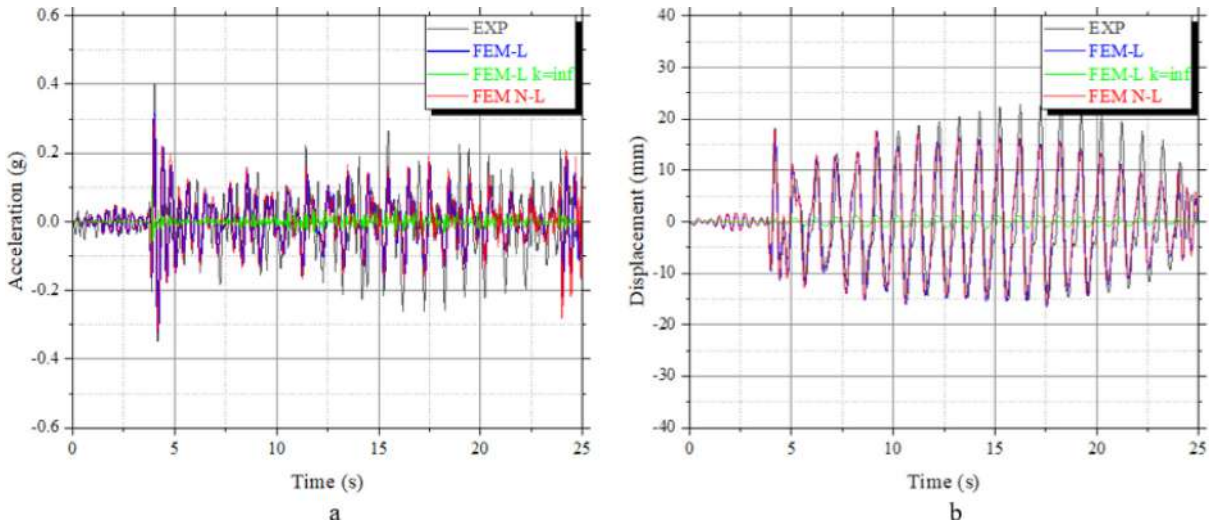

Fig. 26. Results on Loaded-L model, test T11 actions: (a) accelerations; (b) displacements.

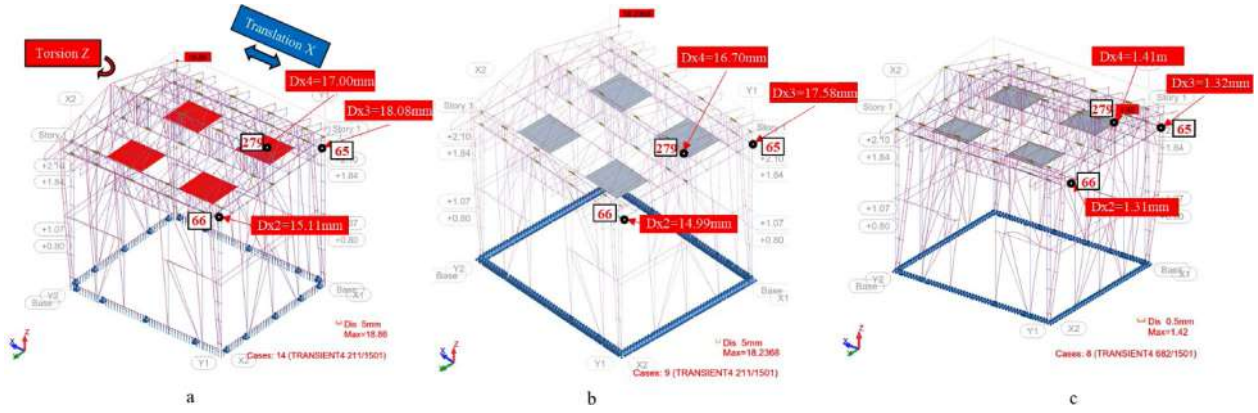

Fig. 27. Time History analysis maximum displacements: (a) Nonlinear model-k_x = 2300 N/mm; (b) linear model-k_x = 2300 N/mm; (c) linear model k_x = inf.

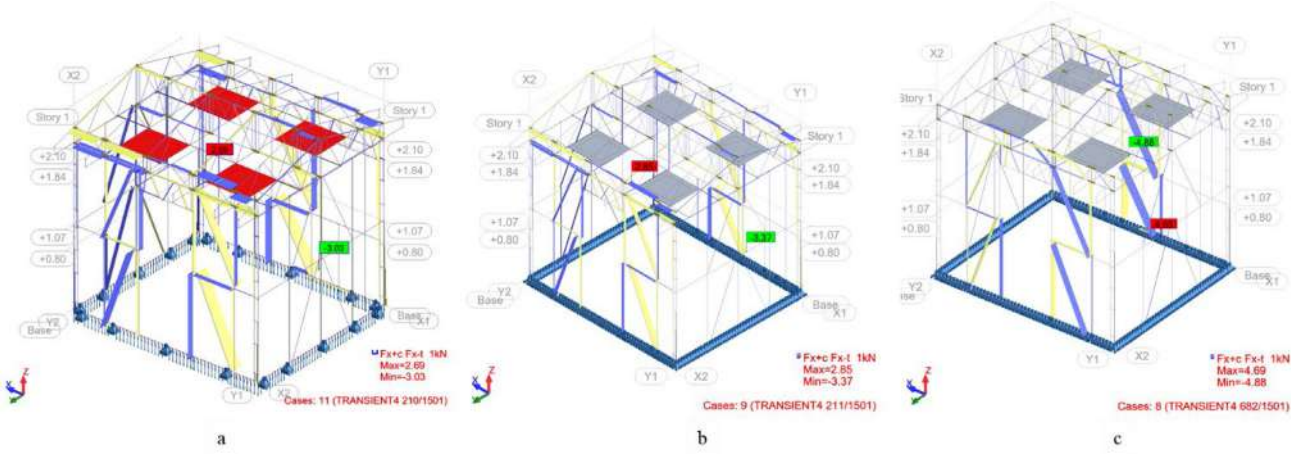

Fig. 28. Maximum axial forces (a) Nonlinear model-k_x = 2300 N/mm; (b) linear model-k_x = 2300 N/mm; (c) linear model k_x = inf.

values of the lateral displacements at node 66, located at the same level as node 65 but on the opposite wall, are different than the ones obtained at node 65 which suggests that a torsional movement was also present. Considering the geometry of the model and the locations for the door and windows openings, this torsional effect was somehow expected.

The maximum intensity of the axial force, 3.03 kN, occurred in the diagonal element of the lower central panel belonging to West wall where window openings were located. For comparison, in case of the model with infinite axial rigidity at the nodes, the corresponding axial force was 4.69 kN.

6. Discussions

Laboratory cyclic tests conducted on the T-joints showed that they have a lower bearing capacity and a lower stiffness compared to the values obtained from direct tensile tests. Even though on the compression side of the cyclic test the initial tendency of the joint was to behave more rigidly compared to the tensile side, the rigidity in compression was significantly reduced after 20 loading cycles and becomes similar to the one in tension. Similar behavior was observed during the experimental tests on the shake table. The obtained results for the axial rigidity of the joints were used in calibrating the numerical model.

The shaking motions at low frequencies of 1 Hz and 1.5 Hz did not produce significant damages into the structure and resulted in an almost rigid body motion response from the model. Very low values of relative accelerations and displacements were obtained even though the amplitude of the input acceleration was increased up to 0.71 g in case of T6. One possible explanation could be the fact that the frequency of the input motion was far away from the fundamental frequency of vibration of the model, 8.28 Hz. However, based on the determined fundamental frequency after each series of tests, it resulted those slight damages could be present in the model since the fundamental frequency decreased to 8.21 Hz, a 0.8% decrease. This small difference may also be due to the inherent measurement errors.

When the frequency of the input motion increased to 6 Hz, larger lateral displacements could be observed. However, the model was still in the linear elastic range of material behavior and the decrease in the fundamental frequency of vibration to 8.09 Hz after the third series of tests could be attributed to the small displacements starting to occur at the joints. This would lead to a more flexible model. The maximum relative displacements increased to 13.44 mm and the relative acceleration reached 1.76 g. The large amplification of the shaking motion, especially in terms of accelerations, could be explained by the ratio of 0.8 between the frequency of the input motion and the fundamental frequency of the model.

The model was loaded with additional masses which would amount to an equivalent load of 1.80 kN/m^2. The increased weight resulted in a 63% decrease in the value of the fundamental frequency from 8.09 Hz to 2.98 Hz. For the loaded model, only a sine beat input motion with a frequency of 1 Hz was selected but with different amplitudes of the input signal. It was observed that during test T11 the relative displacement increased to 22 mm which exceeded the maximum values for ULS by 100%. The fundamental frequency of the model decreased by 16.8% to 2.48 Hz.

During the test T12 the response of the structure was significantly amplified due to damages in the elements and joints and possible resonance phenomenon on higher modes of vibration. After 20 s the relative displacement exceeded 86 mm and failure mechanisms started to develop. This led to further amplification in the response of the structure due to the fact that the fundamental frequency of the model dropped below 2 Hz and became very close to the frequency of the input motion.

The experimental program revealed a complex failure mechanism which can be considered as:

- Global Rocking — a slight uplift of the lower chords of the framing walls between the connection points between the model and the shake table;
- Local buckling of compressed elements such as diagonal elements and even vertical ones near the joints;
- Local buckling of horizontal elements;
- Plastic deformations at the edges of the pre-drilled holes in the CFS profiles;
- Tilting and pulling out of the screws at the joints;
- Tearing of elements in the joint area corresponding to the net cross-sectional area of CFS profile.
- Unfasten of screws at the joints.
- The overall stiffness of the whole structure during the tests decreased due to damages located in general in connections between structural elements. The level of energy absorption is low.

The information collected during the experimental program serves as the starting point for a new series of experiments on similar models with different cladding options such as OSB or gypsum boards. They also served as calibration data for the numerical model developed within the framework of the present research.

The numerical investigation included both linear and non-linear analyses with finite values of axial stiffness at the end of the bar elements determined from cyclic tests. It was observed that for a value of the axial stiffness of 2300 N/mm the results obtained by means of FEA matched the experimental ones very well. Moreover, the values of the relative displacements and accelerations were very close to the ones obtained during the shake table tests. However, the fact that the numerical model did not consider any material non-linearities, only geometrical ones, resulted in quite large differences between the obtained results especially after the experimental model started to exhibit damages due to repeated shaking motions.

7. Conclusions

The paper presents the results obtained after a complex experimental program coupled with numerical simulations on a scaled-down model, 1/1.2 scale, of a CFS structure made of 89 × 41×12× x1 mm lipped channel elements. It represents a replica of constructive solutions for ground floor or ground floor and one or two storeys structures that are frequently met in South-East Europe, including highly active seismic areas.

The main purpose of the research program is to gather both quantitative but more importantly, accurate information in terms of structural response to dynamic actions characterized by input accelerations equal in amplitude to the maximum values specified in seismic design codes, PGA=0.40 g. Comparing both experimental and numerical results obtained for the relative displacements with the maximum allowed values specified in the code for ULS (0.005H) and SLS (0.025H) it can be concluded that the overall stiffness of the structure is able to fulfill the imposed conditions. It was observed that the small values of damping from 0.01 to 0.02 for such structural systems without cladding materials, means they have low energy dissipation capabilities.

The damage of the joints and the reduction in the structural stiffness due to cyclic loads, such as the ones produced by earthquakes, change the eigen period of the structure and has a significant influence on the response of the structure to seismic actions. Larger gravitational loads lead to more extensive damage to the joints.

The developed numerical model based on the experimentally determined connection axial rigidity is able to offer accurate results in terms of the fundamental frequency of vibration, relative accelerations and displacements. This accuracy can be obtained even by running simple linear static and THA analyses, without the need for complex and computationally intensive non-linear approaches. However, for a more accurate capturing of the local damages and onset of failure mechanisms, more complex numerical models are needed, which take into account non-linear material behavior.

The results presented in this paper serve as a starting point for future research works aimed at assessing the influence of the sheathing on the response of CFS structures to seismic actions. Additionally, research in the direction of improved joints with better energy dissipation properties is also pursued by the authors.

CRediT authorship contribution statement

George Taranu: Writing – original draft, Software, Project administration, Methodology, Investigation, Funding acquisition, Data curation, Conceptualization. **Viorel Ungureanu:** Writing – review & editing, Validation, Supervision, Conceptualization, Investigation, Writing – original draft. **Zsolt Nagy:** Writing – review & editing, Validation, Supervision, Investigation, Writing – original draft. **Mihai-Sergiu Alexa-Stratulat:** Methodology, Data curation. **Ionut-Ovidiu Toma:** Writing – original draft, Investigation, Methodology, Writing – review & editing. **Septimiu-George Luca:** Software, Formal analysis, Data curation.

Declaration of competing interest

The authors declare that they have no known competing financial interests or personal relationships that could have appeared to influence the work reported in this paper.

Data availability

Data will be made available on request.

Acknowledgments

The authors acknowledge the contribution of UNIC-ROTAREX, Romania, for supplying the materials, joints and accessories needed for conducting the laboratory investigations.

Additional information

Video shaking table experiment: https://youtu.be/IcGuz9mW8l4
Video Time History vs. Experiment: https://youtu.be/tZVaSpgGxy4
Video of direct tensile tests on T-joints: https://youtu.be/v0yRbs4fWvM
Video of cyclic tests on T-joints: https://youtu.be/eujWg-R-O2U

References

[1] EN 1998-1, Eurocode 8: Design of Structures for Earthquake Resistance – Part 1: General Rules, Seismic Actions and Rules for Buildings, CEN, Brussels, Belgium, 2004.
[2] P100/2013-1, Seismic Design Code - Part I: Design Rules for Buildings, M.D.L.P.A Romania, 2013, (in Romanian).
[3] EN 1993-1-3, Eurocode 3: Design of Steel Structures, Part 1.3: General Rules, Supplementary Rules for Cold-Formed Thin Gauge Members and Sheeting, CEN, Brussels, Belgium, 2006.
[4] EN 1993-1-5, Eurocode 3: Design of Steel Structures-Part 1-5: Plated Structural Elements, CEN, Brussels, Belgium, 2006.
[5] S.K. Naman, B.J. Goodno, Seismic evaluation of a low rise steel building, Eng. Struct. 8 (1986) 9–16, http://dx.doi.org/10.1016/0141-0296(86)90014-3.
[6] R.T. Severn, D.P. Stoten, Y. Tagawa, The contribution of shaking tables to earthquake engineering, in: 15 WCEE, 2012.
[7] B.W. Schafer, D. Ayhan, J. Leng, P. Liu, D. Padilla-Llano, K.D. Peterman, M. Stehman, S.G. Buonopane, M. Eatherton, R. Madsen, B. Manley, C.D. Moen, N. Nakata, C. Rogers, C. Yu, Seismic response and engineering of cold-formed steel framed buildings, Structures 8 (2016) 197–212, http://dx.doi.org/10.1016/j.istruc.2016.05.009.
[8] K.D. Peterman, M.J.J. Stehman, R.L. Madsen, S.G. Buonopane, N. Nakata, B.W. Schafer, Experimental seismic response of a full-scale cold-formed steel-framed building. I: System-level response, J. Struct. Eng. 142 (2016) http://dx.doi.org/10.1061/(asce)st.1943-541x.0001577.
[9] B.W. Schafer, Cold-formed steel structures around the world, Steel Constr. 4 (2011) 141–149, http://dx.doi.org/10.1002/STCO.201110019.
[10] N. Nakata, B.W. Schafer, R.L. Madsen, Seismic design of multi-story cold-formed steel buildings: The CFS-NEES archetype building, in: Structures Congress 2012 - Proceedings of the 2012 Structures Congress, 2012, http://dx.doi.org/10.1061/9780784412367.134.
[11] K.D. Peterman, R.L. Madsen, B.W. Schafer, Experimental seismic behavior of the CFS-NEES building: System- level performance of a full-scale two-story light steel framed building, in: 22nd International Specialty Conference on Recent Research and Developments in Cold-Formed Steel Design and Construction, 2014.
[12] P. Liu, K.D. Peterman, C. Yu, B.W. Schafer, Cold-formed steel shear walls in ledger-framed buildings, in: Structural Stability Research Council Annual Stability Conference, 2012.
[13] X. Wang, T.C. Hutchinson, Evolution of modal characteristics of a mid-rise cold-formed steel building during construction and earthquake testing, Int. J. Earthq. Eng. Struct. Dyn. 49 (2020) 1539–1558, http://dx.doi.org/10.1002/EQE.3316.
[14] R. Landolfo, O. Iuorio, L. Fiorino, Experimental seismic performance evaluation of modular lightweight steel buildings within the ELISSA project, Earthq. Eng. Struct. Dyn. 47 (2018) http://dx.doi.org/10.1002/eqe.3114.
[15] V. Macillo, L. Fiorino, R. Landolfo, Seismic response of CFS shear walls sheathed with nailed gypsum panels: Experimental tests, Thin-Walled Struct. 120 (2017) 161–171, http://dx.doi.org/10.1016/j.tws.2017.08.022.
[16] L. Fiorino, V. Macillo, R. Landolfo, Shake table tests of a full-scale two-story sheathing-braced cold-formed steel building, Eng. Struct. 151 (2017) 633–647, http://dx.doi.org/10.1016/j.engstruct.2017.08.056.
[17] R. Landolfo, A. Campiche, O. Iuorio, L. Fiorino, Seismic performance evaluation of CFS strap-braced buildings through experimental tests, Structures 33 (2021) http://dx.doi.org/10.1016/j.istruc.2021.05.098.
[18] S. Shakeel, B. Bucciero, A. Campiche, T. Pali, L. Fiorino, R. Landolfo, Shake table testing and numerical modelling of LWS strap-braced structures for seismic performance evaluation, in: AIP Conference Proceedings, 2019, http://dx.doi.org/10.1063/1.5114270.
[19] A. Campiche, S. Shakeel, B. Bucciero, T. Pali, L. Fiorino, R. Landolfo, Seismic behaviour of strap-braced LWS structures: Shake table testing and numerical modelling, in: IOP Conference Series: Materials Science and Engineering, 2019, http://dx.doi.org/10.1088/1757-899X/473/1/012032.
[20] M.T. Terracciano, B. Bucciero, T. Pali, V. Macillo, L. Fiorino, R. Landolfo, Shake table tests of structures with CFS strap-braced stud walls, Key Eng. Mater. 763 (2018) http://dx.doi.org/10.4028/www.scientific.net/KEM.763.432.
[21] V. Macillo, A. Campiche, S. Shakeel, B. Bucciero, T. Pali, M.T. Terracciano, L. Fiorino, R. Landolfo, Seismic behaviour of sheathed CFS buildings: Shake-Table testing and numerical modelling, Key Eng. Mater. 763 (2018) http://dx.doi.org/10.4028/www.scientific.net/KEM.763.584.
[22] A. Campiche, S. Shakeel, V. Macillo, M.T. Terracciano, B. Bucciero, T. Pali, L. Fiorino, R. Landolfo, Seismic behaviour of sheathed CFS buildings: Shake table tests and numerical modelling, Ingen. Sismica 35 (2018).
[23] D. Dubina, Behavior and performance of cold-formed steel-framed houses under seismic action, J. Construct. Steel Res. 64 (2008) 896–913, http://dx.doi.org/10.1016/J.JCSR.2008.01.029.
[24] L.A. Fülöp, D. Dubina, Performance of wall-stud cold-formed shear panels under monotonic and cyclic loading: Part II: Numerical modelling and performance analysis, Thin-Walled Struct. 42 (2004) 339–349, http://dx.doi.org/10.1016/S0263-8231(03)00064-8.
[25] D. Dubina, L. Fülöp, V. Ungureanu, I. Szabo, Z. Nagy, Cold-Formed Steel Structures for Residential and Non-Residential Buildings, Timisoara, 2000.
[26] D. Dubina, L.A. Fülöp, A. Aldea, S. Demetriu, Z. Nagy, Seismic performance of cold-formed steel framed houses, in: Proceedings of 5th International Conf. on Behaviour of Steel Structures in Seismic Areas (STESSA), Yo1kohama, 2006, pp. 429–435.
[27] D. Dubina, A. Stratan, A. Ciutina, L. Fulop, Z. Nagy, Strength, stiffness and ductility of cold-formed steel bolted connections, in: International Workshop on Connections in Steel Structures V, Behaviour, Strength & Design, 2004.
[28] V. Ungureanu, I. Both, M. Burca, B. Radu, C. Neagu, D. Dubina, Experimental and numerical investigations on built-up cold-formed steel beams using resistance spot welding, Thin–Walled Struct. 161 (2021) http://dx.doi.org/10.1016/j.tws.2021.107456.
[29] O. Senkardesler, G. Goler, S. Soyoz, Dynamic and cyclic response of a full-scale 2-storey cold-formed steel structure with and without infill materials, Bull. Earthq. Eng. 15 (2017) 3207–3226, http://dx.doi.org/10.1007/s10518-016-0042-1.
[30] C. Hui, L. Gardner, D.A. Nethercot, Moment redistribution in cold-formed steel continuous beams, Thin-Walled Struct. 98 (2016) 465–477, http://dx.doi.org/10.1016/J.TWS.2015.10.009.
[31] P. Kyvelou, L. Gardner, D.A. Nethercot, Composite Action Between Cold-Formed Steel Beams and Wood-Based Floorboards, vol. 15, 2015, http://dx.doi.org/10.1142/S0219455415400295.
[32] J. Wang, W. Wang, Y. Xiao, B. Yu, Cyclic test and numerical analytical assessment of cold-formed thin-walled steel shear walls using tube truss, Thin-Walled Struct. 134 (2019) 442–459, http://dx.doi.org/10.1016/J.TWS.2018.09.038.
[33] X. Wang, T.C. Hutchinson, G. Hegemier, Seismic behavior of cold-formed steel shear walls during full-scale building shake table tests, in: Wei-Wen Yu International Specialty Conference on Cold-Formed Steel Structures 2018 - Recent Research and Developments in Cold-Formed Steel Design and Construction, 2018.
[34] C. Wang, Z. Yang, Z. Zhang, R. Qi, Experimental study on shear behavior of cold-formed steel shear walls with bracket, Structures 32 (2021) 448–460, http://dx.doi.org/10.1016/j.istruc.2021.03.064.
[35] Y. Zou, X. Zhou, Y. Shi, Z. Wang, K. Ke, Z. Zhang, Y. Guan, Shear resistance of cold-formed thin-walled steel inter-story connections, J. Construct. Steel Res. 183 (2021) http://dx.doi.org/10.1016/j.jcsr.2021.106757.

[36] A. Singh, X. Wang, S. Torabian, T.C. Hutchinson, K.D. Peterman, B.W. Schafer, Seismic performance of symmetric unfinished CFS in-line wall systems, in: Structures Congress 2020 - Selected Papers from the Structures Congress 2020, 2020, http://dx.doi.org/10.1061/9780784482896.058.

[37] H.J. Kim, D.H. Shin, Shake table test program of cold-formed steel in-plane partition walls, Structures 30 (2021) http://dx.doi.org/10.1016/j.istruc.2021.01.026.

[38] Y. Guan, X. Zhou, X. Yao, Y. Shi, Seismic performance of prefabricated sheathed cold-formed thin-walled steel buildings: Shake table test and numerical analyses, J. Construct. Steel Res. 167 (2020) http://dx.doi.org/10.1016/j.jcsr.2019.105837.

[39] J. Jing, G.C. Clifton, K. Roy, J.B.P. Lim, Three-storey modular steel building with a novel slider device: Shake table tests on a scaled down model and numerical investigation, Thin-Walled Struct. 155 (2020) 106932, http://dx.doi.org/10.1016/J.TWS.2020.106932.

[40] L. Jiang, K. Yu, J. Ye, Y. Hu, L. Jiang, Seismic damage assessment and shaking-table test validation of midrise cold-formed steel composite shear wall buildings, J. Struct. Eng. 148 (2022) 04022093, http://dx.doi.org/10.1061/(ASCE)ST.1943-541X.0003387.

[41] Y. Hu, L. Jiang, J. Ye, X. Zhang, L. Jiang, Seismic responses and damage assessment of a mid-rise cold-formed steel building under far-fault and near-fault ground motions, Thin-Walled Struct. 163 (2021) 107690, http://dx.doi.org/10.1016/J.TWS.2021.107690.

[42] L. Jiang, J. Ye, Redundancy of a mid-rise CFS composite shear wall building based on seismic response sensitivity analysis, Eng. Struct. 200 (2019) 109647, http://dx.doi.org/10.1016/J.ENGSTRUCT.2019.109647.

[43] L. Jiang, J. Ye, Quantifying the effects of various uncertainties on seismic risk assessment of CFS structures, 18, 2020, pp. 241–272, http://dx.doi.org/10.1007/s10518-019-00726-w.

[44] I.-O. Toma, M. Budescu, G. Albu, Seismic behaviour of an experimental model made of thin-walled cold formed steel profiles - Hardell structures, in: The Bulletin of the Polytechnic Institute of Jassy, Construction. Architecture Section, vol. 67, 2009.

[45] A. Firouzianhaij, N. Usefi, B. Samali, P. Mehrabi, Shake table testing of standard cold-formed steel storage rack, Appl. Sci. 2021 (2021) 1821, http://dx.doi.org/10.3390/app11041821.

[46] G. Taranu, I.O. Toma, Experimental investigation and numerical simulation of c-shape thin-walled steel profile joints, Buildings 11 (2021) http://dx.doi.org/10.3390/buildings11120636.

[47] TR Group, Self Drilling Screw, DIN 7504N ~ISO 15481. (n.d.). https://www.trfastenings.com/Products/Catalogue/Screws-and-Bolts/Self-Drilling-Screws/Pan-Head/Cross-Recess-H-Drive (accessed May 4, 2022).

[48] TR Group, Screws Mechanical Properties ISO 898-1 EN 20898-1, (n.d.). https://www.trfastenings.com/products/knowledgebase/steel-fasteners/screws-and-bolts-mechanical-properties (accessed May 4, 2022).

[49] TR Group, Self Tapping Screw, DIN 7981C ~ISO 7049. (n.d.). https://www.trfastenings.com/Products/Catalogue/Screws-and-Bolts/Self-Tapping-Screws/Pan-Head/Cross-Recess-H-Drive/Form-C (accessed May 4, 2022).

[50] P.D. Moncarz, Helmut Krawinkler, Theory and Application of Experimental Model Analysis in Earthquake Engineering, Stanford, California, 1981.

[51] P. Candeias, A. Campos Costa, E. Coelho, Shaking TableTests of 1:3 Reduced Scale Models of Four Story Unreinforced Masonry Buildings, in: 3 Th World Conference on Earthquake Engineering S, 2004.

[52] Mapping Europe's earthquake risk | Research and Innovation, (n.d.), https://ec.europa.eu/research-and-innovation/en/horizon-magazine/mapping-europes-earthquake-risk (accessed April 1, 2022).

[53] ISO 12106:2017(E) - Metallic materials-fatigue testing - Axial-strain-controlled method, 2017.

[54] ASTM E606/E606M-12 - Standard Test Method for Strain-Controlled Fatigue Testing, 2012, http://dx.doi.org/10.1520/E0606-04E01.

[55] M. Kotełko, J. Grudziecki, V. Ungureanu, D. Dubina, Ultimate and post-ultimate behaviour of thin-walled cold-formed steel open-section members under eccentric compression. Part I: Collapse mechanisms database (theoretical study), Thin-Walled Struct. 169 (2021) 108366, http://dx.doi.org/10.1016/J.TWS.2021.108366.

[56] Ł. Borkowski, J. Grudziecki, M. Kotełko, V. Ungureanu, D. Dubina, Ultimate and post-ultimate behaviour of thin-walled cold-formed steel open-section members under eccentric compression. Part II: Experimental study, Thin-Walled Struct. 171 (2022) 108802, http://dx.doi.org/10.1016/J.TWS.2021.108802.

[57] N. Usefi, P. Sharafi, H. Ronagh, Numerical models for lateral behaviour analysis of cold-formed steel framed walls: State of the art, evaluation and challenges, Thin-Walled Struct. 138 (2019) 252–285, http://dx.doi.org/10.1016/J.TWS.2019.02.019.

[58] I. Shamim, C.A. Rogers, Numerical modelling and calibration of CFS framed shear walls under dynamic loading, in: 21st International Specialty Conference on Cold-Formed Steel Structures - Recent Research and Developments in Cold-Formed Steel Design and Construction, 2012.

[59] A.A. Kasimzade, S. Tuhta, G. Atmaca, S. Ozdemir, Analytical and experimental modal analysis of a model cold formed steel (CFS) structures using microtremor excitation, in: Seismic Isolation, Structural Health Monitoring, and Performance Based Seismic Design in Earthquake Engineering: Recent Developments, 2018, http://dx.doi.org/10.1007/978-3-319-93157-9_9.

[60] A. Campiche, L. Fiorino, R. Landolfo, Numerical modelling of CFS two-storey sheathing-braced building under shaking-table excitations, J. Construct. Steel Res. 170 (2020) http://dx.doi.org/10.1016/j.jcsr.2020.106110.

[61] EN 1993-1-8, Eurocode 3: Design of steel structures - Part 1-8: Design of joints, CEN, Brussels, Belgium, 2005.

[62] EN 1993-1-1, Eurocode 3: Design of Steel Structures - Part 1-1: General Rules and Rules for Buildings, CEN, Brussels, Belgium, 2005.

[63] Robot Structural Analysis Professional, (n.d.). https://www.autodesk.com/products/robot-structural-analysis/overview (accessed January 13, 2022).

buildings

MDPI

Article

Experimental Investigation and Numerical Simulation of C-Shape Thin-Walled Steel Profile Joints

George Taranu * and Ionut-Ovidiu Toma

Department of Structural Mechanics, Faculty of Civil Engineering and Building Services, The "Gheorghe Asachi" Technical University of Iasi, 700050 Iași, Romania; ionut.ovidiu.toma@tuiasi.ro
* Correspondence: george.taranu@academic.tuiasi.ro; Tel.: +40-722-722-786

Abstract: The versatility of steel, its high resistance in relation to its low mass, as well as the easily accessible technology in the context of using recyclable materials and the low negative impact on the environment represent important arguments in using thin-walled steel profiles to make structures for buildings with a low height regime. This paper presents the results of an experimental program that investigated the behavior of three types of joints in a T-shape form made of thin-walled steel profiles to make shear wall panels or truss beam floors. Due to the small dimensions of the C-profiles of 89 × 41 × 12 × 1 mm, and of the technology of their joining, manufacturers prefer the hinged connections of elements with self-drilling screws. The purpose of the research presented in this paper is to assess the maximum capacity of the joints, the elastic and post-elastic behavior until failure, and also the mechanisms failure. The types of joints analyzed are commonly used in the production of structural systems for houses. The experimental program, which consisted of testing 5 specimens for each type of joint in tension (shear on screws), showed different behavior in terms of load-displacement. The experimental, tested models were analyzed by finite element simulations in an ANSYS nonlinear static structure with 3D solid models. The materials were defined by a bilinear true stress–strain curve obtained after some experimental tensile tests of the steel. The results of the experimental tests showed that the main failure mechanism is a yielding of the holes where the screws were mounted and a shearing of the profile walls. Adding an additional screw on each side increases the capacity of the joints, but not until a yield loss is obtained. In conclusion, it is shown that the solution is suitable for a low level of loading in a static manner; however, additional studies are necessary in order to develop and verify other solutions, thus improving the strength of the connection.

Keywords: thin-walled steel profiles; screwed connection; joint tension experiment; failure mechanism; 3D solid FEM; nonlinear analysis

check for updates

Citation: Taranu, G.; Toma, I.-O. Experimental Investigation and Numerical Simulation of C-Shape Thin-Walled Steel Profile Joints. *Buildings* **2021**, *11*, 636. https://doi.org/10.3390/buildings11120636

Academic Editors: Luís Filipe Almeida Bernardo and Miguel Nepomuceno

Received: 25 October 2021
Accepted: 6 December 2021
Published: 10 December 2021

Publisher's Note: MDPI stays neutral with regard to jurisdictional claims in published maps and institutional affiliations.

Copyright: © 2021 by the authors. Licensee MDPI, Basel, Switzerland. This article is an open access article distributed under the terms and conditions of the Creative Commons Attribution (CC BY) license (https://creativecommons.org/licenses/by/4.0/).

1. Introduction

Since the introduction of steel as a building material in the field of construction, it has constantly evolved in terms of increasing the performance of the material by obtaining alloys with very high strengths and a ductile behavior. This was done to ensure the sufficient deformation capacity required for structural elements. Construction steel products that can be hot-rolled or cold-formed from thin sheets have also evolved through the development of multiple cross-sectional shapes.

Cold-formed profiles began to be used in 1850, but their use as structural elements was accepted only after 1925. The first design standards for hot-rolled steel appeared after 1930, but they could not be applied to cold-formed profiles. In the United States, the first edition of the design rules for cold-formed lightweight profiles was based on research conducted at Cornell University and published in 1946 [1]. Several countries use the American code, and those in the European Union use Eurocode 3 [2–5]. During the past two decades, the structures made of thin-walled profiles have become more and more popular. The

numerous advantages compared to other construction materials, coupled with an increase in the number of technological solutions for the production of these profiles, have led to the adoption of these structural solutions for residential buildings, including those located in active seismic areas.

Today, technology and industrial machines have facilitated the emergence of various entrepreneurs producing custom profiles. Some proposed structural systems for buildings, as shown in Figure 1, are made of wall panels stiffened by a system of diagonals at the ends. Sometimes profiles with larger sections and a sheet thickness of 3–5 mm are required in cases of bordering the gaps for windows or doors. Different research programs have been carried out regarding the overall behavior of cold-formed steel profile beams or their connections [6–9].



Figure 1. Example of structure for housing made of spatial frames and trusses from thin-walled C-shaped steel profiles, Germany 2018 (authors' collection).

The floor system for roofs can also be made of truss beams spaced, for example, at 60 cm apart. Figure 2 presents an example of such an adopted solution in the case of a roof for a residential complex building located in Cluj-Napoca city, Romania.



Figure 2. Example of a floor system for a roof made of truss beams with thin-walled steel profiles Cluj-Napoca, Romania 2019 (authors' collection).

Apart from the realization and obtainment of cold-formed profiles from thin steel sheets up to 1 mm used for the purpose of creating structural elements for buildings, there still remains the very important issue of joining these profiles. There are numerous studies in the scientific literature presenting a variety of connecting solutions such as welding, riveting, screws, self-tapping screws, bolting, blind rivets, self-drilling screws, fired pins, arc-welding, imprint holes or a combination of these [8,10–21].

For example, on spot welded specimens tested experimentally [6], a good capacity and ductility was observed, but in comparison with self-drilling screws the ductility was smaller.

Given the large number of alternatives to conceive the joints of cold-formed thin-walled elements, there is still a need for further investigations in order to completely understand the behavior under various loading scenarios. This article presents the results of an experimental and numerical study carried out on a system of profiles and joints used by a Romanian manufacturer [22]. The fully equipped manufacturing facility can produce a large number of geometrical configurations for trusses as load bearing subsystems for roofs, floors (Figure 2) or wall panels (Figure 1). Unlike previously proposed solutions [6,23–26], in the case of these new systems, the structural concept is based on the truss beams and panels for walls. The joints are based on self-drilling and self-tapping screws with holes prepared in advance.

The joints between the profiles are made by drilling and stamping the sheets during the formation of the profiles on the rolling line. The parts are labeled with bar codes which, according to the sketches, are mounted later with self-drilling screws of Ø 4.8 × 19 mm or Ø 4.8 × 22 mm. The assembly of the structural elements are positioned according to the structural drawings and are connected to each other with the same types of self-drilling screws. Over these elements are added 18 mm thick OSB boards with fasteners at a distance of 20 cm on the outer faces, with plasterboards mounted on the inside. The thermal insulation layer of basalt wool is then added between these boards.

According to the current design practice, the numerical model used during the design stage of such structural systems considers the connection between the component elements as joints. Moreover, the contribution to the strength and rigidity of the OSB or gypsum board is neglected. In the case of seismic actions, the structures are subjected to cyclic axial forces, which makes the compressed elements vulnerable to the loss of stability and the tensioned ones prone to being torn from the joints. Additionally, the overloaded floor elements above the design limit may exhibit a fragile behavior, which was observed in a previous study by experimental testing of some floor elements [27]. Some details from the tested system are presented in Figures 3 and 4. At a maximum load capacity, the failure mechanism was brittle, but the maximum displacement before collapse for a 5 m opening around 60 kN/sqm was 4 cm, two times bigger than the maximum admissible one.



Figure 3. Detail of a floor truss system with the 5 m opening gravitationally tested.



Figure 4. The floor truss system after the experimental test with the detail of the failure mechanism.

In this context, an experimental investigation and numerical validation was necessary to understand the behavior of joints and correctly assess the load transfer mechanisms. Experimental and numerical investigations of the overall strength and rigidity of a new type of joint consisting of a drawn-socket can offer insightful information on the behavior of the joint, as well as the structural element the joint was extracted from. Moreover, the load-displacement graphs may provide information that can be used in the design process of such types of joints as the ones presented in the paper.

Additionally, the numerical simulations of joints consisting of 1d-elements may not be so accurate, overestimating the real strength and stiffness capacity of the joint, if it was not for the use of joints with a limited predefined axial rigidity expressed by polynomial functions derived from load–displacement curves. Further research should be conducted in this direction for the numerical models to be improved in order to be able to capture the complex phenomena taking place in such a joint. This could represent the first step in introducing new design procedures to accommodate the large number of joint types with different geometries used in the market.

2. Materials and Methods

The main objective was to check the maximum load capacity of 3 distinct sets of joints with self-drilling and self-tapping screws. A total of 5 specimens were prepared for each considered set, amounting to 15 specimens in all. The 3 types of joints and the test layout are presented in Figure 5. In this context, it is important to experimentally investigate and assess the mechanical properties of the steel from which the profiles were made. This information is of significant importance from the point of view of the subsequent numerical simulations that needed validation and calibration from a material behavior point of view. The geometry of the joints is the simplest one in a T form. Figure 5 presents the schematic geometry and loading process, as well as the 3 types of joints (A, B, C).

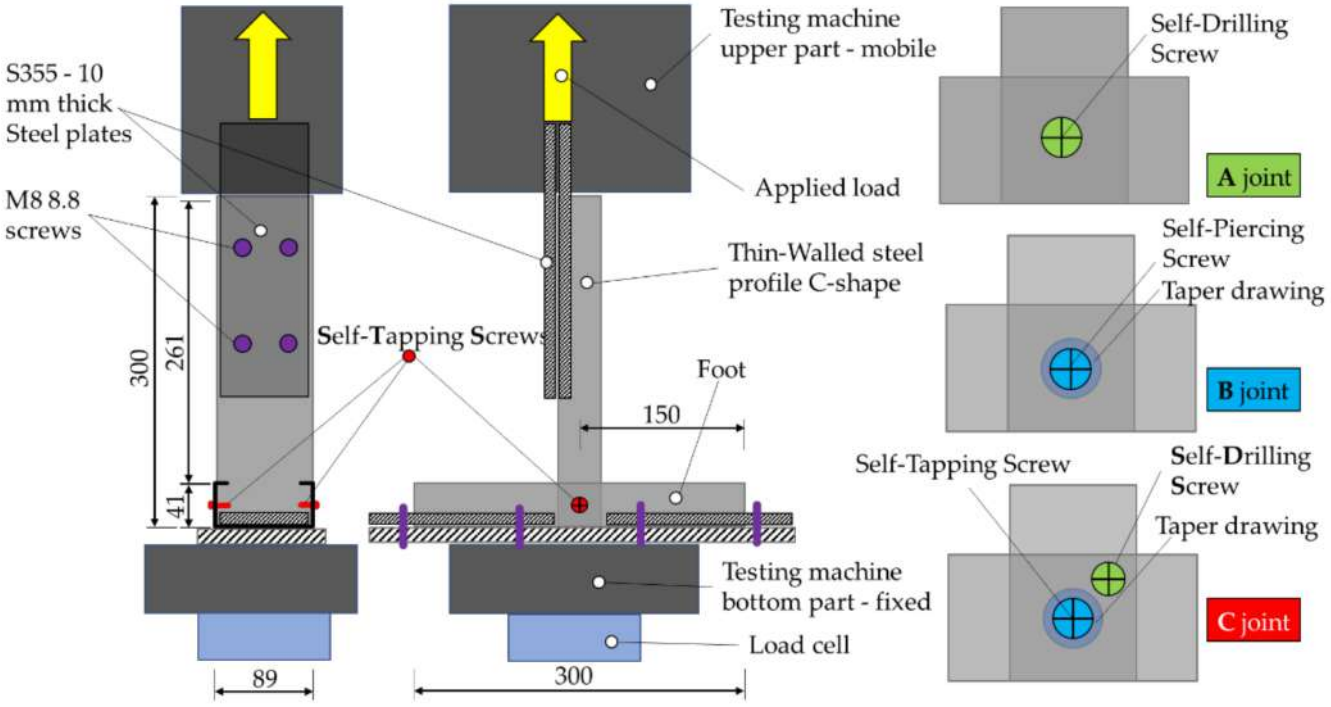

Figure 5. Geometry of the joints and the loading schema.

The details of the components that make up the joints are shown in Figure 6. The C-profiles made of DX51D+Z steel sheet with a thickness of 1 mm were placed at a 90 degrees angle in the shape of the letter T. The C-shape section dimensions are presented in Figure 6. The horizontal profile at the bottom of the joint was fixed in the testing machine by means of thick metal plates attached to the thin-walled cold-formed element by M8 screws. The vertical profile was also fastened with thick metal plates and screws to the top of the testing machine. As already mentioned, 3 types of joint layouts were considered. In the A-type joint, yellow galvanized 4.8 × 19 mm self-drilling screws were used (Figure 7), whereas in the type B joint, gray galvanized 4.8 × 22 mm self-tapping screws were positioned in a tapper drawing on each side (Figure 8).

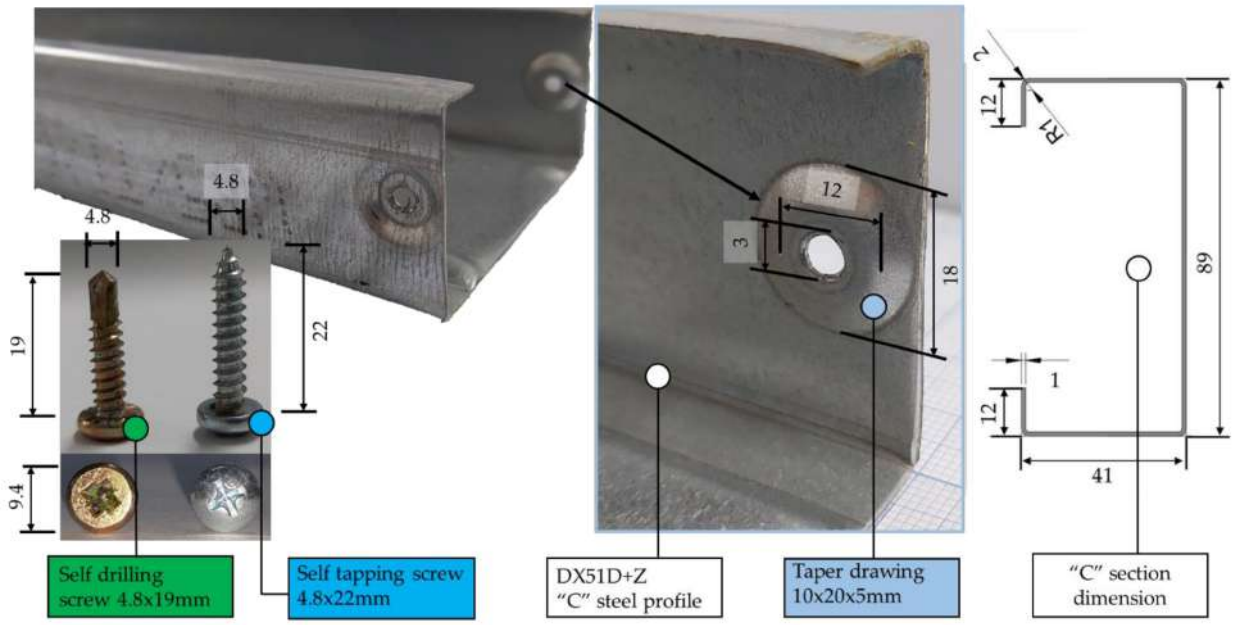

Figure 6. Types of screws and tapper drawing used for the joints.



Figure 7. Specimens for A joint.



Figure 8. Specimens for B joint.

The investigated joints belong to scaled-down models of shear walls and trusses used in flooring systems. The use of DX51D+Z steel for structural applications is not, in general, a good choice compared to their better counterparts S280G+Z and S350GD+Z steel. Taking into account its lower yield strength (120 MPa) and lower ultimate strength (250 MPa) compared to the other types of steel, but its higher ductility, it was intended to investigate whether this type of steel was suitable for structural applications, in the sense of representing the lower limit of the strength interval.

Sometimes, the ability to undergo large deformations before collapse, in case of certain loading scenarios, may prove a viable solution in comparison to a more brittle failure mode. Therefore, an investigation of deformation and load bearing capacities offers useful data related to the possible application of these types of steel in structural elements subjected to static loads. Additionally, the use of this type of steel in structures built in highly seismic areas should be avoided.

The type C joint (Figure 9) is a combination between A and B, with the self-drilling screw being additionally added to the type B joint.



Figure 9. Specimens for C joint.

In order to determine the tensile strength and modulus of elasticity of the material the elements were made of, 5 specimens with the dimensions and shape shown in Figure 10 were cut from the web of the profiles and tested in direct tension. These were tested according to ISO 6892-1: 2019 [28]. The secant modulus of elasticity was automatically assessed by means of the TestXpert II v3.5 software as part of the control unit for the Zwick/Roell SP 1000 universal test machine. The test speed was based on a stress rate of 30 MP/s for the dog-bone specimens (Figure 10). After the tests, 2 specimens were invalidated because of abnormal values. The specimens made of DX51D+Z are shown before and after the tests in Figures 10 and 11. An external extensometer connected to the machine software interface was used for measuring the axial strains.

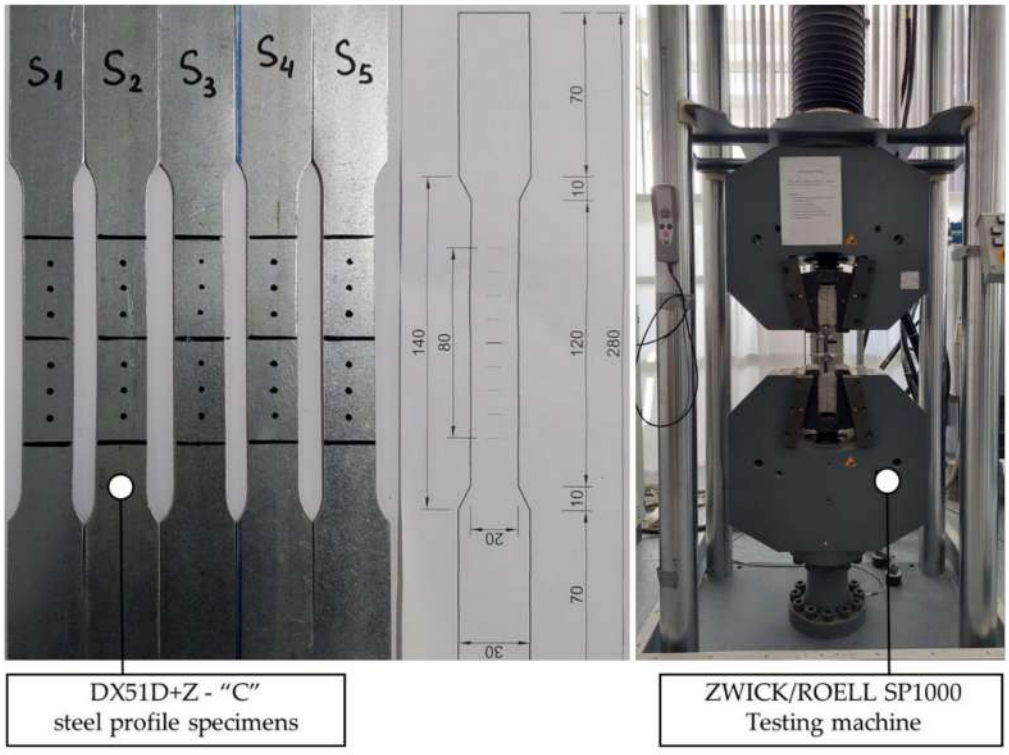

Figure 10. Tensile test specimen prepared and Zwick/Roell SP1000 machine testing.

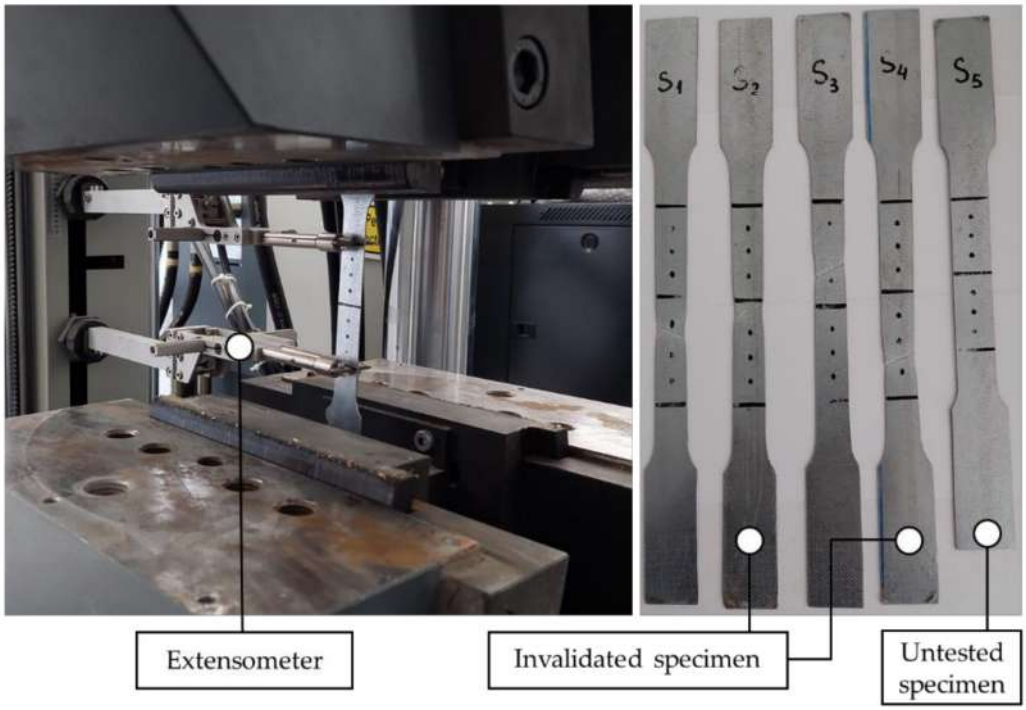

Figure 11. Specimens mounted with extensometer during the tests and specimens tested.

The material properties of the steel, experimentally determined, and for the screws, as supplied by the manufacturer, are summarized in Table 1.

Table 1. Materials properties.

Component	Type	Elastic Modulus (GPa)	Tensile Strength (MPa)	Shear Strength (MPa)
Profile steel sheet 	DX51D+Z	210	250	-
Self-drilling screw—SDR 	4.8 × 19 mm [29]	210	1531	1313
Self-tapping screw—STR 	4.8 × 22 mm [30]	210	1000	500

The T joints were subjected to a tensile force applied along the centerline of the vertical element, as shown in Figure 12 and video recorded available on-line with links presented in Section: Supplementary Materials at the end of the paper. In order to prevent local crushing or tearing of the steel profile, a 10 mm steel sheet was attached to the vertical element, as schematically represented in Figure 5, and then fixed in the upper grip of the testing equipment (Figure 12). The horizontal element was attached via M8 screws to a rigid T-shaped steel component that was fixed in the lower grips of the universal testing machine. The loading of the specimens was performed at a constant speed of 50 N/s.

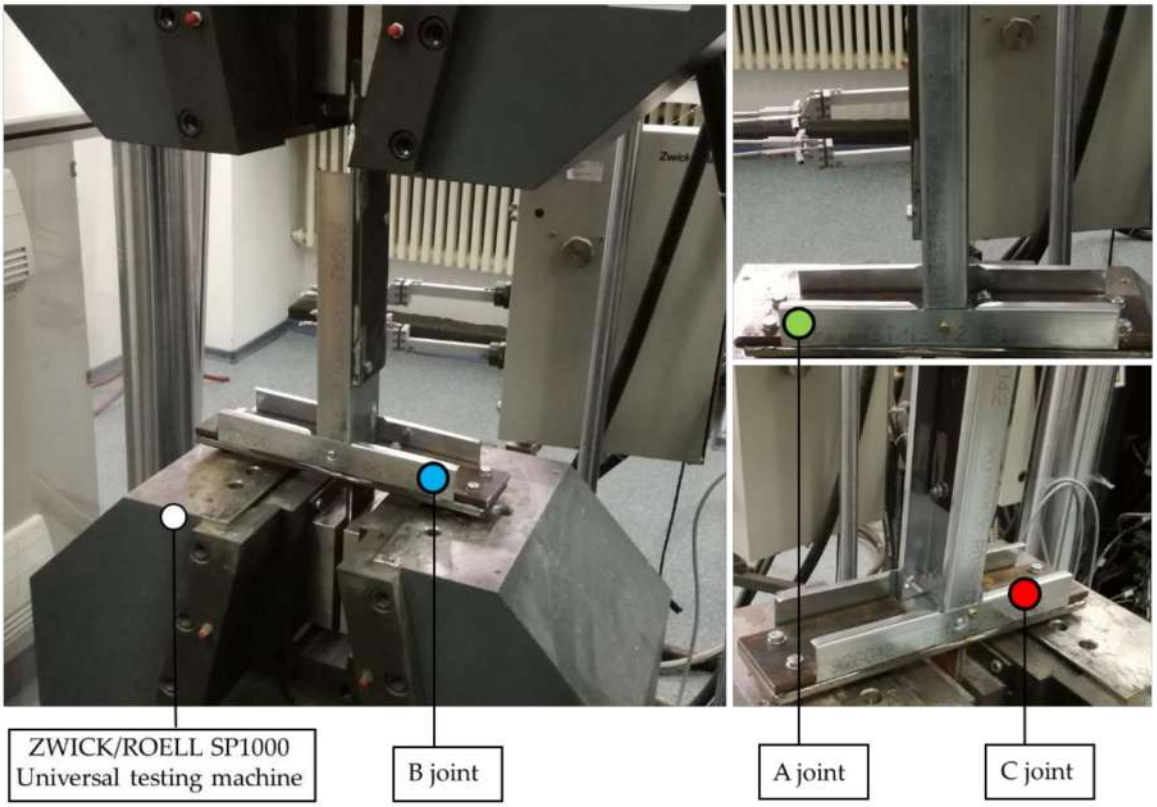

Figure 12. Universal Testing Machine Zwick/Roell SP 1000 and the tested joints A, B, C.

3. Experimental Results

The test results are presented in a graphical manner as a stress–strain curve. For each set of the results, the average curve was calculated and a comparison between the three considered joint configurations was made. The results presented below are discussed in the next chapter.

3.1. Sheet DX51D+Z Results

The stress–strain curves obtained from the three validated specimens are shown in Figure 13a. The averaged stress–strain curve, termed as the "experimental engineering" curve in Figure 13b, was transformed into a true stress–strain curve, used in the numerical analyses as a bilinear curve, for the nonlinear definition of the material behavior [31–33]. The yielding stress was 120 MPa with a corresponding axial strain of 0.36%. The maximum tensile stress was 250 MPa, and the maximum strain at the end of the test was 21.39%.

The engineered stress–strain curve was converted into a true stress–strain curve using the relations:

$$\varepsilon_{true} = ln(1 + \varepsilon_{nom}); \quad (1)$$

$$\sigma_{true} = \sigma_{nom}(1 + \sigma_{nom}); \quad (2)$$

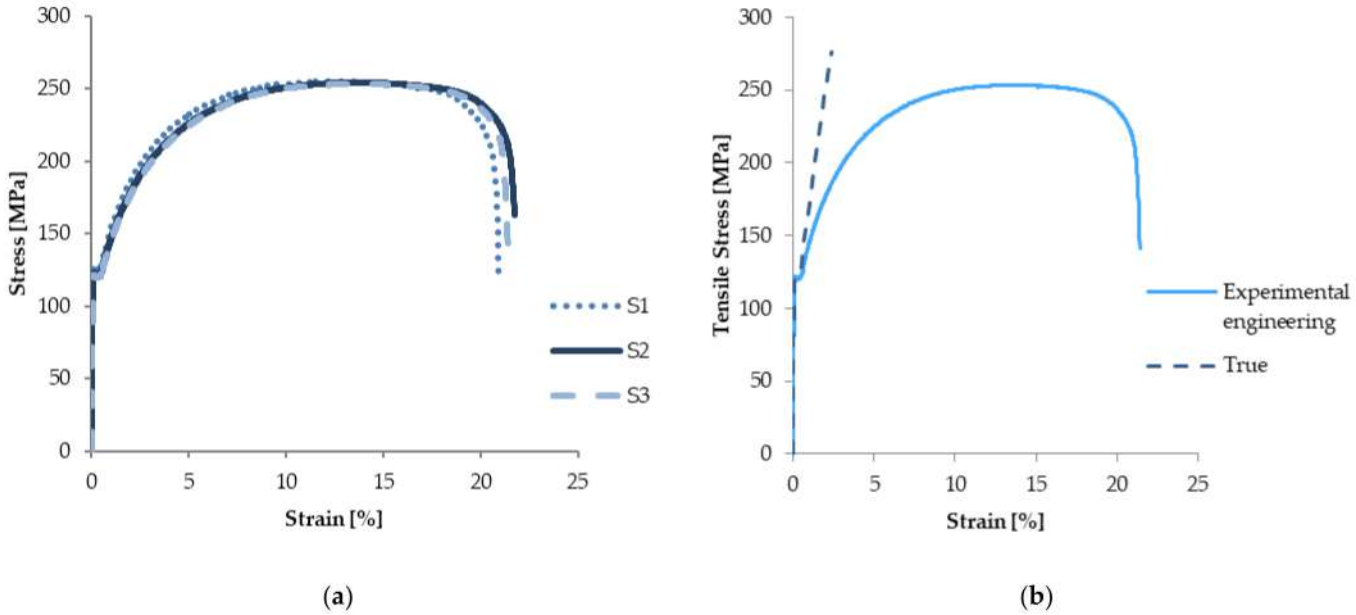

Figure 13. Engineering Stress-Strain curve of the DX51D+Z steel sheet; (**a**) experimental; (**b**) averaged experimental vs. True.

3.2. Joint Results

The load–displacement curves for joint A and B are presented in Figure 14a,b, respectively. For joint A, the maximum load as an averaged value was 8.7 kN, with a corresponding 7 mm displacement. From the graph it can be observed that the elastic behavior of the joint is between 0 and 2 kN. In the case of joint B, the maximum averaged load was 9.8 kN, for which a 5 mm displacement was recorded. The failure is initiated due to stress concentrations occurring at the edges of the steel sheet in the area of the holes where the contact between the steel profile and the self-drilling screw is present. These stress concentrations favor the occurrence of stress values larger than the yield strength of the steel in the C-profile.

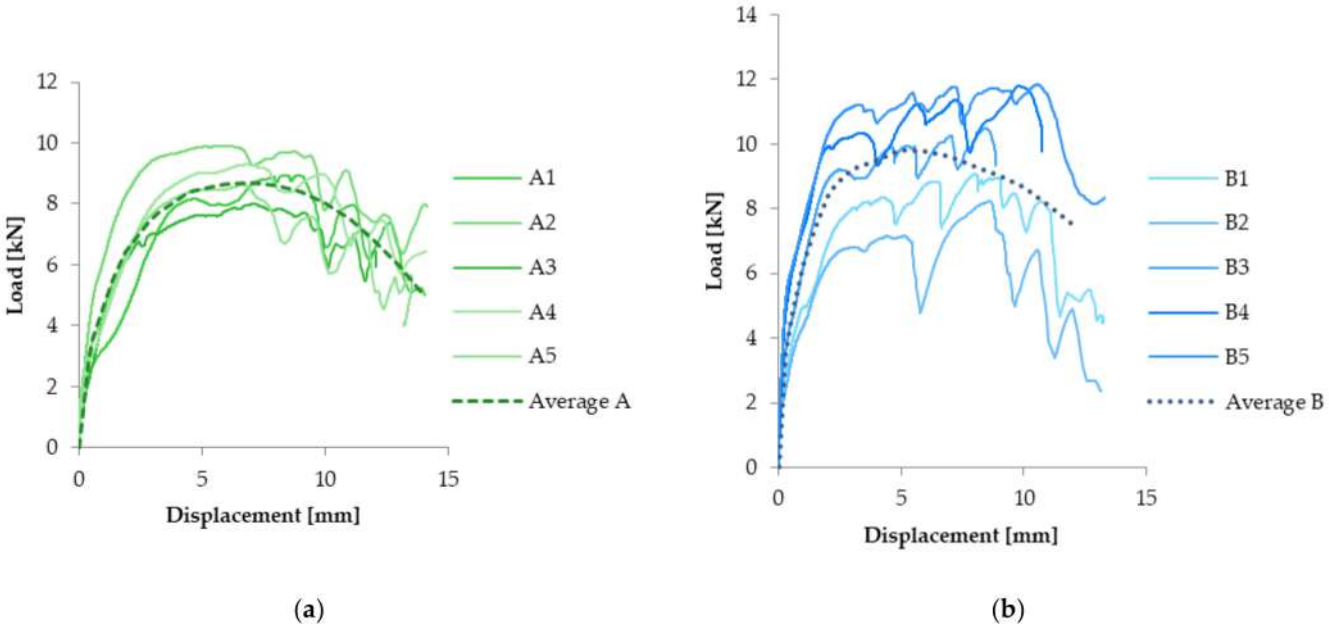

Figure 14. Load-displacement curves: (**a**) joint A; (**b**) joint B.

The T-joints were fixed in the grips of the universal testing machine by means of additional thick steel plates connected to the T-joint by means of screws. This introduced additional deformations and increased the chance of supplementary slips in the connecting areas. Moreover, the estimation of the load-displacement behavior is accurate only in the linear-elastic range of material behavior. A soon as the yield limit of the steel in the thin-walled cold-formed elements was reached, additional deformations were recorded. The jumps in the load-displacement graph were produced by the passing of the steel profile in the connecting area (the hole area) over each twist on the shank of the self-drilling bolts. This behavior was caused by the fact that the screws tilted upwards due to the applied load.

Figure 15a presents the load–displacement curves for the C joint. One of the tested samples, C5, failed at a load approximately 40% lower than the average value of the other 4. Therefore, the load–displacement curve was removed from the calculation procedure. In the case of this joint, two specimens were invalidated due to some abnormal failure. The maximum load for this joint was 15.1 kN at a 9 mm vertical displacement. A comparison between the experimental load–displacement curves of the joints is shown in Figure 15b.

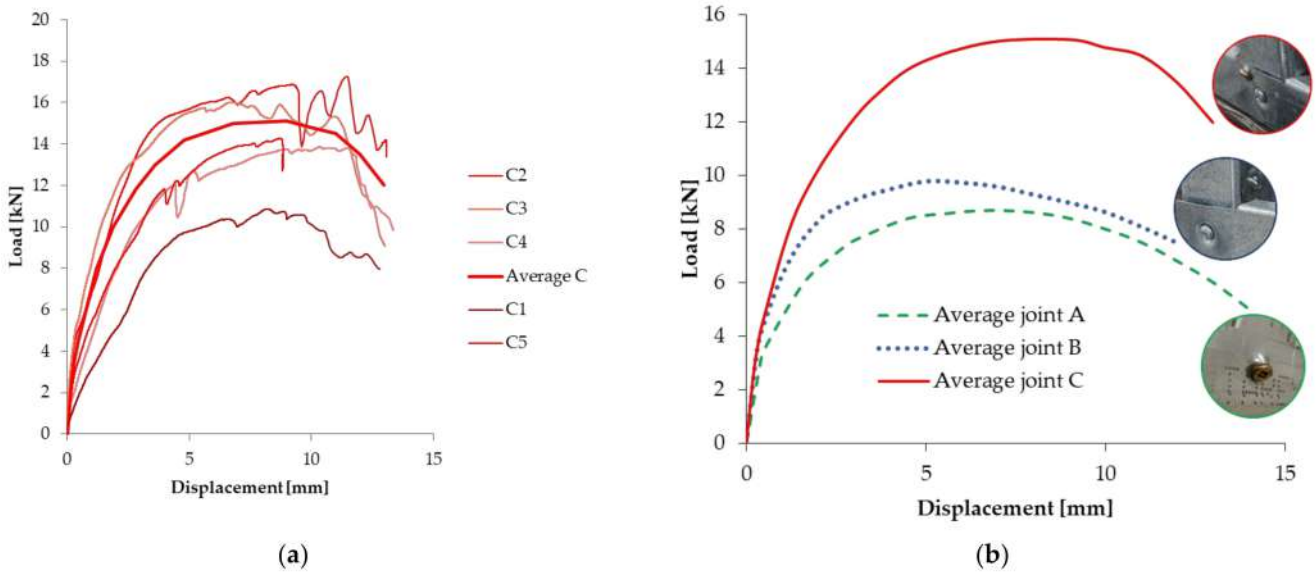

Figure 15. Load–displacement curves: (**a**) joint C; (**b**) Comparison of Average A, B, C.

The aspects of the tested specimens are presented in Figures 16–18. It can be observed that 3 of 5 specimens were pulled-out in case of joint A. The failure was preceded by tilting of the screw, followed by lateral deformations of the flanges in the horizontal element. This resulted in a loss of grip between the elements of the joint and the vertical element was pulled-out.

In the case of joint B and C, there are large, visible deformations and a failure mechanism which is similar to joint A. One of the specimens, C3, failed with shearing the entire section of the edge of the profile.



Figure 16. Joint A tested specimens.



Figure 17. Joint B tested specimens.



Figure 18. Joint C tested specimens.

4. Finite Element Modelling

4.1. Nonlinear Analysis of the DX51D+Z Sheet Tensile Specimen

In order to calibrate the nonlinear behavior of the material, some numerical simulations were carried out. The material was defined in ANSYS as a nonlinear with bilinear stress–strain curve, a yield stress of 120 MPa, maximum strength of 250 MPa, elastic modulus of 210 GPa and tangent modulus of 6750 MPa. Figure 19a,b present the environment of the structural analysis. The bottom of the specimen was fixed, and the upper part had a 2 mm displacement defined in an X direction, the longitudinal axis of the specimen. The discretization of the solid model is presented in Figure 19b with an element quality map distribution. The total number of nodes was 11,548, and the total number of elements was 5525. The elements are defined with nonlinear behavior. Below are presented some characteristics of the analysis:

- Problem dimensionality: 3-d;
- Degrees of freedom: ux, uy, uz;
- Analysis type: static (steady-state);
- Offset temperature from absolute zero: 273.15;
- Nonlinear geometric effects: on;
- Equation solver option: sparse;
- Plastic material properties included: yes;
- Newton-Raphson option: program chosen;
- Globally assembled matrix: symmetric.

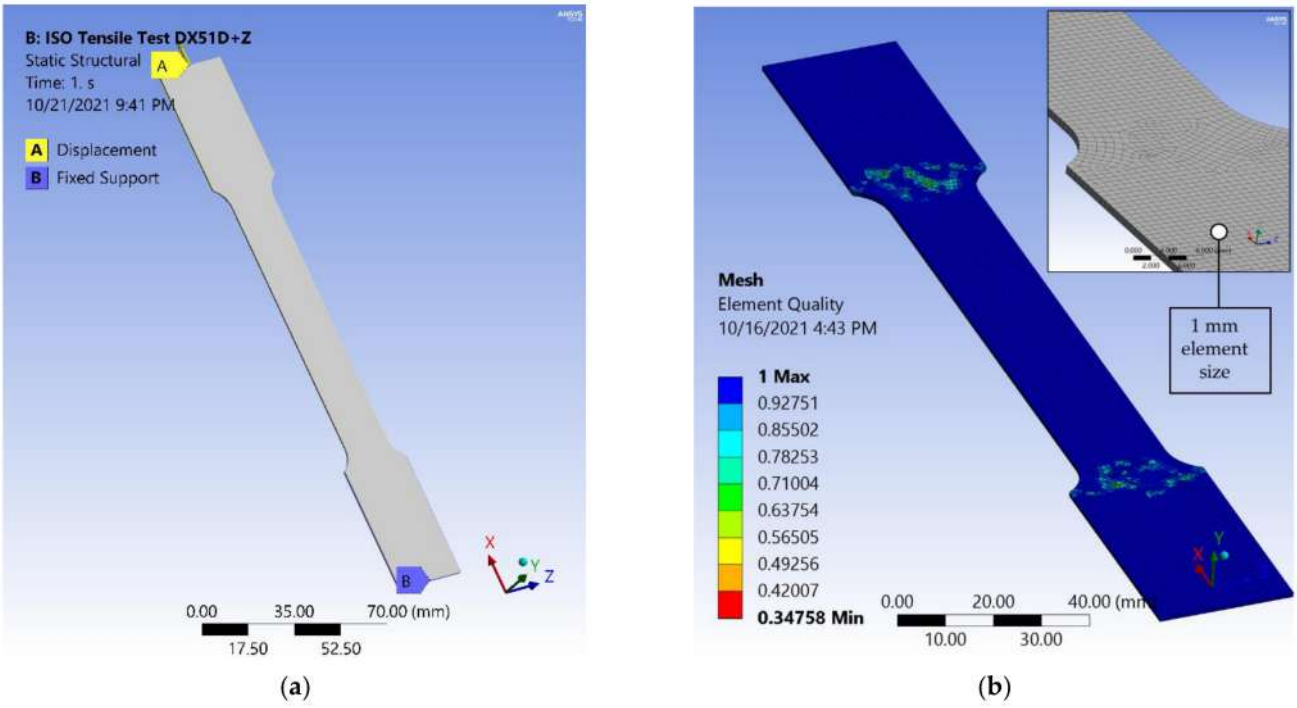

Figure 19. Finite Element Model for tensile stress–strain test calibration: (**a**) loading schema; (**b**) mesh element quality discretization and detail.

4.2. Results on Tensile Simulation Test

Figure 20a presents a map distribution of equivalent (von Mises) stress, which shows the yielding value of the material at 0.1 mm displacement of the upper end. Figure 20b shows the map of equivalent plastic strain at same value of displacement. It can be observed that the maximum values of the equivalent plastic strain occur in the reduction area of the section and also the apparition in the central area of the plastic strain.

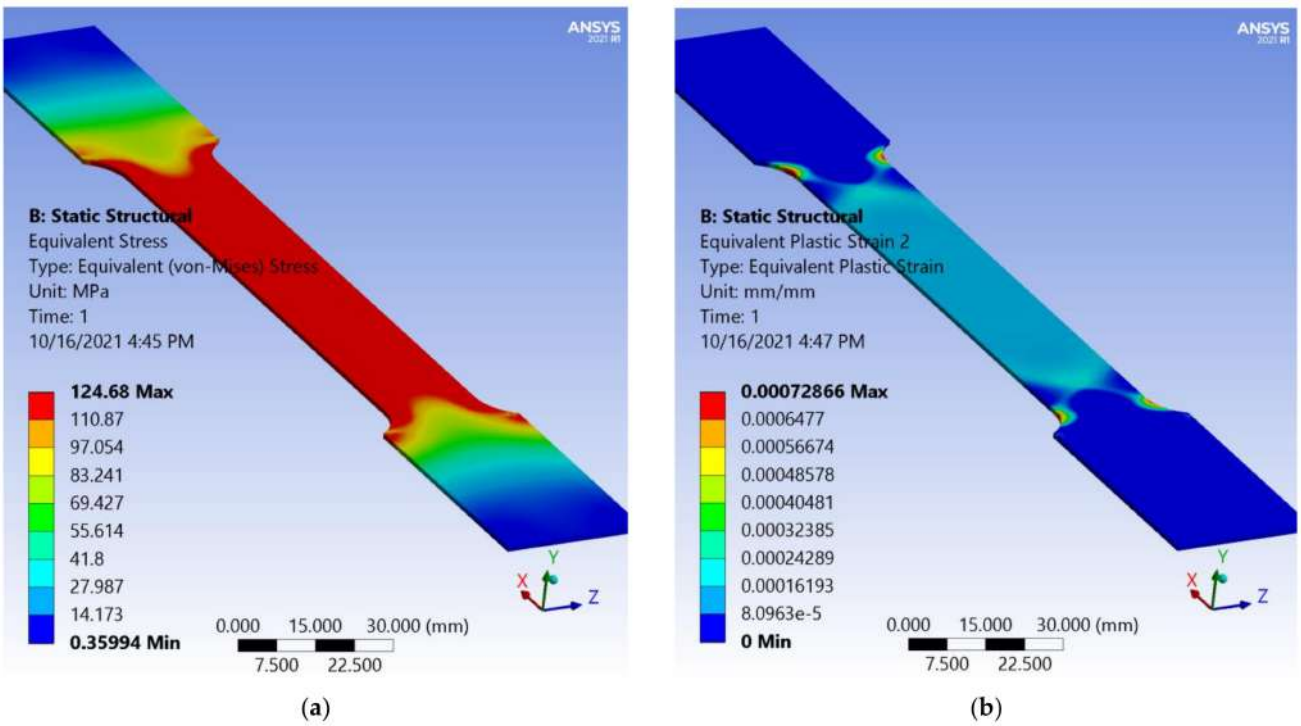

Figure 20. Results at 0.1 mm displacement: (**a**) equivalent von Mises stress; (**b**) equivalent plastic strain.

The results representing the nonlinear behavior of the model are confirmed by the graph presented in Figure 21. The stress–strain curves for the material, considered as a true stress–strain bilinear curve, coincide with the stress–strain results curve at the central node, named a node of interest, positioned in the center of the model.

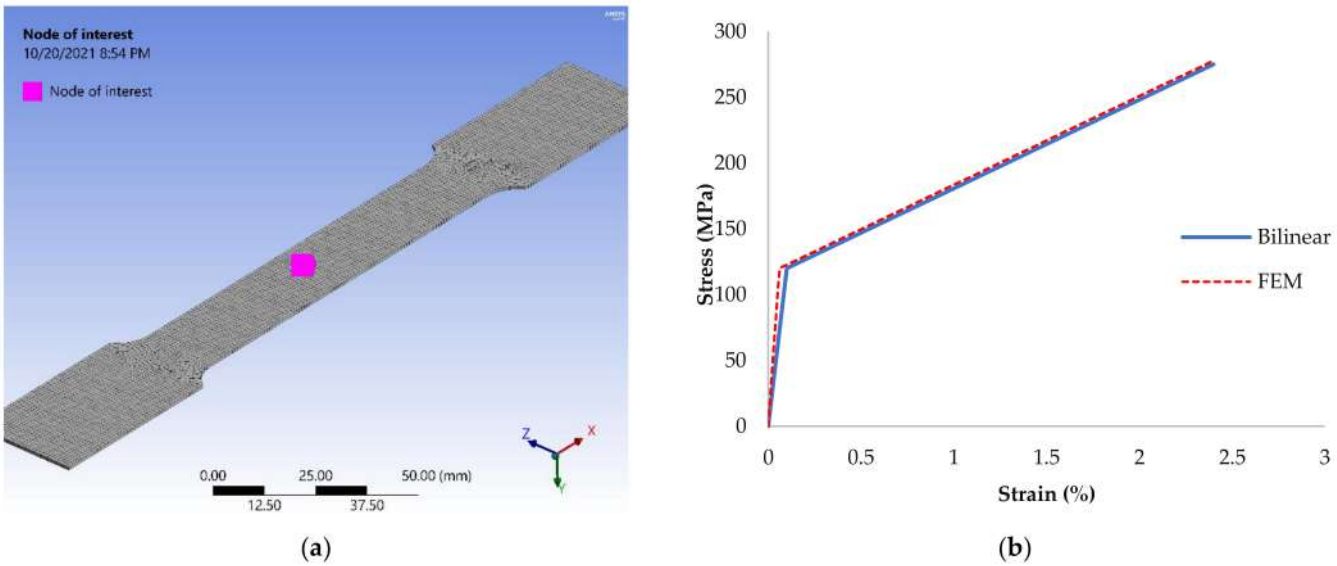

Figure 21. Stress–strain curve: (**a**) node of interest central position; (**b**) stress–strain curves for material definition bilinear and finite element model in node of interest.

4.3. Joint A Modelling and Results

Figure 22 presents joint A's geometry and environment of the model, with a close detail of some hidden parts and a screw description. The screw was shaped considering the two ribs of the thread located between the layers of the profiles. The contacts of the bodies were assumed to be bonded. The mesh discretization and the quality of the finite elements are presented in Figure 23a,b. A SOLID186 brick-type element was used for the thin-walled cold-formed steel profiles, with a maximum grid size of 4 mm. The finite element size decreased to approximately 0.5 mm near the holes and for the screws. Only one layer of the SOLID186 element was considered over the thickness of the steel profile. The screws were modeled by means of tetrahedron SOLID187 element, and three layers were used.

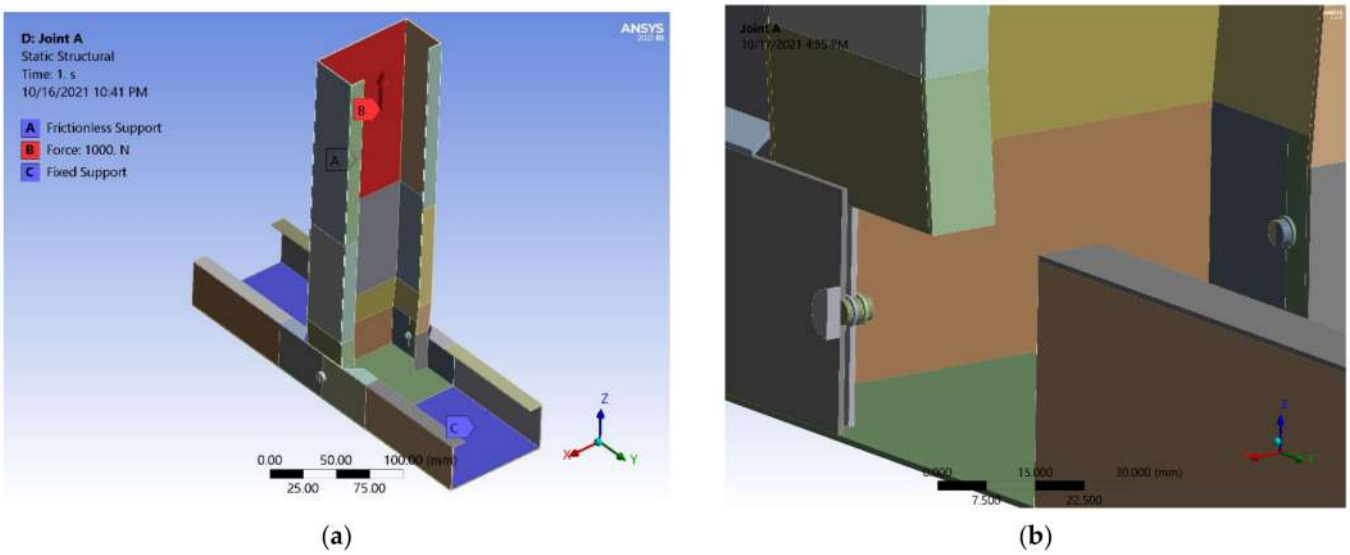

Figure 22. Joint A geometry: (**a**) Static schema; (**b**) detail of screws with hidden body parts.

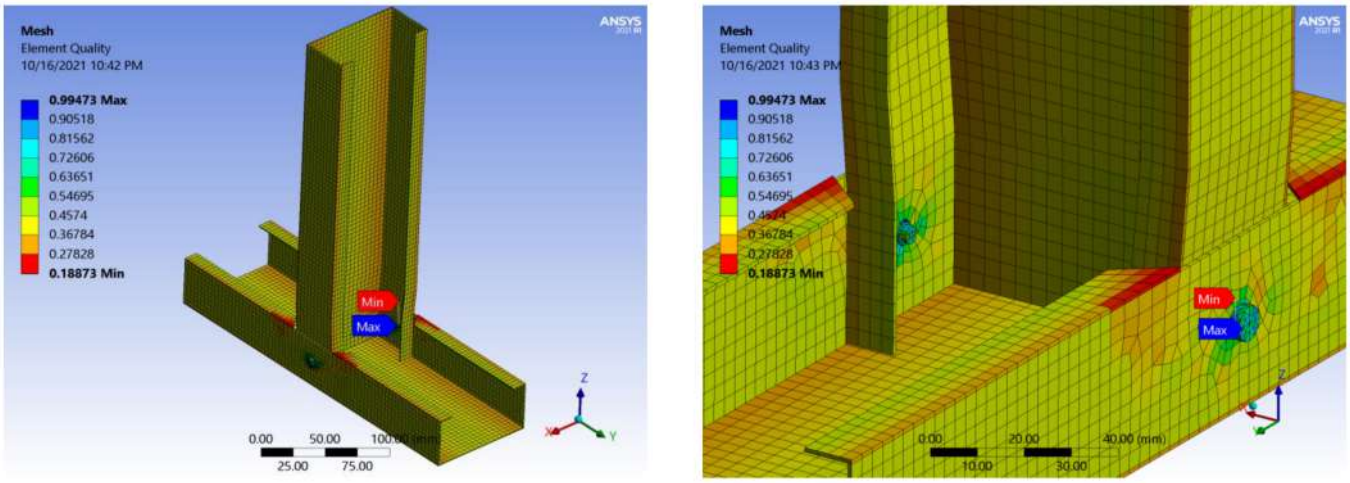

(**a**) (**b**)

Figure 23. Joint A mesh: (**a**) element quality mesh; (**b**) detail of screw connection area.

The shear locking phenomenon was not considered at this stage of the research, with this being identified as the main source for such discrepancies between the experimental and numerical simulation results. Taking into account the raw processing power required for such numerical analyses, coupled with the need for finer mesh discretization as well as the required, at this stage, level of accuracy, the solution presented in the paper was deemed as being the most efficient. It should be pointed out that, for the time being, only a calibration of the model was intended, and a not an optimization process.

The results presented in Figure 24 represent a map distribution of the equivalent von Mises stress with the detail near the holes in profiles at a 2 kN load. The maximum stress value occurred in the screws. Furthermore, at this value of loading it can be seen that the value of the yield stress was exceeded at the points located on the outside part of the vertical element wall, near the circular hole for the screw. In Figure 24b the value of the stress marked is 141 MPa at 2 kN tensile load. Regarding the strain, a map distribution for the equivalent elastic strain at the same value of loading is presented in Figure 25a. The map distribution for plastic strain and those values are presented in detail in Figure 25b. Figure 26a,b present a comparison in terms of deformations in the real experiment and the numerical simulation. It can be seen that the screws are tilting, while the steel sheet of the profiles exhibit local pressure in the area of the screw holes.

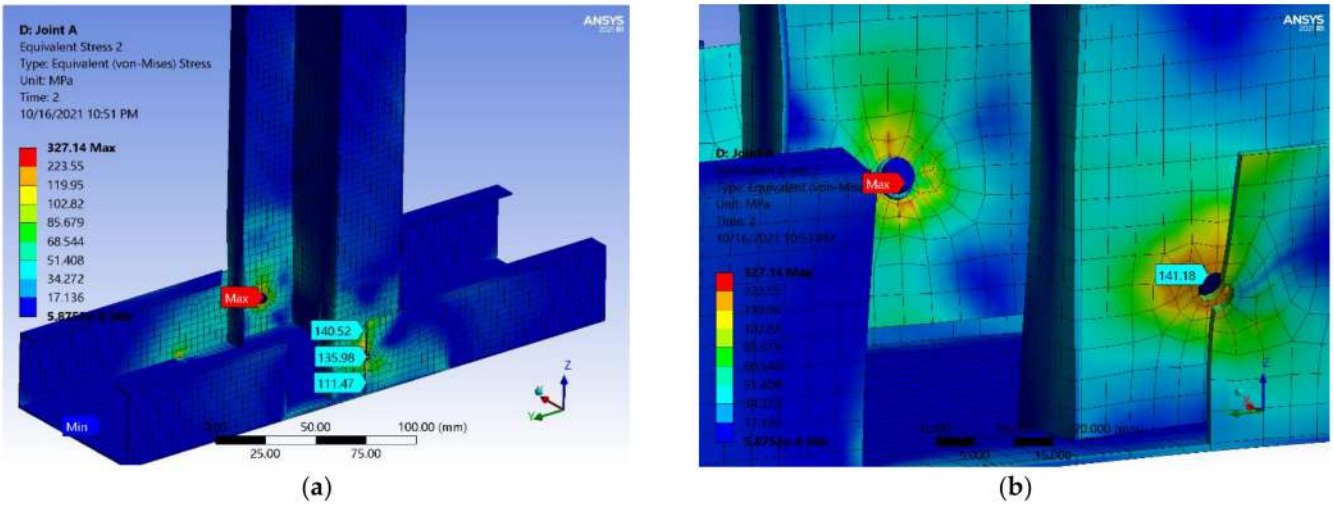

(**a**) (**b**)

Figure 24. Equivalent stress von Mises joint A: (**a**) map distribution; (**b**)detail near hole and screws area.

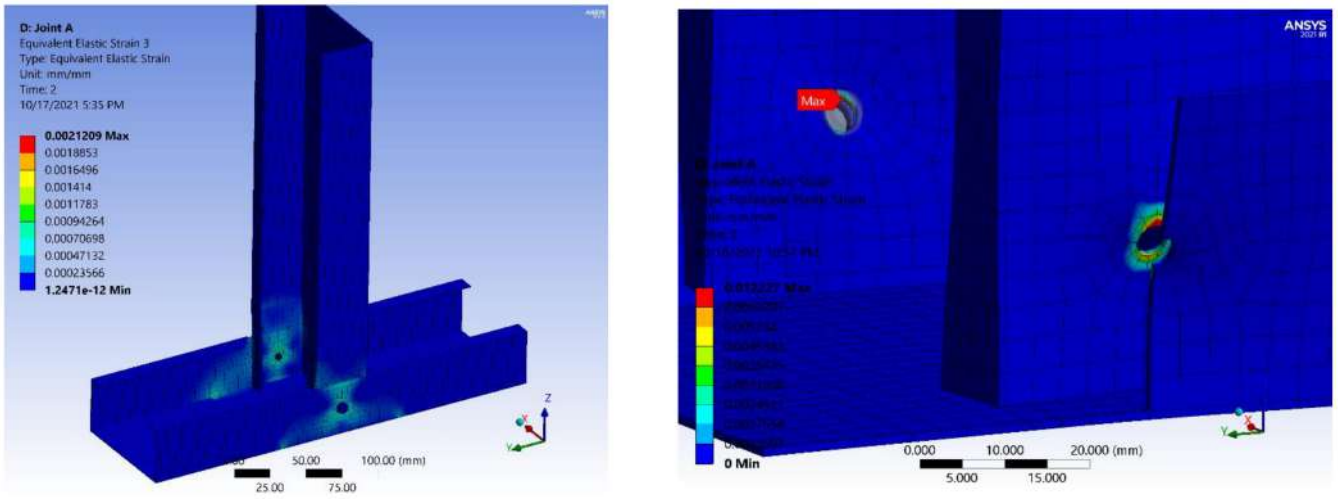

Figure 25. Equivalent strain distribution joint A: (**a**) overall equivalent elastic strain; (**b**) detail near hole and screws area of equivalent plastic strain.

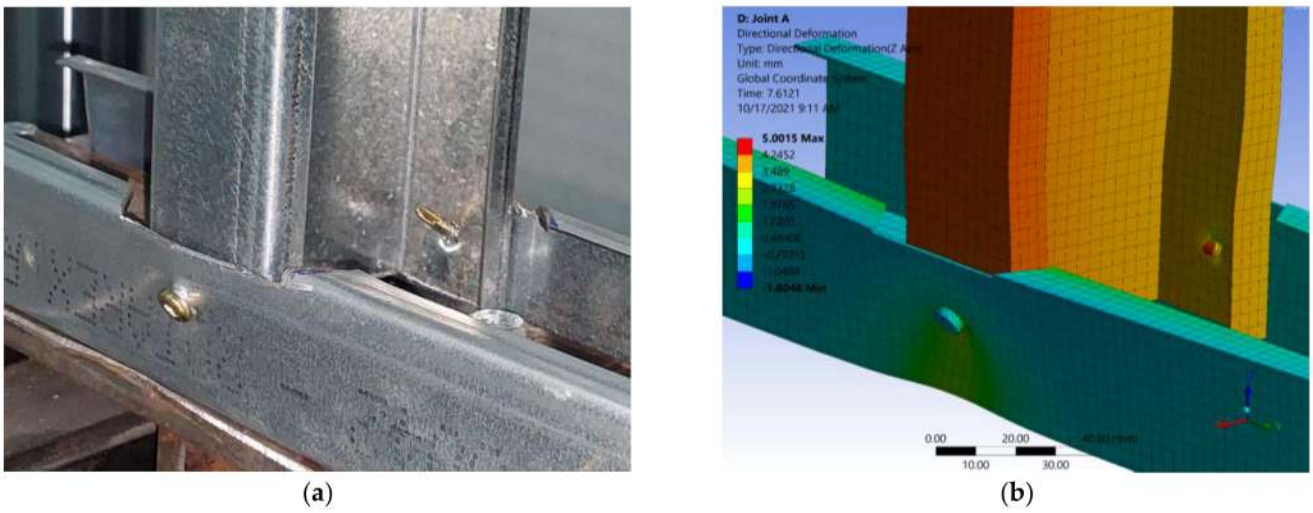

Figure 26. Comparison of displacement joint A: (**a**) experimental; (**b**) numerical model.

4.4. Joint B Modelling and Results

Figure 27 presents joint B's geometry and the environment of the model with a close detail of some hidden parts with a screw and tapper drawing description. The screw was shaped while considering two ribs of the thread located between the layers of the sheet steel of the profiles. The contacts of the bodies were assumed to be bonded. The mesh discretization and the quality of the finite elements are presented in Figure 28a,b. Finite elements were the parallelepipedal solids type, with a maximum size of 4 mm. The screws were modelled with tetrahedron elements.

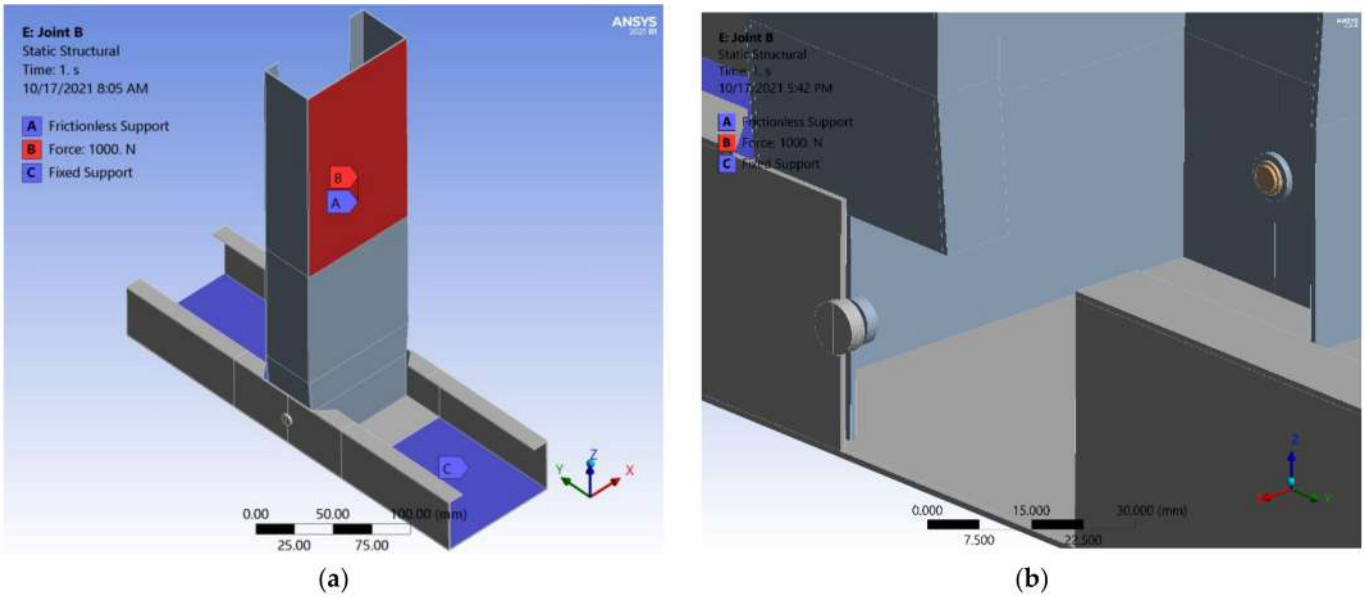

Figure 27. Geometry joint B: (**a**) overall; (**b**) detail.

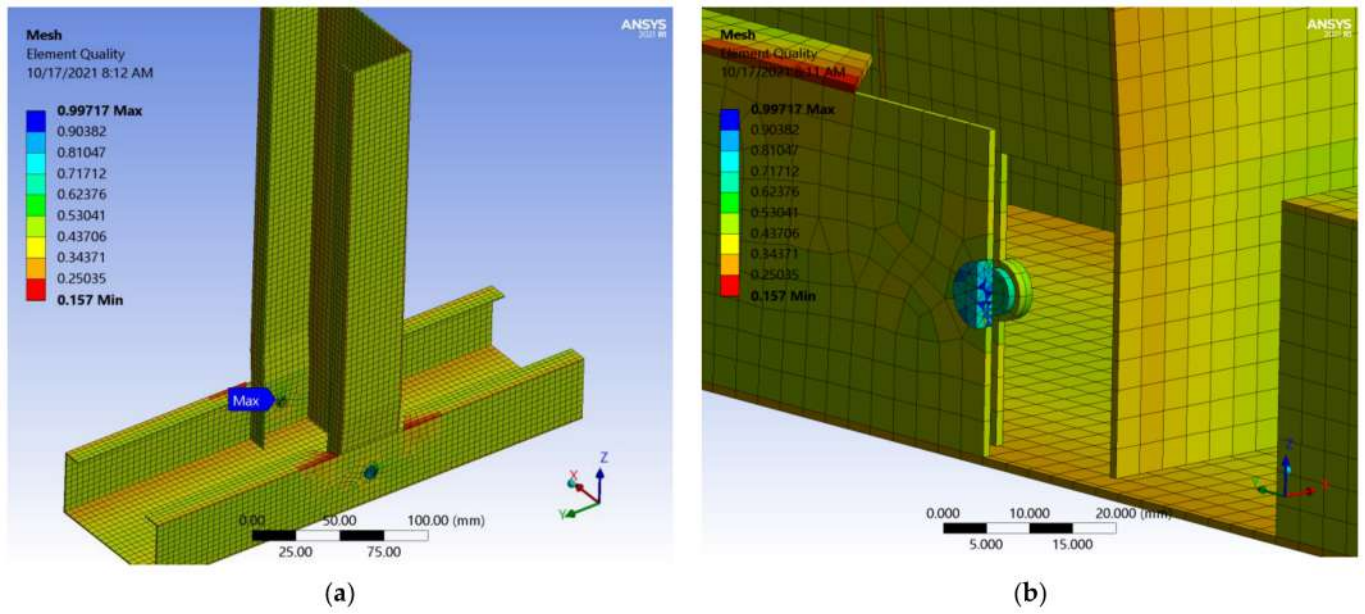

Figure 28. Mesh element quality joint B: (**a**) overall; (**b**) detail.

Figure 29 presents the map distribution of the equivalent von Mises stress. It can be seen that at a same 2 kN load, the values are distributed around the holes and tapper drawings. These values are smaller than those for joint A by up to 10%. In Figure 30a, the map distribution of the equivalent total strain (elastic and plastic) can be seen, while Figure 30b shows a close detail with the plastic deformation on the upper edge of the screw hole.

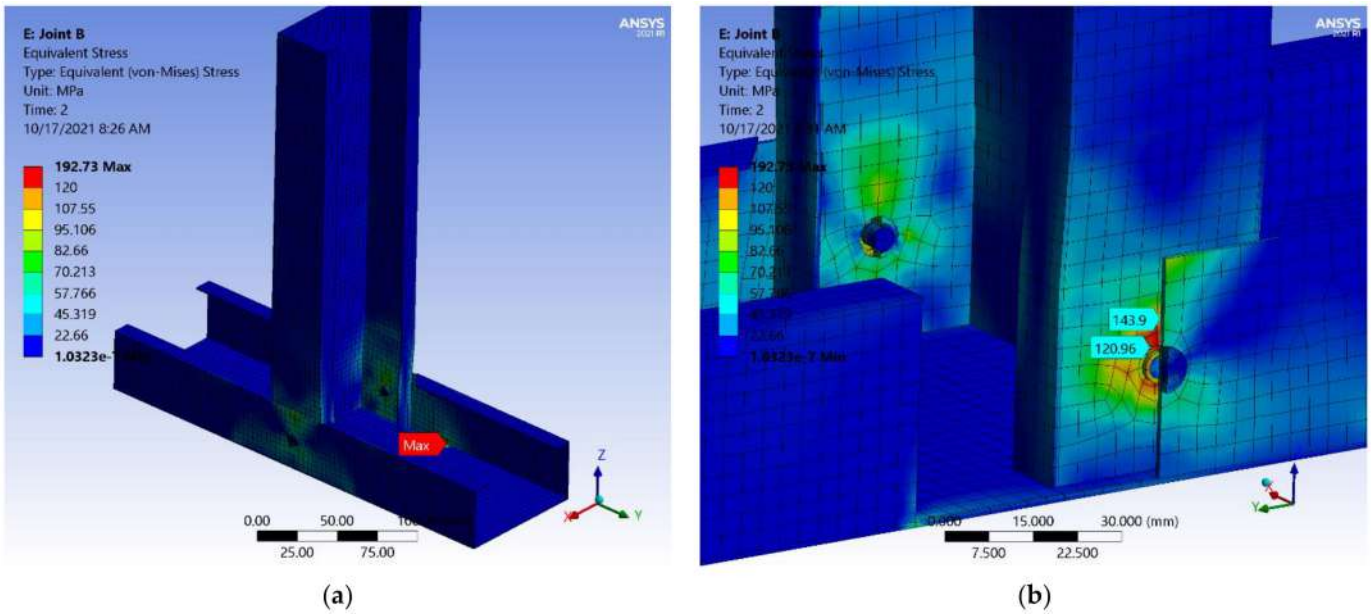

Figure 29. Joint B equivalent stress von Mises: (**a**) map distribution; (**b**) detail near holes and screw area.

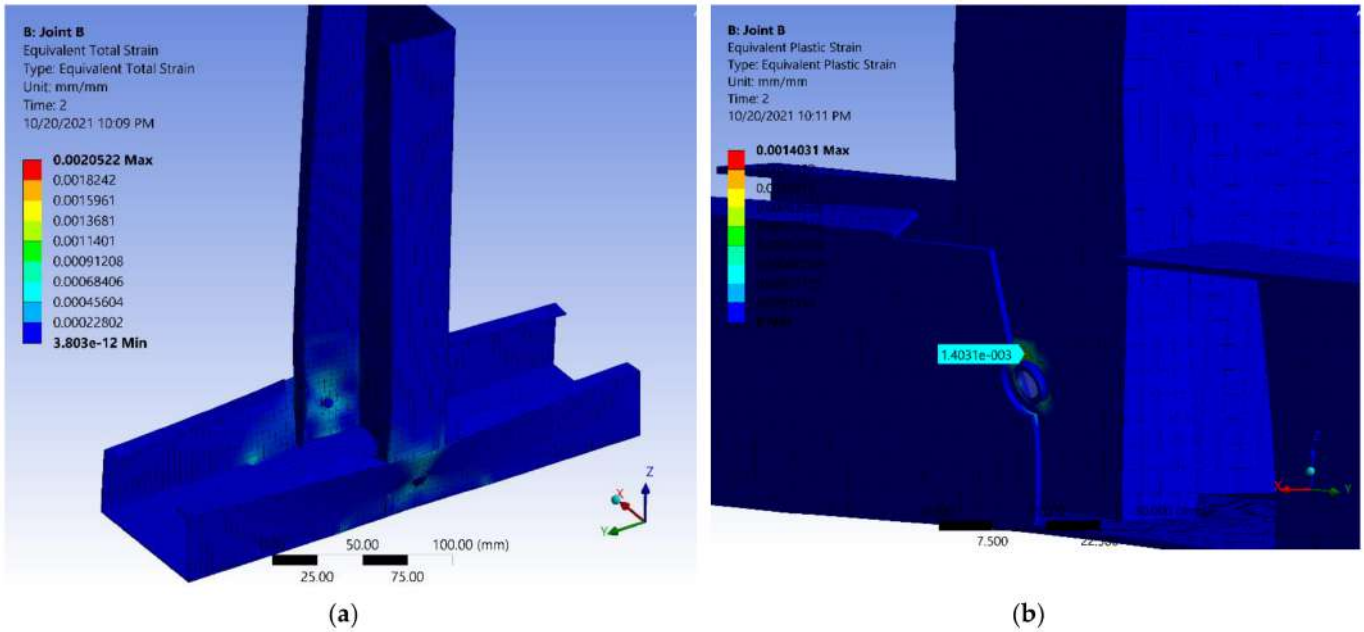

Figure 30. Equivalent strain in joint B at 2 kN—deformed shape: (**a**) overall map total (elastic + plastic) strain; (**b**) detail with plastic strain.

A close detail of tested specimen joint B is shown in Figure 31a. It can be seen that the screw tilted, and the tapper drawings exhibited bearing deformation. The vertical profile failed due to a shearing of the bottom edge of the holes. In the numerical simulation, the deformed model at a maximum load showed similarities with the experimental ones. However, keeping in mind that bonded contacts were considered on the tapper drawing area between the elements, this leads to a better distribution of the stress and a decreased local deformation near the holes. Nevertheless, the values obtained in the experiments and numerical simulation regarding the load and displacements are close as it will shown in subsequent sections Figure 31b.

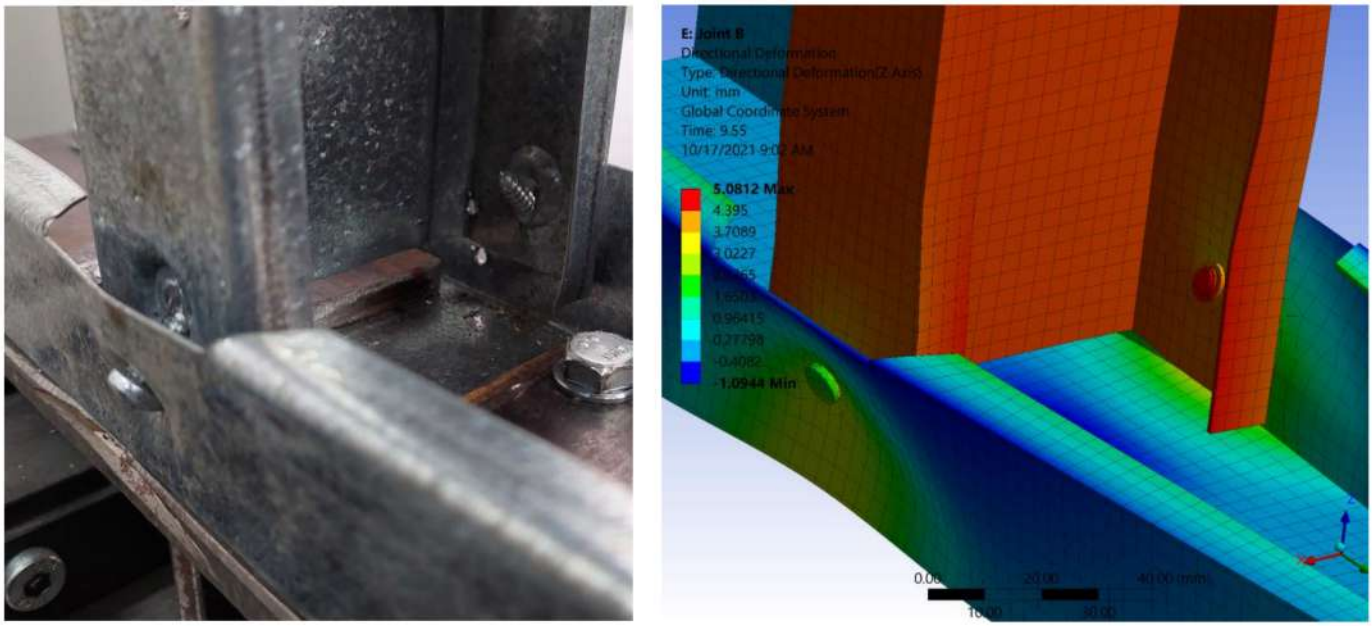

Figure 31. Displacements of joint B—deformed shape: (**a**) experimental; (**b**) numerical model.

4.5. Joint C Modelling and Results

Figure 32 presents joint C's geometry and the environment of the model with a close detail of some hidden parts with a description of the screws and tapper drawings. The screws were shaped considering two ribs of the thread located between the layers of the sheet steel of the profiles. The contacts of the bodies were initially assumed to be bonded. The mesh discretization and the quality of the finite elements are presented in Figure 33a,b. Finite elements were the parallelepipedal solids type, with a maximum size of 4 mm. The structural steel elements, including the screw, were modelled using three-dimensional solid finite elements SOLID186 and SOLID187, respectively. The contact surfaces between the screw head and shank and the steel sheet, as well as the contact between the finite elements in the two steel profiles, were modeled by means of Conta174 and Targe170 elements. The assumption of perfect bond was applied.

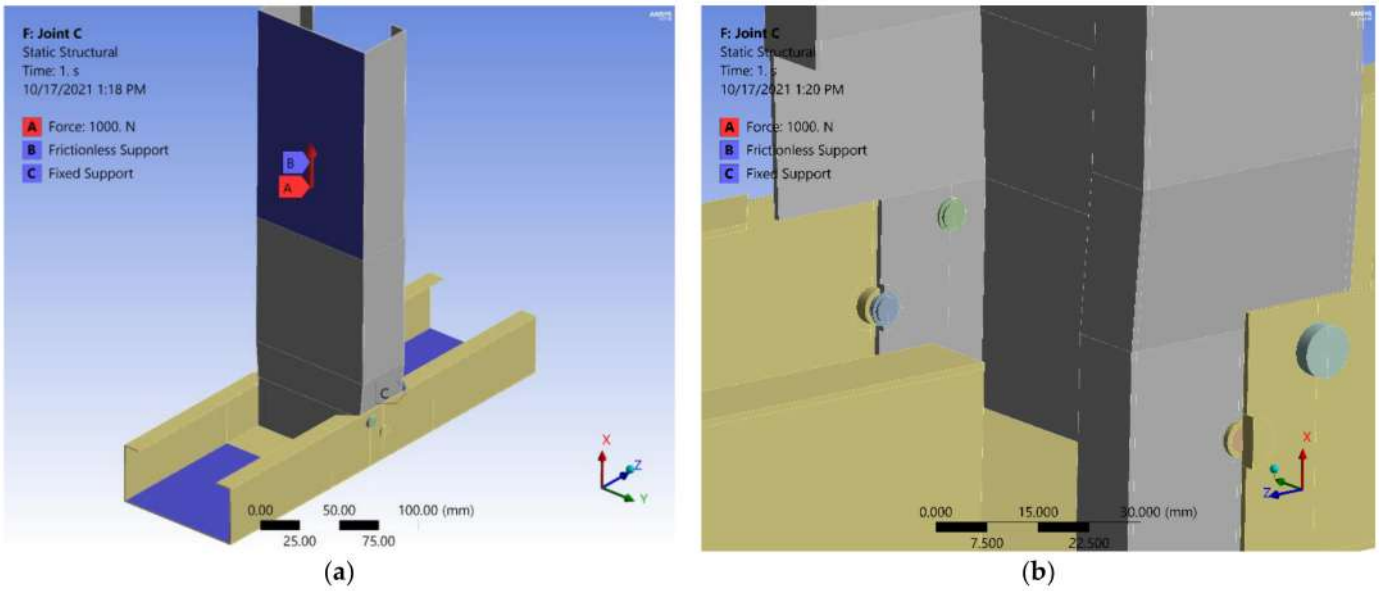

Figure 32. Joint C: (**a**) overall; (**b**) details of screws with hidden parts.

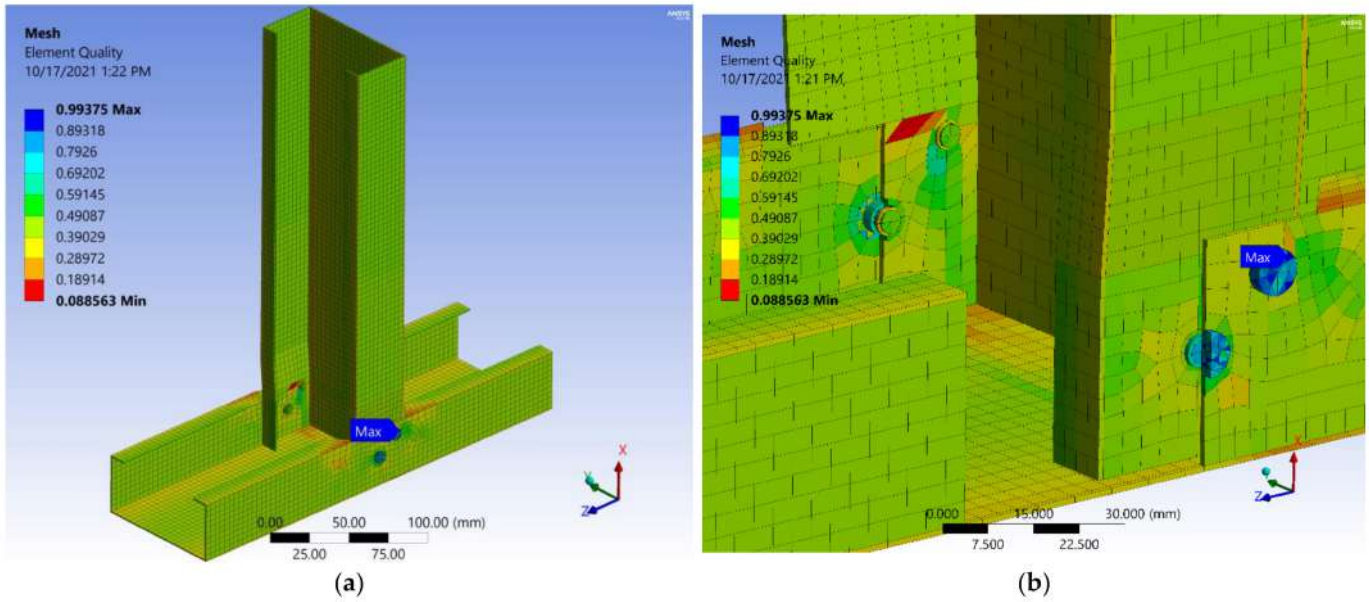

Figure 33. Joint C mesh: (**a**) overall; (**b**) details of screws with hidden parts.

This type of contact is, however, acceptable only for joint types A and B. For joint type C, the influence of the type of contact considered in the numerical model on the overall behavior of the joint was more pronounced compared to the other two. Based on the reviewer's suggestions, the authors conducted additional numerical simulations and concluded that a FRICTIONAL type of contact, available in ANSYS, was a better approach. A comparative load–displacement curve is introduced in this paper to render evident the influence of the type of contact on the overall behavior of the joint. A detailed parametric analysis is considered in the form of a future research stage.

Figure 34 presents the map distribution of the equivalent von Mises stress. It can be seen that at a same 2 kN load, the values are distributed around the holes and tapper drawings, with a concentration in the upper holes. These values are 5% smaller than those obtained for joints A and B. In Figure 35a, the map distribution of the equivalent elastic strain can be seen, while Figure 30b shows a close detail with the plastic deformation on the upper edge of the first screw hole in the upper part.

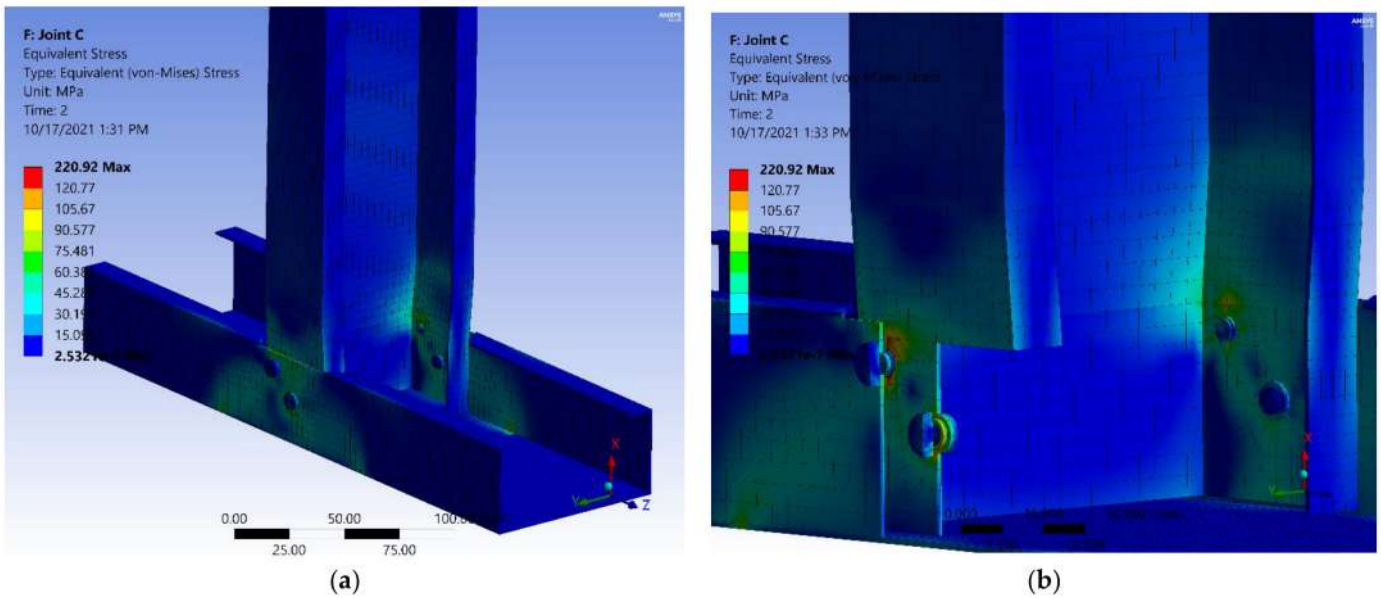

Figure 34. Joint C Equivalent stress: (**a**) overall; (**b**) details of screws with hidden parts.

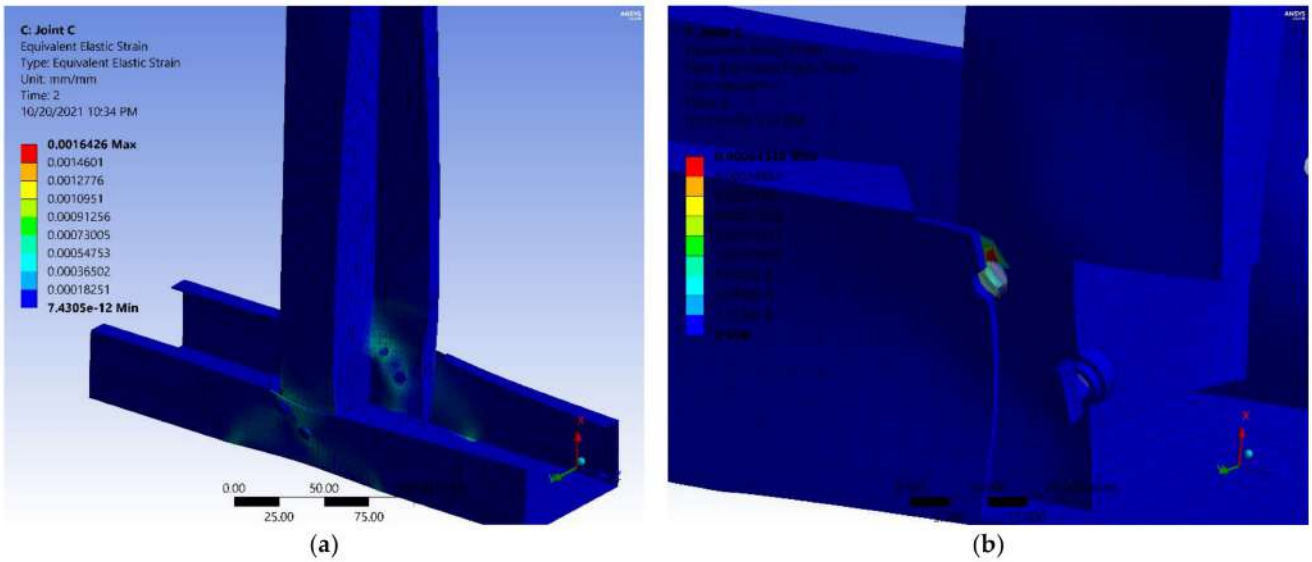

Figure 35. Equivalent strain distribution joint C: (**a**) overall map distribution of equivalent elastic strain; (**b**) detail near hole area of equivalent plastic strain.

In Figure 36a, there is a close detail of the tested specimen joint C, where it can be seen that the screw tilted and the tapper drawings had a bearing deformation. The vertical profile failed due to shearing of the bottom edge of the holes. In the numerical simulation, the deformed model at a maximum load showed similarities with the experimental ones. Considering that the contacts bonded on the tapper drawing area between elements, this leads to a better distribution of stresses and smaller local deformations near the holes. However, the values obtained in the experiments and numerical simulation regarding the load and displacements were much lower compared to the previous two joint types, with joint C being almost two times stiffer (the bonded contact in comparative load-displacement graphs). Comparing the results between the experimental and numerical, we can see, in the case of joint A and joint B, a small influence of contacts definition, while in the case of joint C, the influence is greater, making the model stiffer than the experimented one.

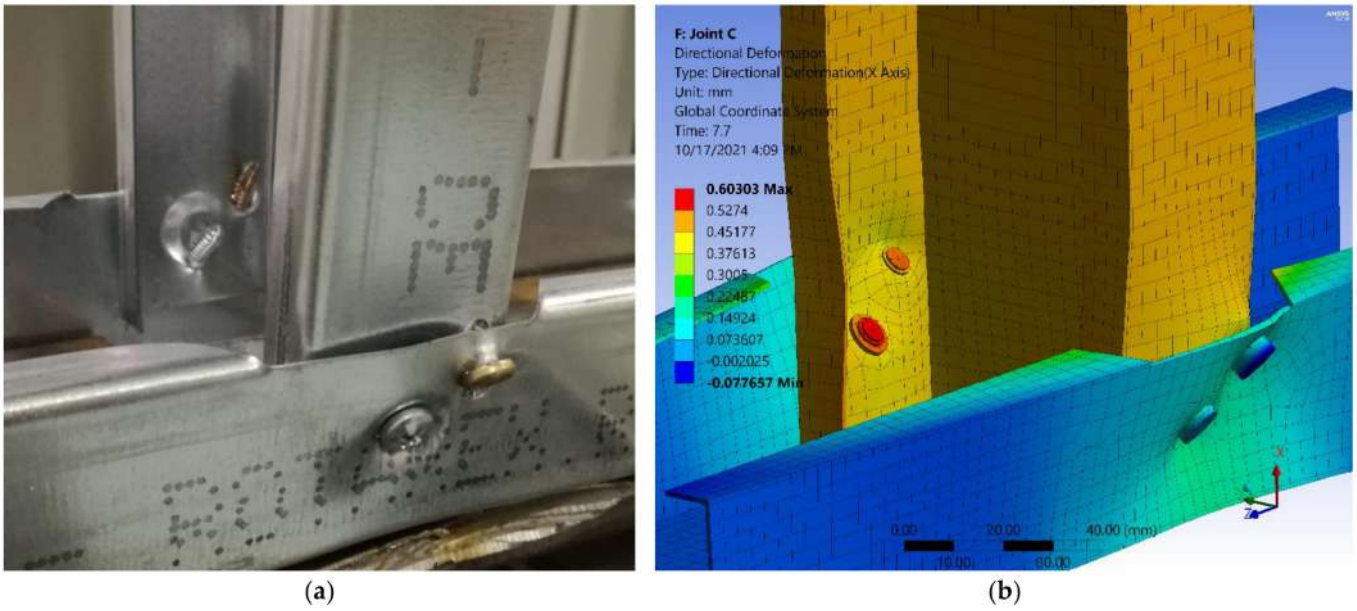

Figure 36. Joint C deformed shape: (**a**) experimental; (**b**) FE model.

Figures 37a,b and 38a present the comparative load–displacement curves for joints A, B and C, respectively. It can be observed that there is a good agreement between the numerical simulations and the experimental results in terms of ultimate loads and corresponding displacements. The numerical models exhibited higher initial stiffness compared to the experiment, mainly due to the assumption of perfect bond between the constitutive parts of the joint. This is very visible, especially for joint type C. The additional models with frictional contacts, which are presented in comparison, show that they are more accurate and closer to the experimental data obtained.

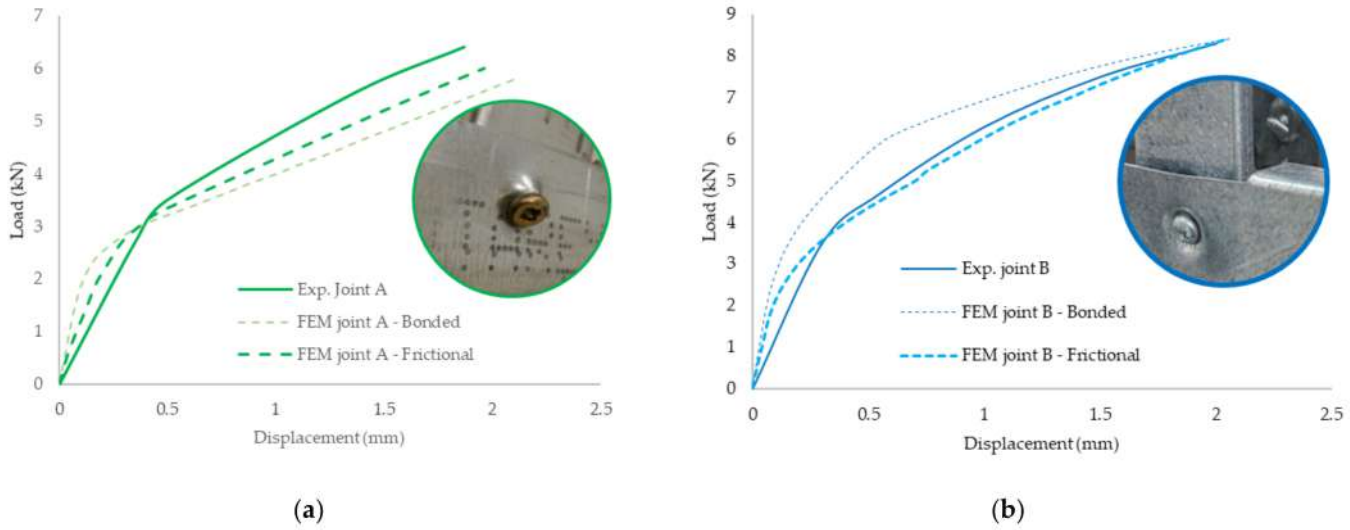

Figure 37. Comparative load–displacement curves: (**a**) joint A; (**b**) joint B.

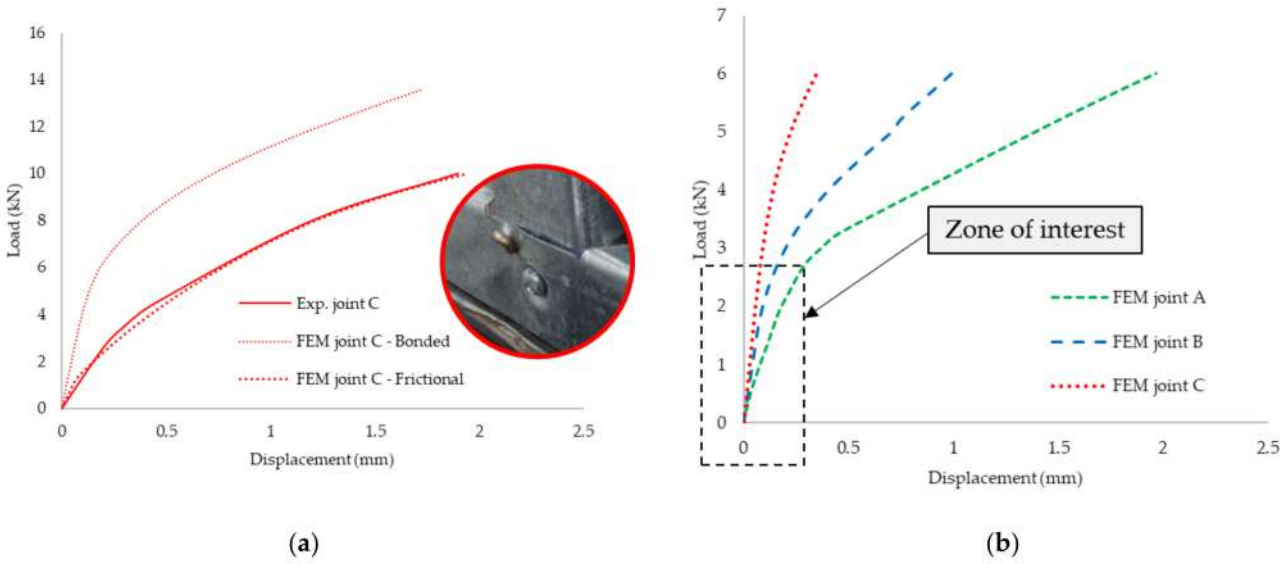

Figure 38. Comparative load–displacement curves: (**a**) Joint C; (**b**) FE models.

The elastic-plastic range, identified on the load-displacement graphs as starting from the point where the graph changes slope, was quite accurately identified in the numerical model and matched the experimental results.

Comparing the values obtained for each type of joint in Figure 38b on the finite element models, there is clearly an increase in the load carrying capacity at the same displacement. The yielding process occurred in joint A sooner than for joints B and C. In Figure 39, the comparative displacements at same value of load at 6 kN show that joint C was 50% stiffer than joint A, and joint B was 41% stiffer than joint A. Comparing joints B and C, it can

be observed that adding a supplementary self-drilling screw on each side increased the overall stiffness and the overall load capacity.

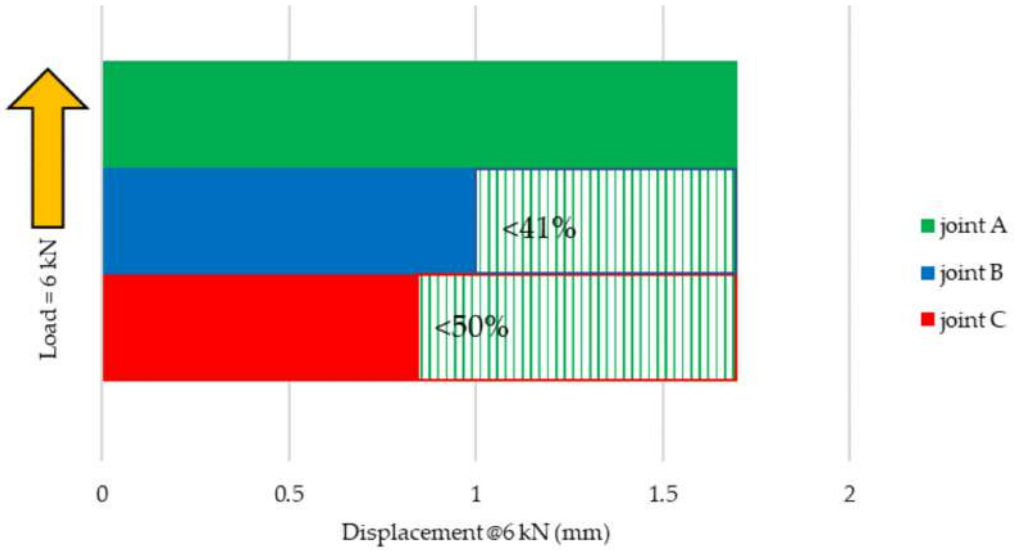

Figure 39. Comparative displacements @ same Load = 6 kN.

4.6. Design Resistance of Joint A, According to EN 1993-1-3

The assessment of the load carrying capacity of a joint, following the recommendations of EN1993-1-3 presented in Table 2, could represent a valuable benchmark for joint type A (Figure 40). Taking into account the fact that the EN1993-1-3 code only gives information on the load carrying capacity of simple joints using self-drilling screws and does not provide any information on the overall rigidity of these joints, the present study brings its contribution to broadening knowledge in the case of joints consisting of drawn-sockets to the deformation capacity of the joint itself.

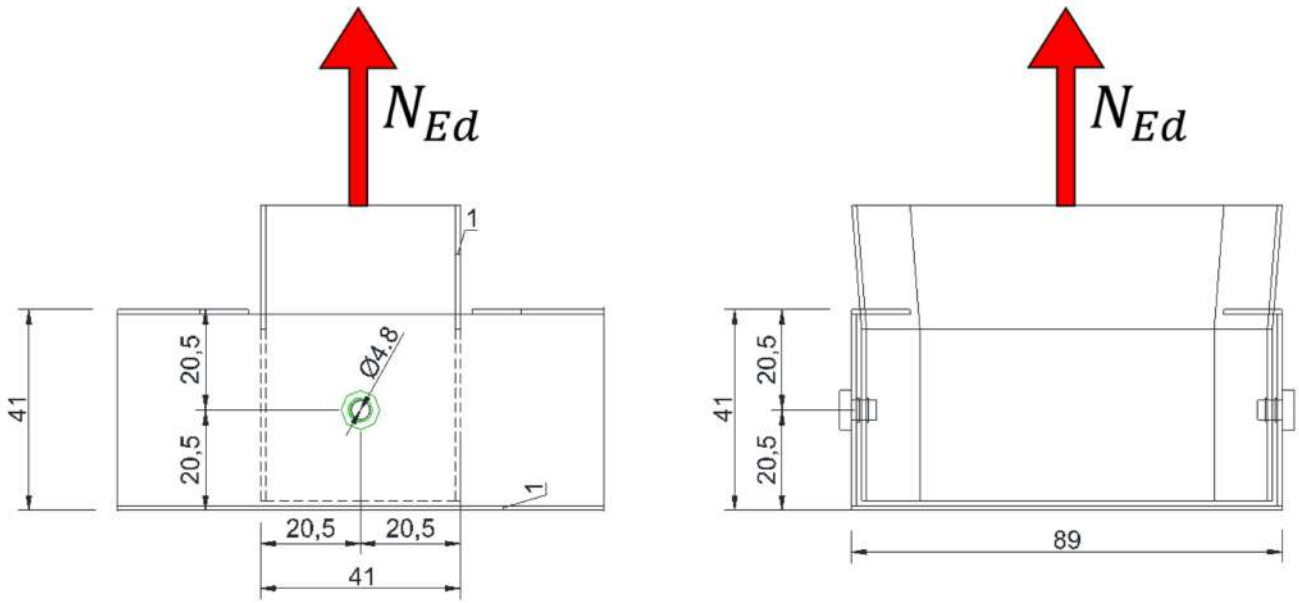

Figure 40. Joint A geometric schema.

Table 2. Joint A design according to EN 1993-1-3.

Basic Data		
Nominal diameter of the screw	$d = 4.8$ mm	(3)
Total number of screws	$n_f = 2$	(4)
End and edge distance for screw	$e_1 = 20.5$ mm; $e_2 = 20.5$ mm	(5)
The dimensions of the stud cross-section:		
Total height	$h_1 = 89$ mm	(6)
Total width of flange	$b_1 = 41$ mm	(7)
Total width of edge fold	$c_1 = 12$ mm	(8)
Nominal thickness	$t_{1,nom} = 1$ mm	(9)
Steel core thickness	$t_1 = 0.96$ mm	(10)
Gross area of the studied cross-section	$A_1 = 185$ mm^2	(11)
The dimensions of the rail cross-section:		
Total height	$h = 89$ mm	(12)
Total width of flange	$b = 41$ mm	(13)
Nominal thickness	$t_{nom} = 1$ mm	(14)
Steel core thickness	$t = 0.96$ mm	(15)
The materials properties are:		
Basic yield strength	$f_{yb} = 125 \frac{\mathrm{N}}{\mathrm{mm}^2}$	(16)
Ultimate strength	$f_u = 420 \frac{\mathrm{N}}{\mathrm{mm}^2}$	(17)
Modulus of elasticity	$E = 210{,}000 \frac{\mathrm{N}}{\mathrm{mm}^2}$	(18)
Poisson's ratio	$\nu = 0.3$	(19)
Shear modulus	$G = \frac{E}{2(1+\nu)} = 81{,}000 \frac{\mathrm{N}}{\mathrm{mm}^2}$	(20)
Partial factor	$\gamma = 1.25$	(21)
The design force on the connection	$N_{Ed} = 2$ kN	(22)
The design shear force per screw in the ultimate limit state is:	$F_{v,\ Ed} = \frac{N_{Ed}}{n_f} = \frac{2}{2} = 1$ kN	(23)
Check the range of validity for design resistance formulas		
The following conditions should be satisfied:		
$e_1 \geq 3d;\ p_1 \geq 3d;\ e_2 \geq 1.5d;\ 3$ mm ≤ 8 mm		(24)
$e_1 = 20.5$ mm $> 3d = 3 \times 4.8 = 14.4$ mm	OK	(25)
$e_2 = 20.5$ mm $> 1.5d = 1.5 \times 4.8 = 7.2$ mm	OK	(26)
3 mm $< d = 4.8$ mm < 8 mm	OK	(27)
Resistance check for self-tapping screws loaded in shear		
Bearing resistance	$F_{b,Rd} = \frac{\propto f_u dt}{\gamma_{M2}}$	(28)
for $t_1 = t = 1$ mm	$\propto = 3.2\sqrt{\frac{t}{d}} = 3.2 \times \sqrt{\frac{0.96}{4.8}} = 1.43$	(29)
The bearing resistance of one screw is:	$F_{b,Rd} = \frac{\propto f_u dt}{\gamma_{M2}} = \frac{1.43 \times 250 \times 4.8 \times 1}{1.25} = 1373$ N$= 1.373$ kN	(30)
Net-section resistance	$F_{n,Rd} = \frac{A_{net} f_u}{\gamma_{M2}}$	(31)
	Where the net cross − sectional area is: $A_{net} = A_1 - 2dt_1 = 185 - 2 \times 4.8 \times 0.96 = 175.8$ mm^2	(32)
The net-section resistance is:	$F_{n,Rd} = \frac{A_{net} f_u}{\gamma_{M2}} = \frac{175.8 \times 250}{1.25} = 35{,}160$ N $= 35.16$ kN	(33)
Shear resistance	$F_{v,Rd} = \frac{F_{v,Rk}}{\gamma_{M2}}$	(34)

Table 2. *Cont.*

$F_{v,Rk} = 9050$ N $= 9.05$ kN according to manufacturer catalogue
$F_{v,Rd} = \frac{9050}{1.25} = 7240$ N $= 7.24$ kN (35)
The resistance of a fastener in shear may be verified using
$\frac{F_{v,Ed}}{\min(F_{b,Rd}; \frac{F_{n,Rd}}{n_f}; F_{v,Rd}} \leq 1$ (36)
$\frac{1}{\min(1.373; 17.58; 7.24)} = \frac{1}{1.373} = 0.72 < 1$ (37)

5. Discussion

All the experimental tested specimens revealed that the main failure mechanism was caused by the exceeding of the strength of the sheet profile on edge holes. After the yielding of the material in the steel profiles, the screws tilted, and this caused a secondary mechanism of bearing deformations in the flanges due to the screw head.

For DX51D+Z steel, a very ductile material, permanent plastic deformations were produced in every case on the hole's edge in the first stage of the loading. Hence, even though higher strength steel could be used, in excess of 250 MPa, the yield strength would be the one controlling the maximum bearing capacity for the design rules. A simple joint with one self-drilling screw on each side of the profile could be loaded with a maximum load of 1.5 kN before the upper limit of the linear-elastic range was attained.

Adding a tapper drawing and a self-tapping screw increased the stiffness of the joint by almost 15% in the elastic zone, and by almost 41% in terms of maximum load. The presence of the tapper drawing had, as a direct effect, the occurrence of an additional friction force, and the contact between the two profiles of the joint could be assumed, at least at the beginning of the loading process, to be perfectly bonded. This resulted in an improved behavior of the joint.

For a stiffer and strengthened joint, two screws on each side of the profile and a tapper drawing were deemed suitable and appropriate for connecting elements in truss beams or wall panels. The maximum loading in the elastic zone could be considered 4 kN.

The simulation results also showed that the failure mechanisms were similar to the real experimented specimens, with a combination of two failure mechanisms: the tilting of the screw and the bearing deformation in the flanges of the cold-formed thin-walled profiles.

The load–displacement curves of the joints obtained by the finite element analyses were similar in behavior and values with those obtained experimentally.

In a comparison between the assessment procedures put forward in Eurocode 3, it can be observed that, up to a value of the load of 2 kN, the considered joint is assumed to be safe, according to the norm. On the other hand, the ultimate strength of the steel considered in Eurocode 3 could lead to an overestimation of the bearing capacity of the joint. A better solution could be to consider the yield strength of the material for the assessment stage. Exceeding the yield strength could lead to the occurrence of plastic deformations that can endanger the safety of the occupants.

For the two remaining cases, joint types B and C, the presence of the drawn-socket is not covered in Eurocode 3. This study could be considered as the starting point for the formulations of design equations for joints with different configurations.

6. Conclusions

This paper presented a detailed study on thin-walled steel profile joints based on two types of screws: self-drilling and self-tapping, in addition to a tapper drawing. The experiments on tension loading showed that the simple self-drilling screws, with one at each side of the profiles, have an elastic behavior until around 1.5 kN; after that, plastic deformation appears on the hole's edge, and the failure mechanism is revealed by a tilting of the screw and bearing deformation of the sheet steel.

Adding a tapper drawing and a self-tapping screw increased the friction between profiles and screw making a stiffer joint. Adding two screws on each side of the profiles with a tapper drawing resulted in a suitable connection for truss element connections or wall panels. When comparing these results with other solutions, such as riveted joints or welded joints, from a technological and strength point of view, it can be said that even if the strengthening is 50% weaker, it is a more practical and accessible technologically for mounting elements on sites. Rivets are also suitable and appropriate, but require holes and a higher precision of positioning of the rivets and holes, which is time consuming on mounting elements.

Supplementary Materials: Joint A video recording of test: https://youtu.be/xqZ65MoHYJs (accessed on 19 October 2021), Joint B video recording: https://youtu.be/v0yRbs4fWvM (accessed on 19 October 2021), Shaking table test of a thin-walled steel profile structure: https://youtu.be/_JnHCGos4mw (accessed on 19 October 2021).

Author Contributions: Conceptualization, G.T.; methodology, G.T.; software, G.T.; validation, I.-O.T.; formal analysis, G.T. and I.-O.T.; investigation, I.-O.T.; resources, G.T.; data curation, G.T.; writing—original draft preparation, I.-O.T.; writing—review and editing, G.T. and I.-O.T.; visualization, I.-O.T.; supervision, G.T.; project administration, G.T.; funding acquisition. All authors have read and agreed to the published version of the manuscript.

Funding: The APC was funded by The "Gheorghe Asachi" Technical University of Iasi under the Publications grant GI/P12/2021.

Institutional Review Board Statement: Not applicable.

Informed Consent Statement: Not applicable.

Data Availability Statement: https://drive.google.com/drive/folders/15I9y-dvw-LmIa6FGANAc2JKDdR164bTM?usp=sharing (accessed on 19 October 2021).

Acknowledgments: The authors acknowledge the contribution of UNIC-ROTAREX, Romania, for supplying the materials, joints and accessories needed for conducting the laboratory investigations. The authors wish to express their gratitude to the partnership between The "Gheorghe Asachi" Technical University of Iasi, INAS S.A. and ANSYS for making available the full research license for Ansys 2021R1 used in conducting the research.

Conflicts of Interest: The authors declare no conflict of interest.

References

1. *Specification for the Design of Light Gage Steel Structural Members*; American Iron and Steel Institute (AISI) Specifications, Standards, Manuals and Research Reports (1946–present); American Iron and Steel Institute: Washington, DC, USA, April 1946.
2. EN 1993-1-3:2006. Eurocode 3: Design of Steel Structures—Part 1–3: General Rules-Supplementary Rules for Cold-Formed Members and Sheeting, 2007 [ECCS]. Available online: https://www.phd.eng.br/wp-content/uploads/2015/12/en.1993.1.3.2006.pdf (accessed on 19 October 2021).
3. Landolfo, R. EUROCODES Background and Applications Cold-Formed (CF) Structures. Available online: https://eurocodes.jrc.ec.europa.eu/doc/WS2008/EN1999_8_Landolfo.pdf (accessed on 19 October 2021).
4. Yu, W. *Cold-Formed Steel Design*; Wiley: Hoboken, NJ, USA, 2000; ISBN 0471-348-090.
5. Blandford, G.E.; Louis, S. Current Research on Cold-Formed Steel Structures; International Specialty Conference on Cold-Formed Steel Structures. 1990. Available online: https://scholarsmine.mst.edu/isccss/10iccfss/10iccfss-session7/3 (accessed on 19 October 2021).
6. Ungureanu, V.; Both, I.; Burcă, M.; Nguyen, T.H.; Grosan, M.; Dubină, D. Experimental Investigations on Spot Welded Built-Up Cold-Formed Steel Beams. *Bull. Polytech. Inst. Jassy Construction. Archit. Sect.* **2018**, *64*, 19–30. [CrossRef]
7. Roşca, O.V. Experimental Tests of Thin-Walled Steel Roof Profiles. *Bull. Polytech. Inst. Jassy Construction. Archit. Sect.* **2011**, *LVII*, 85–96.
8. Ţăranu, G.; Budescu, M. 35 m Large Opening Roof Structural System Made of Hot Rolled and Cold Formed Steel Profiles. *Bull. Polytech. Inst. Jassy Construction. Archit. Sect.* **2018**, *64*, 33–40.
9. Galatanu, T.; Ciongradi, I.P.; Budescu, M.; Rosca, O.V. Experimental Studies of the Back-To-Back Connected Cold Formed Steel Profile Bolted Joints. *Bull. Polytech. Inst. Jassy* **2009**, *55*, 17–28.
10. Sivapathasundaram, M.; Mahendran, M. Pull-out Capacity of Multiple Screw Fastener Connections in Cold-Formed Steel Roof Battens. *J. Constr. Steel Res.* **2018**, *144*, 40–52. [CrossRef]

11. Huynh, M.T.; Pham, C.H.; Hancock, G.J. Experimental Behaviour and Modelling of Screwed Connections of High Strength Sheet Steels in Shear. *Thin-Walled Struct.* **2020**, *146*, 106357. [CrossRef]
12. Huynh, M.T.; Pham, C.H.; Hancock, G.J. Design of Screwed Connections in Cold-Formed Steels in Shear. *Thin-Walled Struct.* **2020**, *154*, 106817. [CrossRef]
13. Roy, K.; Lau, H.H.; Huon Ting, T.C.; Masood, R.; Kumar, A.; Lim, J.B.P. Experiments and Finite Element Modelling of Screw Pattern of Self-Drilling Screw Connections for High Strength Cold-Formed Steel. *Thin-Walled Struct.* **2019**, *145*, 106393. [CrossRef]
14. Wu, H.; Chao, S.; Li, Y.; Sang, L. Experimental Investigation of Strengthened Screw Connection and Application in CFS Shear Walls. *J. Constr. Steel Res.* **2020**, *168*, 105870. [CrossRef]
15. Quan, G.; Ye, J.; Li, W. Computational Modelling of Cold-Formed Steel Lap Joints with Screw Fasteners. *Structures* **2021**, *33*, 230–245. [CrossRef]
16. Nithyadharan, M.; Kalyanaraman, V. A New Screw Connection Model and FEA of CFS Shear Wall Panels. *J. Constr. Steel Res.* **2021**, *176*, 106430. [CrossRef]
17. Feng, R.Q.; Cai, Q.; Ma, Y.; Yan, G. rong Shear Analysis of Self-Drilling Screw Connections of CFS Walls with Steel Sheathing. *J. Constr. Steel Res.* **2020**, *167*, 105842. [CrossRef]
18. Henriques, J.; Rosa, N.; Gervasio, H.; Santos, P.; da Silva, L.S. Structural Performance of Light Steel Framing Panels Using Screw Connections Subjected to Lateral Loading. *Thin-Walled Struct.* **2017**, *121*, 67–88. [CrossRef]
19. Xie, Z.; Yan, W.; Yu, C.; Mu, T.; Song, L. Experimental Investigation of Cold-Formed Steel Shear Walls with Self-Piercing Riveted Connections. *Thin-Walled Struct.* **2018**, *131*, 1–15. [CrossRef]
20. Xie, Z.; Yan, W.; Yu, C.; Mu, T.; Song, L. Improved Shear Strength Design of Cold-Formed Steel Connection with Single Self-Piercing Rivet. *Thin-Walled Struct.* **2018**, *131*, 708–717. [CrossRef]
21. Song, L.; Yan, W.; Zhang, X.; Yu, C.; Xie, Z. Feasibility Research on the Application of Self-Piercing Riveted Connection in Cold-Formed Steel Structures. *J. Constr. Steel Res.* **2020**, *168*, 105957. [CrossRef]
22. Light Steel Structure Factory. Steel House Producer. Available online: https://www.rotarex.ro/en/ (accessed on 19 October 2021).
23. Dubina, D.; Stratan, A.; Ciutina, A.; Fulop, L.; Nagy, Z. Strength, Stiffness and Ductility of Cold-Formed Steel Bolted Connections. Available online: https://scholar.google.com/scholar?cluster=10778266862457140001&hl=en&oi=scholarr (accessed on 19 October 2021).
24. Dubina, D.; Fülöp, L.A.; Aldea, A.; Demetriu, S.; Nagy, Z. Seismic Performance of Cold-Formed Steel Framed Houses. In Proceedings of the 5th International Conference on Behaviour of Steel Structures in Seismic Areas (STESSA), Yokohama, Japan, 14–17 August 2006; pp. 429–435.
25. Dubina, D.; Fülöp, L.; Ungureanu, V.; Szabo, I.; Nagy, Z. Cold-Formed Steel Structures for Residential and Non-Residential Buildings. In Proceedings of the 9th International Conference on Metal Structures, Timisoara, Romania, 19–22 October 2000; pp. 308–317.
26. Thirunavukkarasu, K.; Kanthasamy, E.; Gatheeshgar, P.; Poologanathan, K.; Rajanayagam, H.; Suntharalingam, T.; Dissanayake, M. Sustainable Performance of a Modular Building System Made of Built-Up Cold-Formed Steel Beams. *Buildings* **2021**, *11*, 460. [CrossRef]
27. Taranu, G.; Budescu, M.; Olteanu, I.; Toma, I.-O.; Venghiac, M.; Stratulat, M. Sisteme Structurale de Rezistentă Cu Profile Din Tabla Subtire Indoite La Rece Tip ROTAREX. Available online: http://www.aicps.ro/revista/aicps-review-1-2-2018/content#page/n0/mode/2up (accessed on 16 October 2021).
28. International Organization for Standardization ISO 6892-1:2019(En), Metallic Materials—Tensile Testing—Part 1: Method of Test at Room Temperature. Available online: https://www.iso.org/obp/ui/#iso:std:iso:6892:-1:ed-3:v1:en (accessed on 5 October 2021).
29. Grabber Flat Pan Head Driller 4.8 × 19 mm Heavy Gauge Metal Framing–Self Drilling Screws Technical Data. Available online: https://www.grabberman.com/Media/TechnicalData/512.pdf (accessed on 2 October 2021).
30. INDEX Self Tapping Screw 4.8 × 22 mm DIN 7981 Technical Data Sheet. Available online: https://www.indexfix.com/docs/ft-ros-en.pdf (accessed on 2 October 2021).
31. Flodr, J.; Kałduński, P.; Krejsa, M.; Pařenica, P. Innovative Connection of Steel Profiles, Experimental Verification and Application. *Procedia Eng.* **2017**, *190*, 215–222. [CrossRef]
32. Petrik, A.; Aroch, R. Usage of True Stress-Strain Curve for FE Simulation and the Influencing Parameters. In *IOP Conference Series: Materials Science and Engineering*; Institute of Physics Publishing: Bristol, UK, 2019; Volume 566, p. 012025.
33. Yao, D.; Cai, L.; Bao, C. A New Approach on Necking Constitutive Relationships of Ductile Materials at Elevated Temperatures. *Chin. J. Aeronaut.* **2016**, *29*, 1626–1634. [CrossRef]

Check for updates

Advances in Civil Engineering

WILEY

RESEARCH ARTICLE OPEN ACCESS

Joint Damage Effects on Axial Capacity of Cold-Formed Steel Uprights: Experimental, Numerical, and Machine Learning Study

George Taranu[1] | Casim Yazici[2] | Fatih Mehmet Özkal[3]

[1]Department of Structural Mechanics, Faculty of Civil Engineering and Building Services, The "Gheorghe Asachi" Technical University of Iasi 700050, Iasi, Romania | [2]Department of Construction, Ağrı İbrahim Çeçen University 04400, Ağrı, Türkiye | [3]Department of Civil Engineering, Atatürk University 25240, Erzurum, Türkiye

Correspondence: George Taranu (george.taranu@academic.tuiasi.ro)

Received: 2 September 2025 | **Revised:** 16 January 2026 | **Accepted:** 22 January 2026

Academic Editor: Meng Gao

Keywords: axial load capacity | cold-formed steel | finite-element analysis | joint degradation | machine learning | storage rack systems

ABSTRACT

This study quantifies how beam-to-column joint damage alters the axial resistance and failure modes of cold-formed steel (CFS) uprights used in industrial storage rack systems. Current design-oriented assessments typically neglect the reduction of joint rotational stiffness and moment resistance caused by prior cyclic joint deterioration, which can compromise subsequent compression performance. To address this gap, six commercial perforated upright sections are tested under axial compression in intact and joint-damaged conditions. A unified framework combines experiments, nonlinear finite element analysis (FEA; ANSYS), and machine learning (ML) prediction using geometric descriptors (thickness, area, second moments of area, and radii of gyration) together with experimentally derived joint properties (rotational stiffness and ultimate joint moment). Among the evaluated regressors, the gradient boosting model provides the best predictive performance (cross-validated R^2 and lowest root mean square error [RMSE]/mean absolute error [MAE]), showing close agreement with experimental outcomes and numerical trends. Results indicate axial capacity reductions of up to ~30% after joint degradation and a tendency toward coupled distortional and torsional–flexural (TF) instability. The findings highlight the engineering need to account for joint stiffness degradation in residual capacity checks and support rapid, data-informed decisions for inspection and retrofit of rack uprights. The study provides a practical predictive framework for postdamage capacity evaluation in industrial rack systems.

1 | Introduction

Cold-formed steel (CFS) structural members are widely adopted in modern pallet rack systems because of their low weight, high strength-to-weight ratio, reduced transportation costs, ease of prefabrication, and compatibility with modular construction. In particular, uprights made from CFS are preferred in storage rack systems where efficiency, durability, and rapid assembly are essential. Despite these advantages, perforated and open-section CFS columns exhibit complex and often unstable behavior due to their sensitivity to multiple interactive buckling phenomena. Their thin-walled nature, combined with perforations introduced for assembly or weight reduction, further increases the risk of instability under axial or combined axial and bending loads [1–4].

CFS columns are prone to local, distortional, and global buckling, frequently acting in interaction. This combined-mode behavior challenges traditional design approaches. Although established

This is an open access article under the terms of the Creative Commons Attribution License, which permits use, distribution and reproduction in any medium, provided the original work is properly cited.

Copyright © 2026 George Taranu et al. *Advances in Civil Engineering* published by John Wiley & Sons Ltd.

procedures such as the Direct Strength Method (DSM) and the EN 15512 guideline are commonly used, they may not provide reliable predictions of load-carrying capacity, particularly for perforated profiles [5, 6]. Several studies highlight that these methods can be either overly conservative or unconservative, depending on geometry and loading conditions [7–9]. For perforated members in particular, the shortcomings of classical buckling curves are well documented [10, 11].

To overcome these limitations, researchers have proposed advanced analytical, numerical, and computational methods. Generalized Beam Theory, Koiter asymptotic analysis, and stochastic approaches such as Monte Carlo simulations have been applied to better capture the influence of geometric imperfections and predict collapse mechanisms with higher fidelity. Finite element (FE) modeling has become an essential tool to study nonlinear and postbuckling behavior with accuracy [12–15]. In parallel, analytical formulations based on the mean moment of inertia have been suggested as practical tools for estimating buckling resistance [16].

The structural performance of CFS members is also strongly influenced by the manufacturing process. Cold-forming generates residual stresses, local strain hardening, and nonuniform thickness distribution near corners. These factors may increase strength in some cases but can also unpredictably alter stiffness and failure modes [2, 3]. To improve performance, several reinforcement strategies have been proposed, including bolted connectors, web stiffeners, or edge reinforcements, all of which have been shown to increase both local and global buckling capacity [16–18].

In recent years, attention has also turned toward sustainability and reuse potential. Cold-formed elements, especially those designed for modular construction, may retain structural adequacy after cyclic loading and disassembly, offering opportunities for circular economy applications [9]. However, despite such advances, important aspects of CFS design remain insufficiently addressed.

One critical gap in the literature concerns the role of beam-to-column connections in storage rack systems. These joints are vital for force transfer and overall stability, yet they represent the most damage-prone areas under service and extreme loading. Degradation of rotational stiffness and moment resistance at the connections can severely reduce the axial load-bearing capacity of uprights. Current design methods rarely include this degradation explicitly or fail to quantify it properly [19–21].

Previous research has examined the buckling behavior of perforated CFS columns under axial load through both experiments and numerical studies. Results indicate that local buckling dominates in short columns, distortional or distortional–flexural buckling occurs in medium-length columns, while global buckling governs in long members. Furthermore, numerical predictions have shown close agreement with experimental values, with differences below 5%, and confirmed that the DSM can be applied reliably to such hollow sections without reduction of the net cross-sectional area [22].

Building on these foundations, the present study investigates the effect of joint-induced damage on the axial load capacity of CFS uprights. Axial compression tests were conducted on specimens with different levels of joint degradation, characterized in terms of rotational and moment stiffness. Alongside these parameters, key geometric descriptors such as moment of inertia, wall thickness, and sectional depth were included. A machine learning (ML) model was then developed to predict axial resistance, using both geometric and experimentally derived joint properties as inputs. By integrating physical testing, finite element analysis (FEA), and data-driven modeling, this study provides new insights into the behavior of damaged CFS members and offers a framework for more accurate and resilient design practices in rack systems.

Recent studies have extensively investigated the structural behavior of CFS members with web openings, proposing refined DSM formulations and numerical models to account for the influence of circular and elongated perforations on strength and stability [23–26]. These works demonstrate that perforation geometry and edge stiffening significantly affect local, distortional, and global buckling responses under bending, compression, and shear. However, while such studies provide improved prediction of member resistance, they generally assume idealized boundary conditions and do not explicitly address the effect of beam-to-column joint degradation on the axial capacity of rack uprights subjected to prior cyclic loading.

Despite the progress in modeling perforated CFS members, current rack-system assessment procedures generally treat beam-to-column joints as idealized and do not explicitly incorporate the effects of joint stiffness and moment degradation into upright axial-capacity checks [27]. This represents a practical gap because reduced rotational restraint at the connection may alter the stability path and promote earlier distortional or torsional–flexural (TF) buckling during subsequent compression, even when the upright cross-section remains unchanged [22]. The novelty of the present study is the unified integration of (i) physical testing on intact and joint-damaged uprights; (ii) nonlinear FEA reproducing undamaged, damaged, and bolted-reinforced configurations; and (iii) ML-based capacity prediction using both geometric descriptors and experimentally derived joint properties [28–31]. The objective is to establish and validate a predictive framework for the residual axial capacity of perforated rack uprights that explicitly accounts for connection-induced degradation, thereby supporting practical postdamage assessment and retrofit-oriented decision-making in industrial rack systems [23, 26, 27, 32, 33].

2 | Experimental Program

2.1 | Column Cross-Sections and Material Characterization

Six CFS upright profiles—3.0C1, 2.5C2, 2.0C3, 2.0C4, 2.0U1, and 2.5U2—were selected to represent common members used in storage rack systems. These profiles, manufactured in Türkiye, exhibit different perforation patterns and wall thicknesses (Figure 1). Although the exact geometry of perforations cannot be disclosed for confidentiality reasons, their influence on buckling under axial load is well established. The purpose of the study was to assess the axial capacity of these uprights when subjected to damage occurring at beam-to-column joints.

While the confidential omission of the detailed perforation layout reduces strict reproducibility, the study reports the governing section and material descriptors used in both testing and numerical modeling (e.g., thickness, cross-sectional properties, and measured

7074, 2026, 1, Downloaded from https://onlinelibrary.wiley.com/doi/10.1155/ace/4354889 by Cochrane Romania, Wiley Online Library on [17/10/2026]. See the Terms and Conditions (https://onlinelibrary.wiley.com/terms-and-conditions) on Wiley Online Library for rules of use; OA articles are governed by the applicable Creative Commons License

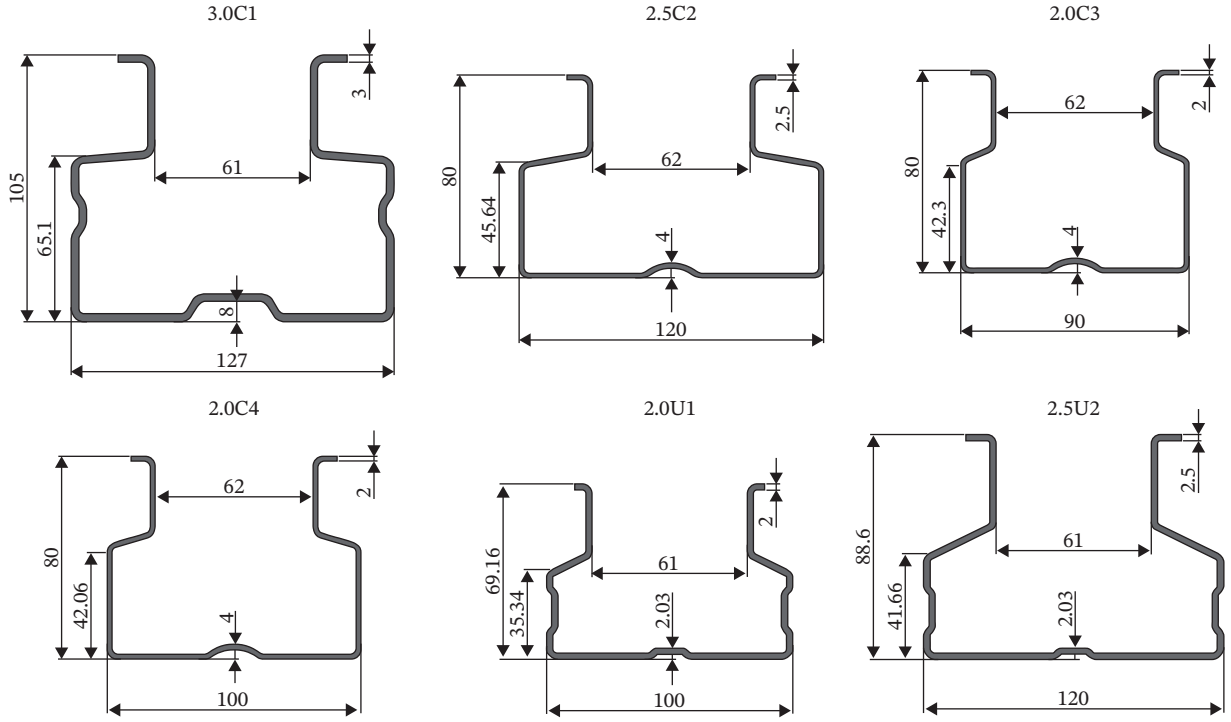

FIGURE 1 | Cross-sectional details of CFS uprights.

steel strength), so that the structural tendencies can be interpreted and checked within the defined geometric framework.

The 760 mm length was also selected to maintain consistency with beam-to-column joint bending tests performed on the same upright families, thereby supporting direct comparisons between connection response and upright axial stability within a common test segment. In addition, the selected segment is sufficiently long to allow representative deformation patterns to develop under axial compression while remaining compatible with the standardized joint-testing configuration.

2.2 | Test Setup and Boundary Conditions

All specimens were tested with a constant length of 760 mm, in accordance with EN 15512 recommendations for beam-to-column joint testing [27]. EN 15512 also specifies that the specimen length shall be greater than three times the greatest flat width of the section (ignoring intermediate stiffeners) and shall include at least five pitches of the perforations [27]. The selected upright length satisfies these geometric requirements for all upright families considered, thereby ensuring that the perforation-induced stiffness reduction is represented over a sufficient number of repeating modules without disclosing the confidential layout. The choice of this uniform length followed the experimental protocol rather than a preliminary buckling analysis; therefore, no dedicated parametric length study was performed prior to testing.

Each specimen was tested with a hybrid support system: one end pinned and the other fixed. This configuration both reflects field conditions and complies with EN 15512 requirements. Posttest visual inspections showed different buckling modes, including local, distortional (symmetric and antisymmetric), torsional, and TF. These observations were based on specimen deformation after testing rather than computational mode decomposition.

In conclusion, although the program did not involve a parametric variation of specimen length or a computational buckling study, the adopted boundary conditions ensured realistic evaluation of axial load behavior in uprights with joint-induced damage. This experimental protocol was intended to replicate field conditions and provide data with high practical relevance. Using a single specimen length may limit the parametric generality of the results; therefore, the present study targets a focused question, namely, the isolated effect of beam-to-column joint damage on the axial capacity and buckling response within a representative rack segment. Despite the confidentiality constraint on perforation details, the close agreement between the numerical models and the experimental responses within the considered upright families supports that the dominant physical tendencies were captured with adequate resolution.

2.3 | Instrumentation, Alignment, and Sources of Variability

Axial load was applied using a 1000 kN hydraulic jack under displacement-controlled loading at a constant rate, and the applied force was recorded by the testing machine/load measurement system. The load measurement accuracy followed the calibration of the laboratory equipment used for the test campaign. Because the primary objective of the present study is the ultimate axial capacity and failure mode identification under standardized boundary conditions, displacement transducers (e.g., LVDTs) were not installed; therefore, the reported outcomes focus on peak load and qualitative buckling classification rather than full load–displacement response.

To minimize unintended eccentricity, the specimens were positioned such that the axial load passed through the effective centroid of the cross-section, and alignment was verified during setup by checking end-plate seating and axiality of the loading

7074, 2026, 1, Downloaded from https://onlinelibrary.wiley.com/doi/10.1155/adce/4354889 by Cochrane Romania, Wiley Online Library on [17/10/2026]. See the Terms and Conditions (https://onlinelibrary.wiley.com/terms-and-conditions) on Wiley Online Library for rules of use; OA articles are governed by the applicable Creative Commons License

line. Despite these measures, small residual eccentricities may remain due to end-plate tolerances, local plate flatness, and assembly clearances. These effects are treated as a potential source of scatter in the measured axial capacities and are addressed through replicate testing where available.

Initial geometric imperfections were not measured systematically prior to testing. This limitation is acknowledged, as thin-walled perforated members are sensitive to imperfection amplitude and shape. The resulting variability is discussed as a modeling assumption/limitation in the FE section. Overall, the experimental program is designed to provide practically representative capacity estimates for intact and joint-damaged configurations under the EN 15512-type boundary conditions, recognizing that unavoidable geometric and setup tolerances contribute to the observed scatter.

3 | Experimental Tests and Results

The experimental program consisted of a sequence of tests designed to characterize the material properties and structural behavior of CFS upright sections under axial compression. Initially, tensile coupon tests were performed to determine the mechanical properties of the steel used in each cross-section. Yield strength and sheet thickness values are summarized in Table 1.

Axial compression tests were then conducted on six upright profiles. Specimens labeled C1, C2, C3, and C4 were derived from a doctoral research study on damaged columns, while U1 and U2 were obtained from a master's thesis focusing on upright behavior [32, 33]. Although originating from different projects, both datasets were produced under comparable testing conditions, ensuring reliable comparison of the influence of prior beam-to-column joint damage on axial performance.

Stub column tests were performed to investigate local buckling. Each profile was tested with one or two replicates depending on its damage state: C1–C4 once and U1 and U2 twice. Undamaged control specimens were also tested in duplicate. Axial loads were applied through the effective centroid of the cross-section in line with European guidelines.

Unlike prior studies that used specific setups to isolate distortional buckling, the present work focused solely on axial compression tests with welded end plates simulating fixed ends. A 1000 kN hydraulic jack applied load at a constant rate of 150 N/s, consistent with literature practice. Loading was stopped when visible buckling occurred. The experimental setup and boundary conditions are shown in Figure 2.



FIGURE 2 | Test setup and loading boundary conditions used in axial compression experiments.

Axial tests were carried out on damaged and undamaged uprights of varying thickness and geometry. Results show that uprights with beam-to-column joint damage exhibited markedly reduced axial capacity compared with intact reference specimens. Visual inspection revealed distortional and TF buckling as the predominant modes in damaged sections, particularly where connection integrity was compromised. In contrast, intact specimens showed delayed buckling and improved axial performance. Typical failure modes are presented in Figure 3.

Specimen-level axial capacities for each profile and configuration are plotted in Figure 4, allowing a direct view of the scatter among individual tests.

To improve the reliability of the comparative evaluation and to explicitly account for experimental variability, the results are also

TABLE 1 | Material characterization of cold-formed steel specimens.

Member	Young's modulus, E (GPa)	Poisson's ratio ν	Thickness, t (mm)	Yield stress, Fy (MPa)	Ultimate stress, Fu (MPa)
3.0C1	210	0.3	3.00	430	576
2.5C2			2.50	430	569
2.0C3			2.00	353	441
2.0C4			2.00	345	437
2.0U1			2.00	336	428
2.5U2			2.50	442	581

7074, 2026, 1, Downloaded from https://onlinelibrary.wiley.com/doi/10.1155/adce/4354889 by Cochrane Romania, Wiley Online Library on [17/10/2026]. See the Terms and Conditions (https://onlinelibrary.wiley.com/terms-and-conditions) on Wiley Online Library for rules of use; OA articles are governed by the applicable Creative Commons License



FIGURE 3 | Typical failure modes observed in tested upright specimens.

summarized statistically by cross-section and condition. Table 2 reports the mean axial capacity, standard deviation (SD), and coefficient of variation (COVID-19) for each group (intact, damaged without bolts, and bolted reinforcement where available). In addition, Figure 5 presents the same comparison graphically, using mean values with error bars (±SD). These statistical descriptors support interpretation of differences between intact and damaged states, and they help contextualize apparent anomalies when the number of specimens is limited.

Geometric and mechanical properties of all sections are summarized in Table 3, while Table 4 compiles axial load capacity, ultimate joint moment, stiffness, and observed failure mode. The labeling system encodes section type, connection arrangement, and reinforcement. For example, in "3.0C1-B120-5T+40-B", "3.0C1" indicates the section and thickness, "B120" the back-to-back configuration, "5T+40" the connector position, and "–B" the bolt reinforcement.

The results show that the axial capacity of uprights is strongly influenced by prior joint testing. Specimen-level capacities are reported in Figure 4, while a statistical comparison by cross-section and condition (mean ± SD) is provided in Table 2 and Figure 5. For 3.0C1, intact specimens averaged 322.96 kN (SD = 5.45 kN), whereas damaged specimens without bolt reinforcement averaged 284.02 kN (SD = 6.59 kN), indicating a clear reduction after joint degradation. For 2.5C2, damaged specimens without bolts averaged 207.17 kN (SD = 18.33 kN), compared to 186.06 kN (SD = 1.44 kN) for intact specimens; this counterintuitive trend is discussed in the dedicated subsection and is interpreted as an observation within the scatter range rather than a general strengthening effect. More pronounced reductions were observed for thinner sections, particularly 2.0C3 (113.63 kN intact vs. 86.19 kN damaged) and 2.0U1 (99.67 kN intact vs. 81.39 kN damaged), where joint-induced stiffness loss is more likely to promote coupled instability. Overall, the statistical summaries confirm that connection-induced degradation can reduce axial capacity and is frequently associated with a shift from distortional to coupled TF buckling modes, highlighting the need to consider joint condition in rack upright assessment and retrofit decisions.

7074, 2026, 1, Downloaded from https://onlinelibrary.wiley.com/doi/10.1155/adce/4354889 by Cochrane Romania, Wiley Online Library on [17/10/2026]. See the Terms and Conditions (https://onlinelibrary.wiley.com/terms-and-conditions) on Wiley Online Library for rules of use; OA articles are governed by the applicable Creative Commons License

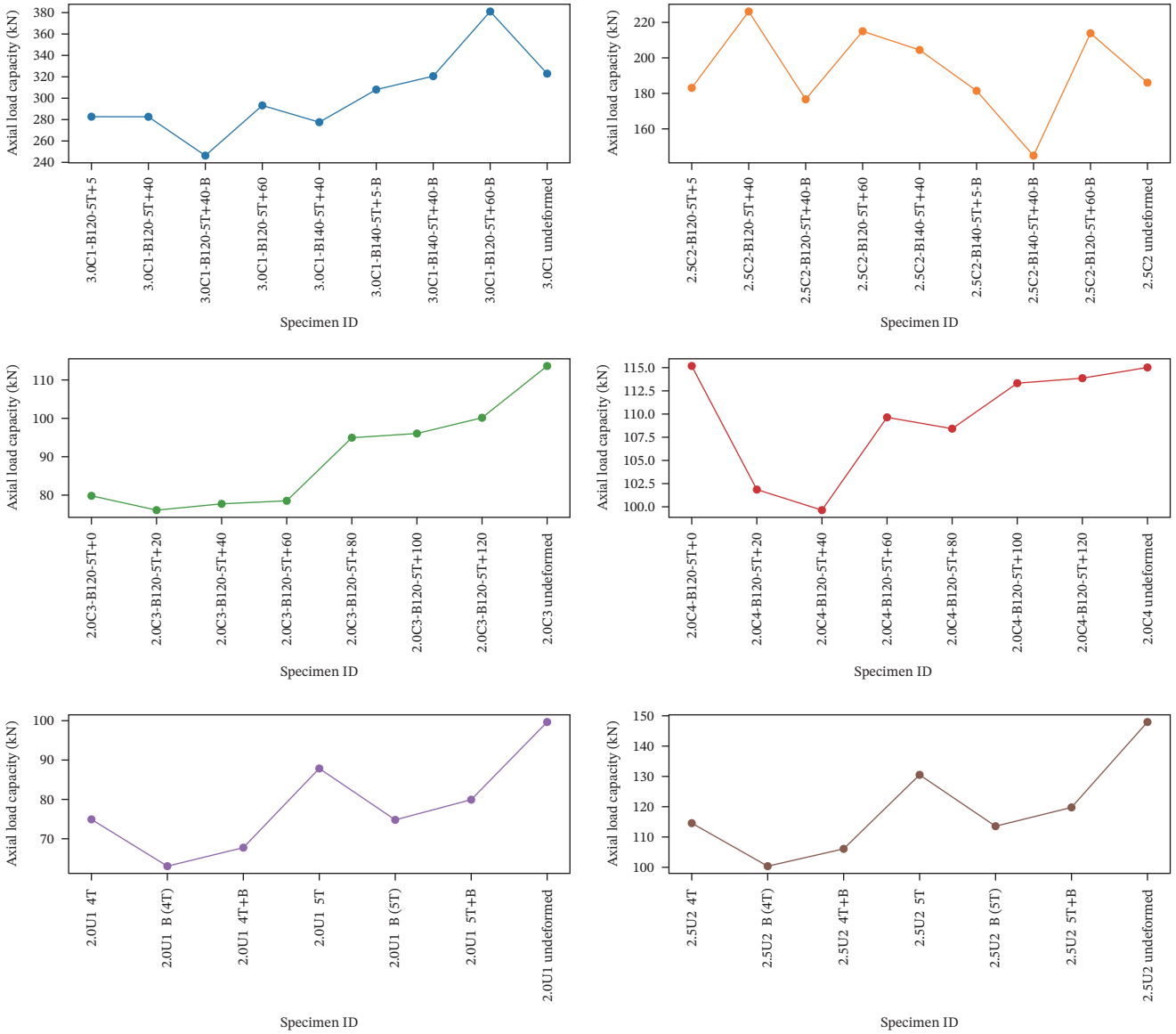

FIGURE 4 | Axial load capacities by cross-section and damage condition.

3.1 | Mechanistic Interpretation of the Failure-Mode Transition

Joint-induced degradation reduces the effective rotational restraint provided by the beam-to-upright connection region. After cyclic joint loading, local damage and stiffness loss may facilitate out-of-plane deformations and warping in the vicinity of the connector zone, increasing the torsional participation of the upright segment during subsequent axial compression. As a result, the stability response can shift from predominantly distortional buckling (D) toward coupled TF behavior (D+TF) because torsional rotation and lateral bending become less restrained once connection stiffness is reduced. This mechanism is consistent with the experimental observations in Figure 3 and the mode labels reported in Table 4, where several damaged configurations exhibit D+TF. The numerical results presented later for predamaged FE models also follow the same trend, supporting the interpretation that connection stiffness degradation promotes coupled instability modes.

3.2 | Sources of Variability and Statistical Treatment

Scatter in axial capacity is expected for thin-walled perforated members and is influenced by multiple factors. The main contributors include (i) material heterogeneity and batch-to-batch variation in yield stress and strain hardening, (ii) initial geometric imperfections and local plate waviness, and (iii) postyield stiffness reduction and localized damage accumulation near the connector region after prior joint tests. In the present experimental campaign, initial imperfections were not measured systematically before testing; therefore, their influence is treated as an inherent source of variability. The reported SD and COVID-19 values in Table 2 should be interpreted in light of the limited number of replicates for some groups, particularly where only two specimens are available. Nevertheless, presenting mean values and variability indicators improves transparency and supports more robust comparison between intact, damaged, and reinforced configurations.

7074, 2026, 1, Downloaded from https://onlinelibrary.wiley.com/doi/10.1155/ade/4354889 by Cochrane Romania, Wiley Online Library on [17/10/2026]. See the Terms and Conditions (https://onlinelibrary.wiley.com/terms-and-conditions) on Wiley Online Library for rules of use; OA articles are governed by the applicable Creative Commons License

TABLE 2 | Statistical summary of axial capacities by section and condition.

Section	Condition	*n*	Mean *P* (kN)	SD (kN)	COVID-19 (%)
3.0C1	Intact	2	322.96	5.45	1.69
3.0C1	Damaged	4	284.02	6.59	2.32
3.0C1	Bolted	4	314.01	55.26	17.60
2.5C2	Intact	2	186.06	1.44	0.78
2.5C2	Damaged	4	207.17	18.33	8.85
2.5C2	Bolted	4	179.22	28.21	15.74
2.0C3	Intact	2	113.63	23.70	20.86
2.0C3	Damaged	7	86.19	10.34	12.00
2.0C4	Intact	2	115.03	1.04	0.90
2.0C4	Damaged	7	108.85	6.05	5.56
2.0U1	Intact	2	99.67	6.33	6.35
2.0U1	Damaged	4	81.39	8.29	10.18
2.0U1	Bolted	8	71.38	8.62	12.08
2.5U2	Intact	2	147.95	7.82	5.29
2.5U2	Damaged	4	122.54	11.59	9.46
2.5U2	Bolted	8	109.94	10.40	9.46

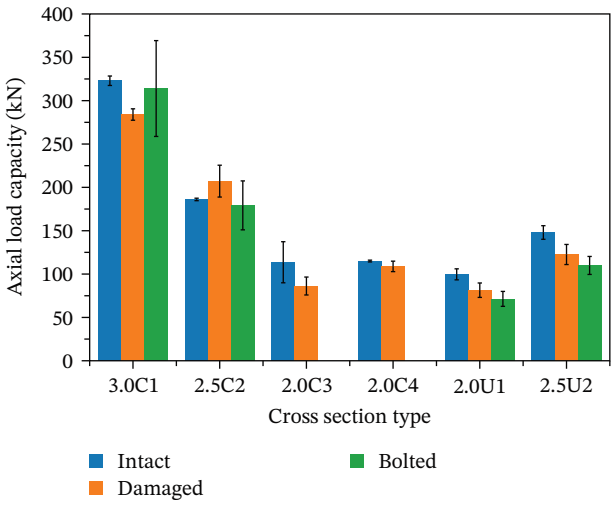

FIGURE 5 | Mean axial load capacity of cold-formed steel uprights for intact, joint-damaged, and bolted-reinforced conditions. Error bars represent ±1 standard deviation based on replicate tests.

3.3 | Comparative Analysis by Cross-Section

The comparative analysis confirms that axial capacity is strongly influenced by prior joint testing. For the 3.0C1 profile, intact specimens averaged 322.96 kN, while damaged specimens without bolt reinforcement averaged 284.02 kN, indicating a reduction of about 12.1%. The bolted configurations show a mean of 314.01 kN but with higher scatter due to the wide range of reinforced configurations included in the dataset (Table 2 and Figure 5). For the 2.5C2 profile, intact specimens averaged 186.06 kN, while the damaged nonbolted group averaged 207.17 kN. This counterintuitive increase is discussed below and should not be interpreted as a systematic strengthening effect, especially given the measured scatter (SD = 18.33 kN) in the damaged group.

For the 2.0C3 profile, intact specimens averaged 113.63 kN, whereas damaged specimens averaged 86.19 kN, corresponding to a reduction of about 24.2%. This section also shows large scatter in the intact group due to the two available replicates. For the 2.0C4 profile, intact specimens averaged 115.03 kN, while damaged specimens averaged 108.85 kN, corresponding to a smaller reduction of about 5.4%.

For the 2.0U1 profile, intact specimens averaged 99.67 kN, while damaged specimens averaged 81.39 kN. Bolted configurations averaged 71.38 kN, indicating that, for this dataset, bolting does not necessarily recover capacity for all configurations and highlights the role of local damage state and connector details. For the 2.5U2 profile, intact specimens averaged 147.95 kN, while damaged specimens averaged 122.54 kN, and bolted configurations averaged 109.94 kN (Table 2 and Figure 5).

3.4 | Discussion of Anomalous Trend in 2.5C2

For the 2.5C2 group, the damaged nonbolted mean capacity exceeds the intact mean. This trend may be explained by imperfection sensitivity and limited sample size. Thin-walled members can exhibit significant capacity variation for small changes in the initial imperfection field, and since imperfections were not measured, a favorable imperfection pattern for the damaged specimens cannot be excluded. In addition, the joint loading phase may induce local straightening or redistribution of residual stresses that could slightly affect subsequent axial behavior. Finally, the difference between intact and damaged means is within the variability range indicated by the damaged group SD (Table 2 and Figure 5). For these reasons, the 2.5C2 increase is reported as an observation rather than a general conclusion, and additional replicates are recommended to confirm the trend.

7074, 2026, 1, Downloaded from https://onlinelibrary.wiley.com/doi/10.1155/adce/4354889 by Cochrane Romania, Wiley Online Library on [17/10/2026]. See the Terms and Conditions (https://onlinelibrary.wiley.com/terms-and-conditions) on Wiley Online Library for rules of use; OA articles are governed by the applicable Creative Commons License

TABLE 3 | Geometric and mechanical properties of upright sections.

Label	Thickness (mm)	Area (mm^2)	Perimeter (mm)	Bounding box X (min)	Bounding box X (max)	Bounding box Y (min)	Bounding box Y (max)	Moment of inertia X (mm^4)	Moment of inertia Y (mm^4)
3.0C1	3.0	1224.11	825	−63.31	63.69	−41.43	63.57	1,508,284	2,591,830
2.5C3	2.5	825.59	665	−60.00	60.00	−29.27	51.23	595,318	1,534,702
2.0C3	2.0	545.46	549	−45.00	45.00	−30.31	49.69	411,242	673,922
2.0C4	2.0	581.08	585	−50.00	50.00	−29.63	50.37	428,283	831,151
2.0U1	2.0	513.26	517	−48.50	48.50	−23.61	45.05	266,054	661,603
2.5U2	2.5	849.21	684	−59.00	59.00	−32.41	56.19	764,901	1,481,970

TABLE 4 | Summary of axial compression test results and failure characteristics.

Specimen ID	Axial load capacity (kN)	Ultimate moment (kN m)	Stiffness (kNm/rad)	Material class	Mode
3.0C1-B120-5T+5	282.69	4.73	458.47	S355	D
3.0C1-B120-5T+40	282.61	4.98	220.34	S355	D
3.0C1-B120-5T+40-B	246.31	4.37	297.83	S355	D+TF
3.0C1-B120-5T+60	293.23	4.89	343.70	S355	D
3.0C1-B140-5T+40	277.55	5.59	410.38	S355	D
3.0C1-B140-5T+5-B	308.06	5.08	157.24	S355	D+TF
3.0C1-B140-5T+40-B	320.59	5.00	187.76	S355	D+TF
3.0C1-B120-5T+60-B	381.08	4.81	211.86	S355	D+TF
3.0C1 undeformed	319.10			S355	D
3.0C1 undeformed	326.81			S355	D
2.5C2-B120-5T+5	183.09	4.45	323.51	S355	D
2.5C2-B120-5T+40	226.14	4.78	209.90	S355	D
2.5C2-B120-5T+40-B	176.65	2.55	236.55	S355	D+TF
2.5C2-B120-5T+60	214.99	3.80	244.49	S355	D
2.5C2-B140-5T+40	204.47	5.38	247.61	S355	D+TF
2.5C2-B140-5T+5-B	181.44	4.71	188.74	S355	D+TF
2.5C2-B140-5T+40-B	144.93	4.28	135.32	S355	D+TF
2.5C2-B120-5T+60-B	213.87	3.71	76.36	S355	D+TF
2.5C2 undeformed	187.08			S355	D
2.5C2 undeformed	185.04			S355	D
2.0C3-B120-5T+0	79.82	3.62	257.23	S235	D
2.0C3-B120-5T+20	76.09	4.15	261.81	S235	D
2.0C3-B120-5T+40	77.72	4.30	234.84	S235	D
2.0C3-B120-5T+60	78.52	3.98	199.53	S235	D
2.0C3-B120-5T+80	94.95	3.58	182.23	S235	D+TF
2.0C3-B120-5T+100	96.05	3.13	174.90	S235	D+TF
2.0C3-B120-5T+120	100.15	2.65	169.93	S235	D+TF
2.0C3 undeformed	130.39			S235	D+TF
2.0C3 undeformed	96.87			S235	D+TF

(Continues)

7074, 2026, 1, Downloaded from https://onlinelibrary.wiley.com/doi/10.1155/adce/4354889 by Cochrane Romania, Wiley Online Library on [17/10/2026]. See the Terms and Conditions (https://onlinelibrary.wiley.com/terms-and-conditions) on Wiley Online Library for rules of use; OA articles are governed by the applicable Creative Commons License

TABLE 4 | (Continued)

Specimen ID	Axial load capacity (kN)	Ultimate moment (kN m)	Stiffness (kNm/rad)	Material class	Mode
2.0C4-B120-5T+0	115.18	4.05	213.15	S235	D
2.0C4-B120-5T+20	101.86	4.32	227.33	S235	D
2.0C4-B120-5T+40	99.64	4.41	199.82	S235	D
2.0C4-B120-5T+60	109.65	4.11	173.14	S235	D
2.0C4-B120-5T+80	108.42	3.55	160.81	S235	D+TF
2.0C4-B120-5T+100	113.33	3.11	150.27	S235	D+TF
2.0C4-B120-5T+120	113.86	2.56	145.86	S235	D+TF
2.0C4 undeformed	114.29			S235	D+TF
2.0C4 undeformed	115.76			S235	D+TF
2.0U1 4T	74.77	2.01	101.19	S235	D
2.0U1 4T	75.08	2.25	110.88	S235	D
2.0U1 B (4T)	66.77	2.78	68.36	S235	D+TF
2.0U1 B (4T)	59.29	2.60	76.43	S235	D+TF
2.0U1 4T+B	60.56	3.10	132.03	S235	D+TF
2.0U1 4T+B	74.93	3.29	121.18	S235	D+TF
2.0U1 5T	83.46	2.44	152.01	S235	D
2.0U1 5T	92.26	2.22	165.65	S235	D
2.0U1 B (5T)	70.45	2.93	87.90	S235	D+TF
2.0U1 B (5T)	79.15	3.05	95.64	S235	D+TF
2.0U1 5T+B	82.72	3.48	181.40	S235	D+TF
2.0U1 5T+B	77.14	3.22	193.44	S235	D+TF
2.0U1 undeformed	95.19			S235	D
2.0U1 undeformed	104.14			S235	D
2.5U2 4T	109.59	2.39	127.35	S355	D
2.5U2 4T	119.54	2.73	141.58	S355	D
2.5U2 B (4T)	109.71	3.21	82.15	S355	D+TF
2.5U2 B (4T)	91.01	2.90	87.21	S355	D+TF
2.5U2 4T+B	109.50	4.06	153.94	S355	D+TF
2.5U2 4T+B	102.65	3.62	161.67	S355	D+TF
2.5U2 5T	137.55	2.95	179.81	S355	D
2.5U2 5T	123.48	2.89	192.43	S355	D
2.5U2 B (5T)	120.72	3.69	110.99	S355	D+TF
2.5U2 B (5T)	106.38	3.98	123.37	S355	D+TF
2.5U2 5T+B	116.34	4.21	228.60	S355	D+TF
2.5U2 5T+B	123.18	3.96	209.52	S355	D+TF
2.5U2 undeformed	153.48			S355	D
2.5U2 undeformed	142.42			S355	D

In summary, specimen-level results in Figure 4 show that damage at beam-to-column joints can reduce axial capacity depending on cross-section type and damage state, and that failure modes often shift toward coupled TF behavior in damaged configurations. The statistical summary in Table 2 and the mean ± SD comparison in Figure 5 confirm that reductions are generally more pronounced for thinner and lower-grade steel sections. These findings emphasize that connection-induced degradation should be considered in

7074, 2026, 1, Downloaded from https://onlinelibrary.wiley.com/doi/10.1155/adce/4354889 by Cochrane Romania, Wiley Online Library on [17/10/2026]. See the Terms and Conditions (https://onlinelibrary.wiley.com/terms-and-conditions) on Wiley Online Library for rules of use; OA articles are governed by the applicable Creative Commons License

the structural assessment of CFS rack uprights and motivate the subsequent ML and FEA for predictive evaluation.

4 | Estimating the Axial Load Capacity of Damaged Columns Using ML

Accurate estimation of the axial load capacity of damaged columns is essential for structural safety assessment and performance evaluation. Conventional analytical approaches often fail to provide reliable predictions when sections are geometrically complex or affected by degradation. Consequently, ML methods have emerged as flexible and robust alternatives for predictive modeling in structural engineering [28–30].

4.1 | Dataset and Feature Selection

In this study, a dataset was constructed by combining experimental results from axial compression tests with corresponding geometric and mechanical properties. The input features include ultimate moment (kNm), rotational stiffness (kNm/rad), yield strength (MPa), wall thickness, cross-sectional area, moments of inertia (about X and Y axes), radii of gyration (X and Y axes), and a binary indicator for bolted reinforcement. The target variable is the axial load capacity (kN).

A correlation matrix was generated to identify relationships between variables. As shown in Figure 6, strong positive correlations were observed between axial capacity and parameters such as moment of inertia, area, and wall thickness. These results are consistent with published findings emphasizing the decisive role of cross-sectional geometry in structural resistance [28–31].

The dataset employed in this study comprises 46 experimental observations, all derived from original axial compression tests on CFS columns subjected to joint-induced damage. Unlike conventional column compression studies, the investigated specimens incorporate damage originating from beam-to-column connection degradation, a condition that has not been experimentally

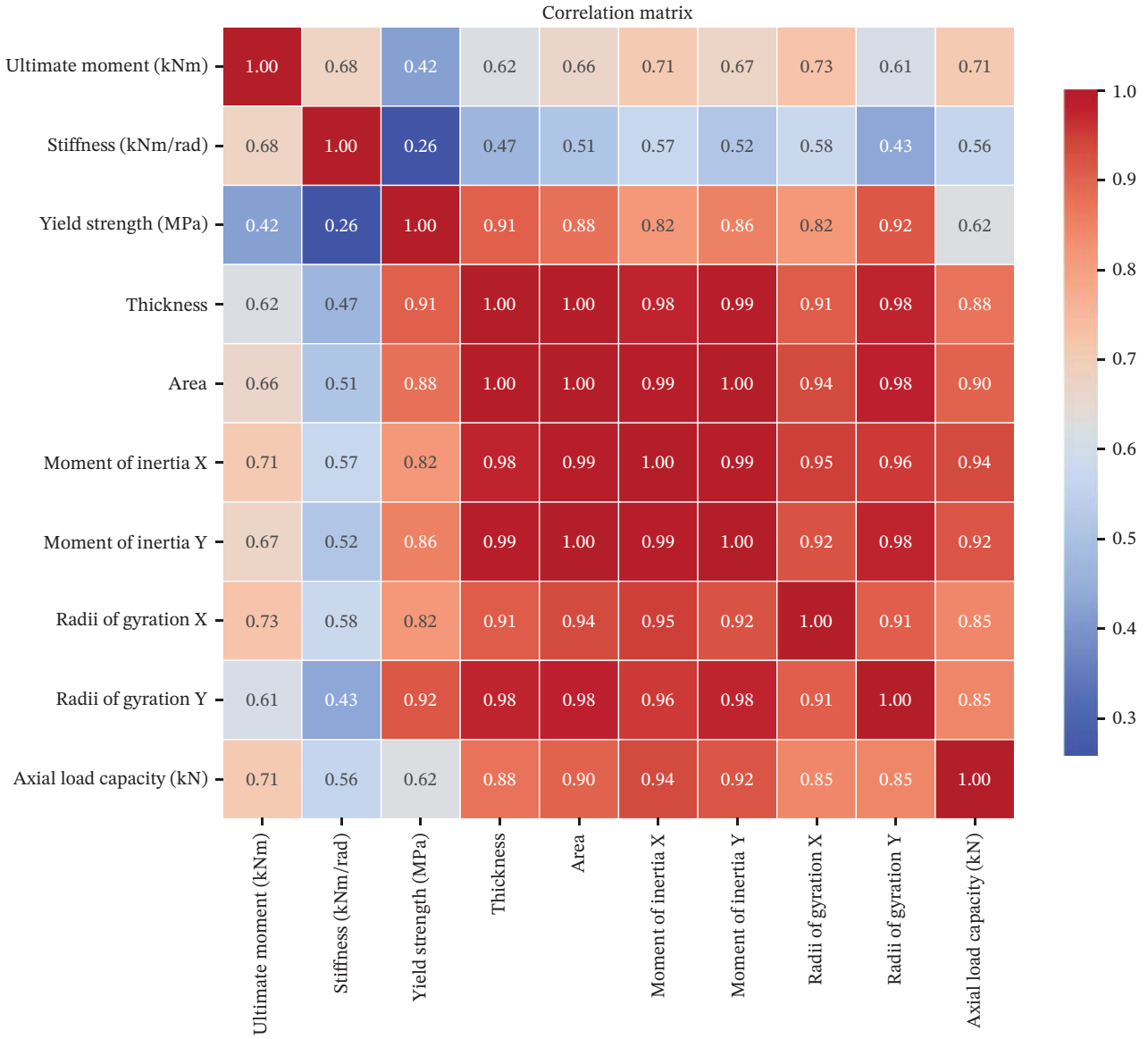

FIGURE 6 | Correlation matrix of all numerical variables in the model.

7074, 2026, 1, Downloaded from https://onlinelibrary.wiley.com/doi/10.1155/ace/4354889 by Cochrane Romania, Wiley Online Library on [17/10/2026]. See the Terms and Conditions (https://onlinelibrary.wiley.com/terms-and-conditions) on Wiley Online Library for rules of use; OA articles are governed by the applicable Creative Commons License

examined in previous literature. Consequently, the dataset size reflects the novelty and experimental complexity of the problem rather than a limitation in data selection.

To mitigate overfitting risks associated with limited sample size, a k-fold cross-validation scheme ($k = 5$) was adopted across the full dataset. Model performance was evaluated using cross-validated root mean square error (RMSE) and mean absolute error (MAE), in addition to the coefficient of determination (R^2). This strategy ensures that the reported predictive accuracy is representative of the model's generalization capability rather than a single train–test split.

The input feature set includes geometric properties, joint-related mechanical parameters, and material characteristics. The presence of bolt reinforcement in the damaged connection region is encoded as a binary variable, where 0 indicates unbolted specimens and 1 represents bolted specimens, allowing the model to explicitly distinguish the contribution of mechanical reinforcement to axial capacity.

While the present dataset is sufficient to demonstrate the feasibility and interpretability of the proposed framework, future studies will focus on expanding the experimental database through additional test campaigns, enabling further enhancement of model robustness and broader applicability.

4.2 | Model Training and Performance Comparison

The dataset was divided evenly into training and testing subsets (50% each) to provide an initial assessment of model performance. Six regression-based ML algorithms were implemented, namely, gradient boosting, random forest, extra trees, bagging, AdaBoost, and ridge regression, in order to examine different learning paradigms ranging from ensemble tree-based methods to linear regularized models. To reduce the potential bias associated with a single train–test split, an additional cross-validation-based evaluation strategy was adopted, as described below.

Rather than relying solely on the coefficient of determination (R^2) obtained from a single data split, model performance was systematically evaluated using a 5-fold cross-validation procedure applied to the entire dataset. Predictive accuracy was quantified using the RMSE and MAE, in addition to R^2, providing a more comprehensive assessment of model generalization capability under limited data conditions.

To ensure a fair and stable comparison between algorithms, baseline hyperparameter configurations recommended in the scikit-learn framework were adopted for all models, followed by moderate manual adjustments to prevent excessive model complexity. Key parameters were kept at conservative defaults to avoid overfitting. An exhaustive grid-search optimization was deliberately avoided, as such approaches may introduce optimistic bias and unstable parameter selection when applied to small experimental datasets. This strategy allowed each model to be evaluated under comparable and controlled conditions.

The average training time required for each algorithm was also recorded and included in the comparison to assess computational efficiency alongside predictive accuracy. A summary of the cross-validated performance metrics, including R^2, RMSE, MAE, and training time, is provided in Table 5.

Figure 7 presents a comparative evaluation of the ML models based on their cross-validated RMSE values. Among the evaluated algorithms, the gradient boosting regressor demonstrated the most favorable balance between prediction accuracy and computational efficiency, consistently achieving the lowest RMSE and MAE values across validation folds. Accordingly, this model was selected for subsequent interpretation and for integration into the graphical user interface (GUI) developed in this study.

4.3 | Detailed Analysis of the Best Model

Based on the cross-validated performance metrics discussed in the previous section, the gradient boosting regressor was selected as the optimal predictive model. This selection was justified by its

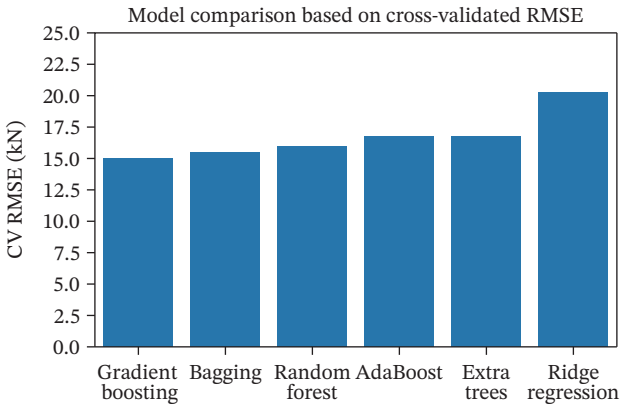

FIGURE 7 | Comparison of machine learning models based on cross-validated root mean square error (RMSE). The results demonstrate that the gradient boosting regressor achieves the lowest prediction error among the evaluated algorithms, indicating superior generalization performance under limited data conditions.

TABLE 5 | Cross-validated performance comparison of machine learning models for axial load capacity prediction.

Model	R^2 (CV mean)	MAE (kN, CV mean)	RMSE (kN, CV mean)	Training time (s)
Gradient boosting	0.96	10	15	34.6
Bagging	0.96	9.9	15.4	66
Random forest	0.95	10	15.9	191.3
AdaBoost	0.95	11.3	16.7	39.1
Extra trees	0.94	10.3	16.8	120.2
Ridge regression	0.91	12.6	20.3	0.6

7074, 2026, 1, Downloaded from https://onlinelibrary.wiley.com/doi/10.1155/adce/4354889 by Cochrane Romania, Wiley Online Library on [17/10/2026]. See the Terms and Conditions (https://onlinelibrary.wiley.com/terms-and-conditions) on Wiley Online Library for rules of use; OA articles are governed by the applicable Creative Commons License

superior generalization capability, as evidenced by the lowest cross-validated RMSE and MAE values among all evaluated algorithms, while maintaining reasonable computational efficiency.

To ensure that the predictive behavior of the selected model is both statistically reliable and physically meaningful, the model predictions were compared against the experimental axial load capacity values together with uncertainty bounds derived from cross-validation. Figure 8 presents the predicted versus experimental axial load capacities, including ± RMSE error bands, providing a direct visual assessment of prediction accuracy and dispersion.

To further investigate the physical consistency of the selected model, the contribution of each input feature was examined using SHAP-based explainability analysis. The SHAP summary plot shown in Figure 9 illustrates the global influence and directionality of the model input parameters on the predicted axial load capacity.

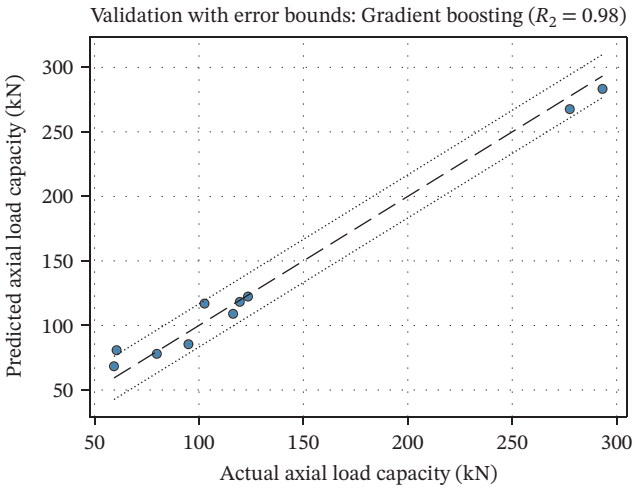

FIGURE 8 | Comparison of predicted and experimental axial load capacities with ± RMSE uncertainty bounds.

Stability-related section properties, particularly the second moments of inertia and radii of gyration, emerged as dominant predictors. This outcome is mechanically consistent with the governing response of damaged thin-walled steel columns under axial compression. Following joint-induced damage, axial resistance becomes increasingly sensitive to flexural stiffness and instability effects, as local damage, geometric imperfections, and potential eccentricities amplify second-order responses. Consequently, parameters controlling flexural rigidity (EI) and column slenderness ($\lambda = L/r$) naturally exert strong influence on the axial load-bearing capacity.

In contrast, yield strength and joint-related rotational stiffness exhibited comparatively lower influence in the explainability analysis. This observation does not imply a lack of physical relevance; rather, it reflects the characteristics of the present dataset and the governing failure mechanisms. Yield strength was introduced as a nominal mapped value based on material class, resulting in limited variability relative to geometric descriptors. Moreover, rotational stiffness primarily characterizes joint-level behavior, whereas axial capacity after damage is governed predominantly by global or coupled instability mechanisms. As a result, these parameters contribute indirectly and appear secondary in the model predictions.

4.4 | User Interface for Practical Implementation

To facilitate practical use of the proposed ML framework, a GUI was developed to provide rapid estimates of axial load capacity from user-defined geometric and mechanical inputs. The GUI directly implements the trained gradient boosting model and applies the same preprocessing workflow used during model development, ensuring full consistency with the training feature set.

The predictive reliability of the GUI output was assessed by comparing model predictions with the corresponding experimental axial capacities. Figure 8 presents the validation in terms of

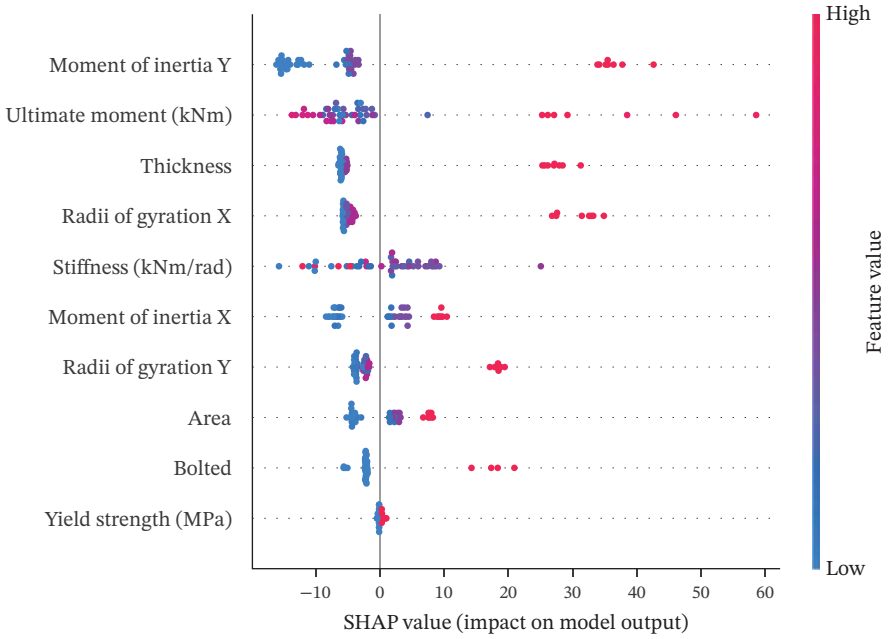

FIGURE 9 | SHAP summary plot showing the global influence of input features on axial load capacity predictions.

7074, 2026, 1, Downloaded from https://onlinelibrary.wiley.com/doi/10.1155/ace/4354889 by Cochrane Romania, Wiley Online Library on [17/10/2026]. See the Terms and Conditions (https://onlinelibrary.wiley.com/terms-and-conditions) on Wiley Online Library for rules of use; OA articles are governed by the applicable Creative Commons License

predicted versus experimental capacities, together with uncertainty bounds defined as ±RMSE obtained from *k*-fold cross-validation. Reporting this error band visualizes the expected dispersion of predictions and provides a practical confidence interval for engineering interpretation.

Overall, most predictions lie within the ±RMSE limits, indicating that the GUI-based implementation preserves the predictive performance of the underlying model. Within the range of profiles, joint conditions, and parameter values represented in the dataset, the GUI therefore serves as a practical decision-support tool for rapid screening of residual axial capacity in damaged CFS uprights.

5 | FEA of Section 3.0C1

5.1 | General Approach

To ensure consistency between experimental and numerical results, three FE models were defined to match the tested configurations:

- Model A (undeformed): Represents the pristine upright and corresponds to specimens 3.0C1 undeformed.
- Model B (Ppredamaged): Simulates degradation from cyclic joint loading without reinforcement. This reflects specimens such as 3.0C1-B120-5T+40, 3.0C1-B120-5T+60, and 3.0C1-B140-5T+40.
- Model C (predamaged + bolts): Includes reinforcement with two bolts above and below the connector zone, corresponding to specimens such as 3.0C1-B120-5T+40-B, 3.0C1-B140-5T+5-B, 3.0C1-B140-5T+40-B, and 3.0C1-B120-5T +60-B.

All models were developed in ANSYS 2023 R1 to assess the influence of joint degradation and reinforcement on the axial resistance of CFS uprights. Geometry, material properties, boundary conditions, and meshing strategies were identical across models; only the connector region was varied to simulate damage or reinforcement.

In the baseline FE models, the upright geometry is idealized (nominal dimensions), and residual stresses from cold-forming are not explicitly modeled. These assumptions are common in capacity-oriented simulations but may lead to slight overestimation of the ultimate load compared to experiments, particularly for thin-walled members where initial geometric imperfections and residual stress patterns influence the stability path. The observed ~5% overestimation of the undamaged model is therefore attributed primarily to the absence of measured initial imperfections and residual stresses. No explicit geometric imperfection sensitivity analysis was performed; the numerical results are based on nominal geometry calibrated against experimental data, and the effect of imperfection amplitude is acknowledged as a limitation of the present study.

5.2 | Geometry and Mesh

The simulated upright replicated the experimental geometry, consisting of two back-to-back C-shaped profiles (B120 configuration) with a total length of 760 mm. The net area of the 3.0C1 section was 1229 mm^2.

A mesh of SOLID186 hexahedral and tetrahedral elements was adopted for the uprights, connector zones, and end plates. This strategy ensured fine resolution at stress concentration zones while maintaining computational efficiency. Mesh sensitivity confirmed convergence. The final mesh included 34,518 nodes and 6293 elements, with a minimum element quality of 0.34 and an average of 0.68. The meshed geometry is shown in Figure 10.

This modeling approach is consistent with previous studies validating FE models for perforated CFS uprights under axial loading [22].

A formal multilevel mesh convergence study was not repeated in the present revision. Instead, mesh adequacy was ensured through an engineering-based discretization strategy and mesh-quality verification. The characteristic element size in the thin-walled regions was selected with direct reference to the sheet thickness ($t = 2$ mm), ensuring sufficient resolution across the plate elements and in the connector region where stress gradients are highest. The mesh was locally refined in the connector zone and other expected localization areas, while a coarser discretization was used away from these regions to maintain computational efficiency. Mesh quality was assessed using standard quality indicators; the minimum element quality and average element quality values reported for the final mesh confirm that the adopted discretization is within an acceptable range for nonlinear collapse simulations. In addition, the predicted deformation patterns and localization zones at peak load were stable and mechanically consistent with the experimentally observed failure modes, providing further confidence that the selected mesh is adequate for the objectives of this study.

5.3 | Material Definition

The constitutive model was based on tensile test data. A true stress–strain curve was derived, capturing strain hardening behavior observed experimentally.

The material was defined as S355 steel with isotropic elasticity ($E = 210$ GPa and $\nu = 0.3$) and multilinear isotropic hardening. The stress–strain relationship is illustrated in Figure 11.

Residual stresses induced by cold-forming were not explicitly included due to the lack of direct residual stress measurements for the tested sections. This modeling choice is stated as a limitation and is expected to contribute to a modest overestimation of strength for the undamaged configuration. This is acknowledged as a limitation.

5.4 | Boundary Conditions and Loading

In the FE simulations, boundary conditions were implemented through remote constraints applied to the end plates. The bottom end plate was fully fixed (all translations and rotations). At the top end plate, lateral translations and rotations were constrained, and only the vertical displacement degree of freedom was released to apply axial compression through a prescribed remote displacement (Figure 12). This "guided" boundary condition was adopted to ensure stable axial loading, avoid rigid-body motion, and replicate the constrained end-plate loading arrangement used in the experimental setup. No additional intermediate lateral bracing or stabilizing constraints were introduced along the member length. The potential influence of constraining lateral

7074, 2026, 1, Downloaded from https://onlinelibrary.wiley.com/doi/10.1155/adce/4354889 by Cochrane Romania, Wiley Online Library on [17/10/2026]. See the Terms and Conditions (https://onlinelibrary.wiley.com/terms-and-conditions) on Wiley Online Library for rules of use; OA articles are governed by the applicable Creative Commons License

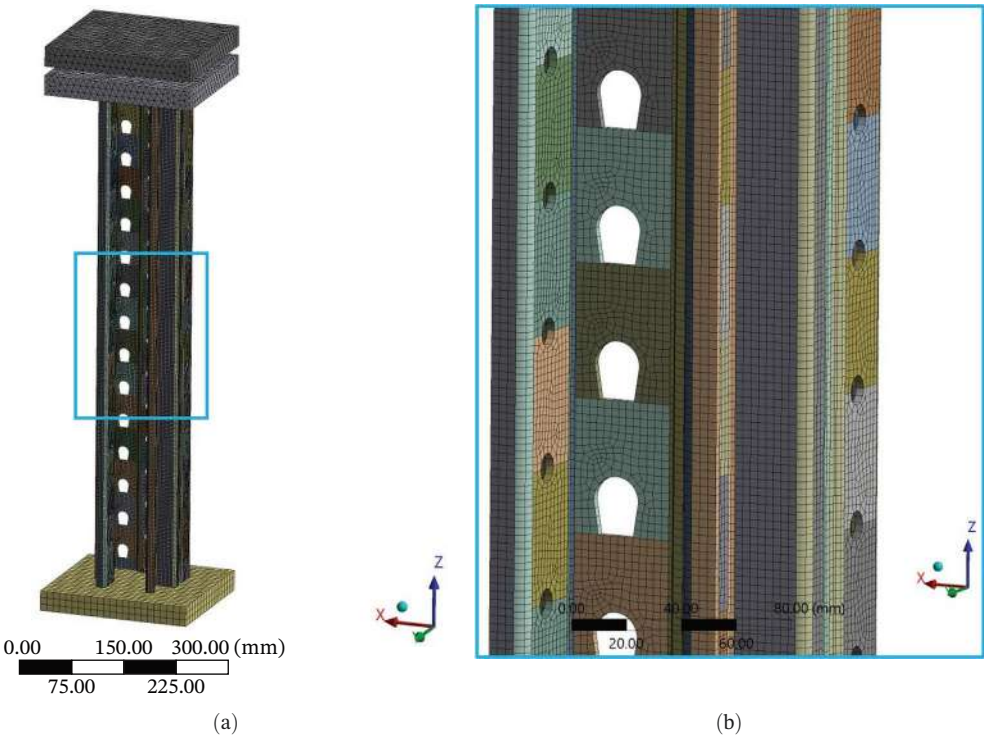

(a) (b)

FIGURE 10 | (a) Finite element mesh of the undamaged Model A (3.0C1). (b) Detail of the mesh.

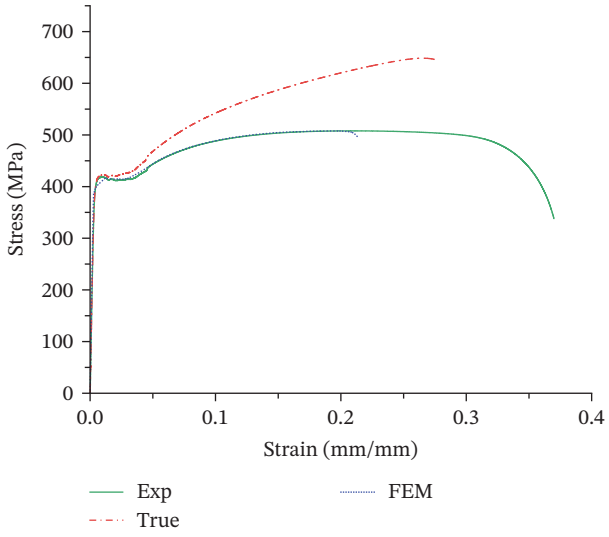

FIGURE 11 | True stress–strain curve derived from experimental tensile testing of S355 cold-formed steel.

degrees of freedom at the loaded end—i.e., an increase in effective lateral restraint compared to an ideal pin—is acknowledged and discussed as a modeling assumption when interpreting the predicted capacity and buckling response.

5.5 | Results and Discussion by Model

5.5.1 | Model A: Undeformed Column

Figures 13–15 illustrate the deformed shape and stress distribution. Maximum stresses occurred at critical regions, matching expectations. The FE-predicted axial capacity was 341 kN, slightly above the experimental mean of 326.8 kN. The overestimation reflects the absence of imperfections and residual stresses in the model.

5.5.2 | Model B: Predamaged Column

Connector degradation was simulated through localized stiffness reduction and notch-type defects, as illustrated in Figure 16. The results, shown in Figures 17–19, revealed reduced axial capacity and asymmetric deformation consistent with damaged specimens such as 3.0C1-B120-5T+40.

5.5.3 | Model C: Predamaged Column With Bolts

Model C introduced bolt reinforcement around the connector region (Figure 20). The redistribution of stresses and stabilized deformations are shown in Figures 21–23. Results confirm partial recovery of axial capacity compared with Model B, though not to the level of Model A.

The increased TF involvement observed in the predamaged configurations can be explained by the reduction of rotational restraint and local stiffness in the connector region. In the undamaged state, the intact connector zone and end-plate assembly provide stronger restraint against torsional rotation and warping-related deformation. After joint degradation, local stiffness loss and geometric disturbance around the connector reduce this restraint and facilitate out-of-plane deformations, so lateral bending and torsional rotation develop in a coupled manner under axial compression. This leads to asymmetric deformation patterns and stress localization consistent with TF participation, as observed in the numerical results for the predamaged models. Direct experimental measurements of displacement or strain were not available in the test campaign; therefore, quantitative FE–experiment

7074, 2026, 1, Downloaded from https://onlinelibrary.wiley.com/doi/10.1155/adce/4354889 by Cochrane Romania, Wiley Online Library on [17/10/2026]. See the Terms and Conditions (https://onlinelibrary.wiley.com/terms-and-conditions) on Wiley Online Library for rules of use; OA articles are governed by the applicable Creative Commons License

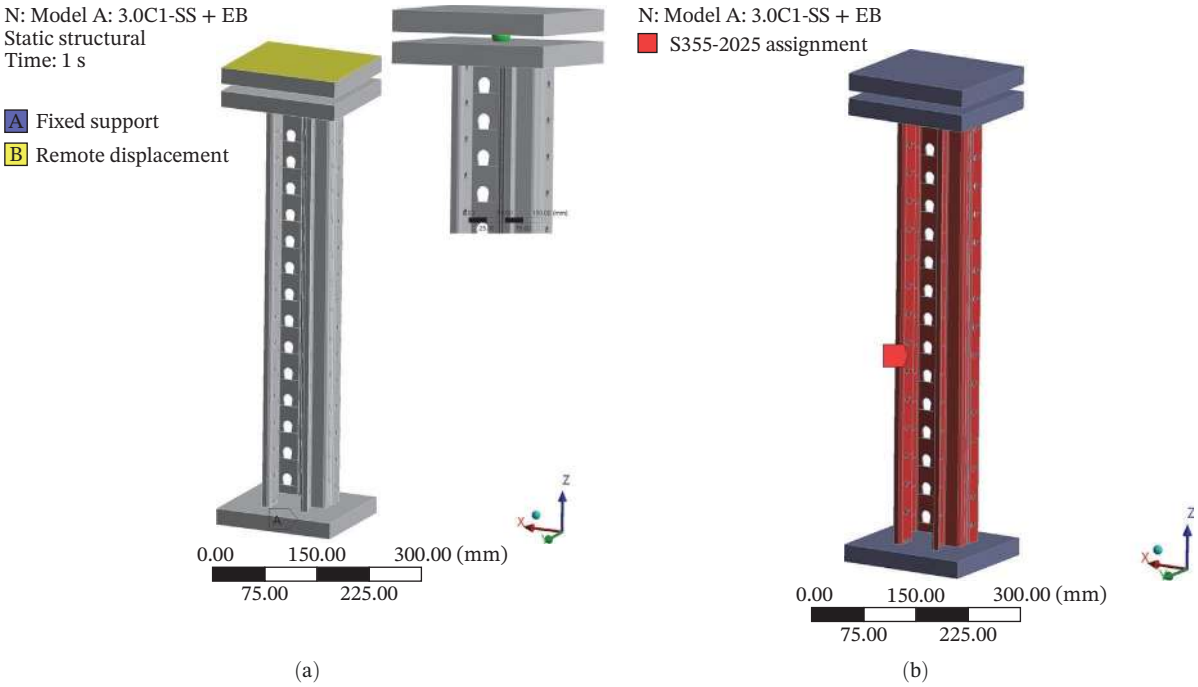

FIGURE 12 | (a) Boundary condition and load application scheme. (b) Material assignment.

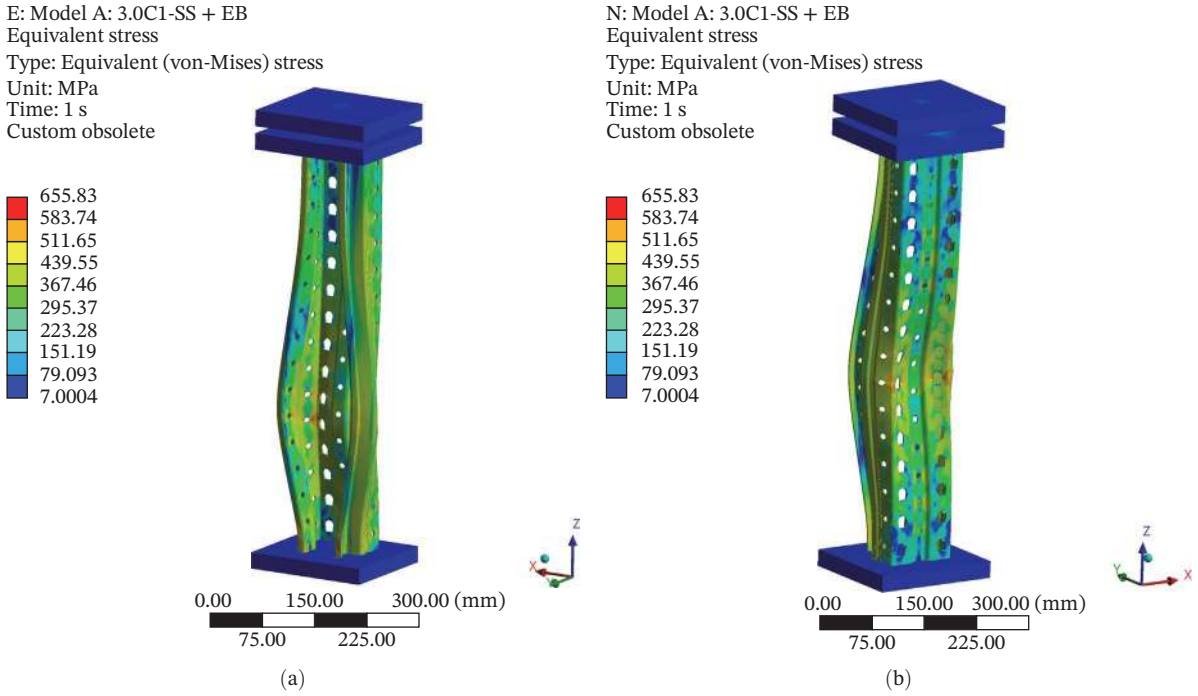

FIGURE 13 | Deformed shape and von Mises stress distribution in Model A: (a) front view and (b) rear lateral view.

comparisons of deformation or strain fields cannot be provided, and validation is based on ultimate capacity and observed failure mode correspondence.

5.6 | Summary of Results

The load–displacement responses of the three models are compared in Figure 24. Model A (undeformed) reached a peak axial capacity of 341 kN, compared with an experimental mean of 326.8 kN. Model B (predamaged) reached 305 kN, compared with an experimental mean of 290 kN, while Model C (predamaged with bolt reinforcement) reached 335 kN, compared with an experimental mean of 320 kN. Overall, the numerical results reproduce the experimentally observed capacity hierarchy (undeformed > reinforced > predamaged) and remain within a few percent of the corresponding test values.

These results support two key observations. First, connection-induced degradation reduces axial load capacity and promotes

7074, 2026, 1, Downloaded from https://onlinelibrary.wiley.com/doi/10.1155/adce/4354889 by Cochrane Romania, Wiley Online Library on [17/10/2026]. See the Terms and Conditions (https://onlinelibrary.wiley.com/terms-and-conditions) on Wiley Online Library for rules of use; OA articles are governed by the applicable Creative Commons License

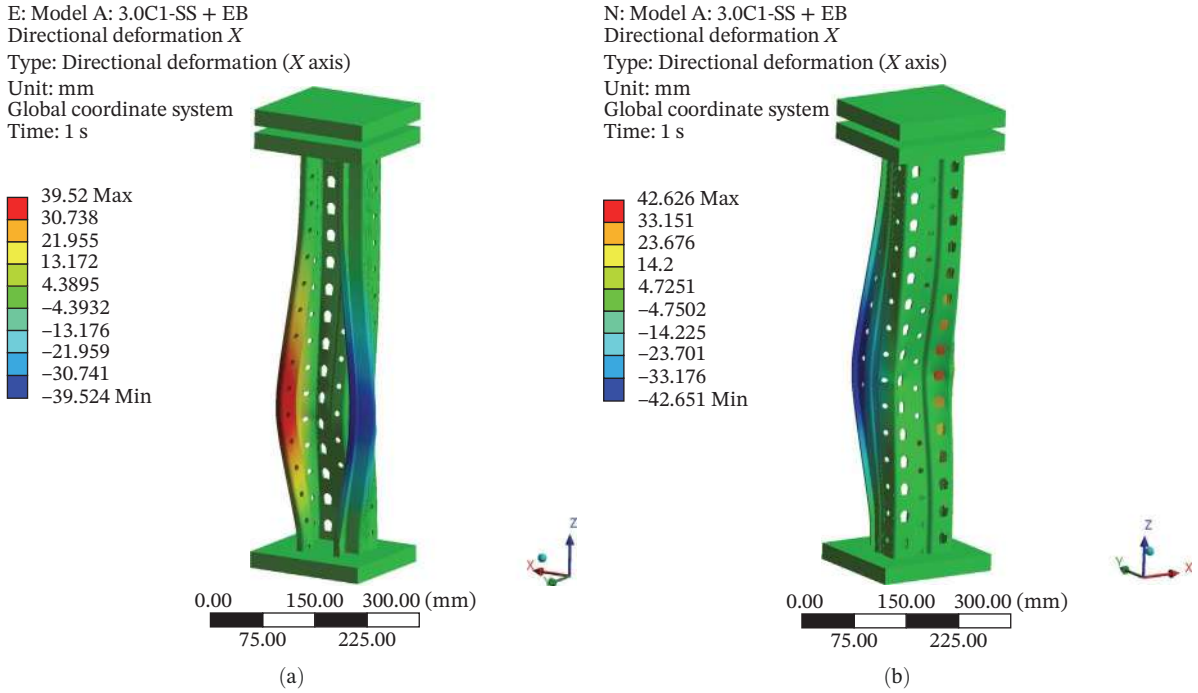

FIGURE 14 | Directional deformation (*X*–axis) in Model A: (a) front view and (b) rear view.

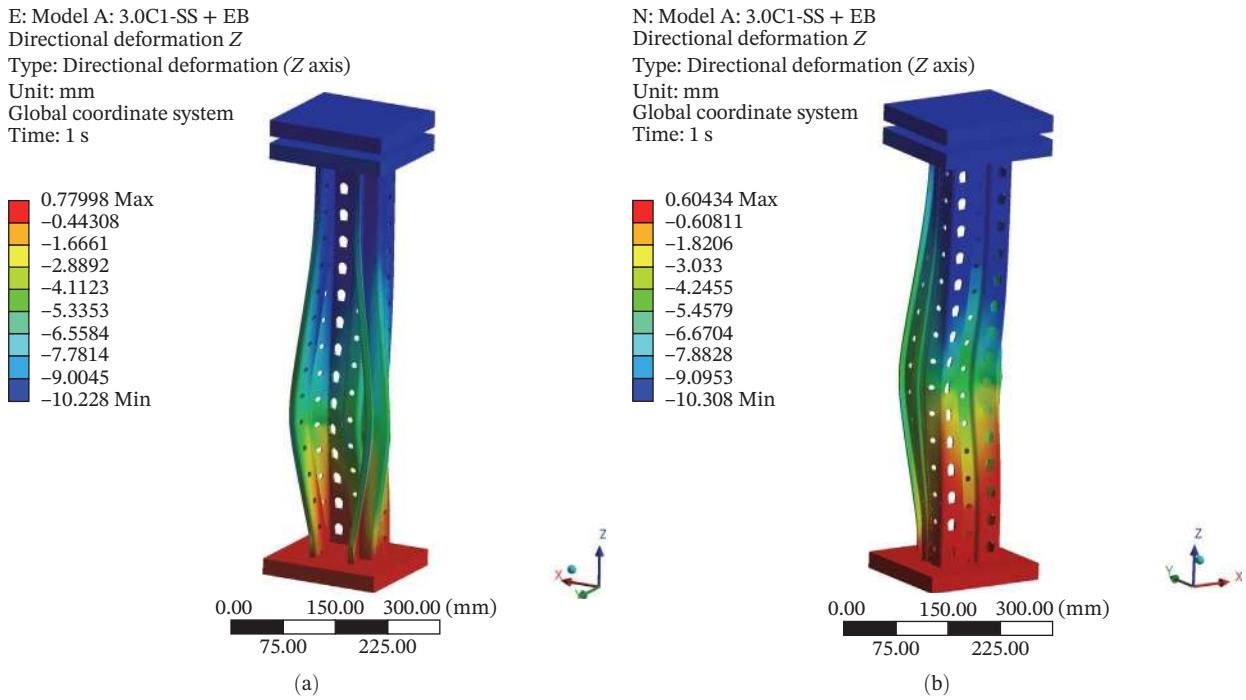

FIGURE 15 | Directional deformation (*Z*–axis) in Model A: (a) front view and (b) rear view.

earlier instability, consistent with the damaged test configurations. Second, bolt-based reinforcement provides a measurable recovery of axial resistance relative to the predamaged state, although full restoration to the undeformed capacity is not achieved.

The predictive consistency across approaches was further evaluated by comparing the FE results with the ML framework developed in Section 4. Using the trained gradient boosting model and the same set of geometric and joint-related descriptors, the ML predictions follow the same capacity trends across undamaged, damaged, and reinforced states. This agreement supports the use of the ML model as a rapid screening tool for residual axial capacity, while the FE simulations provide detailed insight into stress localization and deformation mechanisms governing the observed stability transitions.

7074, 2026, 1, Downloaded from https://onlinelibrary.wiley.com/doi/10.1155/adce/4354889 by Cochrane Romania, Wiley Online Library on [17/10/2026]. See the Terms and Conditions (https://onlinelibrary.wiley.com/terms-and-conditions) on Wiley Online Library for rules of use; OA articles are governed by the applicable Creative Commons License

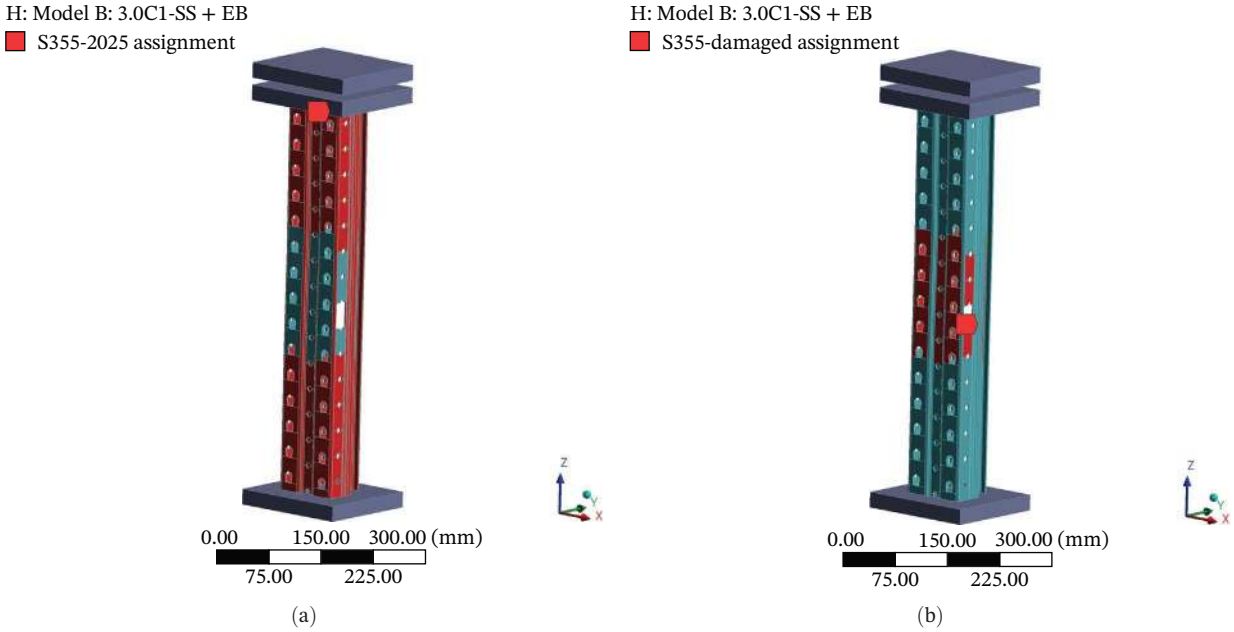

FIGURE 16 | Local degradation modeling in Model B: (a) stiffness reduction zone and (b) notch simulation.

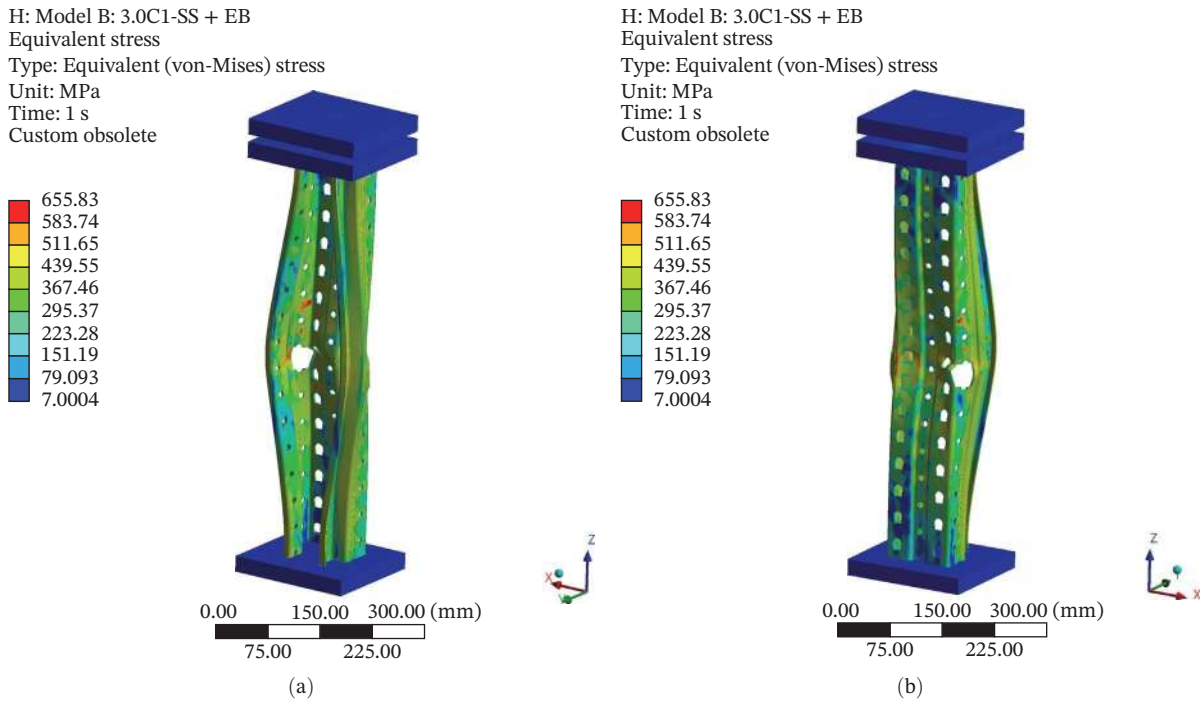

FIGURE 17 | Von Mises stress distribution for Model B: (a) front view and (b) rear lateral view.

6 | Conclusions

This study investigated the axial load-bearing behavior of CFS uprights affected by beam-to-column joint damage. A combined framework of full-scale compression testing, ML, and FEA was used to clarify the interaction between joint rigidity, geometric properties, and structural performance in storage rack systems.

The main conclusions are as follows:

1. Connection-induced degradation leads to significant strength loss. Experimental results show that reductions in joint rotational stiffness and moment resistance can decrease axial capacity by up to ~30%, and damaged uprights tend to exhibit a shift toward coupled TF involvement compared with intact reference specimens.
2. Geometric properties remain decisive predictors of axial resistance. Second moments of area, wall thickness, and radii of gyration correlate strongly with capacity, and their influence becomes more pronounced when connection restraint is reduced by joint degradation.
3. ML enables rapid residual-capacity estimation when calibrated with physically meaningful inputs. Using geometric

7074, 2026, 1, Downloaded from https://onlinelibrary.wiley.com/doi/10.1155/adce/4354889 by Cochrane Romania, Wiley Online Library on [17/10/2026]. See the Terms and Conditions (https://onlinelibrary.wiley.com/terms-and-conditions) on Wiley Online Library for rules of use; OA articles are governed by the applicable Creative Commons License

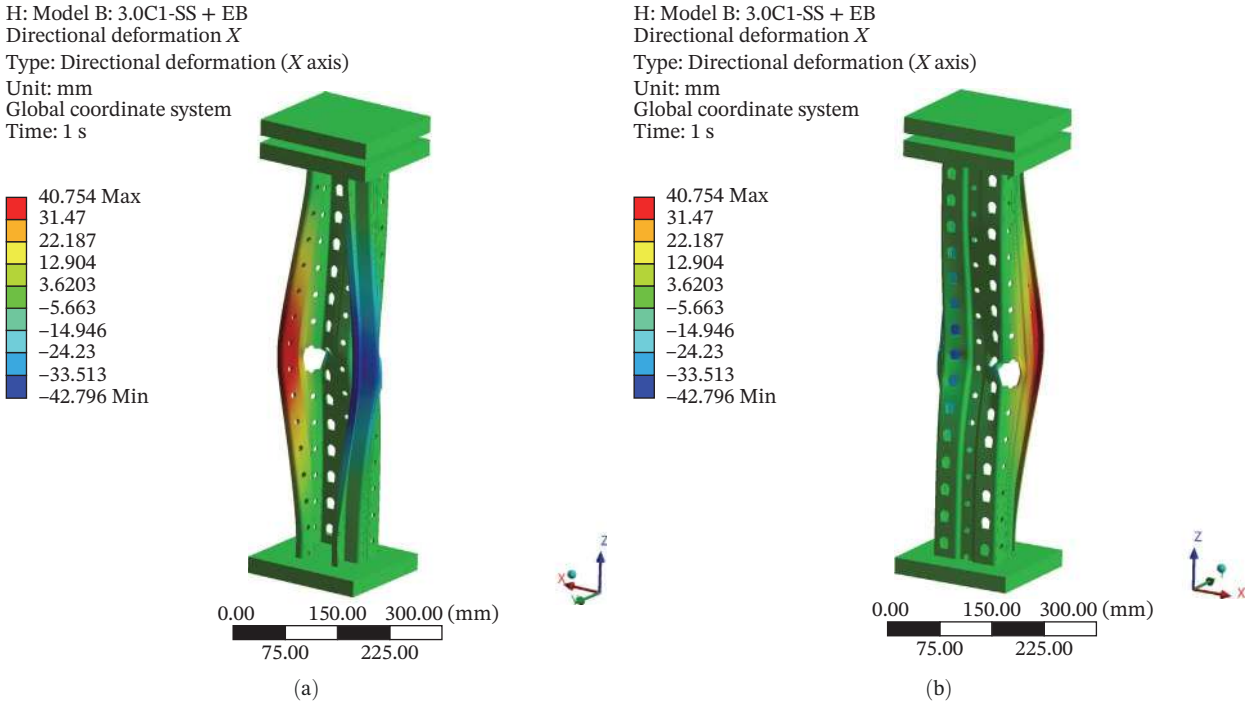

FIGURE 18 | Directional deformation (*X*–axis) in Model B: (a) front view and (b) rear lateral view.

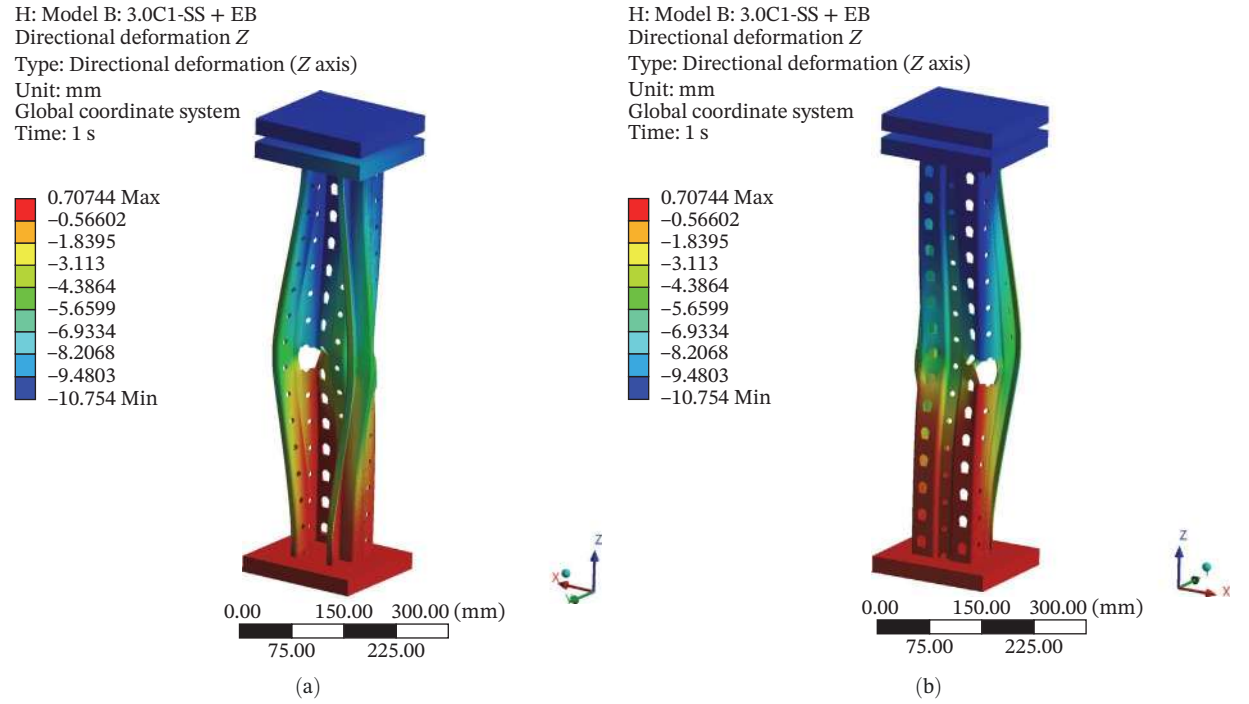

FIGURE 19 | Directional deformation (*Z*–axis) in Model B: (a) front view and (b) rear lateral view.

descriptors together with experimentally derived joint properties, the best-performing ML model achieved high predictive accuracy and captured the capacity reduction trends associated with joint damage.

Nonlinear FE simulations reproduce the observed response trends and provide mechanistic insight. The numerical results for the representative 3.0C1 profile captured the reduction in axial capacity due to connector-region degradation and the partial recovery associated with bolt reinforcement, in close agreement with experimental and ML-based predictions.

Design and assessment implications are significant. Current design-oriented approaches for rack systems typically assume idealized joint behavior; the present results highlight the need to explicitly consider joint stiffness degradation in postdamage evaluation and retrofit-oriented decision-making.

7074, 2026, 1, Downloaded from https://onlinelibrary.wiley.com/doi/10.1155/adce/4354889 by Cochrane Romania, Wiley Online Library on [17/10/2026]. See the Terms and Conditions (https://onlinelibrary.wiley.com/terms-and-conditions) on Wiley Online Library for rules of use; OA articles are governed by the applicable Creative Commons License

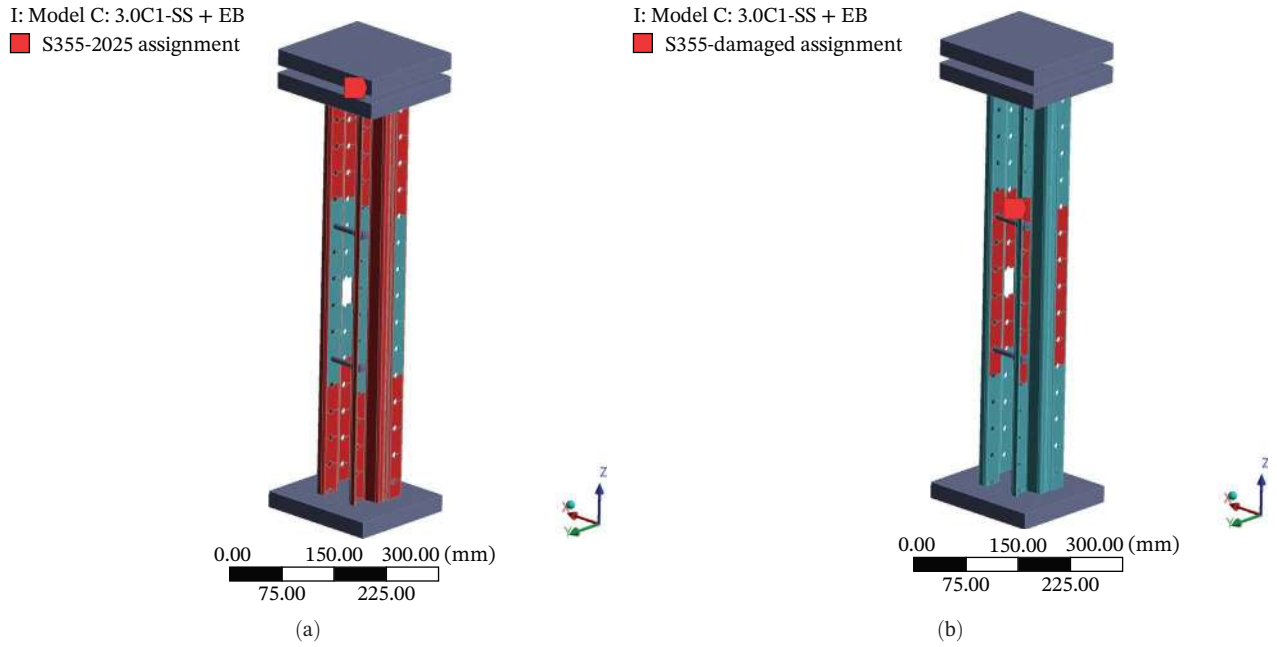

FIGURE 20 | Finite element model showing the bolted reinforcement in Model C: (a) initial material assignment and (b) deformed zone material assignment.

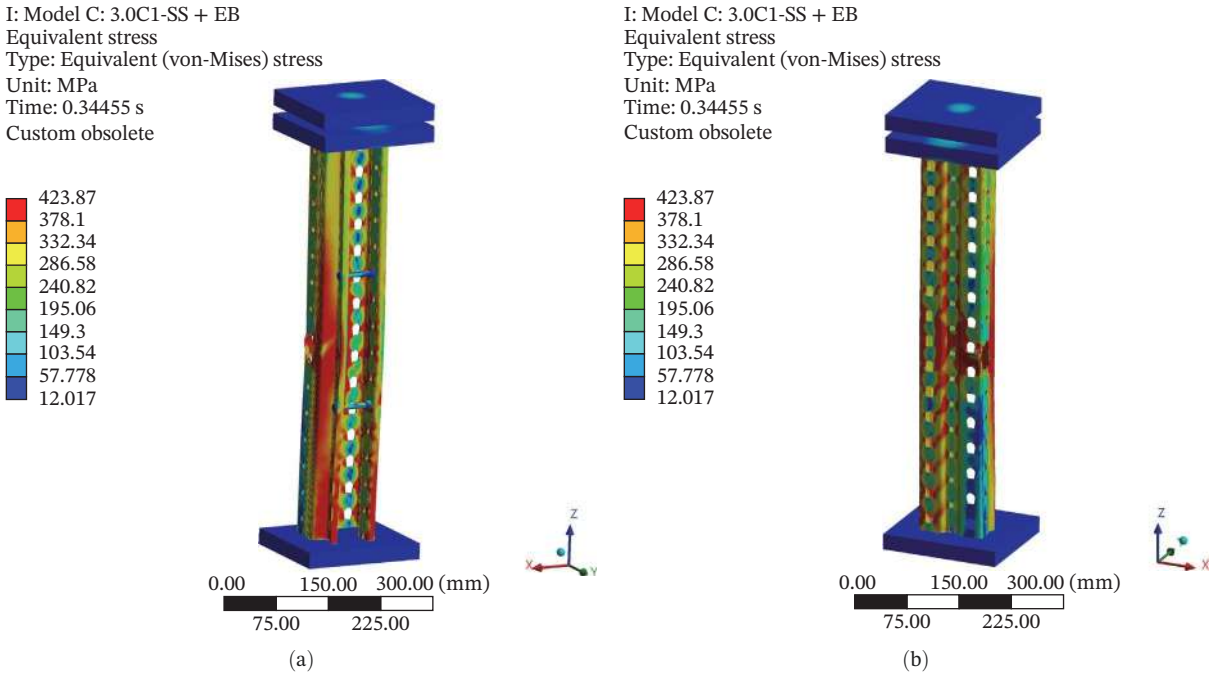

FIGURE 21 | Stress distribution and buckling shape in reinforced Model C: (a) front view and (b) rear lateral view.

The experimental campaign was conducted using a single specimen length (760 mm), consistent with the adopted testing framework, and therefore the conclusions do not explicitly quantify slenderness effects on axial capacity reduction. The tests focused on monotonic axial compression following prior joint degradation, and cyclic or dynamic effects were not investigated. In addition, detailed perforation geometry is commercially proprietary, and initial imperfections were not measured systematically prior to testing, which may contribute to scatter in measured capacities. For the ML component, the dataset size is limited by the availability of full-scale tests, and future dataset expansion is required to further improve generalization. Finally, the FE models use idealized geometry and do not explicitly include measured residual stresses or experimentally measured displacement/strain fields for detailed deformation validation; the numerical results were therefore validated primarily against ultimate capacity and observed failure modes.

Future studies should explore cyclic degradation, multilength columns, and integration of digital twin monitoring for postdamage assessment. Extending the database across additional upright

7074, 2026, 1, Downloaded from https://onlinelibrary.wiley.com/doi/10.1155/adce/4354889 by Cochrane Romania, Wiley Online Library on [17/10/2026]. See the Terms and Conditions (https://onlinelibrary.wiley.com/terms-and-conditions) on Wiley Online Library for rules of use; OA articles are governed by the applicable Creative Commons License

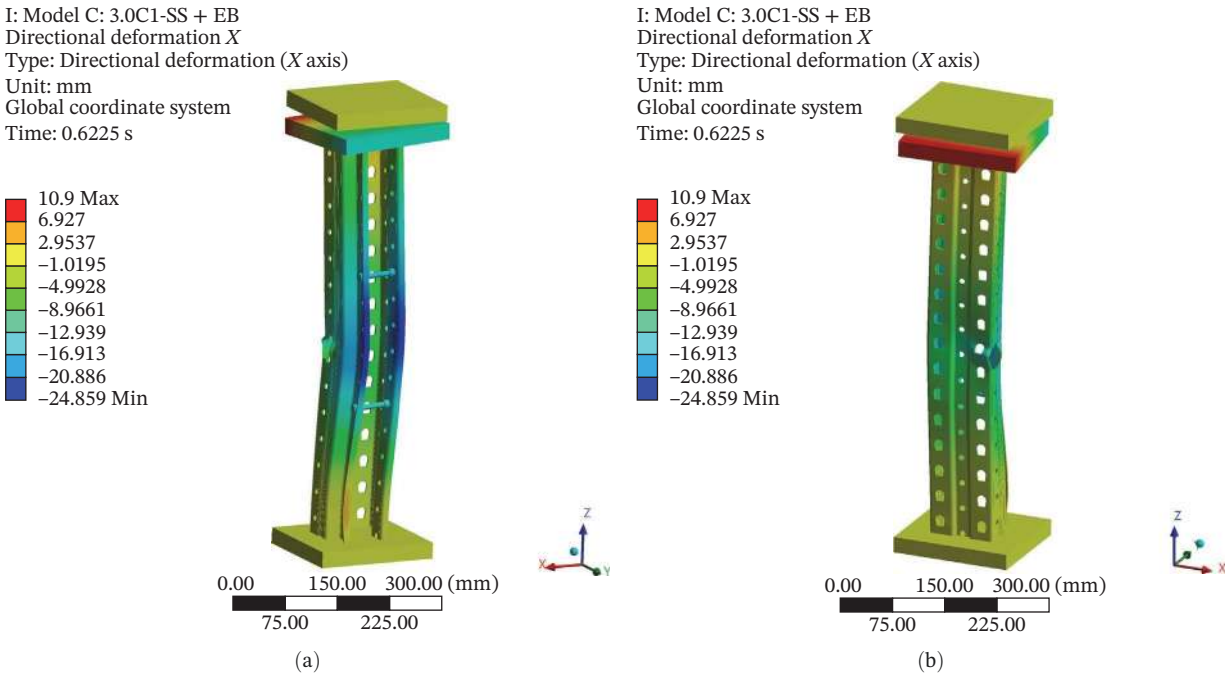

FIGURE 22 | Directional deformation (*X*–axis) in Model C: (a) front view and (b) rear lateral view.

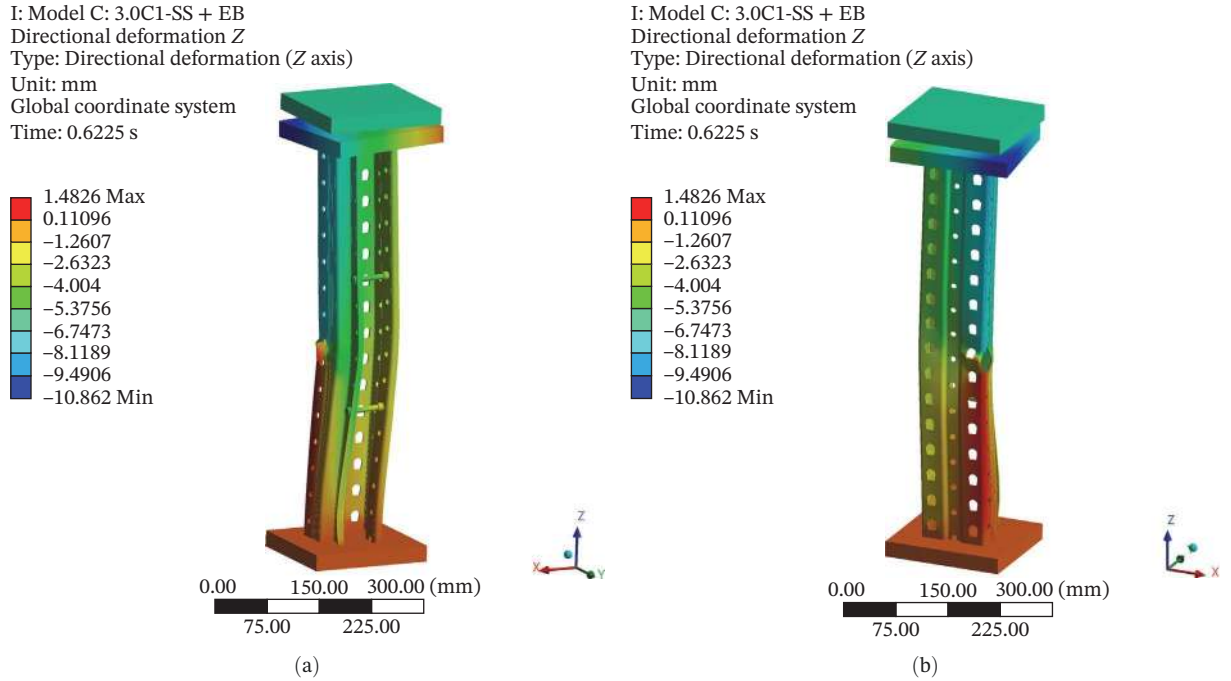

FIGURE 23 | Directional deformation (*Z*–axis) in Model C: (a) front view and (b) rear lateral view.

geometries, perforation schemes, and slenderness ratios will enable more explicit treatment of stability scaling and improve the robustness of data-driven predictions. Further numerical work should incorporate joint hysteresis and progressive local damage modeling to strengthen the connection between joint degradation mechanisms and upright residual capacity.

7074, 2026, 1, Downloaded from https://onlinelibrary.wiley.com/doi/10.1155/adce/4354889 by Cochrane Romania, Wiley Online Library on [17/10/2026]. See the Terms and Conditions (https://onlinelibrary.wiley.com/terms-and-conditions) on Wiley Online Library for rules of use; OA articles are governed by the applicable Creative Commons License

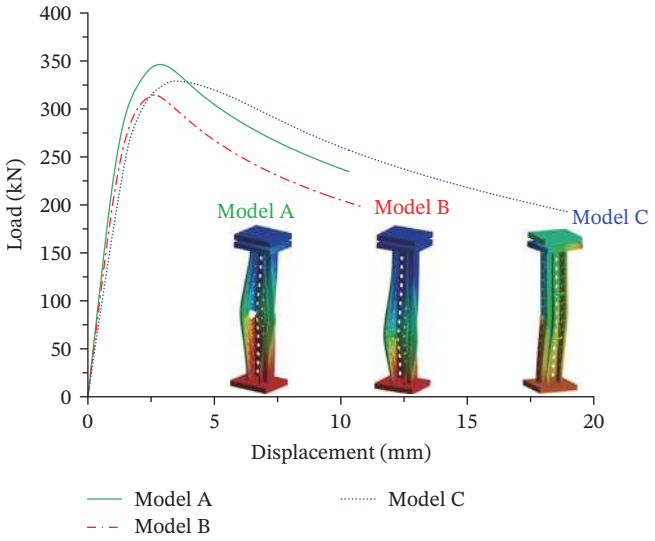

FIGURE 24 | Comparison of load–displacement curves for all three models.

Funding

No funding was received for this manuscript.

Conflicts of Interest

The authors declare no conflicts of interest..

Data Availability Statement

The data that support the findings of this study are available from the corresponding author upon reasonable request.

References

1. J. Bonada, M. Casafont, F. Roure, and M. M. Pastor, "Selection of the Initial Geometrical Imperfection in Nonlinear FE Analysis of Cold-Formed Steel Rack Columns," *Thin-Walled Structures* 51 (2012): 99–111.

2. J. Bonada, M. M. Pastor, F. Roure, and M. Casafont, "Influence of the Cold Work Effects in Perforated Rack Columns Under Pure Compression Load," *Engineering Structures* 97 (2015): 130–139.

3. J. Bonada, M. M. Pastor, F. Roure, and M. Casafont, "Distortional Influence of Pallet Rack Uprights Subject to Combined Compression and Bending," *Structures* 8 (2016): 275–285.

4. X. Zhao, C. Ren, and R. Qin, "An Experimental Investigation Into Perforated and Non-Perforated Steel Storage Rack Uprights," *Thin-Walled Structures* 112 (2017): 159–172.

5. Z. He, Y. Zhang, X. Zhou, B. Zou, and Z. Zhang, "Post-Buckling Behavior and DSM Design of Cold-Formed Steel Lipped Channel Columns Experiencing Local-Distortional-Global Interaction," *Structures* 67 (2024): 106945.

6. C. Ren, B. Wang, and X. Zhao, "Numerical Predictions of Distortional-Global Buckling Interaction of Perforated Rack Uprights in Compression," *Thin-Walled Structures* 136 (2019): 292–301.

7. G. C. Elias, L. H. de Almeida Neiva, A. M. C. Sarmanho, V. N. Alves, and A. F. Barbosa e Castro, "Ultimate Load of Steel Storage Systems Uprights," *Engineering Structures* 170 (2018): 53–62.

8. P. Zhang and M. S. Alam, "Elastic Buckling Behaviour of Σ-Shaped Rack Columns Under Uniaxial Compression," *Engineering Structures* 212 (2020): 110469.

9. R. R. Umaraj, S. K. Selvaraj, T.-M. Chan, and A. Y. Elghazouli, "If Rockets are Reusable Why Not Buildings? Reuse Evaluation for Cold-Formed Steel Unequal-Leg Lipped Angle Columns," *Thin-Walled Structures* 216 (2025): 113463.

10. L. H. de Almeida Neiva, G. C. Elias, J. A. B. Starlino, A. M. C. Sarmanho, and V. N. Alves, "Industrial Storage System Continuous Perforated Uprights: A Combined Design Proposal," *Revista de la construcción* 21, no. 2 (2022): 204–214.

11. L. H. de Almeida Neiva, A. M. C. Sarmanho, V. O. Faria, F. T. de Souza, and J. A. B. Starlino, "Numerical and Experimental Analysis of Perforated Rack Members Under Compression," *Thin-Walled Structures* 130 (2018): 176–193.

12. V. Ungureanu, A. Madeo, G. Zagari, G. Zucco, D. Dubina, and R. Zinno, "Koiter Asymptotic Analysis of Thin-Walled Cold-Formed Steel Uprights Pallet Racks," *Structures* 8 (2016): 286–299.

13. M. M. Pastor, M. Casafont, J. Bonada, and F. Roure, "Imperfection Amplitudes for Nonlinear Analysis of Open Thin-Walled Steel Cross-Sections Used in Rack Column Uprights," *Thin-Walled Structures* 76 (2014): 28–41.

14. J. Bonada, M. Casafont, F. Roure, and M. M. Pastor, "Geometrically Nonlinear Analysis of Perforated Rack Columns Under a Compression Load by Means of Generalized Beam Theory," *Thin-Walled Structures* 166 (2021): 108102.

15. P. Leach and L. Weekes, "Axial Capacity of Perforated Steel Columns," *Steel Construction* 6, no. 2 (2013): 144–149.

16. F. M. Özkal and C. Yazici, "Effects of Steel Bolts on Retrofitting the Buckling Performance of Storage Rack System Uprights," *Structures* 64 (2024): 106578.

17. E. Taheri, A. Firouzianhaji, N. Usefi, P. Mehrabi, H. Ronagh, and B. Samali, "Investigation of a Method for Strengthening Perforated Cold-Formed Steel Profiles Under Compression Loads," *Applied Sciences* 9, no. 23 (2019): 5085.

18. F. M. F. Shaker, Z. Mamdooh, A. Deifalla, and M. M. Yehia, "Experimental Investigations of the Behavior of Stiffened Perforated Cold-Formed Steel Sections Subjected to Axial Compression," *Buildings* 12, no. 6 (2022): 812.

19. P. B. Dinis, B. Young, and D. Camotim, "Local-Distortional Interaction in Cold-Formed Steel Rack-Section Columns," *Thin-Walled Structures* 81 (2014): 185–194.

20. A. Crisan, V. Ungureanu, and D. Dubina, "Behaviour of Cold-Formed Steel Perforated Sections in Compression. Part 1-Experimental Investigations," *Thin-Walled Structures* 61 (2012): 86–96.

21. C. Yazici, E. Arik, and F. M. Özkal, "Influence of Design Parameters on Beam-to-Column Connections of Steel Storage Rack Systems," *Engineering Failure Analysis* 152 (2023): 107439.

22. G. Taranu, S. Iacob, and N. Taranu, "Buckling Behavior of Perforated Cold-Formed Steel Uprights: Experimental Evaluation and Comparative Assessment Using FEM, EWM, and DSM," *Buildings* 15, no. 9 (2025): 1561.

23. W. Wang, K. Roy, B. G. Ananthi, L. Lu, Z. Fang, and J. B. P. Lim, "Simplified Direct Strength Method for the Design of Cold-Formed Steel Channels With Circular Web Openings Under Two-Flange Loadings," *Engineering Structures* 319 (2024): 118840.

24. D. L. Chandramohan, K. Roy, Z. Fang, B. G. Ananthi, and J. B. P. Lim, "Moment Capacity of Cold-Formed Steel Channel Beams With Edge-Stiffened and Unstiffened Elongated Web Holes," *Thin-Walled Structures* 206 (2025): 112605.

25. D. L. Chandramohan, K. Roy, G. B. Gnana Ananthi, Z. Fang, and J. B. P. Lim, "Structural Behaviour and Capacity of Cold-Formed Steel Channel Sections With Elongated Edge-Stiffened and Unstiffened Web Holes Under Compression," *Journal of Constructional Steel Research* 218 (2024): 108681.

7074, 2026, 1, Downloaded from https://onlinelibrary.wiley.com/doi/10.1155/adce/4354889 by Cochrane Romania, Wiley Online Library on [17/10/2026]. See the Terms and Conditions (https://onlinelibrary.wiley.com/terms-and-conditions) on Wiley Online Library for rules of use; OA articles are governed by the applicable Creative Commons License

26. D. L. Chandramohan, K. Roy, Z. Fang, G. B. Gnana Ananthi, and J. B. P. Lim, "Numerical Investigation of Cold-Formed Steel Channels With Edge-Stiffened and Unstiffened Elongated Web Holes Under Shear," *Thin-Walled Structures* 196 (2024): 111472.

27. EN 15512:2009, *Steel Static Storage Systems—Adjustable Pallet Racking Systems—Principles for Structural Design* (CEN, 2009).

28. Y. A. K. Sayed, A. A. Ibrahim, A. G. Tamrazyan, and M. F. M. Fahmy, "Machine-Learning-Based Models Versus Design-Oriented Models for Predicting the Axial Compressive Load of FRP-Confined Rectangular RC Columns," *Engineering Structures* 285 (2023): 116030.

29. C. Yazici and F. J. Domínguez-Gutiérrez, "Machine Learning Techniques for Estimating High–Temperature Mechanical Behavior of High Strength Steels," *Results in Engineering* 25 (2025): 104242.

30. C. Cakiroglu, K. Islam, G. Bekdaş, S. Kim, and Z. W. Geem, "Interpretable Machine Learning Algorithms to Predict the Axial Capacity of FRP-Reinforced Concrete Columns," *Materials* 15, no. 8 (2022): 2742.

31. Y. Yılmaz, F. Öztürk, S. Demir, and A. D. Demir, "Prediction of Load-Bearing Capacity of Sigma Section CFS Beam-Column Members Using Ensemble and Deep Learning Algorithms," *Journal of Constructional Steel Research* 228 (2025): 109458.

32. C. Yazici, "*Experimental and Numerical Investigation on the Storage Rack System Members and Proposal of a Mechanical Model for Beam*," PhD Thesis, Ataturk University, 2022).

33. E. Arık, "*Comparative Investigation on Tabbed and Bolted Beam-to-Column Connections of Storage Rack Systems*," Master's Thesis, Ataturk University, 2023).

7074, 2026, 1, Downloaded from https://onlinelibrary.wiley.com/doi/10.1155/adce/4354889 by Cochrane Romania, Wiley Online Library on [17/10/2026]. See the Terms and Conditions (https://onlinelibrary.wiley.com/terms-and-conditions) on Wiley Online Library for rules of use; OA articles are governed by the applicable Creative Commons License

sustainability

MDPI

Article

Time History Analyses of a Masonry Structure for a Sustainable Technical Assessment According to Romanian Design Codes

Vasile-Mircea Venghiac [1], Cerasela-Panseluta Neagu [1], George Taranu [1,*] and Ancuta Rotaru [2]

[1] Department of Structural Mechanics, Faculty of Civil Engineering and Building Services, Technical University "Gheorghe Asachi" of Iasi, 1 Prof. Dr. Doc. Dimitrie Mangeron St., 700050 Iași, Romania
[2] Department of Transportation Infrastructure and Foundations, Faculty of Civil Engineering and Building Services, Technical University "Gheorghe Asachi" of Iasi, 1 Prof. Dr. Doc. Dimitrie Mangeron St., 700050 Iași, Romania
* Correspondence: george.taranu@academic.tuiasi.ro

Abstract: Computer simulations are challenging in terms of modeling the appropriate behavior of brick masonry structures. These numerical simulations are becoming increasingly difficult due to several design code requirements considered for the technical assessment of brick masonry structures for rehabilitation. In Romania, many brick masonry structures have withstood powerful earthquakes during their lifetime and require rehabilitation works. This paper aims to further assess various simulation challenges regarding the boundary conditions of spandrels and masonry structural behavior. This paper presents a comparative numerical study of two different spandrel-piers scenarios: one considers the link between them as unaffected, and the other attempts to simulate the occurrence of damage by replacing the spandrel's presence in the initial structure. The proposed model follows the "strong pier–weak spandrel model" and is aimed at practicing engineers. Models are computed with ordinary design software such as Robot Structural Analysis with 2D shells finite elements for masonry walls and, in a more complex manner, software such as Ansys with 3D solid finite elements. Time history analyses are carried out for three distinct accelerograms recorded in Romania. A comparison of the results acquired from these two models is presented and discussed. The purpose of this research is to highlight the importance of proper modeling of unreinforced brick masonry structures to optimize operational and maintenance practices.

Keywords: time history analyses; brick masonry spandrel modeling; solid brick masonry structures; sustainable retrofitting techniques; life cycle monitoring

check for updates

Citation: Venghiac, V.-M.; Neagu, C.-P.; Taranu, G.; Rotaru, A. Time History Analyses of a Masonry Structure for a Sustainable Technical Assessment According to Romanian Design Codes. *Sustainability* **2023**, *15*, 2932. https://doi.org/10.3390/su15042932

Academic Editors: Humberto Varum and Claudia Casapulla

Received: 30 December 2022
Revised: 20 January 2023
Accepted: 1 February 2023
Published: 6 February 2023

Copyright: © 2023 by the authors. Licensee MDPI, Basel, Switzerland. This article is an open access article distributed under the terms and conditions of the Creative Commons Attribution (CC BY) license (https://creativecommons.org/licenses/by/4.0/).

1. Introduction

The extended meaning of sustainability refers to the ability of something to maintain or "sustain" itself over time.

The construction industry impacts all four aspects of sustainable development: ecological, economic, social, and cultural.

The main goal of sustainable development is to preserve the ecological systems that are, globally, the basis for human life and nature's biodiversity.

The challenges of the construction sector are the use environmentally friendly construction materials, the energy efficiency of buildings, reuse of construction and demolition waste materials, water conservation and health in structures, building-related transport aspects, urban sustainability, and societal impacts arising from construction activities and the built environment [1]. The main reasons for difficulties are the political, technological, and cultural differences between countries. They originate in the dependence of a subjective evaluation applied to each general method developed so far.

While the definition of sustainable building design is ever-changing, the National Institute of Building Sciences, established by the United States Congress, defines six fundamental principles that involve sustainability in the building industry: optimize site

potential; optimize energy use; protect and conserve water; optimize building space and material use; enhance indoor environmental quality (IEQ); optimize operational and maintenance practices [2].

Consuming vast amounts of materials and being a significant producer of harmful gases because of the raw materials and energy provided by non-renewable sources, the construction industry faces a new challenge. It meets increasing demands for new or renovated sustainable building designs balanced with safe, secure, and effective environments.

One of the main tasks of the civil engineer, faced with assessing the state of an old structure, is to find solutions for its rehabilitation to increase its service life. This leads to significantly less disruptions in the activities taking place in the building, reduced relocation periods for the inhabitants, and significantly less wastes, rather than demolishing the structure and building it again.

Through collaboration, engineers, architects, and other site contractors can specify materials and systems that simplify operational practices and reduce maintenance requirements. On site and within the facility, these practices, apart from reducing water and energy requirements and demanding less toxic chemicals usage, are cost-effective and reduce life-cycle costs. It is imperative to create strategies for sustainable development, especially for the rehabilitation of old urban areas [3].

Great interest is applied to the rehabilitation of the built environment. The concept of rehabilitation of old urban areas allows the achievement of sustainable development since it provides the use of existing structures, avoids the increase of constructed zones, and provides reduction of material consumption and waste production. It also sustainably preserves the regional cultural heritage [3].

The majority of old or historical buildings that require rehabilitation are masonry structures. Brick masonry structures are complex systems [4]. The complexity comes from the inhomogeneity of the material. The geometry variation can also create design difficulties [5]. All these issues create great challenges for structural engineers. The design process is also affected by different types of degradations. In the design process, the degradations are considered by means of safety factors, which reduce certain mechanical characteristics of the materials, such as compressive strength and modulus of elasticity.

Two main structural elements are identified in a masonry wall: the vertical panels, known as piers; and the horizontal elements which couple two adjacent piers, known as spandrels. The piers are the most important elements, being subjected to both static and seismic loads [6].

International codes, such as FEMA 356 [7], propose two simplified models: the "strong pier–weak spandrel" model; and the "strong spandrel–weak pier". Generally, the strong spandrel–weak pier model is consistent with new buildings in which the spandrels are always connected to lintels, tie-beams, and slabs, which provide a consistent coupling between the piers. As a consequence, the piers crack first. However, this is not always true for old or historic buildings where the spandrels are weak elements. The lintels in this case are usually made of wood or masonry, the tie-beams are either missing or made of wood and the floors are also made of wood [8].

According to [9,10] two types of cracking patterns were observed in masonry spandrels: flexural cracking patterns; and shear cracking patterns. These failure modes are generally related to spandrel geometric proportions, lintel type, and brick interlocking at the end-sections [9–12]. Slender spandrels typically fail in flexural mode while squat spandrels fail because of shear.

More complex modeling methods, analysis methods, and elaboration of analysis results can be used for accurate results, such as the derivation of analytical capacity curves and fragility functions [13], non-linear static analysis procedures [14–17], equivalent frame model [18,19]; or for identifying the weakest component, such as the component method for steel structures [20], the capacity design rule [19,21]. However, these methods are overly complex and impractical for practicing structural engineers, who require time-efficient models rather than very high-accuracy ones.

In Romania, the technical assessment of existing buildings is being performed in accordance with the provisions of Code P100-3/2019. The procedure is explained in Chapter 2. The hand calculations presented in the code are simplified to reduce complexity. However, for complex buildings, with many structural elements to be assessed, the procedure becomes difficult, and the risk of human error is high. In this paper, the authors propose a simplified numerical model for assessing the design pier forces in masonry structures. The scientific contribution of the study presented in the article is an approach to numerical models based on previous work [22–26]. Observations during the shaking table tests presented in Figure 1 show that the initial structural masonry wall transforms into the mechanism shown in Figure 2.

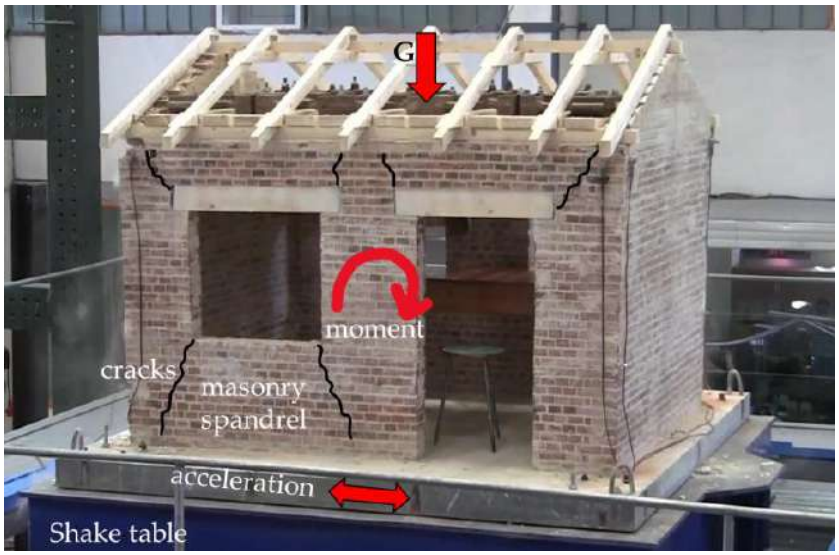

Figure 1. Mechanism of a 1:2 scaled unreinforced masonry structure model tested on the shaking table test [27,28].

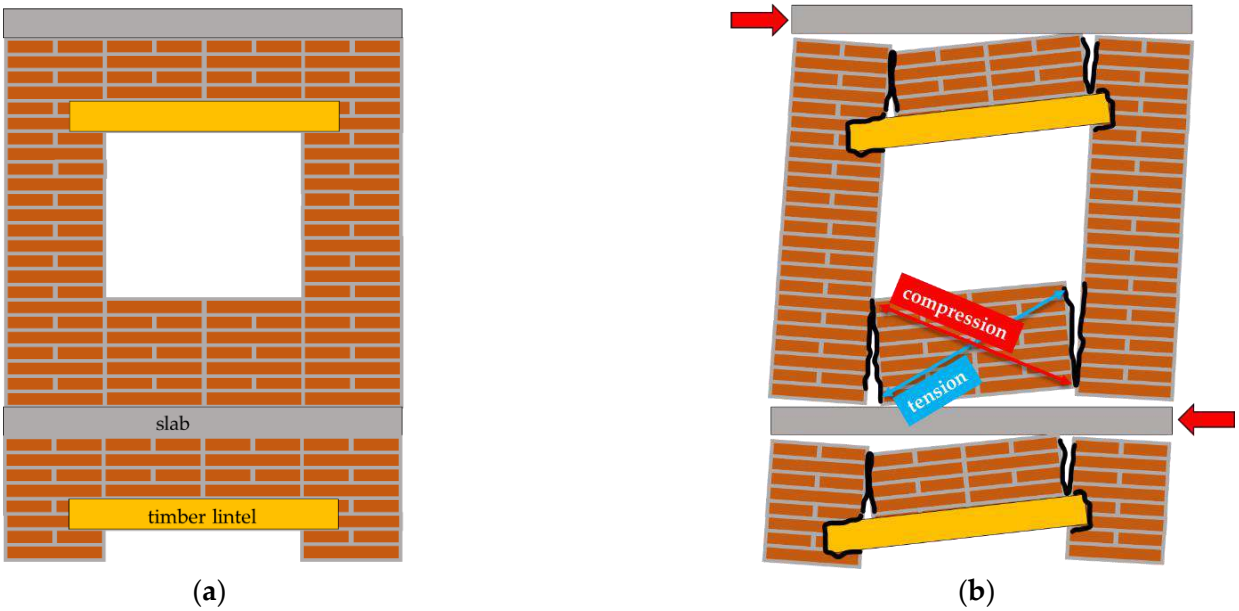

Figure 2. Masonry wall with window hole: (**a**) undeformed shape; (**b**) rocking mechanism during seismic action.

Finite elements models are considered as 3D solids and 2D shells in linear and nonlinear behavior. The material is considered homogeneous in both cases. The hypothesis in approaching the finite element models consists in a continuous rigid double-hinged

spandrel model used for unreinforced brick masonry, following the strong pier–weak spandrel model as shown in Figure 2. The proposed model is intended for slender spandrels rather than squat ones, which are also not connected to lintels, tie-beams, and floors. The models were subjected to three of the most important earthquakes which occurred and were recorded in Romania. The Vrancea region of Romania, the epicenter of the large tectonic earthquakes associated with Eastern Europe, has experienced a series of earthquakes with magnitudes over 6 degrees on the Richter scale in the past decades, namely: in 1977—M = 7.4; in 1986—M = 7.1 and 1990—M = 6.7 [25].

Table 1 shows the major earthquakes recorded in the Vrancea region and their particularities.

Table 1. Characteristics of major recorded earthquakes in the Vrancea region.

No.	Earthquake–Magnitude	LatN	LongE	h(km)	Date	Mw
1	Vrancea M= 7.2	45.34	26.30	109	1977.03.04	7.5
2	Vrancea M = 7.0	45.53	26.47	133	1986.08.30	7.3
3	Vrancea M = 6.7	45.82	26.90	91	1990.05.30	7.0
4	Vrancea M = 6.1	45.83	26.89	79	1990.05.31	6.4
5	Vrancea M = 6.0	45.79	26.71	100	2004.10.27	6.0

The finite element models proposed for designing rehabilitation solutions corresponds more closely to the real behavior of masonry structures than the analytical model proposed by the P100-3/2019 [29]. The latter method overestimates the values of internal forces in the structure. Moreover, by using a computer software technique, the accuracy of the results is higher than hand calculations. Another benefit of automatic calculation is time efficiency and the possibility of running a complex parametric analysis.

2. Materials and Methods

The Romanian code P100-3/2019 presents evaluation and estimation methods of the design forces produced by earthquakes (axial force, shear force, bending moments). The approaches presented in the code are simplistic in terms of the real structural behavior and that is because the process needs to be time-efficient. Some of the formulae do not consider all parameters required to do an accurate estimation, being the reason for the discussions presented in the annexes regarding the errors encountered in the design process.

The assessment is carried out according to one of three methodologies presented in the code. The methodology is chosen based on building importance class, site characteristics, an available information about the construction, such as preliminary technical project, year of construction, structural system, and material characteristics. The first level methodology is the simplest one ("low complexity"), and it is based on evaluating the ratio between the overall shear capacity of the building and the total base shear force. This methodology is rarely used because it is targeted at low-importance class buildings located in areas with low seismic impact (class of importance and seismic exposure III and IV as per P100-1/2013), and which comply with strict regularity and structural layout conditions.

Level 2 and 3 methodologies are considered advanced and may be applied to all types of structures. The assessment is conducted by evaluating the ratio between the sum of shear capacities of all vertical structural elements and the total base shear force. The main difference between the two methodologies is that the second methodology, which is the most widely used procedure, uses linear static analysis, while the third uses non-linear analysis. In the linear static analysis, the degradations of the building are taken into account by means of safety factors which reduce certain mechanical characteristics of materials (e.g., compressive or tensile strength, modulus of elasticity).

The Romanian code stipulates that an appropriate methodology for the seismic assessment of an existing building has to be chosen based on building importance class, site characteristics including seismic hazard, and available information about the construction, defined by P100-3/2019 as the "level of knowledge", such as the initial technical project, year of construction, structural system, and material characteristics.

The levels of knowledge are defined in Section 4.3 of the P100-3/2019 code as follows: KL1—limited knowledge; KL2—normal knowledge; KL3—complete knowledge.

For masonry structures, the code P100-3/2019 stipulates (Annex D.3.1.(6)) that "the third level methodology can only be applied to buildings where, following data collection for the structural assessment, the level of knowledge is KL3".

The factors considered in establishing a complete knowledge level (KL3) are as follows: (a) the geometry of structure (determined from the original overall project and from a comprehensive survey of the building); (b) the composition of structural and non-structural elements; (c) the materials of the structural and non-structural elements. Points (b) and (c) are determined from the original technical design documentation, from the original reports on the quality of works, and from a comprehensive inspection in the field.

For old masonry buildings, many of which suffered the impact of repeated earthquakes, reaching the requirements imposed by KL3 level of knowledge is difficult/not possible in Romania [29].

For these reasons, the authors propose a simple numerical model for the technical assessment of the design pier forces in unreinforced masonry structures, using the second level methodology, namely, linear static analysis.

The second level methodology (Chapter D.3.3.1.4, P100-3/2019) presents the formulae for the bearing capacity of the structural walls. Only the in-plane loading carrying capacity was considered in this article.

The shear capacity for eccentric compression failure (Figure 3a), V_{f1}, is:

$$V_{f1} = \frac{N_d}{c_p \lambda_p}(1 - 1.15\nu_d), \tag{1}$$

where:

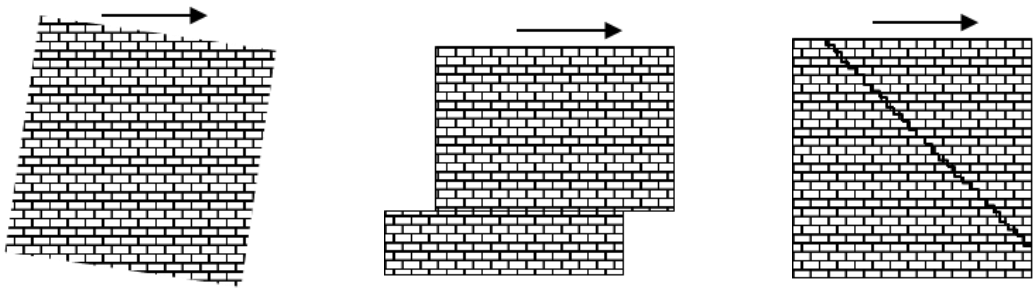

Figure 3. Masonry failure modes: (**a**) eccentric compression failure; (**b**) bed joint sliding; (**c**) diagonal shear cracking.

N_d is the design axial force;
c_p—coefficient which takes into account the bearing conditions at both ends of the pier;
$\lambda_p = \frac{H_p}{l_w}$—masonry wall shape factor;
H_p—height of the wall;
l_w—length of the wall;
$\nu_d = \frac{\sigma_0}{f_d}$ and $\sigma_0 = \frac{N_d}{A_w}$—vertical compression stress acting on the wall;
A_w—horizontal section area of the wall;
f_d—masonry design compression strength.

The shear capacity for bed joint sliding (Figure 3b), V_{f21}, is:

$$V_{f21} = \frac{1.33}{CF\gamma_M}\left(f_{vk0}\frac{l_{ad}}{l_c} + 0.4\sigma_d\right)tl_c, \tag{2}$$

where:

CF is the confidence factor;
γ_M—material partial safety coefficient;
f_{vk0}—initial characteristic shear strength of masonry;
t—thickness of the wall;
$l_{ad} = 2l_c - l_w$—length of active adherence;
$l_c = 1.5l_w - 3\frac{M_d}{N_d}$–length of compressed zone which takes into account the alternating effect of the seismic force;
M_d—design bending moment.
The shear capacity for diagonal shear cracking (Figure 3c), V_{f22}, is:

$$V_{f22} = \frac{tl_w f_{td}}{b}\sqrt{1 + \frac{\sigma_0}{f_{td}}}, \quad (3)$$

where:
f_{td} is the tensile strength of masonry;
b—coefficient computed according to: $1.0 \leq b = \lambda_p \leq 1.5$.
The shear capacity, V_{f2}, is:

$$V_{f2} = \min\left(V_{f21}, V_{f22}\right). \quad (4)$$

The design bearing capacity, V_{Rd}, is:

$$V_{Rd} = \min\left(V_{f1}, V_{f2}\right). \quad (5)$$

According to P100-3/2019, Chapter 8.1, three indicators (R_1, R_2, and R_3) establish the seismic risk class of the building. R_1 is a score based on the structural make-up of the building, R_2 is a score based on the structural degradations, and R_3 relies on the bearing capacity computation of the structure in the ultimate limit state. This paper considers only the R_3 indicator, evaluating it as follows:

$$R_3 = \frac{\sum V_{Rdi}}{\sum V_{Edi}}, \quad (6)$$

where:
V_{Rdi} is the design shear capacity in structural element i;
V_{Edi}—the design shear force in structural element i.
According to Chapter 8.1.3 of P100-3/2019, the seismic risk class associated to the R_3 indicator (expressed in %) is established as follows:

- seismic risk class Rs I, if $R_3 < 35\%$;
- seismic risk class Rs II, if $35\% \leq R_3 < 65\%$;
- seismic risk class Rs III, if $65\% \leq R_3 < 90\%$;
- seismic risk class Rs IV, if $R_3 \geq 90\%$ [22].

The first two risk classes (Rs I and Rs II) refer to buildings in danger of collapse and in need of structural rehabilitation. Class Rs III refers to buildings where non-bearing structural elements (partition walls, claddings) may be damaged, but structural collapse is unlikely. Class Rs IV refers to buildings that perform as expected under the design value of the seismic action, namely, new buildings.

3. Modeling of the Structure

3.1. Finite Element Model Description

The model analyzed in this case study is similar to that presented and computed in P100-3/2019 Annex H, using the specific provisions of the code. It is a 3-story residential building made of unreinforced solid brick masonry with RC slabs in 1925. The structure is asymmetrical in the plane as presented in Figure 4, but it has the same structural

layout on all levels as shown in Figures 5 and 6. There are no visible degradations from previous earthquakes.

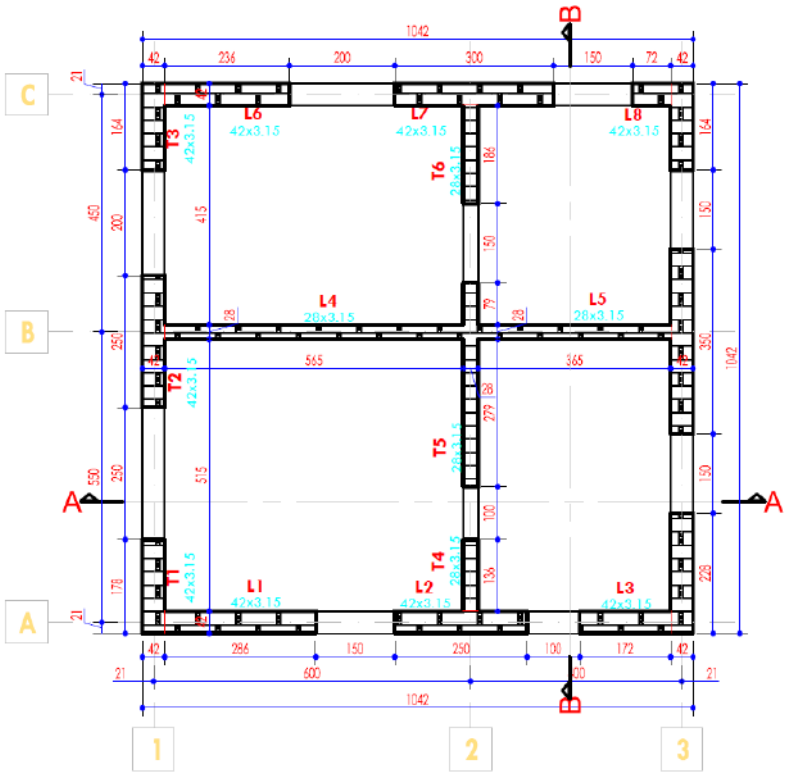

Figure 4. Floor plan with pier labels and building axes (longitudinal A, B, C and transversal 1, 2, 3).

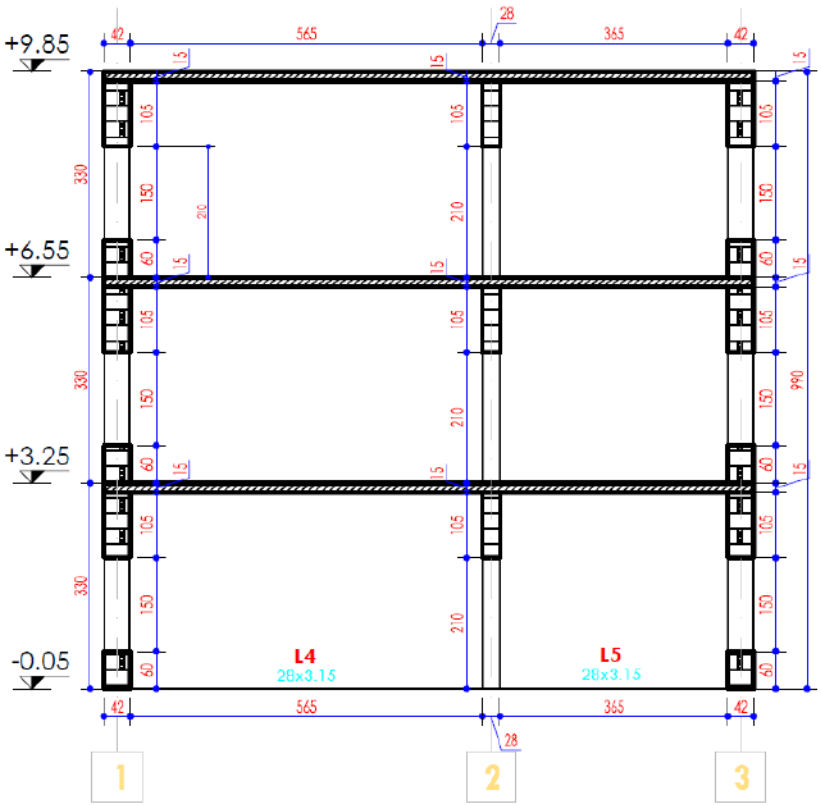

Figure 5. Section A-A with transversal building axes 1, 2, 3.

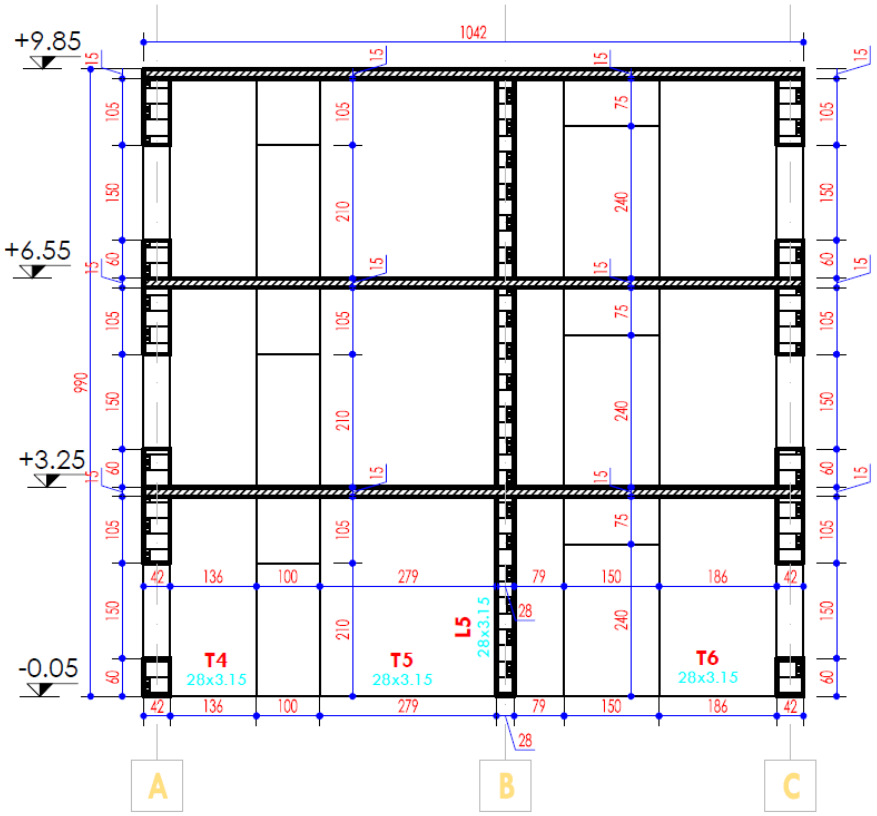

Figure 6. Section B-B with longitudinal building axes A, B, C.

There are no original plans or other technical documentation from the time of building completion, which leads to the second level of knowledge (KL2) according to P100/3-2019 Chapter 4.3 and adopting a confidence factor CF = 1.2.

The exterior wall thickness is 42 cm, and the thickness of the interior walls is 28 cm. The depth of the reinforced concrete slab is 15 cm. The story height is 3.3 m [29]. Figure 2 shows the floor plan dimensions (in centimeters) as they appear from the building survey.

Figure 3 presents mainmasonry failure modes for piers. The active piers along the *X*-axis are labelled L1 ÷ L9 and those along the *Y*-axis are labelled T1÷T9.

The two finite element software environments used for all simulations are Ansys [30] for the 3D non-linear model and Robot Structural Analysis for 2D linear models [31].

The article approaches two types of models, each one with two cases of structural integrity (initial and damaged).

All the finite element models ignore the lintels. The names of the FE models considered are given in Table 2.

Table 2. Description and names of the finite element models.

Recorded Seismic Action	2D Shell Linear		3D Solids Non-Linear	
	Bonded	Rigid Links	Bonded	Frictionless
Bucharest 1977	2D-L-B_Buc_77	2D-L-R_Buc_77	3D-NL-B_Buc_77	3D-NL-F_Buc_77
Bucharest 1986	2D-L-B_Buc_86	2D-L-R_Buc_86	3D-NL-B_Buc_86	3D-NL-F_Buc_86
Bucharest 1990	2D-L-B_Buc_90	2D-L-R_Buc_90	3D-NL-B_Buc_90	3D-NL-F_Buc_90

3.1.1. 2D Shells Linear Modeling

For the 2D shell model presented in Figure 7, the masonry piers and spandrels were the modelled with rectangular shell finite elements. The dimensions of elements are

210 × 210 mm. For concrete slabs, the element type is rigid diaphragm, because they are considered floor as part of the structure.

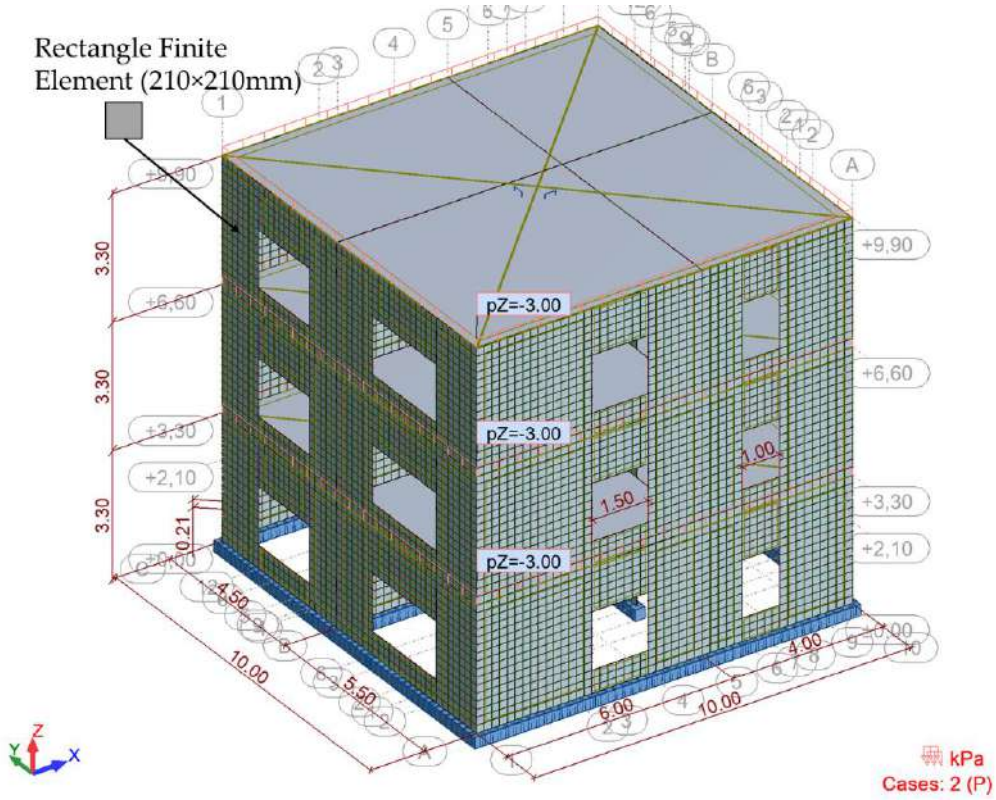

Figure 7. 2D shell linear model—bonded.

Simulations performed with this model are closer to the behavior of the weak pier–strong spandrel model. This is because the shells used to model the spandrels are fully connected to the piers. No additional boundary conditions were defined to simulate their detachment from the piers under seismic actions, and degradation in the spandrels was not considered. The total number of finite elements is 11,955, with a total number of nodes of 12,515.

The second 2D linear model discussed is called the 2D linear shell model, with rigid links instead of spandrels. It consists of brick masonry walls modeled with finite shell elements and brick masonry spandrels modelled with hinged rigid links, as shown in Figure 8.

The 2D linear model with rigid links is defined as double-hinged at the top and bottom of the window and door holes, as seen in Figure 8. These characteristics allow the rocking of the spandrel between two adjacent piers, simulating a weak link between the spandrel and piers. The hypothesis is that the spandrel does not provide any flexural stiffness. This hypothesis is true for many historic buildings which already show degradation in the spandrel area from previous earthquakes. Spandrels in this type of building are not connected to lintels, tie-beams, or floors. The total number of planar finite elements is 9984, with a total number of nodes of 10,538. The number of rigid links is 731.

The chosen arrangement of linear elements in the spandrels and their behavior under seismic actions are shown in Figure 8. This arrangement allows the spandrel to transmit loads between adjacent piers as in the diagonal compression strut model [8].

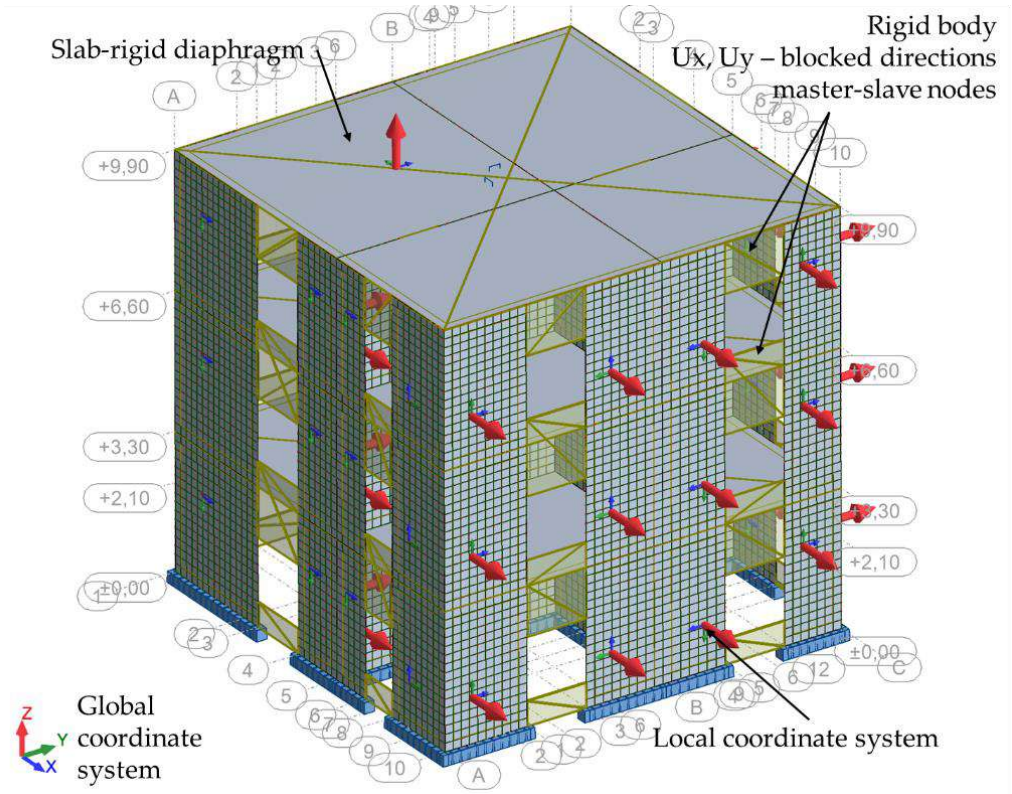

Figure 8. 2D shell linear model—rigid links.

3.1.2. 3D solid non-linear modeling

For the 3D solid model, two types of non-linearities were considered. One is for the homogenous masonry material with a uniaxial bilinear stress–strain curve in compression shown in Figure 9 and the second is based on the contacts between spandrels and piers which are frictionless with $\mu = 0$, presented in Figure 10a.

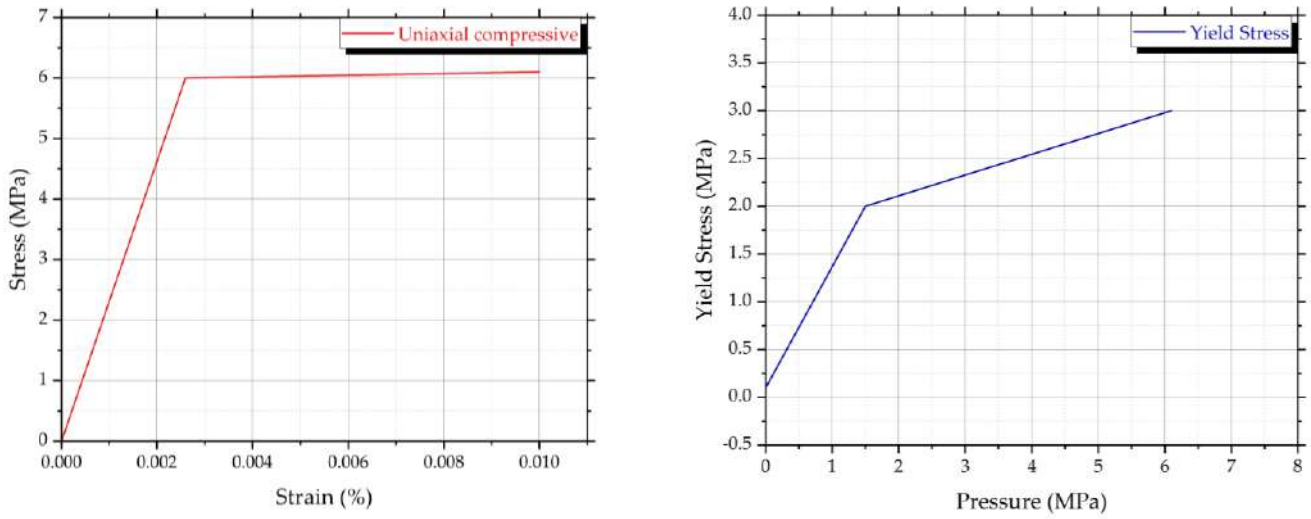

(**a**) (**b**)

Figure 9. Masonry homogenous material definition in Ansys: (**a**) uniaxial compressive; (**b**) Drucker–Prager Strength Piecewise yield criterion.

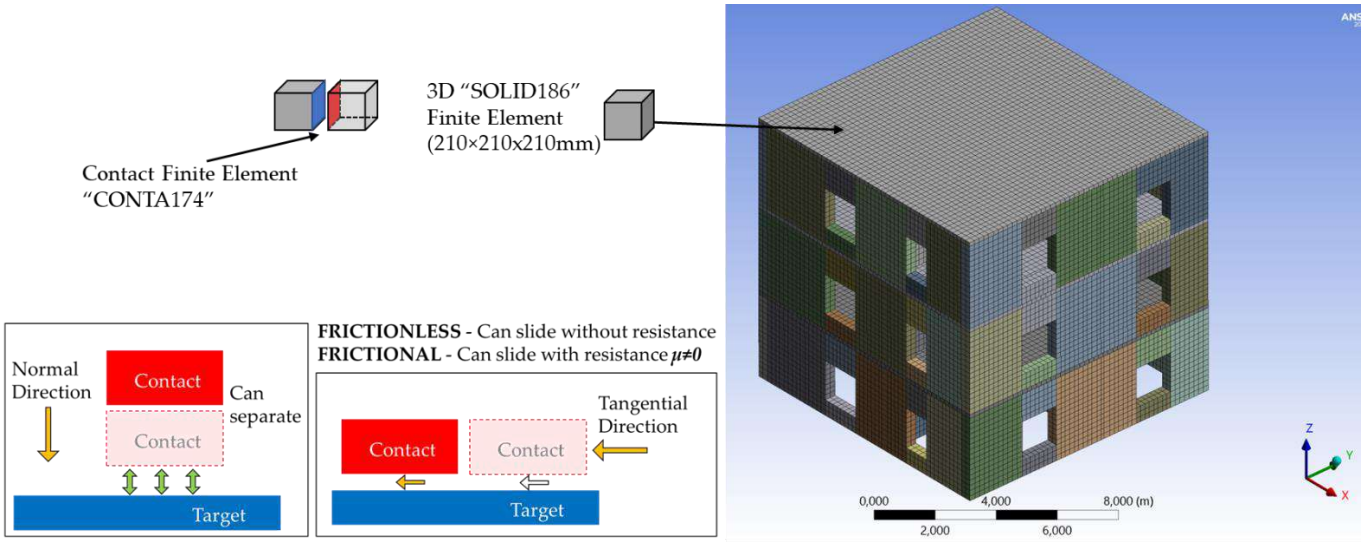

Figure 10. 3D solid model: (**a**) finite element units and contact definition: (**b**) mesh discretization of the 3D solid structural model.

In the frictional contact type setting, "the two contacting geometries can carry shear stresses up to a certain magnitude across their interface before they start sliding relative to each other. This state is known as "sticking." The model defines an equivalent shear stress at which sliding on the geometry begins as a fraction of the contact pressure. Once the shear stress is exceeded, the two geometries will slide relative to each other. The coefficient of friction can be any non-negative value" [32]. In case of frictionless contact type, the elements in contact can slide tangentially without resistance and the normal pressure equals zero if separation occurs. "Thus gaps can form in the model between bodies depending on the load. This solution is non-linear because the contact area may change under load. A zero coefficient of friction is assumed, allowing free sliding" [32].

The mesh discretization and the environment considered in the analyzed model are shown in Figure 10. The total number of solid elements is 31,578 with a size of 210 × 210 × 210 mm. The type of 3D solid elements is "solid186" and the type of contact is "conta174". The total number of the elements is 63,732.

Even though masonry is not a homogeneous material, the modeling process assumes that the material is homogenous for simplicity. This type of modeling, called macro-modeling [33,34], provides reasonable accuracy for stress and strain distribution in large structures. For the same reason, shell elements are considered linear in analysis. The macro-block model with 3D solid elements for masonry walls and the spandrel is based on the assumption that failure occurs at the interface between the spandrel and piers. To simulate this mechanism, tensionless and frictionless behavior is assumed at the interfaces (Coulomb failure criterion [35,36]). Masonry wall piers and spandrels are considered separated blocks. The aim of the numerical study was to observe the general tendency, model stiffness, and structural behavior in comparison with the 2D analysis. Therefore, the quantitative evaluation of stresses and the failure mechanism of the masonry walls were not investigated, considering the plastic behavior of masonry. Table 3 shows the properties of the materials used in all numerical models. Similar approaches of masonry structural systems were also used in the scientific literature [37–45].

3.2. Finite Element Loads Description

The applied loads presented in Figure 11 are described in Table 4.

The recorded accelerograms of the considered earthquakes are in the NS longitudinal direction. Figure 12 illustrates the time history accelerograms recorded for the previously mentioned earthquakes.

Table 3. Material properties used in the models.

Concrete Class C16/20	Density (kg/m^3)		2000
	Young's Modulus (MPa)		29,000
Masonry homogeneous material	Density (kg/m^3)		
	Isotropic elasticity	Derive from Young's modulus and Poisson's ratio	
		Young's modulus (MPa)	2310
		Poisson's ratio (MPa)	0.15
		Bulk modulus (MPa)	1100
		Shear modulus (MPa)	1004
	Uniaxial test data	Compressive stress–strain curve	Figure 9a
	Drucker–Prager strength piecewise	Yield stress–pressure curve	Figure 9b
	Tensile pressure failure	Maximum tensile pressure (MPa)	−0.1
	Crack softening failure	Flow rule	No Bulking
		Fracture energy Gf (J/m^2)	10

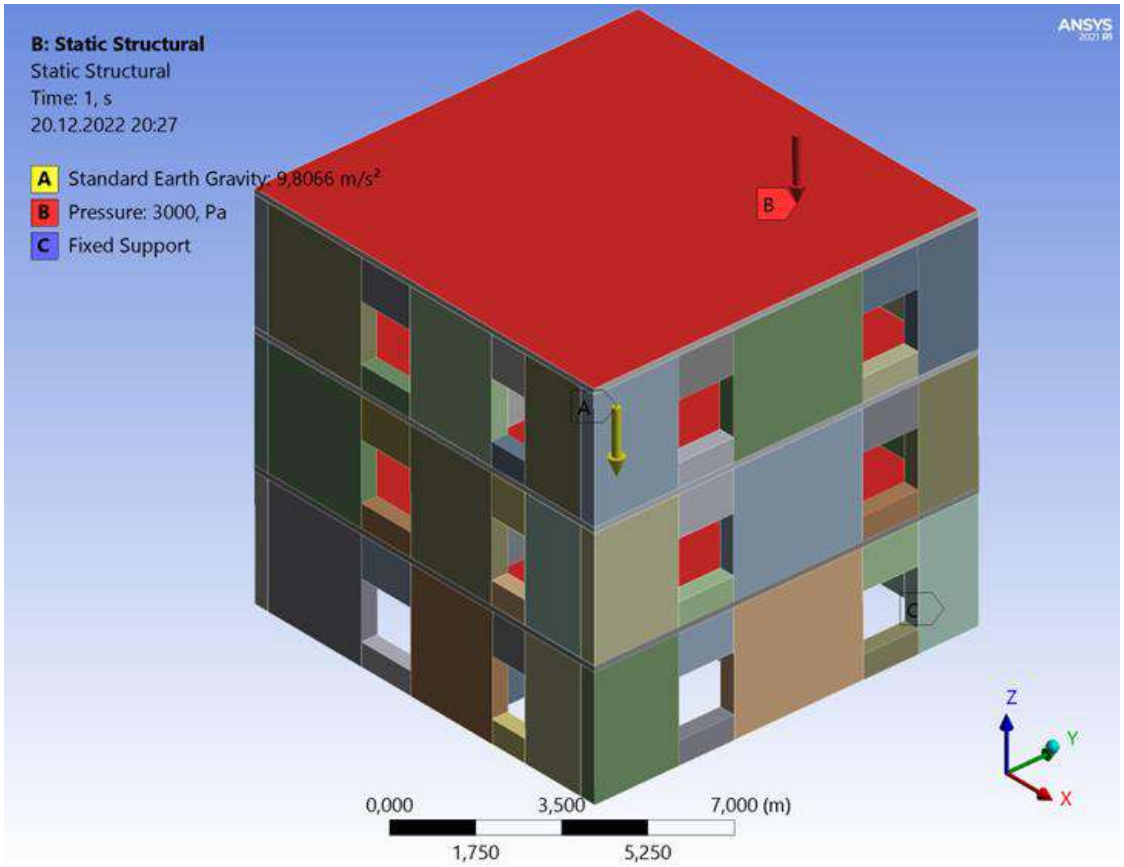

Figure 11. The applied loads on the 3D model.

Table 4. Applied loads [46].

Load Type	Load Name	Characteristic Load Value
Permanent	Self-weight:	
	- Masonry	18 kN/m^3
	- Reinforced concrete	25 kN/m^3
	Plaster 2 cm thickness	0.40 kN/m^2
	Levelling layer + Finishing	1.40 kN/m^2
	Partition walls	1.25 kN/m^2
Variable	Live load: people, furniture	1.50 kN/m^2

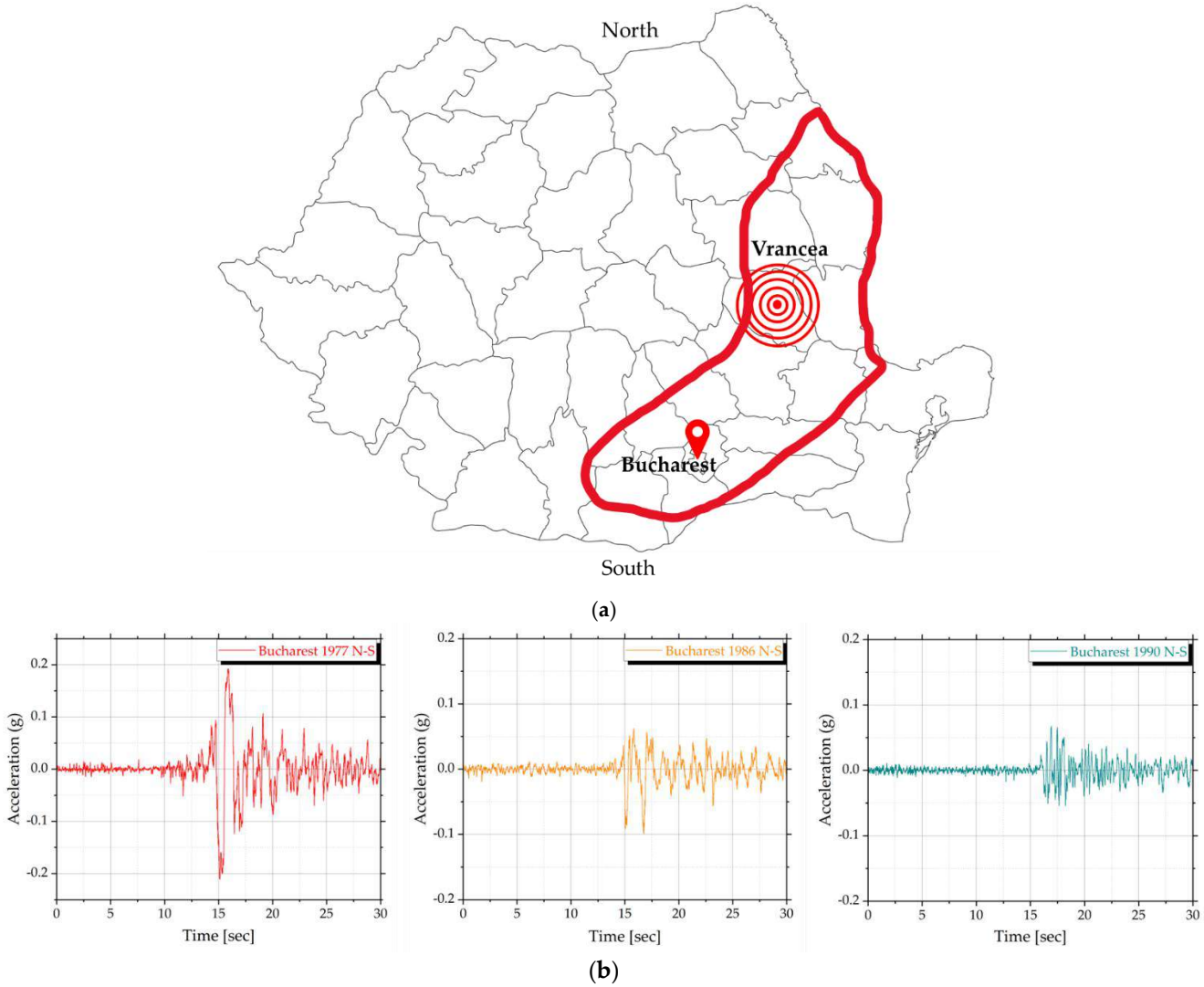

Figure 12. Romania Vrancea's earthquake: (**a**) N–S direction with Vrancea's epicenter and Bucharest capital; (**b**) time history recorded accelerograms in Bucharest, [47].

Time history analysis does not usually apply to assess the seismic response of structures in comparison to conventional methods such as response spectrum or modal analysis method because of the lack of knowledge and availability of the actual ground motion data inputs [48].

In this dynamic analysis, the method may apply the earthquake motion directly at the structure's base by using finite element software environments.

Time history history analysis is a powerful numerical which tool that can provide a structural model response in the time domain to a specific earthquake ground motion

accelerogram [49]. The main advantages of the time history analysis are that it provides a time-dependent history of the structure's responses to a specific ground motion input, providing detailed information about the structure's stress and strain states over the response period. Path-dependent effects such as damping can be computed based on history responses [50].

The analysis is carried out at each incremental time interval and structural responses are evaluated at each time step. The method consists of a step-by-step direct integration in which the time domain is divided into many small time increments δt. At each time interval, the equations of motion are solved with displacements and velocities of the previous step serving as initial functions. Integration of time acceleration history gives the velocity history, integration of which, in turn, gives the displacement history [51].

Details of the input data of seismic actions used in the studied models are shown in Table 5.

Table 5. Input data of recorded Vrancea earthquakes accelerograms [47].

Earthquake Year	Peak Acceleration [m/s^2]	Total Duration [sec]	No. of Points	Spaced Interval	Damping [%]
1977	1.94927	40.14	2008	0.02	5
1986	0.66900	47.98	9596	0.005	5
1990	9.58×10^{-3}	52.9	9870	0.005	5

4. Results and Discussion

4.1. Modal Analysis Results

The modal shapes are shown in Figure 13. It can be observed that the first two modes are translational, having the periods of vibration and modal participating mass ratios given in Table 6. The fundamental period of vibration of the model solved by using the hand calculations shown in the P100-3/2019 code is empirically evaluated based on the number of levels, and is equal to 0.251 s. This value is closer to the fundamental period of vibration of the non-linear 3D model with frictionless contact between the spandrel and piers, as seen in Table 6.

The dynamic analysis results show that in both modeling cases, approaching the link between spandrels and piers contributes to the overall stiffness and dynamic behavior of the masonry structure. In post-earthquake damaged buildings, the separation between spandrels and piers can lead to a more flexible structure and also to the most unfavorable stress distribution in the element structure. The 2D linear shell model with the spandrel replaced by a hinged rigid link body has the most increased fundamental period, followed by the 3D solid non-linear–frictionless model. The presence of spandrel 3D solid elements affects the stiffness of the structure.

4.2. Time History Analysis Results in Terms of Stresses

Figure 14 shows the stress distribution versus time for the 3D solid analyzed models for seismic action recorded in Bucharest in 1977, 1986, and 1990.

Figures 15–17 show the von Mises stress distribution maps for the 2D linear shell model and the 3D solid non-linear model.

A comparison of the results for the seismic action recorded in Bucharest in 1977 shows that the maximum values obtained are similarly distributed. For the 2D linear shell model with rigid links, the maximum value of the von Mises stress is located at the base of the central wall near the door hole because this element is the stiffer and thicker one in the overall structure. The same location is observed for the 3D solid model with frictionless contacts.

For the seismic action recorded in Bucharest in 1986, the values of the von Mises stress are smaller than the previous seismic action. Moreover, for Bucharest 1990, the values are closer to Bucharest 1986 due to the close level of accelerations. Figure 18 shows a comparative graph for the maximum von Mises stress values.

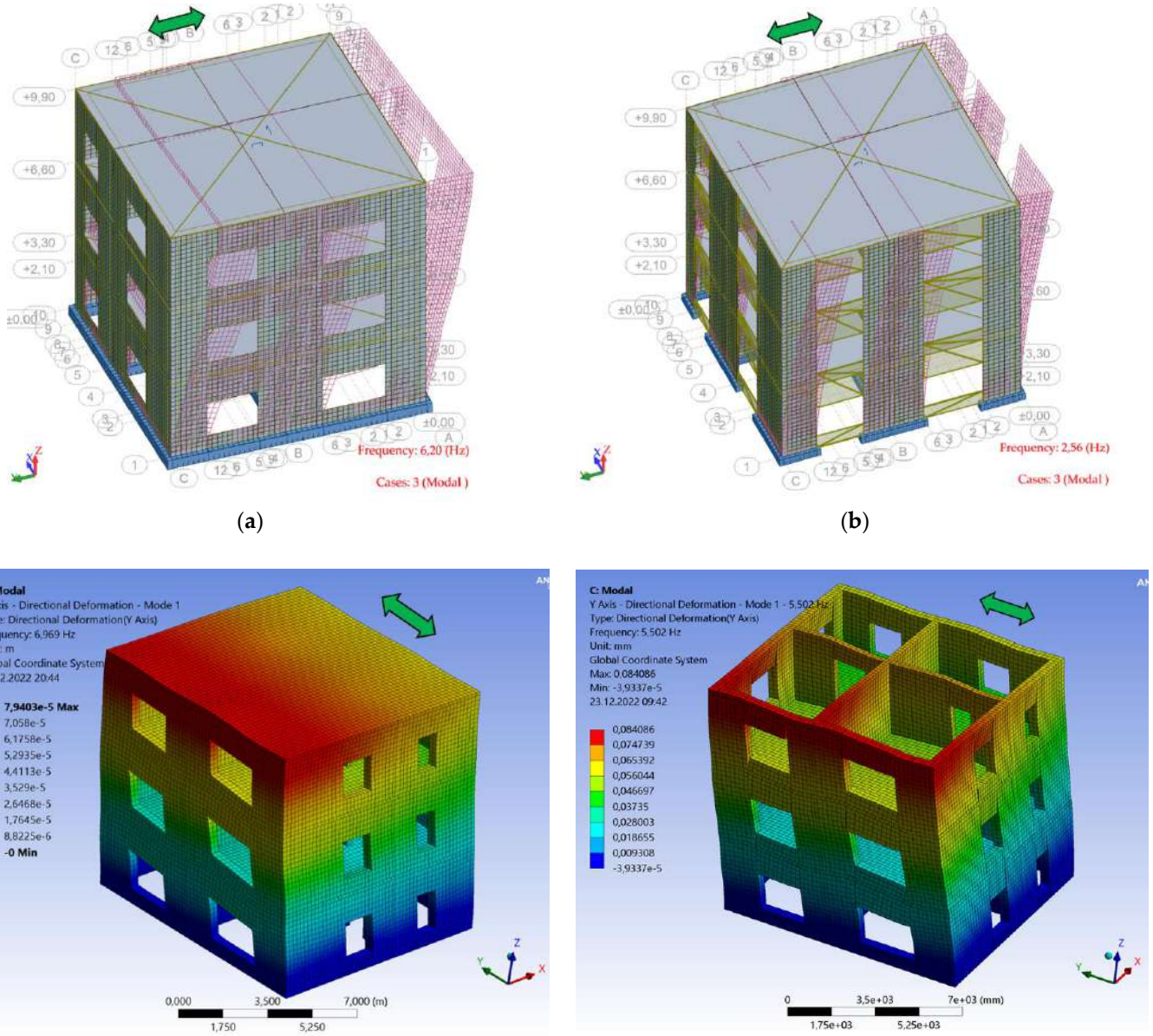

(**a**) (**b**)

(**c**) (**d**)

Figure 13. Modal shapes in first mode of vibration: (**a**) 2D shell linear model—bonded; (**b**) 2D shell linear model—rigid; (**c**) 3D solid model–bonded; (**d**) 3D solid model—frictionless.

Table 6. Dynamic characteristics for the analyzed models.

Numerical Model	Mode	Period [s]	Frequency [Hz]	Modal Participating Mass Ratio on X Direction	Modal Participating Mass Ratio on Y Direction
2D-L-B	1	0.16	6.20	0.001	0.7698
2D-L-R	1	0.39	2.56	0.002	0.6514
3D-NL-B	1	0.14	6.969	0.00073	0.746
3D-NL-F	1	0.18	5.502	0.0014	0.722

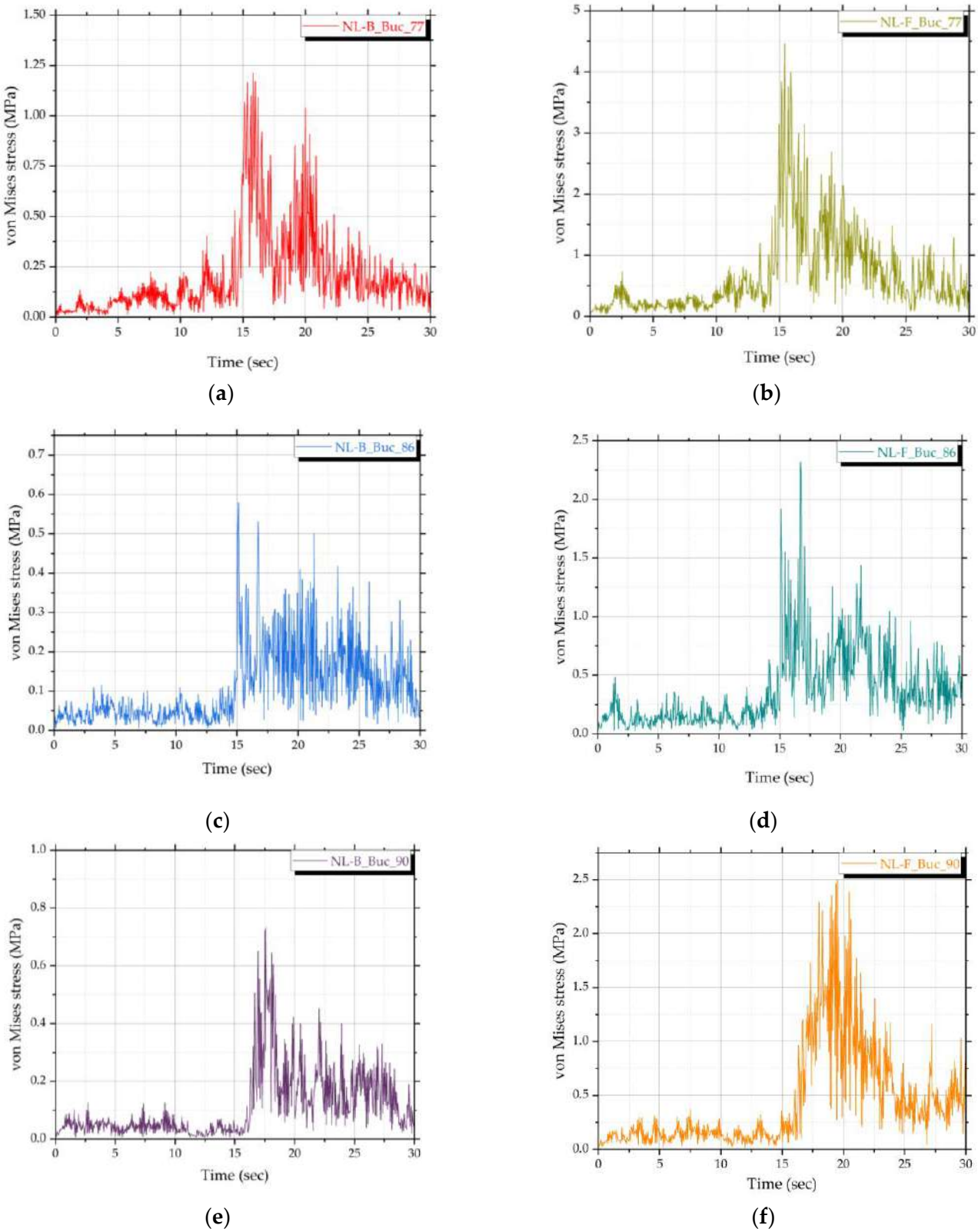

Figure 14. Von Mises stress distribution vs. time for 3D solid models: (**a**) 3D solid non-linear—bonded, Bucharest 1977; (**b**) 3D solid non-linear—frictionless, Bucharest 1977; (**c**) 3D solid non-linear—bonded, Bucharest 1986; (**d**) 3D solid non-linear—frictionless, Bucharest 1986; (**e**) 3D solid non-linear—bonded, Bucharest 1990; (**f**) 3D solid non-linear—frictionless, Bucharest 1990.

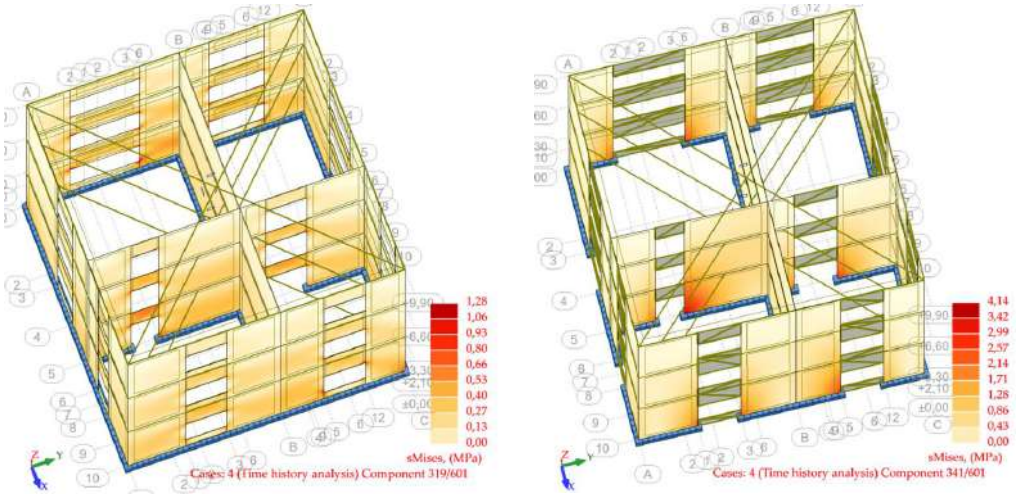

(**a**) (**b**)

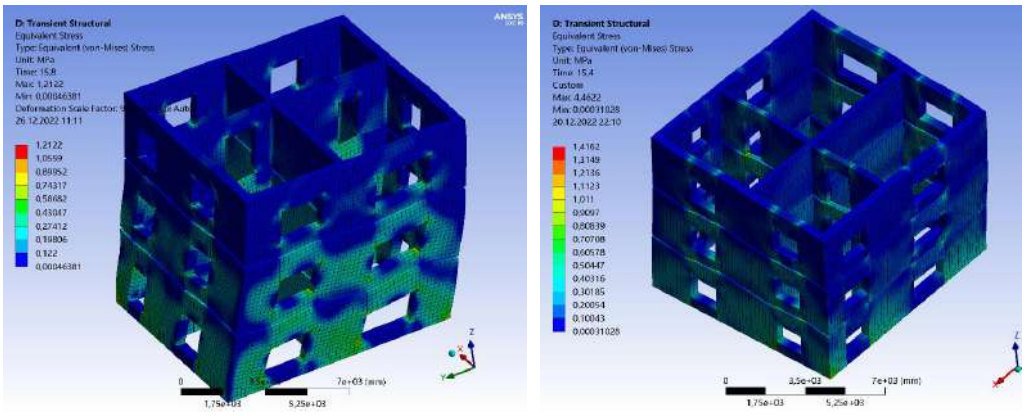

(**c**) (**d**)

Figure 15. Von Mises stress distribution for the seismic action recorded in Bucharest in 1977: (**a**) 2D linear shell model—bonded; (**b**) 2D linear shell model—rigid; (**c**) 3D solid model—bonded; (**d**) 3D solid model—frictionless.

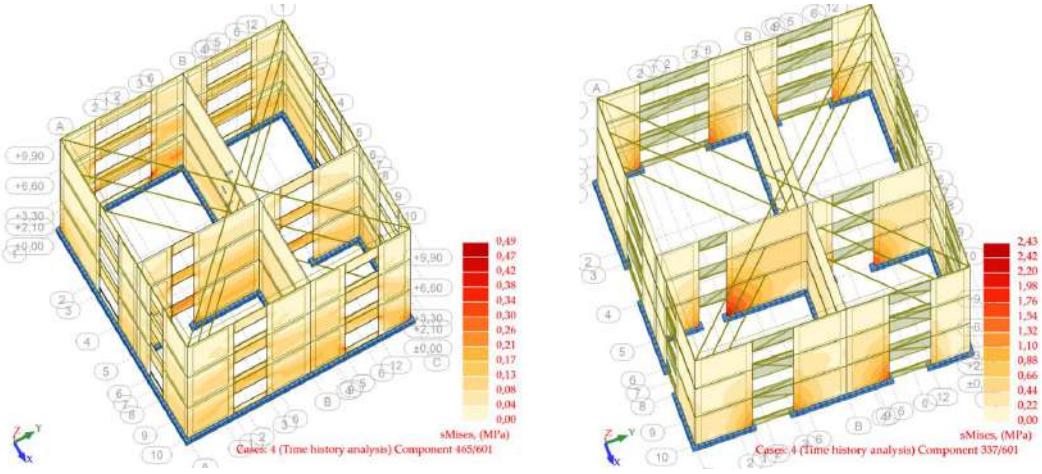

(**a**) (**b**)

Figure 16. *Cont.*

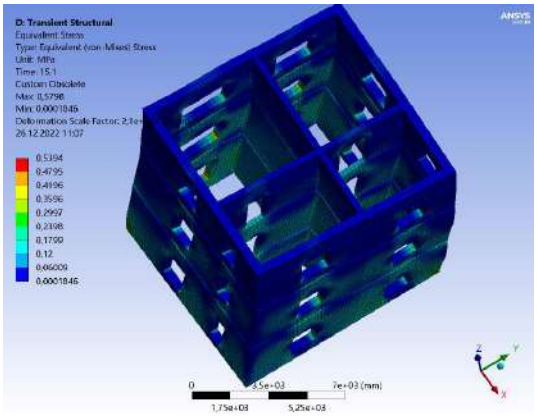

(**c**)

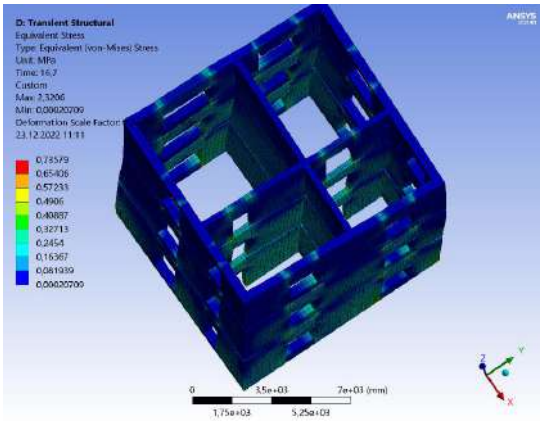

(**d**)

Figure 16. Von Mises stress distribution for the seismic action recorded in Bucharest in 1986: (**a**) 2D linear shell model—bonded; (**b**) 2D linear shell model—rigid; (**c**) 3D solid model—bonded; (**d**) 3D solid model—frictionless.

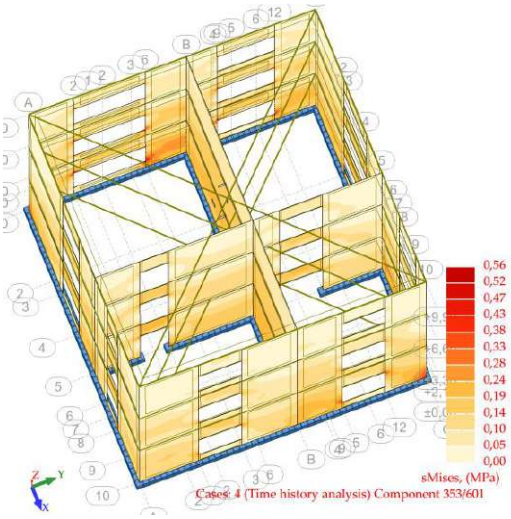

(**a**)

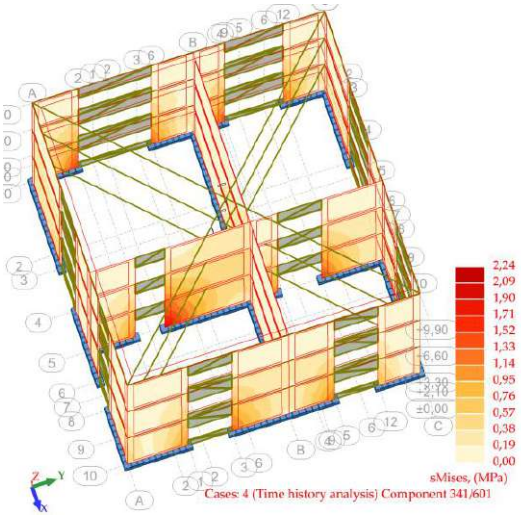

(**b**)

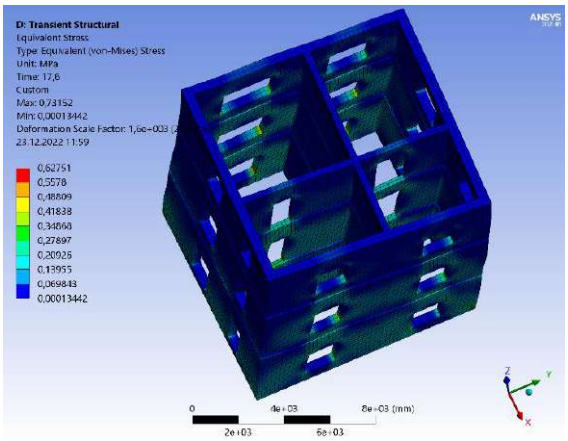

(**c**)

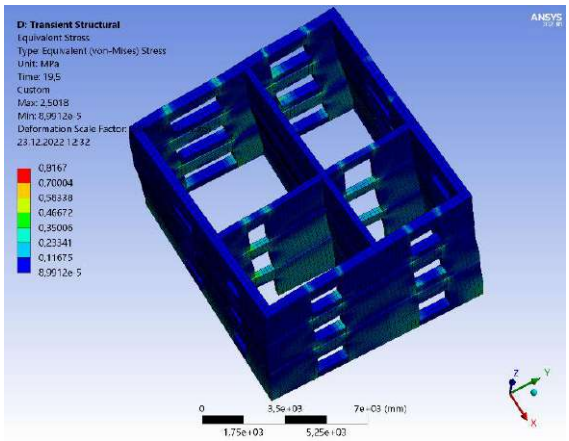

(**d**)

Figure 17. Von Mises stress distribution for the seismic action recorded in Bucharest in 1990: (**a**) 2D linear shell model—bonded; (**b**) 2D linear shell model—rigid; (**c**) 3D solid model—bonded; (**d**) 3D solid model—frictionless.

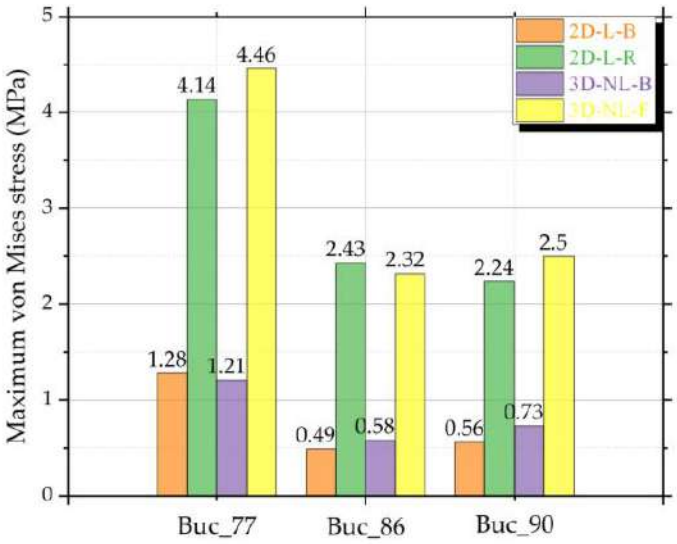

Figure 18. Von Mises stress comparison between time history analyses.

4.3. Time History Analysis Results in Terms of Displacements

Figure 19 presents the displacement versus time graph for the analyzed models in case of Bucharest 1977, 1986, and 1990 recorded seismic action.

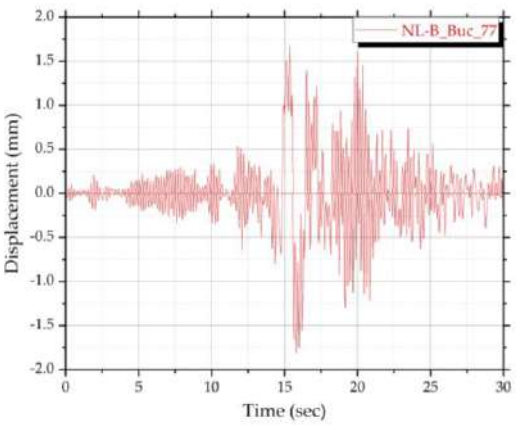

(**a**)

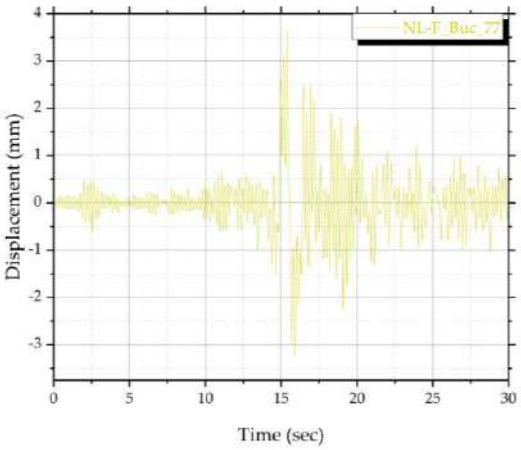

(**b**)

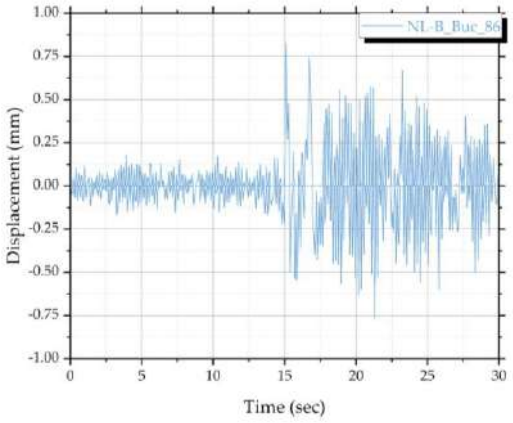

(**c**)

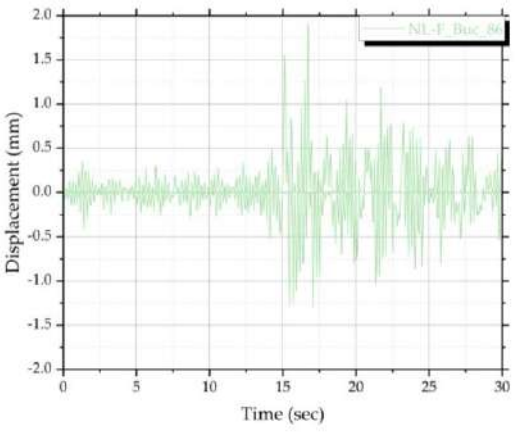

(**d**)

Figure 19. *Cont.*

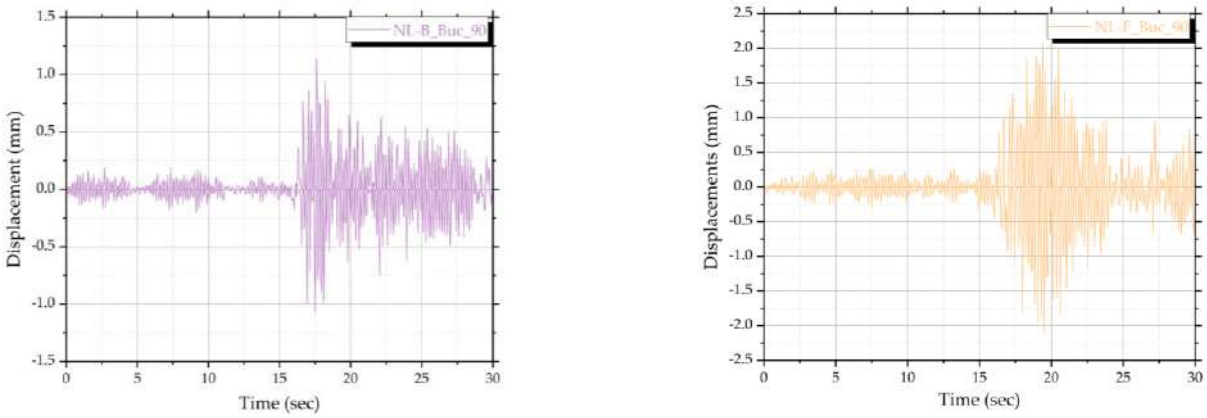

(**e**) (**f**)

Figure 19. Von Mises stress distribution vs. time for 3D solid models: (**a**) 3D solid non-linear—bonded, Bucharest 1977; (**b**) 3D solid non-linear—frictionless, Bucharest 1977; (**c**) 3D solid non-linear—bonded, Bucharest 1986; (**d**) 3D solid non-linear—frictionless, Bucharest 1986; (**e**) 3D solid non-linear—bonded, Bucharest 1990; (**f**) 3D solid non-linear—frictionless, Bucharest 1990.

Figures 20–22 show the deformed shape of the analyzed models and the maximum displacement values from time history analyses.

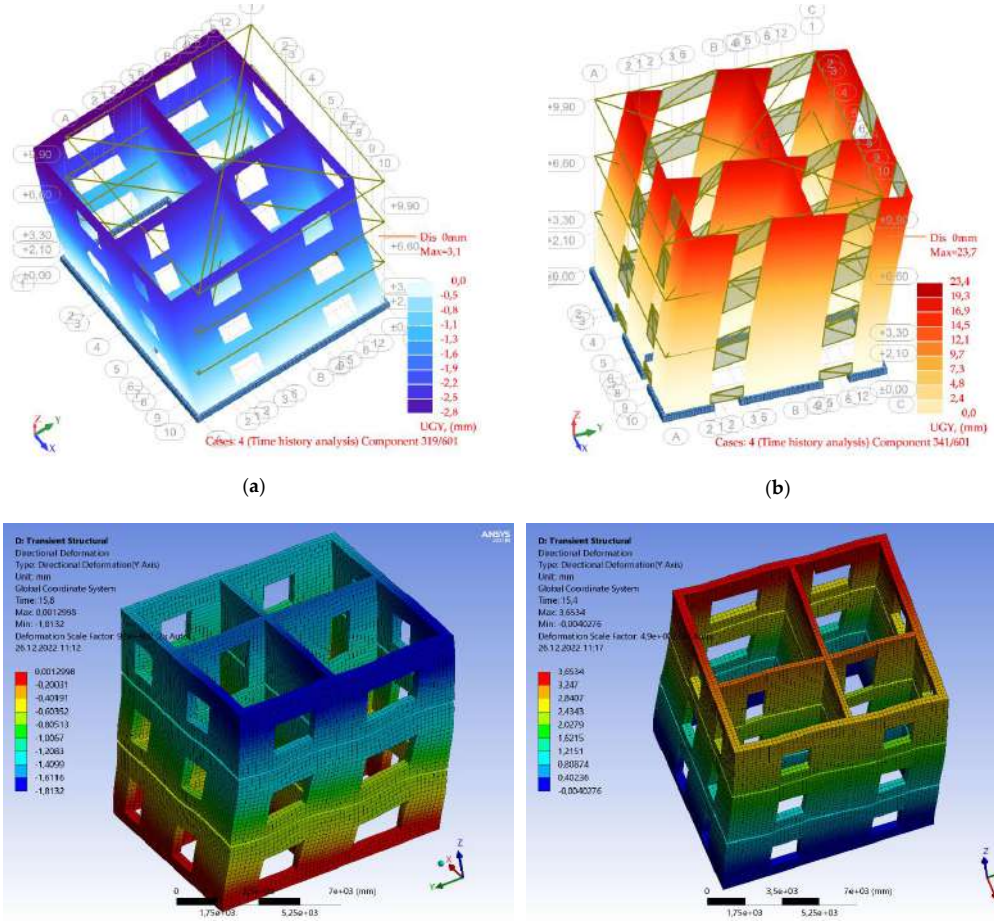

(**a**) (**b**)

(**c**) (**d**)

Figure 20. Displacement distribution map for the seismic action recorded in Bucharest in 1977: (**a**) 2D linear shell model—bonded; (**b**) 2D linear shell model—rigid; (**c**) 3D solid model—bonded; (**d**) 3D solid model—frictionless.

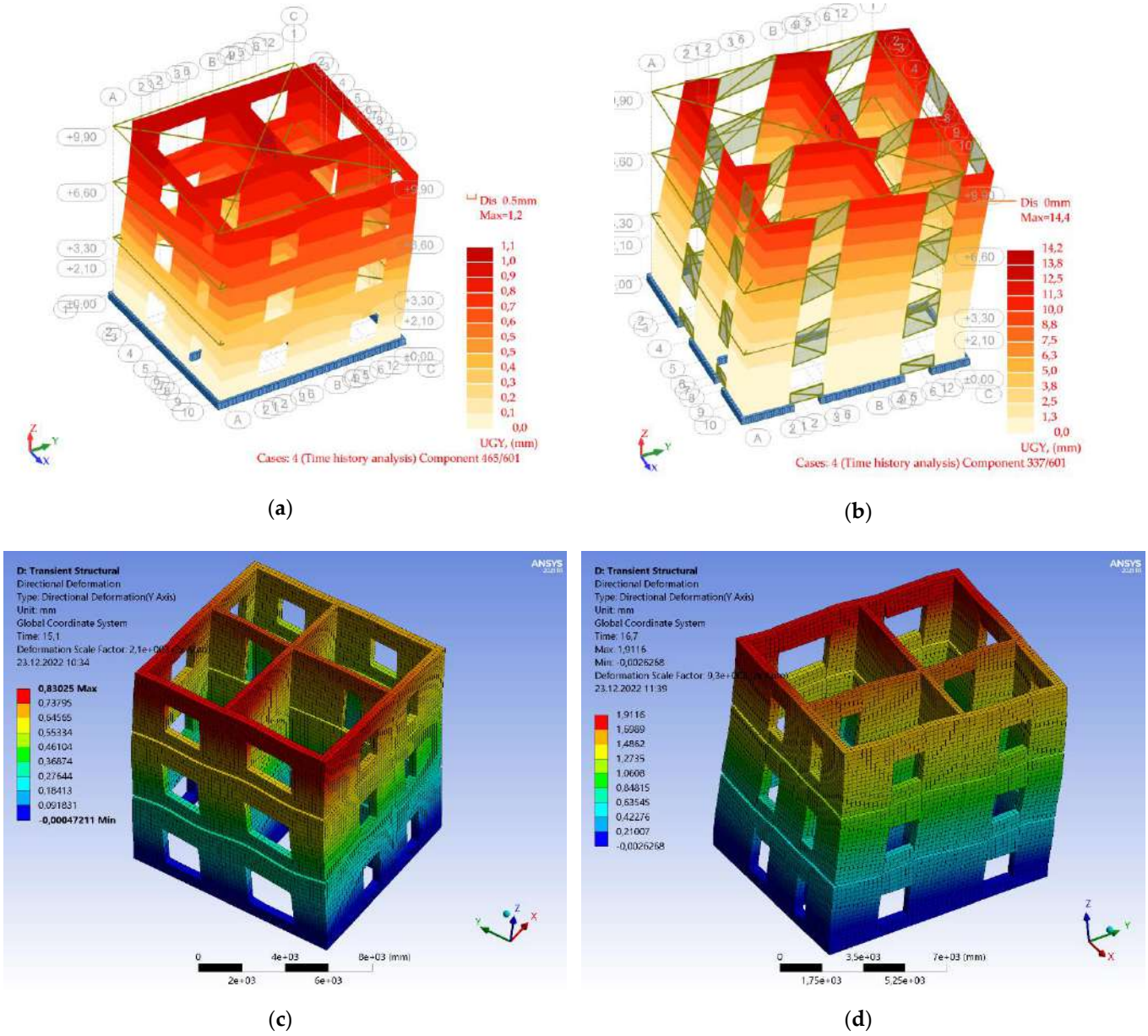

(**a**) (**b**)

(**c**) (**d**)

Figure 21. Displacement distribution map for the seismic action recorded in Bucharest in 1986: (**a**) 2D linear shell model—bonded; (**b**) 2D linear shell model—rigid; (**c**) 3D solid model—bonded; (**d**) 3D solid model—frictionless.

A comparison of the maximum absolute Y-direction displacements for both 2D shell and 3D solid model types, under the three inputs, is shown in Figure 23. The displayed values are under the seismic combination on the Y direction, as this is the weakest axis of the building.

The story displacement values obtained for the 2D linear shell model with rigid links are approximately 8 times larger in comparison with the others for the 1977 earthquake, and at least 13 times larger for the 1986 and 1990 earthquakes. The reason for this difference lies in the lack of flexural rigidity of the linear spandrels and their complete absence. These spandrels are only subjected to compression forces between adjacent piers. Therefore, the piers fully carry the bending moments and shear forces. There is no redistribution of bending moments between vertical structural elements, and for this reason, the design internal forces are larger for the 2D shell model with rigid links instead of spandrel elements. This can also be observed in the results shown in Tables 7–13.

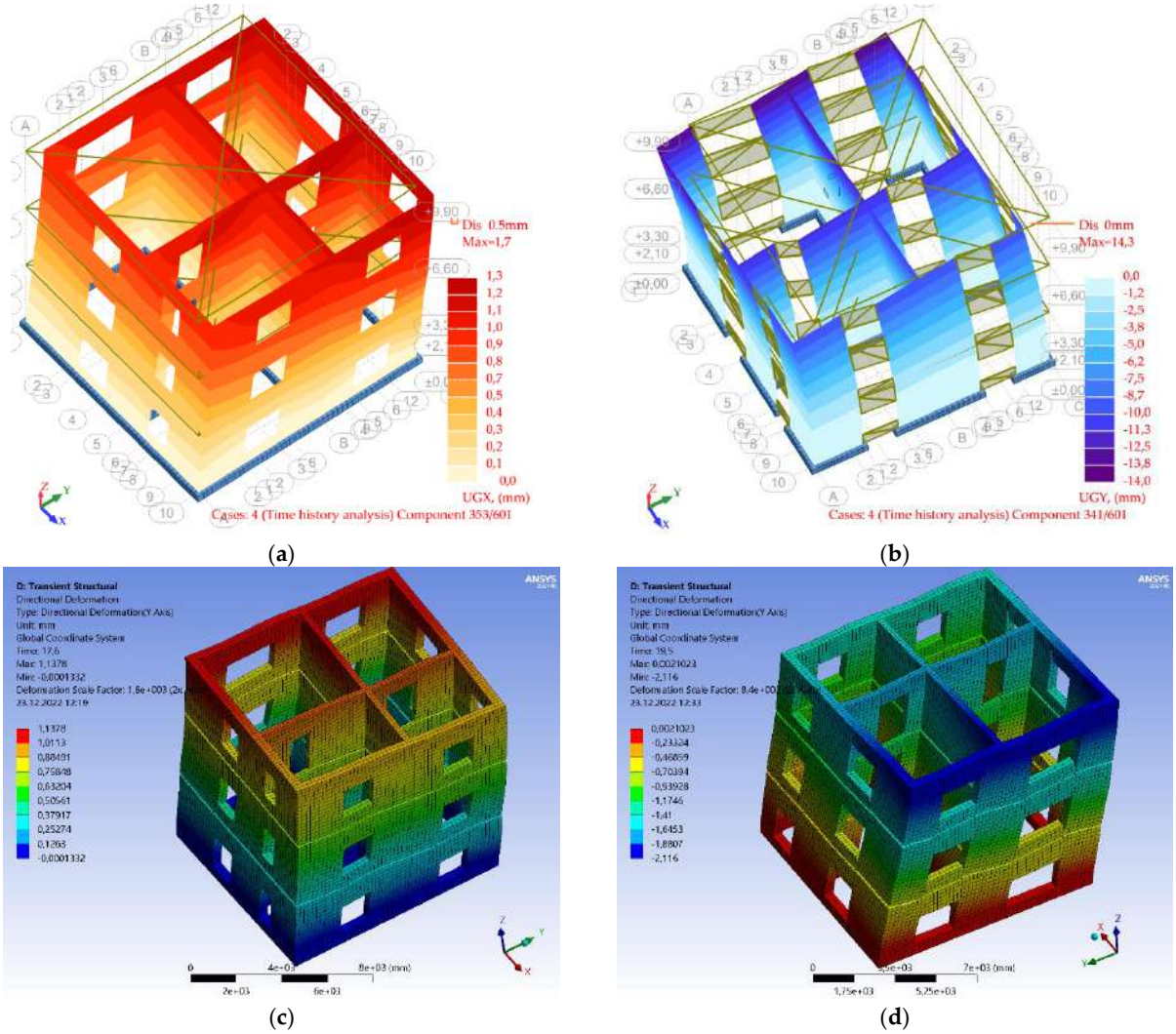

Figure 22. Displacement distribution map for the seismic action recorded in Bucharest in 1990: (**a**) 2D linear shell model—bonded; (**b**) 2D linear shell model—rigid; (**c**) 3D solid model—bonded; (**d**) 3D solid model—frictionless.

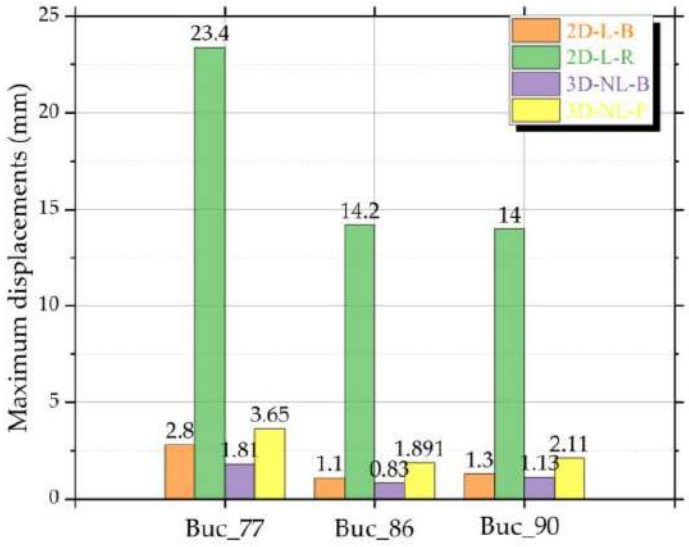

Figure 23. Maximum absolute displacement comparative graph.

Tables 7–13 present the pier internal design forces, shear capacity, R_3 indicator, and seismic risk class for each model obtained from all three recorded earthquakes and hand calculations.

Even though there is no difference in the risk class for the 1977 and 1986 earthquakes, the results show that the R_3 indicator of the linear spandrel model decreased by 10% and 26%, respectively. For the 1990 earthquake, the risk classes are very different; the risk class for the shell spandrel model is Rs IV and the risk class for the linear spandrel model is Rs II, in which case the reduction is 48%. This difference represents a safe construction in the event of a severe earthquake according to design codes (risk class Rs IV) compared to a structure at risk of collapse (risk class Rs II), the latter requiring structural rehabilitation. Furthermore, the results presented in P100-3/2019, obtained after manual calculations of the structure analyzed in this paper, classify the structure into seismic risk class Rs I with $R_3 = 0.25$. The reduction between the shell spandrel model R_3 indicator and manual calculations is 72%. This difference highlights the conservative nature of the design codes, which implies excessive structural rehabilitation demands.

Table 7. Seismic risk class assessment according to P100-3/2019 for the shell spandrel model from 1977 Vrancea earthquake input.

Pier	Load Combo	N_d kN	V_{Ed} kN	M_d kNm	V_{f1} kN	V_{f2min} kN	V_{Rd} kN	$R3_i$
T1	GSY	−238.7	34.359	37.585	107.16	52.842	52.842	1.5379
T2	GSY	−452.4	93.901	138.04	265.2	96.811	96.811	1.031
T3	GSY	−245.6	49.703	50.712	109.63	53.534	53.534	1.0771
T4	GSY	−153.2	17.391	20.931	69.314	34.631	34.631	1.9913
T5	GSY	−495.3	89.91	161.86	457.98	137.61	137.61	1.5305
T6	GSY	−202.1	34.27	37.309	116.44	46.587	46.587	1.3594
T7	GSY	−223	25.557	21.418	135.22	60.908	60.908	2.3833
T8	GSY	−466	75.102	125.63	411.98	155.35	155.35	2.0686
T9	GSY	−168.7	25.315	41.653	80.205	45.253	45.253	1.7876
L1	GSX	−469.8	59.736	74.211	454.55	162.64	162.64	2.7226
L2	GSX	−329.7	46.359	50.011	208.57	83.695	83.695	1.8054
L3	GSX	−166	27.966	36.663	79.114	44.942	44.942	1.607
L4	GSX	−174.2	14.891	17.522	76.726	36.715	36.715	2.4656
L5	GSX	−556.4	96.921	167.61	582.77	155.11	155.11	1.6004
L6	GSX	−147.2	23.479	20.519	67.093	34.009	34.009	1.4485
L7	GSX	−346.1	32.393	30.262	246.15	100.83	100.83	3.1127
L8	GSX	−426.1	56.702	82.537	318.6	124.67	124.67	2.1988
L9	GSX	−117.8	10.223	17.933	40.442	32.131	32.131	3.1429
		R_{3T} = 1.53427 R_{3L} = 2.101445			R_3 =1.53427		Risk class RsIV	

Table 8. Seismic risk class assessment according to P100-3/2019 for the shell spandrel model from 1986 Vrancea earthquake input.

Pier	Load Combo	N_d kN	V_{Ed} kN	M_d kNm	V_{f1} kN	V_{f2min} kN	V_{Rd} kN	$R3_i$
T1	GSY	−239.3	35.572	38.29	107.38	52.903	52.903	1.4872
T2	GSY	−451.2	95.285	141.27	264.69	96.691	96.691	1.0147
T3	GSY	−243.8	50.832	51.386	108.98	53.353	53.353	1.0496
T4	GSY	−152.8	16.283	20.013	69.159	34.588	34.588	2.1241
T5	GSY	−495.4	85.6	157.09	458.01	137.62	137.62	1.6067
T6	GSY	−204.2	32.553	35.895	117.4	46.807	46.807	1.4378
T7	GSY	−218	21.808	19.138	132.59	60.304	60.304	2.7651
T8	GSY	−464.7	67.786	117.47	411.07	155.16	155.16	2.2889
T9	GSY	−164.9	23.128	40.334	78.653	44.81	44.81	1.9374

Table 8. *Cont.*

Pier	Load Combo	N_d kN	V_{Ed} kN	M_d kNm	V_{f1} kN	V_{f2min} kN	V_{Rd} kN	$R3_i$
L1	GSX	−467.3	55.545	71.296	452.52	162.23	162.23	2.9208
L2	GSX	−329.3	44.195	47.998	208.4	83.658	83.658	1.8929
L3	GSX	−166.7	26.761	35.973	79.404	45.025	45.025	1.6825
L4	GSX	−173.8	14.017	16.836	76.579	36.674	36.674	2.6162
L5	GSX	−556	93.282	163.70	582.47	155.06	155.06	1.6622
L6	GSX	−148.6	22.591	19.845	67.611	34.154	34.154	1.5118
L7	GSX	−345.3	31.125	29.199	245.69	100.73	100.73	3.2361
L8	GSX	−425.7	55.096	81.327	318.34	124.61	124.61	2.2618
L9	GSX	−117.1	9.9959	17.790	40.211	32.039	32.039	3.2052
		R_{3T} = 1.59063 R_{3L} = 2.19556				R_3 = 1.59063		Risk class RsIV

Table 9. Seismic risk class assessment according to P100-3/2019 for the shell spandrel model from 1990 Vrancea earthquake input.

Pier	Load Combo	N_d kN	V_{Ed} kN	M_d kNm	V_{f1} kN	V_{f2min} kN	V_{Rd} kN	$R3_i$
T1	GSY	−227.8	64.85	68.83	103.1	51.73	51.730	0.797
T2	GSY	−442.8	157.1	234.8	261.1	95.850	95.850	0.609
T3	GSY	−237.3	80.11	81.41	106.6	52.70	52.703	0.657
T4	GSY	−150.07	31.14	35.01	68.14	34.304	34.304	1.101
T5	GSY	−488.4	145	273.8	453.5	136.713	136.71	0.942
T6	GSY	−192.31	52.30	61.93	111.8	45.5482	45.548	0.870
T7	GSY	−188.20	44.64	49.54	116.6	56.5789	56.578	1.267
T8	GSY	−456.71	117.5	201.5	405.3	153.937	153.93	1.309
T9	GSY	−128.80	36.54	57.20	63.19	40.2977	40.297	1.102
L1	GSX	−435.52	99.49	147.8	427.0	157.184	157.18	1.579
L2	GSX	−323.76	68.95	79.58	205.5	83.0144	83.014	1.203
L3	GSX	−143.07	39.73	48.70	69.41	42.1377	42.137	1.060
L4	GSX	−169.05	24.08	28.51	74.94	36.2124	36.212	1.503
L5	GSX	−537.33	145.3	282.7	568.6	152.614	152.61	1.050
L6	GSX	−145.53	34.10	31.54	66.46	33.833	33.833	0.992
L7	GSX	−327.63	58.86	69.23	235.3	98.377	98.377	1.671
L8	GSX	−420.64	86.93	134.3	315.3	123.937	123.93	1.425
L9	GSX	−103.75	15.69	23.39	36.16	30.411	30.411	1.937
		R_{3T} = 0.91535 R_{3L} = 1.32193				R_3 = 0.91535		Risk class RsIV

Table 10. Seismic risk class assessment according to P100-3/2019 for the linear spandrel model from 1977 Vrancea earthquake input.

Pier	Load Combo	N_d kN	V_{Ed} kN	M_d kNm	V_{f1} kN	V_{f2min} kN	V_{Rd} kN	$R3_i$
T1	GSY	−71.72	36.943	58.725	36.735	11.731	11.731	0.3175
T2	GSY	−366.9	62.793	223.4	226.96	87.884	87.884	1.3996
T3	GSY	−90.54	30.765	63.959	45.733	14.811	14.811	0.4814
T4	GSY	−97.67	20.645	33.115	47.261	28.379	28.379	1.3746
T5	GSY	−456.1	101.59	315.91	431.85	132.42	132.42	1.3035
T6	GSY	−139.3	35.815	59.212	85.229	39.47	39.47	1.1021
T7	GSY	−192.1	25.259	43.538	118.76	57.084	57.084	2.26
T8	GSY	−420.8	71.91	199.61	379.24	148.35	148.35	2.063
T9	GSY	−122	17.755	45.817	60.147	39.384	39.384	2.2182

Table 10. *Cont.*

Pier	Load Combo	N_d kN	V_{Ed} kN	M_d kNm	V_{f1} kN	V_{f2min} kN	V_{Rd} kN	$R3_i$
L1	GSX	−441.9	78.313	167.06	432.22	158.22	158.22	2.0203
L2	GSX	−297.6	42.773	77.403	191.92	79.922	79.922	1.8685
L3	GSX	−159.5	24.211	41.718	76.413	44.167	44.167	1.8242
L4	GSX	−126.5	17.853	27.705	59.131	31.774	31.774	1.7798
L5	GSX	−538.5	111.44	326.13	569.52	152.77	152.77	1.3709
L6	GSX	−104.8	18.262	26.619	50.284	29.255	29.255	1.602
L7	GSX	−315.3	42.122	76.665	227.98	96.707	96.707	2.2959
L8	GSX	−386	55.798	140.07	294.44	119.18	119.18	2.136
L9	GSX	−110.5	7.8918	17.913	38.235	31.248	31.248	3.9595
		R_{3T} = 1.38674 R_{3L} = 1.86434			R_3 = 1.38674		Risk class RsIV	

Table 11. Seismic risk class assessment according to P100-3/2019 for the linear spandrel model from 1986 Vrancea earthquake input.

Pier	Load Combo	N_d kN	V_{Ed} kN	M_d kNm	V_{f1} kN	V_{f2min} kN	V_{Rd} kN	$R3_i$
T1	GSY	−93.45	44.607	71.304	47.1	15.287	15.287	0.3427
T2	GSY	−358.5	73.021	271.45	222.92	54.538	54.538	0.7469
T3	GSY	−46.33	38.515	76.594	24.175	7.5782	7.5782	0.1968
T4	GSY	−103.4	22.42	36.421	49.685	29.082	29.082	1.2971
T5	GSY	−448.3	109.8	356.52	426.48	131.38	131.38	1.1965
T6	GSY	−131.8	38.257	65.985	81.192	38.53	38.53	1.0071
T7	GSY	−168.6	22.474	47.338	105.74	53.992	53.992	2.4024
T8	GSY	−418.1	69.725	205.78	377.21	147.92	147.92	2.1215
T9	GSY	−129.1	16.011	47.72	63.308	40.332	40.332	2.5191
L1	GSX	−439.6	64.487	141.87	430.29	157.83	157.83	2.4475
L2	GSX	−294.3	36.795	66.837	190.12	79.514	79.514	2.161
L3	GSX	−157.8	20.946	37.999	75.678	43.955	43.955	2.0985
L4	GSX	−133.8	15.274	24.252	61.98	32.575	32.575	2.1328
L5	GSX	−543.4	97.423	286.85	573.19	153.41	153.41	1.5747
L6	GSX	−110	15.62	23.184	52.449	29.877	29.877	1.9128
L7	GSX	−314.6	35.6	65.57	227.51	96.6	96.6	2.7135
L8	GSX	−382.6	48.967	124.95	292.38	118.72	118.72	2.4245
L9	GSX	−111.6	6.8775	16.759	38.573	31.384	31.384	4.5632
		R_{3T} = 1.19273 R_{3L} = 2.17513			R_3 = 1.19273		Risk class RsIV	

Table 12. Seismic risk class assessment according to P100-3/2019 for the linear spandrel model from 1990 Vrancea earthquake input.

Pier	Load Combo	N_d kN	V_{Ed} kN	M_d kNm	V_{f1} kN	V_{f2min} kN	V_{Rd} kN	$R3_i$
T1	GSY	120.27	75.719	124.23	59.391	19.673	19.673	0.2598
T2	GSY	−322	123.94	465.17	204.68	52.679	52.679	0.425
T3	GSY	92.971	69.868	129.72	46.873	15.208	15.208	0.2177
T4	GSY	−44.71	36.741	59.344	22.979	7.3131	7.3131	0.199
T5	GSY	−408.1	177.07	595.65	397.52	66.752	66.752	0.377
T6	GSY	−82.31	60.748	110.79	53.017	13.464	13.464	0.2216
T7	GSY	−108.5	31.906	84.892	70.484	17.743	17.743	0.5561
T8	GSY	−385.2	100.62	312.39	352.31	142.59	142.59	1.4171
T9	GSY	−15.58	20.313	67.073	8.3103	2.5481	2.5481	0.1254

Table 12. *Cont.*

Pier	Load Combo	N_d kN	V_{Ed} kN	M_d kNm	V_{f1} kN	V_{f2min} kN	V_{Rd} kN	$R3_i$
L1	GSX	−424.3	123.72	275.11	417.83	155.36	155.36	1.2557
L2	GSX	−273.2	63.076	118.32	178.67	76.912	76.912	1.2194
L3	GSX	−120.5	34.279	57.096	59.506	39.19	39.19	1.1432
L4	GSX	−105.8	27.576	42.888	50.701	29.375	29.375	1.0652
L5	GSX	−505.1	166.37	523.93	543.81	146.85	146.85	0.8827
L6	GSX	−83.88	28.266	41.727	41.246	25.642	25.642	0.9072
L7	GSX	−295.6	71.656	138.11	215.92	93.963	93.963	1.3113
L8	GSX	−362.2	86.458	224.59	279.59	115.82	115.82	1.3396
L9	GSX	−98.56	13.039	23.952	34.55	29.751	29.751	2.2817
		R_{3T} = 0.48495 R_{3L} =1.16019			R_3 = 0.48495		Risk class RsII	

Table 13. Seismic risk class assessment according to P100-3/2019–hand calculations from Annex H.

Pier	Load Combo	V_{Ed} kN	V_{f1} kN	V_{f2min} kN	V_{Rd} kN	$R3_i$
T1	GSY	59.97	26.69	46.7	26.69	0.445
T2	GSY	134.97	57.5	74.1	57.5	0.426
T3	GSY	59.97	26.69	46.7	26.69	0.445
T4	GSY	53.43	17.42	30.3	17.42	0.326
T5	GSY	325	99.98	81.9	81.9	0.252
T6	GSY	95.61	28.78	39.1	28.78	0.301
T7	GSY	166.05	36.2	46.9	36.2	0.218
T8	GSY	364.28	94.36	81.6	81.6	0.224
T9	GSY	93.18	23.67	39.9	23.67	0.254
L1	GSX	418.93	108.23	86.3	86.3	0.206
L2	GSX	172.43	55.87	72.0	55.87	0.324
L3	GSX	77.61	23.67	39.9	23.67	0.305
L4	GSX	41.57	17.42	30.3	17.42	0.419
L5	GSX	324.12	127.91	92.7	92.7	0.286
L6	GSX	41.51	17.56	30.6	17.56	0.423
L7	GSX	144.37	53.85	57.2	53.85	0.373
L8	GSX	170.47	69.38	70.0	69.38	0.407
L9	GSX	21.67	12.22	28.7	12.22	0.564
		R_{3T} = 0.258 R_{3L} =0.257		R_3 = 0.257		Risk class RsI

5. Conclusions

Masonry structures are very difficult to assess for structural rehabilitation. The Romanian design codes presents hand calculation methods with many limitations, such as high volume of work, time-consuming, poor accuracy, overlooked errors, and so on.

Damage occurrence by earthquakes located at the interface between spandrels and piers requires an adequate numerical model in a reasonable manner affordable for ordinary designers. The transformation of the initial structural integrity is validated by experimental data and scientific research literature on past earthquakes. To achieve such a numerical model in the current study, spandrels were replaced by rigid body hinged connections in a 2D linear shell model and with frictionless contact in a 3D solid non-linear model. Time history analyses were performed using three accelerograms recorded during the 1977, 1986, and 1990 Romanian earthquakes. After each time history analysis, it was observed that the numerical model of the initial structure, treated as bonded, exhibited stress concentration at the spandrel corners with maximum values larger than the strength of the masonry. The second stage of the analysis ignores the bond between the spandrel and piers, considering the links damaged, so the analyzed structure behaves very differently.

The results on the analysis show large variations between the two models, some of them making the difference in classifying a structure as either safe or under risk, which imposes some consolidation measures to ensure its strength and safety. A comparison is made between the results presented in this paper and the results of hand calculation provided by the Romanian design code P100-3/2019, which places the model in a risk class that is less favorable than the one obtained with the linear spandrel model. This was not surprising, as design codes are conceived to increase safety. Thus, the methods provided by these codes overestimate the actions applied to structures, usually resulting in unnecessary consolidation measures. This highlights the importance of using a model that best reflects reality and ensures the safety and time efficiency necessary to properly evaluate the structure.

However, this model presents some limitations, such as the fact that when modeling brick masonry as homogeneous, the behavior of spandrels depends on their geometry (slender vs. squat spandrels), undulations in the brick masonry, and the presence and type of lintels. The user of the proposed model should carefully assess the spandrel type and other parameters to model the structure correctly. In addition, using this type of modeling leads to more accurate results, resulting in more accurate consolidation solutions. This is reflected in cost and material efficiency, which, in turn, translates into sustainable consolidation solutions.

Author Contributions: Conceptualization, V.-M.V. and C.-P.N.; methodology, G.T.; software, V.-M.V., G.T.; validation, C.-P.N.; formal analysis, V.-M.V.; investigation, V.-M.V. and C.-P.N.; resources, V.-M.V.; data curation V.-M.V., G.T.; writing—original draft preparation, V.-M.V. and C.-P.N.; writing—review and editing C.-P.N., G.T., A.R.; visualization, C.-P.N.; supervision, V.-M.V., A.R.; project administration, V.-M.V.; funding acquisition, V.-M.V. and C.-P.N. All authors have read and agreed to the published version of the manuscript.

Funding: This research received no external funding. The APC was funded by the Erasmus+ project KA2–Higher education strategic partnerships no. 2018-1-RO01-KA203-049214, Rehabilitation of the Built Environment in the Context of Smart City and Sustainable Development Concepts for Knowledge Transfer and Lifelong Learning–RE-BUILT.

Institutional Review Board Statement: Not applicable.

Informed Consent Statement: Not applicable.

Data Availability Statement: Not applicable.

Conflicts of Interest: The authors declare no conflict of interest.

References

1. Jenkins, R.; Barton, J. *Environmental Regulation in the New Global Economy: The Impact of Industry and Competitiveness*; Edward Elgar Publishing: Cheltenham, UK, 2002.
2. KMB Energy Engineering Company Unveils 6 Fundamental Principles of Sustainable Building Design. Available online: https://www.kmbdg.com/news/energy-engineering-company-sustainable-building-design/ (accessed on 26 December 2022).
3. Almeida, C.P.; Ramos, A.F.; Silva, J.M. Sustainability Assessment of Building Rehabilitation Actions in Old Urban Centres. *Sustain. Cities Soc.* **2018**, *36*, 378–385. [CrossRef]
4. Almssad, A.; Almusaed, A.; Homod, R.Z. Masonry in the Context of Sustainable Buildings: A Review of the Brick Role in Architecture. *Sustainability* **2022**, *14*, 4734. [CrossRef]
5. Ministerul Dezvoltării, Lucrărilor Publice și Administrației. Masonry Structures Design Code—CR 6—2013. 2013. Available online: https://www.mdlpa.ro/userfiles/reglementari/Domeniul_V/V_9_3_CR_6_2013.pdf (accessed on 30 January 2023).
6. Cattari, S.; Beyer, K. Influence of Spandrel Modelling on the Seismic Assessment of Existing Masonry Buildings. In Proceedings of the Tenth Pacific Conference on Earthquake Engineering Building an Earthquake-Resilient Pacific, Sydney, Australia, 6–8 November 2015.
7. *FEMA 356*; Pre-Standard and Commentary for the Seismic Rehabilitation of Buildings. American Society of Civil Engineers: Reston, VA, USA, 2000.
8. Cattari, S.; Lagomarsino, S. A Strength Criterion for the Flexural Behaviour of Spandrel in Un-Reinforced Masonry Walls. In Proceedings of the 14th World Conference on Earthquake Engineering, Beijing, China, 12–17 October 2008.
9. Beyer, K.; Mangalathu, S. Review of Strength Models for Masonry Spandrels. *Bull. Earthq. Eng.* **2012**, *11*, 521–542. [CrossRef]
10. Beyer, K.; Dazio, A. Quasi-Static Cyclic Tests on Masonry Spandrels. *Earthq. Spectra* **2012**, *28*, 907–929. [CrossRef]

11. Beyer, K. Peak and Residual Strengths of Brick Masonry Spandrels. *Eng. Struct.* **2012**, *41*, 533–547. [CrossRef]
12. Dazio, A.; Beyer, K. Seismic Behaviour of Different Types of Masonry Spandrels. In Proceedings of the 4th European Conference on Earthquake Engineering, Ohrid, Macedonia, 30 August–3 September 2010.
13. Ahmad, N.; Ali, M. Displacement-Based Seismic Assessment of Masonry Buildings for Global and Local Failure Mechanisms. *Cogent Eng.* **2017**, *4*, 1414576. [CrossRef]
14. Guerrini, G.; Graziotti, F.; Penna, A.; Magenes, G. Improved Evaluation of Inelastic Displacement Demands for Short- Period Masonry Structures. *Earthq. Eng. Struct. Dyn.* **2017**, *46*, 1411–1430. [CrossRef]
15. Esposito, R.; Messali, F.; Ravenshorst, G.; Schipper, R.; Rots, J. Seismic Assessment of a Lab-Tested Two-Storey Unreinforced Masonry Dutch Terraced House. *Bull. Earthq. Eng.* **2019**, *17*, 4601–4623. [CrossRef]
16. Kim, G.-W.; Song, J.-K.; Jung, S.-J.; Song, Y.-H.; Yoon, T.-H. Lateral Load Distribution Factor for Modal Pushover Analysis. In Proceedings of the Council on Tall Buildings and Urban Habitat, Seoul, Republic of Korea, 10–13 October 2004.
17. Rostami, A.; Poursha, M. A Lateral Load Distribution for the Static Analysis of Base-Isolated Building Frames under the Effect of Far-Fault and near-Fault Ground Motions. *Structures* **2021**, *34*, 2384–2405. [CrossRef]
18. Quagliarini, E.; Maracchini, G.; Clementi, F. Uses and Limits of the Equivalent Frame Model on Existing Unreinforced Masonry Buildings for Assessing Their Seismic Risk: A Review. *J. Build. Eng.* **2017**, *10*, 166–182. [CrossRef]
19. Dumitraş, M.; Cobîrzan, N.; Dumitraş, D. Considerations Regarding the Analysis of Masonry Walls to Horizontal Loads Using Equivalent Frame Method Building. *Bull. Polytech. Inst. Jassy Constr. Archit. Sect.* **2013**, *59*, 41.
20. Gusella, F.; Orlando, M.; Thiele, K. Evaluation of Rack Connection Mechanical Properties by Means of the Component Method. *J. Constr. Steel Res.* **2018**, *149*, 207–224. [CrossRef]
21. Kasaeian, S.; Usefi, N.; Ronagh, H.; Dareshiry, S. Seismic Performance of CFS Strap-Braced Walls Using Capacity-Based Design Approach. *J. Constr. Steel Res.* **2020**, *174*, 106317. [CrossRef]
22. Soveja, L.; Budescu, M.; Gosav, I. Modelling Methods for Unreinforced Masonry Structures. *Bull. Polytech. Inst. Jassy Constr. Archit. Sect.* **2013**, *59*, 19.
23. Taranu, G. *Strengthening of Masonry Arches and Vaults at Historical Monuments/Consolidarea Arcelor si Boltilor din Zidarie la Monumentele Istorice*; Loghin, C., Ed.; Politehnium: Iasi, Romania, 2021; ISBN 978-973-621-497-4.
24. Pleşu, R.; Ţăranu, G.; Covatariu, D.; Grădinariu, I.-D. Strengthening and Rehabilitation Conventional Methods for Masonry Structures. *Bul. Inst. Politeh. Sect. Constr. Arhit.* **2011**, *57*, 165.
25. Venghiac, V.M.; Olariu, C.P.; Budescu, M. Structural Rehabilitation Analyses for a Romanian Cultural Heritage Building Located in Seismic Area. *Adv. Eng. Forum* **2017**, *21*, 196–203. [CrossRef]
26. Pleşu, R.; Taranu, G.; Budescu, M. FEM Analyses of a 1:2 Scale Historical Unreinforced Masonry Building. In Proceedings of the Computational Civil Engineering—CCE2013, International Symposium, Iasi, Romania, 24 May 2013.
27. Ple, R. Contributii Privind Metodele de Reabilitare a Structurilor din Zidarie/ Contributions Regarding the Rehabilitation Methods of Masonry Structures. Ph.D. Thesis, The "Gheorghe Asachi" Technical University of Iasi, Iasi, Romania, 2013.
28. Taranu, G.; Toma, I.-O.; Taranu, N. Shake Table Test of a 1:2 Scale Historical Unreinforced Masonry Building. In Proceedings of the 1st Croatian Conference on Earthquake ENgineering, 1 CroCEE, Zagreb, Croatia, 22–24 March 2021.
29. Ministerul Dezvoltării, Lucrărilor Publice și Administrației. Code for Earthquake Design P100-3/2019 Provisions for the Seismic Assessment of Existing Buildings 2019. Available online: https://www.mdlpa.ro/userfiles/reglementari/Domeniul_I/P100 partea%20a%20iiia.pdf (accessed on 14 January 2023).
30. Ansys | Engineering Simulation Software. Available online: https://www.ansys.com/ (accessed on 19 October 2021).
31. Robot Structural Analysis Professional. Available online: https://www.autodesk.com/products/robot-structural-analysis/overview (accessed on 13 January 2022).
32. Ansys Contact Types and Explanations. Available online: https://www.mechead.com/contact-types-and-behaviours-in-ansys/ (accessed on 14 January 2023).
33. Casapulla, C.; Portioli, F.; Maione, A.; Landolfo, R. A Macro-Block Model for in-Plane Loaded Masonry Walls with Non-Associative Coulomb Friction. *Meccanica* **2013**, *48*, 2107–2126. [CrossRef]
34. Sassu, M.; Andreini, M.; Casapulla, C.; de Falco, A. Archaeological Consolidation of UNESCO Masonry Structures in Oman: The Sumhuram Citadel of Khor Rori and the Al Balid Fortress. *Int. J. Arch. Herit.* **2012**, *7*, 339–374. [CrossRef]
35. Casapulla, C.; Argiento, L.U.; Maione, A.; Speranza, E. Upgraded Formulations for the Onset of Local Mechanisms in Multi-Storey Masonry Buildings Using Limit Analysis. *Structures* **2021**, *31*, 380–394. [CrossRef]
36. Casapulla, C.; Portioli, F. Experimental and Analytical Investigation on the Frictional Contact Behavior of 3D Masonry Block Assemblages. *Constr. Build. Mater.* **2015**, *78*, 126–143. [CrossRef]
37. Hafner, I.; Lazarević, D.; Kišiček, T.; Stepinac, M. Post-Earthquake Assessment of a Historical Masonry Building after the Zagreb Earthquake–Case Study. *Buildings* **2022**, *12*, 323. [CrossRef]
38. Croce, P.; Landi, F.; Puccini, B.; Martino, M.; Maneo, A. Parametric HBIM Procedure for the Structural Evaluation of Heritage Masonry Buildings. *Buildings* **2022**, *12*, 194. [CrossRef]
39. Manzini, C.F.; Ottonelli, D.; Degli Abbati, S.; Marano, C.; Cordasco, E.A. Modelling the Seismic Response of a 2-Storey URM Benchmark Case Study: Comparison among Different Equivalent Frame Models. *Bull. Earthq. Eng.* **2022**, *20*, 2045–2084. [CrossRef]

40. Croce, P.; Landi, F.; Formichi, P.; Beconcini, M.L.; Puccini, B.; Zotti, V. Non-Linear Methods for the Assessment of Seismic Vulnerability of Masonry Historical Buildings. In *Protection of Historical Constructions*; Lecture Notes in Civil Engineering; Springer: Cham, Switzerland, 2022; Volume 209.
41. Asad, M.; Zahra, T.; Thamboo, J.; Song, M. Finite Element Modelling of Reinforced Masonry Walls under Axial Compression. *Eng. Struct.* **2022**, *252*, 113594. [CrossRef]
42. Cannizzaro, F.; Castellazzi, G.; Grillanda, N.; Pantò, B.; Petracca, M. Modelling the Nonlinear Static Response of a 2-Storey URM Benchmark Case Study: Comparison among Different Modelling Strategies Using Two- and Three-Dimensional Elements. *Bull. Earthq. Eng.* **2022**, *20*, 2085–2114. [CrossRef]
43. Beconcini, M.L.; Formichi, P.; Giresini, L.; Landi, F.; Puccini, B.; Croce, P. Modeling Approaches for the Assessment of Seismic Vulnerability of Masonry Structures: The E-PUSH Program. *Buildings* **2022**, *12*, 346. [CrossRef]
44. Cattari, S.; Calderoni, B.; Caliò, I.; Camata, G.; de Miranda, S.; Magenes, G.; Milani, G.; Saetta, A. Nonlinear Modeling of the Seismic Response of Masonry Structures: Critical Review and Open Issues towards Engineering Practice. *Bull. Earthq. Eng.* **2022**, *20*, 1939–1997. [CrossRef]
45. D'Altri, A.M.; Cannizzaro, F.; Petracca, M.; Talledo, D.A. Nonlinear Modelling of the Seismic Response of Masonry Structures: Calibration Strategies. *Bull. Earthq. Eng.* **2022**, *20*, 1999–2043. [CrossRef]
46. *EN 1991-1-1*; European Committee for Standardization Eurocode 1: Actions on Structures—Part 1-1: General Actions—Densities, Self-Weight, Imposed Loads for Buildings. European Committee for Standardization: Brussels, Belgium, 2002.
47. INFP Bridging the Gap between Seismology and Earthquake Engineering: From the Seismicity of Romania towards a Refined Implementation of Seismic Action EN 1998-1 (2004) in Earthquake Resistant Design of Buildings (BIGSEES Project). Available online: http://bigsees.infp.ro/ (accessed on 26 December 2022).
48. *FEMA 450*; Building Seismic Safety Council of the National Institute of Building Sciences NEHRP. Recommended Provisions for Seismic Regulations for New Buildings and Other Structures, Part 1-15. Building Seismic Safety Council of the National Institute of Building Sciences NEHRP: Washington, DC, USA, 2003.
49. Chopra, A.K. *Dynamics of Structures*, 3rd ed.; Pearson Education: Noida, India, 2006.
50. Ministerul Dezvoltării, Lucrărilor Publice și Administrației. Romania P100-1/2013: Seismic Design Code—Part I: Design Rules for Buildings (in Romanian). 2013. Available online: https://www.mdlpa.ro/userfiles/reglementari/Domeniul_I/I_22_P100_1_2013.pdf (accessed on 26 January 2023). (In Romanian).
51. Hartmann, F.; Katz, C. *Structural Analysis with Finite Elements*; Springer: Berlin, Germany, 2007.

Disclaimer/Publisher's Note: The statements, opinions and data contained in all publications are solely those of the individual author(s) and contributor(s) and not of MDPI and/or the editor(s). MDPI and/or the editor(s) disclaim responsibility for any injury to people or property resulting from any ideas, methods, instructions or products referred to in the content.

sustainability

MDPI

Article

Sustainable Design for CFS Structures: Experimental Data and Numerical Models of Hinged Connections

George Taranu [1,*], Vasile-Mircea Venghiac [1], Ioana Olteanu-Dontov [1], Ancuta Rotaru [2] and Ionut-Ovidiu Toma [1]

[1] Department of Structural Mechanics, Faculty of Civil Engineering and Building Services, Technical University Gheorghe Asachi of Iasi, 700050 Iasi, Romania; vasile-mircea.venghiac@academic.tuiasi.ro (V.-M.V.); ioana.olteanu-dontov@academic.tuiasi.ro (I.O.-D.); ionut.ovidiu.toma@tuiasi.ro (I.-O.T.)

[2] Department of Transportation Infrastructure and Foundations, Faculty of Civil Engineering and Building Services, Technical University Gheorghe Asachi of Iasi, 700050 Iasi, Romania; ancuta.rotaru@academic.tuiasi.ro

* Correspondence: george.taranu@academic.tuiasi.ro; Tel.: +40-232-70-14-55

Abstract: Cold-formed steel structures represent a suitable alternative to classical, by now, structural solutions considering the recycling/reuse tendency worldwide as part of the circular economy paradigm. The paper presents a new design approach for CFS profile joints to accurately predict their realistic behavior, based on experimental and numerical investigation of two types of connectors frequently used in the construction industry for manufacturing joints made of CFS profiles: steel-steel pop-rivets (SSPR) and self-tapping screws (STS). The experiments carried out in the case of T-joints subjected to tensile forces tested both solutions. Another significant parameter of the research was the thickness of the steel sheet used to make the CFS profiles. A number of 20 specimens of T-joints made of Cold-Formed Steel (CFS) profiles in total were tested. These consist of five specimens for each of two types of steel sheet thicknesses. The results are relevant for designers because they provide relevant data concerning the limited axial rigidity of T-joints, which are an important instrument in numerical models for achieving the optimum design of the structural system in terms of strength and overall rigidity. Experimental tests calibrate the numerical model that accounts for the axial stiffness of the hinged joints between the CFS profiles. The main parameters of the research are the thickness of the steel sheet and the connector type. The calibrated numerical model used in a case study highlights the advantages of the new approach compared to the classical design procedure based on a conventional hinged connection. Based on the results, the conclusion is that, besides the geometry of the joint and the connector type, the joint stiffness plays a crucial role in the overall behavior of the structural system and should be accounted for in the design process.

Keywords: cold-formed steel profiles; connector; T-joint; axial stiffness; numerical model

check for updates

Citation: Taranu, G.; Venghiac, V.-M.; Olteanu-Dontov, I.; Rotaru, A.; Toma, I.-O. Sustainable Design for CFS Structures: Experimental Data and Numerical Models of Hinged Connections. *Sustainability* **2022**, *14*, 7813. https://doi.org/10.3390/su14137813

Academic Editor: Elena Mele

Received: 30 May 2022
Accepted: 24 June 2022
Published: 27 June 2022

Publisher's Note: MDPI stays neutral with regard to jurisdictional claims in published maps and institutional affiliations.

Copyright: © 2022 by the authors. Licensee MDPI, Basel, Switzerland. This article is an open access article distributed under the terms and conditions of the Creative Commons Attribution (CC BY) license (https://creativecommons.org/licenses/by/4.0/).

1. Introduction

In a constantly changing society with increasing needs and problems, identifying appropriate material and structural solutions for a sustainable design remains of great interest. Cold-formed steel (CFS) profile structures may represent a solution for this new challenge of achieving a sustainable design process. There are already over 100 years of experience in using CFS [1], but intensive research has been carried out only in the last 50 years [2–5], while in the last 30 years it has begun to increase even more [6–8]. Some of that research focused on profile section or structural systems and others on the connection types between profiles under different type of loadings. The use of CFS structures has seen an increasing interest all over the world from Europe in Italy [9–11], Romania [12–15], Turkey [16], UK [17–19], USA [20–22] or Asia [23–28]. CFS structures may tick some of the requirements in terms of sustainability, such as efficiency ratio (strength vs. consumed material quantity, which allows for an assessment by the proportion between

the strength of a structural element and the mass). According to the Steel Framing Industry Association [29], section C profiles have the highest efficiency ratio among construction products. Bending the thin steel sheets obtains a section with stiffness able to undergo various stresses, in which the kinks themselves represent areas of increased stiffness. On the other hand, CFS profiles present stability over time since they do not bend unless excessive loads are applied, do not crack and can have a lifespan of tens or hundreds of years. Adequate insulation significantly avoids and reduces the risk of subsequent repairs or frequent maintenance checks.

When it comes to the new circular economy paradigm, one of the features that place this product in a top position is the possibility to recycle and reuse the steel into other similar products for several cycles. In the last ten years, the responsibility (urge) of designing and carrying out sustainable constructions to preserve and improve the environment has entered the public consciousness [30].

Flexibility in space repartitioning can be made according to the owner's requirements. This feature is available for constructions with interior walls of CFS profiles that can be modified concerning their position and size during the life cycle of the building, according to the needs. The possibility to mount and dismantle these profiles while using appropriate joints is an advantage because it is no longer necessary to rebuild the covered space completely; it can be converted easily according to architectural needs and without additional structural material consumption.

Green buildings and specific standards according to the Leadership in Energy and Environmental Design (LEED) National Green Building Standard (ICC-700) include the qualities of this material (steel) in the list of those certificated for green buildings because of the ability to reuse and recycle CFS profiles [30] according to architectural needs and without additional material consumption.

Understanding and adopting sustainable construction solutions also means cost-effective results. Energy-saving for steel construction profiles, including costs for material production, saving water and the labor costs can lead to efficient and economically attractive buildings.

CFS thin sheets can be transformed in various complex profile section shapes such as "C", "U", "Z", "∑" and others. The main advantage of structures with steel profiles is the degree of prefabrication of the parts. In particular, "C" section has the advantage of positioning the connected parts in joints with enough space for access to mount with different types of connectors. Due to transport and assembly conditions, the pieces can be connected in the factory or on-site. The joints between the resulting compounds can often fulfil constructive requirements only (without any specific bearing function), but there are cases when they also have a structural role and must be able to properly transmit forces between the elements or ensure sufficient global stiffness to abide by the code requirements [31,32]. The CFS profiles can be mounted in different structural system combinations such as frames, lattice systems, rigid structural panels or combinations of the above. Depending on the dimensions of the covered space and the considered structural approach, various research studies investigate the connection types of joints. The most common connections are made with rivets, self-drilling screws, threaded and nut screws, welds or stampings [33–36]. Many research papers study the nonlinear behavior of both profiles and connectors but address only 3D or 2D finite element modelling and emphasize the profile response [37–41].

The scientific literature presents results on CFS profiles for which the main parameter was the connector type, whether be it rivets, blind-rivets, screws or self-drilling screws. The most used configuration of the investigated joints consisted in two plates of thin steel sheets with different numbers of connectors. The parameters of the considered T-joints presented in the present paper were the thickness of the steel sheet as well as the type of connectors. Numerical and laboratory investigations were conducted in order to calibrate the numerical model and to assess, as accurately as possible, the behavior of the considered joints in direct tensile tests. The optimum combination was selected after careful analysis of

both numerical and experimental investigations. The current research uses C150 × 45 mm profiles to enlarge the possible structural system, as this CFS profile is designed to frame structures, structures with lattice beams and lattice columns reaching an opening of 5.00 m and modulated longitudinally at various distances. Currently available design codes, such as Eurocode 3 [42–45], provide reasonable information on the analytical approach to account for the behavior of elements. Consequently, numerical models based on the analytical approach provided in Eurocode 3 may require further significant calibration to match the experimental programs. For example, considering a hinged lattice beam with infinite axial stiffness, the general rigidity of the truss may be overestimated, and the strength capacity of some of its components may be exceeded due to a redistribution of internal forces.

The current study highlights the importance of using force–displacement curves assessed through experiments on the joint types between the profiles of a structural system. Experimental results are comparable to those obtained in other research works available in the scientific literature [46,47].

2. Materials and Methods

2.1. Steel Quality and Connectors

The considered materials are among those available on the market for cold-formed steel profile products. The steel sheets used to form the C profiles have S355 steel grade. The initial purpose of the research was to study the behavior of this type of steel to establish whether these profiles are suitable for load-bearing structural elements. Table 1 presents the steel-steel pop-rivets and self-tapping screws considered for the connections.

Table 1. Materials properties.

Joint part	Material	Strength	
Flange Post C150 × 45 × 10 t = 1.2/1.6 mm	S355 [42]	355 MPa—Yield strength experimental	490 MPa—Maximum strength experimental
Steel-Steel pop-rivets 4.8 × 10 mm [48] 	Zinc coated steel	 2900 N—Shear strength [48]	 3100 N—Tensile strength [48]
Self-tapping screw 5.5 × 22 mm [48] 	Zinc coated steel	 500 MPa—Shear strength [48]	 1000 MPa—Tensile strength [48]

To correctly identify the material and its behavior, experimental tests were carried out according to ISO 6892-1:2019 specifications [23] on samples cut from steel sheet. The steel specimens were cut from the web of the CFS profiles. In the laboratory, five specimens were tested in the ZWICK/ROELL 1000 SP universal test machine. The universal testing machine is hydraulic and has a single central hydraulic drive. The bottom part of the machine is fixed and the upper part can move in a range of 0 to 60 cm. The maximum test speed of the machine is 200 mm/min. The universal testing machine is fully automated and controlled by the TestXpert II v3.5 software. The test speed was based on stress at a rate of 30 MPa/s.

Figure 1 shows the considered specimens extracted from the CFS profiles. The strains were measured using an external extensometer attached by contact to the specimen. Figure 2 shows the stress–strain curves obtained on all the tested samples.



(**a**) (**b**)

Figure 1. Laboratory experimental test on S355 steel sheets: (**a**) samples with extensometer mounted in universal testing machine; (**b**) samples tested.

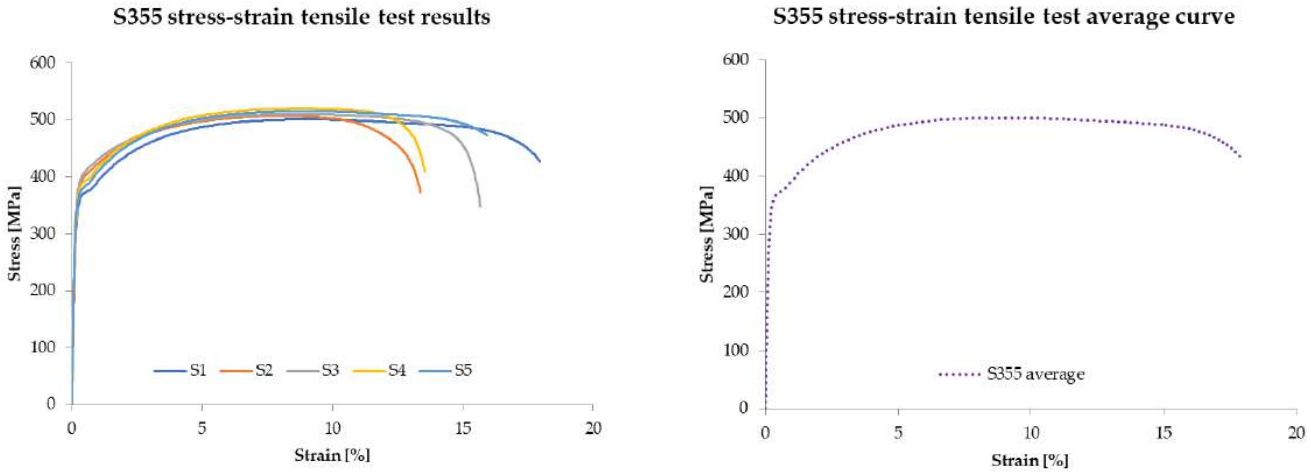

(**a**) (**b**)

Figure 2. Stress–strain curves for S355 steel sheet in tensile test: (**a**) curves for the 5 specimens; (**b**) average curve.

2.2. Connection's Geometry and Testing Methodology

Figure 3 presents the geometry of the elements making up the T-joint and the geometry of the joint itself. Both interconnected parts have a hole located in the center of the contact area of the C-profile flange where the connector sets in.

The specimens were mounted in the universal testing machine employing steel adaptors, with the primary role being to align the joint with the direction of the applied tensile load. A 10 mm thick welded T-shaped steel adaptor connected the joint to the lower grips of the testing machine. The experiment uses a 300 × 150 × 10 mm steel sheet in the upper part, as shown in Figure 3. 4 M14 screws fastened these adaptor pieces at the upper and lower regions of the T-joint. A constant loading rate of 50 N/s was applied until the failure occurred. The internal transducer of the testing machine recorded the absolute displacements.

The labelling of the tested specimens shown in Figure 3, which depends on the connector type and the thickness of the steel sheet, is explained in detail in Table 2. Two series of specimens operated based on the steel sheet thickness of the CFS profiles. For

each of the two series, two different connector types were considered. Furthermore, each sub-grouping consisted of five specimens for 20 specimens in total. Hence, the specimen labeling had in view the specimens (S), the sample number within the sub-group (1–5), the series type based on steel sheet thickness (A or B) and the type of connector (SSPR or STS).

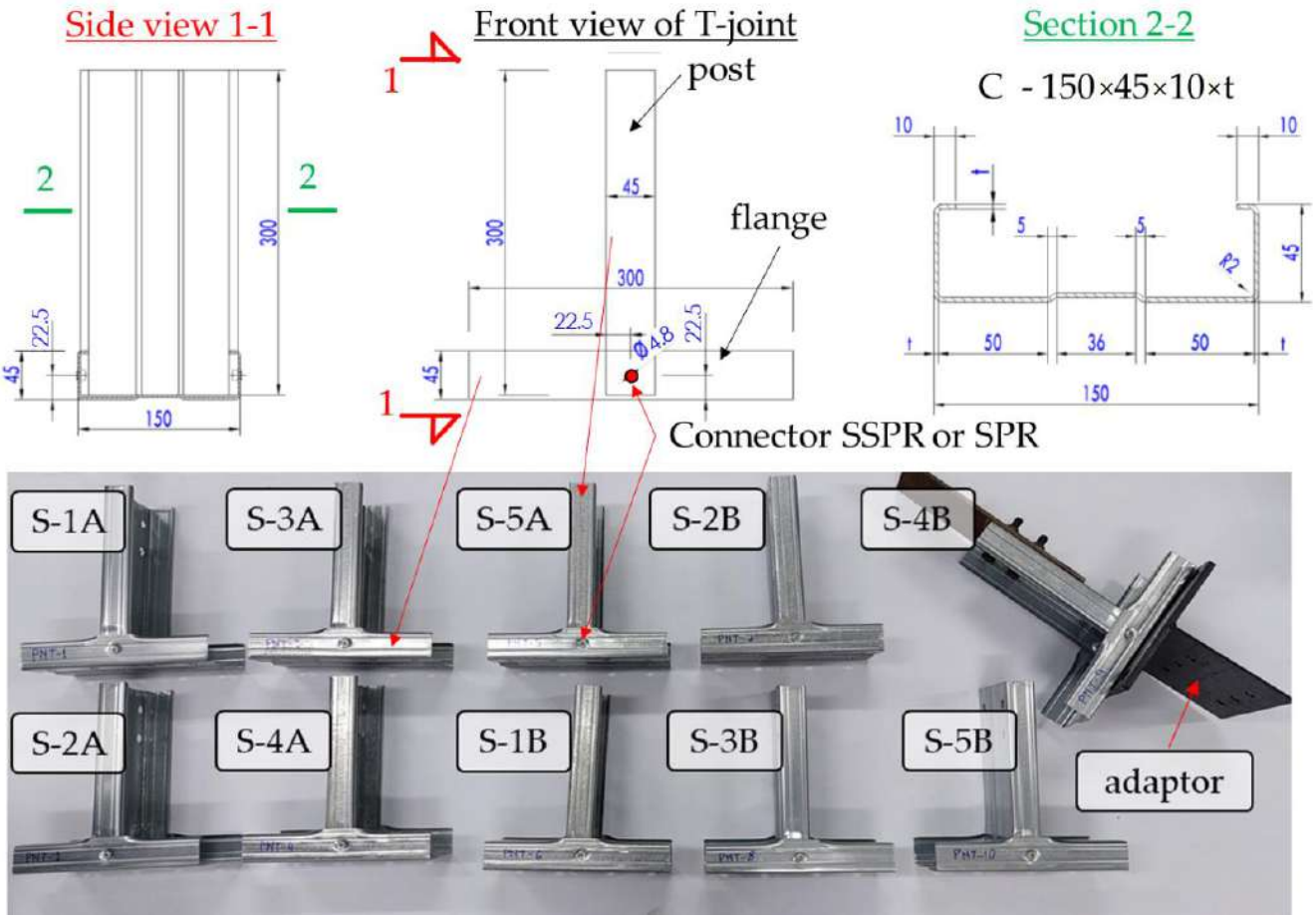

Figure 3. Geometry and dimensions for the tested joints, C-profile characteristics, respectively.

Table 2. Experimental tested specimen label and description.

Specimen		C-Profile Thickness (mm)	Connector
S-1A SSPR	S-1A STS	A = 1.2	(SSPR) Steel-Steel Pop-Rivet
S-2A SSPR	S-2A STS		
S-3A SSPR	S-3A STS		
S-4A SSPR	S-4A STS		
S-5A SSPR	S-5A STS		
S-1B SSPR	S-1B STS	B = 1.6	(STS) Self-Tapping Screw
S-2B SSPR	S-2B STS		
S-3B SSPR	S-3B STS		
S-4B SSPR	S-4B STS		
S-5B SSPR	S-5B STS		

Figure 4 shows the details of mounting the joint specimens in the Zwick/Roell 1000SP universal testing machine and details of the used connectors.

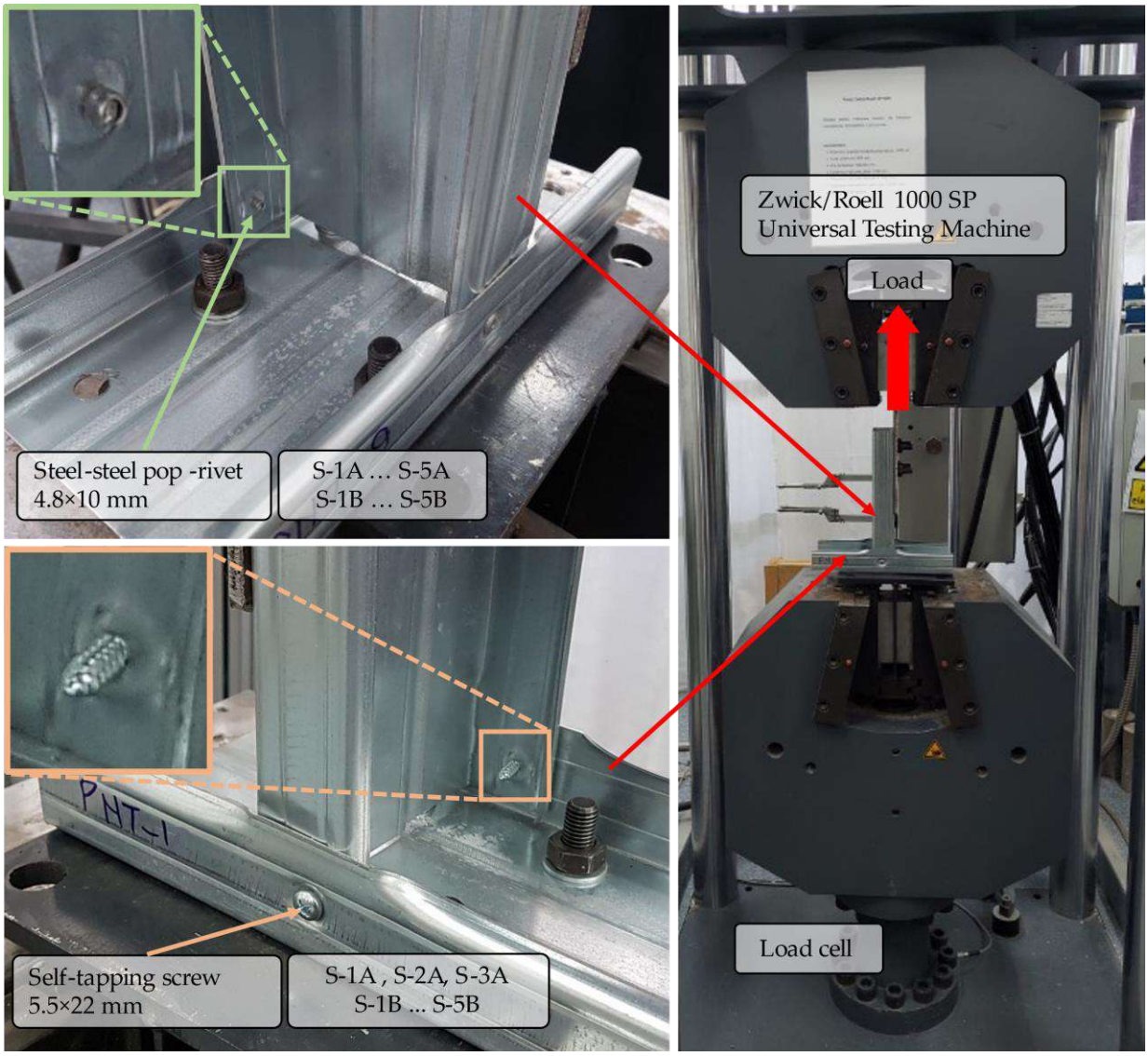

Figure 4. Testing equipment, specimens and connector details.

A 10 T-joint sample set with SSPR connectors was ready during the first stage. After their failure and the investigation of the pre-drilled holes, the elements met together again using self-drilling screws of Ø5.5 × 22 mm. The new joints were tested again with the same test parameters to assess an aspect of the sustainability properties for CFS presented at the beginning, namely their capacity to be reused after a dismantling process. The number of the reuse cycle evaluation and the effect on the residual strength capacity of the elements to be recycled are topics of future research.

3. Experimental Testing Results

3.1. Experimental Results for Connections with Rivets—SSPR

The TestExpert control program recorded and exported the force–displacement curves (P-Δ) for post-processing and analysis. Figure 5 shows the comparative overlapping curves for each of the five distinct situations mentioned in Table 2.

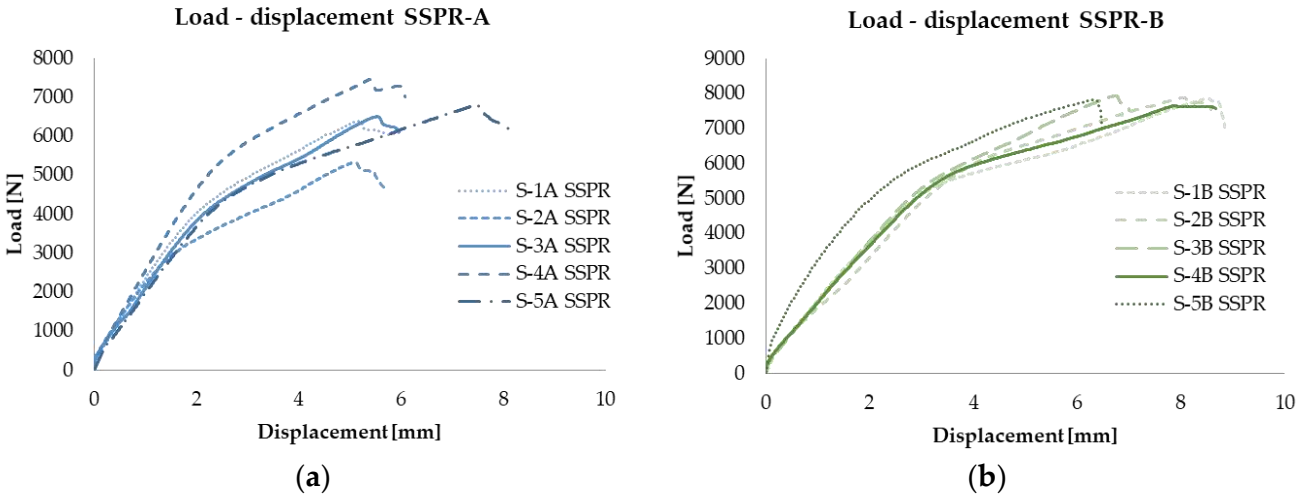

Figure 5. Force–displacement results for (**a**) joint connection type SSPR-A; (**b**) joint connection type SSPR-B.

The graph in Figure 5a shows that the maximum load value for SSPR-A joints reached approximately 7400 N per node only for specimen number 4 and a displacement of 5.4 mm, while all the others were around 6500 N with a 5.5 mm maximum displacement. That shows that in the 1.2 mm steel sheet case, the shearing and crushing of the rivet caused the failure. In the case of the increased thickness, the B series with a 1.6 mm thickness, which used SSPR joints, experienced a complex stress state in the rivets located on the larger contact surface between sheets and rivets, which were crushed, bent and sheared. The maximum recorded value was 7900 N, which was 21% higher than in the case of SSPR-A, at a displacement of 6.40 mm, as shown in Figure 5b.

3.2. Experimental Results for Connections with Screws STS

In the case of the A series with STS connectors, only three results were allowed due to technical causes, as shown in Figure 6a. Thus, a maximum load value of 16,500 N, with a corresponding displacement of 15 mm, was obtained in the case of S-1A STS. Meanwhile, the average peak load value was 15,300 N with a 16.85 mm corresponding displacement. In the case of the B series, Figure 6b, the STS-B samples reached a maximum value of 20,100 N and a corresponding displacement of 19.6 mm for S-3B STS. The average load value for STS-B samplings was 18,500 N, recording a 17.5 mm displacement.

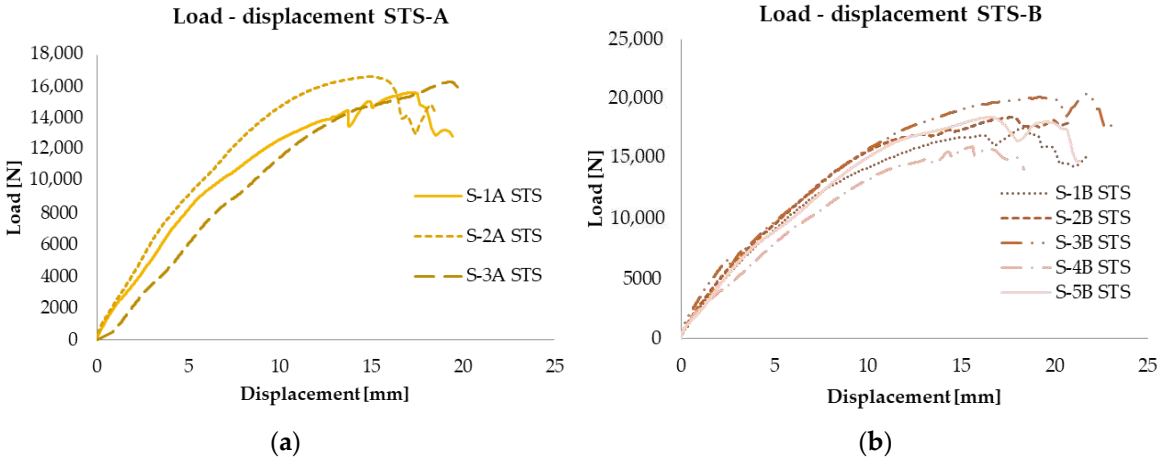

Figure 6. Force–displacement results for (**a**) joint connection STS-A; (**b**) joint connection STS-B.

All average force–displacement curves are compared graphically in Figure 7. The results show that both sheet thickness and connector type influence the behavior and the load-carrying capacity of these joints. Four distinct areas allow identification from the force–displacement curve analysis for the SSPR-A and SSPR-B joints. The four areas indicated on load-displacement SSPR-A average curve in Figure 7 are similar for other types of joints tested.

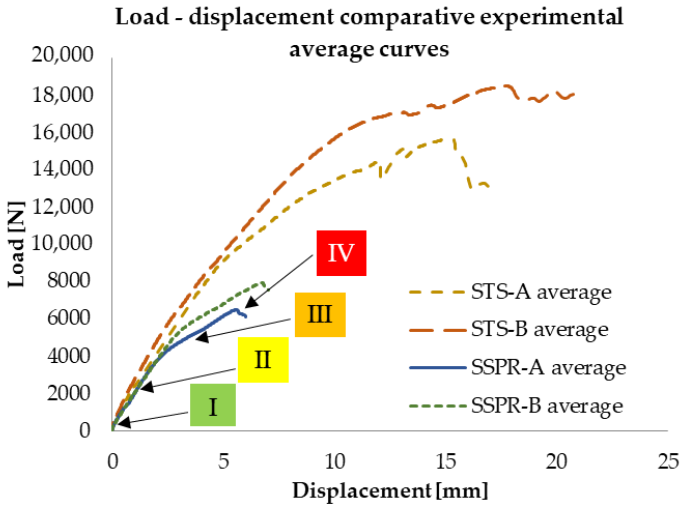

Figure 7. Comparison of the experimentally obtained average force–displacement curves.

According to the stiffness highlighted in Figure 7, the four distinct areas of the joint's behavior consider the stiffness of the connection as follows:

1. In Area I, the initial stiffness attained 2150 N/mm for SSPR-A and 2170 N/mm for SSPR-B. For the screw joints, the initial stiffness reached 2295 N/mm for STS-A and 2360 N/mm for STS-B, respectively. These initial values are about 40% higher than the stiffness in the elastic Area II due to the presence of embedded drawings.
2. Area II, with elastic behavior, is wider compared to the initial one. The average stiffness value was 1520 N/mm for SSPR-A and 1598 N/mm for STS-B.
3. Area III corresponds to the plastic range when the displacements increase more than the loads. The average stiffness was 628 N/mm for SSPR-A and 677 N/mm for STS-B.
4. Area IV represents the failure area when the node can no longer take loads, and the displacements increase until the rivets break or the screws are torn-up due to the shearing of the material around holes.

These stiffness values and the idealized bilinear curves of the node behavior obtained through experiments are the input data for the finite element numerical simulation. Namely, they are in the definition of the nonlinear behavior of hinged joints. Section 4 of the paper summarizes the stiffness values and idealized curves according to the Robot Structural Analysis calculation software requirements [49].

3.3. Failure Modes of the SSPR and STS Connections

Figure 8 shows the failure mechanism of the SSPR-A joint connection with a detail of the rivet status after failure. Small surfaces indicating little worn-out areas on the steel profile are also noticeable between the drawn areas around the holes of the profile. The marked area presence showed increased friction between the elements and an initial stiffness increase of up to 10% from the maximum loading value. The areas with plastic deformations were not visible to the naked eye after the failure of the rivets in the connection area.

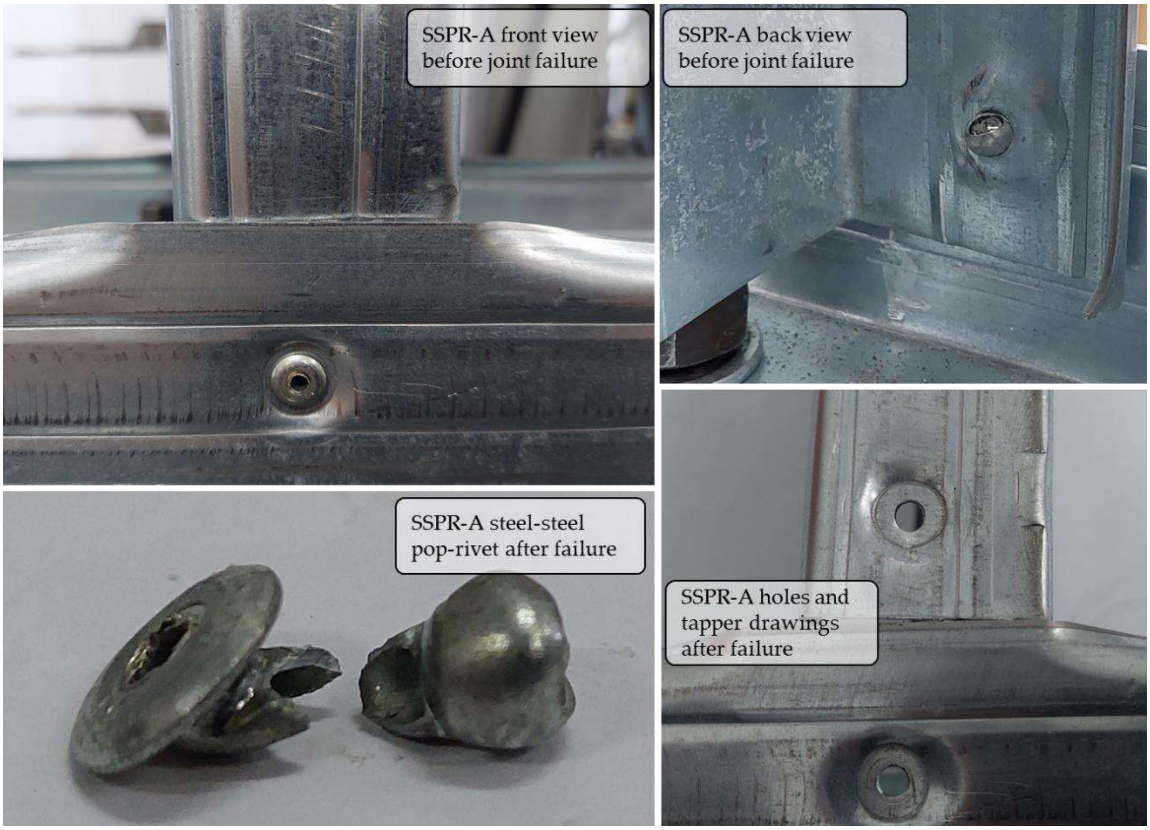

Figure 8. Failure mechanism of steel-steel pop-rivets joints SSPR-A.

Figure 9 presents the failure of an SSPR-B joint and the contact areas between elements, highlighting their post-failure aspect. Slight worn-out surfaces appearing in the lower part of the drawing areas of the strut elements and the upper part of the drawing areas of the horizontal component denoted by 1 in Figure 9 were identified, which means that the friction between the elements during the tests was significant in the first stage. Plastic deformation areas develop to a small extent at the hole level in the strut. The rivets failed due to a combination of bending, crushing and shearing.

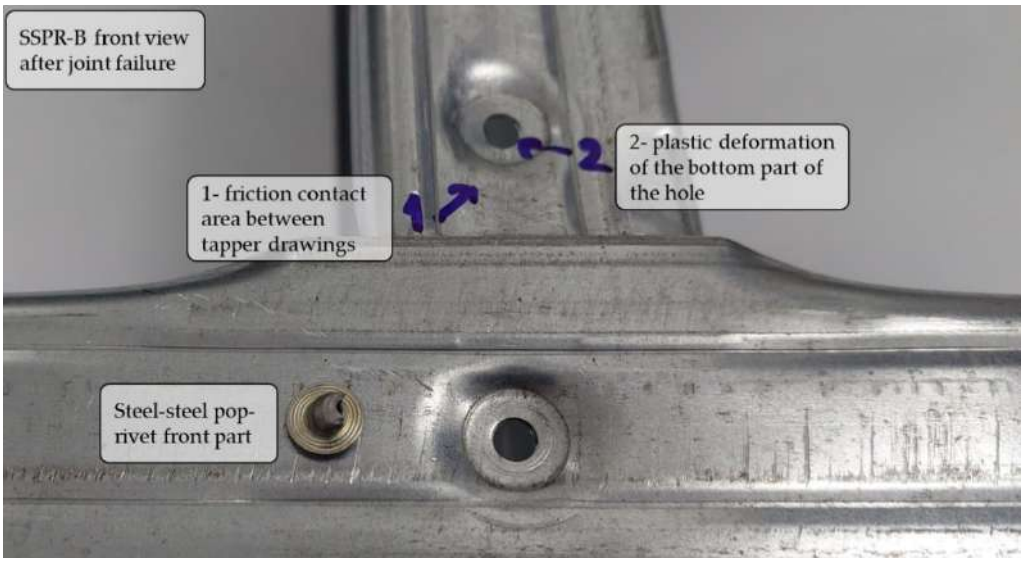

Figure 9. Failure mechanism of steel-steel pop-rivets joints SSPR-B.

Figure 10 shows details of the failure mechanism of a STS-A joint regarding the rotation of screws, the local bending of drawing cups and the plastic deformation of holes. Figure 11 presents a similar failure mechanism observed for the case of STS-B joints. The existence of screws and their thread favored a more ductile behavior, the final failure mechanism being gradual as opposed to the failure mechanism observed for the joints with rivets that failed in a brittle manner.



Figure 10. Failure mechanism of self-tapping screw joints STS-A.



Figure 11. Failure mechanism of self-tapping screw joints STS-B.

4. Numerical Simulation of Joints with 1D Finite Elements

4.1. Input Data

According to Chapter 5, Section 5.1.1 from EN 1993-1-1 [42], the structural model and the simplifying assumptions must reflect, as accurately as possible, the actual behavior of the structures in the limit states and show the factual behavior of the sections, elements, joints and supports. In the Section 5.1.2 of the same norm [42] it is stated that "Generally, the effects of the joint behavior on the distribution of internal force and moment distribution within a structure and the overall deformations of the structure, may not count. However, where such effects are significant, such as for semi-continuous joints, they should be included, EN 1993-1-8" [42,44]. Moreover, the checking procedure of the joint's strength according to EC 3 1-1-3 [26] does not take into account the non-linear behavior of the joints.

Generally, the finite element modelling of structures with bar-type elements considers the hinged connections free to rotation and restrained against translations, respectively, having infinite axial stiffness. In the case of CFS profile structures, how the bond between bars is defined has a considerable influence on results in both static and dynamic responses, sometimes underestimating them. A comparative analysis with 1D finite elements and hinged links observed in three different scenarios the effect of nonlinear behavior on element connection. The material used to model the joints and truss is S355 with modulus

of elasticity E = 210 GPa. The finite elements are beam type and the distance between nodes varies from 100 mm to 300 mm. The modelling of axial rigidity in end releases of the elements is based on next types of behavior:

- Linear (conventional);
- Nonlinear, of bilinear type;
- Nonlinear, of parabolic type.

Figure 12a shows the experimentally tested joint, which was analyzed in Robot Structural Analysis software [24], and Figure 12b defines the degrees of freedom in the nodes for the bar-type finite elements. Thus, the experimental results with bilinear (Figure 13a) and polynomial (Figure 13b) behaviors define the axial stiffness kx.

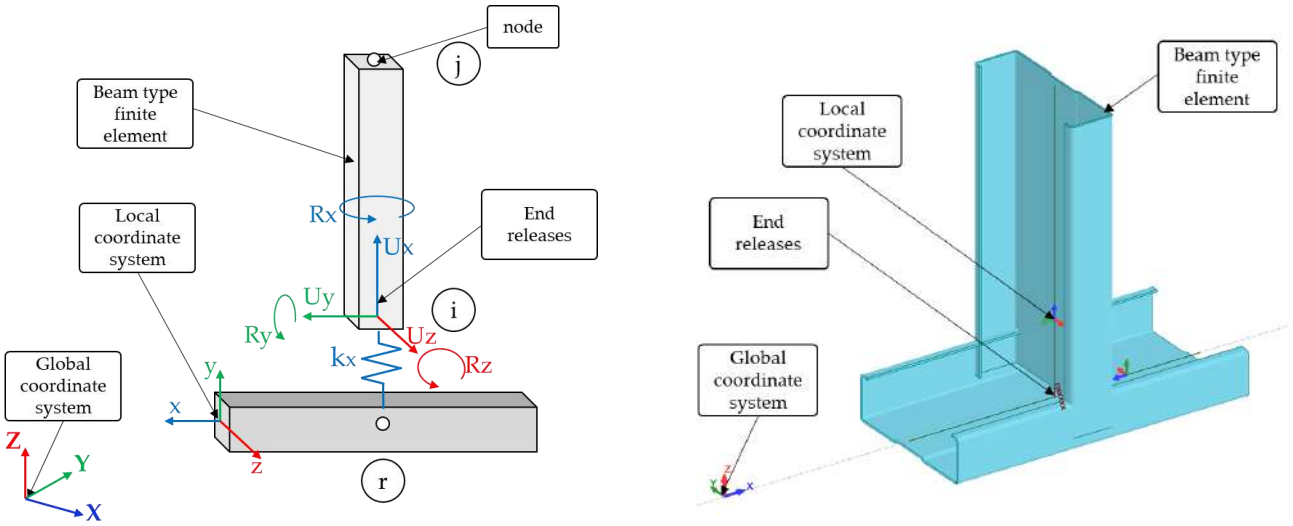

(**a**) (**b**)

Figure 12. Hinged joint with nonlinear behavior (**a**) conceptual sketch for the degree of freedom for the T-joint of beam type elements; (**b**) numerical model geometry.

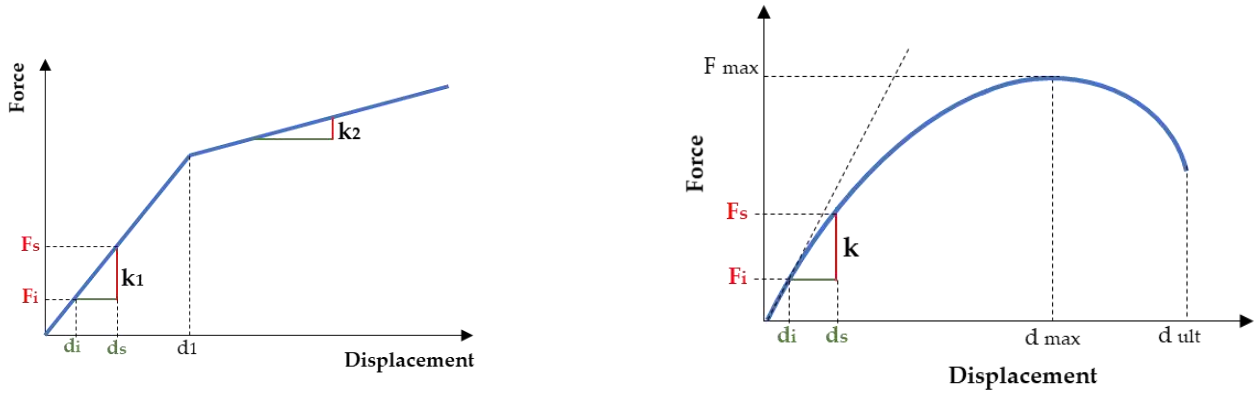

(**a**) (**b**)

Figure 13. Characteristic curves for the axial stiffness, k_x: (**a**) Idealized bilinear representation; (**b**) Polynomial curve.

The considered relation computing the stiffness is:

$$k = \frac{F_s - F_i}{d_s - d_i} \quad (1)$$

where F_s and F_i represent the limit values of the considered interval, d_s and d_i the displacements corresponding to the forces, according to the curves in Figure 13.

The stiffness values acquired based on the recorded experimental data for each area are summarized in Table 3 and presented graphically in Figure 14. Although the initial axial stiffness is slightly higher, its small influence on the overall behavior of the joint made it neglected. Therefore, $k_x = k_e = k_1 = k$, which is the first value of the axial rigidity in the elastic behavior presented in Figures 13a and 14, respectively, and $k_p = k_2$ mentioned also in Figures 13a and 14, were adopted.

Table 3. Stiffness values with respect to the sheet thickness and the connector type.

Joint Type	Stiffness [N/mm]			F_{max} [N]	d_1 [mm]	d_{ult} [mm]
	k_i	$k_x = k_e = k_1 = k$	$k_p = k_2$			
SSPR-A	2150	1520	628	6150	2.65	5.50
SSPR-B	2170	1560	644	7800	3.20	7.00
STS-A	2295	1575	669	14,500	5.85	12.50
STS-B	2360	1598	677	17,400	8.40	13.20

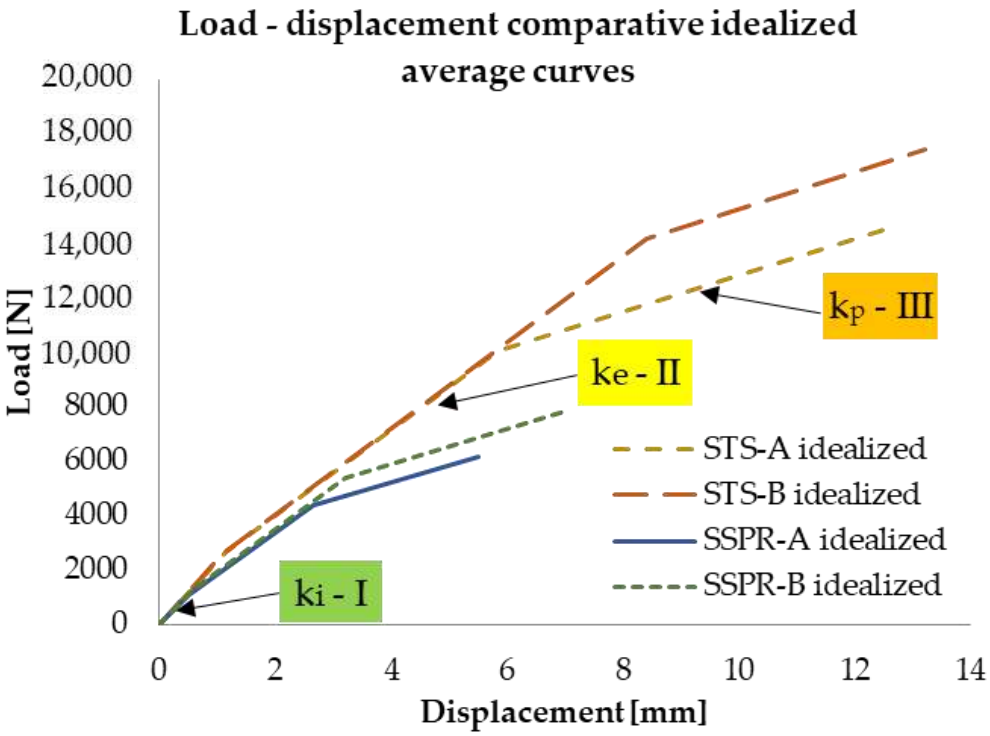

Figure 14. Comparison between the experimental idealized curves.

4.2. Joints Modelling

Figure 15 presents the geometric model for the joint. The flange of the joint was fixed by four pinned supports arranged according to the layout shown in Figure 15a. At the top part, in node 6, the translations in the X and Y directions of the global coordinate system were restrained. The force was applied at node 6 with 1000 N increments from 1 to 10,000 N and with 2000 N step size from 10,000 N to 20,000 N.

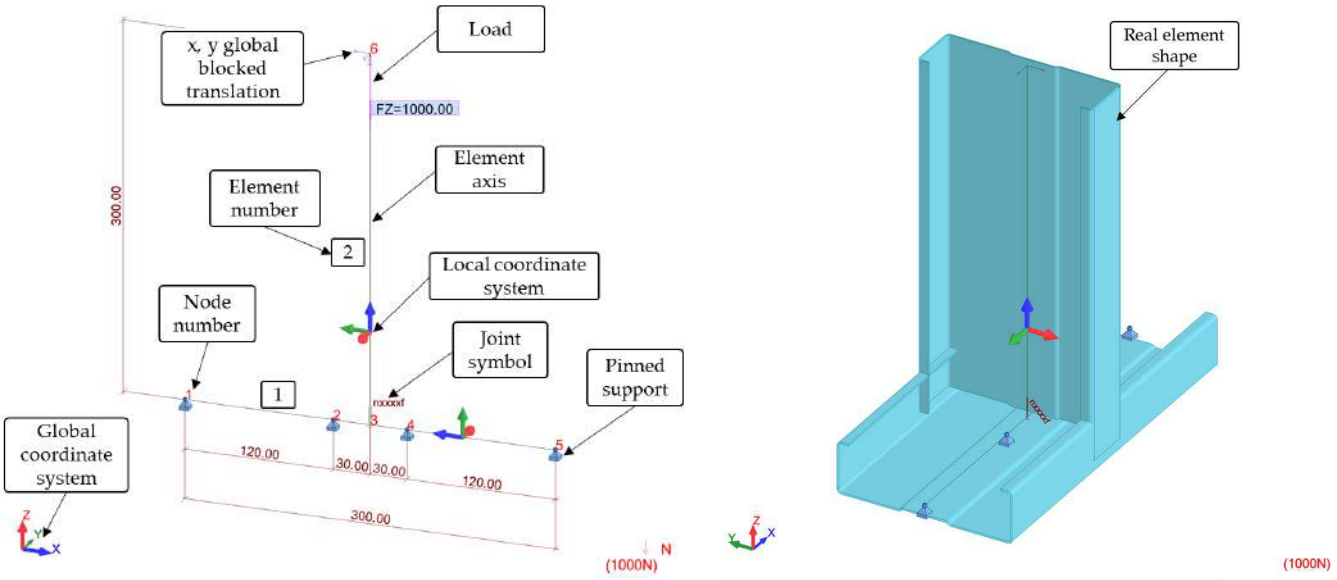

(**a**) (**b**)

Figure 15. (**a**) Conceptual diagram of the joint; (**b**) 3D view.

The degrees of freedom for node 3 of element 2, Figure 15a, are shown in Table 4.

Table 4. Considered scenarios for the degrees of freedom at the pin-connection/hinge.

Degree of Freedom (DOF)	Conventional Joint Linear	Nonlinear SSPR-A	Nonlinear SSPR-B	Nonlinear STS-A	Nonlinear STS-B
U_x	blocked	Nonlinear SSPR-A bil/pol	Nonlinear SSPR-B bil/pol	Nonlinear STS-B bil/pol	Nonlinear STS-B bil/pol
U_y	blocked	blocked	blocked	blocked	blocked
U_z	blocked	blocked	blocked	blocked	blocked
R_x	blocked	blocked	blocked	blocked	blocked
R_y	blocked	blocked	blocked	blocked	blocked
R_z	free	free	free	free	free

4.3. Numerical Analysis Results for the Joints

In the case of conventional linear analysis in which the bar 2 was hinged, by applying the increasing force from 0 to 10,000 N the maximum displacement of node 6 was 0.1 mm at a 14,000 N maximum load. In the graphs from Figure 16a,b the comparative curves present the five distinct models:

- Joint A/B lin—the basic model with a hinged joint;
- SSPR-A/B bil—model with bilinear behavior of the axial stiffness of bar 2;
- SSPR-A/B pol—model with polynomial behavior of the axial stiffness of bar 2;
- STS-A/B bil—model with bilinear behavior of the axial stiffness of bar 2;
- STS-A/B pol—model with polynomial behavior of the axial stiffness of bar 2.

In the bilinear model case, SSPR-A bil, when reaching the limit displacement value of 2.7 mm, the observed change in the slope by a faster increase of displacements did not interrupt the convergence. In the STS-A bil case, at a 5.8 mm displacement, the slope of the graph changed. These values coincide with those introduced by the bilinear curves of the axial bond.

In the case of modelling the SSPR-A pol joints with the polynomial function when reaching the 2.7 mm displacement, the stiffness of the node changed until reaching the final displacement of 4.8 mm at a force of 6000 N when the solution became non-convergent.

That represents the failure point marked on the graph with a red star. The situation was similar in the case of STS-A pol, the final displacement being 10.7 mm at 14,000 N.

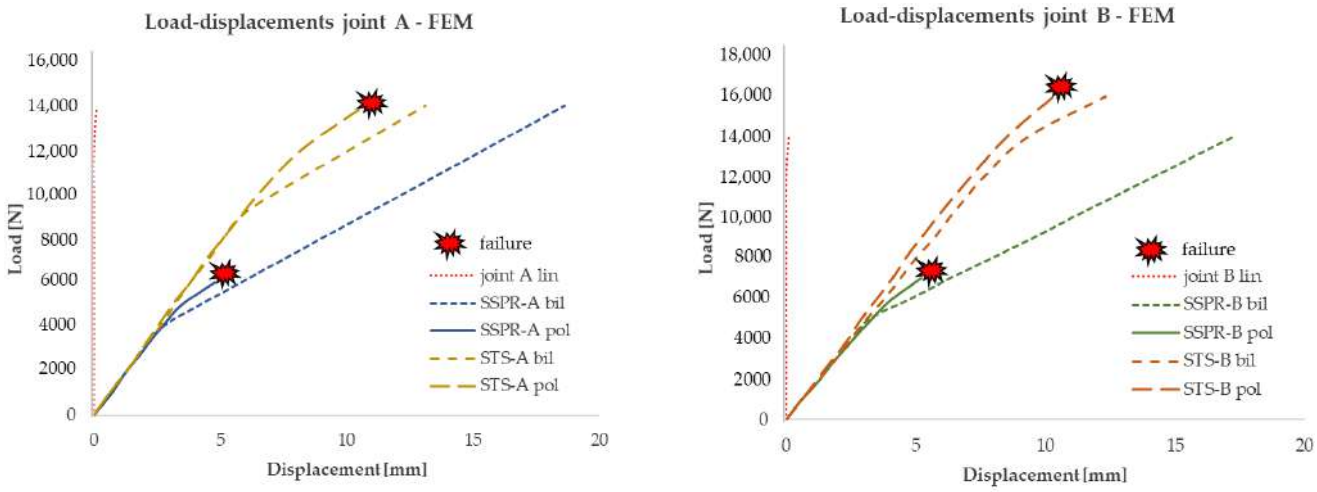

(**a**) (**b**)

Figure 16. (**a**) Numerical results for joint type A; (**b**) Numerical results for joint type B.

The results for the type B joints shown in Figure 16b are similar to those of the type A, the ultimate displacement, which in the SSPR-B bil case was 2.6 mm and 5.2 mm for SSPR-B pol, representing the main differences between them. By increasing the thickness of the sheet profile in the case of the model with polynomial function at the same load of 7000 N, the node type B was stiffer than A, with a total displacement smaller by 10%.

For the STS-B bil model, the limit value for the displacement was 9.3 mm at 14,000 N and in the case of STS-B pol, it was a 10.3 mm ultimate displacement corresponding to an applied force of 16,000 N. In the case of the joint type B with polynomial function, the maximum force value was 16,000 N, at which the convergence of the solution stopped.

In Figure 17, a comparison between the curves of the analyzed models, defined through a polynomial curve for the axial stiffness, was performed. These are very similar to those experimentally obtained. The curves are separated based on the profile thickness to simplify the comparison and identify the differences, as seen in Figure 18a for type A and b for type B.

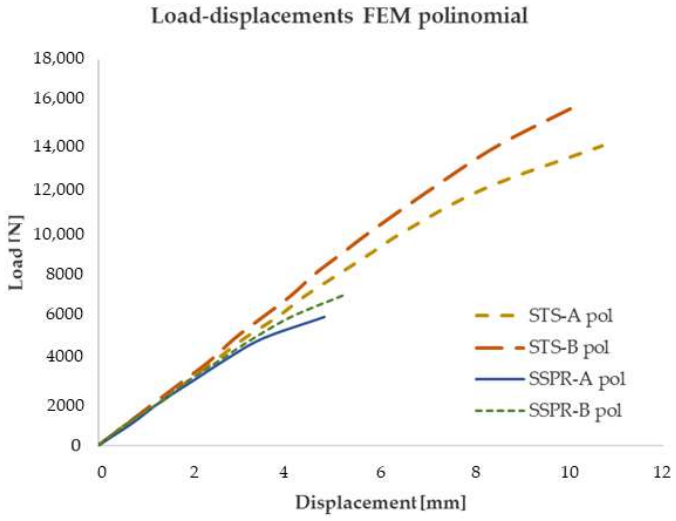

Figure 17. Comparison of the curves from numerical simulation with the polynomial function.

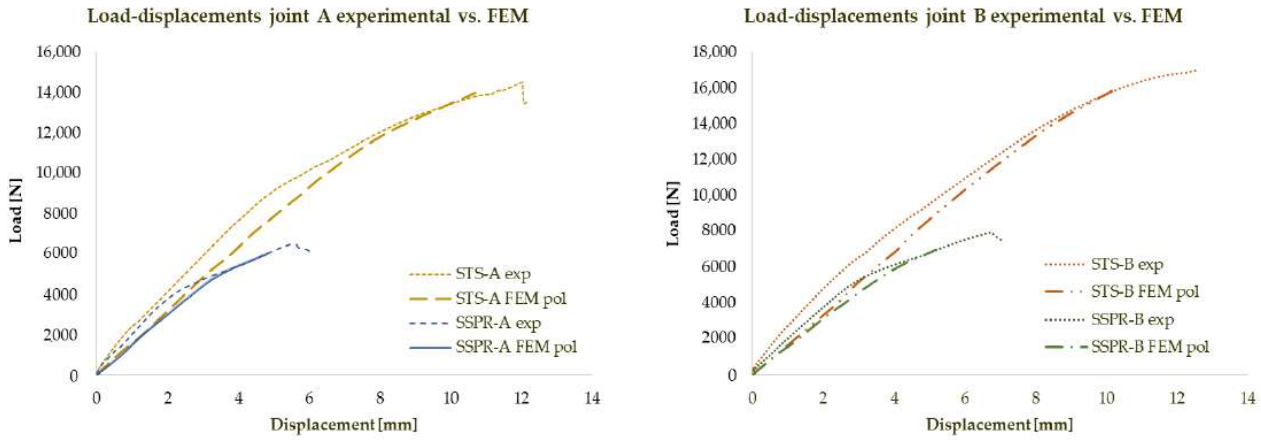

(**a**) (**b**)

Figure 18. (**a**) Comparison of experimental and numerical curves for type A joint; (**b**) Comparison of experimental and numerical curves for type B joint.

The maximum stress in the joint type A identified in bar 2 at a load value of 6000 N was 20.17 N/mm^2. At a force of 10,000 N, the maximum stress was 33.61 N/mm^2, except for the SSPR-A pol case, which no longer converged after reaching the failure point.

In the case of the joint type B, the maximum stress obtained in element 2 was 15.12 N/mm^2 at a load of 6000 N, and at 10,000 N, the maximum stress was 25.21 N/mm^2 except for SPRB-pol, which no longer converged.

5. Case Study on a 2D Truss Beam

5.1. Structural Analysis Assumptions

The proposed comparative analysis of a 2D truss beam highlighted the influence of the authentic behavior of joints connected with self-tapping screws. The truss modeling assumes two approaches: conventional with linear hinged joints and nonlinear with joints defined using the STS-B pol—the polynomial model.

The beam shown in Figure 19 has an opening of 5000 mm and a height of 500 mm. It was simply supported at joints 1 and 17 and restrained against translations in the global y-direction for all the joints positioned in the top chord. It was divided into eight panels 625 mm in length. The diagonal positions were eccentrical concerning the nodes of the struts with an eccentricity of 50 mm on the flange. The forces were applied concentrated at the nodes at the top chord. The load intensity varied from 250 N to 3500 N for ten loading scenarios, as shown in Table 5.

Table 5. Loading scenarios.

Case	Nodes	Load F_z (N)
1	18, 20, 22, 24, 26, 28, 30, 32, 34	−250
2		−500
3		−700
4		−1000
5		−2000
6		−3000
7		−3250
8		−3350
9		−3400
10		−3500

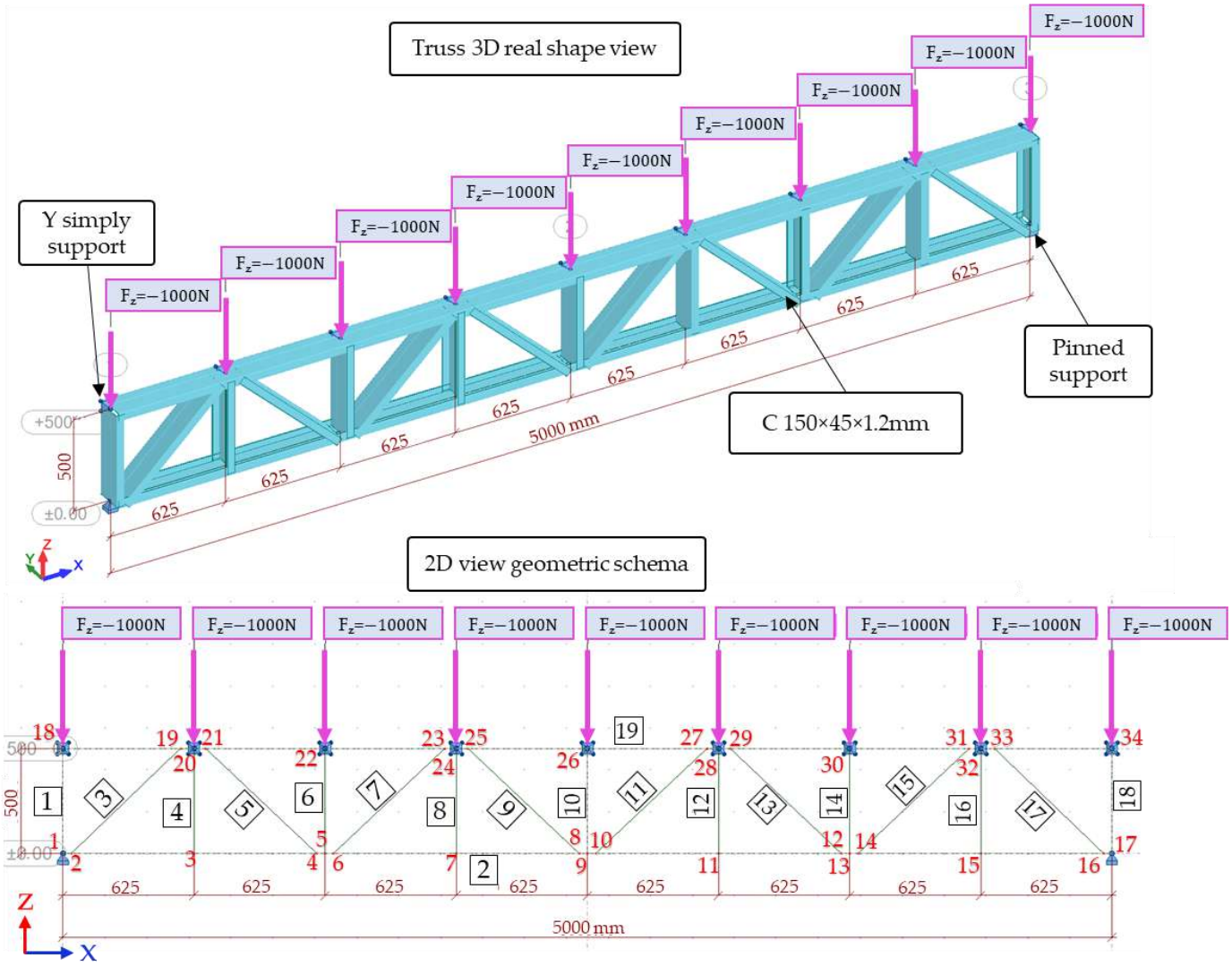

Figure 19. Geometry and static model for the truss structure.

5.2. Results

The monitored results assessed the maximum vertical displacements occurring at joints 9 and 26, located at the mid-span on the bottom and top chords, respectively. Considering the stiffness, the maximum displacement should occur below L/250 = 20 mm which is the maximum allowable displacement according to design codes. That resulted in the case of a load intensity of 700 N on each node. Figure 20 shows the deformed shape of the truss model to the undeformed one in both configurations; that is, conventional hinged nodes and node behavior defined by the polynomial function.

Comparing the maximum displacements shown in Figure 20, the maximum displacement at node 26 was 1.0 mm at a load intensity of 700 N on each node in the model with conventional joints, which means a total beam load of 6.30 kN. In the case of the model with non-linear defined joints, the maximum displacement at the same node was 19.8 mm, representing 99% of the maximum allowable displacement. Accordingly, the difference is almost 20 times the overall stiffness of the truss beam.

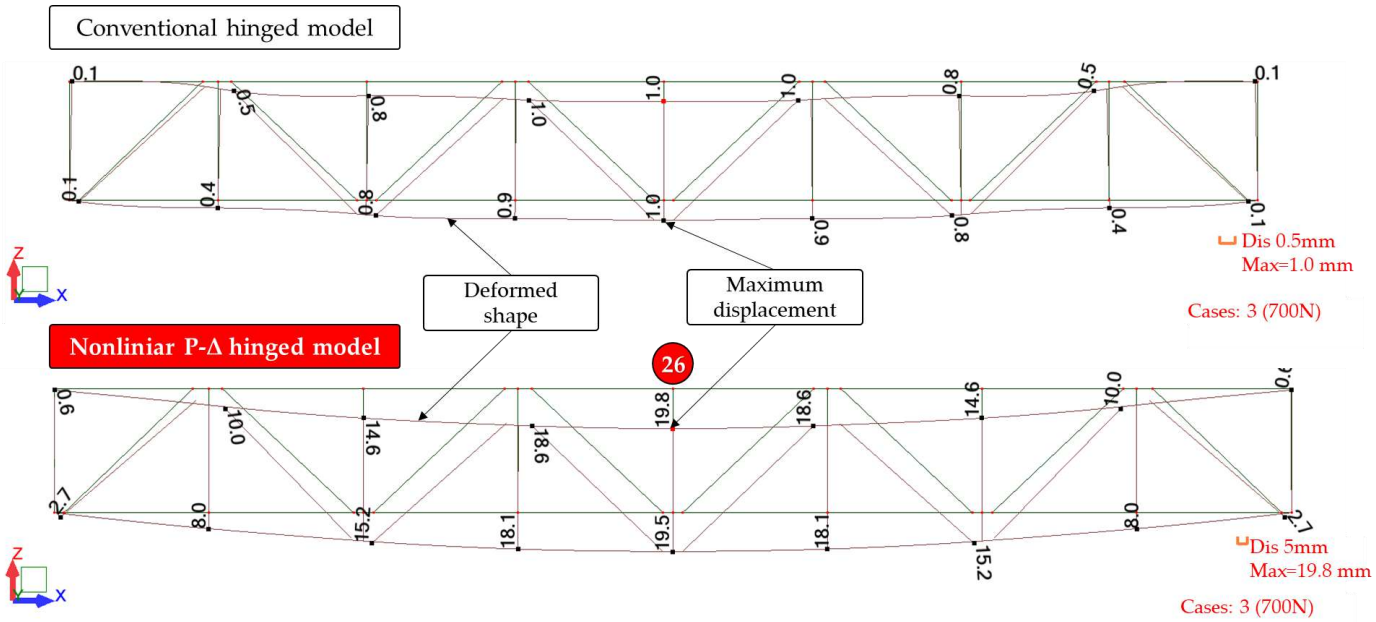

Figure 20. Deformed shape for the truss at a load of 700 N per node considering both case studies.

Figure 21 shows the distribution of the axial forces in the bars of the truss structure considering the same loading case as for the displacement computation (700 N/joint) in both model approaches. The maximum value of axial forces shows a relatively small difference. In the case of the compressed top chord, bar 19, the maximum axial force was 6953 N, 7.5% higher in the conventional hinged model in contrast to the nonlinear model, which had a 6436 N axial force. In the case of the lower chord, bar number 2, the maximum obtained value for the axial force was 2205 N, 8% higher in the conventional model than 2025 N in the nonlinear model. The differences are also inverse in bars 1 and 18, which are more stressed in the nonlinear model, and also in bars with reversed loading states from tension to compression (bars 4 and 16).

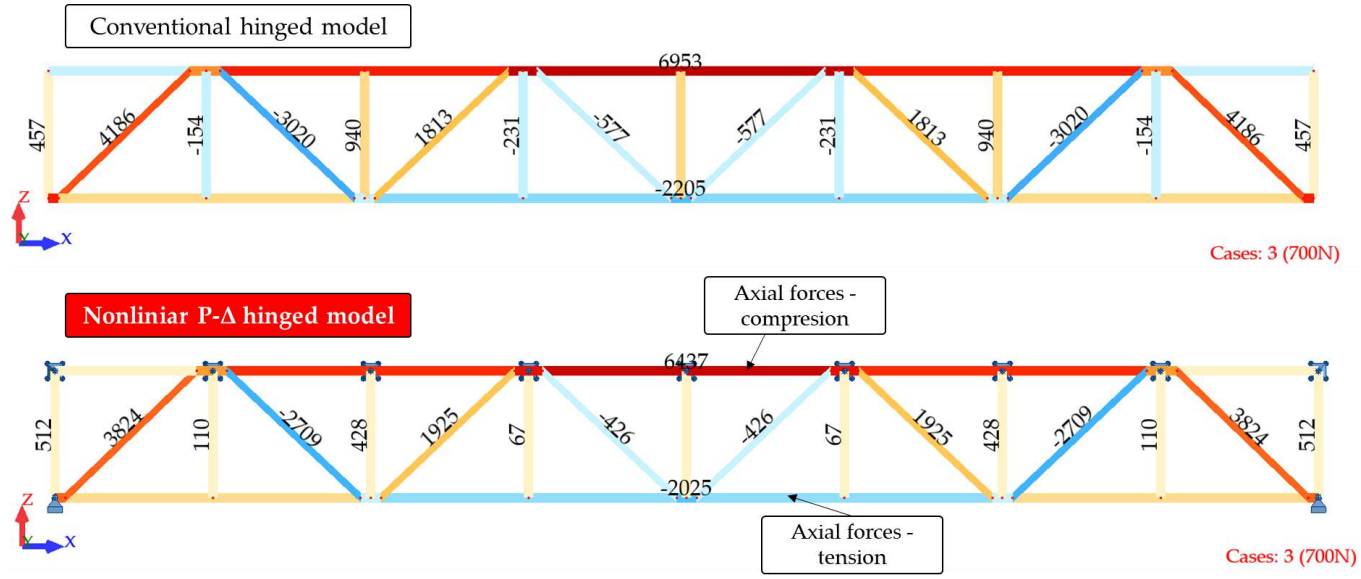

Figure 21. Axial force distribution in loading case 3, considering both case studies.

Analyzing the stress state in the truss bars (Figure 22), they reach the value of 283 N/mm^2 in the conventional model at joints 19 and 33, located on the top chord and belonging to the first and last panels of the truss. For the nonlinear model, the maximum

stress of 343 N/mm^2 occurs at nodes 21 and 31, also located on the top chord but belonging to the second and the last panels of the truss. The total load applied to the truss for both models was 30 kN.

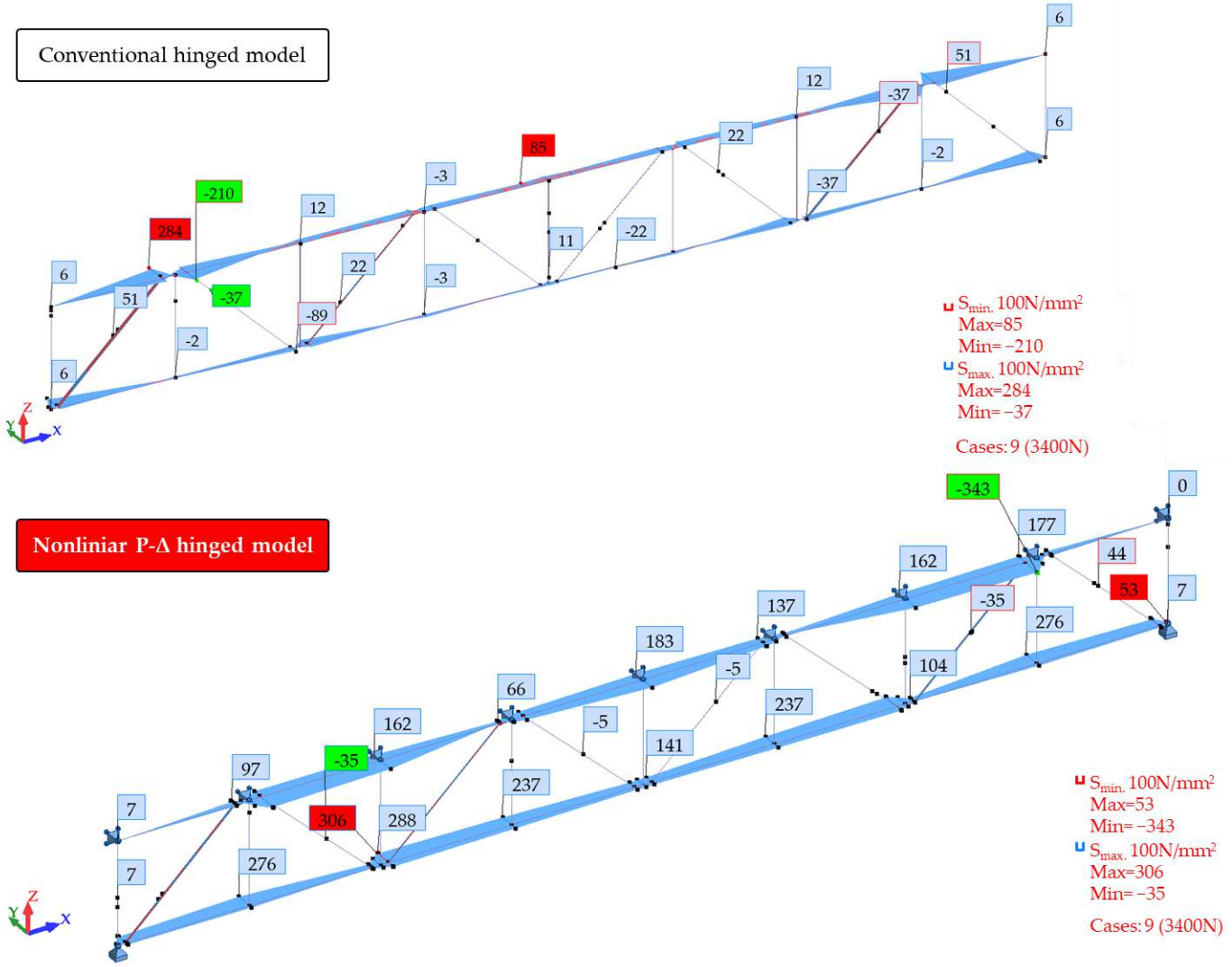

Figure 22. Maximum normal stress distribution.

Figure 23 shows a force–displacement curve computed on the relation between the total loads on the truss as the sum of all the forces per node applied up until the failure of all the non-linearly defined connections occurs. The nonlinear model is much more flexible at a maximum displacement of about 100 mm, reaching a load of around 30 kN. The structure yields; this did not occur in the conventional linear model. Moreover, the maximum displacement of only 5 mm at the same value is significantly reduced.

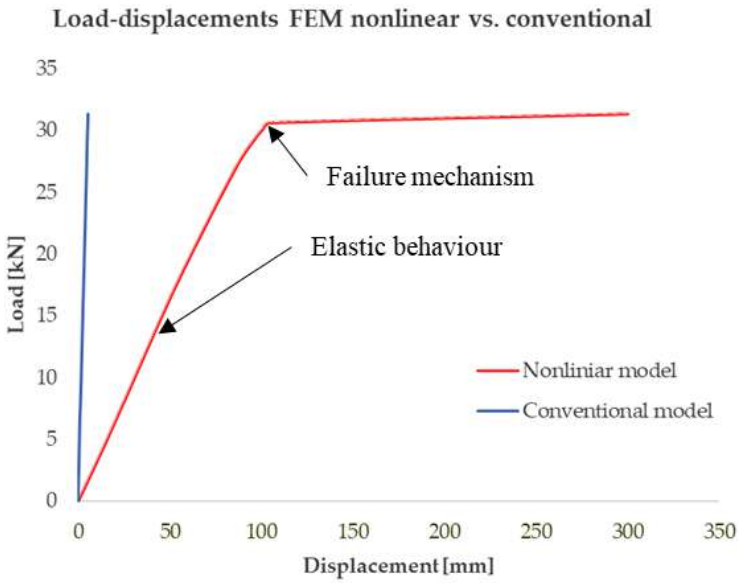

Figure 23. Force–displacement curve for the truss beam.

6. Discussion

The laboratory tests have led to similar results reported in the scientific literature to record force–displacement curves [39] with maximum load from 8 to 30 kN and maximum displacement from 3 to 8 mm. The difference is that the tests were not carried out on the T-joint, just on steel sheets with different patterns and numbers of screws. The use of SSPR and STS connectors in daily practice is the preferred solution by contractors as they are technologically accessible. The STS connectors lead to a higher load-carrying capacity of the joint against rivets for the same thickness and geometry of connected elements. Moreover, the failure mode in the case of STS connectors is more ductile in contrast to the brittle failure of rivets. Another significant advantage of STS connectors, considering the recycle/reuse paradigm in a sustainability context, is that it allows the disassembling of elements and their reuse in different configurations.

The thickness of the steel sheet has a significant influence on the overall behavior of joints, in contempt of the connector type. The experimental results determined the average load-displacement curves. These curves highlighted that the highest load-carrying capacity occurred for the B series (thicker steel sheet). The connector type played a secondary role in the carrying capacity; the STS connectors yield higher applied force values than the SSPR connectors. The latter resulted in a 60% drop in the ultimate load values concerning the SRS connector for both the A and B series of samples. Moreover, the SRS joint failure occurred gradually and was more ductile than the brittle behavior of SSPR joints.

The presence of drawn-cups leads to a 10% increase in the initial stiffness of the joints and facilitates an easier alignment of the pre-drilled CFS profiles to be connected.

The FEA models of the tested joints using linear elements ran in two ways: considering the conventional hinged joints between the elements and hinged joints with axial stiffness based on either bilinear or polynomial definition of the P-Δ curve. The paper presents both linear and non-linear static analyses. The FE model using the polynomial behavior of the hinge leads to obtaining the closest results to the experiments being 12–15% more flexible than the manufactured joints. The presence of drawings, not considered in the numerical model, can explain this slight difference.

The calibrated model was used in a case study of a truss element frequently used in the flooring systems. Further investigating the obtained results and running a comparative analysis on the reported data from the scientific literature lead to the conclusion that the use of linear static analysis may produce erroneous results because there is a tendency of underestimating the structural response.

There are a currently growing number of scientific papers using complex numerical models and proposing joining solutions using self-tapping screws and/or rivets to improve the overall behavior of CFS elements and sub-systems. However, their applicability in practical design and construction processes is not an easy process. Moreover, the currently available design regulation, e.g., Eurocode 3, covers partly only the checking of the CFS elements joints, mainly in terms of strength, somehow neglecting the influence of joint stiffness. The present study did not focus on checking the strength requirement for T-joints but mainly on joint behavior influence regarding stiffness and connector type.

Although the strength requirement was fulfilled, with the maximum normal stress values being well below the strength of the steel sheet or the screw strength, the truss element considered for the case study proved to be quite flexible. The maximum intensity of the applied load that could produce normal stress equal to 98% of the material strength has given rise to a maximum vertical displacement of 100 mm, five times larger than the allowable limit. Consequently, such elements should also be checked concerning stiffness requirement, not only regarding strength. Additionally, the numerical models should account for the non-linear behavior of the joints based on laboratory tests since the classical approach of perfect hinged elements does not reflect the authentic truss system behavior.

7. Conclusions

The sustainability of civil engineering structures can and should matter from the early design stages. That is probable to turn up through an optimum design in terms of chosen construction materials coupled with a realistic behavior of structural elements in numerical models. That ensures the best use of employed materials and, at the same time, the degree of safety required by norms.

Cold-formed steel profiles are a promising alternative to their hot-rolled counterparts, especially when considering their beneficial load-carrying capacity to material consumption ratio. Another significant advantage of their recycling/reuse approach is the ability to be reused in different configurations, especially when STS connectors are in use.

The paper presents the experimental and numerical investigation of two types of connectors frequently used in the construction industry for manufacturing joints made of CFS profiles: steel-steel pop-rivets (SSPR) and self-tapping screws (STS). The experiments carried out in the case of T-joints subjected to tensile forces tested both solutions. The recorded videos of the experiments are available online [50,51]. Another significant parameter of the research was the thickness of the steel sheet used to make the CFS profiles.

The goal of the experimental program was to obtain valuable information on T-joint behavior in terms of strength and stiffness and to render evidence on failure mechanisms considering the connector type and thickness of CFS profiles.

A case study was considered for which the obtained load-displacement curves for the T-joints were used in the modeling of a truss structure by means of 1D finite elements and the behavior of hinges derived from the experimental program. The numerical models considered three distinct approaches in terms of hinge behavior: classical linear elastic analysis and two non-linear analysis cases. The non-linear cases considered bilinear and polynomial load-displacement curves for hinges based on experimentally obtained data.

Based on the obtained results from the FEA, it can be concluded that the linear model with infinite axial stiffness and only rotational degree free yields result that do not match the real behavior of the T-joint, whereas out of the two non-linear cases, the polynomial approach leads to the most accurate prediction of the authentic behavior.

The outcomes have a significant impact on the design stage of CFS elements. Although Eurocode 3 provides information on the design steps of CFS members connected using either SSPR or STS, it recommends taking in account the P-Δ effect for the influence of the joint stiffness on the overall behavior of the structural sub-systems. The investigated case study of the truss structure by the calibrated numerical model of the joints reveals the fact that for similar intensities of the applied load, the corresponding vertical displacement is 20 times lower for the case of linear static analysis based on classical hinged joints with

infinite axial stiffness compared to the non-linear approach accounting for the joint stiffness experimentally uniaxial determined.

The main conclusion of the research presented in this paper is that the design process should be as accurate as possible and account for all phenomena occurring either at the joints or within the elements themselves to obtain safe and sustainable structures using CFS elements. The numerical models, calibrated using experimental data, may lead to accurate results for overall structural rigidity, and may also have a significant influence on fulfilling strength requirements.

Presented outcomes should further progress to provide statistically relevant interpretations summarized in the form of load-displacement curves defining the behavior of different joint geometries using various types of connectors. Moreover, supplementary tests on cyclic loading at tension and compression are necessary because the fatigue of the joint influences the behavior and the axial stiffness of the connected elements. Presented results could serve as a starting point for further research on the spatial structural system behavior subjected to static loads.

Author Contributions: Conceptualization, G.T. and V.-M.V.; methodology, G.T., V.-M.V. and I.O.-D.; software, G.T. and V.-M.V.; validation, I.O.-D., A.R. and I.-O.T.; formal analysis, G.T., V.-M.V.; investigation, G.T. and V.-M.V.; resources, V.-M.V.; data curation V.-M.V. and I.-O.T.; writing—original draft preparation, G.T. and I.O.-D.; writing—review and editing A.R. and I.-O.T.; visualization, G.T.; supervision, V.-M.V., I.-O.T. and A.R.; project administration, A.R.; funding acquisition, A.R. All authors have read and agreed to the published version of the manuscript.

Funding: The APC was funded by the Erasmus+ project KA2—Higher education strategic partnerships no.2018-1-RO01-KA203-049214, *Rehabilitation of the Built Environment in the Context of Smart City and Sustainable Development Concepts for Knowledge Transfer and Lifelong Learning*—RE-BUILT.

Institutional Review Board Statement: Not applicable.

Informed Consent Statement: Not applicable.

Data Availability Statement: Not applicable.

Acknowledgments: The authors would like to thank SC Panoterm SRL, Iasi, Romania for supplying the T-joints in the various configurations used in the research. Their interest and continuous support is greatly acknowledged.

Conflicts of Interest: The authors declare no conflict of interest.

References

1. Thirunavukkarasu, K.; Kanthasamy, E.; Gatheeshgar, P.; Poologanathan, K.; Rajanayagam, H.; Suntharalingam, T.; Dissanayake, M. Sustainable Performance of a Modular Building System Made of Built-Up Cold-Formed Steel Beams. *Buildings* **2021**, *11*, 460. [CrossRef]
2. Liang, H.; Roy, K.; Fang, Z.; Lim, J.B.P. A Critical Review on Optimization of Cold-Formed Steel Members for Better Structural and Thermal Performances. *Buildings* **2022**, *12*, 34. [CrossRef]
3. Schafer, B.W. Cold-Formed Steel Structures around the World. *Steel Constr.* **2011**, *4*, 141–149. [CrossRef]
4. Blandford, G.E.; Louis, S. *Current Research on Cold-Formed Steel Structures*; Missouri University of Science and Technology: Rolla, MO, USA, 1990.
5. Ungureanu, V.; Both, I.; Burcă, M.; Nguyen, T.H.; Grosan, M.; Dubină, D. Experimental Investigations on Spot Welded Built-Up Cold-Formed Steel Beams. *Bull. Polytech. Inst. Jassy Constr. Archit. Sect.* **2018**, *64*, 19–30. [CrossRef]
6. Koh, H.; Blum, H.B. A Review of Current Practice for Testing by Analysis of Cold-Formed Steel Structures. *Structures* **2022**, *37*, 871–880. [CrossRef]
7. Sani, M.S.H.M.; Muftah, F.; Osman, A.R. A Review and Development of Cold-Formed Steel Channel Columns with Oriented Strand Board Sections. *Mater. Today Proc.* **2019**, *17*, 1078–1085. [CrossRef]
8. Moga, L.; Petran, I.; Santos, P.; Ungureanu, V. Thermo-Energy Performance of Lightweight Steel Framed Constructions: A Case Study. *Buildings* **2022**, *12*, 321. [CrossRef]
9. Campiche, A.; Shakeel, S.; Macillo, V.; Terracciano, M.T.; Bucciero, B.; Pali, T.; Fiorino, L.; Landolfo, R. Seismic Behaviour of Sheathed CFS Buildings: Shake Table Tests and Numerical Modelling. *Ing. Sismica* **2018**, *35*, 106–123.
10. Terracciano, M.T.; Bucciero, B.; Pali, T.; Macillo, V.; Fiorino, L.; Landolfo, R. Shake Table Tests of Structures with CFS Strap-Braced Stud Walls. *Key Eng. Mater.* **2018**, *763*, 432–439. [CrossRef]

11. Macillo, V.; Fiorino, L.; Landolfo, R. Seismic Response of CFS Shear Walls Sheathed with Nailed Gypsum Panels: Experimental Tests. *Thin-Walled Struct.* **2017**, *120*, 161–171. [CrossRef]
12. Gălăţanu, T.F.; Ungureanu, V. *The Experimental Tests of the Joint Assembly of Thin Walled Steel Profiles KB*; Transilvania University Publishing House Braşov: Braşov, Romania, 2012.
13. Ungureanu, V.; Luka•ević, I.; Both, I.; Dubina, D. Numerical Investigations on Built-up Cold-formed Steel Beams for Long Spans. *Ce/Papers* **2021**, *4*, 2277–2284. [CrossRef]
14. Lukačević, I.; Ungureanu, V.; Valčić, A.; Ćurković, I. Numerical Study on Bending Resistance of Cold-formed Steel Back-to-back Built-up Elements. *Ce/Papers* **2021**, *4*, 487–494. [CrossRef]
15. Taranu, G.; Toma, I.O. Experimental Investigation and Numerical Simulation of C-Shape Thin-Walled Steel Profile Joints. *Buildings* **2021**, *11*, 636. [CrossRef]
16. Senkardesler, O.; Goler, G.; Soyoz, S. Dynamic and Cyclic Response of a Full-Scale 2-Storey Cold-Formed Steel Structure with and without Infill Materials. *Bull. Earthq. Eng.* **2017**, *15*, 3207–3226. [CrossRef]
17. Hui, C.; Gardner, L.; Nethercot, D.A. Moment Redistribution in Cold-Formed Steel Continuous Beams. *Thin-Walled Struct.* **2016**, *98*, 465–477. [CrossRef]
18. Kyvelou, P.; Gardner, L.; Nethercot, D.A. Composite Action between Cold-Formed Steel Beams and Wood-Based Floorboards. *Int. J. Struct. Stab. Dyn.* **2015**, *15*, 1540029. [CrossRef]
19. Kyprianou, C.; Kyvelou, P.; Gardner, L.; Nethercot, D.A. Characterisation of Material and Connection Behaviour in Sheathed Cold-Formed Steel Wall Systems—Part 2: Analytical Modelling. *Structures* **2021**, *30*, 1184–1199. [CrossRef]
20. Liu, P.; Peterman, K.D.; Yu, C.; Schafer, B.W. Characterization of Cold-Formed Steel Shear Wall Behavior under Cyclic Loading for the CFS-NEES Building. In *Proceedings of the 21st International Specialty Conference on Cold-Formed Steel Structures—Recent Research and Developments in Cold-Formed Steel Design and Construction*; Missouri University of Science and Technology: Rolla, MO, USA, 2012.
21. Foroughi, H.; Wei, G.; Torabian, S.; Eatherton, M.R.; Schafer, B.W. *Seismic Behavior of Steel SCBF Buildings Including Consideration of Diaphragm Inelasticity*; Cold-Formed Steel Research Consortium Report Series; Johns Hopkins University: Baltimore, MD, USA, 2021.
22. Singh, A.; Wang, X.; Torabian, S.; Hutchinson, T.C.; Peterman, K.D.; Schafer, B.W. Seismic Performance of Symmetric Unfinished CFS In-Line Wall Systems. In *Structures Congress 2020*; American Society of Civil Engineers: Reston, VA, USA, 2020.
23. Xu, Y.; Zhou, X.; Shi, Y.; Zou, Y.; Xu, L.; Xiang, Y.; Ke, K. Lateral Resistance of OSB Sheathed Cold-Formed Steel Shear Walls. *Thin-Walled Struct.* **2021**, *161*, 107451. [CrossRef]
24. Wang, C.; Yang, Z.; Zhang, Z.; Qi, R. Experimental Study on Shear Behavior of Cold-Formed Steel Shear Walls with Bracket. *Structures* **2021**, *32*, 448–460. [CrossRef]
25. Zhao, J.; Peng, Y.; Su, W.; Dong, J. Finite Element Analysis of the Shear Capacity of Stainless-Steel Blind-Rivet Connections. *J. Constr. Steel Res.* **2021**, *179*, 106558. [CrossRef]
26. Roy, K.; Lau, H.H.; Ting, T.C.H.; Chen, B.; Lim, J.B.P. Flexural Capacity of Gapped Built-up Cold-Formed Steel Channel Sections Including Web Stiffeners. *J. Constr. Steel Res.* **2020**, *172*, 106154. [CrossRef]
27. Chen, B.; Roy, K.; Fang, Z.; Uzzaman, A.; Raftery, G.; Lim, J.B.P. Moment Capacity of Back-to-Back Cold-Formed Steel Channels with Edge-Stiffened Holes, Un-Stiffened Holes, and Plain Webs. *Eng. Struct.* **2021**, *235*, 112042. [CrossRef]
28. Dar, M.A.; Subramanian, N.; Rather, A.I.; Dar, A.R.; Lim, J.B.P.; Anbarasu, M.; Roy, K.; Dar, M.A.; Subramanian, N.; Rather, A.I.; et al. Effect of Angle Stiffeners on the Flexural Strength and Stiffness of Cold-Formed Steel Beams. *Steel Compos. Struct.* **2019**, *33*, 225. [CrossRef]
29. SFIA-Steel Framing Industry Association. Available online: https://sfia.memberclicks.net/sustainable-steel (accessed on 23 February 2022).
30. Maribeth Rizzuto Building with Sustainable Green Materials. Available online: https://www.buildings.com/articles/32274/building-sustainable-green-materials (accessed on 23 February 2022).
31. Jaspart, J.-P.; Weynand, K. *Design of Joints in Steel and Composite Structures*; ECCS–European Convention for Constructional Steelwork: Brussels, Belgium, 2016; ISBN 9789291471324.
32. Ye, J.; Jiang, L. Simplified Analytical Model and Shaking Table Test Validation for Seismic Analysis of Mid-Rise Cold-Formed Steel Composite Shear Wall Building. *Sustainability* **2018**, *10*, 3188. [CrossRef]
33. Lee, Y.H.; Tan, C.S.; Mohammad, S.; Md Tahir, M.; Shek, P.N. Review on Cold-Formed Steel Connections. *Sci. World J.* **2014**, *2014*, 951216. [CrossRef]
34. Tunca, O.; Erdal, F.; Sağsöz, A.E.; Çarbaş, S. Structural Features of Cold-Formed Steel Profiles. *Chall. J. Struct. Mech.* **2018**, *4*, 77. [CrossRef]
35. Pekoz, T.; Louis, S. *Design of Cold-Formed Steel Screw Connections*; Missouri University of Science and Technology: Rolla, MO, USA, 1990; pp. 575–579.
36. Flodr, J.; Lehner, P.; Krejsa, M. Experimental and Numerical Evaluation of Clinch Connections of Thin-Walled Building Structures. *Sustainability* **2020**, *12*, 5691. [CrossRef]
37. Huynh, M.T.; Pham, C.H.; Hancock, G.J. Design of Screwed Connections in Cold-Formed Steels in Shear. *Thin-Walled Struct.* **2020**, *154*, 106817. [CrossRef]

38. Alpatov, V.; Soloviev, A. Thin-Walled Profiles and Their Joint Assembly Units Built with Screws: Numerical Studies of Load Bearing Capacity. In Proceedings of the MATEC Web of Conferences, Wellington, New Zealand, 10–12 December 2018; EDP Sciences: Les Ulis, France; Volume 196.
39. Roy, K.; Lau, H.H.; Ting, T.C.H.; Masood, R.; Kumar, A.; Lim, J.B.P. Experiments and Finite Element Modelling of Screw Pattern of Self-Drilling Screw Connections for High Strength Cold-Formed Steel. *Thin-Walled Struct.* **2019**, *145*, 106393. [CrossRef]
40. Huynh, M.T.; Pham, C.H.; Hancock, G.J. Experimental Behaviour and Modelling of Screwed Connections of High Strength Sheet Steels in Shear. *Thin-Walled Struct.* **2020**, *146*, 106357. [CrossRef]
41. Kechidi, S.; Fratamico, D.C.; Bourahla, N.; Castro, J.M.; Schafer, B.W. Numerical Study of Screw Fasteners in Built-up CFS Chord Studs. *Ce/Papers* **2017**, *1*, 1543–1552. [CrossRef]
42. *EN 1993-1-1*; Eurocode 3: Design of Steel Structures—Part 1-1: General Rules and Rules for Buildings. CEN: Brussels, Belgium, 2005.
43. *EN 1993-1-3*; Eurocode 3: Design of Steel Structures—Part 1-3: General Rules, Supplementary Rules for Cold-Formed Thin Gauge Members and Sheeting. CEN: Brussels, Belgium, 2006.
44. *EN 1993-1-8*; Eurocode 3: Design of Steel Structures—Part 1-8: Design of Joints. CEN: Brussels, Belgium, 2005.
45. *EN 1993-1-5*; Eurocode 3: Design of Steel Structures—Part 1-5: Plated Structural Elements. CEN: Brussels, Belgium, 2006.
46. Kalo, R. High Fidelity Modeling of Cold-Formed Steel Single Lap Shear Screw Fastened Connections. Master's Thesis, University of Massachusetts Amherst, Amherst, MA, USA, 2019.
47. Rautenbach, E. Finite Element Modelling of Thin Sheet Steel Screw Connections. Master's Thesis, University of Pretoria, Pretoria, South Africa, 2016.
48. ROCAST—Catalog. Available online: https://vinix.cld.bz/ROCAST/html-Catalog-Rocast-2017-2018/125#zoom=z (accessed on 4 December 2021).
49. Robot Structural Analysis Professional. Available online: https://www.autodesk.com/products/robot-structural-analysis/overview (accessed on 13 January 2022).
50. S1 Pop-Rivets T-Joint Test of Thin-Walled Steel Profiles. Available online: https://youtu.be/3COo5riXSuk (accessed on 13 January 2022).
51. Self-Tapping Screw T-Joint Test. Available online: https://youtu.be/7zbe4oWyAmQ (accessed on 13 January 2022).

Construction and Building Materials 438 (2024) 137229



Contents lists available at ScienceDirect

Construction and Building Materials

journal homepage: www.elsevier.com/locate/conbuildmat

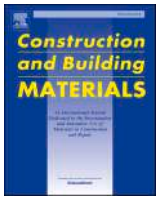



Effect of expanded perlite aggregates and temperature on the strength and dynamic elastic properties of cement mortar

Sergiu-Mihai Alexa-Stratulat, George Taranu, Ana-Maria Toma *, Ioana Olteanu, Cristian Pastia, Georgiana Bunea, Ionut-Ovidiu Toma *

The "Gheorghe Asachi" Technical University of Iasi, Faculty of Civil Engineering and Building Services, Iasi, Romania

ARTICLE INFO

Keywords:
Expanded perlite aggregate mortar
Dynamic modulus of elasticity
Flexural strength
Compressive strength
Elevated temperature

ABSTRACT

The residential market consumes nearly half of the world's concrete production, and it is anticipated that 68 % of the global population will reside in urban areas by 2050. Researchers have focused their efforts on exploring alternative options to natural aggregates in concrete and mortar. In line with the principles of circular economy, construction and demolition waste has been repurposed for the manufacture of cement-based materials. Volcanic products, which are abundant but underutilized, have been identified as an alternative to recycled aggregates. They offer several advantages over natural river aggregates, including reduced weight, enhanced thermal and acoustic insulation, improved fire resistance and pozzolanic characteristics. While there has been a significant amount of research on the use of expanded perlite as a supplementary cementitious material, studies involving the use of expanded perlite aggregates (EPA) in cement-based construction materials are relatively limited. This paper seeks to address this knowledge gap by investigating the use of EPA in cement-based mortar at both room and elevated temperatures. The study examines the impact of varying replacement percentages (10 %, 20 % and 30 % - by volume) of natural sand with EPA having a maximum grain size of 4 mm, and the exposure temperature of mortar prisms at the age of 28 days. Specifically, temperatures of 100ºC, 150ºC and 200ºC were selected for analysis. The impact of these parameters on the flexural and compressive strength of mortar, as well as its dynamic elastic properties, was experimentally determined. The findings indicate that, at room temperature, higher replacement percentages of natural sand by EPA result in decreased flexural and compressive strengths, by as much as 50 % and 30.71 %, respectively. However, the dynamic moduli values for replacement percentages up to 20 % are similar to those of the reference mix. Conversely, when subjected to temperatures up to 200ºC, significant improvements were observed in the flexural strength values, e.g. over 20 % for temperatures of 150°C and 200°C, with only marginal improvements in compressive strength, 3 % ÷ 20 % for temperatures of 150°C and 200°C, compared to values obtained at room temperature.

1. Introduction

Concrete is the most widely used construction material with a total worldwide production of 14 billion cubic meters in 2020, according to Global Cement and Concrete Association [1]. Nearly half of this quantity served the residential sector. Projections indicate that 68 % of the world's population will inhabit urban areas by 2050, leading to an estimated annual concrete production of 20 billion cubic meters. Given that aggregates constitute 60 %-75 % of the total concrete volume, it follows that the demand for natural resources will increase substantially. It is estimated that approximately 50 % of the world's raw material consumption is necessary to sustain this demand [2].

Finding alternative solutions to natural aggregates has been actively pursued by many researchers. The use of ferrochrome waste slag aggregates in limestone-calcined clay cement mortar resulted in an increase in both tensile strength (up to 22.2 %) and compressive strength (up to 71 %), as the percentage of natural sand replacement increased [3]. In addition, when natural sand was completely replaced with ferrochrome waste slag aggregates, the water absorption coefficient decreased by 16 %. In line with the principles of circular economy,

* Corresponding authors.
E-mail addresses: sergiu-mihai.alexa-stratulat@academic.tuiasi.ro (S.-M. Alexa-Stratulat), george.taranu@academic.tuiasi.ro (G. Taranu), ana-maria.toma@academic.tuiasi.ro (A.-M. Toma), ioana.olteanu@academic.tuiasi.ro (I. Olteanu), cristian.pastia@academic.tuiasi.ro (C. Pastia), georgiana.bunea@academic.tuiasi.ro (G. Bunea), ionut.ovidiu.toma@tuiasi.ro (I.-O. Toma).

https://doi.org/10.1016/j.conbuildmat.2024.137229
Received 7 December 2023; Received in revised form 13 June 2024; Accepted 24 June 2024
Available online 26 June 2024
0950-0618/© 2024 The Authors. Published by Elsevier Ltd. This is an open access article under the CC BY-NC-ND license (http://creativecommons.org/licenses/by-nc-nd/4.0/).

construction and demolition waste has been repurposed as a resource for cement-based materials production. A recent study used recycled aggregates to substitute natural sand in mortar at rates of 25 %, 50 %, 75 %, and 100 %.Apart from demonstrating their effectiveness in structural applications, such as masonry elements, completely replacing natural with recycled aggregates with particle size smaller than 2.4 mm resulted in a 64 % reduction of CO_2 emissions associated with production processes. However, after considering both the strength properties and carbon footprint, it was concluded that optimal replacement percentage was 50 % [2].

The use of recycled aggregates from construction and demolition waste in concrete typically results in a decrease in mechanical properties. This is primarily attributed to the quality of the aggregates, which weakens the interfacial transition zone between the porous mortar adhering to the surface of the recycled aggregates and the fresh cement paste [4,5]. A possible solution to this issue involves treating the recycled aggregates with a silica fume slurry. This yielded a notable 16 %-26 % increase in concrete compressive strength at various curing ages, with complete replacement of natural aggregates. The inclusion of carbon fibers resulted in a 38 % increase in the flexural strength of concrete with recycled aggregates and a 34 % increase in the modulus of elasticity [6]. In a separate study, different combinations of recycled aggregates and nano-silica were examined to assess their impact on the mechanical and durability properties of concrete. Researchers employed gene expression programming to predict the compressive strength of concrete incorporating recycled aggregates and nano-silica as a pozzolan [7]. The proposed optimal mix comprised a 26 % replacement of natural coarse aggregates with recycled aggregates and 4 % nano-silica. According to the mathematical model, this mix demonstrated the highest flexural and compressive strength, modulus of elasticity and, simultaneously, the lowest water absorption coefficient.

An alternative to recycled aggregates has been identified in the form of volcanic products, which, despite their substantial potential, are not fully exploited. Volcanic rocks such as pumice, lapillus, tuff, zeolites, and perlite offer several advantages over natural river aggregates, including their lightweight nature, improved thermal and acoustic insulation properties, fire resistance, and pozzolanic properties [8]. The use of volcanic scoria, a type of volcanic rock formed by rapid cooling of lava in air, in concrete led to a 15 % reduction of bulk density and a 22.3 % increase in modulus of elasticity. Furthermore, due to secondary pozzolanic reactions, the compressive strength increased between 28 and 90 days by 15.23 %-22.3 %. However, the obtained values were approximately 70 %-75 % of the compressive strength obtained for the reference mix [9]. The use of zeolites as lightweight aggregates in concrete proved to be advantageous from the point of view of self-weight reduction. Additionally, a smaller interfacial transition zone between the aggregates and the cement paste was achieved, depending on the type of cement used in the concrete mix [10]. High quantities of ettringite and calcium hydroxide (CH) at early ages, and correspondingly high levels of calcium silicate hydrates (CSH) at later ages, were identified as the main factors influencing the quality of the interfacial transition zone, with a pronounced dependence on cement dosage and water-to-cement ratio.

Perlite, an amorphous aluminosilicate volcanic glass, has the ability to expand approximately 5–20 times its original volume when heated to its softening temperature, ranging between 900ºC and 1200ºC [11]. This expansion process, caused by the water trapped inside the perlite ore, results in a lightweight, cellular aggregate with bulk densities ranging from 80 kg/m^3 to 240 kg/m^3 [12]. Expanded perlite, with its high surface area, low sound transmission, low thermal conductivity [12,13] and chemical inertness, finds a wide range of applications, from horticulture to pharmaceutical and filtering applications in municipal drainage systems. In the construction industry, it has been used as a replacement for cement [14] and/or aggregates [11]. Taking into account the many applications of perlite, its worldwide production steadily increased during the last decade, as shown in Fig. 1.

One of the earliest uses of perlite in the construction industry has been in the development of building insulation materials, such as renders and mortars. Considering that approximately 40 % of a building's total energy consumption is dedicated to maintaining a comfortable indoor climate [12,16], there has been a growing demand for improved insulating materials and more efficient cooling and heating systems. Laboratory investigations and numerical analyses have demonstrated that panels composed of a mixture of cement, expanded perlite and pumice exhibit superior thermal performance in both standard (no vegetation) and green roof scenarios compared to reference panels [12]. Combining perlite powder with a sodium hydroxide solution and a foaming agent result in an ultra-lightweight foam concrete-like material, with enhanced thermal properties and fire performance. Heat treatment, particularly at a curing temperature of 850ºC, was identified as an important parameter, yielding the best results in terms of density and thermal conductivity [13]. Additionally, owing to the pozzolanic activity of perlite, a denser and stronger structure of renders and mortars is obtained [17]. A similar densification effect has been observed in the case of a magnesium potassium phosphate cement-expanded perlite composite, used as a fire-resisting coating. The presence of perlite

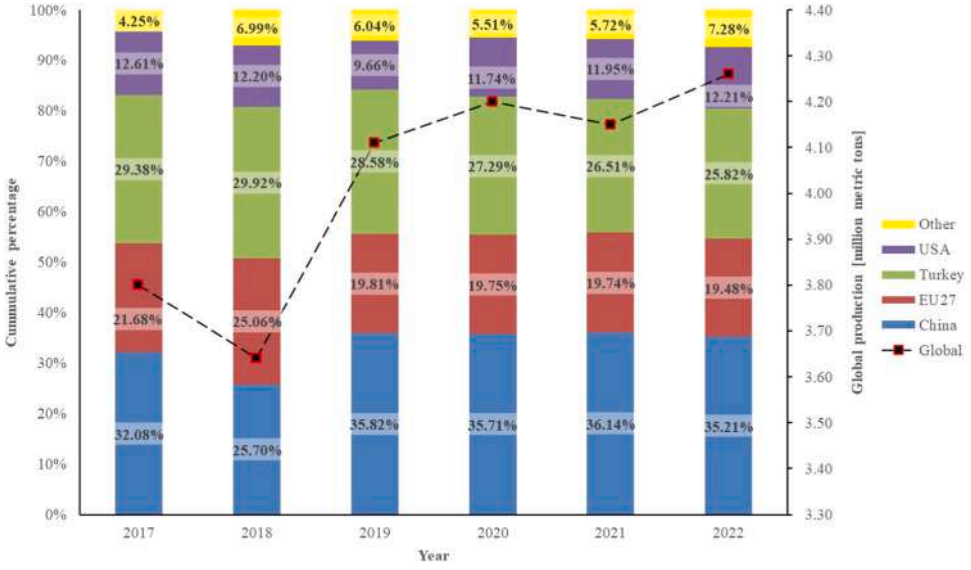

Fig. 1. Worldwide perlite ore production (based on data from USGS [15]).

increased residual bond strength after the fire test and reduced the occurrence of visible cracks on the coating surface [18].

The production of cement is a significant contributor to greenhouse gas (GHG) emissions in the construction industry, accounting for approximately 5 % - 7 % of the global CO_2 emissions [19,20]. To address this environmental impact, the use of supplementary cementitious materials (SCMs) has been proposed as a feasible solution. SCMs can be classified based on their source into industrial wastes, such as silica fume and fly ash, and natural pozzolans, such as pumice, metakaolin, perlite, zeolite and others. Natural pozzolans are aluminosilicate materials capable of reacting with calcium hydroxide (CH) to form calcium silicate hydrates (CSH) gels, contributing to a denser structure in cementitious materials and enhancing strength and durability properties [21]. Research has shown that using perlite powder in self-compacting concrete (SCC) requires an increase in superplasticizer content to achieve similar workability to the reference mix. Compressive strength values were found to be nearly identical to the reference mix at the age of 91 days, with significant improvements observed with increasing the fineness of perlite powder from the age of 28 days [22]. The use of perlite powder in SCC resulted in improved mechanical properties when exposed elevated temperatures, up to 600ºC, with reduced spalling [23]. Replacing cement with high percentages of perlite powder, such as 20 % and 30 %, had a detrimental effect on concrete protection of reinforcement to corrosion in aggressive environments [24]. However, a 40 % replacement of cement by expanded perlite powder yielded comparable 28-day compressive strength values in ultra-high performance concrete (UHPC) but slightly reduced the chloride ion penetration resistance of concrete [25].

In an effort to prevent the depletion of natural resources used in concrete production, researchers have explored alternatives to conventional aggregates. Other forms of natural aggregates, such as expanded perlite, zeolites, and volcanic tuff, were identified, and their impact on the mechanical properties of concrete were evaluated. A recent study focused on the replacement of coarse natural aggregates with perlite aggregates concluded that concrete density is significantly reduced due to perlite porous structure [26]. However, as perlite possesses lower strength than traditional aggregates, the compressive strength of concrete decreased with increasing replacement percentage. Conversely, concrete with expanded perlite aggregates (EPA) demonstrated higher compressive strength values at both 7 and 28 days compared to other lightweight concrete mixes based on pumice aggregates [27]. Moreover, replacing natural sand with EPA in proportions of 75 %-100 % resulted in obtaining ultra-high performance concrete with similar fluidity, mechanical strength and durability properties as conventional UHPC [25].

The existing scientific literature contains a significantly higher number of studies dedicated to perlite as a supplementary cementitious material compared to those investigating expanded perlite as an aggregate substitute. This paper seeks to address this knowledge gap by investigating the use of EPA in cement-based mortar at both room temperature and after exposure to elevated temperatures. Previous research has shown that concrete incorporating powdered perlite exhibited enhanced mechanical properties at temperatures up to 300ºC [23,28]. Therefore, this study focused on evaluating the impact of replacing natural sand with EPA, with a maximum grain size of 4 mm, at varying percentages (10 %, 20 % and 30 % by volume) as well as subjecting mortar prisms to temperature exposure at 28 days. The temperatures selected for the experiment were 100ºC, 150ºC and 200ºC. Experimental determinations were made regarding the impact of both parameters on the flexural and compressive strength of mortar, and on its dynamic elastic properties.

The results indicate that, at room temperature, an increase in replacement percentage of natural sand with EPA leads to decreased flexural strength and compressive strength. However, replacement percentages of up to 20 % exhibit dynamic moduli values similar to those of the reference mix. Conversely, when exposed to temperatures up to 200ºC, there are significant improvements in the flexural strength and minimal gains in compressive strength, compared to the values obtained at room temperature. The most substantial increases were observed at 150ºC.

2. Materials and methods

2.1. Materials

A CEM II B-M (S-LL) 42.5 R cement (StructoPlus), complying with SR EN 197–1:2011 [29] guidelines, was considered in this research. It is widely available on the market, and it comprises 65 %-79 % clinker and a 21 %-35 % combination of blast furnace slag and limestone. The chemical composition of the cement, as provided by the manufacturer (HOLCIM, Romania), is detailed in Table 1. According to Favier et al. [30], CEM II cement is the predominant type in Europe, holding a 47 % market share in 2015.

The aggregate used in this study was river sand with a maximum grain size of 4 mm and a specific weight of 2.69. Expanded perlite, having a specific weight of 0.129 and complying to SR EN 1097–3:2002 [31] and SR EN 933–2:2020 [32], was selected as a substitute for the natural sand, with replacement volumes of 10 %, 20 % and 30 %. Table 1 provides the chemical composition of the expanded perlite, as supplied by the manufacturer (ProcemaPerlit). The sieve analysis of the two types of aggregates is presented in Fig. 2. It can be observed that EPA had almost 60 % of its volume consisting of grains larger than 1 mm [33], whereas in case of sand the percentage was significantly lower, 18.16 %. However, since EPA aggregates have a lower Mohs hardness compared to natural sand, it is expected that particle size distribution of EPA will change during mixing, namely the volume of fine grains to increase, as previously reported [33]. The percentage shown in Fig. 3 for 0.125 mm sieve corresponded to even lower than 0.063 mm sieve, which basically falls in the category of powders. In case of sand, the corresponding percentage was only 3.4 %.

Based on the specifications provided by ASTM C618:2022 [34], expanded perlite falls in the category of natural pozzolans due to the combined content of SiO_2, Al_2O_3 and Fe_2O_3 exceeding 70 % [35]. Fig. 3a depicts the porous structure of expanded perlite. When further magnified, the microstructure shows a series of flakes/sheets [36] separated by gaps, as shown in Fig. 3b. These features contribute to the thermal insulation and water absorption properties of expanded perlite [37].

2.2. Mix proportion

A reference mortar mix ratio of 1:4:0.6 (cement:sand:water) by volume was employed. Table 2 shows the proportions, per cubic meter, for all mixes used in the study. For mortars modified by EPA, a higher water/cement ratio was required to achieve a consistency similar to that of the reference mix [14]. In other previous studies, superplasticizer was used in order to keep the same water/cement ratio [33]. However, according to earlier findings, there are large compatibility issues between various superplasticizers and natural pozzolans [38]. For similar water/binder ratio it was found that there is a need to increase the superplasticizer content by as much as 50 % to counteract the loss of slump caused by the use of zeolite (having similar chemical composition to perlite). Moreover, different superplasticizers required different dosages in order to achieve similar workability of mortar.

Aside of the reference, the mixtures were labeled by EPA (expanded perlite aggregate) and a number indicating the percentage of sand replacement. For each mix outlined in Table 2, twelve standard prisms, each measuring 40 mm×40 mm×160 mm in height, width, and length respectively [39], were cast. This resulted in a total of 48 specimens. The prismatic steel molds were mount on a jolting table (drop height of 15 mm) and vibrated in accordance with specifications of SR EN 196–1:2016 [39]. After vibration, there was no bleeding water visible on the surface of the mortar prisms.

The mortar prisms were demolded after 24 hours from casting and

Table 1
Chemical composition of CEM II cement and expanded perlite (expressed in %).

	CaO	SiO_2	Al_2O_3	Fe_2O_3	MgO	SO_3	Na_2O	K_2O	Cl
CEM II	58.49	16.32	4.83	2.24	1.39	2.85	0.34	0.46	0.035
	CaO	**SiO_2**	**Al_2O_3**	**Fe_2O_3**	**MgO**	**SO_3**	**Na_2O+K_2O**		**Cl**
Expanded Perlite	1.3–1.7	74–77	12–15	1.1–1.6	0.1–0.7	-	5.0–8.0		-

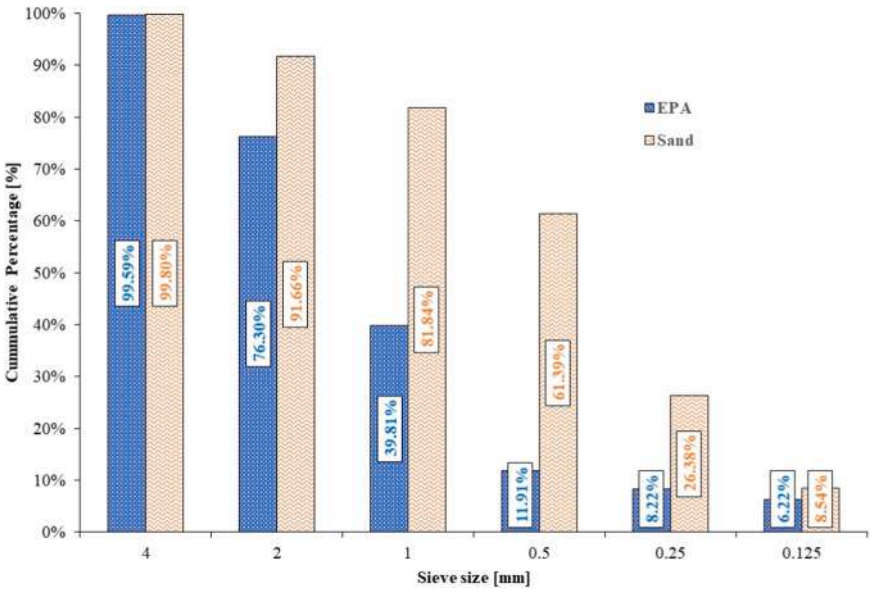

Fig. 2. Sieve analysis of EPA and natural sand.

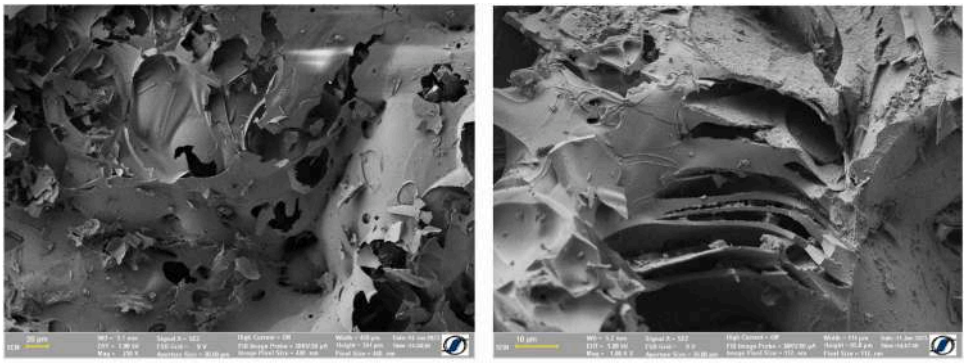

Fig. 3. SEM images of expanded perlite.

Table 2
Mix proportions of mortars used in this study.

Mix designation	Cement [kg/m^3]	Sand [kg/m^3]	EPA [kg/m^3]	Water / Cement -
Ref	380	1550	-	0.60
EPA10		1395	7.42	0.65
EPA20		1240	14.85	
EPA30		1085	22.28	

stored in water at 22°C±1°C for 27 days, until the day of testing. Prior to storing the mortar prisms in water, their geometrical dimensions were measured, as presented in Section 2.3.2, to check for compatibility with the dimensions of the steel mold. Additionally, there were no large voids on the surface of the mortar prisms, suggesting that the mortar fully filled the steel mold.

2.3. Methods

2.3.1. Slump test

The slump was assessed using a mini-slump test with a cone of dimensions 100 mm×70 mm×60 mm (bottom diameter × top diameter × height) [40,41]. Once the cone was lifted and the spread of the mortar ceased, the average of three measured diameters was taken into account. In addition, the height reduction was measured relative to the height of the cone.

2.3.2. Dimensions and mass

At the age of 28 days, the mortar prisms were taken out of the water, wiped clean with a thick cloth to remove the excess of water. Afterwards, they were weighed, using a digital scale with an accuracy of 0.01 g, and then measured with the digital caliper, accuracy of 0.01 mm, to check for dimensional stability and also to be able to compute the bulk

density of the obtained mortars. Measurements were recorded for both length (four values) and width/height (six values) of the prisms.

2.3.3. Dynamic moduli of elasticity

The dynamic moduli of elasticity were determined in accordance with ASTM C215:19 specifications [42]. The determination of longitudinal dynamic modulus of elasticity and dynamic shear modulus were based on the first resonant frequencies in longitudinal and transversal directions, respectively, obtained by means of Impact Echo Method (Fig. 4).

The dynamic longitudinal modulus of elasticity was calculated on the basis of Eq. 1 [42]:

$$E_{dyn} = D \cdot M \cdot (n')^2 \quad (1)$$

where: M is the mass of specimen (kg), n' is the fundamental longitudinal frequency of vibration (Hz) and $D = \frac{4 \cdot L}{b \cdot t}$ is a coefficient ($\frac{N \cdot s^2}{kg \cdot m^2}$) that depends on the length L (m) and the cross sectional dimensions b(m) and t (m) of the specimen.

The dynamic shear modulus was calculated using Eq. 2 [42]:

$$G_{dyn} = B \cdot M \cdot (n'')^2 \quad (2)$$

where: M is the mass of specimen (kg), n'' is the fundamental torsional frequency of vibration (Hz) and $B = \frac{4 \cdot L \cdot R}{A}$ is a coefficient ($\frac{N \cdot s^2}{kg \cdot m^2}$) that depends on the length L (m), of the specimen the cross-sectional area A (m^2) and the shape factor R which takes the value of 1.183 for a square cross-section prism [42].

The experimental arrangement depicted in Fig. 4a was used to record the longitudinal free vibration response of all specimens. The signal for each prism consisted of at least 10 impact responses, as exemplified in Fig. 5a for the Ref mix. This signal underwent the Fast Fourier Transform (FFT) analysis, and the frequency spectrum was obtained (Fig. 5b). The fundamental longitudinal frequency was identified by applying a Pseudo-Voigt fitting function on the FFT spectrum (Fig. 5c). The dynamic modulus of elasticity was calculated using Eq. 1.

A similar method was applied to obtain the torsional vibration frequency, employing the set-up outlined in Fig. 4b. Upon obtaining the FFT spectra, two main peaks, closely positioned, were observed, as depicted in Fig. 6a for the Ref mix. Consequently, the fundamental transversal frequency of vibration was also measured, employing the set-up presented in Fig. 4c. This frequency was then neglected in the analysis of the torsional response, which was fitted with the same Pseudo-Voigt function (Fig. 6b). The fundamental torsional frequency was then used to compute the dynamic shear modulus of each prism using Eq. 2.

The dynamic Poisson ratio was computed by means of Eq. 3:

$$\nu_{dyn} = \frac{E_{dyn}}{2G_{dyn}} - 1 \quad (3)$$

where E_{dyn} is the dynamic modulus of elasticity and G_{dyn} is the dynamic shear modulus determined based on Eqs. (1) and (2), respectively.

2.3.4. Temperature

Cement-based materials, such as mortar, concrete and reinforced concrete, may be exposed to severe environmental conditions, including high temperatures. Under extreme circumstances, fire incidents may occur either due to natural disasters or human error. Exposure to high temperatures triggers a series of internal changes in the material that negatively impact its mechanical properties. Previous research indicates that the cement paste is the most vulnerable component or mortar or concrete to high temperatures [43,44]. When exposed to temperatures higher than 900°C the cement paste loses 80 % of its strength [45]. The initial effect is the loss of free and capillary water, with the evaporation process starting at approximately 100ºC. However, given the pore pressure inside the cement-based material, this process takes place within the 100ºC-140ºC temperature range [46]. While the loss of water may lead to shrinkage in the cement paste, its impact on the dimensional stability of elements is generally counteracted by the expansion of non-hydrated products, such as un-hydrated cement grains and calcium hydroxide [47].

The dehydration of ettringite occurs between 80ºC and 150ºC, while the decomposition of gypsum takes place at 150ºC-170ºC. The dehydration process of calcium silicate hydrate (CSH) initiates around 200ºC [48]. Previous studies indicated that cement-based materials do not experience substantial strength reduction when exposed to temperatures up to 300ºC. Any strength loss that occurs is reversible, due to the rehydration process occurring during and after the cooling phase [49].

The selection of temperature values was based on previously mentioned studies on concrete, coupled with the findings of Castellote et al. [50] on cement pastes. Considering the information presented above, the temperature thresholds chosen for this study were 100ºC (marking the onset of evaporation of free and capillary water), 150ºC (indicating the end of free and capillary water evaporation, as well as the dehydration of ettringite) and 200ºC (concluding gypsum decomposition and the beginning of CSH dehydration, but still well below 300ºC). For the purpose of this study, the prisms were placed in an oven, heated to the target temperature, and maintained at that temperature for 4 hours. Once the heating process was terminated, the prisms were allowed to cool gradually to room temperature inside the oven at a cooling rate of 0.5 °C/min. The temperature increase rate was consistent for all specimens, at 6ºC per minute, as shown in Fig. 7.

After being exposed to elevated temperature, the specimens were measured to check for any changes in the geometrical dimensions and weighted to account for the mass loss due to evaporation processes. The dynamic elastic properties were determined following the procedure outlined in Section 2.3.3.

2.3.5. Flexural-tensile strength and compressive strength

The flexural tensile strength and compressive strength of all mortar prisms were assessed in compliance with SR EN 196–1:2016 [39]. Three-point bending test, with a loading rate of 50 N/s, was used to determine the flexural tensile strength. The resulting broken parts of the prism were examined for signs of visible cracks and then subjected to uniaxial compression test with a loading rate of 2400 N/s.

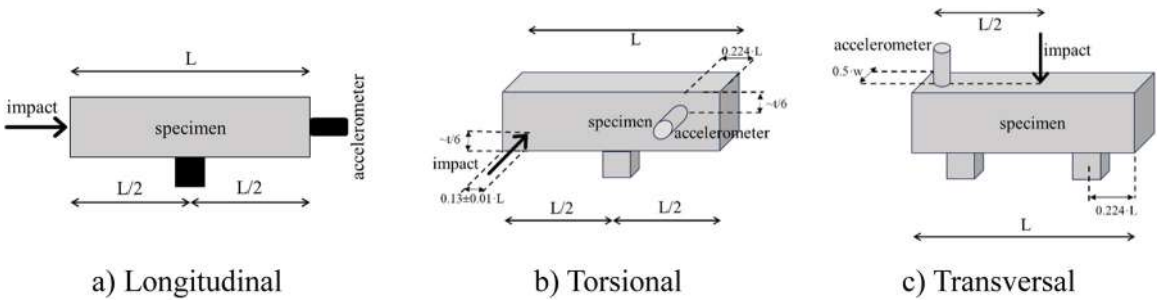

Fig. 4. Set-up for determination of fundamental frequency of vibration [42].

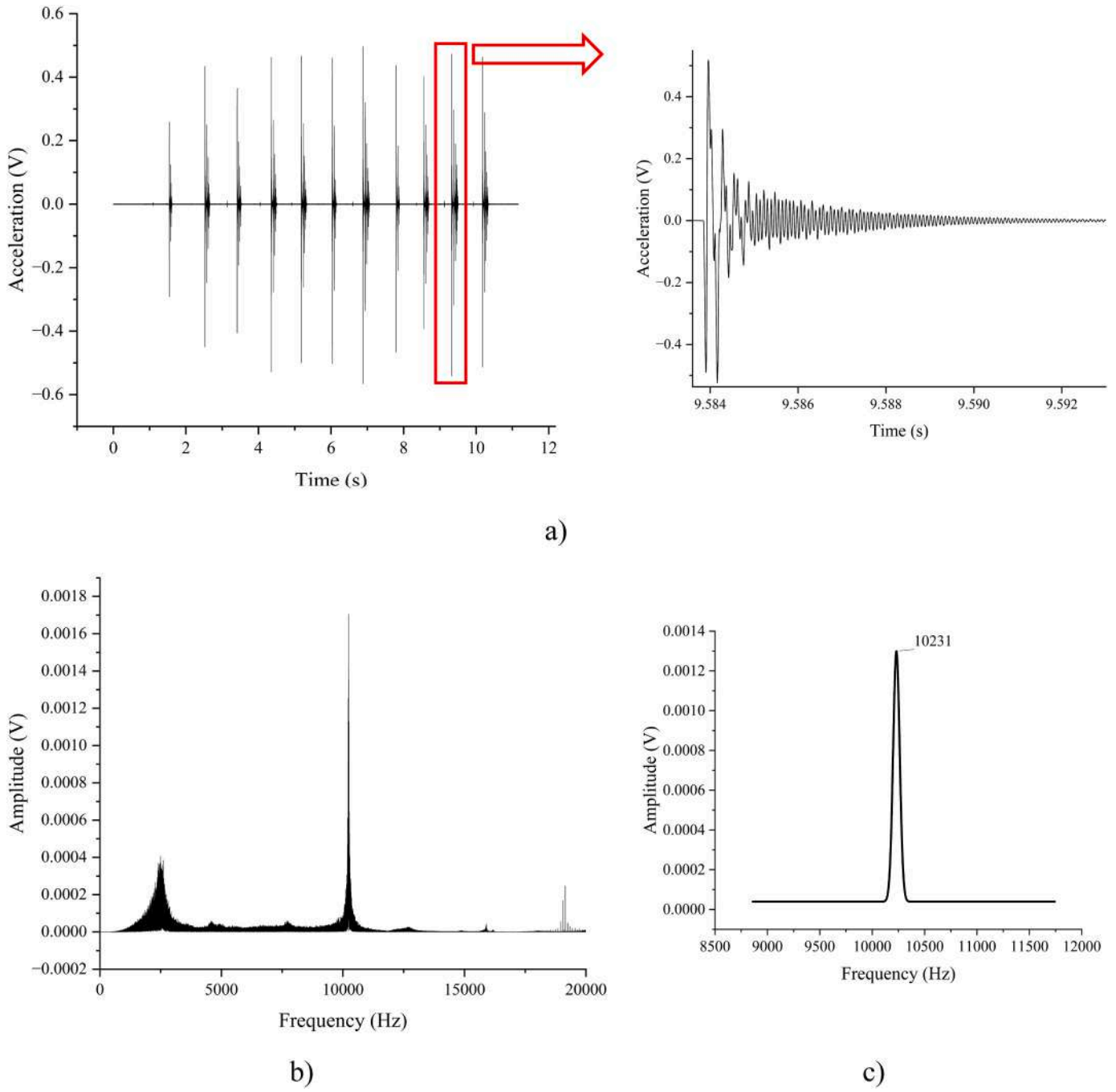

Fig. 5. Procedure for the determination of the fundamental longitudinal frequency of vibration of a prism belonging to the Ref mix: a) Free vibration response (longitudinal impact), b) Overlapped FFT spectra for a single prism, c)Fitting result of the FFT analysis of a longitudinal impact response.

The final values of the flexural strength for the mixes presented in Table 2 were obtained by averaging three measurements for each set of prisms, categorized according to the temperature they were previously exposed to (room temperature, 100ºC, 150ºC and 200ºC). Similarly, the final values of the compressive strength were calculated by averaging six measurements for each set of prisms.

3. Results and discussions

3.1. Effect of EPA

3.1.1. Mortar slump

Workability and consequently, the slump, are influenced by the water content of the mix. A high water/cement ratio results in more workable mortar/concrete but it leads to increased chance of segregation, during casting and vibration, and a decrease in the values of mechanical properties. On the other hand, a stiff mix, results in poor compaction, leading also to a decrease in strength [51].

The results obtained from the mini slump cone [52,53] are summarized in Table 3. The replacement of natural sand by EPA did not result in significant changes of the cone base diameter. The EPA10 mix showed identical behavior with the Ref mix, the same base diameter of the mini cone and the same slump, even though the water/cement ratio was increased. However, increasing the replacement percentage to 20 % and 30 % resulted in higher values of the slump even for marginal changes of the base diameter and without visible swelling of the mortar cone.

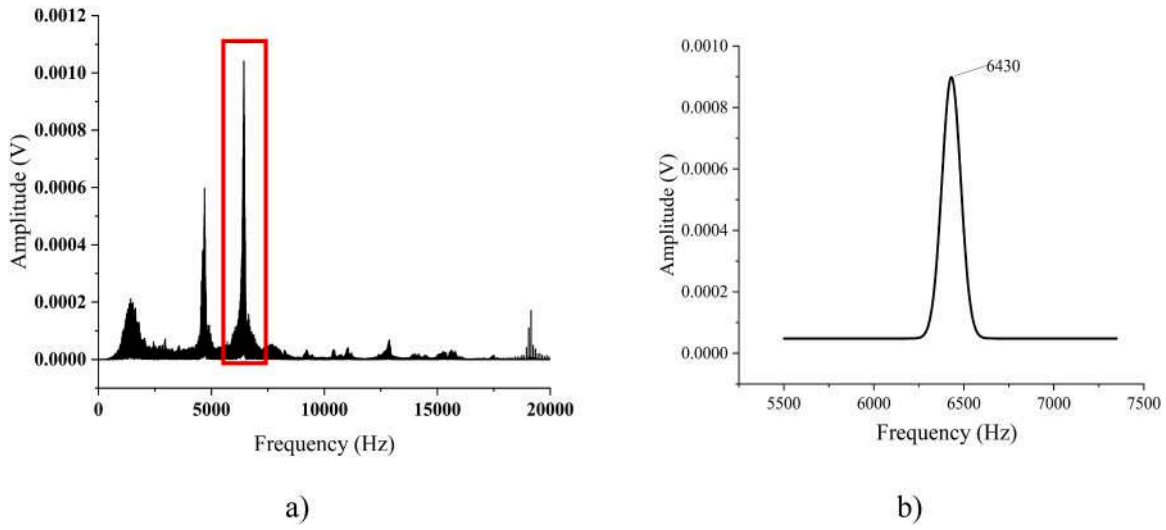

Fig. 6. Determination of the fundamental torsional frequency of vibration of a prism belonging to the Ref mix: a) Overlapped FFT spectra for a single prism, b) Fitting result of a FFT of the torsional impact response.

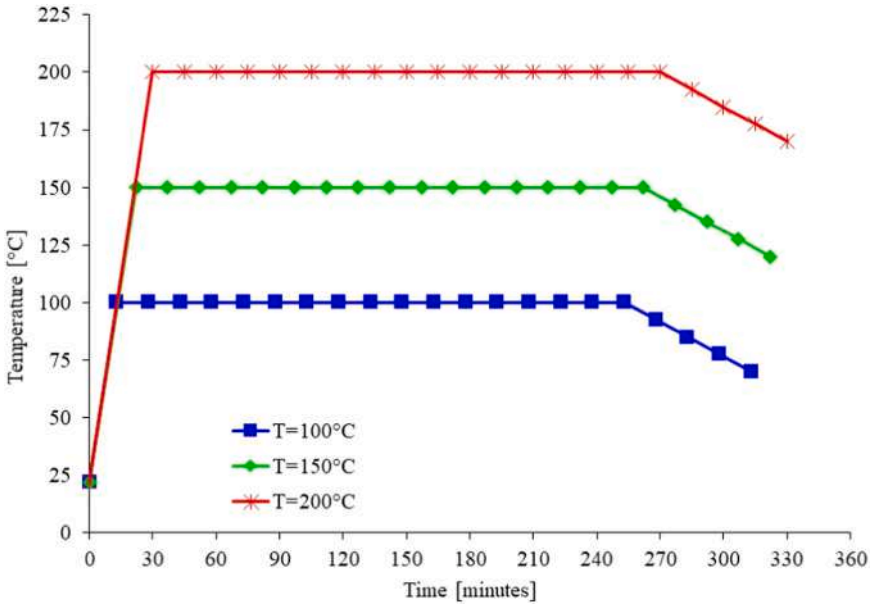

Fig. 7. Temperature-time history.

Table 3
Properties of fresh mortar.

Mix	Ref	EPA10	EPA20	EPA30
				
Diameter at the base [mm]	100	100	102	103
Slump [mm]	1	1	13	15

All mixes exhibited similar workability as perceived during casting the specimens. A similar approach of increasing the water/cement ratio to obtain similar workability was previously reported [54], although additives were also used, in fixed percentages for all considered mixes, to adjust the water retentivity of EPA.

3.1.2. Bulk density

The variation of density with the replacement percentage of natural sand by EPA, at the age of 28 days, is presented in Fig. 8.

A decrease in density can be observed with the increase of the replacement percentage. Compared to the reference mix, the EPA30 mix exhibited a 7.73 % reduction in density. The substitution of natural sand

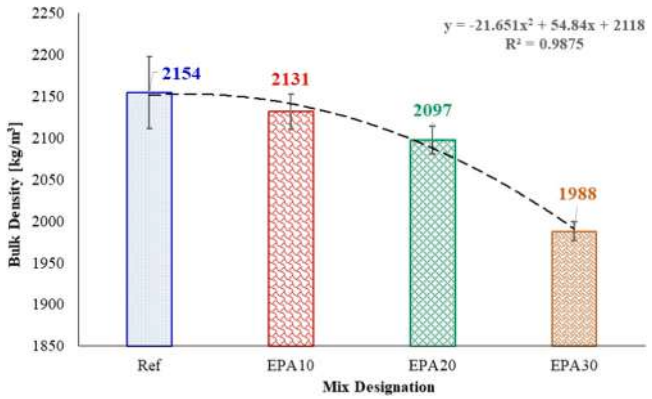

Fig. 8. Variation of density with EPA content.

with EPA led to a 1.06 % and 2.65 % decrease in density values for the EPA10 and EPA20 mixes, respectively. This downward trend appears to follow a quadratic equation, as depicted in Fig. 8.

Similar trends were reported in the scientific literature either in the case of using perlite as cement substitution in mortar [55–57] or as aggregates in lightweight concrete [26].

3.1.3. Dynamic elastic properties

The graphs in Fig. 9 illustrate the distribution of dynamic modulus of elasticity values, relative to the median, for all 12 prisms of each mix show in Table 2. It can be observed that Ref, EPA10 and EPA20 mixes exhibit a good distribution of the values, falling within one standard deviation from the median. In contrast, the EPA30 mix displays scattered results, with some values lying outside the standard deviation interval. These values were excluded from computing the dynamic elasticity modulus median value. The dispersion could be the result of the higher replacement percentage, considering the high porosity of EPA

The distribution of the values of the dynamic shear modulus, with respect to the median, is presented in Fig. 10 for all 12 prisms of each mix shown in Table 2. It can be observed that all mixes exhibit good distribution of the values of the modulus of elasticity, within one standard deviation from the median.

The influence of sand replacement by EPA on the dynamic elastic

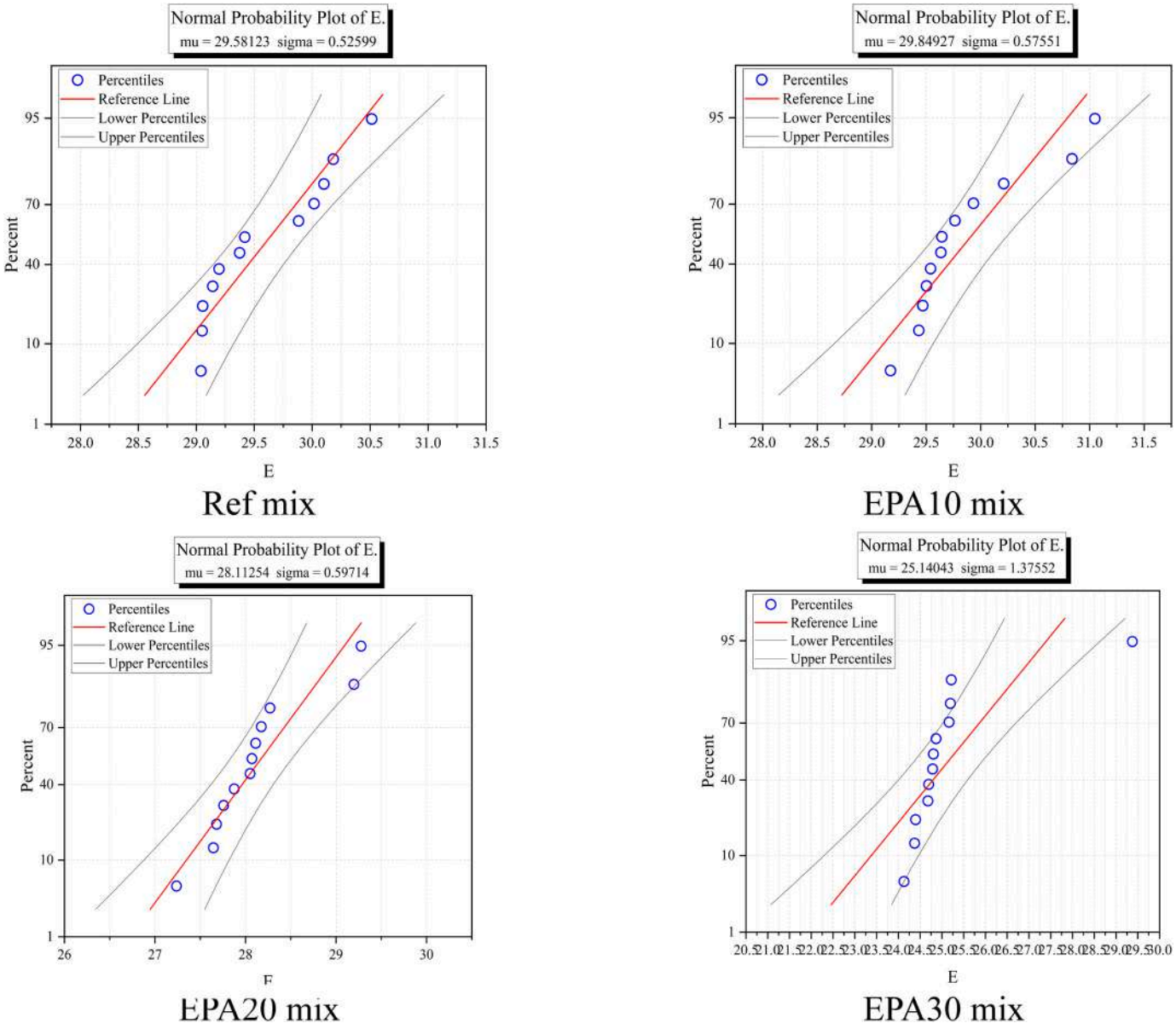

Fig. 9. Distribution of dynamic modulus of elasticity values with respect to the median.

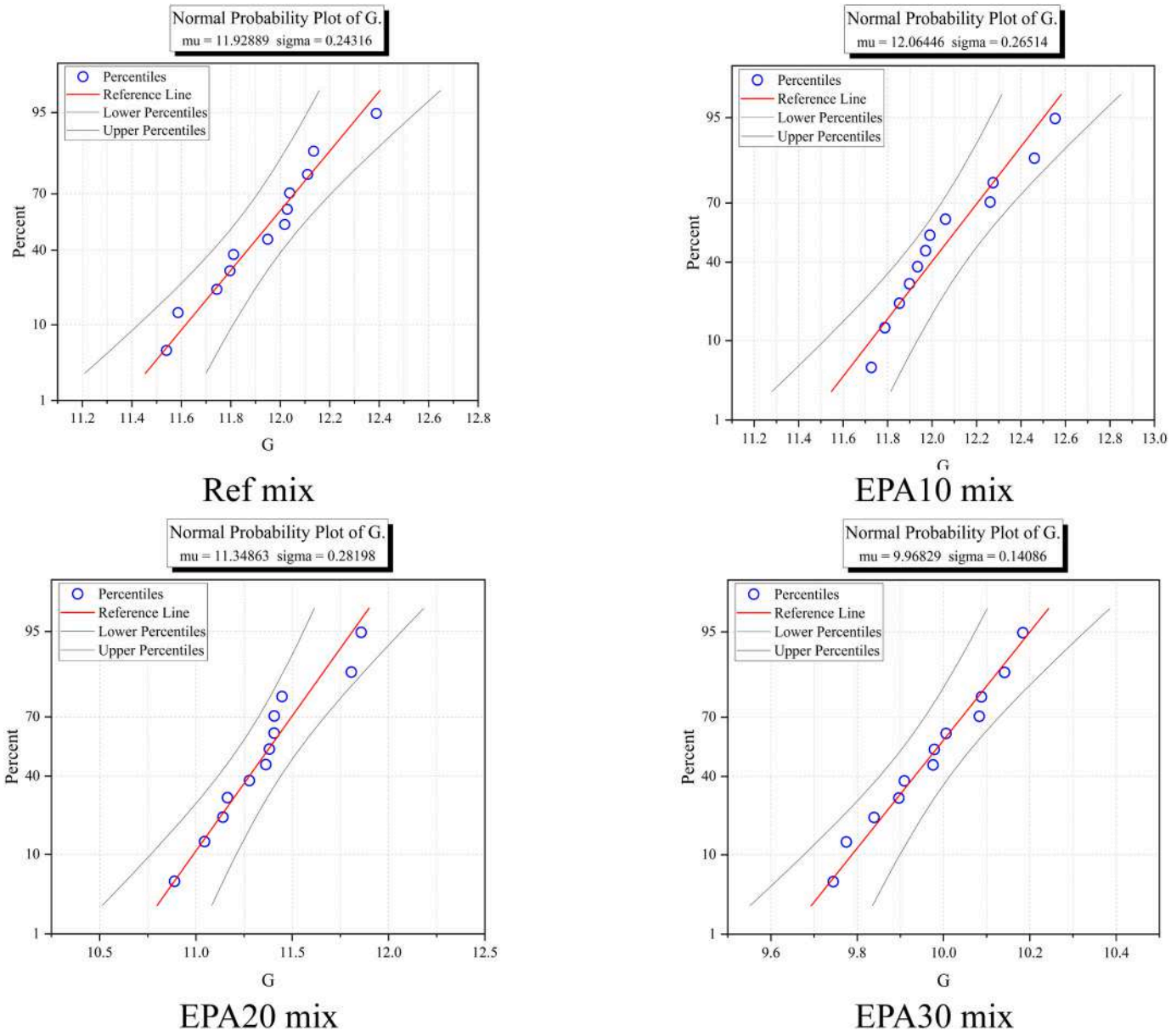

Fig. 10. Distribution of dynamic shear modulus values with respect to the median.

properties of mortar is presented in Fig. 11.

Taking into account Eqs. (1) and (2) for the calculation of the two dynamic elastic moduli, the observed trend in Fig. 11 is consistent with the data presented in Fig. 8. Since the bulk density of the mix did not change significantly, Fig. 8, and D and B coefficients from Eq. (1) and Eq. (2), respectively, are based on the geometrical dimensions of the samples, it follows that the values of the fundamental frequency of vibration for all specimens could be similar to one another. Although sand was replaced by EPA, the mass was also similar among the mixes, with small variations and showing a slight decreasing trend with increasing replacement percentage. This could be attributed to the fact that all prisms were stored in water. The data is summarized in Table 4, as average of 12 values corresponding to the 12 prisms for each mix.

The values of longitudinal (Edyn) and shear (Gdyn) dynamic moduli increased slightly when replacing 10 % of sand by EPA. For higher substitution amounts, the values for these parameters are decreasing. Nevertheless, it can be observed that the Poisson's ratio is directly proportional with the perlite quantity. This implies that Young's modulus is less affected than shear modulus, especially for over 20 % replacement percentages, suggesting a decrease in the transversal deformability

3.1.4. *Flexural tensile strength*

The substitution of natural sand with EPA led to a significant reduction, ranging between 40 % and 51 %, in the flexural tensile strength values. Three prisms from each mix were tested following the procedure presented in Section 2.3.5. The results of the tests are presented in Fig. 12. Similar decreasing trends have been reported in previous research [58] although, in most cases, this was observed in specimens where perlite powder replaced Portland cement rather than sand [55,59].

3.1.5. *Compressive strength*

The decrease in compressive strength values was less pronounced compared to flexural strength when natural sand was replaced by EPA. The reduction ranges from 18.33 % for EPA10 to 30.71 % for EPA30, as shown in Fig. 13. Three prisms from each mix were tested, following the procedure presented in Section 2.3.5. Similar behavior regarding

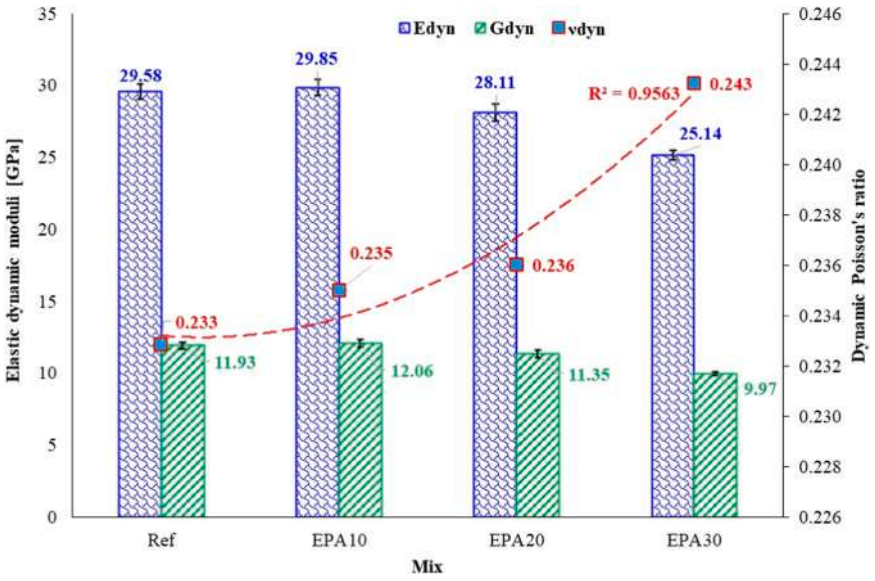

Fig. 11. Influence of EPA replacement percentage on the dynamic elastic properties of mortar.

Table 4
Dynamic characteristics of considered mixes (average values of 12 data sets).

Mix	Mass [kg]	n' (Eq. 1) [Hz]	E_{dyn} (Eq. 1) [GPa]	n'' (Eq. 2) [Hz]	G_{dyn} (Eq. 2) [GPa]	ν_{dyn} (Eq. 3) -
Ref	0.568	11523	**29.58**	6728	**11.93**	**0.233**
EPA10	0.561	11684	**29.85**	6829	**12.06**	**0.235**
EPA20	0.543	11440	**28.11**	6682	**11.35**	**0.236**
EPA30	0.532	11102	**25.14**	6429	**9.97**	**0.243**

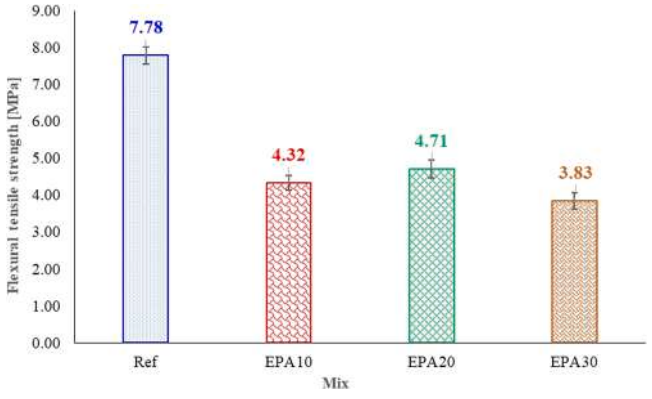

Fig. 12. Influence of EPA replacement percentage on the flexural tensile strength of mortar.

compressive strength was reported previously [58] but mostly for specimens with perlite powder replacing Portland cement instead of sand [55,59].

From the analysis of the obtained data, in terms of average values, an equation linking the dynamic longitudinal modulus of elasticity (E_{dyn}) and the compressive strength (f_c) of mortar with EPA aggregates was proposed, as shown in Eq. (4).

$$f_c = 9.08e^{-4} \cdot E_{dyn} \quad (4)$$

where both the compressive strength and the dynamic longitudinal modulus of elasticity are expressed in MPa. The accuracy of the proposed formula is checked against the experimental obtained values for the compressive strength of mortar mixes. The obtained results are

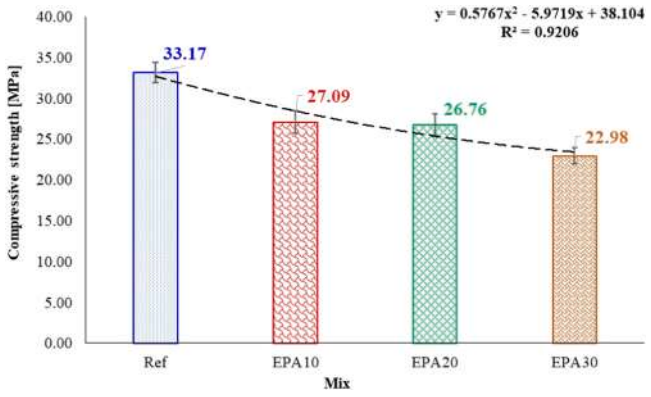

Fig. 13. Influence of EPA replacement percentage on the compressive strength of mortar.

shown in Fig. 14, in terms of average values, and in Fig. 15 in terms of individual values obtained on mortar prisms for each mix containing EPA.

From Fig. 14 it can be observed that there is a very good correlation between the values of the compressive strength given by the proposed

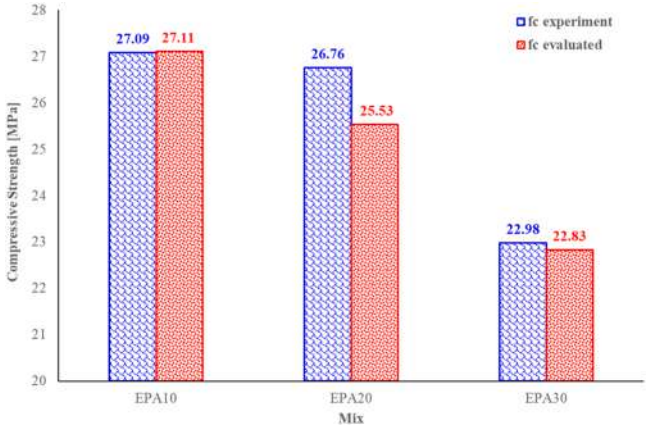

Fig. 14. Analytical vs. experimental results for the compressive strength of mortar mixes (average values).

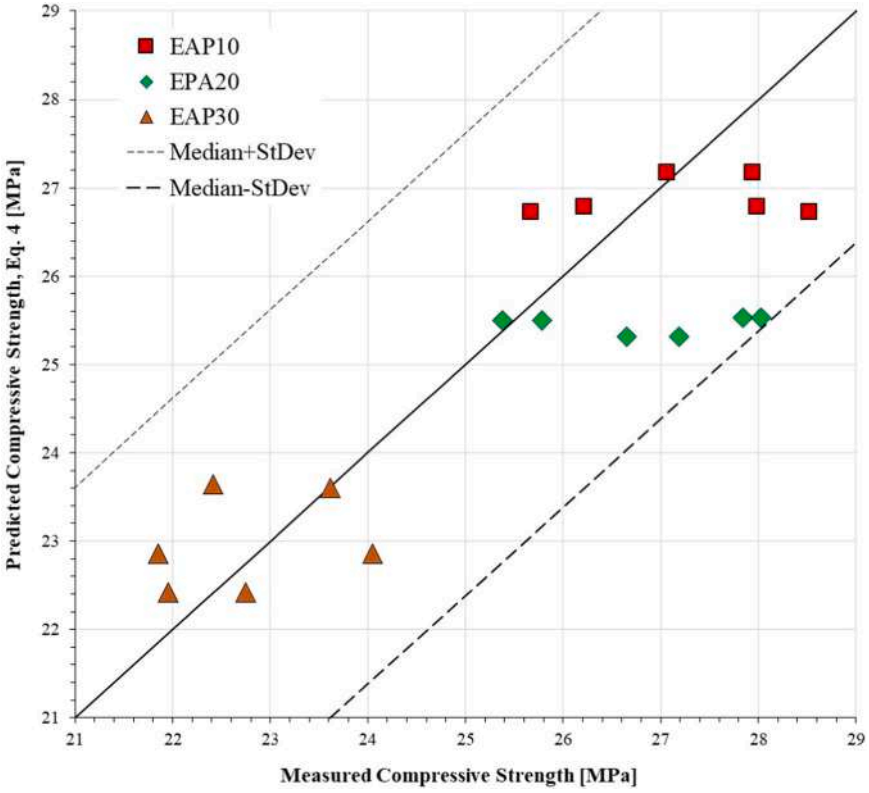

Fig. 15. Distribution of predicted/measured compressive strength values with respect to the median.

formula and the experimentally obtained data. The largest difference was obtained for EPA20 mix, 4.59 %. All other values where less than 1 % apart from the laboratory test values. The data shown in Fig. 15, obtained for individual prisms of each mix, shows that the results obtained from Eq. (4) fall within ±1 standard deviation from the median. There is an underestimation tendency of the experimental results for 20 % and 30 % replacement rates whereas for 10 % EPA content using Eq. (4) leads to slightly overestimated results.

Surveying of the scientific literature revealed no other studies that present both dynamic elastic properties and compressive strength of mortars with EPA, thus the proposed equation could not be validated against other data sets. It is important to note that, upon further validation, the significance of the proposed equation lies in its ability to directly and accurately determine the compressive strength of mortar with EPA once the dynamic modulus of elasticity is known. This could potentially eliminate the need for destructive tests.

The proposed equation has limitations, since it was derived for a specific cement/sand volumetric ratio, a water/cement ratio and a certain cement type. Further investigations are necessary in order to improve this equation, as reported by similar studies investigating the properties of cement-lime laying mortar [60].

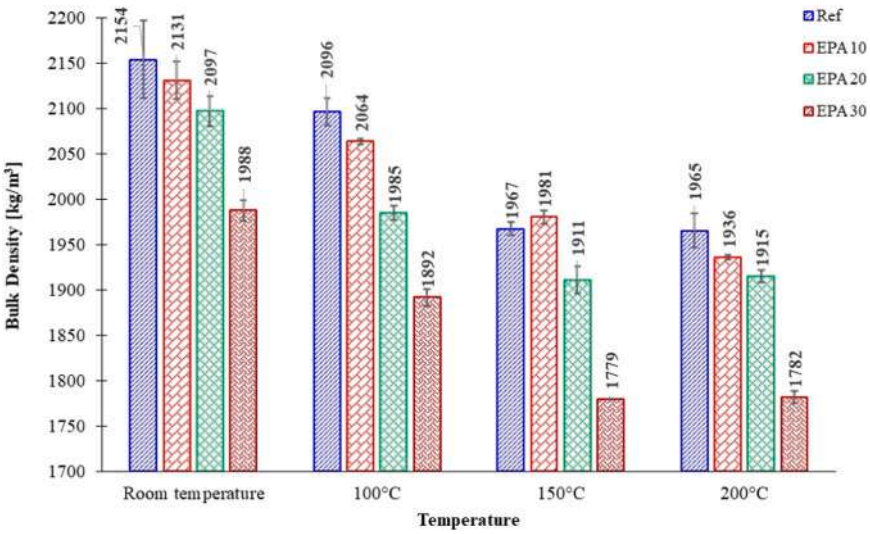

Fig. 16. Influence of temperature on the bulk density of considered mortar mixes.

3.2. Effect of temperature

As outlined in Section 2.3.4, the prismatic specimens were heated up to temperatures of 100ºC, 150ºC and 200ºC at a rate of 6ºC per minute. Subsequently, they were kept for 4 hours and then gradually cooled down back to room temperature. Specimens were analyzed in terms of density, dynamic moduli, and flexural and compressive strength.

3.2.1. Bulk density

After the thermal treatment, specimens were measured again to check for dimensional stability and weighed to account for changes in mass due to water loss. Bulk density values are presented in Fig. 16.

It can be observed that exposure to higher temperatures resulted in lower values for bulk density. Reference, EPA20 and EPA30 mixes appear to stabilize at 150ºC, since exposure at 200ºC does not have a notable impact on density values. EPA10 mix displays an almost linear decrease for density with the increase in temperature.

Fig. 17 illustrates the mass loss resulting from the evaporation process for each mortar mix under consideration. At 100ºC, all EPA mixes exhibited a lower mass loss (4.35 %-4.56 %) compared to the reference (5.25 %). When specimens were exposed to 150ºC, both EPA20 and EPA30 mix showed a higher mass loss than Ref by 0.85 % and 1.56 %, respectively. The EPA10 mix registered the lowest mass loss at this temperature. At 200ºC, the reference mix, EPA10 and EPA20 exhibited nearly identical mass loss values (8.77 %, 9.10 % and 9.20 %). In contrast, EPA30 experienced the highest mass loss of 10.93 %.

The variation of mass loss with temperature can be divided into two intervals: from room temperature to 150ºC, and from 150ºC to 200ºC. In the first range of temperatures, Ref and EPA10 mixes exhibit similar trends, with a steeper slope up to 100ºC, followed by a reduced rate between 100ºC and 150ºC. On the other hand, EPA20 and EPA30 mixes demonstrated a higher rate of mass loss from 100ºC to 150ºC. This phenomenon could be attributed to the increased porosity of specimens with higher percentages of EPA.

Within the temperature range of 150ºC to 200ºC, Ref, EPA20 and EPA30 showed little mass loss variation. This observation is supported by bulk density values depicted in Fig. 16. EPA10 exhibited an almost identical slope to the previous interval.

The observed trends can be explained by considering the internal structure of mortar. EPA are highly porous, as depicted in Fig. 3. Their use in mortar is expected to result in the formation of internal pores that are either closed or open. During heating, capillary water and water from open pores evaporates, accounting for most of the overall mass loss. It was previously reported that ettringite undergoes thermal decomposition at 90ºC, while CSH begins dehydrating between 200ºC and 450ºC, corroborating earlier findings [47]. Additionally, excessive shrinkage of the cement paste was reported at temperatures higher than 200°C with detrimental effects in terms of strength and durability [48]. While ettringite dehydrates between 80ºC and 150ºC, gypsum decomposes at 150ºC-170ºC and CSH starts to dehydrate at 200ºC [48]. Partially saturated internal, sealed pores, resulted from water consumption during the hydration of cement grains, allow the remaining water to transform into vapors. Simultaneously, they provide enough space to prevent vapor pressure from damaging the mortar matrix. A similar phenomenon was reported in earlier research works on EPP (expanded perlite powder) used to suppress the alkali-silica reaction in cement mortar [61,62].

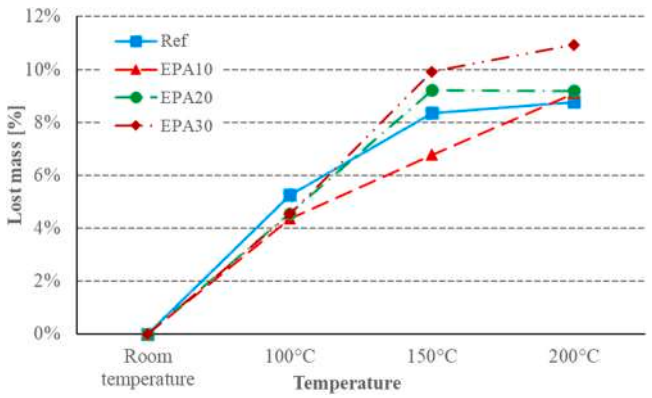

Fig. 17. Lost mass of mortar prisms as function of temperature.

3.2.2. Dynamic elastic properties

Upon cooling to room temperature, the prisms were used to determine dynamic moduli, as outlined in Section 2.3.3. For each considered temperature, 3 specimens were tested, resulting in a total of 30 data sets per mix for the computation of the dynamic modulus of elasticity and the dynamic shear modulus. Results are presented in Fig. 18.

It can be observed that as the temperature increases, the values for the dynamic moduli decrease. Similar to results at room temperature, EPA10 exhibited higher dynamic elasticity modulus compared to Ref, showing improvements of 5.6 %, 5.48 % and 3.85 % at 100ºC, 150ºC and 200ºC, respectively. The dynamic shear modulus of EPA10 showed the highest improvement, with respect to Ref, at 150ºC (6.05 %). Improvements in both moduli, compared to Ref, can be seen only for EPA20 at 150ºC, but they are half the ones observed for the EPA10 mix. Compared to the reference, the EPA30 mix showed consistently lower values, for both E and G, by as much as 14 %.

Values for both moduli decrease almost linearly with temperature for all mixes, as it can be seen in Fig. 19. For both E and G, the temperature of 100ºC represents a threshold corresponding to the most significant decrease. At this temperature, values are reduced for all mixes with percentages between 18.71 % for EPA10 and 20.86 % for Ref. Another important observation is that the EPA20 mix is the least affected by exposure at 150ºC in comparison to 100ºC.

Considering the pozzolanic nature of expanded perlite, if can be inferred that smaller pores were present in mortars with EPA [14,44]. Also, given the porous nature of EPA, modified mortars are expected to exhibit a higher total porosity compared to Ref. Nevertheless, considering bulk density values and the observed temperature effects, pore size and quantity would represent a reasonable underlying mechanism. While using 10 % EPA has a beneficial effect on elastic properties, higher percentages prove detrimental, possibly due to the availability of calcium hydroxide (CH) in the cementitious matrix [63].

3.2.3. Flexural tensile strength

The impact of temperature exposure on the flexural tensile strength of all mortar mixes is shown in Fig. 20. It can be observed that all EPA mixes exhibit lower values than Ref, at both room temperature and 100ºC. Conversely, at higher temperatures all EPA mortars show higher tensile strengths, compared to both the reference mix and to lower treatment temperature values.

At the same time, it can be seen that while the flexural tensile strength of the Ref mix exhibits a decreasing trend with the increase in temperature, EPA mixes showed an opposite behavior. All recorded values of the flexural tensile strength at 100ºC, 150ºC and 200ºC were higher than the value obtained at room temperature. EPA10 and EPA20 mixes registered a peak increase at 150ºC while the value for the EPA30 mix continuously increased with the increase in the exposure temperature, although only a 3.5 % increase was observed from 150ºC to 200ºC.

Tensile strength values of EPA mortars at all temperatures, normalized to the Ref value at each temperature, are presented in Fig. 21. The EPA10 can be seen to exhibit a steeper increase compared to the other two mixes. Comparing Fig. 20 and Fig. 21, it can be inferred that EPA20 and EPA30 display similar trends in both absolute and normalized values. On the other hand, normalized values of EPA10 are seen to continuously increase, suggesting that flexural strength is more affected for Ref than for EPA10, when increasing the temperature from 150ºC to 200ºC.

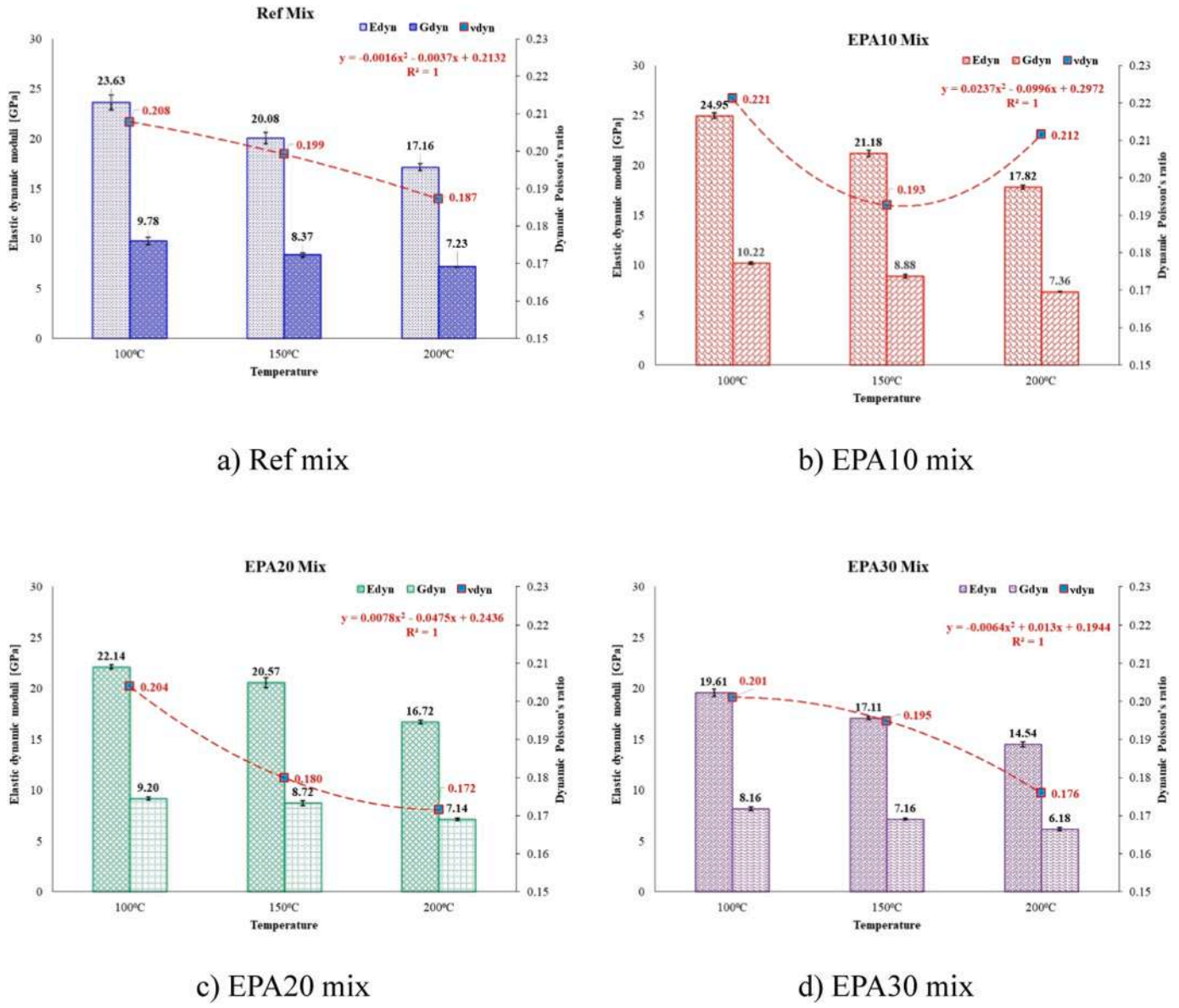

Fig. 18. Temperature influence on the dynamic elastic properties of mortars.

A possible explanation of the obtained results may reside in the pozzolanic nature of expanded perlite aggregates. Recent studies confirmed that, due to pozzolanic activity, the larger pores in the cement matrix are transformed into smaller pores because of the hydration products [44,64,65]. At the same time, no deteriorations in the cementitious matrix were reported for temperatures up to 400ºC [44]. However, pozzolanic reaction needs time and requires a higher activation energy than the case of using Portland cement alone. This accounts for the lower early age mechanical properties in cement-based materials with various pozzolans. One method to accelerate the rate of pozzolanic activity is to increase the curing temperature. However, this approach was reported to influence the degree of crystallinity of the resulting CSH [63]. On the other hand, when subjecting cement-based mortar to elevated temperature, lower mass losses were reported for mixes with calcined perlite [66]. This implies that the presence of expanded perlite positively influences the behavior of mortar at elevated temperatures.

3.2.4. *Compressive strength*

The effect of exposure temperature on compressive strength for all mortar mixes is presented in Fig. 22. An increase in temperature resulted in decreasing values of the Ref compressive strength, with a steep decrease of 19.35 % at 100ºC, and additional reductions of 4 % for 150ºC and 200ºC. The compressive strength values of EPA10 and EPA20 mixes decreased when exposed to 100ºC. However, at 150ºC and 200ºC, both mixes showed higher values compared to both the Ref mix at the same temperature and to their room temperature values. This suggests that a lower content of EPA led to an improved internal structure, potentially related to lower porosity. Additionally, subjecting the EPA specimens to higher temperatures and subsequent cooling to room temperature may have promoted an acceleration of the pozzolanic reaction [44,63–66] and the rehydration of cement grains [49].

The substitution of natural sand by EPA resulted in higher normalized values of the compressive strength with respect to the Ref mix, Fig. 23, compared to the flexural strength, Fig. 21. At the same time, the compressive strength gains when subjected to elevated temperature are lower than in the case of flexural strength for all EPA mixes. This may be attributed to a different CSH crystallinity, due to the promotion of pozzolanic reaction at elevated temperatures, that had a more significant influence on the values of the compressive strength. Similar trends as the ones shown in Figs. 21 and 23 were previously reported [67],

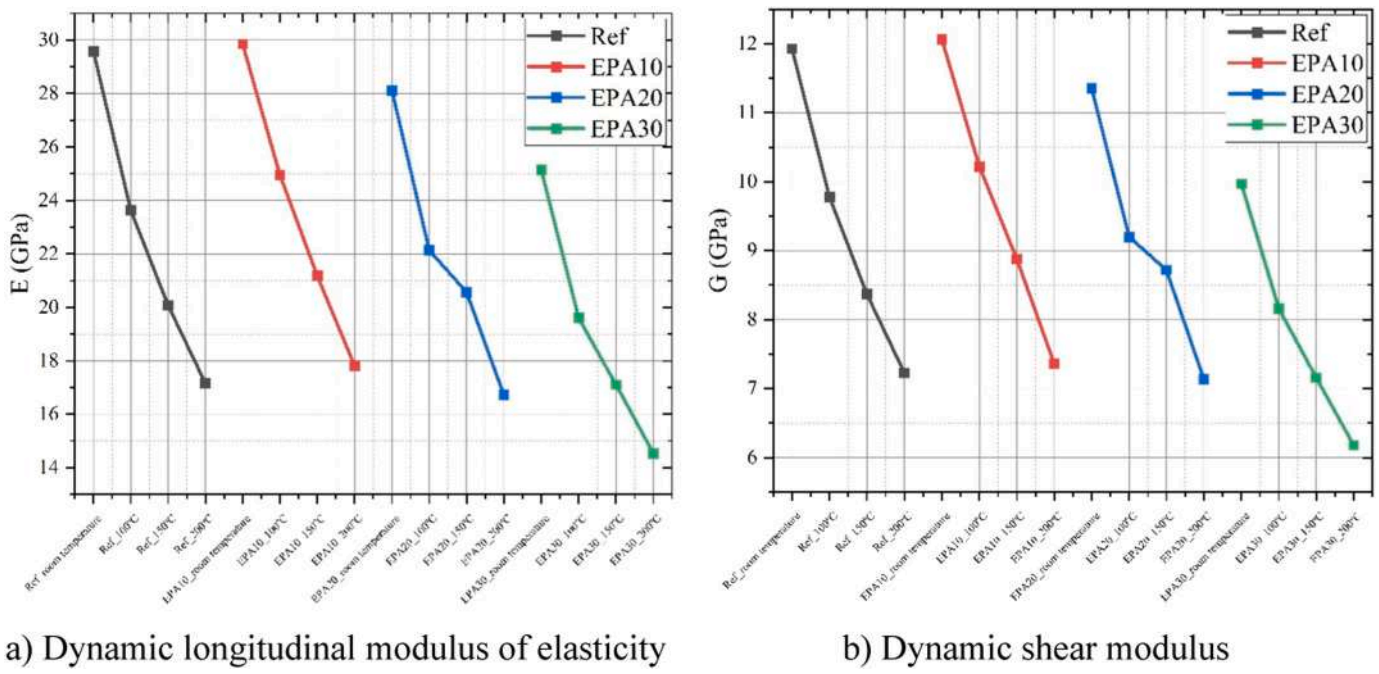

Fig. 19. Decreasing trends of the two dynamic moduli as function of temperature.

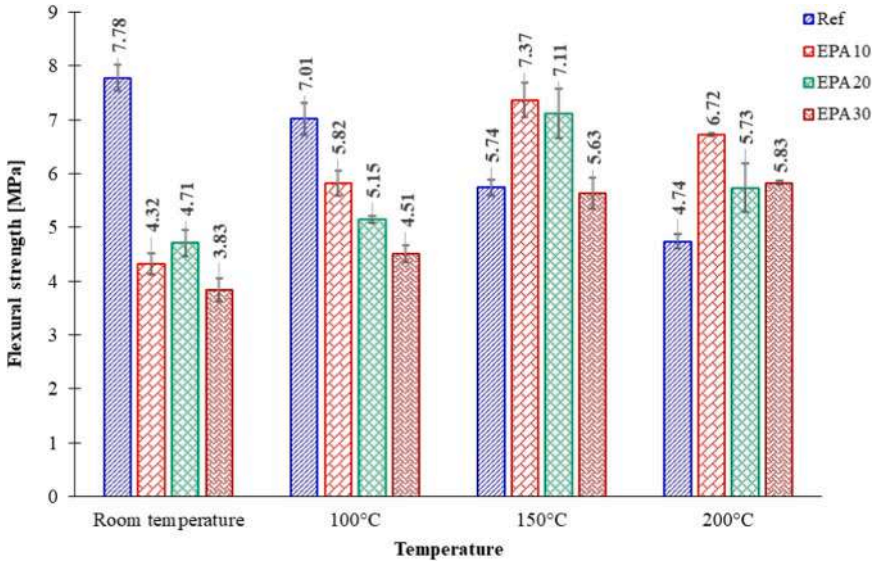

Fig. 20. Influence of temperature on the flexural tensile strength values.

although for higher temperatures and higher replacement percentages [68].

4. Conclusions

The present paper aims at bringing its contribution to narrowing the knowledge gap on the use of EPA in cement-based mortar, both at room and at temperatures up to 200°C. Previous studies reported improvements in the mechanical properties of concrete containing powder perlite for temperatures up to 300°C. Therefore, the parameters considered in this research were: the replacement percentage (10 %, 20 % and 30 % by volume) of natural sand by EPA with a maximum grain size of 4 mm and the temperature treatment of mortar prisms at the age of 28 days. The selected temperatures were 100°C, 150°C and 200°C. The influence of both parameters on the flexural and compressive strength of mortar as well as dynamic elastic properties were experimentally determined. Based on the results presented in the paper, the following conclusions can be drawn:

1. Substituting sand by expanded perlite aggregates, by volume, results in a decrease in the values of density, flexural strength and compressive strength at the age of 28 days. The higher the substitution percentage, the higher the decrease.
2. When substitution percentage of sand by EPA is 10 % or 20 %, very little influence is observed from the point of view of dynamic longitudinal modulus of elasticity and shear modulus of prismatic specimens.
3. An empirical equation is proposed to obtain the compressive strength of mortar with EPA aggregates when the dynamic longitudinal modulus of elasticity (E_{dyn}) is known. The proposed equation shows

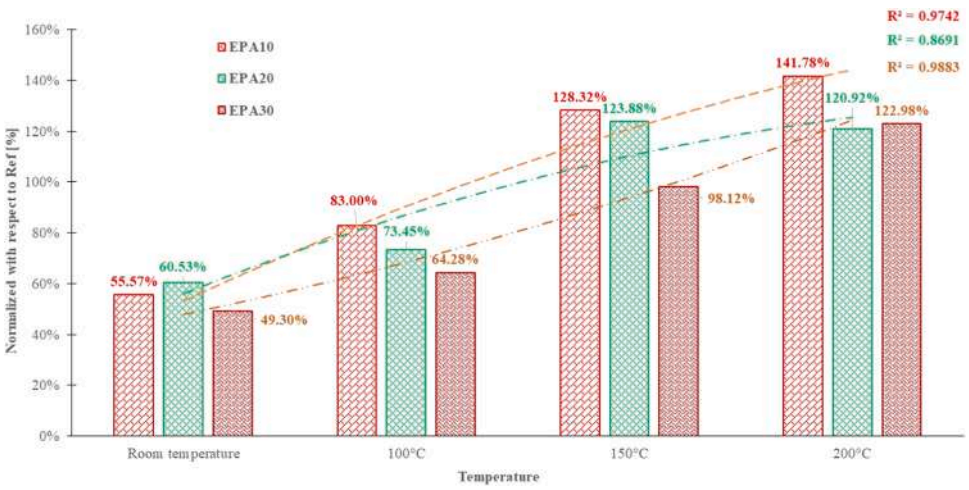

Fig. 21. Flexural tensile strength of EPA mixes normalized with respect to the Ref mix.

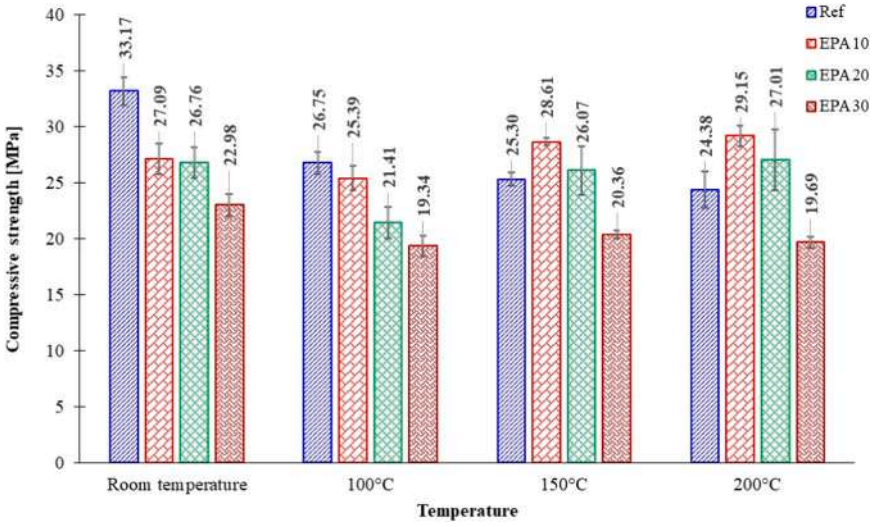

Fig. 22. Influence of temperature on the compressive strength values.

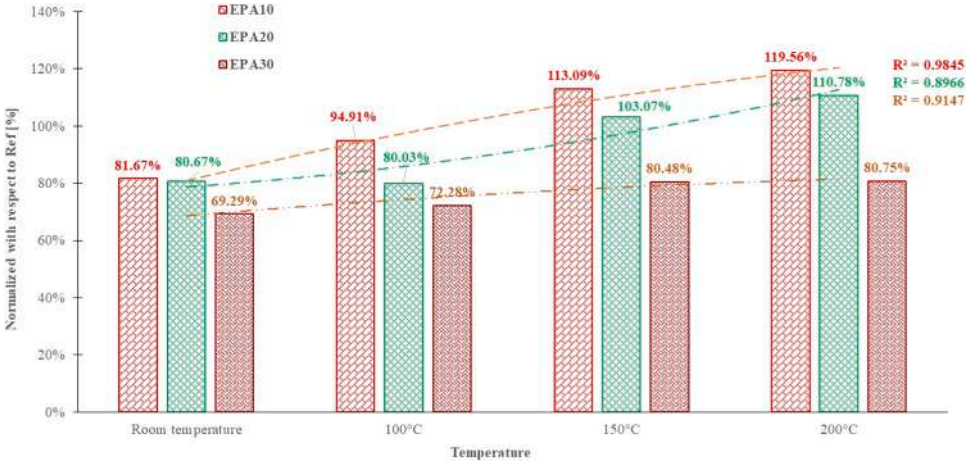

Fig. 23. Compressive strength of EPA mixes normalized with respect to the Ref mix.

good accuracy of the predicted values when compared to experimental data. While further validation is necessary, the scientific literature currently lacks reports on these parameters for cement mortar with EPA.

4. Exposing the specimens to temperatures of 100ºC, 150ºC and 200ºC results in a decrease in the values of bulk density due, mostly, to the evaporation process of capillary water. Expanded perlite mortar mixes exhibit a more pronounced density reduction due to the porous nature of these aggregates.
5. Similar decreasing trends are reported for the values of dynamic moduli of all considered mortar mixes. However, for EPA10 and EPA20 mixes, higher values are reported compared to the Ref mix, without expanded perlite aggregates. This can be attributed to smaller internal pores dimensions. However, further research is necessary to confirm this hypothesis by either computed tomography (CT) or mercury intrusion porosimetry (MIP).
6. While the flexural tensile strength of Ref mix decreased with the increase in temperature, all EPA mixes show higher values after being subjected to selected temperatures compared to the one obtained at room temperature. The highest values are obtained for the EPA10 and EPA20 mixes at 150ºC. The obtained values are also higher than the one obtained for the Ref mix at the considered temperature
7. A similar conclusion can be drawn from the point of view of the compressive strength of mortar mixes. The highest values are obtained for EPA10 and EPA20 mixes at 200ºC, although the increase is only marginal. At both 150ºC and 200ºC the compressive strength of EPA10 and EPA20 mixes are higher than the Ref mix.
8. When taking into account both the temperature and the replacement percentage of natural sand by EPA, the optimum combinations are obtained for 10 % and 20 % replacement percentages at temperatures between 100ºC and 150ºC for the dynamic moduli of elasticity. The same replacement percentages result in improved flexural and compressive strength values at 150ºC. Higher replacement percentages, e.g. 30 % as considered in this research, results in consistently lower values for the investigated parameters, with the exception of flexural strength, at both room and temperatures up to 200°C.

CRediT authorship contribution statement

Ana-Maria Toma: Writing – original draft, Validation, Methodology, Conceptualization. **Ioana Olteanu:** Writing – original draft, Methodology, Investigation, Formal analysis. **George Taranu:** Writing – review & editing, Methodology, Investigation, Formal analysis. **Ionut-Ovidiu Toma:** Writing – original draft, Supervision, Resources, Project administration, Methodology, Investigation, Funding acquisition, Formal analysis, Data curation, Conceptualization. **Cristian Pastia:** Writing – review & editing, Methodology, Investigation, Formal analysis. **Georgiana Bunea:** Writing – review & editing, Visualization, Methodology, Investigation, Formal analysis. **Sergiu-Mihai Alexa-Stratulat:** Writing – original draft, Validation, Supervision, Software, Methodology, Investigation, Formal analysis, Data curation.

Declaration of Competing Interest

The authors declare that they have no known competing financial interests or personal relationships that could have appeared to influence the work reported in this paper.

Data availability

Data will be made available on request.

Acknowledgment

The research presented in this paper was conducted as part of the PN-III-P2–2.1-PED-2021-0677 research grant “Sustainable Concrete for Energy Efficient Buildings” funded by Executive Agency for Higher Education, Research, Development and Innovation Funding – UEFISCDI.

References

[1] GCCAssociation, Cement and Concrete Around the World, Glob. Cem. Concr. Assoc. (2020). https://gccassociation.org/concretefuture/cement-concrete-around-the-world/.
[2] P.M. Borges, J.Z. Schiavon, S.R. da Silva, E. Rigo, A. Neves Junior, E. Possan, J.J. de O. Andrade, Mortars with recycled aggregate of construction and demolition waste: mechanical properties and carbon uptake, Constr. Build. Mater. 387 (2023) 131600, https://doi.org/10.1016/j.conbuildmat.2023.131600.
[3] H. Shoukry, P. Perumal, A. Abadel, H. Alghamdi, M. Alamri, H.A. Abdel-Gawwad, Performance of limestone-calcined clay cement mortar incorporating high volume ferrochrome waste slag aggregate, Constr. Build. Mater. 350 (2022) 128928, https://doi.org/10.1016/j.conbuildmat.2022.128928.
[4] P. Matar, J. Barhoun, Effects of waterproofing admixture on the compressive strength and permeability of recycled aggregate concrete, J. Build. Eng. 32 (2020) 101521, https://doi.org/10.1016/j.jobe.2020.101521.
[5] U. Chandru, B. A, S. R, Systematic comparison of different recycled fine aggregates from construction and demolition wastes in OPC concrete and PPC concrete, J. Build. Eng. (2023) 106768, https://doi.org/10.1016/j.jobe.2023.106768.
[6] M.J. Ashraf, M. Idrees, A. Akbar, Performance of silica fume slurry treated recycled aggregate concrete reinforced with carbon fibers, J. Build. Eng. 66 (2023) 105892, https://doi.org/10.1016/j.jobe.2023.105892.
[7] F. Rezaei, A. Memarzadeh, M.-R. Davoodi, M.-A. Dashab, M. Nematzadeh, Mechanical features and durability of concrete incorporating recycled coarse aggregate and nano-silica: experimental study, prediction, and optimization, J. Build. Eng. 73 (2023) 106715, https://doi.org/10.1016/j.jobe.2023.106715.
[8] L. Barbieri, F. Altimari, F. Andreola, B. Maggi, I. Lancellotti, Characterization of volcano-sedimentary rocks and related scraps for design of sustainable materials, Materials 16 (2023) 3408, https://doi.org/10.3390/ma16093408.
[9] W.H. Juimo Tchamdjou, T. Cherradi, M.L. Abidi, L.A. Pereira-de-Oliveira, Mechanical properties of lightweight aggregates concrete made with cameroonian volcanic scoria: destructive and non-destructive characterization, J. Build. Eng. 16 (2018) 134–145, https://doi.org/10.1016/j.jobe.2018.01.003.
[10] M. Pekgöz, İ. Tekin, Microstructural investigation and strength properties of structural lightweight concrete produced with Zeolitic tuff aggregate, J. Build. Eng. 43 (2021) 102863, https://doi.org/10.1016/j.jobe.2021.102863.
[11] A.M. Rashad, A synopsis about perlite as building material – a best practice guide for Civil Engineer, Constr. Build. Mater. 121 (2016) 338–353, https://doi.org/10.1016/j.conbuildmat.2016.06.001.
[12] S. Celik, R. Family, M.P. Menguc, Analysis of perlite and pumice based building insulation materials, J. Build. Eng. 6 (2016) 105–111, https://doi.org/10.1016/j.jobe.2016.02.015.
[13] M. Davraz, M. Koru, A.E. Akdağ, Kılınçarslan, Y.E. Delikanlı, M. Çabuk, Investigating the use of raw perlite to produce monolithic thermal insulation material, Constr. Build. Mater. 263 (2020) 120674, https://doi.org/10.1016/J.CONBUILDMAT.2020.120674.
[14] E. Kapeluszna, Ł. Kotwica, W. Nocuń-Wczelik, Comparison of the effect of ground waste expanded perlite and silica fume on the hydration of cements with various tricalcium aluminate content – comprehensive analysis, Constr. Build. Mater. 303 (2021) 124434, https://doi.org/10.1016/j.conbuildmat.2021.124434.
[15] United States Geological Survey (USGS), Mineral commodity summaries 2023, 2023. doi:10.3133/mcs2023.
[16] M. Zukowski, G. Haese, Experimental and numerical investigation of a hollow brick filled with perlite insulation, Energy Build. (2010), https://doi.org/10.1016/j.enbuild.2010.03.009.
[17] M. Vyšvařil, M. Pavlíková, M. Záleská, A. Pivák, T. Žižlavský, P. Rovnaníková, P. Bayer, Z. Pavlík, Non-hydrophobized perlite renders for repair and thermal insulation purposes: influence of different binders on their properties and durability, Constr. Build. Mater. 263 (2020) 120617, https://doi.org/10.1016/j.conbuildmat.2020.120617.
[18] Y. Fang, X. Yin, P. Cui, X. Wang, K. Zhuang, Z. Ding, F. Xing, Properties of magnesium potassium phosphate cement-expanded perlite composites applied as fire resistance coating, Constr. Build. Mater. 293 (2021) 123513, https://doi.org/10.1016/j.conbuildmat.2021.123513.
[19] S.M. Motahari Karein, P. Vosoughi, S. Isapour, M. Karakouzian, Pretreatment of natural perlite powder by further milling to use as a supplementary cementitious material, Constr. Build. Mater. (2018), https://doi.org/10.1016/j.conbuildmat.2018.08.012.
[20] H. Li, L. Wang, Y. Zhang, J. Yang, D.C.W. Tsang, V. Mechtcherine, Biochar for sustainable construction industry. in: Curr. Dev. Biotechnol. Bioeng., Elsevier, 2023, pp. 63–95, https://doi.org/10.1016/B978-0-323-91873-2.00015-7.
[21] Ł. Kotwica, W. Pichór, E. Kapeluszna, A. Różycka, Utilization of waste expanded perlite as new effective supplementary cementitious material, J. Clean. Prod. 140 (2017) 1344–1352, https://doi.org/10.1016/j.jclepro.2016.10.018.
[22] S.M.M. Karein, A. Joshaghani, A.A. Ramezanianpour, S. Isapour, M. Karakouzian, Effects of the mechanical milling method on transport properties of self-compacting concrete containing perlite powder as a supplementary cementitious material, Constr. Build. Mater. 172 (2018) 677–684, https://doi.org/10.1016/j.conbuildmat.2018.03.205.

[23] S. Alexander, S. Juhi Manohar, S. Shino John, K. Varun Teja, T. Meena, Mechanical and micro-structural properties of perlite powder incorporated SCC, Mater. Today Proc. 45 (2021) 3374–3382, https://doi.org/10.1016/j.matpr.2020.12.776.
[24] D. Fodil, M. Mohamed, Compressive strength and corrosion evaluation of concretes containing pozzolana and perlite immersed in aggressive environments, Constr. Build. Mater. 179 (2018) 25–34, https://doi.org/10.1016/j.conbuildmat.2018.05.190.
[25] X. Wang, D. Wu, Q. Geng, D. Hou, M. Wang, L. Li, P. Wang, D. Chen, Z. Sun, Characterization of sustainable ultra-high performance concrete (UHPC) including expanded perlite, Constr. Build. Mater. 303 (2021) 124245, https://doi.org/10.1016/J.CONBUILDMAT.2021.124245.
[26] M. Bakhshi, A. Dalalbashi, H. Soheili, Energy dissipation capacity of an optimized structural lightweight perlite concrete, Constr. Build. Mater. 389 (2023) 131765, https://doi.org/10.1016/j.conbuildmat.2023.131765.
[27] R. Demirboğa, I. Örüng, R. Gül, Effects of expanded perlite aggregate and mineral admixtures on the compressive strength of low-density concretes, Cem. Concr. Res. (2001), https://doi.org/10.1016/S0008-8846(01)00615-9.
[28] M. Abed, J. de Brito, Evaluation of high-performance self-compacting concrete using alternative materials and exposed to elevated temperatures by non-destructive testing, J. Build. Eng. 32 (2020) 101720, https://doi.org/10.1016/j.jobe.2020.101720.
[29] ASRO (Romanian Standards Association), SR EN 197–1: Cement. Part I: Composition, specifications and conformity criteria for normal use cements, (2011).
[30] A. Favier, C. De Wolf, K. Scrivener, G. Habert, A Sustainable Future for the European Cement and Concrete Industry, Zurich, 2018. ⟨https://europeanclimate.org/wp-content/uploads/2018/10/AB_SP_Decarbonisation_report.pdf⟩.
[31] ASRO (Romanian Standards Association), SR EN 1097-2:2002 Tests for mechanical and physical properties of aggregates - Part 2: Methods for the determination of resistance to fragmentation, (2020). ⟨https://magazin.asro.ro/ro/standard/274070⟩.
[32] ASRO (Romanian Standards Association), SR EN 933-2:2020 Tests for geometrical properties of aggregates. Determination of particle size distribution. Test sieves, nominal size of apertures, (2020). ⟨https://magazin.asro.ro/ro/standard/274810⟩.
[33] S. Grzeszczyk, G. Janus, Lightweight reactive powder concrete containing expanded perlite, Materials 14 (2021) 3341, https://doi.org/10.3390/ma14123341.
[34] ASTM International, ASTM C618-22: Standard Specification for Coal Fly Ash and Raw or Calcined Natural Pozzolan for Use in Concrete, (2022). doi:10.1520/C0618-22.
[35] ASTM International, ASTM C 618: Standard Specification for Coal Fly Ash and Raw or Calcined Natural Pozzolan for Use in Concrete, (2022). ⟨https://www.astm.org/c0618-22.html⟩.
[36] D. Adi Darmawan, A. Wahyudi, H. Eric Mamby, I. Suherman, Characterization of perlite and expanded perlite from West Sumatera, Indonesia, IOP Conf. Ser. Earth Environ. Sci. 882 (2021) 012010, https://doi.org/10.1088/1755-1315/882/1/012010.
[37] M. Lanzón, F.J. Castellón, M. Ayala, Effect of the expanded perlite dose on the fire performance of gypsum plasters, Constr. Build. Mater. 346 (2022) 128494, https://doi.org/10.1016/j.conbuildmat.2022.128494.
[38] H. AzariJafari, A. Kazemian, B. Ahmadi, J. Berenjian, M. Shekarchi, Studying effects of chemical admixtures on the workability retention of zeolitic Portland cement mortar, Constr. Build. Mater. 72 (2014) 262–269, https://doi.org/10.1016/j.conbuildmat.2014.09.020.
[39] ASRO (Romanian Standards Association), SR EN 196–1:2016, Methods of testing cement - Part 1: Determination of Strength, (2016).
[40] H. Dilbas, Effect of cement type and water-to-cement ratio on fresh properties of superabsorbent polymer-modified cement paste, Materials 16 (2023) 2614, https://doi.org/10.3390/ma16072614.
[41] I.-O. Toma, G. Stoian, M.-M. Rusu, I. Ardelean, N. Cimpoeşu, S.-M. Alexa-Stratulat, Analysis of pore structure in cement pastes with micronized natural zeolite, Materials 16 (2023) 4500, https://doi.org/10.3390/ma16134500.
[42] ASTM International, ASTM C215-19 - Standard Test Method for Fundamental Transverse, Longitudinal, and Torsional Resonant Frequencies of Concrete Specimens, (2019).
[43] D.P. Thanaraj, A.N., P. Arulraj, K. Al-Jabri, Investigation on structural and thermal performance of reinforced concrete beams exposed to standard fire, J. Build. Eng. 32 (2020) 101764, https://doi.org/10.1016/j.jobe.2020.101764.
[44] M. Sarıdemir, A. Yıldırım, Effect of elevated temperatures on properties of high strength mortars containing ground calcined diatomite with limestone sand, J. Build. Eng. 56 (2022) 104748, https://doi.org/10.1016/j.jobe.2022.104748.
[45] S. Alani, M.S. Hassan, A.A. Jaber, I.M. Ali, Effects of elevated temperatures on strength and microstructure of mortar containing nano-calcined montmorillonite clay, Constr. Build. Mater. 263 (2020) 120895, https://doi.org/10.1016/j.conbuildmat.2020.120895.
[46] I. Fletcher, S. Welch, J. Torero, R. Carvel, A. Usmani, Behaviour of concrete structures in fire, Therm. Sci. 11 (2007) 37–52, https://doi.org/10.2298/TSCI0702037F.
[47] J. Piasta, Heat deformations of cement paste phases and the microstructure of cement paste, Mater. Struct. 17 (1984) 415–420, https://doi.org/10.1007/BF02473981.
[48] I. Hager, Behaviour of cement concrete at high temperature, Bull. Pol. Acad. Sci. Tech. Sci. 61 (2013) 145–154, https://doi.org/10.2478/bpasts-2013-0013.
[49] P. Sikora, K. Cendrowski, E. Horszczaruk, E. Mijowska, The effects of Fe3O4 and Fe3O4/SiO2 nanoparticles on the mechanical properties of cement mortars exposed to elevated temperatures, Constr. Build. Mater. 182 (2018) 441–450, https://doi.org/10.1016/j.conbuildmat.2018.06.133.
[50] M. Castellote, C. Alonso, C. Andrade, X. Turrillas, J. Campo, Composition and microstructural changes of cement pastes upon heating, as studied by neutron diffraction, Cem. Concr. Res. 34 (2004) 1633–1644, https://doi.org/10.1016/S0008-8846(03)00229-1.
[51] M. Vijayalakshmi, A.S.S. Sekar, G. Ganesh prabhu, Strength and durability properties of concrete made with granite industry waste, Constr. Build. Mater. 46 (2013) 1–7, https://doi.org/10.1016/j.conbuildmat.2013.04.018.
[52] F. Šoukal, L. Bocian, R. Novotný, L. Dlabajová, N. Šuleková, J. Hajzler, O. Koutný, M. Drdlová, The effects of silica fume and superplasticizer type on the properties and microstructure of reactive powder concrete, Materials 16 (2023) 6670, https://doi.org/10.3390/ma16206670.
[53] H. Varela, G. Barluenga, I. Palomar, A. Sepulcre, Synergies on rheology and structural build-up of fresh cement pastes with nanoclays, nanosilica and viscosity modifying admixtures, Constr. Build. Mater. 308 (2021) 125097, https://doi.org/10.1016/j.conbuildmat.2021.125097.
[54] M. Lanzón, P.A. García-Ruiz, Lightweight cement mortars: advantages and inconveniences of expanded perlite and its influence on fresh and hardened state and durability, Constr. Build. Mater. 22 (2008) 1798–1806, https://doi.org/10.1016/J.CONBUILDMAT.2007.05.006.
[55] F. Guenanou, H. Khelafi, A. Aattache, Behavior of perlite-based mortars on physicochemical characteristics, mechanical and carbonation: case of perlite of Hammam Boughrara, J. Build. Eng. 24 (2019) 100734, https://doi.org/10.1016/j.jobe.2019.100734.
[56] D. Kramar, V. Bindiganavile, Impact response of lightweight mortars containing expanded perlite, Cem. Concr. Compos. 37 (2013) 205–214, https://doi.org/10.1016/j.cemconcomp.2012.10.004.
[57] A. Łagosz, D. Olszowski, W. Pichór, Ł. Kotwica, Quantitative determination of processed waste expanded perlite performance as a supplementary cementitious material in low emission blended cement composites, J. Build. Eng. 40 (2021) 102335, https://doi.org/10.1016/j.jobe.2021.102335.
[58] V. Akyuncu, F. Sanliturk, Investigation of physical and mechanical properties of mortars produced by polymer coated perlite aggregate, J. Build. Eng. 38 (2021) 102182, https://doi.org/10.1016/j.jobe.2021.102182.
[59] K. Şengül, S.T. Erdoğan, Influence of ground perlite on the hydration and strength development of calcium aluminate cement mortars, Constr. Build. Mater. 266 (2021) 120943, https://doi.org/10.1016/j.conbuildmat.2020.120943.
[60] G.H. Nalon, M.A. Alves, L.G. Pedroti, J.C. Lopes Ribeiro, W.E. Hilarino Fernandes, D. Silva de Oliveira, Compressive strength, dynamic, and static modulus of cement-lime laying mortars obtained from samples of various geometries, J. Build. Eng. 44 (2021) 102626, https://doi.org/10.1016/j.jobe.2021.102626.
[61] F. Bektas, L. Turanli, P.J.M. Monteiro, Use of perlite powder to suppress the alkali–silica reaction, Cem. Concr. Res. 35 (2005) 2014–2017, https://doi.org/10.1016/j.cemconres.2004.10.029.
[62] R. Chihaoui, H. Siad, Y. Senhadji, M. Mouli, A.M. Nefoussi, M. Lachemi, Efficiency of natural pozzolan and natural perlite in controlling the alkali-silica reaction of cementitious materials, Case Stud. Constr. Mater. 17 (2022) e01246, https://doi.org/10.1016/j.cscm.2022.e01246.
[63] H. Maraghechi, M. Maraghechi, F. Rajabipour, C.G. Pantano, Pozzolanic reactivity of recycled glass powder at elevated temperatures: reaction stoichiometry, reaction products and effect of alkali activation, Cem. Concr. Compos. 53 (2014) 105–114, https://doi.org/10.1016/j.cemconcomp.2014.06.015.
[64] M.R. Karim, F.I. Chowdhury, H. Zabed, M.R. Saidur, Effect of elevated temperatures on compressive strength and microstructure of cement paste containing palm oil clinker powder, Constr. Build. Mater. 183 (2018) 376–383, https://doi.org/10.1016/j.conbuildmat.2018.06.147.
[65] I. Garcia-Lodeiro, P.M. Carmona-Quiroga, R. Zarzuela, M.J. Mosquera, M. T. Blanco-Varela, Chemistry of the interaction between an alkoxysilane-based impregnation treatment and cementitious phases, Cem. Concr. Res. 142 (2021) 106351, https://doi.org/10.1016/j.cemconres.2020.106351.
[66] S. Çelikten, M. Sarıdemir, K. Akçaözoğlu, Effect of calcined perlite content on elevated temperature behaviour of alkali activated slag mortars, J. Build. Eng. 32 (2020) 101717, https://doi.org/10.1016/j.jobe.2020.101717.
[67] Z. Li, X. Zhou, B. Shen, Fiber-cement extrudates with perlite subjected to high temperatures, J. Mater. Civ. Eng. 16 (2004) 221–229, https://doi.org/10.1061/(ASCE)0899-1561(2004)16:3(221).
[68] I.E. Ariyaratne, A. Ariyanayagam, M. Mahendran, Bushfire-resistant lightweight masonry blocks with expanded perlite aggregate, Fire 5 (2022) 132, https://doi.org/10.3390/fire5050132.

Design–Build–Test in a First-Year Civil Engineering Laboratory: A Thin-Cardboard Truss Bridge Case Study

George Taranu, Ph.D.[1]

Abstract: This case study describes the implementation of a resource-light design–build–test laboratory project embedded in a first-year civil engineering course, where many students begin with limited competence in statics and mechanics. Student teams designed and fabricated a thin-cardboard truss bridge under geometric constraints and a strict self-weight limit. Bridges were tested to failure using incremental loading with force and displacement measurements. Required deliverables included a force–displacement plot, failure-mode documentation, and a short reflection linking observed behavior to introductory mechanics concepts. An optional, supervised body-weight proof demonstration complemented the instrumented test as a human-scale illustration of resistance and stiffness. To examine the usefulness of the implementation, evidence was collected through anonymous pre- and post-activity surveys (pre: $N = 107$; post: $N = 111$, representing response rates of approximately 71% and 74% of the ∼150 eligible students), a retrospective alumni survey (years 2–4; $N = 58$, representing approximately 21.4% of the ∼270 eligible students from prior cohorts), and team-level performance logs. Both surveys were administered to the same first-year cohort, but participation was voluntary and attendance-dependent at two separate laboratory sessions. Some students who were absent during the presurvey administration completed the postsurvey, while some presurvey respondents did not participate in the postsurvey. No students from other cohorts were included. Because responses were anonymous, the two samples were overlapping but nonidentical, and pre–post analyses are therefore reported as unpaired cohort-level comparisons. The case study reports observed patterns in conceptual understanding, self-efficacy calibration, teamwork, and perceived relevance and summarizes implementation lessons and conditions that can support replication in similar first-year settings. Findings are consistent with the activity supporting the interpretability of load paths, stiffness, and failure mechanisms for students, while providing a scalable, low-cost protocol for early structural education.
DOI: 10.1061/JCEECD.EIENG-2550. *This work is made available under the terms of the Creative Commons Attribution 4.0 International license, https://creativecommons.org/licenses/by/4.0/.*

Practical Applications: Many first-year civil engineering students struggle to connect equations and simplified models to what structures actually do. This article presents a low-cost classroom project designed to reduce that gap through a structured design–build–test activity. Student teams design and construct a small cardboard truss bridge under a strict weight limit and then test it incrementally to failure while recording load and deflection. They are also required to plot the load–deflection response and document the observed failure mode, including a brief explanation of why failure occurred. In this way, abstract concepts such as load path, stiffness, instability, and structural efficiency become visible, discussable, and easier to interpret. The case study combines survey evidence, alumni feedback, and team-level test records to identify practical conditions that support effective implementation. These include a standardized loading setup, a simple recording sheet, a rubric that rewards explanation and measurement quality rather than peak load alone, and clear safety procedures. The activity can be adapted in other civil engineering programs that seek a scalable, hands-on approach for strengthening early structural understanding, student engagement, and evidence-based reasoning without requiring expensive equipment.

Author keywords: Experiential learning; Project-based learning; Design–build–test; Structural mechanics; Force–displacement; Self-efficacy.

This work is made available under the terms of the Creative Commons Attribution 4.0 International license.

Introduction

Students in the context of this study encountered the design–build–test (DBT) activity before completing formal coursework in Statics and Strength of Materials. In early mechanics learning, students often approach problems procedurally, matching equations to familiar exercise types before developing a stable conceptual understanding of structural behavior (Felder and Brent 2005, 2024). In introductory structures contexts, this gap becomes visible when students can compute reactions but struggle to explain load paths, relate internal forces to deformation, or anticipate failure mechanisms influenced by detailing and imperfections. The activity was therefore designed to provide an early experiential anchor for concepts developed more formally later in Mechanics, Statics, and Strength of Materials.

Recent reviews indicate that experiential, project-based, and active learning approaches remain prominent in undergraduate engineering education, but their effectiveness depends strongly on scaffolding, assessment alignment, and context-specific implementation choices (Bindal 2022; Jamison et al. 2022; Sukacké et al. 2022;

[1]Lecturer, Dept. of Structural Mechanics, Faculty of Civil Engineering and Building Services, "Gheorghe Asachi" Technical Univ. of Iasi, Iasi 700050, Romania. ORCID: https://orcid.org/0000-0002-5662-8484. Email: george.taranu@academic.tuiasi.ro

Note. This manuscript was submitted on February 25, 2026; approved on July 31, 2026; published online on September 12, 2026. Discussion period open until February 12, 2027; separate discussions must be submitted for individual papers. This paper is part of the ***Journal of Civil Engineering Education***, ASCE, ISSN 2643-9107.

Tembrevilla et al. 2024). A practical way to address this early barrier is to provide a controlled experience in which behavior can be observed, discussed, and documented. Engineers routinely build judgment by iterating between observation and representation: observing response, proposing a model, testing it, and revising assumptions. This process supports intuition about stiffness, strength, stability, and redundancy (Salvadori 1980). For novices, small build–and–test structures can make internal force flow and failure mechanisms visible and therefore easier to connect to introductory mechanics representations (Ressler 2001).

Bridge and truss projects remain widely used in engineering education because they offer visible structural behavior, clear constraints, and accessible testing formats. Recent implementations and reviews show continuing interest in these formats, while also emphasizing that learning benefits depend strongly on scaffolding, assessment design, and the quality of evidence linking testing to explanation (Carroll and Mitchell 2022; Fredette and Kennedy 2022; Hughes and Merrill 2021; Jamison et al. 2022; Sundman et al. 2025; Tembrevilla et al. 2024). Earlier first–generation implementations established the format in first–year and mechanics teaching contexts (Gavin 2011; Mahendran 1995; Malmqvist et al. 2004; Mills and Treagust 2003; O'Kelly 2007; Palmquist 2006) with simple materials, clear constraints, and an intuitive performance goal. Published implementations span several formats. Some are early first–year bridge projects intended to introduce structural reasoning through design and construction (Barry et al. 2013; Carroll and Mitchell 2022; Phillips 2007; Wolfe and LaPlante 1999), while others embed bridge or truss work in statics and mechanics courses through design competitions, model construction, load testing, or authentic inspection activities (Lange et al. 2022; Naito 2005; Steif et al. 2005; Wolfe and LaPlante 1999). Across this literature, the dominant emphases vary: some studies foreground teamwork, project organization, and general engagement; others focus on design realism, material testing, competition performance, field authenticity, or member–force recording and optimization. Ressler (2001) explicitly argued that many model bridge contests overemphasize strength-to-weight and underemphasize authentic design, mathematical reasoning, and iteration, motivating more structured DBT formats with analysis and reflection. First–year bridge–building implementations have also reported modular structures and constraint–driven design, supporting the relevance of low–cost bridge DBT formats in introductory curricula (Naito 2005).

Against this background, the present case study does not claim novelty for using a truss bridge project per se, nor for combining design, testing, and reflection in general. Rather, the distinctive element is narrower and lies in the specific combination, in a first-year setting, of three implementation choices treated simultaneously as graded learning outputs. First, a strict self-weight limit (200 g) was enforced not as a soft target but through a graded penalty proportional to the excess mass, so that efficiency reasoning became a scored dimension of the activity rather than a rhetorical constraint. Second, every team was required to submit a standardized force–displacement plot as a graded deliverable, so that measured response and its interpretation became mandatory evidence for all teams rather than an optional by-product of testing. Third, each team was required to classify the observed failure mode within a fixed category set explicitly mapped back to the truss idealization used for analysis, so that failure explanation became a required reasoning task rather than an instructor-led observation or a competition outcome. In this way, mass efficiency, measured-response interpretation, and failure-mode explanation became mandatory, jointly graded learning outputs for every team, not optional discussion points, competition by-products, or instructor-led commentary. This combination is what the present case study positions as its original element relative to the closest prior implementations, including Abdel Sattar and Labib (2019), Ayan (2009), Fredette and Kennedy (2022), Godfrey et al. (2025), Kolil et al. (2023), Mahendran (1995), May et al. (2023), and O'Kelly (2007), which are important precedents but do not frame this specific combination of graded mass constraint, standardized response plotting, and failure-mode classification as a required deliverable for every team. A related practical gap also remains: even when bridge or truss projects are reported, implementation details that support replication, troubleshooting, and assessment alignment are often brief or unevenly documented.

This case study addresses that gap by documenting a resource-light DBT truss bridge activity implemented in a first-year course on fundamentals of structural design. Student teams designed and fabricated a thin-cardboard truss bridge under geometric constraints and a strict self-weight limit. Each team then tested the bridge to failure using incremental loading in a standardized laboratory setup. Force and displacement were recorded, and failure modes were documented. Required deliverables included a justified configuration, basic constructability decisions, and a short technical submission with plots and reflections connecting observations to equilibrium, internal forces, stiffness, and stability prior to more formal calculations.

The assessment rubric used for evaluating team deliverables is presented in Table 1. The rubric was designed to operationalize constructive alignment (Biggs and Tang 2011; Maffei et al. 2022) by linking each assessment dimension directly to the learning objectives stated previously: modeling rationale (25%), measurement quality and force–displacement interpretation (30%), failure-mode documentation (20%), and reflection comparing observed and predicted behavior (25%).

To examine the usefulness of the implementation and to provide evidence relevant for replication, data were collected through anonymous pre- and post-activity surveys, a retrospective alumni survey, and team-level performance logs. This case study focuses on the following implementation–oriented questions: (RQ1) What cohort–level changes are observed in students reported conceptual understanding of load paths and force transfer after the DBT activity? (RQ2) What changes are observed in students' self–efficacy regarding early–stage structural modeling and design tasks? (RQ3) How do students describe teamwork and engagement during the activity? (RQ4) How do students and alumni perceive the relevance of the activity to engineering practice and later coursework? These questions are taken up explicitly in the section "Results."

The contribution of this case study is a replicable DBT protocol that treats force–displacement interpretation and failure-mode documentation as required learning outputs and reports practical conditions, materials, and testing procedures intended to support adoption in similar first-year contexts.

Theoretical Background and Related Work

Learning Lenses Used to Design the Activity

This case study uses experiential learning as a practical design lens rather than a hypothesis–testing framework. Experiential learning describes a cycle from concrete experience to reflection, conceptualization, and experimentation (Jamison et al. 2022; Morris 2020; Sundman et al. 2025; Tembrevilla et al. 2024). In a DBT sequence, the artefact and its measured response provide the experience, while post-test explanation and redesign support reflection and abstraction. This framing helps specify which activity elements are essential for replication.

A complementary perspective is situated learning, which argues that learning develops through participation in socially

This work is made available under the terms of the Creative Commons Attribution 4.0 International license.

Table 1. Assessment rubric for the design–build–test truss bridge activity

Assessment dimension	Weight (%)	Exemplary (3–4 points)	Developing (2 points)	Beginning (0–1 point)
1. Modeling and design rationale	25	Truss configuration is justified with reference to load path, member roles (tension/compression), and geometry–stiffness trade-offs. Assumptions are stated and linked to introductory mechanics.	Configuration is described but justification is partial or generic. Some connection to mechanics concepts present.	Configuration is stated without rationale. No connection to mechanics or structural reasoning.
2. Measurement quality and F–D interpretation	30	Force–displacement data are complete and correctly plotted. Initial slope (stiffness), slope change, peak capacity, and postpeak behavior are identified and interpreted.	Data are mostly complete. F–D plot is present but interpretation is limited to peak load. Slope and damage onset not discussed.	Data are incomplete or incorrectly recorded. F–D plot absent or uninterpreted.
3. Failure-mode documentation	20	Failure mode is correctly identified (e.g., out-of-plane sway, compression buckling, joint failure) and linked to the truss idealization and internal force flow. Location of failure is noted.	Failure mode is named but not linked to mechanics. Location is noted without interpretation.	Failure mode is absent, vague, or incorrect. No connection to internal forces.
4. Reflection: observed versus predicted behavior	25	Discrepancies between predicted and observed response are identified and explained with reference to modeling assumptions, workmanship, or material behavior. Reflection is specific and evidence-based.	Some comparison between predicted and observed is attempted. Explanation is generic or unsupported.	Reflection is absent or restates the task description. No comparison between model and observation.

Note: Total points = 10 (exemplary = 3–4 pts per dimension; weighted as shown). Assessment was conducted by the course instructor on the written technical report submitted by each team after the testing session. Rubric criteria align directly with the learning objectives stated in the section "Course Context and Learning Objectives."

Table 2. Mapping of theoretical lenses to specific design decisions in the activity

Theoretical lens	Core claim relevant to this study	Specific design decision it motivated	Where evident in the protocol
Experiential learning (Jamison et al. 2022; Tembrevilla et al. 2024)	Learning proceeds through a cycle of concrete experience, reflective observation, abstract conceptualization, and active experimentation.	The design–build–test sequence instantiates Kolb's cycle: teams design (abstract), build (active), test (concrete), and reflect in the F–D plot and report (reflective).	Sections "Experiential Design–Build–Test Activity," "Procedure and Experimental Data Collection," "Data Analysis"; deliverables: F–D plot and written reflection.
Situated learning (Lave and Wenger 1991)	Knowledge is most durably acquired when embedded in authentic practice, not abstracted exercises.	Authentic materials (thin cardboard), genuine fabrication variability, real load–displacement response, and visible failure provide conditions for legitimate peripheral participation in structural reasoning.	Section "Experiential Design–Build–Test Activity": material constraints, joint fabrication, failure classification.
Constructive alignment (Biggs and Tang 2011)	Learning objectives, teaching and learning activities, and assessment tasks must be aligned for deep learning to occur.	The rubric criteria (Table 1) directly mirror the stated learning objectives: modeling clarity, measurement quality, F–D interpretation, and reflection grounded in observed behavior.	Section "Course Context and Learning Objectives" (objectives); Table 1 (rubric); Section "Instruments and Measures" (assessment).
Predict–observe–explain (White and Gunstone 1992)	Students develop conceptual understanding by first predicting, then observing, then reconciling discrepancies through explanation.	The predict–observe–explain sequence: teams predict bridge behavior from their truss analysis, observe the measured F–D response and failure, and then explain discrepancies in the reflection report.	Sections "Experiential Design–Build–Test Activity," "Procedure and Experimental Data Collection"; deliverable: written reflection (Section "Procedure and Experimental Data Collection").

Note: DBT = design–build–test; and F–D = force–displacement.

and materially meaningful practice rather than through decontextualized knowledge transmission alone (Lave and Wenger 1991). In this view, novices develop usable judgment more effectively when tasks include authentic features such as trade-offs, tolerances, constructability constraints, and informative failure, while remaining analytically accessible at their stage of preparation. Bridge and truss tasks are suitable for first-year contexts because they make load path, stiffness, redundancy, and constructability visible through mechanisms that students can observe, discuss, and relate to simplified structural models (Ghareeb 2026; Lange et al. 2022; Martin et al. 2021; Palmquist 2006; Ressler 2001).

The activity is also shaped by constructive alignment, where intended outcomes, learning activities, and assessment criteria are deliberately matched (Biggs and Tang 2011). This matters in DBT implementations because students optimize what is assessed. If evaluation rewards only peak load, teams may pursue "winning" strategies at the expense of modeling clarity, measurement quality, and explanation. Alignment therefore motivates rubrics that reward justification, data quality, and reflection grounded in observed behavior. Table 2 maps each theoretical lens to the specific design decisions it motivated in the activity protocol, making these connections explicit and traceable.

Evidence Base, Implementation Choices, and Boundary Conditions

Across STEM, active learning is often associated with improved learning outcomes compared with lecture-only instruction, although effects vary by context and implementation quality (Freeman et al. 2014; Prince 2004). For the present case study, however, the more relevant issue is not active learning in the abstract, but how these general findings translate into structured design–build–test tasks in

This work is made available under the terms of the Creative Commons Attribution 4.0 International license.

early engineering education. Recent reviews confirm that experiential, project–based, and challenge–based formats are widely used in undergraduate engineering, but also show that their educational value depends strongly on scaffolding, assessment alignment, and the quality of the link between activity and explanation (García-Ramírez 2025; Jamison et al. 2022; Sukackė et al. 2022; Tembrevilla et al. 2024).

Within this broader evidence base, bridge and truss activities provide an intermediate level of relevance because they make load path, member action, stiffness, and failure mechanisms directly observable to novice learners. Prior implementations suggest that their educational value depends not only on building and testing, but also on requiring students to connect observations to simplified models, measured response, and explicit explanation (Carroll and Mitchell 2022; Chang and Peterson 2009; Fredette and Kennedy 2022; Gavin 2011; Hughes and Merrill 2021; O'Kelly 2007; Ressler 2001). These studies collectively support recurring implementation choices that are also relevant in the present case: explicit constraints that create trade-offs, standardized loading that yields interpretable response data, and required documentation of force–displacement behavior and failure mechanisms. In this sense, the present activity is positioned not simply within the general active-learning literature, but more specifically within an emerging body of DBT bridge/truss implementations in early engineering education.

Case-study reporting in civil engineering design education has shown that outcomes depend strongly on implementation structure and scaffolding, supporting the need to document protocol details for replication (Gavin 2011). DBT bridge/truss projects are common in early engineering education because they make structural behavior observable and discussable. Their educational value depends on guiding students to connect observations to an interpretable model and to evidence–based explanation (Ressler 2001). Prior implementations suggest recurring choices that support replicability and learning-oriented outcomes: explicit constraints that create trade-offs, standardized loading that produces interpretable response data, and required documentation of failure mechanisms. These features can turn variability and unexpected outcomes into learning opportunities when reflection is structured and assessment rewards explanation, not only peak capacity.

Several boundary conditions are relevant when interpreting implementation evidence in first-year settings. Conceptual gains can depend strongly on the quality of reflection and feedback. Self-efficacy may not increase and can decrease when initially optimistic self-assessments are recalibrated after students confront authentic task difficulty, imperfections, and failure behavior; in this sense, a lower postactivity rating may reflect more accurate self-appraisal rather than diminished learning (Felder and Brent 2024; Kruger and Dunning 1999; Pajares 1996). Transfer to new problems is also not automatic and may require explicit prompts linking observed behavior to general principles and later analytical methods. The teamwork dimension of DBT projects also deserves attention. Employers consistently identify teamwork, communication, and collaborative problem-solving among the most valued entry-level competencies (Hirudayaraj et al. 2021), providing a practice-oriented rationale for including RQ3 alongside the conceptual and self-efficacy questions. These considerations motivate cautious language and support triangulation rather than reliance on a single indicator.

Positioning and Contribution of This Case Study

This case study documents a resource-light DBT truss bridge implementation designed for the first-year transition from "calculating" to "explaining and justifying." The protocol draws on a predict–observe–explain (POE) sequence, in which students first predict structural response, then observe measured behavior during testing, and finally explain discrepancies between the idealized model and the experimental outcome (White and Gunstone 1992). It also applies constructive alignment through rubric-based criteria that value modeling justification, measurement quality, force–displacement interpretation, and failure-mode documentation. To support replication, the paper reports constraints, testing procedures, deliverables, and practical lessons learned. To document usefulness, it reports cohort-level pre/post patterns, team performance summaries, and retrospective alumni perceptions, without making causal claims beyond the limits of the design. Consistent with JCEE case study expectations, the present paper emphasizes an evidence-informed instructional practice and provides sufficient implementation detail to support replication (Brown 2021).

Study Context and Intervention

Course Context and Learning Objectives

The case study was conducted in a first-year civil engineering course focused on basic structural reasoning for design. The course introduces equilibrium, internal actions, and simple structural elements, and it targets early judgment skills such as selecting a structural configuration and explaining load transfer. The laboratory framework and project brief are documented in the course practical guide (Taranu 2023), which is publicly accessible online in Romanian.

The DBT activity was aligned with introductory learning objectives assessed through project work and surveys. Students were expected to (1) interpret equilibrium conditions and relate them to support reactions; (2) explain load paths and distinguish axial tension, axial compression, shear, and bending effects; (3) analyze a simple truss bridge using introductory internal-force methods; (4) connect geometric choices (span, depth, layout) to stiffness and capacity; (5) interpret a force–displacement response and relate slope changes to stiffness degradation and failure onset; and (6) justify modeling assumptions and explain observed failure modes using structural reasoning. These objectives follow common introductory bridge DBT formats that combine design reasoning with reduced-scale experimental verification (Ressler 2001). To make efficiency nontrivial while remaining feasible for first-year teams, the bridge mass was limited to 200 g. This threshold was selected empirically from prior implementation experience as an upper reference value, not as a design target in itself. It was chosen so that a well-designed bridge could still reach a load capacity above 100 kg, making the later optional supervised body-weight proof demonstration feasible. At the same time, the instructional goal was not to maximize bridge mass up to this limit, but to promote an efficient relationship between material consumption and load-bearing capacity. The 200 g value therefore functioned as a maximum reference constraint intended to preserve structural efficiency rather than to reward heavier solutions.

Experiential Design–Build–Test Activity

The activity followed a structured design–build–test sequence. Teams reviewed constraints and performance criteria, generated alternative truss configurations, and selected one solution based on explicit reasoning. The design stage required definition of the structural scheme and supports, idealization of the applied load, basic internal-force calculations, and introductory member sizing aligned with first-year mechanics.

The workflow and modeling idealization used for student analysis are summarized in Fig. 1. In the experiment, load was introduced through a rigid load-transfer plate connected to a hook-and-chain loading arrangement. For teaching purposes, the plate was assumed sufficiently rigid to distribute the central force

This work is made available under the terms of the Creative Commons Attribution 4.0 International license.

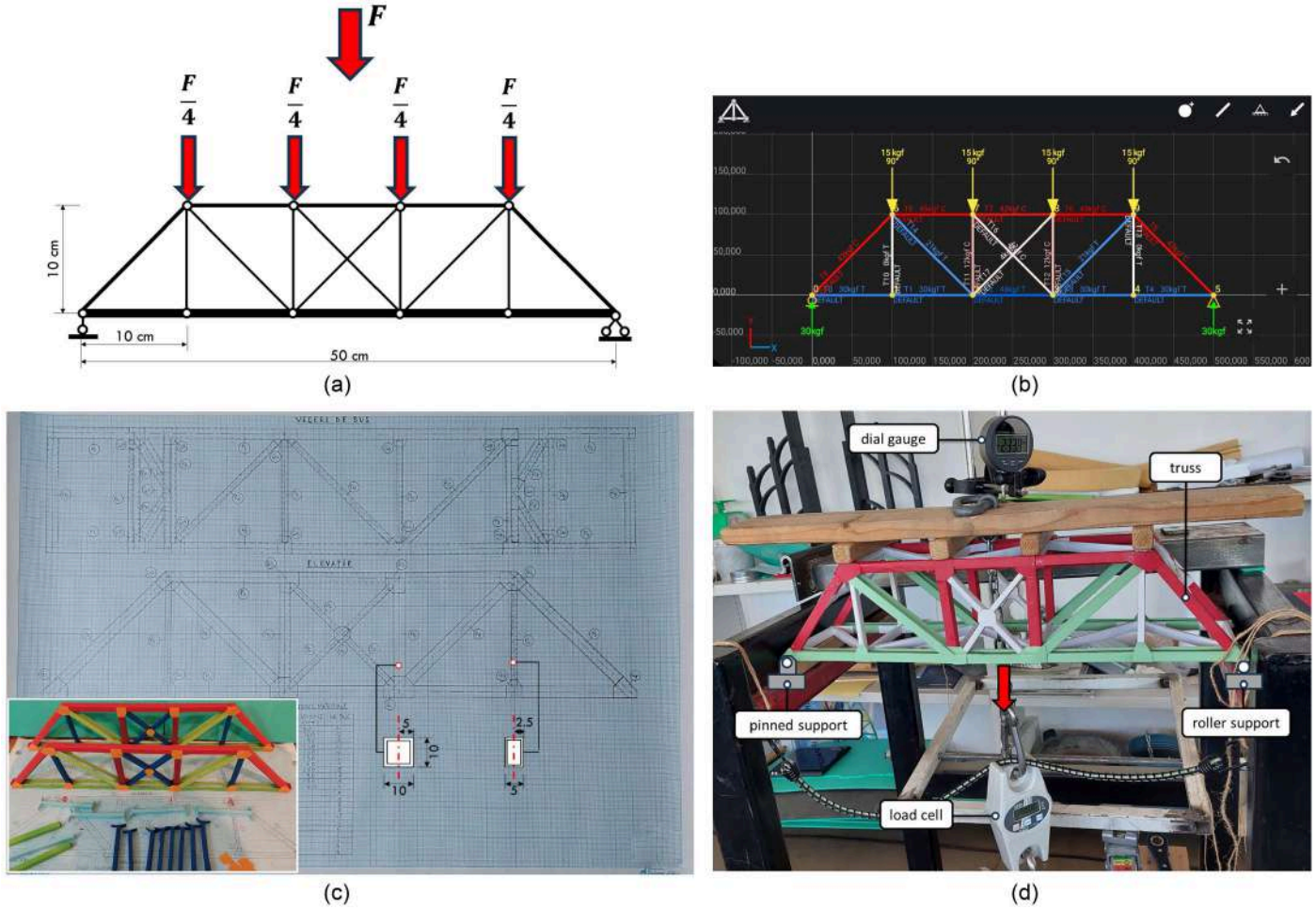

Fig. 1. Design–build–test workflow and modeling idealization used in the bridge activity: (a) idealized loading model; (b) example of truss internal-force analysis output; (c) typical student design documentation (sketches/drawings) and a physical prototype during fabrication; and (d) experimental test setup with pinned and roller supports.

uniformly to the four top-chord panel points in contact; therefore, students represented the applied load as four equal nodal forces. For replication, the span between supports (pinned and roller) was 50 cm and the truss height was 10 cm [Fig. 1(a)]. The same contact layout on the top chord was used for all teams. Load was then increased in 2.5 kg increments while the bridge response and damage progression were observed at each stabilized step. Fig. 1 also illustrates a typical truss analysis output, examples of student documentation and prototypes, and the laboratory test rig.

During fabrication, teams used low-cost materials (thin cardboard members) and glued joints. Workmanship variability and local imperfections were treated as learning features, supporting discussion of constructability, detailing, and limits of idealized modeling. Testing used incremental static loading in 2.5 kg steps. Force and deflection were recorded at each step, and failure progression was documented. The test was stopped when the bridge could not sustain an additional 2.5 kg increment or when instability or local failure prevented continued loading. A strict self-weight limit (below 200 g) promoted structural efficiency and discouraged brute-strength solutions. The 200 g limit was enforced as a grading criterion rather than as an exclusion rule: teams exceeding it received a scoring penalty proportional to the excess mass, but their bridges were still tested to preserve the learning value of the full POE sequence. In practice, bridge masses ranged from 78 to 270 g; a small number of teams exceeded the limit, typically because of imprecise trimming or overreinforcement of joints. These cases were retained in the performance dataset to reflect the full variability of implementation outcomes. Where relevant, results should therefore be interpreted with the awareness that the highest-mass bridges did not satisfy the intended 200 g mass-budget rule, even though they were tested under the same loading and measurement protocol.

The deliverables produced after testing, including the force-displacement plot and the written reflection, are described in Section 4.4. Examples of bridges produced by different teams under the same constraints are shown in Fig. 2, illustrating variation in configuration and detailing within a common brief. After the standard instrumented test, an optional body-weight proof challenge was offered. When a bridge satisfied a preliminary proof load, one student could stand on the bridge under supervision using the safety frame/hand support (Fig. 3). This provided a human-scale validation of resistance and stiffness that complemented the quantitative interpretation of the force–displacement curve. The challenge was not graded as a stand-alone outcome; it was used as a motivational prompt and a trigger for reflection. A one–page data sheet standardized recording of load steps, displacement, and observed failure progression across teams.

Teams worked in groups of three to four students with rotating roles covering analysis, fabrication, measurement, and documentation. A short safety briefing addressed tool use, stable

This work is made available under the terms of the Creative Commons Attribution 4.0 International license.



Fig. 2. Examples of student-built thin-cardboard truss bridges meeting the project constraints.



Fig. 3. Optional body-weight proof challenge performed after the standard instrumented loading protocol.

This work is made available under the terms of the Creative Commons Attribution 4.0 International license.

setup, controlled placement of loads, and clear communication during loading.

Methods

Research Design

A mixed-methods design combined three complementary evidence streams. As a case study, analyses are reported as descriptive cohort-level patterns intended to inform replication rather than to establish causal effects. The primary stream comprised anonymous pre- and post-activity surveys administered to the same first-year cohort. Because responses were not linkable across time, pre- and post-results were analyzed as independent samples. A second stream was a retrospective alumni survey (years 2–4) probing perceived transfer and longer-term relevance. A third stream comprised team-level performance evidence from experimental testing and rubric-based evaluation of deliverables. The overall design and data sources are summarized in Fig. 4, and Table 3 summarizes datasets, timing, and purpose.

This design was selected because the intervention was embedded in a compulsory laboratory sequence and a parallel control group was not feasible without altering course structure. The study therefore prioritizes convergent evidence across perception, performance, and reflection rather than single-metric claims.

Participants, Datasets, and Ethics

Three anonymous survey datasets were collected (Table 3). The presurvey was administered before the DBT activity and collected $N = 107$ responses; the postsurvey was administered after

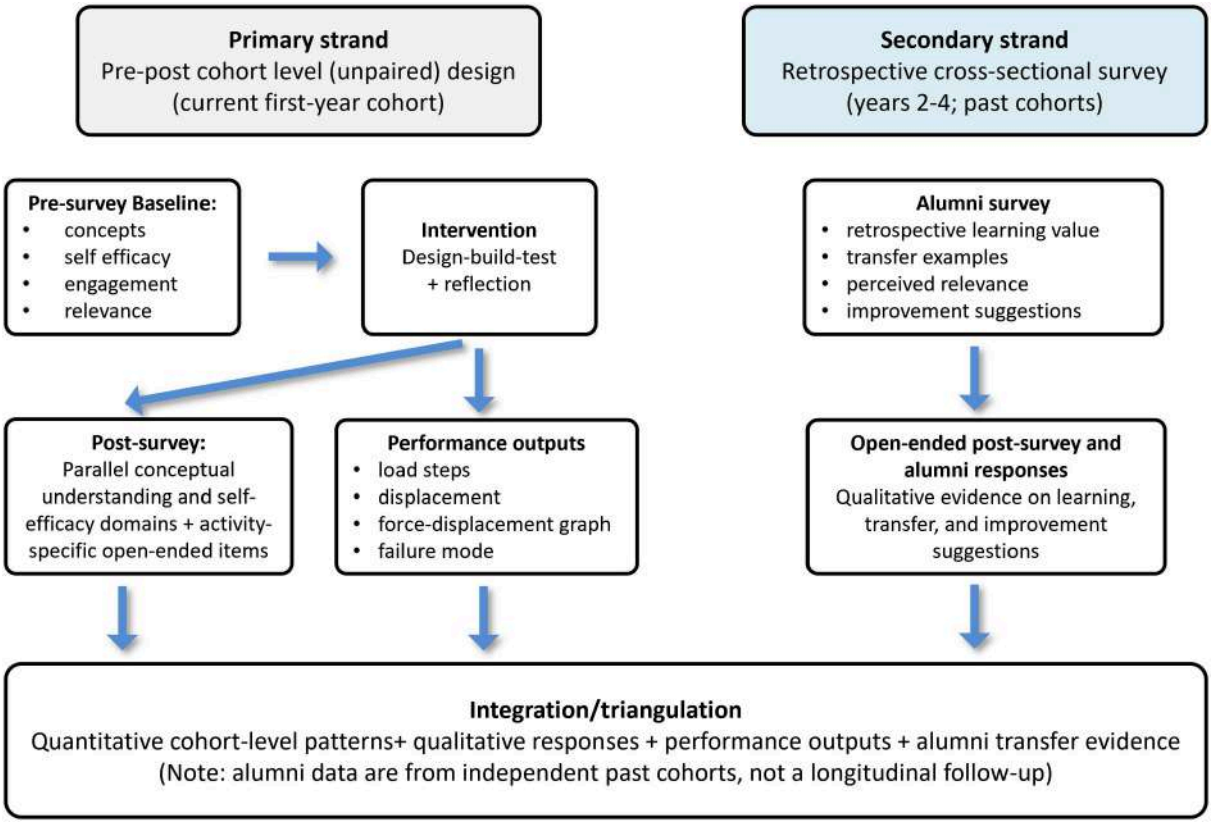

Fig. 4. Research design overview and evidence streams used in the study.

Table 3. Datasets and evidence streams used in the study

Dataset	Target group	*N*	Timing	Linkable across time	Main purpose
Preactivity survey	Year 1 cohort	107	Before DBT activity	No	Baseline concepts, self-efficacy, motivation, prior exposure
Postactivity survey	Year 1 cohort	111	After testing + reporting	No	Perceived learning, parallel domains, implementation feedback
Alumni survey	Years 2–4	58	Retrospective	No	Perceived transfer and longer-term value
Team performance logs	Student teams	30 teams with complete records	During testing	Team-level only	Force–displacement, peak load, failure modes, efficiency indicators
Rubric-based deliverables	Student teams	Full course cohort (team-level deliverables)	After activity	Team-level only	Evidence of justification, data quality, reflection and reporting quality

testing and reporting and collected $N = 111$ responses from the same first-year cohort. Out of an eligible first-year population of approximately 150 students, this corresponds to a response rate of about 71% (pre) and 74% (post), reflecting participation only from those who actually attended the laboratory sessions in which the anonymous questionnaires were administered. Both surveys were voluntary and administered at different points in the semester. The difference in sample size reflects voluntary participation: some students who were absent during the presurvey session participated in the postsurvey, and vice versa. No students from other cohorts were included in either the pre- or post-survey dataset; the additional postsurvey respondents came from the same first-year cohort.

Because surveys were anonymous, individual matching was not possible. To assess sample overlap descriptively, the postsurvey included the control item, "Did you also complete the preactivity questionnaire administered earlier in the semester?" with response options yes/no/not sure. Responses were 62.2% yes ($n = 69$), 9.9% no ($n = 11$), and 27.9% ($n = 31$) not sure (Table 4). This item was used only as a descriptive check on overlap. Because no individual identifiers or anonymous linking codes were collected, it did not permit response matching and was not used for inferential subgroup analysis. Its purpose was to confirm that the pre- and post-survey samples were overlapping but nonidentical, which supports the decision to analyze pre–post comparisons as unpaired cohort-level differences rather than paired individual trajectories. Key participation indicators and prior exposure are summarized in Table 4.

The alumni survey yielded $N = 58$ responses out of approximately 270 eligible alumni from cohorts in years 2–4, corresponding to a response rate of about 21.4%. This lower response rate is consistent with the fact that participation was entirely voluntary, the questionnaire was distributed by email for completion

J. Civ. Eng. Educ., 2027, 153(1): 05026020

This work is made available under the terms of the Creative Commons Attribution 4.0 International license.

Table 4. Key participation indicators and prior exposure

Indicator	Response options	Count	Percent (%)
Presurvey: prior participation in similar DBT activities ($N = 107$)	Yes	21	19.6
	No	86	80.4
Postsurvey: completed the presurvey ($N = 111$)	Yes	69	62.2
	No	11	9.9
	Not sure	31	27.9

in respondents' own time, and no direct in-class contact with the instructor was possible at that stage.

Surveys were voluntary and did not collect direct identifiers (names, student IDs, or contact details). Survey participation was not required for grading, and responses were analyzed in aggregate. Photographs used for illustration were handled independently from survey datasets and were not linked to individual responses. Ethical approval was obtained under institutional procedures.

Instruments and Measures

Three questionnaires and two performance-based sources were used. The instruments were purpose-built for this study and were not adapted from validated standardized questionnaires. Multi-item constructs were therefore treated as context-specific scales, and internal consistency is reported in the Results section for the relevant constructs.

Items were developed by the course instructor on the basis of three explicit sources: (1) the intended learning outcomes of the DBT activity; (2) the four research questions; and (3) the concrete stages of the project—design, construction, incremental testing to failure, force–displacement plotting, failure-mode observation, and reflection on the differences between the idealized model and the observed behavior. Each construct was operationalized through items referring directly to these stages, providing a transparent rationale for item selection and supporting content relevance for the activity studied. The construct composition and the full wording of all items are documented in Table S1.

The instruments were not subjected to formal pilot testing, structured expert-panel review, or a dedicated psychometric construct-validation procedure prior to administration. Accordingly, the multi-item scores are interpreted as exploratory, context-specific indicators rather than validated standardized scales, and Cronbach's alpha values are reported as internal-consistency diagnostics within the present samples rather than as evidence of established construct validity. In addition, the pre- and post-activity item sets address parallel domains but are not textually identical—several postactivity items use comparative wording (e.g., "I understand better")—so pre–post comparisons are interpreted as exploratory cohort-level patterns. These constraints are acknowledged in the section "Limitations and Future Work."

The pre-, post-, and alumni surveys included five-point Likert items and open-ended prompts on learning outcomes, useful activity components, difficulties, and suggested improvements. The presurvey measured conceptual preparedness, selfefficacy for introductory design and interpretation tasks, teamwork disposition, and motivation/perceived relevance.

The postsurvey included parallel conceptual-understanding and self-efficacy domains and added implementation-focused items targeting the DBT mechanisms (constraints, detailing, incremental loading, failure observation, and force–displacement plotting).

The alumni survey focused on remembered conceptual value, transfer/relevance, and perceived skills development. The number of items included in each construct is reported in Tables 5–7, and the full wording of all survey items is provided in Table S1. Performance evidence included (1) team-level force–displacement records obtained during testing; and (2) rubric-based evaluation of deliverables aligned with the intended outcomes.

Procedure and Experimental Data Collection

During testing, one team member recorded each load step and the corresponding displacement on a standardized data sheet while another monitored the dial gauge and called out readings. Force was recorded from the applied suspended mass at each stabilized increment, displacement was read before the next increment was added, and completeness checks were carried out immediately after each test to verify that all load steps, the peak load, and the final observed failure mode had been entered.

After testing, each team submitted a short technical report including final geometry and assumptions, measured mass, a load–displacement table, a force–displacement plot used to identify

Table 5. Pre- and post-activity parallel-domain ratings for the first-year cohort (1–5 scale)

Construct	Instrument	N	Mean	SD	Cronbach's α	Welch t (df)	p	Hedges' g
Conceptual understanding (equilibrium, force flow, truss action, geometry, load path, stiffness, F–D meaning)	Pre	107	3.744	0.648	0.850	—	—	—
	Post	111	4.028	0.568	0.835	−3.445 (210.1)	0.00069	0.47
Self-efficacy (basic sizing, contribution to design, technical discussion, experimental interpretation)	Pre	107	4.026	0.670	0.791	—	—	—
	Post	111	3.858	0.720	0.875	1.779 (215.7)	0.0766	−0.24
Teamwork and coordination	Pre	107	4.210	0.882	0.794	—	—	—
	Post	111	4.288	0.716	0.769	—	—	—
Motivation and perceived value	Pre	107	4.601	0.531	0.691	—	—	—
	Post	111	4.602	0.508	0.861	—	—	—

Note: Positive Hedges' g values indicate higher post-activity ratings. Conceptual understanding and self-efficacy are reported as exploratory unpaired cohort-level comparisons. Teamwork and coordination and motivation and perceived value are presented as descriptive parallel-domain profiles only because the corresponding pre- and post-activity item sets differ more substantially in wording and composition. These descriptive profiles should not be interpreted as equivalent repeated-scale comparisons or as evidence of individual change.

This work is made available under the terms of the Creative Commons Attribution 4.0 International license.

Table 6. Postsurvey implementation-focused constructs (first-year cohort, $N = 111$)

Construct (post only)	Items covered	Mean	SD	Cronbach's α
Activity learning mechanisms	Mass limit; use of cardboard-property information; clarity of stages; building details; incremental loading; observing failure; F–D plotting; explanation of behavior	4.111	0.573	0.816
Teamwork and coordination	Teamwork; communication; planning	4.288	0.716	0.769
Motivation and perceived value	Motivation for course; preference versus "paper-only" labs; overall interest; perceived contribution; recommendation; desire for similar activities	4.602	0.508	0.861

Table 7. Alumni survey constructs (years 2–4, $N = 58$; 1–5 scale)

Alumni construct	Items covered	Mean	SD	Cronbach's α
Recall	General memory of the activity	4.276	0.790	—
Conceptual value	Equilibrium; internal forces; geometry; stiffness; seeing behavior and failure	4.248	0.806	0.896
Transfer	Use in later courses; concrete reuse examples	3.612	1.162	0.815
Intuition and relevance	Structural intuition; attention to real structures; perceived formative value	4.069	1.014	0.896
Skills	Teamwork; technical communication; planning; confidence for simple structures	4.013	0.892	0.821
Preference	Better than paper-only labs; recommend continuation; desire for similar activities	4.586	0.726	0.838

This work is made available under the terms of the Creative Commons Attribution 4.0 International license.

stiffness (initial slope), damage onset, peak capacity, postpeak behavior, and a short reflection comparing expected and observed response (Taranu 2023).

Data Analysis

Quantitative results are reported as descriptive statistics and cohort-level comparisons intended to summarize observed patterns. Construct scores were computed from Likert items and summarized using means and standard deviations. For the two parallel domains used for exploratory cohort-level comparison—conceptual understanding and self-efficacy—pre- and post-activity scores were compared using Welch's t-tests for unpaired samples, and effect sizes were reported using Hedges' g. Teamwork-related ratings and motivation/perceived-value ratings were summarized descriptively because their pre- and post-activity item sets addressed related domains but were not compositionally equivalent. These descriptive profiles are visualized in Fig. 5 but are not interpreted as inferential pre–post shifts. Where distributional assumptions were questionable, nonparametric sensitivity checks were used. Item-level analyses were treated as exploratory and were corrected for multiple comparisons within each construct family using the Holm adjustment. Given the unpaired design and the absence of a control group, the inferential comparisons are interpreted as exploratory cohort-level patterns rather than as evidence of individual change or causal effects.

Performance data were analyzed at the team level. For teams with complete records, bridge mass, peak supported load, and a load-to-weight efficiency indicator were summarized. The

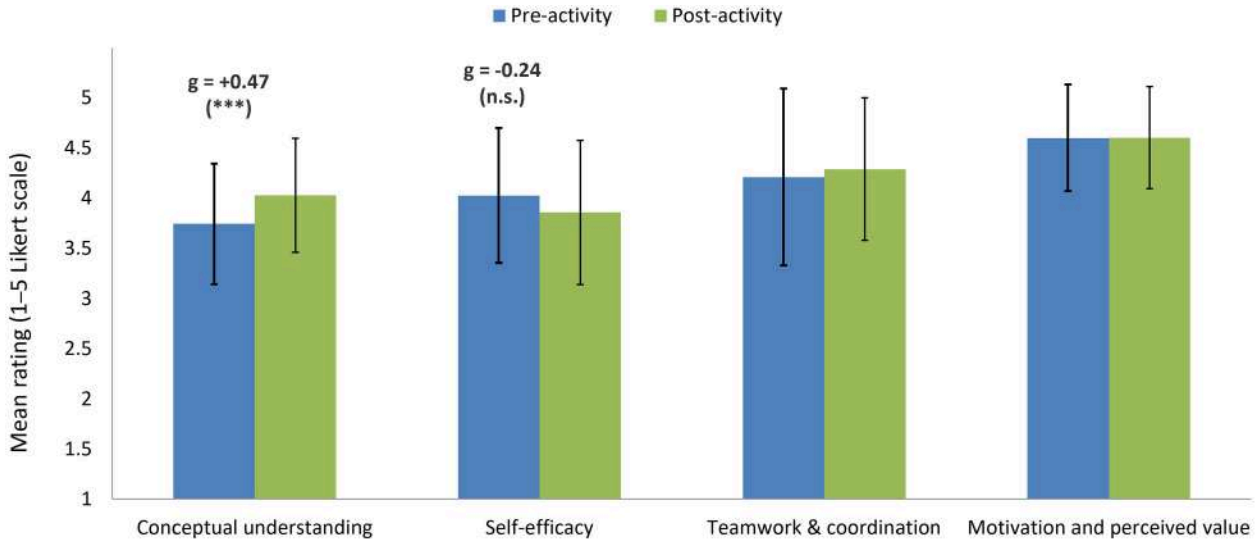

Note: Error bars indicate ±1 SD. Hedges' g effect sizes and significance levels are reported only for conceptual understanding and self-efficacy. Teamwork and coordination and motivation and perceived value are shown as descriptive parallel-domain profiles only because the pre- and post-activity item sets differ in wording and composition and should not be interpreted as equivalent repeated scales.

Fig. 5. Pre- and post-activity parallel-domain ratings for the first-year cohort, shown with ±1 SD error bars. Hedges' g effect sizes and significance levels are reported only for conceptual understanding and self-efficacy; teamwork, coordination, motivation, and perceived value are shown descriptively.

efficiency indicator was defined as peak load normalized by self–weight (grams)

$$E = \frac{P_{\max} \cdot 1{,}000}{m} \quad (1)$$

reported as a dimensionless load–to–weight ratio. Load-displacement curves were used as objective anchors for discussion of stiffness, damage onset, and failure progression.

Open-ended responses were analyzed manually using a hybrid thematic content-analysis procedure conducted by the author. The postsurvey prompts and the alumni open-ended prompts were analyzed separately because they addressed distinct aspects of the activity, and the unit of analysis was the individual respondent's answer to each prompt. In the first pass, all available responses were read in full, prompt by prompt, and recurrent meanings were assigned preliminary codes generated inductively from the data, without a rigid predefined coding list. In the second pass, semantically related preliminary codes were consolidated into a smaller set of stable categories and organized deductively in relation to RQ1–RQ4 to support triangulation with the quantitative findings; after the categories had been refined, all responses were reviewed again using the final coding framework.

A single response could receive more than one code when it contained multiple substantive ideas, but each theme was counted at most once per respondent within the same prompt. Because the complete fixed datasets were analyzed, no saturation-based stopping rule was applicable; coding ended when the final review pass produced no further changes to the category set. Entries without substantive content (e.g., "-", ".", or "no comment") were retained in the source datasets but were not assigned a substantive thematic code. Coding was conducted by a single coder; intercoder reliability statistics are therefore not available, and this constraint is acknowledged in the section "Limitations and Future Work." For the postsurvey findings reported in the section "Qualitative Evidence from Open-Ended Responses," percentages were calculated as the number of respondents expressing each theme divided by the full post-survey sample ($N = 111$) and rounded to the nearest whole number; for alumni prompts the denominator was $N = 58$. Because multiple themes could be assigned to one response, percentages within a prompt are not mutually exclusive and do not sum to 100%. Selected quotations were translated from Romanian and used to illustrate dominant patterns and informative outliers without including identifiable details.

Results

For clarity, the Results section is organized to mirror the four implementation-oriented research questions introduced in the section "Introduction": RQ1 is addressed through pre-/post-conceptual ratings, implementation-focused learning mechanisms, qualitative responses, and team performance evidence; RQ2 through pre-/post-self-efficacy ratings and qualitative comments on interpretation and confidence; RQ3 through teamwork/coordination ratings and related qualitative responses; and RQ4 through postsurvey relevance comments and the alumni dataset.

Sample and Scale Properties

This section reports the main quantitative pre-/post-patterns relevant to RQ1 (conceptual understanding) and RQ2 (self–efficacy). The preactivity survey included $N = 107$ first–year students and the postactivity survey included $N = 111$ students from the same cohort. Responses were anonymous and not linkable across time; therefore, pre–post comparisons are reported as cohort-level differences. Table 5 summarizes construct descriptives and internal consistency (1–5 scale). Conceptual understanding ratings were higher in the postactivity sample ($M = 4.028$, SD = 0.568) than in the preactivity sample ($M = 3.744$, SD = 0.648); the Welch comparison was statistically significant, $t(210.1) = -3.445$, $p = 0.00069$, Hedges' $g = 0.47$, indicating a small-to-moderate cohort-level shift. Self-efficacy ratings were slightly lower in the postactivity sample than in the preactivity sample (pre: $M = 4.026$, SD = 0.670; post: $M = 3.858$, SD = 0.720), but the Welch comparison was not statistically significant, $t(215.73) = 1.779$, $p = 0.0766$, Hedges' $g = -0.24$ (Table 5). These cohort-level pre-/post-patterns are also visualized in Fig. 5, which shows construct means, variability, and effect sizes. The two patterns are interpreted subsequently in relation to RQ1 (conceptual understanding) and RQ2 (self-efficacy). Fig. 5 also presents descriptive pre- and post-activity profiles for teamwork and coordination and for motivation and perceived value. Teamwork-related ratings were positive at both measurement points (pre: $M = 4.210$, SD = 0.882; post: $M = 4.288$, SD = 0.716). Motivation and perceived-value ratings were similarly high before and after the activity (pre: $M = 4.601$, SD = 0.531; post: $M = 4.602$, SD = 0.508). These values are reported descriptively only. The corresponding pre- and post-activity item sets addressed related domains but differed in wording and composition and should not be interpreted as equivalent repeated-scale measures or as evidence of individual change.

Perceived Learning Mechanisms in the DBT Protocol (RQ1, RQ3)

To address RQ1 and RQ3, the postsurvey also targeted the specific activity mechanisms intended to support learning, including the mass constraint, incremental loading, failure observation, and force–displacement plotting. These items formed a coherent scale ($\alpha \approx 0.82$) and are summarized in Table 6. The postactivity teamwork and motivation/value constructs are also summarized in Table 6 and should be interpreted together with the descriptive parallel-domain profiles shown in Fig. 5. Fig. 6 complements Table 6 by showing item-level postsurvey means and variability across the main constructs.

The three postactivity constructs were rated positively overall. At the construct level, the highest ratings were recorded for motivation and perceived value ($M = 4.60$, SD = 0.51), followed by teamwork and coordination ($M = 4.29$, SD = 0.72) and activity learning mechanisms ($M = 4.11$, SD = 0.57) (Table 6). Teamwork and coordination showed greater variability than the other two constructs, suggesting that collaborative work was generally valued but was also experienced as challenging—a pattern corroborated by the qualitative evidence reported in the section "Qualitative Evidence from Open-Ended Responses."

Item-level inspection reveals a more differentiated pattern. The highest-rated engagement/value items were the preference for practical over paper-only laboratories ($M = 4.73$, SD = 0.57), the overall interest and attractiveness of the project ($M = 4.68$, SD = 0.61), the recommendation to retain the activity ($M = 4.65$, SD = 0.70), and the desire for similar activities in other courses ($M = 4.64$, SD = 0.71). Among the implementation-focused learning mechanisms, the most highly rated items were observing failure ($M = 4.58$, SD = 0.63), construction and detailing ($M = 4.49$, SD = 0.74), and incremental loading ($M = 4.38$, SD = 0.74). This pattern suggests that the tangible and directly observable components of the protocol were especially salient to students. By contrast, the use of information about cardboard properties in design ($M = 3.66$, SD = 1.15)

This work is made available under the terms of the Creative Commons Attribution 4.0 International license.

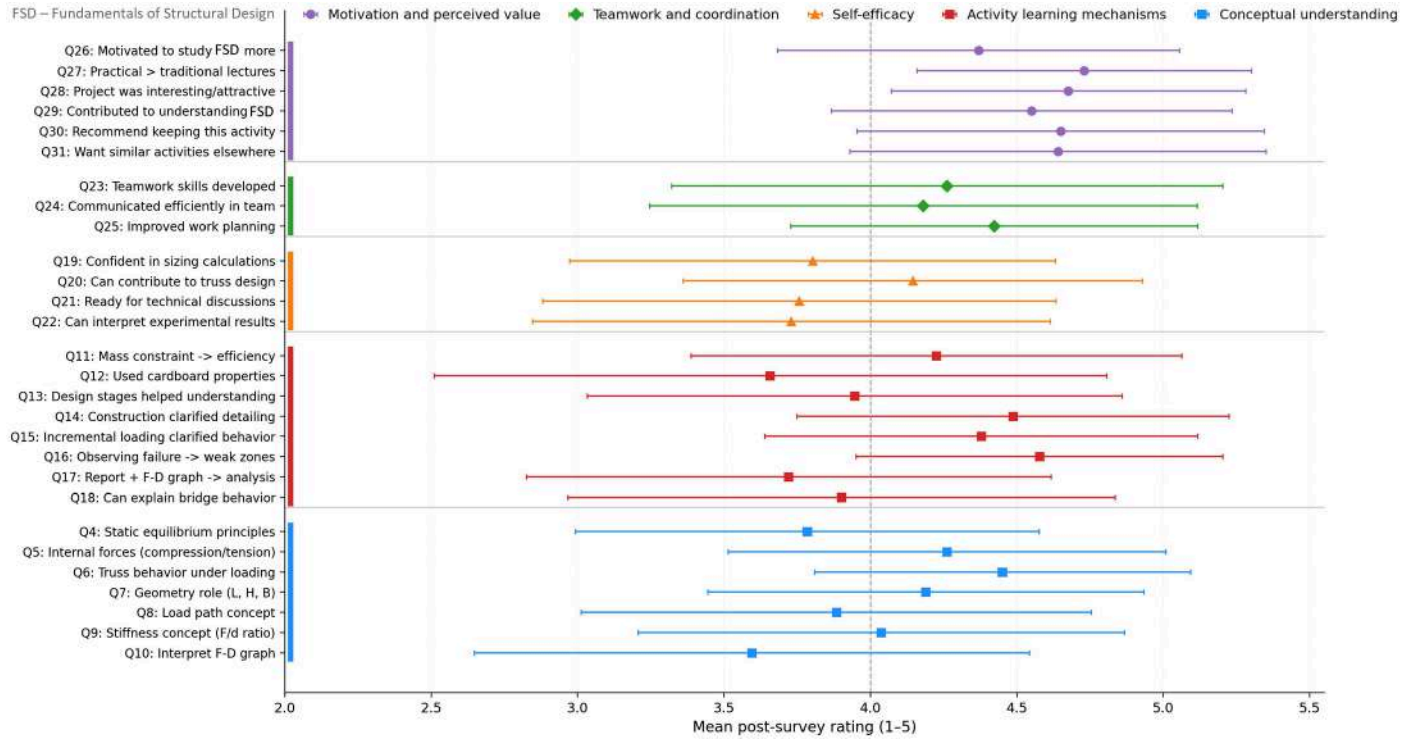

Fig. 6. Item-level post-survey ratings (means ± 1 SD) grouped by construct for the first-year cohort.

and the use of the report and F–D graph for quantitative analysis ($M = 3.72$, SD = 0.90) received the lowest ratings among the activity mechanisms. These more analytical and material-informed components may benefit from more explicit instructional scaffolding in future iterations.

Alumni Retrospective Evidence on Durability and Transfer (RQ4)

The alumni survey (years 2–4, $N = 58$) provides a longer–term perspective on perceived value and transfer, addressing RQ4. Table 7 summarizes the main constructs. Ratings were highest for preference and recommendation ($M = 4.59$, SD = 0.73) and conceptual value ($M = 4.25$, SD = 0.81), indicating that the perceived learning benefit persisted beyond the initial course. Transfer ratings were lower and more variable ($M = 3.61$, SD = 1.16), which is consistent with the expectation that perceived transfer depends on individual course pathways and the extent to which later coursework explicitly revisits truss–related concepts. The variability in transfer ratings suggests that while some alumni found direct connections to later courses (particularly statics and structural analysis), others did not encounter contexts where the bridge experience was directly applicable. Skills-related ratings (teamwork, technical communication, planning: $M = 4.01$, SD = 0.89) were positive and comparable to the postsurvey teamwork ratings, suggesting that the collaborative dimension of the activity was remembered as formative. This contrast between very high preference ratings and more moderate transfer ratings suggests that the activity was remembered as educationally worthwhile even when later curricular opportunities for explicit reuse were uneven across students.

Qualitative Evidence from Open–Ended Responses

Open-ended items in the postsurvey (five prompts; $N = 111$ respondents) and alumni survey ($N = 58$) were analyzed using the hybrid thematic content–analysis procedure described in the section "Data Analysis." Percentages reported in the following subsections and in Fig. 7 are respondent-level proportions: each theme was counted at most once per respondent and divided by the full sample of the corresponding survey ($N = 111$ postsurvey; $N = 58$ alumni), with rounding to the nearest whole percent. Because a response could express more than one theme, percentages within a prompt are not mutually exclusive and do not sum to 100%. Themes were identified independently for each prompt and then consolidated across instruments. Selected quotations below have been translated from Romanian. Fig. 7 provides a compact visual summary of the dominant coded themes across the five open-ended postsurvey prompts. Taken together, these qualitative patterns are consistent with the quantitative results: students most strongly valued the visible and hands-on elements of the protocol, while coordination demands and more analytical tasks emerged as the main sources of difficulty.

Conceptual Understanding (RQ1)

When asked what they learned about structural behavior, 45% of postsurvey respondents described load path and force transmission mechanisms. A recurring pattern was the recognition that structural form matters more than material quantity: "The most important thing I learned is that shape and arrangement of elements are more important than material quantity." Several responses connected observation to conceptual refinement: "I learned that structural composition and details decisively influence behavior under loading, not just the general shape." Failure modes were explicitly named in approximately 9% of responses: "Testing showed that failure of a single beam can lead to loss of load–bearing capacity of the entire structure."

Most Useful Activity Component (RQ1, RQ2)

Testing was cited most frequently by 55% of postsurvey respondents, followed by design (22%) and an integrated view of the

This work is made available under the terms of the Creative Commons Attribution 4.0 International license.

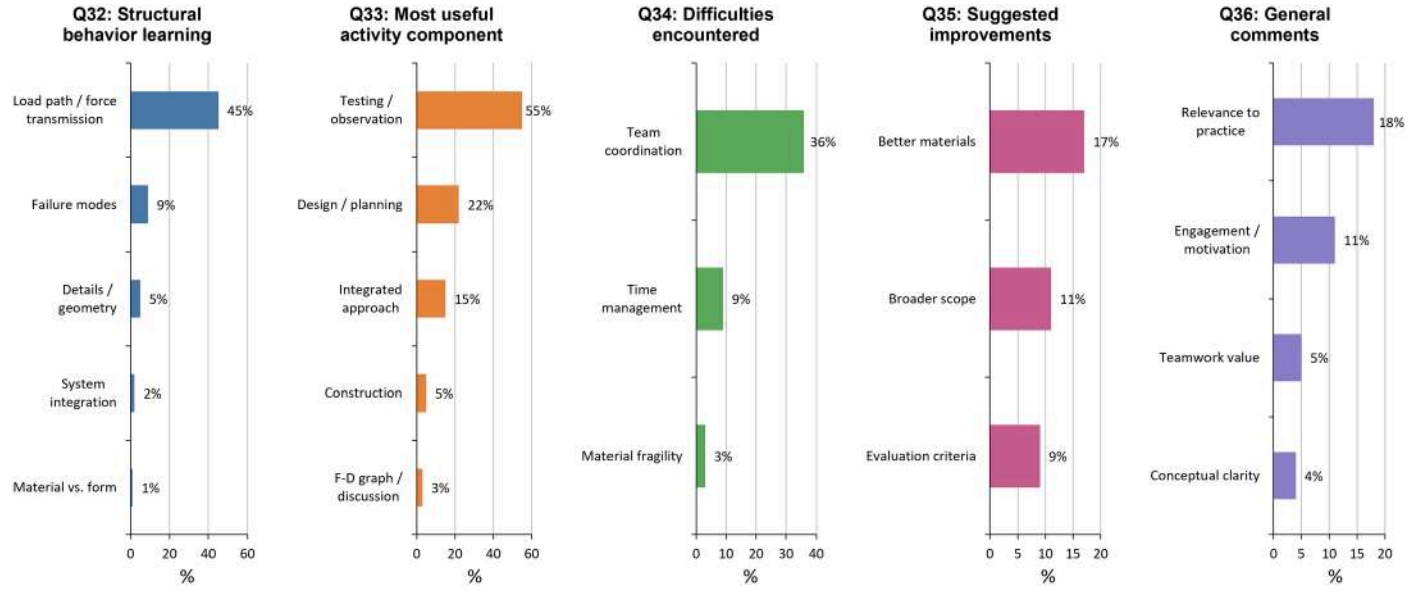

Fig. 7. Summary of dominant coded themes across five open-ended post-survey prompts. Percentages indicate the share of all postsurvey respondents ($N = 111$) who expressed each theme; each theme was counted at most once per respondent. Multiple themes could be assigned to a single response, so percentages do not sum to 100%. Values are rounded to the nearest whole percent; nonsubstantive entries and low-frequency residual codes are not displayed.

full sequence (15%). A representative response illustrated the testing-to-concept link: "The most useful part was testing correlated with the F–D graph, because it linked theory directly to the actual behavior of the structure." Students who valued the design phase emphasized its role in forcing structural reasoning: "Design trains you to think and understand in more detail the structure you will build and the forces that appear in each component element."

Teamwork and Engagement (RQ3)

Difficulties related to team coordination and communication were reported by 36% of respondents. Typical challenges included role negotiation, schedule alignment, and resolving disagreements about design choices: "The team wasn't organized at the beginning of the project; everyone had a different opinion and it was hard to reach a conclusion." Despite these challenges, general comments reflected high engagement with the hands–on format: "Practical activities are much more interesting than traditional lectures. I would like to have more projects like this." The combination of reported difficulty and sustained engagement is consistent with the teamwork and coordination ratings in Table 6 ($M = 4.29$, SD = 0.72).

Perceived Relevance (RQ4)

In postsurvey comments, 18% of postsurvey respondents explicitly connected the activity to engineering practice or professional preparation: "This type of project is essential for training an engineer, because it gives you practical experience that you can't get from a textbook." Alumni retrospective responses reinforced this pattern. When asked to describe a concrete situation where the project helped them understand a concept in a later course, the most frequently cited contexts were statics assignments involving truss analysis, strength-of-materials laboratories, and bridge engineering courses. A representative alumni response was, "In the second year, we had a statics assignment on truss beams, and I remembered the bridge project—it helped me understand force distribution on the beam and the effects of those forces."

Difficulties and Suggested Improvements

Beyond teamwork, reported challenges included time pressure (9%) and material fragility (3%). Suggested improvements centered on providing more durable materials (17%), refining evaluation criteria (9%), and broadening the range of structural types (11%). These responses inform the implementation lessons discussed in the section "Lessons Learned for Replication."

Team Performance Outcomes from Experimental Testing

Team performance evidence was extracted from experimental logs for teams with complete records ($N = 30$). Across recorded teams, bridge mass ranged from 78 to 270 g. Of the 30 teams included in the mass-capacity dataset, six exceeded the 200 g reference mass limit, one was exactly at the limit, and 23 remained below it. These overweight bridges (20.0%) were still tested under the protocol described in the section "Experiential Design–Build–Test Activity"; they were penalized in grading but retained in the descriptive dataset to preserve the full variability of implementation outcomes. A load-to-weight efficiency indicator was computed to support comparison under the mass constraint (Table 8). Fig. 8 complements these summary statistics by showing the relationship between bridge mass and peak load capacity for all tested teams with available mass-capacity records, together with the 200 g mass limit and constant load-to-mass ratio lines. The wide performance range, with efficiency ratios spanning from 219 to 641, illustrates how configuration, detailing, and workmanship produced meaningfully different structural outcomes under a common testing protocol. This variability provided the basis for in-class discussion of why some designs performed better, linking geometry and member-role choices to measurable stiffness and capacity differences.

Representative force–displacement curves from one laboratory group are shown in Fig. 9, highlighting between-team variation in initial stiffness, damage onset, and peak capacity. These curves served as the primary evidence source for student interpretation tasks: teams were required to identify the initial slope, locate

This work is made available under the terms of the Creative Commons Attribution 4.0 International license.

Table 8. Team performance summary from experimental logs

Metric	*N*	Mean	SD	Min	Median	Max
Self-weight (g)	30	166.9	39.0	78.0	164.0	270.0
Peak load (kgf)	30	63.7	15.3	47.5	65.0	110.0
Load-to-weight ratio, *E* (dimensionless)	30	413.7	120.0	219.3	391.3	641.0

Note: $E = P_{max} \cdot 1{,}000/m$. Higher values indicate greater structural efficiency under the mass constraint. Summary includes all teams with complete records, including the small number that exceeded the 200 g reference mass limit and were retained for descriptive completeness.



Fig. 8. Bridge mass versus peak load capacity for tested teams, showing the 200 g mass limit and constant load-to-mass ratio lines (kgf/g). Each point represents one team.

slope changes associated with damage or stiffness degradation, and relate the observed response to their predicted truss behavior. Typical failure mechanisms observed during testing are illustrated in Fig. 10, including global out-of-plane sway, compression-member buckling, and joint-related failures. These mechanisms provide physical explanations for changes in slope and capacity observed in the force–displacement response and can support troubleshooting and refinement in similar implementations. Although team performance logs were not used as stand-alone answers to a separate research question, they provide objective contextual support for interpreting RQ1 by anchoring discussion of stiffness, load path, and failure behavior in measured outcomes.

Discussion

Interpretation of the Main Findings (RQ1)

This case study documented cohort-level patterns consistent with the intended learning loop of the activity. For clarity, the subsequent discussion revisits the four implementation-oriented research questions introduced in the section "Introduction." Conceptual understanding ratings were higher in the postactivity sample (Table 5), and the pattern aligns with repeated exposure to the same core ideas in three forms: an idealized truss representation, measured force-displacement response, and observed damage or failure modes (Figs. 1, 9, and 10). This sequence makes load transfer and stiffness behavior visible before requiring full mathematical fluency, which was a central implementation goal.

Performance evidence provides an objective anchor for interpretation. Differences in stiffness and capacity across teams (Figs. 8 and 9), together with typical failure mechanisms (Fig. 10), illustrate how detailing and member role choices can change response. These observations support discussion of why plotting and interpreting force–displacement data can help novices connect mechanics concepts to tangible behavior.

Self–Efficacy Calibration (RQ2)

Self-efficacy ratings did not increase and showed a small, nonsignificant decrease (Table 5). In a DBT context, this pattern can reflect calibration rather than reduced engagement. Early in a course, students may overestimate their ability before confronting real constraints, imperfections, and failure. After fabrication and testing, self-–assessment may become more realistic. The observed variability in performance and the sensitivity to workmanship and joint behavior make this interpretation plausible.

From an instructional standpoint, calibration should be treated as a normal step and supported through structured reflection and feedback that emphasizes progress and provides actionable next steps, rather than leaving students with an unstructured sense of failure.

Teamwork, Engagement, and Coordination (RQ3)

With respect to RQ3, the findings suggest that the DBT format supported engagement strongly, while also making coordination challenges visible as a meaningful part of the learning experience. Quantitative ratings for teamwork and coordination were positive (Table 6: $M = 4.29$, SD = 0.72), but qualitative evidence adds nuance. More than a third of postsurvey respondents reported

This work is made available under the terms of the Creative Commons Attribution 4.0 International license.

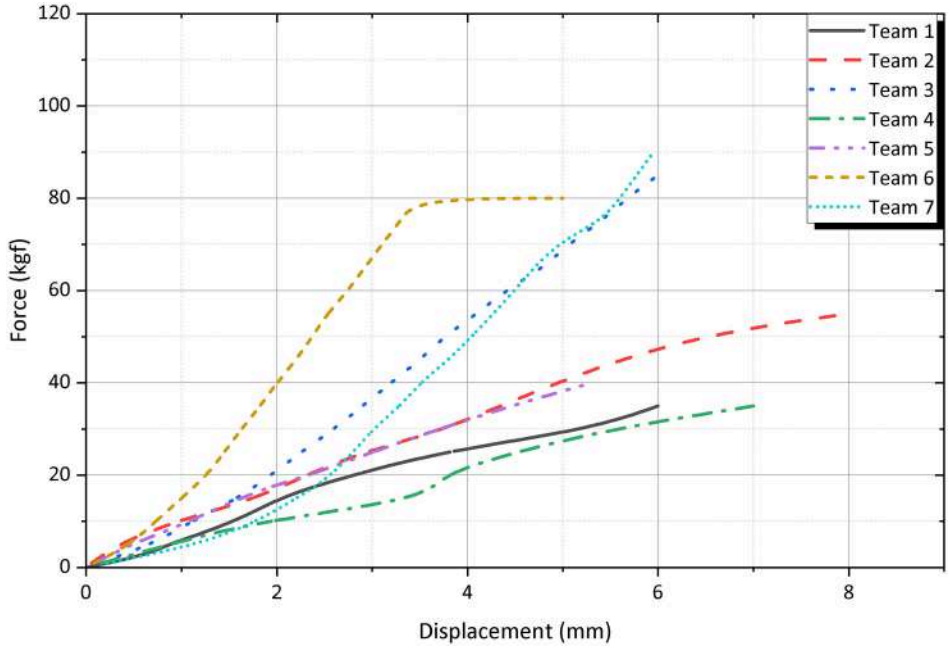

Fig. 9. Representative force–displacement curves from one laboratory group (multiple teams).

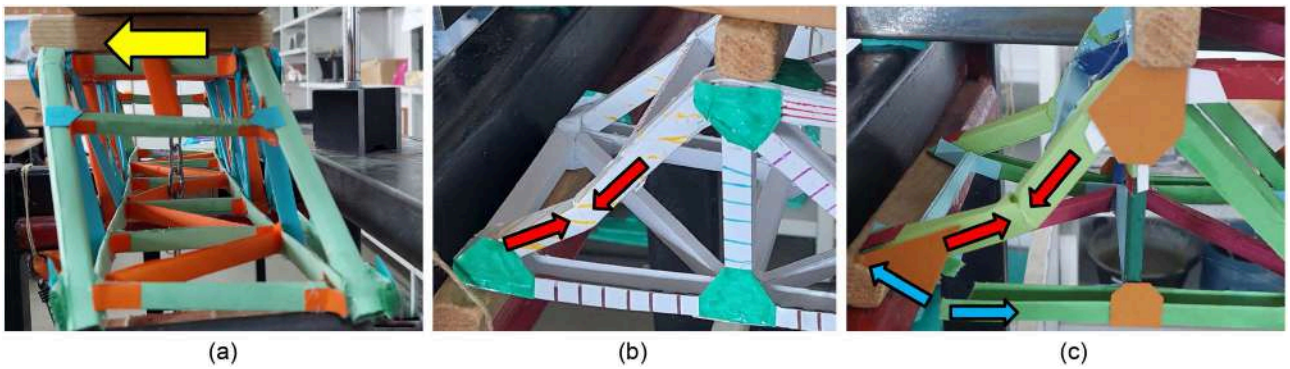

Fig. 10. Typical damage and failure mechanisms observed during testing: (a) out-of-plane sway; (b) local compression-member buckling; and (c) joint-related failure involving interacting tension/compression members.

team coordination as the primary difficulty encountered during the project. Common challenges included negotiating design decisions within the group, distributing fabrication tasks under time pressure, and maintaining communication when team members had different schedules. These difficulties are not unique to this implementation; they reflect the inherent complexity of collaborative project work in early-stage engineering courses (Hirudayaraj et al. 2021). From an instructional standpoint, the coexistence of positive teamwork ratings and reported coordination difficulties suggests that students valued the collaborative experience even when it was challenging—consistent with the view that productive struggle in team contexts can itself be a learning outcome when supported by structured roles and brief coordination guidelines (Felder and Brent 2024). The descriptive parallel-domain profile in Fig. 5 indicates that teamwork-related ratings were positive both before and after the activity. Because the item sets were not compositionally equivalent, the small numerical difference should not be interpreted as a measured pre–post gain. Motivation and perceived-value ratings were already high before implementation and remained high after the activity, suggesting a ceiling-prone profile rather than an interpretable increase.

Alumni Evidence and Perceived Transfer (RQ4)

This subsection discusses the alumni survey findings reported in the section "Alumni Retrospective Evidence on Durability and Transfer (RQ4)" and interprets their implications for longer-term perceived value, relevance to practice, and transfer to later coursework. With respect to RQ4, the alumni evidence suggests that the perceived relevance of the activity remained high over time, although transfer to later coursework was more variable and depended on subsequent curricular opportunities to reactivate the experience. The alumni survey offers a retrospective check on the durability and transfer of the activity's perceived value. Conceptual value and preference ratings remained high 2 to 4 years after the initial experience (Table 7), suggesting that the learning impression was not merely a transient novelty effect. Transfer ratings were lower and more variable ($M = 3.61$, SD = 1.16). This pattern is expected: transfer depends on whether later coursework explicitly engages concepts introduced in the bridge project, and course pathways vary across students.

Qualitative alumni responses provide concrete illustrations. The most frequently cited transfer contexts were statics assignments involving truss analysis and strength-of-materials laboratories. One alumnus noted, "In the second year, we had a statics assignment on

This work is made available under the terms of the Creative Commons Attribution 4.0 International license.

truss beams, and I remembered the bridge project—it helped me understand force distribution on the beam and the effects of those forces." Another described using the project experience during a teaching practicum: "I taught a lesson on beams as structural elements at the pedagogical module, and the bridge project helped me explain truss elements to high-school students." These examples suggest that the activity created anchoring experiences that some students spontaneously connected to later learning contexts, though the connection was not universal. Transfer could potentially be strengthened by explicit cues in later courses that reference the bridge testing experience.

Taken together, the alumni findings suggest that the activity had durable perceived value, but that later transfer depended on whether subsequent courses explicitly reactivated the conceptual anchors created by the bridge project.

Tangible Validation and Authenticity

A distinctive implementation element was the optional body-weight proof challenge. Its function was not to replace measurement, but to provide a human-scale illustration of resistance and stiffness after teams had already collected and interpreted quantitative data. Framed as optional and nongraded, it acted as a motivational prompt and an authenticity cue, while limiting the risk that teams optimize for spectacle rather than for evidence-based reasoning.

Implementation Features That Likely Mattered

Three implementation features are likely to be important for replication. First, the strict self-weight constraint forced trade-offs and made efficiency meaningful, encouraging attention to depth, triangulation, and member roles rather than material mass. Second, incremental loading and force–displacement plotting turned stiffness into an interpretable concept, enabling discussion of slope changes, damage onset, and capacity loss. Third, failure observation and classification made internal force flow tangible; mechanisms such as out-of-plane sway, buckling, and joint failure (Fig. 10) map directly to the truss idealization and to the limits of modeling assumptions. These features align with the educational value often attributed to tangible performance tasks in introductory structures (Ressler 2001; Salvadori 1980).

Boundary Conditions for Interpretation

Because pre- and post-surveys were unpaired, observed differences may partly reflect sampling variation rather than individual change. Instructor and implementation effects are also plausible: differences in briefing, feedback, or rubric emphasis can shift student attention and outcomes. Team performance logs may overrepresent more organized teams, and results should be interpreted accordingly. Finally, the equal nodal load idealization is pedagogically appropriate for first-year analysis but should not be interpreted as a high-fidelity representation of real contact mechanics; its purpose is to keep modeling tractable while preserving meaningful connections between measured response and an interpretable model.

Implications for Teaching Practice

The activity is feasible at scale when the protocol is standardized and the POE sequence is preserved. A rubric that rewards modeling clarity, measurement quality, and evidence-based explanation is important to avoid a competition-only mindset. The load-transfer plate and the explicit equal nodal-load idealization are useful at first-year level because they reduce modeling complexity while preserving discussion of load paths and axial force flow. The mass constraint should remain strict to drive efficiency reasoning. The body-weight proof challenge can be retained as optional and nongraded, with clear safety framing and supervision, and the instrumented test should remain the primary evidence source.

Taken together, the Discussion suggests that RQ1 is addressed mainly through higher postactivity conceptual ratings and performance-anchored interpretation, RQ2 through self-efficacy calibration, RQ3 through the coexistence of strong engagement and real coordination demands, and RQ4 through the contrast between durable perceived value and more variable transfer.

Lessons Learned for Replication

Several lessons became clearer only through implementation and were not fully evident at the design stage. First, the most educationally salient components for students were the visible and tangible parts of the protocol, especially testing, observing failure, and comparing different bridge behaviors, whereas the more analytical components—particularly using material–property information and the report plus force–displacement graph for quantitative interpretation—were valued less strongly and therefore appear to require more explicit scaffolding in future iterations. Second, teamwork was generally rated positively, but coordination difficulties were more frequent than anticipated, especially in role negotiation, scheduling, and reaching agreement on design decisions. Third, the 200 g mass limit functioned as a meaningful efficiency constraint, but implementation showed that a small number of teams still exceeded it, usually because of overreinforcement, joint detailing, or imprecise trimming. Fourth, recurring fabrication errors were more systematic than expected, especially incorrect placement of diagonals, eccentric joints, and member sizing inconsistent with the analysis. Finally, the slight downward shift in self-efficacy suggests that confronting imperfections and failure may calibrate students' judgment, but also indicates the need for a more explicit debrief to frame this calibration as part of learning rather than as a negative outcome. To support practical replication, the subsequent points include not only pedagogical recommendations but also concrete operational parameters such as recurring fabrication errors, approximate material costs, typical student workload, testing duration, and supervision requirements.

Based on these implementation outcomes, several adjustments would strengthen future iterations and may also support replication in other contexts:

1. Retain the mass constraint, but add an earlier checkpoint on projected and measured bridge mass, since implementation showed that some teams exceeded the intended 200 g budget despite understanding the rule.
2. Standardize the load-transfer plate and contact points to improve comparability across teams.
3. Keep the force–displacement plot as a required deliverable, but provide stronger scaffolding for its interpretation, because students appeared to value the testing experience more strongly than the subsequent quantitative analysis.
4. Require failure-mode documentation using a small set of categories (e.g., sway, buckling, joint failure).
5. Use a rubric that rewards explanation and data quality, not only peak load.
6. Treat the body-weight proof as optional, supervised, and nongraded, after the instrumented test.
7. Introduce a brief prfabrication design–review checkpoint focused on diagonal orientation, joint eccentricity, and member sizing, because these errors recurred more systematically

This work is made available under the terms of the Creative Commons Attribution 4.0 International license.

than expected. The most frequently observed errors were misplacement of tension and compression diagonals (tension-strip members placed in compression-diagonal positions), imprecise joints leading to eccentricities, dimensional deviations of up to 2%–5% in member length and width, and member sizing inconsistent with the internal forces determined from analysis. A brief design-review checkpoint before fabrication, in which the instructor verifies diagonal orientation and joint detailing, can reduce these recurring issues.

8. Budget approximately 4–6 EUR per team for materials (thin cardboard sheets, silicone glue sticks, basic cutting tools). Total student time per team ranged from 6 to 12 h across design, fabrication, and reporting phases. The testing session, including setup, incremental loading, and brief discussion with the instructor, required approximately 10 min per team. A single instructor supervised the testing session for one laboratory group (typically 7–10 teams). These practical parameters are reported to support resource planning and to help instructors calibrate expectations for comparable implementations.
9. Include a short structured debrief after testing to help students interpret failure and self-efficacy recalibration productively, especially when bridge performance falls short of expectations.
10. Strengthen teamwork support through explicit interim role allocation and short coordination checkpoints, since student comments showed that collaboration was valued but also one of the main sources of difficulty.

Limitations and Future Work

Reporting follows published best-practice guidance for case study research by prioritizing context, protocol transparency, and lessons learned to support replication (Gomes Araújo and Lucko 2022). This case study has several limitations that constrain generalization and should be considered when interpreting the reported patterns. First, the intervention was implemented at a single institution within one course context; outcomes may therefore reflect local curriculum structure, laboratory culture, and instructor practices. Replication in other programs with different student preparation and staffing resources is needed before broader claims are made.

Second, pre- and post-activity surveys were anonymous and not linkable at the individual level. Pre–post comparisons are therefore reported as unpaired cohort-level differences, which limits causal inference because observed changes may partly reflect sampling variation rather than individual change trajectories. Future implementations could use an anonymous linking procedure (e.g., self-generated codes) to enable paired analysis while preserving confidentiality. In addition, the presurvey ($N = 107$) and postsurvey ($N = 111$) samples were not identical in size and only partially overlapped, because participation depended on attendance and voluntary response at two different survey sessions. Although this discrepancy is explained in the section "Participants, Datasets, and Ethics" and supported by the postsurvey overlap-check item, it remains a design limitation because it introduces an additional source of sampling variation in the cohort-level pre–post comparisons.

Third, the study did not include a parallel control group. As a result, observed patterns cannot be attributed uniquely to the DBT activity rather than to concurrent course learning. A feasible future approach is a quasi-experimental design, such as staggered implementation (different laboratory groups receiving the activity earlier or later) or comparison with a structurally similar paper-based lab targeting the same concepts.

Fourth, several outcomes rely on self-report, which can be influenced by social desirability and by evolving standards of self-evaluation. The small, nonsignificant decrease in self-efficacy may reflect calibration after confronting authentic constraints, but alternative explanations remain plausible. Future work could strengthen triangulation by linking survey measures to objective evidence at the individual level, such as short concept checks, scored explanation tasks, or standardized concept inventories.

In addition, the survey instruments were purpose-built for this case study. Although the item sets were mapped to the learning objectives, the research questions, and the stages of the activity (Table S1), they were not subjected to pilot testing, external expert review, factor analysis, or criterion-related validation before administration. The composite scores should therefore be interpreted as exploratory, context-specific indicators rather than validated psychometric measures. Moreover, the pre- and post-activity item sets addressed parallel domains but were not textually identical, which further limits the interpretation of the unpaired cohort-level comparisons. This limitation is particularly relevant for the teamwork-related and motivation/perceived-value domains, for which the pre- and post-activity item sets differ more substantially in wording and composition. These two domains are therefore presented descriptively only and should not be interpreted as equivalent repeated-scale comparisons or as evidence of individual change. Future replications should incorporate expert content review, student cognitive interviews, pilot testing, and construct-validation analyses.

Similarly, the thematic analysis of open-ended responses was conducted by a single coder. Although a multipass procedure with code consolidation was used, intercoder reliability could not be computed, and the qualitative findings should be interpreted as an author-generated synthesis rather than independently verified categories. Future studies should include independent coding of at least a subset of responses and report an agreement statistic.

Fifth, performance logs and force–displacement records may be incomplete in some implementations, and missingness may not be random. Standardized data sheets, required submission of raw measurements, and brief calibration instructions could improve completeness and comparability across teams.

Finally, the simplified load distribution model (rigid plate represented as equal nodal forces) was adopted to match first-year capabilities and keep analysis tractable. While pedagogically appropriate, it is not a high-fidelity representation of stiffness-dependent load sharing. Future work could introduce staged modeling, where advanced students revisit the same setup using refined distribution assumptions or sensitivity checks.

Future work should therefore focus on methodological strengthening (paired designs and quasi-experimental comparisons), clearer links between conceptual outcomes and performance or later-course achievement, and scalability studies quantifying staff time, material costs, and stability of implementation effects across cohorts and instructors.

Conclusions

This case study suggests that a resource-light design–build–test truss bridge activity can do more than motivate first-year students: when coupled with structured measurement, force–displacement interpretation, and explicit failure-mode explanation, it can support the early transition from "calculating" to "explaining and justifying" structural behavior. For engineering educators, the central implication is that the educational value of DBT does not lie in building and testing alone, but in how the protocol turns observed response into interpretable evidence.

This work is made available under the terms of the Creative Commons Attribution 4.0 International license.

Cohort-level survey patterns were consistent with higher postactivity ratings for conceptual understanding of load paths, internal force mechanisms, and stiffness behavior (Hedges' $g = 0.47$). Self-efficacy did not increase and showed a small, nonsignificant decrease, plausibly reflecting calibration after confronting practical constraints, workmanship variability, and failure behavior rather than reduced competence. For first-year structural engineering contexts, this finding has an important pedagogical implication: a small decrease in self-efficacy after confronting imperfections and failure should not automatically be interpreted as a negative result. Instead, it may indicate calibration from overconfident intuition toward more realistic engineering judgment, provided that the activity includes structured reflection and debriefing. Qualitative evidence reinforced these patterns: students most frequently cited load-path understanding and force transmission as the key learning outcome and identified testing as the most useful activity component for connecting mechanics concepts to tangible behavior. Teamwork ratings were positive but accompanied by substantial reported coordination challenges, suggesting that collaborative project work served simultaneously as a learning mechanism and a source of productive difficulty.

An optional, supervised body-weight proof challenge was used after the instrumented test as a nongraded, human-scale illustration of resistance and stiffness, complementing rather than replacing the measured response. Alumni responses (years 2–4) indicated that conceptual value and preference persisted beyond the initial course, while perceived transfer was more variable and appeared to depend on whether later coursework explicitly revisited truss–related concepts.

For JCEE readers, the main instructional implication is that first-year DBT activities are most defensible educationally when they are designed as evidence–based learning tasks rather than as informal build contests. Standardized force-displacement recording, required failure-mode classification, and rubric-based explanation criteria shift the activity away from performance ranking alone and toward conceptual interpretation, which is more closely aligned with early engineering learning goals.

Given the unpaired pre–post design, single-institution context, and absence of a control group, the conclusions remain appropriately cautious. Even so, the study advances understanding of DBT pedagogy in three ways. First, it shows that in first-year structural engineering education, the educational value of DBT can be strengthened when testing is tied explicitly to force–displacement interpretation and failure-mode explanation, rather than treated mainly as a competition outcome. Second, it contributes to the interpretation of self-efficacy in early engineering education by highlighting that small postactivity decreases require cautious interpretation and may be compatible with a calibration effect after authentic confrontation with structural imperfections and failure. Third, it provides a more replication-oriented account of DBT implementation by documenting not only the activity logic, but also the assessment structure, observed fabrication errors, material costs, and operational constraints that shaped the outcomes. For instructors, the practical conclusion is that effective first-year DBT design requires a complete prediction–observe–explain sequence supported by structured measurement, explicit reflection, and assessment criteria that reward evidence-based reasoning.

Future work should prioritize paired pre–post designs using anonymous linking codes, quasi–experimental comparisons with structurally similar non–DBT laboratories, and longitudinal tracking to assess whether early hands-on bridge experiences produce measurable effects on later structural reasoning and design performance.

Data Availability Statement

Some or all data, models, or code that support the findings of this study are available from the corresponding author upon reasonable request. The available materials include anonymized pre- and post-activity survey datasets, an anonymized alumni survey dataset, team-level experimental testing logs (mass, peak load, load steps, displacement records, and derived force–displacement curves), and the assessment rubric and standardized data sheet used for the activity. The course practical guide cited as Taranu (2023) is publicly accessible online https://py.md/UVmSL, although it is available only in Romanian. The present article reports the core implementation details in English to support replication by international readers.

Author Contributions

George Taranu: Conceptualization; Investigation; Methodology; Project administration; Validation; Writing – original draft; Writing – review and editing.

Supplemental Materials

Supplemental materials associated with this paper are available in a repository online at https://doi.org/10.13140/RG.2.2.23479.69286.

References

Abdel Sattar, A., and W. Labib. 2019. "Active learning in engineering education: Teaching strategies and methods of overcoming challenges." In *Proc., ACM Int. Conf. on Educational and Information Technology*, 255–261. New York: Association for Computing Machinery. https://doi.org/10.1145/3318396.3318449.

Ayan, Ö. 2009. "Cardboard in architectural technology and structural engineering: A conceptual approach to cardboard buildings in architecture." Ph.D. thesis, Dept. of Architecture, ETH Zurich.

Barry, B. E., K. F. Meyer, K. P. Arnett, and B. Spittka. 2013. "Competition-based learning activities within civil engineering education." In *Proc., ASEE Annual Conf. & Exposition*. Washington, DC: American Society for Engineering Education. https://doi.org/10.18260/1-2--19328.

Biggs, J., and C. Tang. 2011. *Teaching for quality learning at university*. 4th ed. New York: McGraw-Hill.

Bindal, N. 2022. "Experiential learning in design education teaching construction and technology through active experimentation in interior and architectural design." *Int. J. Des. Educ.* 16 (2): 91. https://doi.org/10.18848/2325-128X/CGP/v16i02/91-102.

Brown, S. 2021. "Editor's note." *J. Civ. Eng. Educ.* 148 (2): 01621001. https://doi.org/10.1061/(ASCE)EI.2643-9115.0000059.

Carroll, J., and K. Mitchell. 2022. "How to spice up your balsawood bridge competition (other)." In *Proc., 2022 ASEE Annual Conf. & Exposition*. Washington, DC: American Society for Engineering Education.

Chang, G., and W. Peterson. 2009. "Bridge design project: A hands on approach to statics and strength of materials learning." In *Proc., 2009 Annual Conf. & Exposition*, 14–289. Washington, DC: American Society for Engineering Education.

Felder, R. M., and R. Brent. 2005. "Understanding student differences." *J. Eng. Educ.* 94 (1): 57–72. https://doi.org/10.1002/j.2168-9830.2005.tb00829.x.

Felder, R. M., and R. Brent. 2024. *Teaching and learning STEM: A practical guide*. Hoboken, NJ: Wiley.

Fredette, L., and M. Kennedy. 2022. "Work in progress: Reformulation of a truss competition course project to improve educational outcomes."

This work is made available under the terms of the Creative Commons Attribution 4.0 International license.

In *Proc., 2022 ASEE Annual Conf. & Exposition*. Washington, DC: American Society for Engineering Education.
Freeman, S., S. L. Eddy, M. McDonough, M. K. Smith, N. Okoroafor, H. Jordt, and M. P. Wenderoth. 2014. "Active learning increases student performance in science, engineering, and mathematics." *Proc. Natl. Acad. Sci.* 111 (23): 8410–8415. https://doi.org/10.1073/pnas.1319030111.
García-Ramírez, Y. 2025. "Enhancing civil engineering education through innovative STEM-based prototyping: A comparative study of physical models and board games in geometric road design." *Humanit. Social Sci. Commun.* 12 (1): 686. https://doi.org/10.1057/s41599-025-05020-6.
Gavin, K. 2011. "Case study of a project-based learning course in civil engineering design." *Eur. J. Eng. Educ.* 36 (6): 547–558. https://doi.org/10.1080/03043797.2011.624173.
Ghareeb, A. M. 2026. "The effectiveness of using physical models in enhancing students' understanding of structural systems in global architectural projects: An applied study using the project-based learning (PBL) approach." *J. Eng. Res.* 10 (1). https://doi.org/10.21608/JER.2026.463828.1044.
Godfrey, T., D. Hardt, A. J. Perez, K. Sehnawi, and A. Chandar. 2025. "Design, manufacture and testing of structural trusses using additively manufactured polymer composites." In *Proc., 36th Annual Int. Solid Freeform Fabrication Symp*. Austin, TX: Univ. of Texas at Austin.
Gomes Araújo, L., and G. Lucko. 2022. "Best practices for case studies in construction engineering and management research." *J. Constr. Eng. Manage.* 148 (8): 04022062. https://doi.org/10.1061/(ASCE)CO.1943-7862.0002312.
Hirudayaraj, M., R. Baker, F. Baker, and M. Eastman. 2021. "Soft skills for entry-level engineers: What employers want." *Educ. Sci.* 11 (10): 641. https://doi.org/10.3390/educsci11100641.
Hughes, A. J., and C. Merrill. 2021. "Implementing the method of sections to design, build, and test trusses: Combining theory with practice." *Technol. Eng. Teach.* 80 (5): 15–20.
Jamison, C. S. E., J. Fuher, A. Wang, and A. Huang-Saad. 2022. "Experiential learning implementation in undergraduate engineering education: A systematic search and review." *Eur. J. Eng. Educ.* 47 (6): 1356–1379. https://doi.org/10.1080/03043797.2022.2031895.
Kolil, V. K., S. U. Parvathy, and K. Achuthan. 2023. "Confirmatory and validation studies on experimental self-efficacy scale with applications to multiple scientific disciplines." *Front. Psychol.* 14 (Apr): 1154310. https://doi.org/10.3389/fpsyg.2023.1154310.
Kruger, J., and D. Dunning. 1999. "Unskilled and unaware of it: How difficulties in recognizing one's own incompetence lead to inflated self-assessments." *J. Personality Social Psychol.* 77 (6): 1121–1134. https://doi.org/10.1037/0022-3514.77.6.1121.
Lange, J., A. von der Heyden, U. Knaack, and E. Kanli. 2022. "A bridge built of paper—A master's-course project for civil engineering students." *Struct. Eng. Int.* 32 (3): 345–349. https://doi.org/10.1080/10168664.2020.1838250.
Lave, J., and E. Wenger. 1991. *Situated learning: Legitimate peripheral participation*. Cambridge, UK: Cambridge University Press.
Maffei, A., E. Boffa, F. Lupi, and M. Lanzetta. 2022. "On the design of constructively aligned educational unit." *Educ. Sci.* 12 (7): 438. https://doi.org/10.3390/EDUCSCI12070438.
Mahendran, M. 1995. "Project-based civil engineering courses." *J. Eng. Educ.* 84 (1): 75–79. https://doi.org/10.1002/j.2168-9830.1995.tb00149.x.
Malmqvist, J., P. Y. Young, S. Hallström, J. Kuttenkeuler, and T. Svensson. 2004. "Lessons learned from design-build-test-based project courses." In *Proc., 8th Int. Design Conf.*, 665–672. Zagreb, Croatia: Univ. of Zagreb.
Martin, K. M., E. Miskioğlu, C. Noble, A. McIntyre, C. Bolton, and A. R. Carberry. 2021. "Predicting and evaluating engineering problem solving (PEEPS): Instrument development." In *Proc., 9th Research in Engineering Education Symp. and 32nd Australasian Association for Engineering Education Conf.: Engineering Education Research Capability Development*. Perth, WA, Australia: Research in Engineering Education Network and Australasian Association for Engineering Education.
May, D., C. Terkowsky, V. Varney, and D. Boehringer. 2023. "Between hands-on experiments and cross reality learning environments—Contemporary educational approaches in instructional laboratories." *Eur. J. Eng. Educ.* 48 (5): 783–801. https://doi.org/10.1080/03043797.2023.2248819.
Mills, J. E., and D. F. Treagust. 2003. "Engineering education: Is problem-based or project-based learning the answer?" *Australas. J. Eng. Educ.* 3 (Jan): 2–16. https://doi.org/10.3316/aeipt.132462.
Morris, T. H. 2020. "Experiential learning—A systematic review and revision of Kolb's model." *Interact. Learn. Environ.* 28 (8): 1064–1077. https://doi.org/10.1080/10494820.2019.1570279.
Naito, C. 2005. "Freshman level design—Bridge building project." In *Proc., 2005 ASEE Gulf-Southwest Annual Conf.* Washington, DC: American Society for Engineering Education.
O'Kelly, B. C. 2007. "Case study of a problem-based bridge engineering design course." In *Proc., Int. Symp. for Engineering Education*, 91–96. Dublin, Ireland: Dublin City Univ.
Pajares, F. 1996. "Self-efficacy beliefs in academic settings." *Rev. Educ. Res.* 66 (4): 543–578. https://doi.org/10.3102/00346543066004543.
Palmquist, S. 2006. "Project based learning in engineering mechanics: Inspection and analysis of a historic truss bridge." In *Proc., 2006 Annual Conf. & Exposition*, 11–1042. Washington, DC: American Society for Engineering Education.
Phillips, D. 2007. "Bridge building using teamwork." In *Proc., Int. Symp. for Engineering Education*. Dublin, Ireland: Dublin City Univ.
Prince, M. 2004. "Does active learning work? A review of the research." *J. Eng. Educ.* 93 (3): 223–231. https://doi.org/10.1002/j.2168-9830.2004.tb00809.x.
Ressler, S. J. 2001. *Designing and building file-folder bridges: A problem-based introduction to engineering*. West Point, NY: United States Military Academy.
Salvadori, M. 1980. *Why buildings stand up: The strength of architecture*. 1st ed. New York: W. W. Norton and Company.
Steif, P. S., A. Dollár, and J. A. Dantzler. 2005. "Results from a statics concept inventory and their relationship to other measures of performance in statics." In *Proc., Frontiers in Education 35th Annual Conf.* New York: IEEE.
Sukackė, V., A. O. P. D. C. Guerra, D. Ellinger, V. Carlos, S. Petronienė, L. Gaižiūnienė, S. Blanch, A. Marbà-Tallada, and A. Brose. 2022. "Towards active evidence-based learning in engineering education: A systematic literature review of PBL, PjBL, and CBL." *Sustainability* 14 (21): 13955. https://doi.org/10.3390/su142113955.
Sundman, J., X. Feng, A. Shrestha, A. Johri, O. Varis, and M. Taka. 2025. "Experiential learning for sustainability: A systematic review and research agenda for engineering education." *Eur. J. Eng. Educ.* 51 (4): 1173–1203. https://doi.org/10.1080/03043797.2025.2532591.
Taranu, G. 2023. *Bazele Proiectării Structurilor: Îndrumar pentru lucrări practice de laborator* [Fundamentals of structural design: Laboratory practical work guide]. 1st ed. Iasi, Romania: Gheorghe Asachi Technical Univ. of Iaşi.
Tembrevilla, G., A. Phillion, and M. Zeadin. 2024. "Experiential learning in engineering education: A systematic literature review." *J. Eng. Educ.* 113 (1): 195–218. https://doi.org/10.1002/jee.20575.
White, R., and R. Gunstone. 1992. *Probing understanding*. 1st ed. New York: Routledge.
Wolfe, F. A., and C. M. LaPlante. 1999. "Bridge to the future: The freshman capstone design bridge project at union college." In *Proc., 1999 Annual Conf.*, 4–109. Washington, DC: American Society for Engineering Education. https://doi.org/10.18260/1-2--7929.

This work is made available under the terms of the Creative Commons Attribution 4.0 International license.